Coordination Chemistry of Bioinspired Iron Complexes with Tri- and Tetradentate Ligands

Solid State Structures, Solution Behaviour and Reactivity

Von der Fakultät für Mathematik, Informatik und Naturwissenschaften der RWTH Aachen University zur Erlangung des akademischen Grades einer Doktorin der Naturwissenschaften genehmigte Dissertation

vorgelegt von

Henrika Maria Hüppe, M. Sc.

aus

Duisburg

Berichter: Univ.-Prof. Dr. rer. nat. Sonja Herres-Pawlis
Univ.-Prof. Dr. rer. nat. Iris M. Oppel

Tag der mündlichen Prüfung: 09.11.2023

"A scientist in his laboratory is not only a technician:
he is also a child placed before natural phenomena
which impress him like a fairy tale."

— Marie Curie

Eidesstattliche Erklärung

Henrika Maria Hüppe erklärt hiermit, dass diese Dissertation und die darin dargelegten Inhalte die eigenen sind und selbstständig, als Ergebnis der eigenen originären Forschung, generiert wurden.
Hiermit erkläre ich an Eides statt

1. Diese Arbeit wurde vollständig oder größtenteils in der Phase als Doktorand dieser Fakultät und Universität angefertigt;

2. Sofern irgendein Bestandteil dieser Dissertation zuvor für einen akademischen Abschluss oder eine andere Qualifikation an dieser oder einer anderen Institution verwendet wurde, wurde dies klar angezeigt;

3. Wenn immer andere eigene- oder Veröffentlichungen Dritter herangezogen wurden, wurden diese klar benannt;

4. Wenn aus anderen eigenen- oder Veröffentlichungen Dritter zitiert wurde, wurde stets die Quelle hierfür angegeben. Diese Dissertation ist vollständig meine eigene Arbeit, mit der Ausnahme solcher Zitate;

5. Alle wesentlichen Quellen von Unterstützung wurden benannt;

6. Wenn immer ein Teil dieser Dissertation auf der Zusammenarbeit mit anderen basiert, wurde von mir klar gekennzeichnet, was von anderen und was von mir selbst erarbeitet wurde;

7. Ein Teil oder Teile dieser Arbeit wurden zuvor veröffentlicht und zwar in: Auflistung der Veröffentlichungen im Abschnitt **Publikations** s. Seite II.

Aachen, den

Henrika M. Hüppe

Preface

Collaborative Work

Parts of this thesis were obtained as collaborative work:

> Mößbauer measurements and fitting of data were performed by Dr. Linda Iffland-Mühlhaus in the group of Prof. Dr. Ulf-Peter Apfel at Ruhr-Universität Bochum, Germany.
>
> SQUID magnetometry measurements in solution and data correction were performed by Dr. Sophie Schönfeld, Andreas Dürrmann in the working group of Prof. Dr. Birgit Weber at University of Bayreuth, Germany.
>
> SQUID magnetometry measurements of single crystals and data correction were performed by Hend Shahed and Dr. Neetika Sharma from the Jülich Centre for Neutron Science-2, Forschungszentrum Jülich, Germany.
>
> Femtosecond X-ray emission spectroscopy experiments (XES) were carried out at European XFEL (Hamburg/Schenefeld, Germany) at the femtosecond X-ray experiments (FXE) instrument in November 2021. The measurements were performed in cooperation with Dr. Mykola Biednov and support of the whole FXE group under supervision of Dr. Christopher Milne.

Some experiments in this thesis have been obtained in cooperation with students' research projects and lab technician trainees as part of their qualification:

> Sonja D. Mürtz, student assistant, **2019–2020**.
>
> Pauline Durschewski, lab technician trainee, **2020**.
>
> *"Biomimetic pyridinyl-based iron complexes"*
> Maverick Eilers, Bachelor's Thesis, **2020** and student assistant, **2021**.
>
> *"Studies on catalytic oxidation reactions with biomimetic N-donor iron complexes"*
> Ian Krumm, Bachelor's Thesis, **2021** and student assistant, **2021–2022**.

Publications

Parts of this thesis that have been published as journal articles:

"Catalytically Active Iron(IV)oxo Species Based on a Bis(pyridinyl)phenanthrolinylmethane"
Henrika M. Hüppe, Kristina Keisers, Fabian Fink, Sonja D. Mürtz, Alexander Hoffmann, Linda Iffland, Ulf-Peter Apfel and Sonja Herres-Pawlis, *Isr. J. Chem.* **2020**, *60*, 987–998, doi:10.1002/ijch.202000009.

"Triflate vs Acetonitrile: Understanding the Iron(II)-Based Coordination Chemistry of Tri(quinolin-8-yl)amine"
Henrika M. Hüppe, Linda Iffland-Mühlhaus, Joshua Heck, Maverick Eilers, Hans Gildenast, Sophie Schönfeld, Andreas Dürrmann, Alexander Hoffmann, Birgit Weber, Ulf-Peter Apfel, Sonja Herres-Pawlis, *Inorg. Chem.* **2023**, *62*, 4435–4455, doi:10.1021/acs.inorgchem.2c03890.

Parts of this thesis that have been presented on conferences:

"OH-Funktionalisierte Bis(pyrazolyl)methanliganden für die biomimetische Eisen- und Kupferkoordination"
Henrika M. Hüppe, Alexander Hoffmann, Sonja Herres-Pawlis, Poster Presentation, 15. Koordinationschemie-Treffen, **2019**, Munich, Germany.

"Functionalized bis(pyrazolyl)methane ligands for the biomimetic transition metal coordination"
Henrika M. Hüppe, Alexander Hoffmann, Sonja Herres-Pawlis, Poster Presentation, 19th International Conference on Biological Inorganic Chemistry, **2019**, Interlaken, Switzerland.

"Biomimetische Übergangsmetallkomplexe mit funktionalisierten Bis(pyrazolyl)methanliganden"
Henrika M. Hüppe, Alexander Hoffmann, Sonja Herres-Pawlis, Poster Presentation, GDCh-Wissenschaftsforum Chemie, **2019**, Aachen, Germany.

"Vier gewinnt: Tetradentater N-Donorligand für einen katalytisch aktiven Nicht-Häm-Eisen(IV)Oxo-Komplex"
Henrika M. Hüppe, Kristina Keisers, Fabian Fink, Sonja D. Mürtz, Alexander Hoffmann, Linda Iffland, Ulf-Peter Apfel, Sonja Herres-Pawlis, Poster Presentation, 16. Koordinationschemie-Treffen, **2020**, Freiburg, Germany.

"Fantastic four: Tetradentate N-donor ligand enabling a catalytically active non-heme iron(IV)oxo complex"
Henrika M. Hüppe, Kristina Keisers, Fabian Fink, Sonja D. Mürtz, Alexander Hoffmann, Linda Iffland, Ulf-Peter Apfel, Sonja Herres-Pawlis, Oral Presentation, French-BIC Meeting, **2020**, Obernai, France (online).

"Triflate vs. Acetonitrile – Who is Coordinating? Co-Ligand Study for Iron(II) Complexes in Solution and Solid State"
Henrika M. Hüppe, Joshua Heck, Maverick Eilers, Linda Iffland-Mühlhaus, Sophie Schönfeld, Andreas Dürrmann, Alexander Hoffmann, Ulf-Peter Apfel, Birgit Weber, Sonja Herres-Pawlis, Poster Presentation, 44th International Conference on Coordination Chemistry, **2022**, Rimini, Italy.

Other publications that were prepared in the context of this thesis or as collaborative work during this Ph.D. project which are not part of this thesis:

"Interplay of Spin Crossover and Coordination-Induced Spin State Switch for Iron Bis(pyrazolyl)methanes in Solution"
Kristina Keisers, **Henrika M. Hüppe**, Linda Iffland-Mühlhaus, Alexander Hoffmann, Christoph Göbel, Ulf-Peter Apfel, Birgit Weber and Sonja Herres-Pawlis, *Inorg. Chem.* **2020**, *59*, 15343–15354, doi:10.1021/acs.inorgchem.0c02306.

"Sharing is Caring: Guidelines for Sharing in the Electronic Laboratory Notebook (ELN) Chemotion as applied by a Synthesis-oriented Working Group"
Fabian Fink, **Henrika M. Hüppe**, Nicole Jung, Alexander Hoffmann and Sonja Herres-Pawlis, *Chemistry-Methods* **2022**, *2*, e202200026, doi:10.1002/cmtd.202200026.

"The Bridge towards a more stable and active Side-on-Peroxido ($Cu_2^{II}(\mu\text{-}\eta^2\text{:}\eta^2\text{-}O_2)$) complex as a Tyrosinase Model System"
Rosalie Dalhoff, Regina Schmidt, Lena Steeb, Kristina Rabatinova, Matthias Witte, Simon Teeuwen, Salim Benjamaâ, **Henrika M. Hüppe**, Alexander Hoffmann and Sonja Herres-Pawlis, *Faraday Discuss.* **2023**, *244*, 134–153, doi:10.1039/D2FD00162D.

Abstract

Inspired by nature, biomimetic iron complexes can be used to act as catalysts in selective oxidation reactions. In this process, high-valent oxo species of the iron complexes are passed through. Besides the ligand design for such iron complexes, the structure of the precursor complexes and the coordination chemical behaviour in solution are key to the high-valent iron-oxo species and to investigate their catalytic activity.

In this work, tri- and tetradentate ligands with *N*- and *O*-donors were synthesised and investigated. For a bis(pyrazolyl)ethanol ligand, a bisfacial coordination of iron with a $\{N_3\}$-coordination of the ligand was found. The investigated tetradentate ligands ($MeC(Py)_2Phen$, $MeC(Py)_2PicMe$ and NQu_3) with $\{N_4\}$- or $\{N_3O\}$-donor set always leave two *cis*-positioned coordination sites for labile co-ligands in an octahedral coordination environment. These are particularly important for catalytic oxidation reactions with high-valent iron-oxo intermediates. For all three tetradentate ligands, a $[Fe^{IV}L=O]^{2+}$ species could be detected by mass spectrometry. UV/Vis spectroscopic investigations also show typical iron-oxo bands. For complexes with the ligand $MeC(Py)_2Phen$, the catalytic C – H bond oxidation could also be successfully investigated.

The structure of the corresponding precursor complexes was investigated in the solid state and in solution. The main focus was on the co-ligand competition of triflate and acetonitrile. While different species were observed in the solid state, all results in solution suggest that acetonitrile is coordinating when used as a solvent. Furthermore, spin crossover behaviour in solution was observed for complexes with ligands $MeC(Py)_2PicMe$ and NQu_3 in acetonitrile.

A large number of potential precursor complexes with (weakly) coordinating anions could be structurally characterised by single crystal X-ray diffraction. Selected substances were also investigated with magnetometry or Mößbauer spectroscopy. UV/Vis spectroscopy, NMR spectroscopy, magnetometry or Mößbauer spectroscopy were used for coordination chemical investigations in solution.

The low-spin complex $[Fe(MeC(Py)_2Phen)(MeCN)_2](OTf)_2$ was investigated for short-lived excited states by femtosecond X-ray emission spectroscopy and compared with the photophysical properties of a bisfacial iron(II) complex of a bis(pyrazolyl)pyridinylmethane ligand. Both show similar photophysical behaviour to that of the well-studied iron(II) bipyridinyl complex.

Kurzzusammenfassung

Inspiriert von der Natur können biomimetische Eisenkomplexe als Katalysatoren in selektiven Oxidationsreaktionen eingesetzt werden. Dabei werden hochvalente Oxo-Spezies der Eisenkomplexe durchlaufen. Neben dem Ligandendesign für solche Eisenkomplexe ist die Struktur der Präkursorkomplexe und das koordinationschemische Verhalten in Lösung sehr wichtig für die Bildung der hochvalenten Eisen-Oxo-Spezies und ihre katalytische Aktivität.

Im Rahmen dieser Arbeit wurden tri- und tetradentate Liganden mit *N*- und *O*-Donoren synthetisiert und untersucht. Für einen Bis(pyrazolyl)ethanolliganden konnte eine bisfaciale Koordination von Eisen mit einer $\{N_3\}$-Koordination des Liganden festgestellt werden. Die untersuchten tetradentaten Liganden ($MeC(Py)_2Phen$, $MeC(Py)_2PicMe$ und NQu_3) mit $\{N_4\}$- bzw. $\{N_3O\}$-Donoren-Set lassen in einer oktaedrischen Koordinationsumgebung immer zwei *cis*-ständige Koordinationsstellen für labile Coliganden frei. Diese sind besonders wichtig für katalytische Oxidationsreaktionen mit hochvalenten Eisen-Oxo-Intermediaten. Für alle drei tetradentaten Liganden konnte eine $[Fe^{IV}L=O]^{2+}$ Spezies mittels Massenspektrometrie nachgewiesen werden. Auch UV/Vis-spektroskopische Untersuchungen zeigen typische Eisen-Oxo-Banden. Für Komplexe mit dem Liganden $MeC(Py)_2Phen$ konnte zudem die katalytische C – H-Bindungs-Oxidation erfolgreich untersucht werden.

Bei den zugehörigen Präkursorkomplexen wurde die Struktur im Festkörper und in Lösung untersucht. Das Hauptaugenmerk lag dabei auf der Coliganden-Konkurrenz von Triflat und Acetonitril. Während im Festkörper verschiedene Spezies beobachtet wurden, legen alle Ergebnisse in Lösung nahe, dass Acetonitril koordinierend vorliegt, wenn es als Lösungsmittel verwendet wird. Des Weiteren konnte für Komplexe mit den Liganden $MeC(Py)_2PicMe$ und NQu_3 in Acetonitril Spin-Crossover-Verhalten in Lösung beobachtet werden.

Eine Vielzahl an potenziellen Präkursorkomplexen mit (schwach) koordinierenden Anionen konnte im Festkörper mit Einkristallröntgendiffraktometrie strukturell charakterisiert werden. Ausgewählte Substanzen wurden zudem mit Magnetometrie oder Mößbauer-Spektroskopie untersucht. Für koordinationschemische Untersuchungen in Lösung kamen UV/Vis-Spektroskopie, NMR-Spektroskopie, Magnetometrie oder Mößbauer-Spektroskopie zum Einsatz.

Der Low-Spin-Komplex $[Fe(MeC(Py)_2Phen)(MeCN)_2](OTf)_2$ wurde mittels Femtosekunden-Röntgen-Emissions-Spektroskopie auf kurzlebige angeregte Zustände hin untersucht und mit den photophysikalischen Eigenschaften eines bisfacialen Eisen(II)-Komplex mit einem Bis(pyrazolyl)pyridinylmethanliganden verglichen. Beide zeigen ein ähnliches photophysikalisches Verhalten wie der gut untersuchte Eisen(II)-Bipyridinyl-Komplex.

Danksagung

Als erstes möchte ich mich bei Prof. Dr. Sonja Herres-Pawlis bedanken, dass ich diese Doktorarbeit in ihrem Arbeitskreis anfertigen durfte. Vielen Dank für das Vertrauen und Freiheiten innerhalb des Themas, wo ich zwischen bioanorganischer Chemie und Koordinationschemie meiner wissenschaftlichen Neugier folgen konnte. Des Weiteren möchte ich mich dafür bedanken, dass ich an Messzeiten an Großforschungseinrichtungen, Workshops und nationalen sowie internationalen Konferenzen teilnehmen durfte.
Prof. Dr. Iris Oppel möchte ich für die Übernahme des Zweitgutachtens danken, sowie der Möglichkeit die Röntgenkristallographie praktisch zu erlernen.
Ebenfalls möchte ich mich bei Prof. Dr. Arne Lüchow für die Übernahme der Aufgabe des dritten Prüfers und bei Prof. Dr. Frédéric W. Patureau für die Übernahme des Prüfungsvorsitzes bedanken.
Mein Dank gilt Prof. Dr. Ulf-Peter Apfel und Dr. Linda Iffland-Mühlhaus für die äußerst angenehme und konstruktive Kooperation im Bereich der Mößbauermessungen.
Prof. Dr. Birgit Weber, Dr. Sophie Schönfeld und Andreas Dürrmann möchte ich für die SQUID-Magnetometrie-Messungen in Lösung danken.
I would like to thank Dr. Christopher Milne and Dr. Mykola Biednov for the possibility to attend a beam-time at European XFEL. Furthermore, I would like to thank everybody else involved in this beam-time for the help and the welcoming atmosphere.
I am grateful for the cooperation with Dr. Neetika Sharma and Hend Shahed in the field of spin crossover complexes in the solid state.
Mein Dank gilt den Abteilungen für chemische Analytik des Instituts für Anorganische Chemie und des Instituts für Organische Chemie, die mit Messungen zur Charakterisierung der Verbindungen beigetragen haben. Insbesondere möchte ich mich bei Brigitte Pütz für die CSI/ESI-MS und bei Dr. Gerhard Fink und Rachida Bomahrat für die (VT)-NMR-Messungen bedanken. Tobias Storp möchte ich für die PXRD-Messungen und den möglichst reibungslosen Ablauf rund um das SCXRD-Diffraktometer danken. Den Arbeitskreisen Englert und Oppel danke ich für die Unterstützung bei SCXRD-Messungen. Bei Dr. Melanie Paul möchte ich mich für die geduldige Unterstützung beim Erlernen der SCXRD-Messungen bedanken. Zudem danke ich Dr. Melanie Paul und Dr. Hans Gildenast für die Messung einiger der in dieser Arbeit enthaltenen SCXRD-Strukturen. Dr. Alexander Hoffmann danke ich für die Unterstützung beim Kristallstrukturlösen und bei sonstigen Problemen im Laboralltag. Auch möchte ich mich bei Claudia Nelleßen bedanken, die zahllose Dinge im Hintergrund organisiert hat.
Für die Unterstützung bei der Arbeit im Labor möchte ich mich bei Sonja Mürtz, Pauline Durschewski, Maverick Eilers und Ian Krumm bedanken.
Vielen Dank an Hans, Josh, Steven, Mykola, Konstantin, Christian und Ulla, die mir beim Korrekturlesen geholfen haben.

Mein besonderer Dank gilt Hans und Steven. Ihr konntet mir bei allen möglichen Problemen von SCXRD-Strukturen über Latex-Formatierungsprobleme bis hin zur Auswahl der richtigen Schriftart mit Rat und Tat zur Seite stehen.
Ich bin überaus dankbar, ein herausragendes Team im Arbeitskreis um mich haben zu dürfen und möchte mich bei allen aus dem AK Herres-Pawlis für die gute Arbeitsatmosphäre und Unterstützung bedanken. Namentlich möchte ich dabei Alina, Christian, Christine, Fabian F., Fabian T., Felix, Kristina, Konstantin, Larissa, Josh, Martin, Melanie, Regina, Rosalie, Ruth, Patty und Thomas hervorheben, die mich auf diesem Weg im Arbeitskreis begleitet haben. Neben dem lebendigem Austausch über chemische Fragestellungen und Probleme war vom kurzen Kaffee-Stop über Super-Kuchen-Wochen bis zum ausgedehnten Running-Dinner alles dabei, was die Zeit hier unvergesslich gemacht hat.
Bei Felix, Hans, Jil, Johanna, Kira, Paulina, Steven und Susi möchte ich mich dafür bedanken, das ihr darauf geachtet habt, dass das Leben nicht nur aus Chemie besteht. Ohne euch wäre die Zeit in Aachen nicht die selbe gewesen!
Mein Dank gilt zudem Christian, der mich vor allem auf den letzten Metern zum Ziel begleitet hat. Ohne dich wäre ich vermutlich durchgedreht.
Besonders möchte ich mich bei meiner Familie bedanken: Bei meinen Eltern Eva und Paul, bei meinem Bruder Paul, bei meiner Oma Mia und meiner Tante Ulla. Ihr habt mich immer unterstützt, mir den Rücken frei gehalten und mir ein finanziell sorgenfreies Studium ermöglicht. Danke!

List of Compounds

*Compounds marked with * were synthesised according to previous reports from the Herres-Pawlis group. Compounds marked with ‡ were previously synthesised and kindly provided by former co-workers.*

Ligands

1*	$HOCH_2C(Pz)_2Py$	2-(pyridinyl)bis(pyrazolyl)ethanol
2*	$MeC(Py)_2Phen$	2-(1,1-di(pyridin-2-yl)ethyl)-1,10-phenanthroline
3	$MeC(Py)_2PicMe$	methyl 6-(1,1-di(pyridin-2-yl)ethyl)picolinate
4*	NQu_3	tri(quinolin-8-yl)amine
5‡	$HC(3,5\text{-}MePz)_2Py$	bis(3,5-methylpyrazolyl)pyridinylmethane

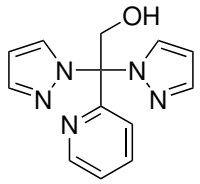

$HOCH_2C(Pz)_2Py$
1

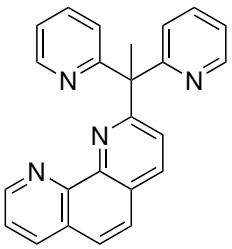

$MeC(Py)_2Phen$
2

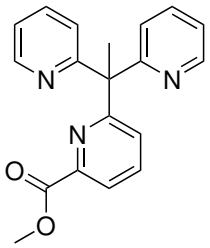

$MeC(Py)_2PicMe$
3

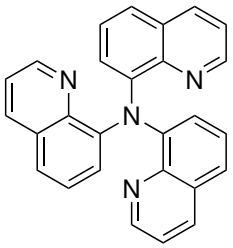

NQu_3
4

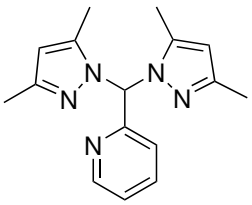

$HC(3,5\text{-}MePz)_2Py$
5

Complexes

1a $[Fe(HOCH_2C(Pz)_2Py)_2]Br_2 \cdot MeCN$
1b $[Fe(HOCH_2C(Pz)_2Py)_2][FeBr_4]Br \cdot C_7H_8$
1c $[Fe(HOCH_2C(Pz)_2Py)_2][FeCl_4]Cl \cdot 2\,MeCN$
1d $[Fe(HOCH_2C(Pz)_2Py)_2](OTf)_2 \cdot 2\,MeCN$

1e $[Zn(HOCH_2C(Pz)_2Py)_2][ZnCl_4]$

1f $[Cu_2(\mu\text{-}Br)Br_2(HOCH_2C(Pz)_2Py)_2]Br \cdot C_7H_8$
1g $[Cu_2(OCH_2C(Pz)_2Py)_2Cl_2]$
1h $[Cu_2(OCH_2C(Pz)_2Py)_2Br_2]$

2a* $[Fe(MeC(Py)_2Phen)(MeCN)_2](OTf)_2$
2b $[Fe(MeC(Py)_2Phen)(MeCN)_2](BF_4)_2 \cdot MeCN$
2c $[Fe(MeC(Py)_2Phen)(\mu\text{-}Cl)_2FeCl_2]$
2d $[Fe(MeC(Py)_2Phen)Cl(\mu\text{-}O)FeCl_3] \cdot MeCN$

3a $[Fe(MeC(Py)_2PicMe)(OTf)_2]$
3b $[Fe_4(\mu\text{-}O)_2(MeC(Py)_2Pic)_4](OTf)_4 \cdot 4\,DCM \cdot THF$
3c $[Fe(MeC(Py)_2PicMe)Cl_2] \cdot 0.5\,MeCN$
3d $[Fe(MeC(Py)_2PicMe)(H_2O)(MeCN)](BF_4)_2 \cdot MeCN$
3e $[Fe(MeC(Py)_2PicMe)(BF_4)Cl] \cdot 3.5\,Et_2O$

4a $[Fe(NQu_3)(MeCN)_2](OTf)_2 \cdot MeCN \cdot 0.5\,Et_2O$
4b $[Fe(NQu_3)(OTf)(MeCN)](OTf) \cdot 0.5\,Et_2O$
4c $[Fe(NQu_3)(OTf)_2]$
4d $[Fe(NQu_3)(OTf)_2] \cdot 0.45\,Et_2O$
4e $[Fe(NQu_3)(OTf)_2][Fe(NQu_3)(OTf)_2]_{0.5}\{[Fe(NQu_3)(OTf)(H_2O)](OTf)\}_{0.5}$
4f $[Fe(NQu_3)(H_2O)(MeCN)](OTf)_2$
4g $[Fe_2(\mu\text{-}O)(NQu_3)_2(OTf)_2](OTf)_2 \cdot 0.85\,MeCN$
4h $[Fe(NQu_3)(OTf)_2] \cdot 1.3\,DCM \cdot Z$
4i $[Fe(NQu_3)(OTf)(H_2O)](OTf) \cdot DCM$
4j $[Fe(NQu_3)(EtCN)_2](OTf)_2$
4k $[Fe(NQu_3)(OTf)(EtCN)](OTf) \cdot 0.5\,Et_2O$
4l $[Fe(NQu_3)(OTf)(MeOH)](OTf)$
4m $[Fe(NQu_3)(OTf)(MeOH)](OTf) \cdot MeOH$
4n $[Fe(NQu_3)Cl_2] \cdot 0.5\,DCM$
4o $[Fe(NQu_3)Br_2] \cdot 0.5\,DCM$
4p $[Fe(NQu_3)Cl]PF_6 \cdot 1.5\,DCM$
4q $[Fe(NQu_3)(MeCN)_2](BF_4)_2 \cdot 0.5\,MeCN$
4r $[Fe(NQu_3)(NCS)_2] \cdot 0.5\,Et_2O$

5a‡ $[Fe(HC(3,5\text{-}MePz)_2Py)_2](CF_3CO_2)_2$

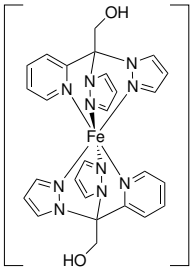

[Fe(HOCH$_2$C(Pz)$_2$Py)$_2$]Br$_2$ · MeCN
1a

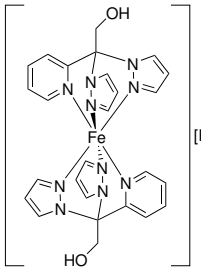

[Fe(HOCH$_2$C(Pz)$_2$Py)$_2$][FeBr$_4$]Br · C$_7$H$_8$
1b

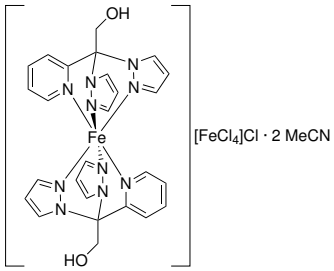

[Fe(HOCH$_2$C(Pz)$_2$Py)$_2$][FeCl$_4$]Cl · 2 MeCN
1c

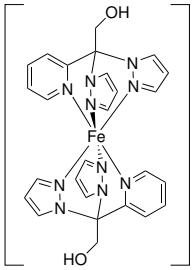

[Fe(HOCH$_2$C(Pz)$_2$Py)$_2$](OTf)$_2$ · 2 MeCN
1d

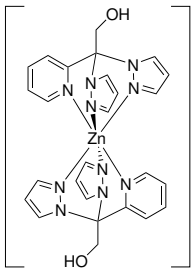

[Zn(HOCH$_2$C(Pz)$_2$Py)$_2$][ZnCl$_4$]
1e

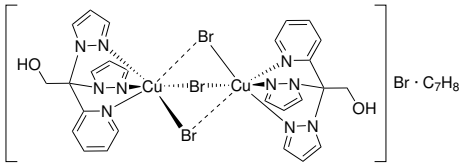

[Cu$_2$(μ-Br)Br$_2$(HOCH$_2$C(Pz)$_2$Py)$_2$]Br · C$_7$H$_8$
1f

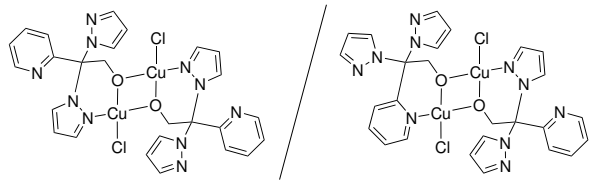

[Cu$_2$(OCH$_2$C(Pz)$_2$Py)$_2$Cl$_2$]
1g

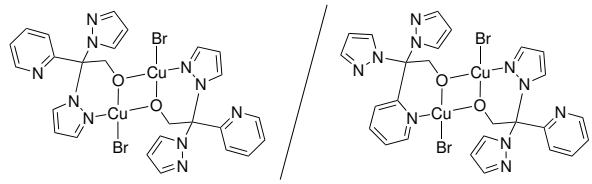

[Cu$_2$(OCH$_2$C(Pz)$_2$Py)$_2$Br$_2$]
1h

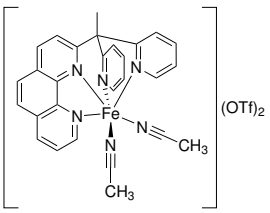

[Fe(MeC(Py)$_2$Phen)(MeCN)$_2$](OTf)$_2$
2a

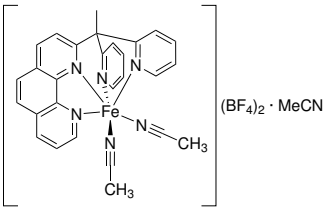

[Fe(MeC(Py)$_2$Phen)(MeCN)$_2$](BF$_4$)$_2$ · MeCN
2b

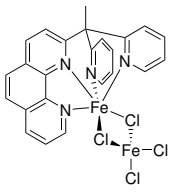

[Fe(MeC(Py)$_2$Phen)(μ-Cl)$_2$FeCl$_2$]
2c

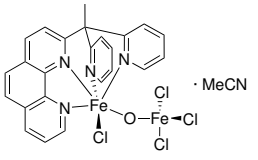

[Fe(MeC(Py)$_2$Phen)Cl(μ-O)FeCl$_3$] · MeCN
2d

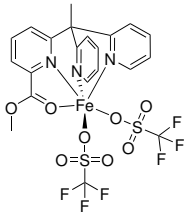

[Fe(MeC(Py)$_2$PicMe)(OTf)$_2$]
3a

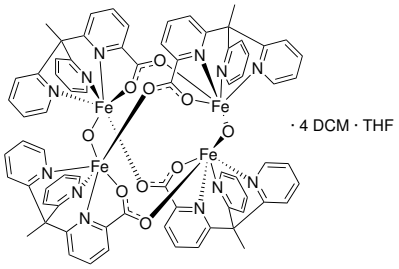

[Fe$_4$(μ-O)$_2$(MeC(Py)$_2$Pic)$_4$](OTf)$_4$ · 4 DCM · THF
3b

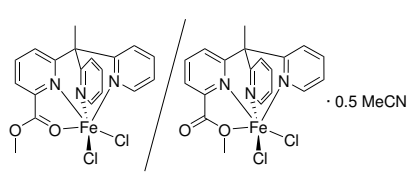

[Fe(MeC(Py)$_2$PicMe)Cl$_2$] · 0.5 MeCN
3c

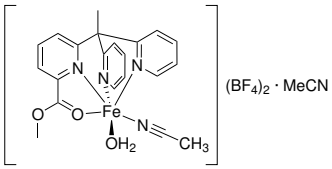

[Fe(MeC(Py)$_2$PicMe)(H$_2$O)(MeCN)](BF$_4$)$_2$ · MeCN
3d

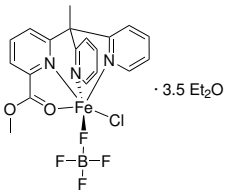

[Fe(MeC(Py)$_2$PicMe)(BF$_4$)Cl] · 3.5 Et$_2$O
3e

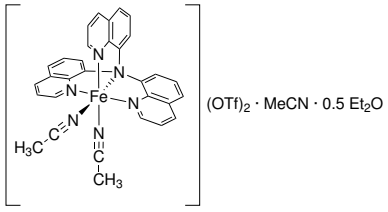

[Fe(NQu$_3$)(MeCN)$_2$](OTf)$_2$ · MeCN · 0.5 Et$_2$O
4a

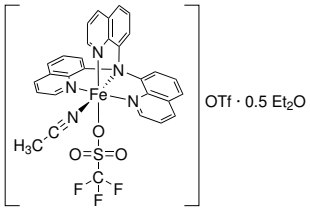

[Fe(NQu$_3$)(OTf)(MeCN)](OTf) · 0.5 Et$_2$O
4b

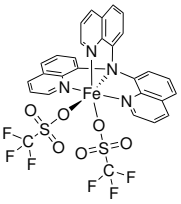

[Fe(NQu$_3$)(OTf)$_2$]
4c

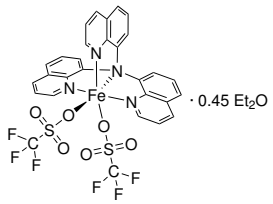

[Fe(NQu$_3$)(OTf)$_2$] · 0.45 Et$_2$O
4d

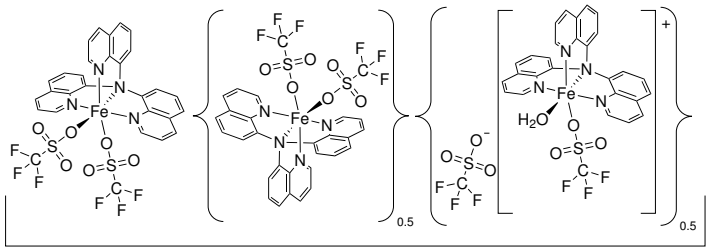

[Fe(NQu$_3$)(OTf)$_2$][Fe(NQu$_3$)(OTf)$_2$]$_{0.5}${[Fe(NQu$_3$)(OTf)(H$_2$O)](OTf)}$_{0.5}$
4e

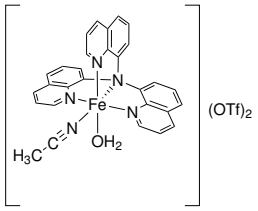

[Fe(NQu$_3$)(H$_2$O)(MeCN)](OTf)$_2$
4f

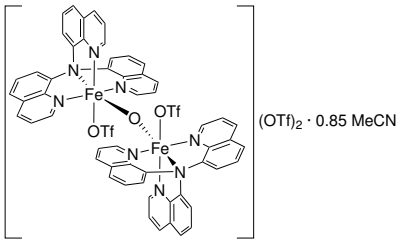

[Fe$_2$(μ-O)(NQu$_3$)$_2$(OTf)$_2$](OTf)$_2$ · 0.85 MeCN
4g

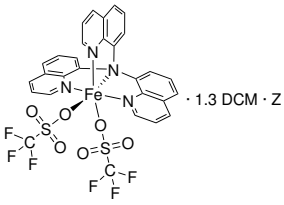

[Fe(NQu$_3$)(OTf)$_2$] · 1.3 DCM · Z
4h

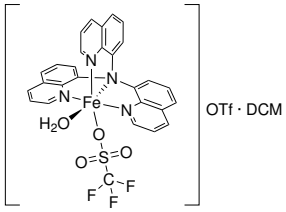

[Fe(NQu$_3$)(OTf)(H$_2$O)](OTf) · DCM
4i

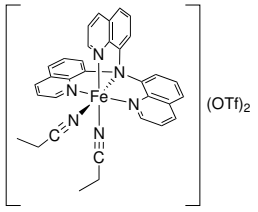

[Fe(NQu$_3$)(EtCN)$_2$](OTf)$_2$
4j

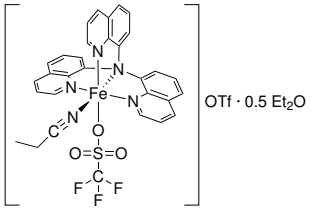

[Fe(NQu$_3$)(OTf)(EtCN)](OTf) · 0.5 Et$_2$O
4k

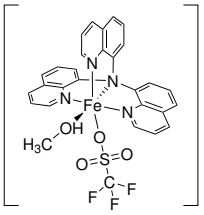

[Fe(NQu$_3$)(OTf)(MeOH)](OTf)
4l

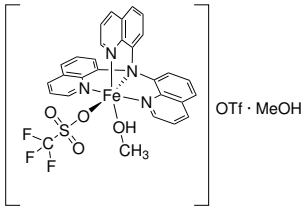

[Fe(NQu$_3$)(OTf)(MeOH)](OTf) · MeOH
4m

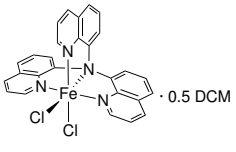

[Fe(NQu$_3$)Cl$_2$] · 0.5 DCM
4n

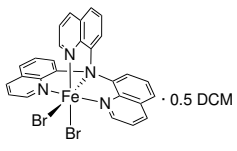

[Fe(NQu$_3$)Br$_2$] · 0.5 DCM
4o

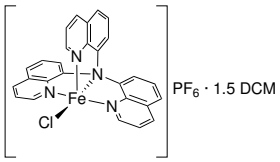

[Fe(NQu$_3$)Cl]PF$_6$ · 1.5 DCM
4p

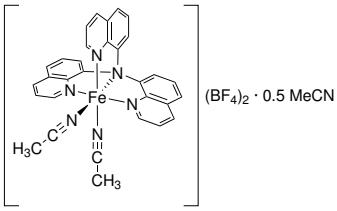

[Fe(NQu$_3$)(MeCN)$_2$](BF$_4$)$_2$ · 0.5 MeCN
4q

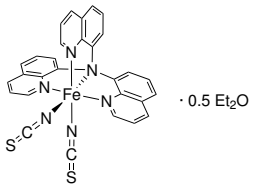

[Fe(NQu$_3$)(NCS)$_2$] · 0.5 Et$_2$O
4r

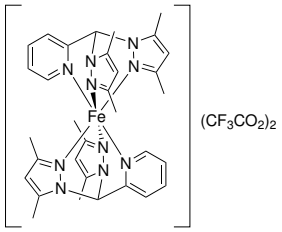

[Fe(HC(3,5-MePz)$_2$Py)$_2$](CF$_3$CO$_2$)$_2$
5a

Abbreviations & Symbols

A	cyclohexanol
A	absorption [-]
A_c	corrected absorption [-]
***A*-d**	cyclohexanol-d_{11}
2°-*A*	2-adamantanol
3°-*A*	1-adamantanol
abs.	absolute
ACV	L-α-Aminoadipyl-L-cysteinyl-D-valine
A*/*K	alcohol-to-ketone ratio
Asp	aspartic acid
BDE	bond dissociation energy
BiPy	bipyridine
C	cyclohexane
c	concentration [$\mathrm{mol\,L^{-1}}$]
***C*-d**	cyclohexane-d_{12}
CDO	cystein dioxygenase
CISSS	coordination-induced spin state switch
CSI-MS	cryospray-ionisation mass spectrometry
CSD	Cambridge Structural Database
CSM	continuous shape measure
CV	cyclic voltammogram
Dke1	acetylacetone dioxygenase
DMSO	dimethyl sulfoxide
ε	extinction coefficient [$\mathrm{L\,mol^{-1}cm^{-1}}$]
$E_{1/2}$	half-wave potential [V]
ΔE	peak-to-peak separation [mV]
EPR	electron paramagnetic resonance
ESI-MS	electrospray ionisation mass spectrometry
Fc/Fc^+	ferrocene redox couple
FCC	field cooled cooling
FCW	field cooled warming
FXE	femtosecond X-ray experiments
γ_{HS}	molar fraction of molecules in high-spin state
GC	gas chromatography
GDO	gentisate 1,2-dioxygenase
Glu	glutamic acid

GoF	goodness of fit
2H1C	2-His-1-carboxy
3H	3-His
His	histidine
HRMS	high resolution mass spectrometry
HS	high-spin
I	intensity [-]
IR	infrared spectroscopy
IS	intermediate-spin
K	cyclohexanone
***K*-d**	cyclohexanone-d_{10}
2°-*K*	2-adamantanone
KG	ketogluterate
KIE	kinetic isotope effect
LS	low-spin
lspl	least-sqares plane
mCPBA	*m*-chloroperoxybenzoic acid
$MeC(Py)_2BiPy$	6-(1,1-di(pyridin-2-yl)ethyl)-2,2'-bipyridine
MMO	methane monooxygenase
MS	mass spectrometry
MW	molecular weight
n-BuLi	*n*-butyllithium
n.d.	not deposited
NIR	near-infrared
NMR	nuclear magnetic resonance
OC	octahedron
PDB	Protein Data Bank
Phen	phenanthroline
PyTACN	1-[(2-pyridyl)methyl]-4,7dimethyl-1,4,7-triazacyclononane
PXRD	powder X-ray diffraction
R	universal gas constant
refl.	reflections
sPhIO	(2-*t*-butylsulfonyl)iodosylbenzene
SCO	spin crossover
SCXRD	single crystal X-ray diffraction
SH	shoulder (XES data)
SQUID	superconducting quantum interference device
struct. param.	structure parameters
$T_{1/2}$	SCO temperature [K]
THF	tetrahydrofuran
TMG_3tren	2,2',2"-(nitrilotris(ethane-2,1-diyl))tris(1,1,3,3-tetramethylguanidine)

TON	turnover number
TPA	tris(2-methylpyridyl)amine
TPR	trigonal prism
TQA	tris(2-quinolylmethyl)amine
UV/Vis	ultraviolet-visible
VT	variable temperature
$\chi_M T$	molar susceptibility [$cm^3\,K\,mol^{-1}$]
XAS	X-ray absorption spectroscopy
XES	X-ray emission spectroscopy
XFEL	X-ray free-electron laser
Z	formula units per unit cell
ZFC	zero field cooled

List of Figures

List of Schemes

List of Tables

Contents

Introduction

1 Motivation & Overview of Related Work

Iron is a life-sustaining element, of which every human body contains about 3–5 g.[1] It is not present in its metallic bulk form as we know it from everyday life, but is mostly bound as cation with 4500 (ferritin) to single iron centres in metalloenzymes.[2] In the latter case, where only one or two iron centres are surrounded by the protective protein scaffold and coordinated by amino acids of the protein, there are specific sites at the metal centre for the coordination of further co-ligands.

Are ligands and co-ligands binding to an iron centre only an issue for coordination chemists? No! Perhaps the most important co-ligand for iron is molecular dioxygen, which binds to the iron-containing metalloprotein hemoglobin in the human bloodstream and is responsible for oxygen transport in the body. In modern medical care, to ensure that this life-sustaining process is working properly, the oxygen saturation of the arterial blood is monitored by pulse oximetry. This non-invasive continuos method of measuring is based on the different ultraviolet-visible (UV/Vis) and near-infrared (NIR) absorption bands of oxy- and desoxy-hemoglobin. Therefore, the photometrical determined concentration of oxy-hemoglobin is divided by the total hemoglobin concentration resulting in an oxygen saturation value.[3–5] Especially in the recent COVID-19 pandemic, where one of the symptoms of infection can be low dioxygen saturation, it is crucial to monitor the dioxygen saturation in the patient's blood.[6] But other co-ligands such as carbon monoxide, which bind to the iron centres of hemoglobin and thus alter the light absorption behaviour, can also be photometrically detected in the human body.[7] Carbon monoxide can block the dioxygen coordination site in hemoglobin due to its higher binding affinity towards the iron centre which dangerously disrupts the oxygen transport.[8]

Bioinorganic chemistry aims at understanding how metal containing proteins work and what we can learn from nature about coordination chemistry. This can be achieved by investigations on the metalloproteins themselves or via model complexes. Modifications of biomimetic compounds deepen insight into nature's design and sometimes even how this can be improved for non-biological catalytic applications.

A key feature of metalloproteins is their ability to perform dioxygen activation and selective oxidation reactions in an atom-economical manner under relatively mild conditions, what is lacking in conventional oxidation methods.[9–11] Without a catalyst, reactions of organic substrates with dioxygen are spin-prohibited and therefore kinetically hindered, although they are thermodynamically favourable.[12] Hence, it is of great interest to develop catalytically active biomimetic complexes. Iron complexes are promising candidates because there are so many natural models in the form of iron metalloenzymes and iron is also the fourth most abundant metal in the earth's crust and is additionally affordable and non-toxic.[9,13–15]

1.1 Iron Metalloproteins

1.1.1 Structures of Iron Metalloproteins

Besides the transport of oxygen, which is performed by hemoglobin, there are more iron metalloproteins that have different functions in the human body. These are e. g. storage of iron (myoglobin, ferritin, hemosiderin), electron transfer (cytochrome *c*, iron-sulphur proteins) or catalysis (cytochrome *c* oxidase, cytochrome P450).[16] Catalytically active metalloproteins are also called metalloenzymes.
Iron contining enzymes display three recurring structural motifs (Figure 1.1): The mononuclear heme motif, mononuclear non-heme enzymes and dinuclear non-heme enzymes.[17]

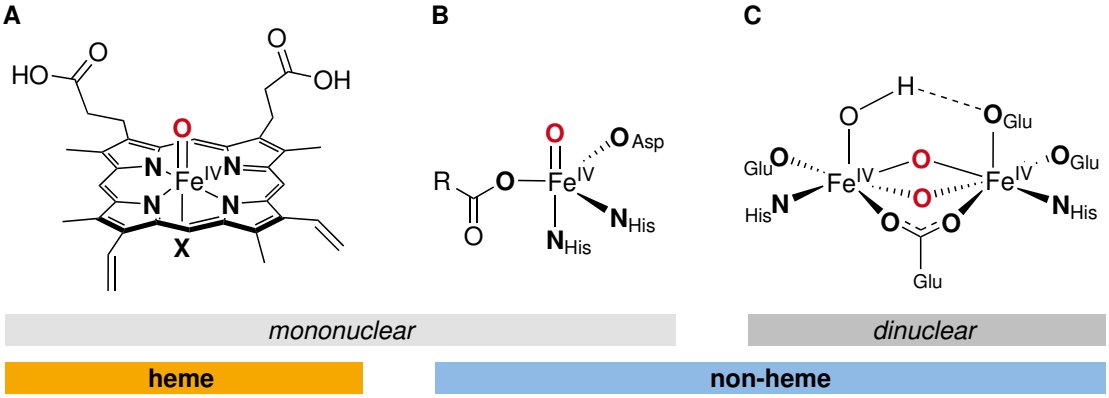

Figure 1.1: Examples of three active centres in oxygen activating iron enzymes. A: heme enzyme: compound-I intermediate (catalyse, peroxidase or cytochrome-P450), B: mononuclear non-heme enzyme: intermediate J of taurine dioxygenase, C: dinuclear non-heme enzyme: intermediate Q of soluble methane monooxygensase. Histidine (His), aspartic acid (Asp) and glutamic acid (Glu). Structures adapted from Hohenberger *et al.*[17]

The heme enzymes are named after the heme complexes which feature a macrocyclic porphyrin moiety with four *N*-donors in the equatorial plane of an octahedral coordination sphere of an iron centre (Figure 1.2).[18,19] Enzymes without this additional heme moiety bind iron cations directly with the amino acid side chains of the protein. For mononuclear metalloenzymes these are usually two histidine (His) and one deprotonated aspartic acid (Asp) or glutamic acid (Glu) side chain in a facial arrangement of the octahedral coordination sphere – the 2-His-1carboxylate (2H1C) facial triad.[19–21] The three remaining coordination sites in the octahedral coordination geometry can be occupied by molecular oxygen, substrate(s) or water. The latter is the case in the enzymes resting state.[22] The first single crystal X-ray diffraction (SCXRD) structures of enzymes in which iron centres are coordinated by a 2H1C facial triad were reported in the mid 1990s. These include the extradiol cleaving 2,3-dihydroxybiphenyl 1,2-dioxygenase*, the pterin-dependent tyrosine

*BphC; PDB (Protein Data Bank) ID[23]: 1HAN[24] and 1DHY[25]

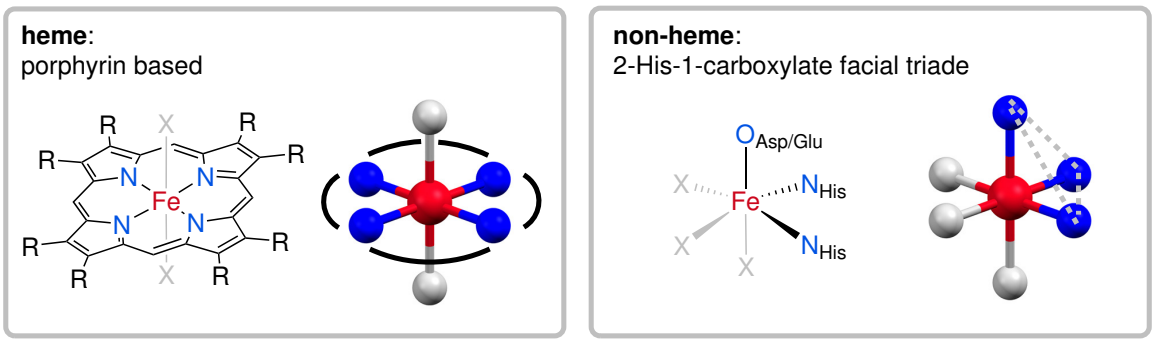

Figure 1.2: Schematic depiction of a porphyrin scaffold[18] coordinating an iron centre in heme iron complexes (left) and a 2-His-1-carboxylate facial triad[20] coordinating an iron centre in non-heme iron complexes (right) for an octahedral coordination sphere. Labile co-ligands (X): O_2, substrate(s) or water. Colour code for octahedron: iron = red, donor atoms = blue, co-ligand positions = grey.

hydroxylase†, isopenicillin N synthase‡, iron superoxide dismutase§ and soybean lipoxygenase¶.[20,21] The structure of isopenicillin N synthase is shown in Figure 1.3. In this structure, the co-ligand positions in the octahedral coordination sphere are occupied by water, nitric oxide and L-D-(α-Aminoadipoyl)-L-cysteinyl-D-valine (ACV). About 10 years later, the number of structures containing the 2H1C facial triad motif has grown to 125 out of 30 different enzymes emphasising the importance of this structural feature.[30]

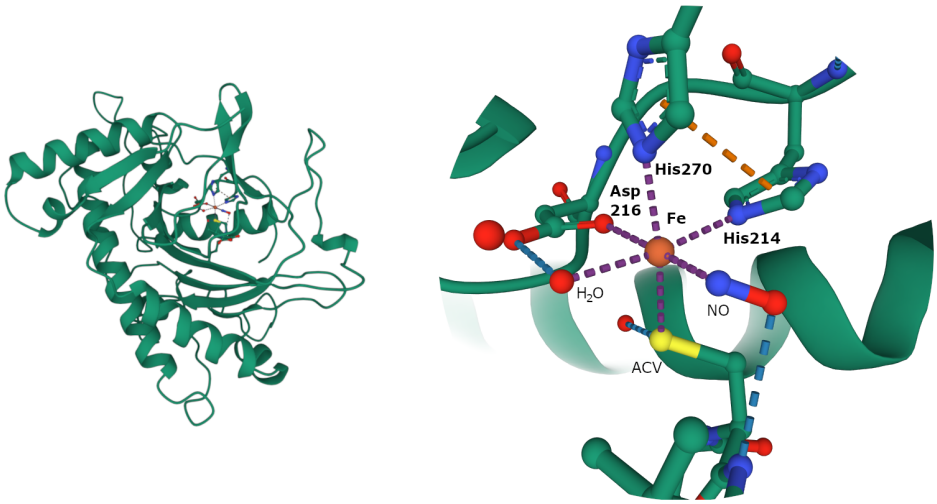

Figure 1.3: Structure of isopenicillin N synthase from apergillus nidulans (INPS; PDB ID: 1BLZ, left) and close up of 2H1C facial triad (His214, His270, Asp216) coordinating an Fe(III) ion in this structure. Co-ligand position are occupied by H_2O, NO and L-D-(α-Aminoadipoyl)-L-cysteinyl-D-valine (ACV).[27] Crystal solvent molecules are omitted for clarity. Colour code: blue = nitrogen, red = oxygen, yellow = sulphur, orange = iron, dark green = protein scaffold.[23,31]

†TyrH; PDB ID: 1TOH[26]
‡IPNS; PDB ID: 1BK0 and 1BLZ[27]
§FeSOD, PDB ID: 1ISB[28]
¶SOL-1; PDB ID: 1YGE[29]

In addition to the 2H1C facial triad, another structural motif of facial coordination has recently been identified: the 3-His facial triad (3H).[32–35] Although it seems to be much rarer, it enables a similar dioxygen activation as the 2H1C triad.[22,34] Examples for enzymes containing a 3H facial triad are cysteine dioxygenase (CDO),[36–38] acetylacetone dioxygenase (Dke1)[39] and gentisate 1,2-dioxygenase (GDO).[40] In Figure 1.4 the 3H coordination motif of human cysteine dioxygenase is shown with cysteine as coordinating substrate.[36] Other atypical non-heme coordination motifs deviating from the commonly occurring 2H1C motif like 2-His, 3-His-1-carboxylate and 4-His have been identified.[22]

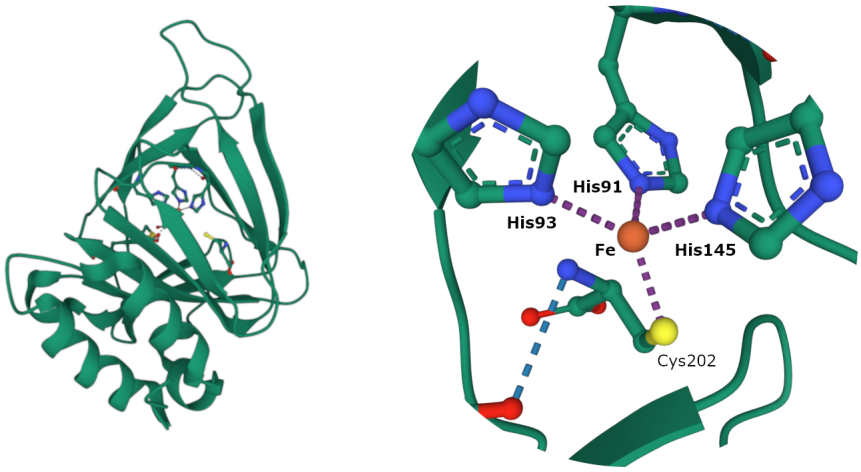

Figure 1.4: Structure of human cysteine dioxygenase (CDO; PDB ID: 2IC1, left) and close up of 3H triad (His91, His93, His145) coordinating an Fe(II) ion in this structure. The substrate cysteine is coordinating as co-ligand.[36] Crystal solvent molecules are omitted for clarity. Colour code: blue = nitrogen, red = oxygen, yellow = sulphur, orange = iron, dark green = protein scaffold.[23,31]

1.1.2 Catalytic Reactivity of Non-Heme Iron Enzymes

In the metabolism of molecular oxygen – as required for aerobic life – mononuclear non-heme iron enzymes play a key role.[22] Although reactions with molecular oxygen are thermodynamically favourable, they are kinetically hindered because the reaction of organic substrates with oxygen are spin-forbidden.[12] Mononuclear non-heme iron enzymes are able to facilitate these spin-forbidden reactions (see Table 1.1 for an overview of common reaction types for enzymes with 2H1C facial triad).[12,20]

For mononuclear metalloenzymes the activation of molecular oxygen proceeds along a common mechanism (Figure 1.5). In the first step molecular oxygen is bound to the metal centre, resulting in a superoxo species. This changes the kinetically inert ground state of dioxygen to a radical anion doublet state, increasing its reactivity. If this species is reduced with one electron to a peroxo species this can subsequently be protonated to a hydroperoxo species. Alternatively, the superoxo species can react with a hydrogen radical to a hydroperoxo species in a single step. The hydroperoxo species can undergo two different O – O cleavage reactions – homolysis or heterolysis – forming high-valent oxo

Table 1.1: Selected sub-classes of mononuclear non-heme iron enzymes of the enzyme super-family with 2H1C facial triad, associated reaction types and examples.[12,20]

Enzyme sub-classes	Reaction type	Enzyme examples
α-KG dependent enzymes	hydroxylation, desaturation, epimerisation, heterocyclic ring formation & expansion, epoxidation, endoperoxide formation	taurine:α-KG dioxygenase clavaminate synthase carbapenem synthase deacetoxycephalosporin C synthase 4'-methoxyviridicatin synthase fumitremorgin B endoperoxidase
pterin-dependent hydroxylases	hydroxylation of aromatic rings	tyrosine hydroxylase
Rieske oxygenases	2 e^- oxidation	naphthalene 1,2-dioxygenase
isopenicillin N synthase	4 e^- oxidative ring closure	isopenicillin N synthase
ethylene forming enzymes	2 e^- oxidation	1-aminocyclopropane-1-carboxylate oxidase
(*S*)-2-hydroxypropyl-1-phosphonate epoxidase	1,3-dehydrogenation to epoxide	(*S*)-2-hydroxypropyl-1-phosphonatepoxidase

KG = ketogluterate.

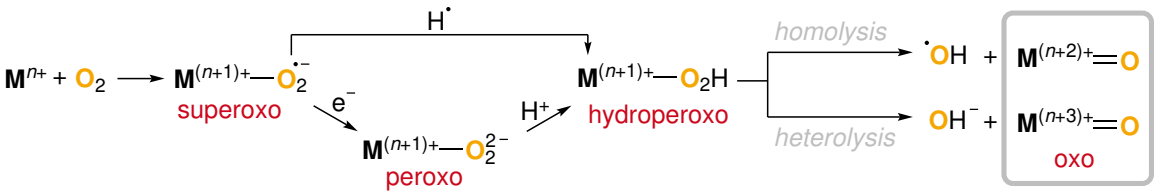

Figure 1.5: Unified mechanism for oxygen activation at mononuclear metalloenzymes with metal centre M. Mechanism adapted from Ray *et al.*[14]

species of different oxidation states.[14] Afterwards, the high-valent oxo species can react with a substrate. This oxygen activation mechanism is the key to many catalytic cycles for metalloenzymes.

Reactions performed by these metalloenzymes are highly selective and work under mild reaction conditions. Inspired by the plethora of different functionalisations made possible by these enzymes, researchers are keen to understand the key reactivity properties of the enzymes as well as to harness catalytic capabilities using model complexes.

1.2 Biomimetic Non-Heme Iron Model Complexes

1.2.1 Design of Model Complexes

In the field of biomimetic chemistry the aim is to synthesise and study model compounds that mimic natural metalloenzymes. These synthetic analogues are needed because, besides

imitating the catalytic properties of natural enzymes, studying the function of metalloenzymes is often challenging on the sophisticated biomolecules themselves.[41] The design of small model complexes that mimic essential parts such as the reactivity or structural features of the biomolecule can help in these investigations. Compared to rather structurally sophisticated enzymes, model complexes are a minimalist version of them. The original protein scaffold is mimicked by more straightforward multidentate ligands with only a fraction of the atoms.[42] In the process, the first (and second) coordination spheres of the metal ion are recreated.[34,43–45] Designing biomimetic model complexes can pursue two objectives: modelling the structure or the catalytic activity of the natural enzyme.[46] Ideally, both objectives are combined in a model compound that can mimic structure and functionality as accurate as possible.[41]

Structural Model Complexes

Structural model complexes that focus on a detailed replica of the active site of a metalloenzyme are synthesised to gain a better understanding of the structure around the metal centre at the active site and deeper insights into the mechanism of the catalytic cycle of the enzyme.[47,48] Also, model systems are used as reference for interpretation of experimental data from natural enzymes.[49] For example, proteins are often very challenging to crystallise for structure investigations via SCXRD, which is easier with smaller molecules like model complexes. And even if the proteins are available as single crystals the obtained structures usually have lower resolutions than the ones of the smaller model complexes.[50] Also, different spectroscopic data from model systems and their natural paragons are collected and compared to gain deeper insights into the processes at the active site.[14,17,47,51,52]
One goal in the field of structural model complexes is the more detailed mimic of the coordination environment at the active site e.g. of the 2H1C facial triad in the low-valent iron(II)/(III) precursor complexes. Therefore, suitable $\{N_2O\}$-donor ligands are needed. To force a facial arrangement of the donors, the model ligands are usually tripodal. However, without the pre-organised structure of a protein, these tripodal ligands tend to form bisfacial complexes with two ligands attached to a single metal cation.[53] This blocks the three coordination sites that should be vacant for an accurate structural model of a 2H1C facial triad. Additionally, most anionic *O*-donors have the tendency to coordinate in a bridging mode.[53] To overcome these problems, there are several strategies like increasing steric demand or the bite-angle of the ligand.[35] Despite that, there is only a small number of complexes exhibiting a monofacial coordination by a tripodal $\{N_2O\}$-donor ligand.[35,53–57] Ligands that have been successfully used for monoligated model complexes analysed by SCXRD are listed in Figure 1.6.
To understand the reaction pathways of metalloenzymes, it is not only important to structurally characterise the resting state, but also to identify the reactive intermediates. Therefore, another important aspect of structural models is the synthesis and characterisation of

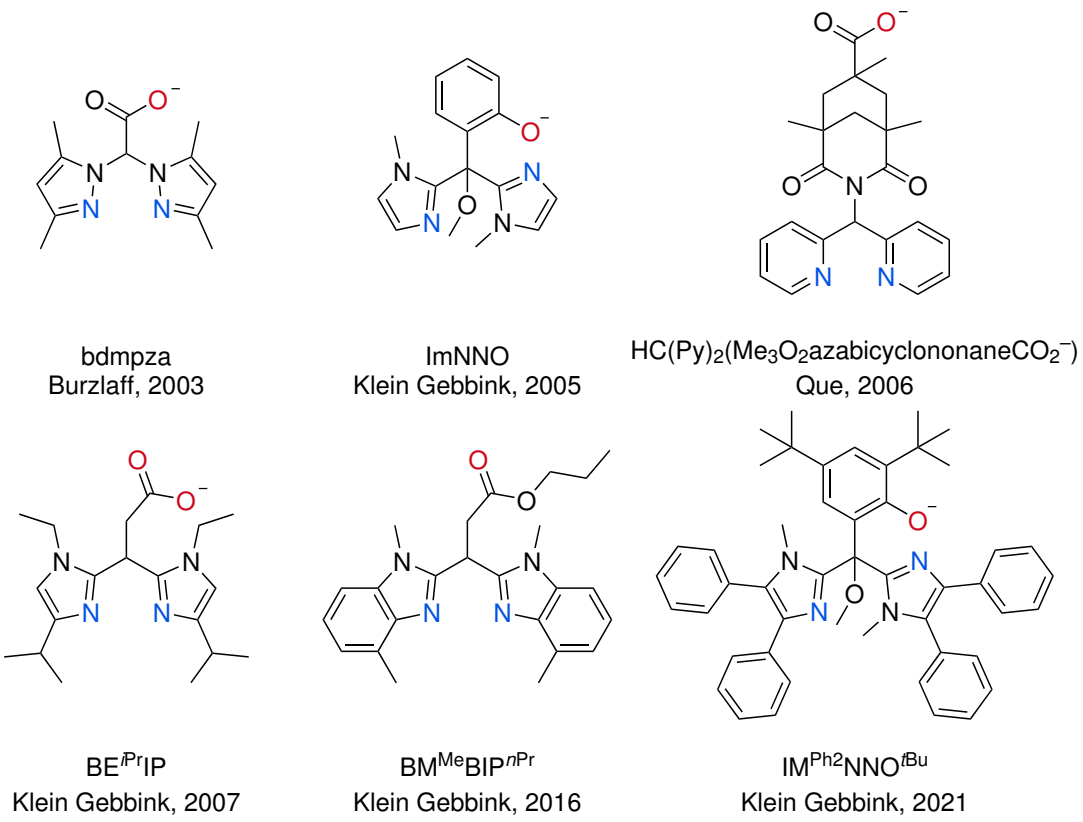

Figure 1.6: Tridentate tripodal $\{N_2O\}$-ligands for modelling 2H1C facial triad with mononuclear monoligated iron complexes characterised by SCXRD.[35,54–57]

the high-valent oxo intermediates. The first non-heme model complex that mimicked the high-valent iron(IV)oxo intermediate of mononuclear iron enzymes and that was structurally characterised by SCXRD was presented by Rohde *et al.* in 2003 (Cambridge Structural Database (CSD)[58] refcode: WUSJOJ).[50] They used the macrocyclic ligand 1,4,8,11-tetramethyl-1,4,8,11-tetraazacyclotetradecane (TMC) which enabled a very stable iron(IV)oxo complex ($S = 1$, at least 1 month @ −40 °C, Figure 1.7, top). There was already a spectroscopic hint (Mößbauer spectroscopy) of an iron(IV)oxo species of non-heme model complexes with a different ligand, but it formed in low yield and was not stable long enough to be crystallised.[59] This development was far behind the heme model systems where the first thoroughly spectroscopically characterised model complex was presented in 1981 by Groves *et al.*[60] In the very beginning, the aim of these model complexes was to prove that mononuclear high-valent iron-oxo species are also possible without a heme-based ligand.[50,61] Parallel to the discovery of the first iron(IV)oxo model complex in 2003, the first non-heme iron(oxo) species was spectroscopically identified in the non-heme enzyme taurine:α-ketoglutarate dioxygenase (TauD).[49,62,63] A second early example for an iron(oxo) species in a model system that was stable enough for crystallisation and characterisation via SCXRD was $[Fe^{IV}(O)(N4Py)]^{2+}$ (*N*,*N*-bis(2-pyridylmethyl)-*N*-bis(2-pyridyl)methylamine) in 2005 by Klinker *et al.*[64] Until today there are 19 structures of mononuclear iron(IV)oxo complexes listed in the CSD (04.07.2023, Table 1.2).[58] No structures of mononuclear non-

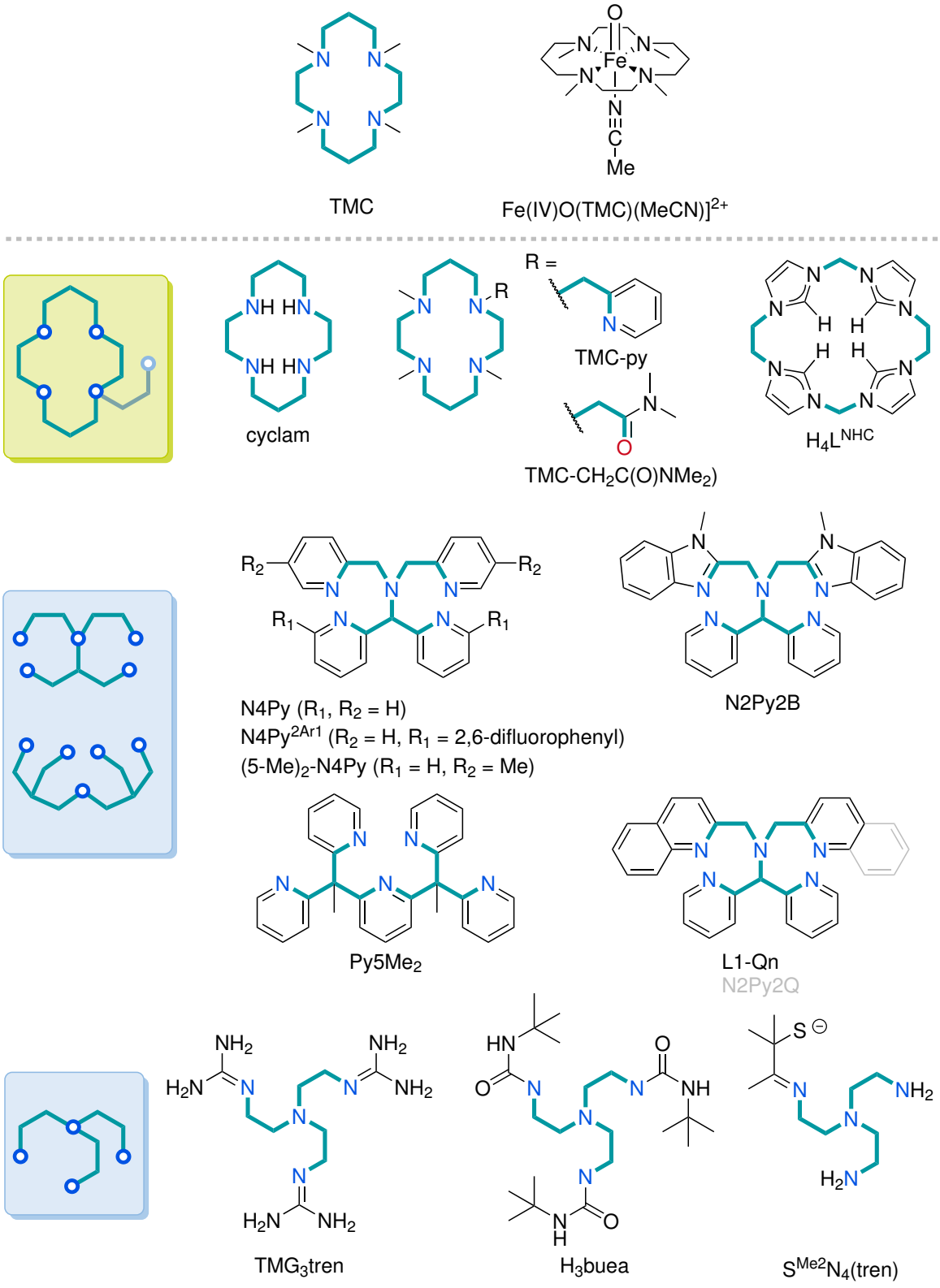

Figure 1.7: First non-heme iron(IV)oxo model complex characterised with SCXRD by Rohde *et al.* (top).[50] Ligands used for non-heme iron(IV)oxo model complexes listed in the CSD (bottom).[58] CSD refcodes and references are listed in Table 1.2. Schematically donor set-up (left) and ligand backbone highlighted in bold.

Table 1.2: Structures of mononuclear non-heme iron(IV)oxo complexes listed in the CDS and their corresponding Fe = O bond lengths and used ligands.[58] Ligands are depicted in Figure 1.7.

CSD refcode	Year	Fe = O [Å]	Ligand
WUSJOJ[50]	2003	1.646	TMC
PASREH[64]	2005	1.638	N4Py
YOHHEJ[65]	2008	1.667	TMC-py
ANEXAT[66]	2010	1.661	TMG_3tren
UPICUS[67]	2010	1.68	H_3buea
FESKEV[68]	2013	1.66	L^{NHC}
ZIYYEN[69]	2014	1.658	TMC-$CH_2C(O)NMe_2$
JUWCUB[70]	2015	1.624	TMC
IXICEZ[71]	2016	1.66	$N4Py^{2Ar1}$
JIKZUB[72]	2018	1.677	N2Py2Q
JILBAK[72]	2018	1.656	N2Py2B
TICHEV[73]	2018	1.65	TMC
TICHIZ[73]	2018	1.636–1.667	TMC
KOGZIS[74]	2019	1.656	$Py5Me_2$
KOGZOY[74]	2019	1.654	$(5\text{-Me})_2$-N4Py
KOGZUE[75]	2019	1.672	L^{NHC}
BUNBUK[76]	2020	1.703	cyclam
FEJCAC[77]	2022	1.603	$S^{Me2}N_4$tren
WAWMAM[78]	2022	1.642	L1-Qn

heme iron(V)oxo complexes were reported. A major part of the structures comprises macrocyclic ligands with four donors very similar to TMC or variations of the parent TMC ligand with an additional pendant fifth donor (Table 1.2, Figure 1.7). The other major class is supported by pentadentate ligands that are derived from N4Py. Only three examples are supported by tetradentate tripodal ligands (Table 1.2, Figure 1.7).
The number of iron-oxo species characterised only spectroscopically is far larger than the structurally characterised ones.[47,48] This is explained by the fact that many of the iron-oxo species are too unstable and reactive to be crystallised for structural characterisation.

Functional Model Complexes

The functional modelling of metalloenzymes is of even greater interest than structural modelling. Nature shows in an elegant way how reactions can be carried out effectively and selectively at ambient conditions. This has been motivation for chemists in the last decades to understand, recreate and extend this reactivity.[9,13,42,79,80]
When it comes to catalytically active model complexes, tridentate ligands allow a bisfacial coordination. As mentioned before, there is a risk of bisfacial coordination of the metal centre blocking labile coordination sites which are important for catalysis.[19] Therefore, many of the catalytically active biomimetic iron complexes are based on tetra- or pentadentate ligands. They shield more of the primary coordination sphere of the iron centre while still

leaving enough well designed space for labile co-ligands.

Although nature uses a mix of *N*- and *O*-donors in its iron enzymes, most ligands used in reactive high-valent iron-oxo model complexes are based solely on *N*-donor functions.[81,82] A reason for this may be that they are often easier to manipulate in their donor ability than *O*-donors. For example, the closest position where sterically or electronically manipulation of carboxylate groups is possible is at the α-carbon behind the carbonyl carbon atom which is three atoms away from the metal centre.[19] *N*-donors like amine, amide, imine or *N*-heterocycles offer a larger variety and manipulation options closer to the metal centre.[19] As mentioned before, anionic *O*-donors can act as bridging ligands.[53]

Park and Lee reviewed tri-, tetra- and pentadentate *N*-donor ligands for biomimetic non-heme iron complexes and tried with a taxonomic approach to categorise the ligands suitable for this kind of chemistry.[19] Their proposed "family tree" and classification of *N*-donor ligands is shown in Figure 1.8.

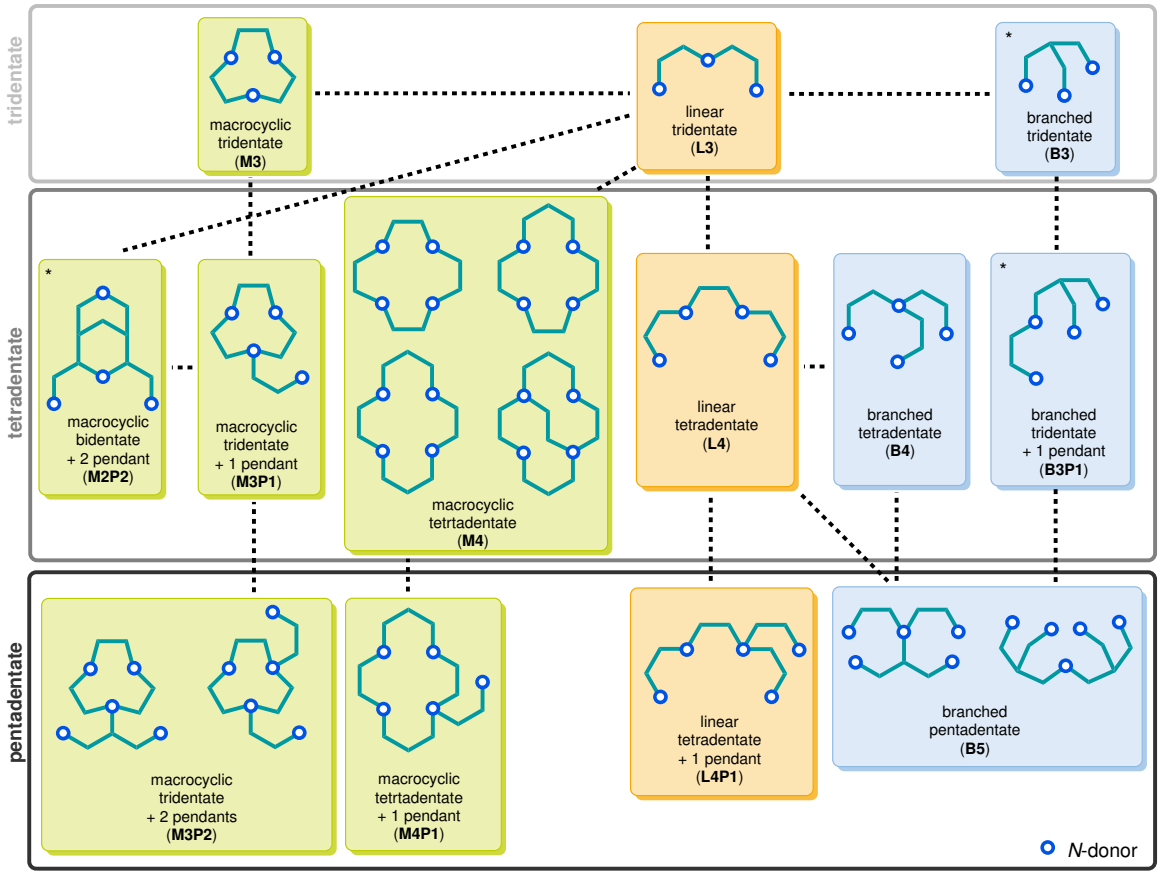

Figure 1.8: Schematic depiction of *N*-donor ligands for biomimetic iron complexes. L = linear (orange), M = macrocyclic (green), B = branched (blue), P = pendant; followed by number of donor atoms. Concept and nomenclature were adapted from Park and Lee and expanded (*).[19]

They divided the ligands in three main scaffolds: linear (L), macrocyclic (M) and branched (B). A number after the letter indicates the number of donor atoms included in this scaffold. Additional ligands that are branching from this scaffold are indicated as pendant (P, including their number). Different from the original by Park and Lee three scaffolds were added

to the illustration (marked with *): the branched tridentate ligand (B3) and the related branched tridentate + 1 pendant (B3P1) and the bidentate macrocyclic + 2 pendant (M2P2) scaffold. Especially the two branched scaffolds added are relevant in context of this thesis. Catalytically active examples for B3 are a complex with the ligand TP^{Ph2} (hydrotris(3,5-diphenylpyrazol-1-yl)borate) by the Que group, for B3P1 with the ligand $MeC(Py)_2BiPy$ by the Jurss group and for M2P2 complexes with bispidine based ligand systems of the Comba group (Figure 1.9).[83–85]

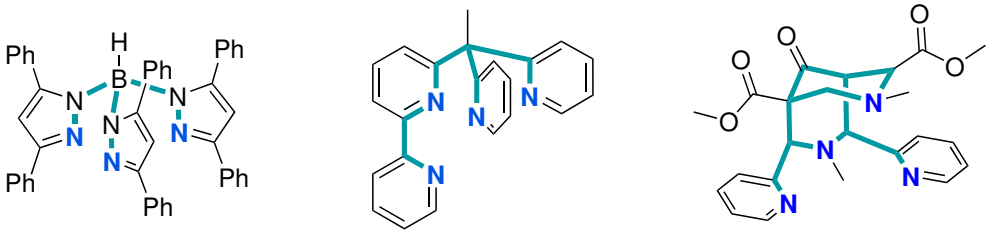

Figure 1.9: Examples for B3, B3P1 and M2P2 ligands.[83–85] Ligand backbone highlighted in bold.

One of the first functional model complexes was synthesised using the ligand tris(2-methylpyridyl)amine (TPA) by the group of Que (Figure 1.10).[86,87] Coordinating the iron centre in a tetradentate tripodal fashion, the ligand offers two labile coordination sites in *cis*-position to each other (*cis*-labile). The two *cis*-labile coordination sites are considered to be beneficial for some catalytic mechanisms.[19] For example, the catalytic activity can be enhanced with a co-ligand (e.g. water or carboxylic acid) in *cis*-position to the intermediate peroxide species and assists with activating the O – O-bond.[13,19,42,88] Similar effects of *cis*-control can be found in 2H1C based enzymes with water or α-ketogluterate involved in the catalytic cycle.[19,20]

Inspired by TPA, similar ligand scaffolds were used for other model complexes. Some of them were obtained by directly altering or extending the TPA ligand.[81] Others changed the connectivity of the pyridine donors as well as their number, but maintained the *cis*-labile coordination sites.[42] Examples for tetradentate ligands with a varying number of pyridine donors are shown in Figure 1.10. These also have been modified in order to obtain more efficient and selective catalysts. Prominent examples of ligands (and their variations) shown here have been studied extensively and include BPMEN,[42] PyTACN[90] and bispidine-based ligands,[89,91] each of which can also be seen as a ligand family in its very own.

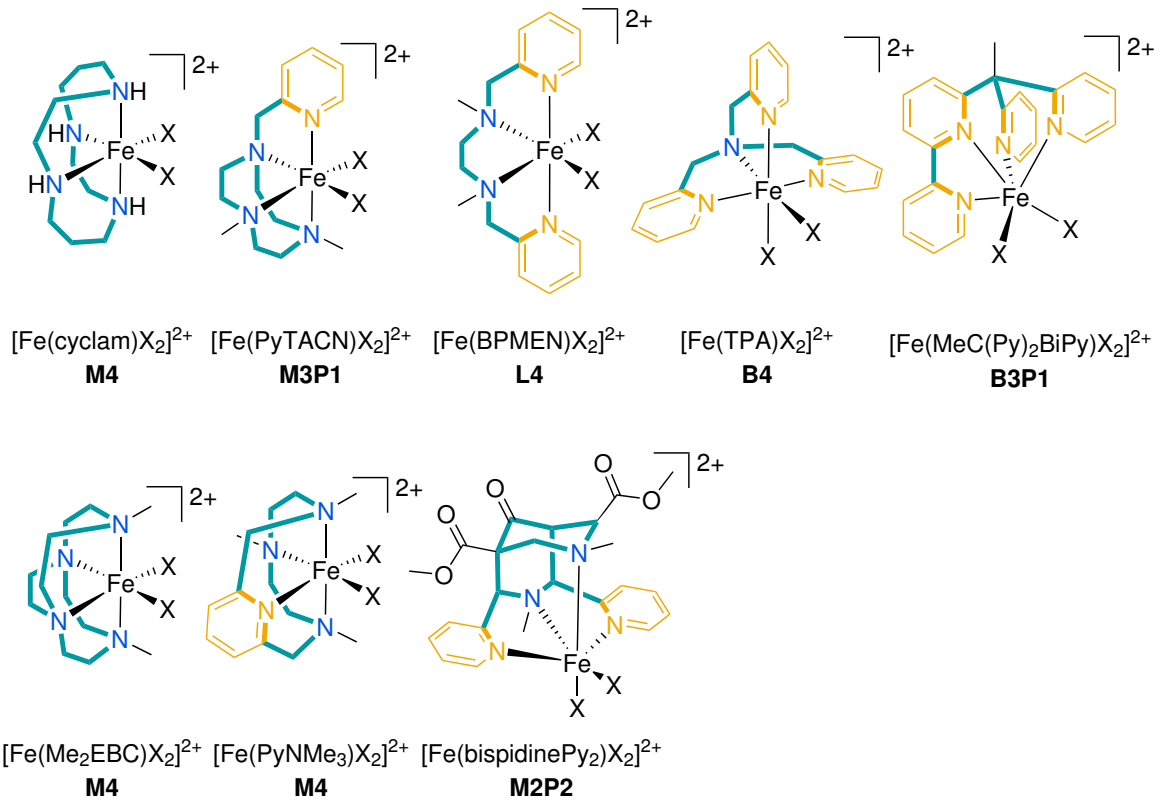

Figure 1.10: Tetradentate neutral ligand systems and their iron(II) precursor complexes with *cis*-labile coordination sites. Ligand backbone highlighted in bold, X denotes labile co-ligands. In case of neutral X ligands the complexes are charged 2+. Examples taken from Vicens *et al.* and Comba *et al.*[42,89]

1.2.2 Generating High-Valent Iron-Oxo Species

In nature, enzymes are able to utilise molecular oxygen for the generation of high-valent iron-oxo species. For model complexes, this is often not possible so there is a need for an oxidation agent. There are single oxygen atom donors like iodosylbenzene (PhIO)/1-(*t*-butylsulfonyl)-2-iodosylbenzene (sPhIO), peroxy acids (e.g. *m*-chloroperoxybenzoic acid (mCPBA)), $KHSO_5$, ozone, NaOCl/NaOBr, R_3NO or NO_2 (Figure 1.11).[92–94] Another option is the use of hydroperoxides (e.g. H_2O_2).[92]

Reaction conditions are low temperatures or room temperature and the reaction medium can be organic solvents or water.[94]

Spin State of Iron(IV)oxo Complexes

Two spin states have been reported for iron(IV)oxo complexes: $S = 2$ high-spin (HS) and $S = 1$ intermediate-spin (IS). The iron(IV)oxo intermediate in natural non-heme enzyme displays a HS ($S = 2$) spin state, whereas most iron(IV)oxo model complexes exhibit an IS ($S = 1$) state.[17,47,50,51,91,92] Examples for octahedral iron(IV)oxo model complexes with $S = 1$ are $[Fe^{IV}O(TPA)(MeCN)]^{2+}$ and $[Fe^{IV}O(N_4Py)(MeCN)]^{2+}$ (Figure 1.12). There

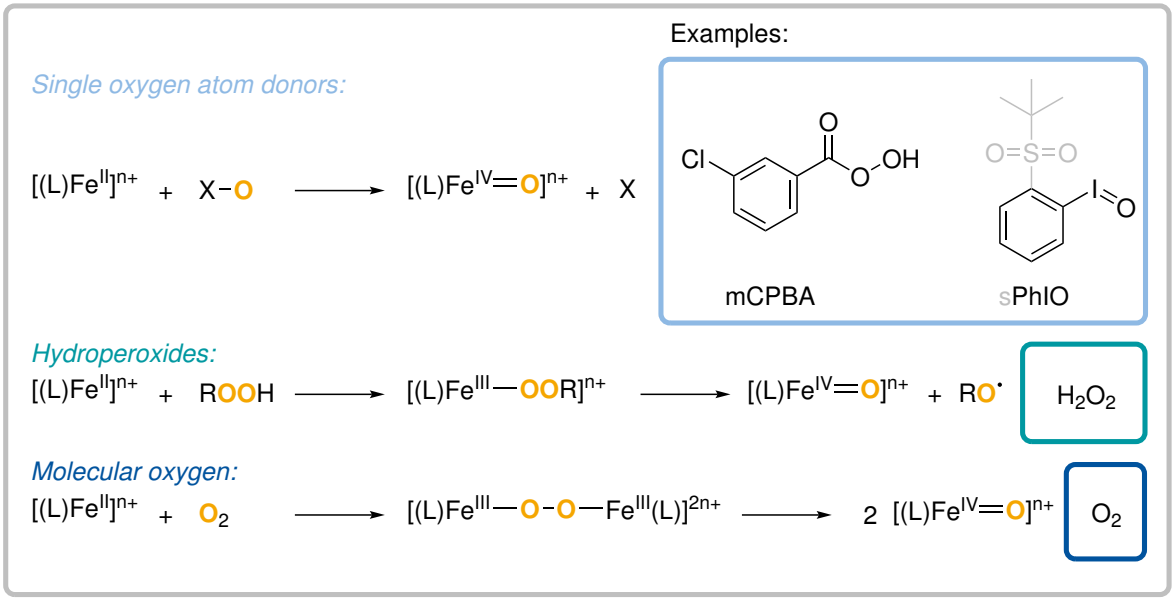

Figure 1.11: Oxidation agents for generating iron(IV)oxo complexes from iron(II) precursor complexes. Reactions adapted from Nam.[92]

are two strategies for adapting the HS ($S = 2$) state with model complexes to mimic the metalloenzymes. Both address the energy level of the d_{xy} and $d_{x^2-y^2}$ orbitals. The first strategy uses bulky tripodal ligands that allow a trigonal bipyramidal coordinated complex with a C_3-symmetric ligand environment. In this coordination geometry, the d_{xy} and $d_{x^2-y^2}$ are degenerated which is favouring a HS ($S = 2$) state.[51] Examples are the complexes $[Fe^{IV}O(TMG_3tren)]^{2+}$ or $[Fe^{IV}O(tpa^{Ph})]^{2+}$ (Figure 1.12).[66,98] The second strategy is to decrease the energy gap between the d_{xy} and $d_{x^2-y^2}$ orbitals with maintaining the (pseudo) octahedral geometry. This was successfully done with the quinoline variant of the TPA ligand which is tris(2-quinolylmethyl)amine (TQA).[51,97] The introduction of the quinolines, which additionally "substitute" the α-position of the *N*-donor, weakens the ligand field in the $[Fe^{IV}O(TQA)(MeCN)]^{2+}$ complex, resulting in a decreased energy gap that enables an $S = 2$ state.[97]

Spin State of Iron(V)oxo Complexes

Apart from iron(IV)oxo complexes, iron(V)oxo species can also be generated. These might be relevant in some metalloenzymes like the Rieske oxygenases, but have not been detected so far.[11] Iron(V)oxo species have been identified in mononuclear non-heme model systems, but are rare due to their high reactivity.[11] In the CSD (04.07.2023) there is no entry of an iron(V)oxo model complex.[58]

Reaction conditions determine whether a homolysis towards an iron(IV)oxo or heterolysis to iron(V)oxo species is taking place (see Figure 1.5). For several ligand systems, iron(IV)oxo as well as iron(V)oxo species have been spectroscopically characterised.[79] There are three typical examples where iron(V)oxo species have been observed more frequently. The first

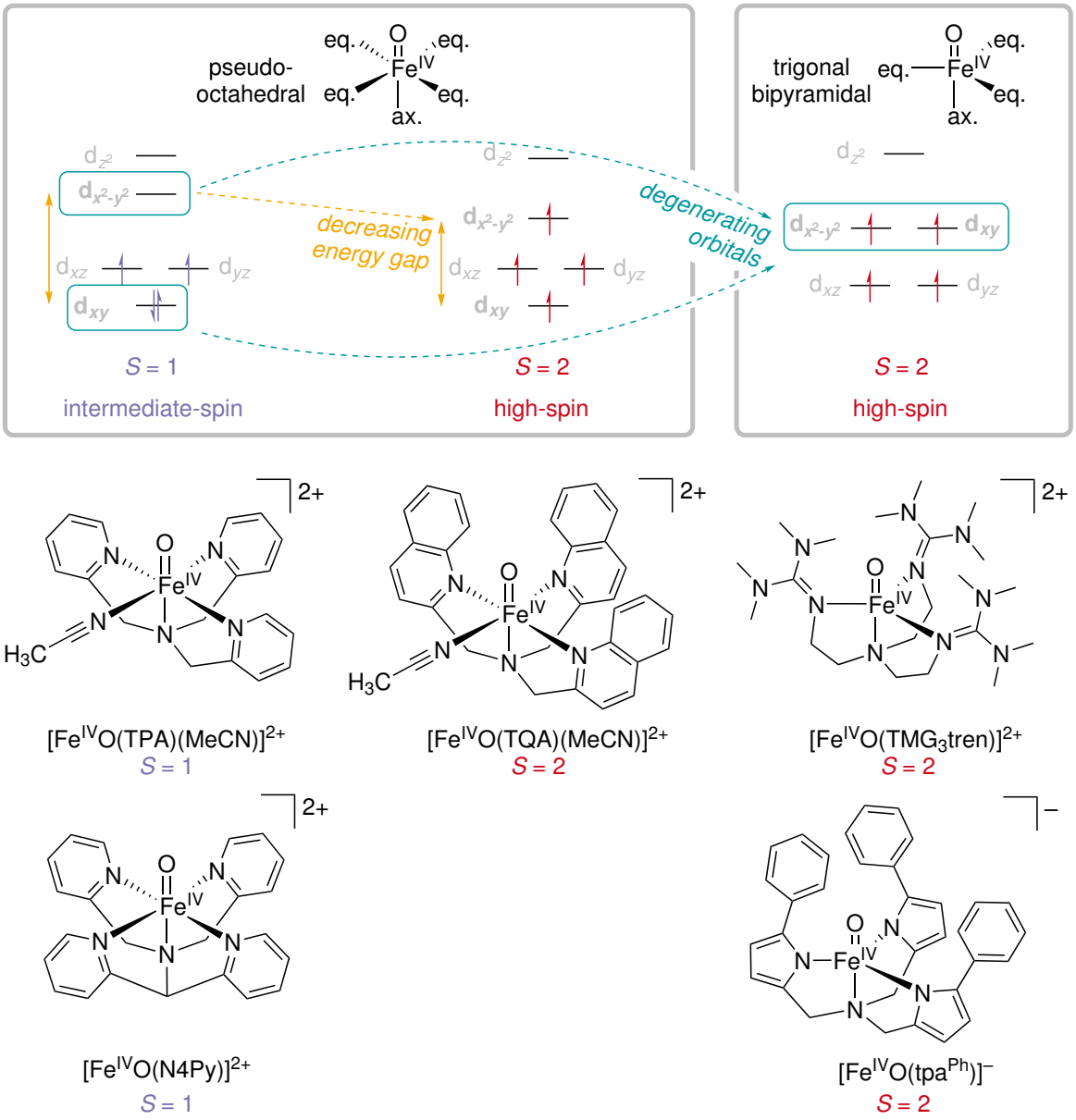

Figure 1.12: Top: Molecular orbital diagram for the HS and IS state of iron(IV)oxo species in an (pseudo) octahedral or trigonal bipyramidal coordination geometry and strategies to obtain a HS state instead of an IS state. Figure cumulated from different references.[17,47,51,91,95] Bottom: Selected examples of iron(IV)oxo complexes with HS (trigonal bipyramidal or octahedral geometry) and IS state (octahedral geometry). References sorted by ligands: TPA,[61,96] TQA,[97] TMG_3tren,[66] N4Py[64] and tpa^{Ph}.[98]

one is species with tetraamido macrocyclic ligands (TAML, Figure 1.13) which were the first model systems where an iron(V)oxo species was detected.[99] Depending on the reaction conditions, iron(IV)- or iron(V)oxo species can be stabilised by TAML (derived) ligands.[11,99]

The other two typical cases of iron(V)oxo are observed in combination with H_2O_2 as oxidant and a catalytic oxidation mechanism assisted by water (e.g. PyTACN) or carboxylic acid (e.g. TPA, $PyNMe_3$, (*S*,*S*)-PDP(^{NMe2})) of complexes with *cis*-labile coordination sites (Figure 1.13).[11,79]

In terms of spin state, two different iron(V)oxo species have been observed: low-spin (LS, $S = 1/2$) and HS ($S = 3/2$).[11,100–102] Examples for both are shown in Figure 1.13. However, high reactivity, low formation yield and transient nature of formed species make iron(V)oxo species challenging to observe spectroscopically.[79]

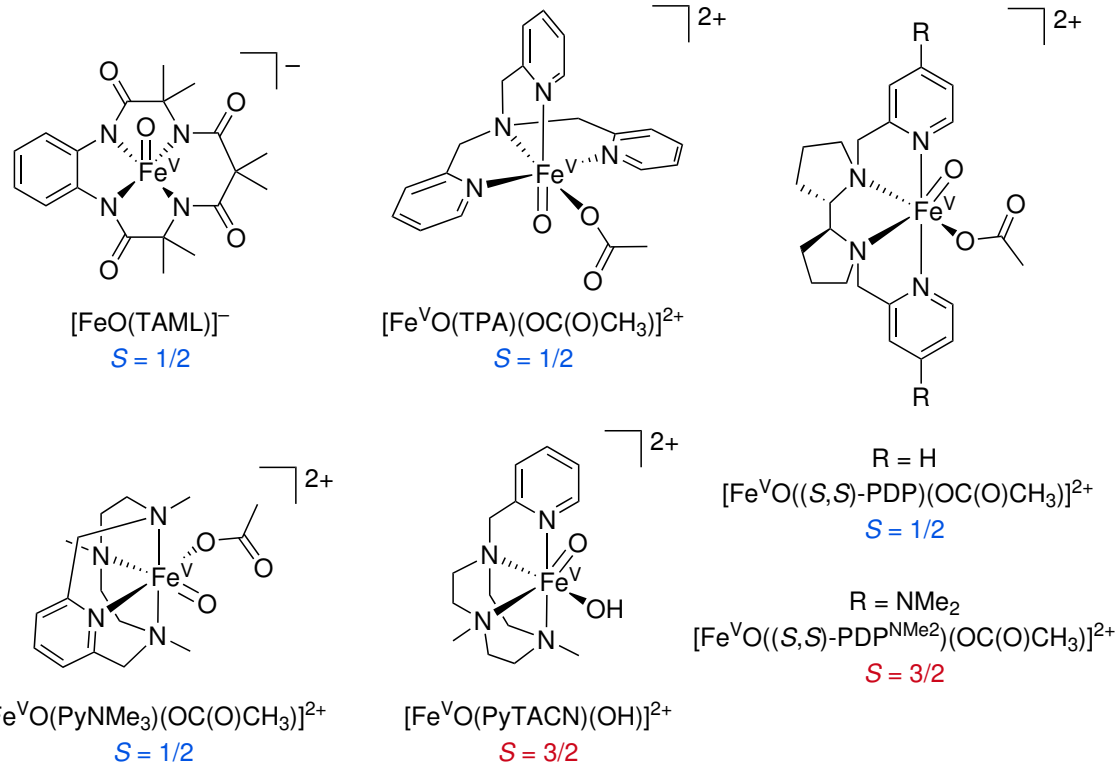

Figure 1.13: Selected examples of proposed structures for iron(V)oxo species with LS ($S = 1/2$) or HS ($S = 3/2$) state. References sorted by ligand: TAML,[99] TPA,[103] $PyNMe_3$,[104] PyTACN,[105] PDP,[106] PDP^{NMe2}.[101]

1.2.3 Experimental Methods for Observation of High-Valent Iron-Oxo Species

The binding of oxygen towards an iron centre changes the UV/Vis absorption spectra of the enzyme or complex. Hence, UV/Vis spectroscopy is one key method to investigate the nature of an high-valent iron-oxo species. Values of absorption maxima for model systems and natural enzymes are listed in Table 1.3 as well as other characteristic experimental values for these species.

Structure determination via SCXRD gives the most clear evidence of the existence an iron-oxo species. However, only a few model systems have half-life times long enough to be crystallised. If SCXRD is not possible, the important Fe = O bond length can be obtained from extended X-ray absorption fine structure (EXAFS) measurements.[47,61] Furthermore, the $\tilde{\nu}$(Fe = O) can be observed with Fourier transform infrared (FT-IR) or resonance Raman spectroscopy.[47] Also, mass spectrometry is an important tool to identify high-valent iron-

Table 1.3: Ranges of values obtained by different experimental methods to identify high-valent iron-oxo species of mononuclear non-heme systems. Values are cumulated from reviews and the CSD.[58]

Method	Physical quantity	$Fe^{IV}=O$			$Fe^{V}=O$
		Model complex		Natural enzymes	Model complex
		$S=1$	$S=2$	$S=2$	$S=1/2$
UV/Vis[11,47]					
	λ_{max} [nm]	435–890	320–412, 803–900	318	410–490, 613–780
	ε [L mol^{-1} cm^{-1}]	100–1200	500–9800, 260–290	1500	4000–5400, 430–4200
SCXRD[58]					
	Fe=O [Å]	1.60–1.70		–	–
EXAFS[11,47]					
	Fe=O [Å]	1.64–1.70	1.62–1.65	1.62	1.58–1.63
IR/Raman[11,47]					
	$\tilde{\nu}$(Fe=O) [cm^{-1}]	752–854	799–850	821	798–817
Mößbauer[11,47,51]					
	δ [mm s^{-1}]	−0.04–0.22	0.02–0.38	0.22–0.30	−0.46–0.10
	ΔE_Q [mm s^{-1}]	−0.22–3.95	−1.05–0.58	−1.09–1.27	−0.5–4.27

oxo species.[50] Especially cryospray-ionisation mass spectrometry is important since a lot of the species used as model systems have longer lifetimes at lower temperatures.[71,107,108] The nature of spin state and the oxidation state of the system can be investigated with Mößbauer and electron paramagnetic resonance (EPR) spectroscopy.[47,50]

1.2.4 Catalytic Oxidation Reactions

Like the natural archetypes, high-valent iron-oxo model complexes can be capable of catalytic substrate oxidation. Examples of reactions performed by biomimetic non-heme iron(IV)oxo species are shown in Scheme 1.1. This includes aliphatic/aromatic hydroxylation, alkylaromatic/alcohol oxidation, alkene epoxidation, N-dealkylation and P-/S-oxidation.[94] In particular, the C – H functionalisation reactions are noteworthy because C – H bonds are quite inert and are considered strong covalent bonds. Common substrates in catalytic studies have a bond dissociation energy (BDE) in the range of 77 to 99 kcal/mol, with cyclohexane typically used as a representative for stronger C – H bonds (BDE: 99.3 kcal/mol).[95,109,110] Conventionally, these molecules are oxidised with strong oxidising agents (e.g. heavy metal oxides or dioxiranes) under harsh reaction conditions, resulting in over-oxidation and large amounts of waste.[11,111] Therefore, a selective, efficient and atom-economical oxidation method for these molecules is of great interest to the chemical industry, which relies on hydrocarbon feedstocks where the C – H bond needs to be functionalised. Mild reaction conditions and the use of complexes with a readily available and non-toxic metal ion are

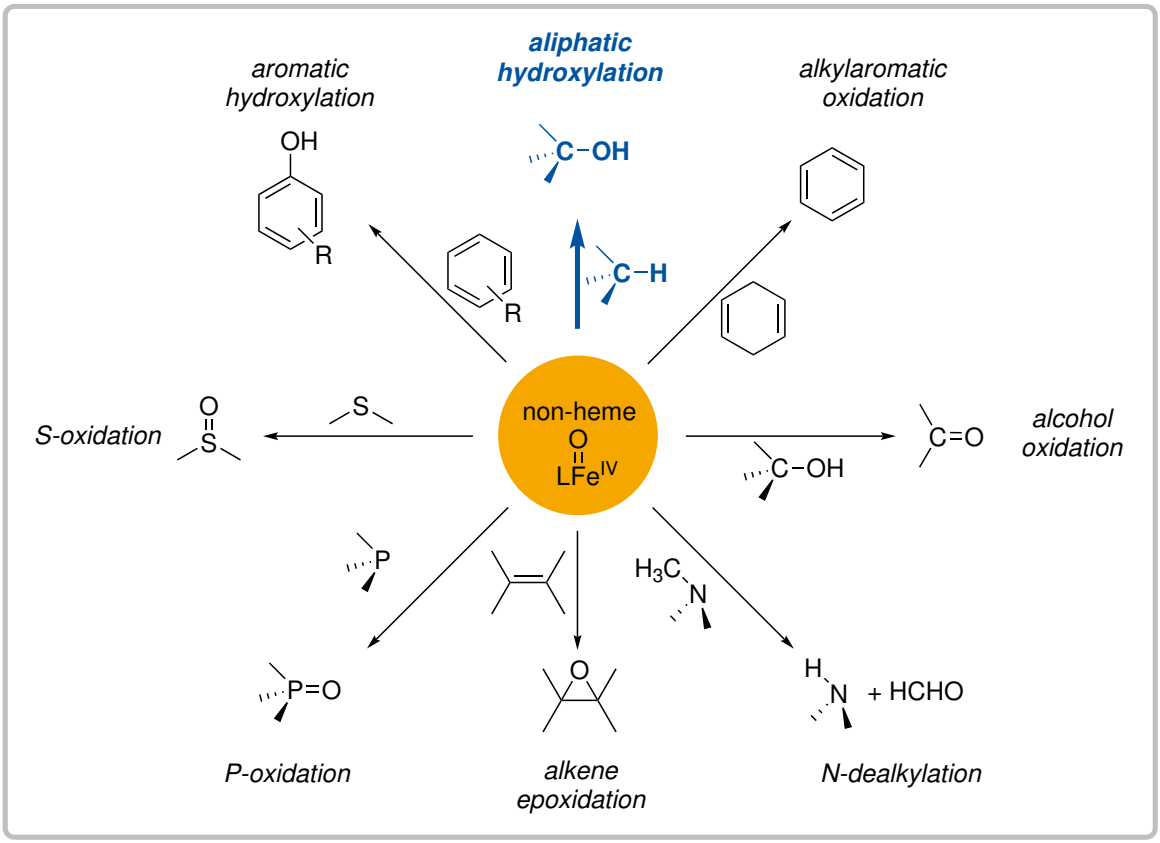

Scheme 1.1: Oxidation reactions performed by non-heme iron(IV)oxo model complexes. Scheme adapted from Nam *et al.*[94]

desirable.[9,11,79,111] The development and use of biomimetic complexes, which mimic the efficient and selective reactions under mild reaction conditions of their natural counterparts, aims to overcome this problem.[111]

While the iron-oxo species may be able to mildly oxidise the organic substrate, the generation of the iron-oxo still requires aggressive oxidants. These may react with the organic substrate directly albeit in a much less selective manner. This influence has to be considered in the substrate scope and it has to be investigated thoroughly in control reactions.

Metal-based oxidants that are formed by the iron complex would be $Fe^{III}-OOH$, $Fe^{IV}=O$ or $Fe^{V}=O$ species. Contrasting this, powerful but unselective radicals would be $HO^{\bullet}$ and $RO^{\bullet}$. They might originate from the reaction between iron and peroxides, which is known as Fenton's Chemistry:[112]

$$Fe^{2+} + ROOH \longrightarrow Fe^{3+} + RO^{\bullet} + OH^{-}$$
$$Fe^{3+} + ROOH \longrightarrow Fe^{2+} + ROO^{\bullet} + H^{+}$$

Iron complexes with *cis*-labile coordination sites have been proven to be beneficial to circumvent Fenton reactions for reactions with H_2O_2.[111] In principle, the oxidation of C – H bond in alkanes by an iron oxidant consists of two steps: 1. the C – H bond cleavage

initiated by a form of oxidant and 2. the formation of an C – O bond:[112]

$$\mathrm{R{-}H + oxidant} \xrightarrow{\text{1. C–H bond cleavage}} \mathrm{R^{\bullet} + Fe{-}OH} \xrightarrow{\text{2. C–O bond formation}} \mathrm{R{-}OH}$$

The timing of these two reaction steps is crucial and is connected to the lifetime of the alkyl radical. An almost concerted execution of the two steps, is observed for short-lived alkyl radicals and metal-based oxidants. A rapid rebound of the alkyl radical with the metal centre takes place to form the C – O bond for the alcohol product. A long separation in time between the two steps results in a long-lived alkyl radical, which can be trapped by O_2 in solution. The reaction of the alkyl radical with molecular oxygen is known as Russell-type termination and results in equimolar amounts of alcohol and ketone product.[112]

$$\mathrm{RCH^{\bullet} + O_2 \longrightarrow RCHOO^{\bullet}}$$
$$\mathrm{RCHOO^{\bullet} + RCHOO^{\bullet} \longrightarrow RCH{-}OH + RC{=}O + O_2}$$

To determine the lifetime of the radical, the alcohol to ketone product ratio can be examined. A widely used substrate for this reaction is cyclohexane.[111,112] It allows easy product identification as it yields six chemically identical carbon atoms and therefore only two main oxidation products are expected: cyclohexanol (***A***) and cyclohexanone (***K***, Scheme 1.2).

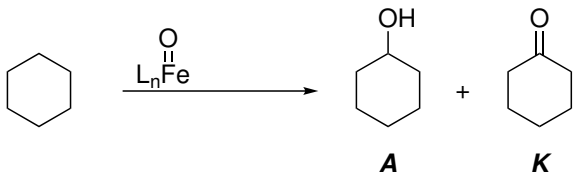

Scheme 1.2: Catalytic oxidation of cyclohexane to cyclohexanol (***A***) and cyclohexanone (***K***).

The product ratio of ***A*** and ***K*** is determined for these reactions. On one hand, equal amounts of alcohol and ketone ($\boldsymbol{A}/\boldsymbol{K} = 1$) are obtained when the radical has a long lifetime and reacts directly with molecular oxygen to a alkylperoxyl radical which leads to a Russell-type reaction termination. If the lifetime on the other hand is short, there is a rapid rebound to the metal centre, the alcohol is the primary product ($\boldsymbol{A}/\boldsymbol{K} >> 1$). However, lower amounts of ketone are formed due to further oxidation of the alcohol.[112]

The regioselectivity between C – H bonds of tertiary and secondary carbon atoms provides further information about the nature of the oxidant and its strength.[79,112] For a metal-based oxidant, the attack of the weaker C – H bond of tertiary carbon atoms should be preferred, while a powerful long-lived radical is less selective.[79] A common substrate is adamantane since it provides four equal tertiary carbon atoms and six equal secondary carbons.[111,112] The number of main oxidation products is limited to three: 1-adamantanol (3°-***A***), 2-adamantanol (2°-***A***) and 2-adamantanone (2°-***K***, Scheme 1.3). For a metal-based oxidant, high amounts of 1-adamantanol (3°-***A***) and low amounts of the secondary carbon

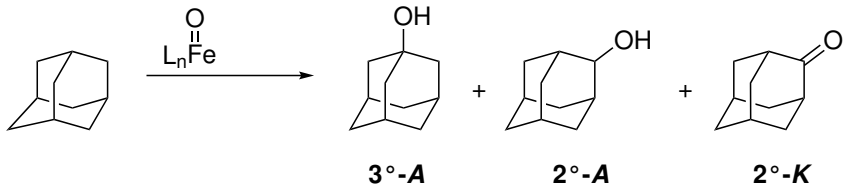

Scheme 1.3: Catalytic oxidation of adamantane to 1-adamantanol (3°-***A***), 2-adamantanol (2°-***A***) and 2-adamantanone (2°-***K***).

products 2-adamantanol (2°-***A***) and 2-adamantanone (2°-***K***) should be observed. It is expressed by the 3°/2° ratio (Equation 1.1).

$$3^\circ/2^\circ = 3 \cdot \frac{3^\circ\text{-}\boldsymbol{A}}{2^\circ\text{-}\boldsymbol{A} \; + \; 2^\circ\text{-}\boldsymbol{K}} \tag{1.1}$$

The factor of 3 is taking the higher number of secondary C – H bonds into account.[112]
A second test for the strength of the oxidant is the determination of the kinetic isotope effect (KIE) by comparing the oxidation of weaker C – H bonds to stronger C – D bonds ($\Delta \sim 1.7$ kcal/mol).[79,112] Hence, a metal based oxidant is expected to preferentially oxidise the non-deuterated substrate.[112] Cyclohexane and the deuterated counterpart cyclohexane-d_{12} are the substrates of choice (Scheme 1.4). A non-heme high-valent iron-oxo complex, that is active in catalytic C – H oxidation reactions, exhibits a high ***A***/***K*** ratio (≥ 5), under aerobic conditions), a high 3°/2° ratio (> 15) and a high KIE (> 2).[79]

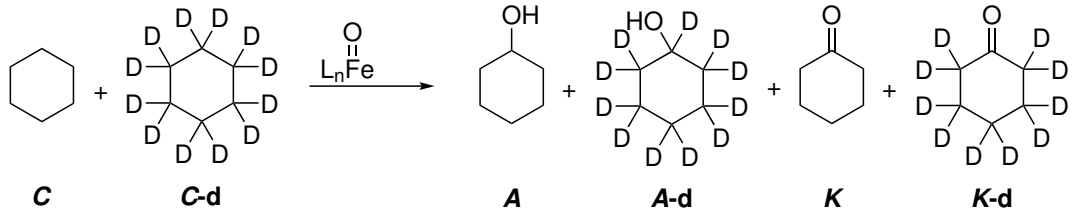

Scheme 1.4: Catalytic oxidation of cyclohexane (***C***) and cyclohexane-d_{12} (***C*-d**) to cyclohexanol (***A***), cyclohexanol-d_{11} (***A*-d**), cyclohexanone (***K***) and cyclohexanone-d_{10} (***K*-d**).

However, cyclohexanol and adamantanol are not the products that are industrially relevant but these reactions are only three examples of model reactions used to shed light on the oxidation reaction mechanism and the role of the iron complex. These are only some of the basic mechanistic tests and for a closer mechanistic investigation further experiments are needed.[79,111]
Due to the large number of possible oxidants and different reaction conditions, it is difficult to name the most selective and efficient reported C – H oxidation catalyst, but two effects regarding the ligand design and the resulting reactivity can be briefly discussed here.
For pyridine-based ligands like TPA, BPMEN and PyTACN, substitution in the α-position of the pyridine has a big influence on the catalytic abilities (Figure 1.14). In the C – H hydroxylation of cyclohexane, the ***A***/***K*** ratio and the turn over number (TON) drop sig-

nificantly, when two or three of the pyridine moieties of the TPA or BPMEN ligands are α-substituted.[11] The methylated PyTACN derivate 6Me-PyTACN, which only has one α-pyridine position for methylation, shows no significant changes in C – H hydroxylation of cyclohexane.[90,113] This is in line with the results for the mono-methylated TPA or BPMEN derivates.[11]

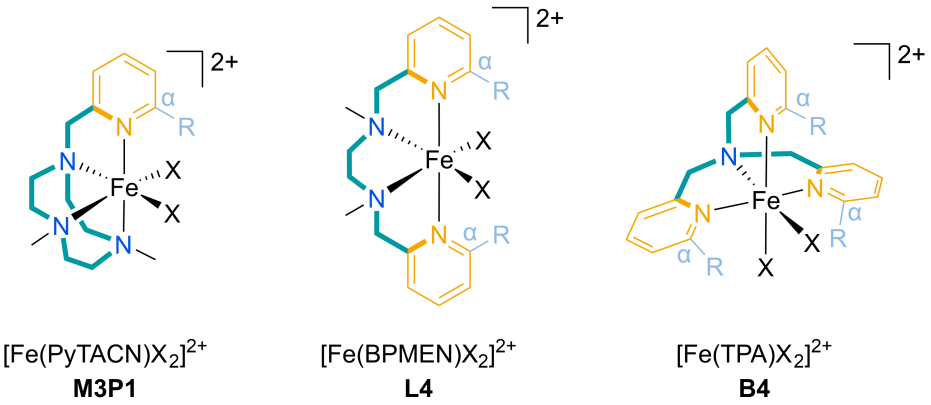

Figure 1.14: Possible α-substitution positions at pyridine moieties on PyTACN, BPMEN and TPA iron(II) complexes. Ligand backbone highlighted in bold, X denotes labile co-ligands. In case of neutral X ligands the complexes are charged 2+. Examples adapted from Dantignana *et al.*[11]

Modifications in α-position can have an electronic influence besides a steric influence. An example for this is the comparison between the iron(IV)oxo compounds with TPA and TQA ligands. As discussed before, the quinoline donors of TQA are rather weak field ligands than the pyridines in TPA and enable an $S = 2$ iron(IV)oxo species instead of an $S = 1$ (see Figure 1.12).[51] The TQA-based iron(IV)oxo complex is one of the fastest catalysts in the C – H oxidation field and the $S = 2$ spin state is the same as in natural enzymes. The TQA-based iron(IV)oxo complex is able to oxidise cyclohexane at −40 °C, whereas the TPA-based iron(IV)oxo species does not show any reaction with cyclohexane at this temperature.[114]

Overall, there are many factors influencing the reaction pathways in reactions involving high-valent iron-oxo species. The potential oxidants are mostly iron(IV) or iron(V) species which can be found in different spin states. Besides the used ligand, the nature of the oxidation agent and auxiliary molecules in the catalytic cycle like water or carboxylic acid enable different reaction pathways which are not fully understood. The more catalysts are developed, the more knowledge is gained about which ligand can stabilise iron in which oxidation states and in which catalytic transformations it can be used.[11,19,42,79]

1.3 Spin State Switching Behaviour

Besides applying iron(II) complexes as precursor species for catalytic active iron complexes, they may show an additional attractive feature: spin state switching. The occupation of

different spin states is usually observed for octahedral complexes of 3*d* metal cations with electronic configurations of d^4–d^7. They can exist in high-spin (HS) or low-spin (LS) state depending on the strength of the provided ligand field (Figure 1.15).[115] The stronger the ligand field, the more likely a stabilisation of a LS state becomes while a weak ligand field induces the occupation of a HS state. In case of an intermediate ligand field, reversible switching between these two bistable states may be enabled.[116,117] Triggering the switch of the spin state in such compounds requires an external stimulus which can be physical – *change of temperature/pressure/magnetic field/electric field/light irradiation* – or chemical – *ligand exchange, complex dissociation, chemical reaction at the ligand or (non-)covalent solvent interactions.*[116,118–121]

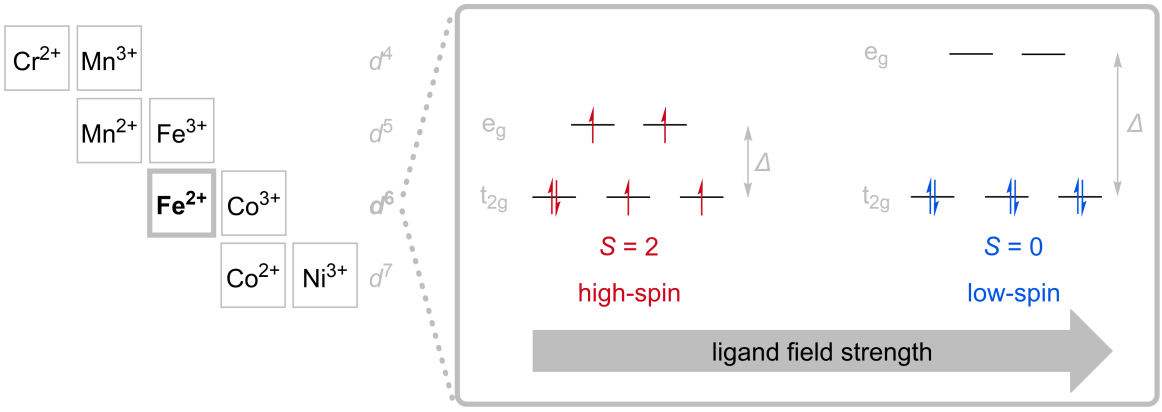

Figure 1.15: Examples for d^4–d^7 metal ions (left) and schematic HS vs. LS electron configuration in correlation with ligand field strength for d^6 metal ions (right).

Switching between HS and LS state can be observed in the solid state and in solution.[122] Since the framework conditions in these two phases are different, the spin switching behaviour can be exclusive to one of these phases.[120,121] In the solid state, the term for switching between two spin states is usually spin crossover (SCO). The SCO behaviour can be abrupt (with hysteresis), in multiple steps or incomplete.[118] Cooperative effects induced by crystal packing, co-crystallised molecules and intermolecular interactions are playing an important role in the solid state.[118,120] In contrast, a distinction is made between two different switching behaviours in solution where the differentiation is based on whether the coordination number changes or not. If the coordination sphere is unchanged during the spin switching event, the phenomenon is termed as SCO. Typical for an SCO in solution is a gradual transition between the two states which follows a Boltzmann distribution.[123,124] This gradual change is caused by the lack of cooperative effects in solution. Influences on the SCO process are based on e.g. ligand field strength or the nature of the solvent.[120,121] If the switching of the spin state in solution is caused by a change of the coordination number, it is called coordination-induced spin state switch (CISSS). It can be influenced by factors like ligand stoichiometry or choice of solvent and counterions.[116,123,125] When

investigating switching behaviour in solution, it can be challenging to verify the nature of the coordination sphere for both states to be able to clearly differentiate between SCO and CISSS.[126]

Nowadays, the most studied ion for SCO is iron(II) with an octahedral $\{N_6\}$-coordination sphere. It exhibits the largest possible difference between HS (four unpaired electrons, paramagnetic) and LS state (no unpaired electrons, diamagnetic; Figure 1.15) in terms of structure and magnetic response.[119,123,127] Structurally, the LS and HS variant of a iron complex can be distinguished by their Fe – N bond lengths: for LS they are typically below 2.0 Å (~ 1.8–2.0 Å) and for HS above 2.0 Å (~ 2.0–2.2 Å) which is a difference of about 10 %.[119] However, this spin state switching feature can also complicate the study and development of iron complexes designed for different applications.

In general, the simplest application for which SCO complexes can be considered is as molecular switches. Other fields where SCO compounds are discussed in terms of potential applications are molecular electronics, data storage, display devices, non-linear optics and photomagnetism.[128]

1.4 Continuous Shape Measure

Iron(II) complexes usually show coordination numbers of four to six. For four- and five-fold coordination, there are the geometry indices τ_4 and τ_5, respectively, which can characterise the coordination geometry in a single and easily understandable parameter.[129,130] The τ_4 value describes whether a fourfold coordination sphere is square planar or tetrahedral. The τ_5 value distinguishes square pyramidal from trigonal bipyramidal coordination spheres in penta-coordinated complexes. However, the coordination number of six, which is very common for iron complexes, cannot be described with such a value. An instrument that is able to describe geometries of six-fold coordinated complexes in a convenient manner is the continuous shape measure (CSM) as provided in the software SHAPE.[131,132] With CSM the N atoms of a complex (central metal atom and donor atoms) and the vertices of a polyhedron (or polygon) of an ideal coordination geometry are described by a set of vectors. The coordinates of the vectors of the perfect polyhedron ($\overrightarrow{P}_k, k = 1, 2, ...N$) are optimised so that the distance between the coordination polyhedron ($\overrightarrow{Q}_k, k = 1, 2, ...N$) and the perfect polyhedron are minimised. The shape measure ($S(G)$) can be calculated by Equation 1.2, where Q_0 is the vector of the geometrical centre of the coordination environment in the complex.[132]

$$S(G) = \frac{\Sigma_{k=1}^{N} |Q_k - P_k|^2}{\Sigma_{k=1}^{N} |Q_k - Q_0|^2} \cdot 100 \tag{1.2}$$

Theoretically values of $0 \leq S(G) \leq 100$ are possible whereby 0 indicates the real and the ideal coordination polyhedron to be identical. Consequently, larger values indicate deviation from the ideal geometry. This CSM is also possible for different coordination numbers, so

that values for geometries of four- and five-fold coordination modes are available.[133,134] An overview of the ideal polyhedra and polygons that geometries can be compared to by using SHAPE are presented in Figure 1.16. The reference geometries are spherical and have equidistant edges if possible. For the polyhedra where more than one alternative exists, the spherical version comprises equidistant bond lengths to the central atom, while the

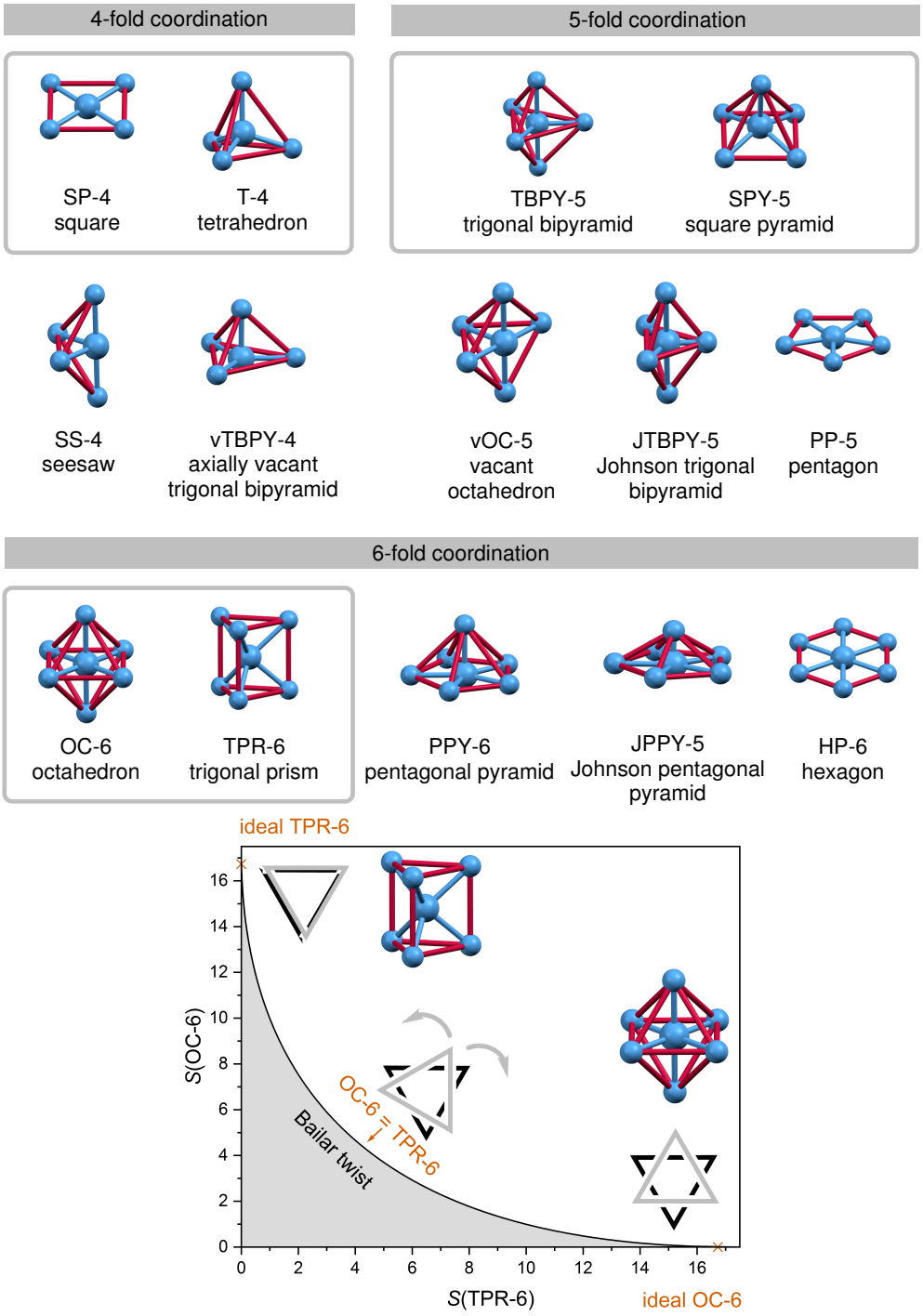

Figure 1.16: Representation of ideal coordination geometries as implemented in SHAPE (top). Interconversion of ideal octahedron and ideal trigonal prism along the Bailar twist and corresponding behaviour of S(OC-6) and S(TPR-6) values (bottom). Atoms and bonds in blue, outlines of geometries in red. Polyhedra: equidistant bonds to the central atom; Johnson type polyhedra: equidistant edges.

Johnson version of the polyhedra exhibits equidistant edges. Equidistant bond lengths are typical geometries for metal complexes and equidistant edges for boranes or clusters.[131] In case of distinguishing six-fold coordination geometries in terms of octahedron (OC-6) or trigonal prism (TPR-6), the intermediate value between both structures is S(OC-6) = S(TPR-6) = 4.42. A perfect octahedron would be S(OC-6) = 0 & S(TPR-6) = 16.73 and a perfect trigonal prism S(OC-6) = 16.73 & S(TPR-6) = 0 (Figure 1.16, bottom).[132] The interconversion of an ideal octahedron to an ideal trigonal prism and vice versa, in which only two opposing faces of the octahedron are rotated, is known as Bailar twist represented as black line in Figure 1.16 (bottom). Since this is the ideal distortion, any additional distortions, e.g. Jahn-Teller or trigonal antiprismatic distortions, would lead to larger values in the pair of S(OC-6) and S(TPR-6) values. Thus, only values outside the grey area in the left corner are obtained.[132]

2 Thesis Outline

2.1 Objectives

The aim of this thesis is the investigation of the coordination chemistry of iron(II) complexes with tri- and tetradentate ligands with *N*- and *O*-donors. The focus is to study the solid state structures and the solution behaviour of these complexes. This fundamental analysis of the coordination behaviour is necessary for the estimation of the reactivity of these complexes in view of their possible application as precursor species for new functional high-valent iron-oxo model complexes. Typically, the structure of a metal complex is determined in the solid state, but bioinorganic model complexes are applied as homogeneous catalysts in solution. Therefore the solution structure, which may differ from the solid state structure, is even more important. It is planned to characterise both the precursor species and the potential oxo-complexes. If an iron-oxo complex can be identified, the aim is to determine whether the species is suitable as a catalyst for C – H oxidation.
Four different ligands for iron complexes were chosen for this thesis (Figure 2.1). They differ in their number of *N*- and *O*-donor atoms and the donor connectivity through the ligand backbone. The first ligand $HOCH_2C(Pz)_2Py$ (**1**) has four different possible donor atoms but the focus is on the $\{N_3\}$-coordination abilities. The second ligand $MeC(Py)_2Phen$ (**2**) is a pure *N*-donor ligand with $\{N_4\}$-coordination. A mixed donor atom variant of this is the $MeC(Py)_2PicMe$ ligand (**3**) which is a tetradentate ligand for $\{N_3O\}$-coordination modes. A differently arranged tetradentate $\{N_4\}$-donor ligand is NQu_3 (**4**).

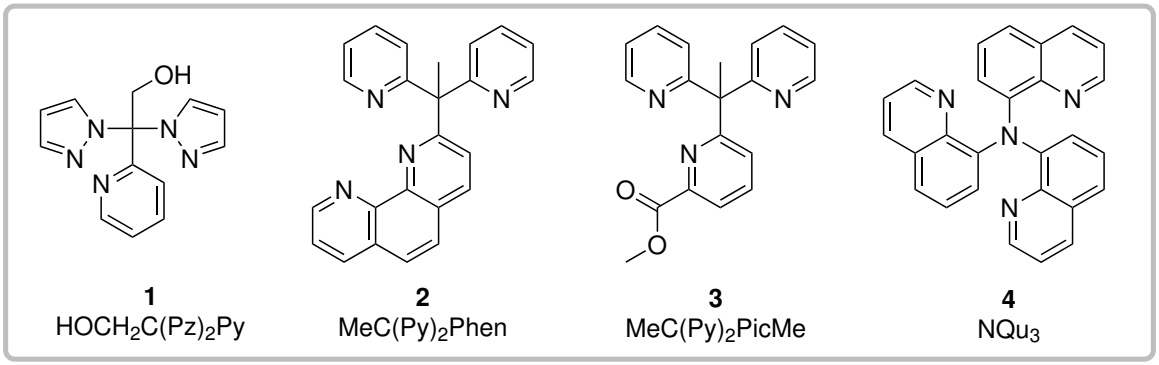

Figure 2.1: Overview of the ligands for this work.

The aim of this work can be divided into several subtasks which are different depending on the ligand: Ligand **1** consists of a bis(pyrazolyl)pyridinylmethane moiety which is known for coordination of biologically relevant 3*d* metal ions such as iron, copper and zinc.[135] The pending hydroxy group was attached to graft this ligand to another molecule or a

surface. The investigation of **1** centres around the question how this anchor changes the coordination behaviour of the ligand and the properties of its metal complexes.
The ligands **2**, **3** and **4** were chosen more from a biomimetic chemistry point of view to obtain complexes with potential for functional biomimetic iron species. All three ligands are designed as tetradentate ligands to enable *cis*-labile coordination sites at a sixfold-coordinated iron centre. As already mentioned in the introduction, this is a well-established concept in the field of functional iron-oxo model complexes. With **2** a high-valent iron-oxo species had been observed in preliminary experiments by Dr. Kristina Keisers.[136] These results promise that this system can also catalyse C – H oxidation reactions which was investigated in the present thesis. The task for this work is to complete the characterisation of the high-valent iron-oxo species and evaluate this species as biomimetic catalyst in C – H oxidation reactions.
To extend the design concept of ligand **2**, the phenanthrolinyl unit is altered by introducing an *O*-donor into the ligand scaffold. The *O*-donor is utilised since many of the known examples are only based on pure *N*-donor ligands and this design is one step closer to the biological motif of the 2H1C facial triad. The choice fell on a pyridinyl-ester unit in form of 6-methyl picolinate inspired by ester-functionalised guanidine ligands that have been successfully used for iron coordination in catalytically active complexes.[137] For this ligand **3**, the tasks are the synthesis and characterisation of the ligand and corresponding iron(II) complexes. The behaviour of these complexes in solution should be investigated as well as their potential as precursor complexes for high-valent iron-oxo complexes.
The fourth ligand **4** is chosen for this thesis due to the similarity to well established ligands in iron-oxo chemistry (TPA, TQA, see section 1.2). The task here includes the synthesis and characterisation of potential iron(II) precursor complexes in solid sate and solution. To gain deeper insights into the iron-based coordination chemistry of **4**, the influence of different co-ligands on the resulting complexes will be investigated. For the iron(II) complexes of TPA, it is known that the variation of the co-ligand can lead to changes in the spin state.[138] It is therefore to be investigated whether similar exchange pathways of co-ligands exist for complexes of **4** and how these affect the spin state. It should not be neglected that structures in solution can differ from those in the solid state. Furthermore, the oxidation to high-valent iron-oxo species and potential application in C – H oxidation reactions are part of the goal. Interesting points in terms of the ligand design of **4** are the different arrangement of weak field quinolines (compared to pyridine donors) than in the TQA ligand: The α-positions next to the *N*-donors remain unsubstituted in **4** and the scaffold offers a more rigid backbone.

2.2 Contents

Overall, this work contains investigations of the solid state structures, the solution behaviour and the reactivity of 3*d* metal complexes – mainly iron – using the four different ligands

1–**4**. Due to the different potential donor groups of these ligands, different coordination modes were found. A schematic illustration of the four ligands and their coordination modes is depicted in Figure 2.2.

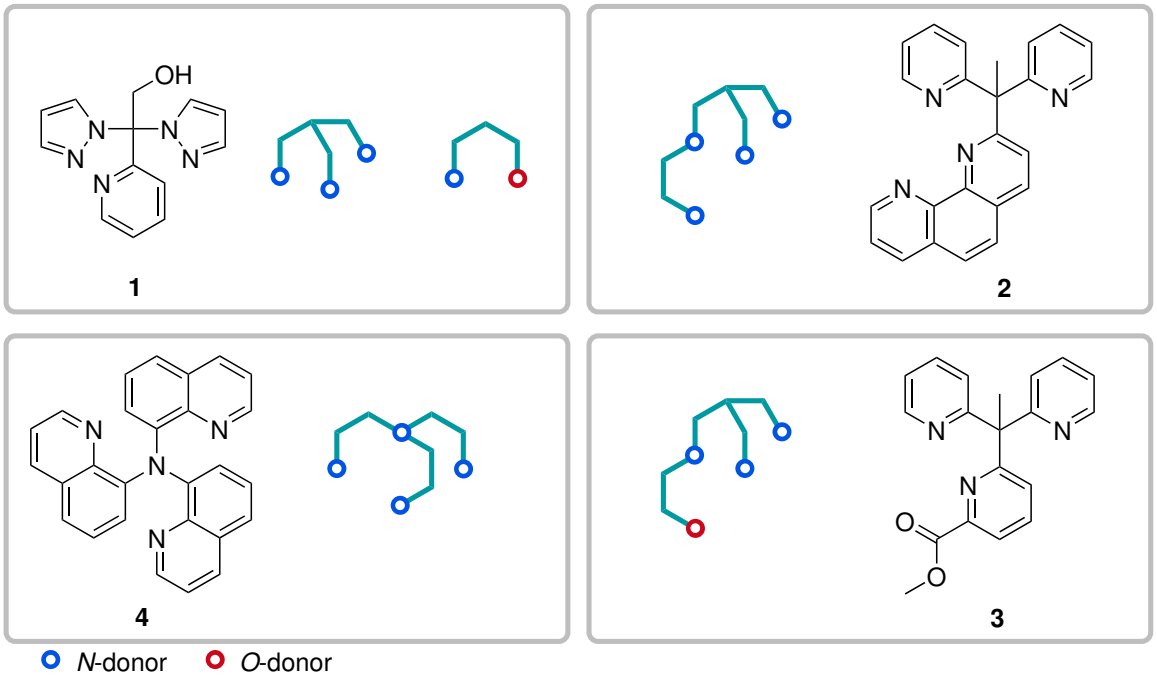

Figure 2.2: Overview of the ligands in this work and their schematic donor arrangement.

The tridentate $\{N_3\}$-coordination mode and the bidentate $\{NO\}$-coordination mode of the ligand **1** for iron, zinc and copper in the solid state are discussed first. This is followed by solution studies of the iron complexes with **1**. Secondly, ligand **2** with a $\{N_4\}$-coordination mode is described in the solid state and in solution followed by the new oxygen derivative **3** with $\{N_3O\}$-coordination mode, which has the same ligand backbone in terms of spacing and connection of the donors. In the following, with **4** a further ligand geometry for a $\{N_4\}$-coordination is studied in solid state and in solution. The last chapter, in which the influences of the different ligand scaffolds on the complex geometry in the solid state are compared, completes the discussion.

Results & Discussion

3 Bis(pyrazolyl)(pyridinyl)ethanol – a Ligand with Two Coordination Modes

*The ligand $HOCH_2C(Pz)_2Py$ (**1**) was synthesised the first time by Isabella Sommer during her Master's thesis.[139] Further characterisation of the ligand and first coordination chemistry experiments with **1** were performed during my Master's thesis from May 2018 until November 2018.[140] In this thesis the coordination chemistry experiments with **1** were continued.*

The bis(pyrazolyl)(pyridinyl)ethanol ligand $HOCH_2C(Pz)_2Py$ (**1**) is a member of the bis(pyrazolyl)(pyridinyl)methane ligand family, which were synthesised in many different variations.[126,135,141–153] Most of the changes of the ligand scaffold affect the substitution of different pyrazolyl or pyridinyl moieties. Substitution of the apical hydrogen atom to introduce a fourth arm of the ligand were also performed in the past, but are much rarer.[142,154] This may be because direct changes at the donor groups have the larger impact on the complex than changes in the backbone of the ligand. Studies with $HOCH_2C(Pz)_2Py$ (**1**) were mainly performed to investigate if the coordination behaviour is not drastically changed when the backbone is further functionalised. Functional groups like OH-group offer the possibility to anchor such a complex to a different molecule or surface e.g. with a esterification reaction, but only if the OH-group is not part of the donating moieties in the resulting complex.

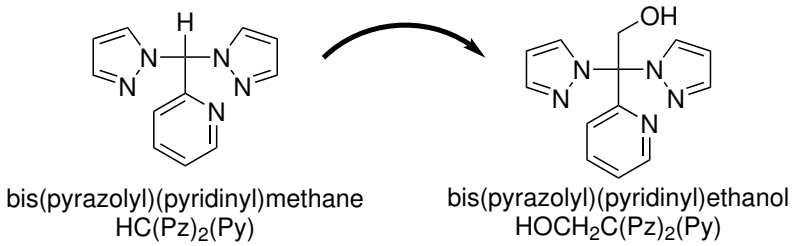

Figure 3.1: Molecular structure of bis(pyrazolyl)(pyridinyl)methane (left) and bis(pyrazolyl)(pyridinyl)ethanol (right).

3.1 Synthesis of Ligand $HOCH_2C(Pz)_2Py$ (1)

The synthesis of $HOCH_2C(Pz)_2Py$ (**1**) is a functionalisation of one of the simplest bis(pyrazolyl)methane ligands – bis(pyrazolyl)(pyridinyl)methane ($HC(Pz)_2Py$).[141] The postfunctionalisation of the apical carbon atom by introducing a methylene alcohol group ($-CH_2OH$) is performed similar to a protocol by Reger *et al.* which was originally developed for

tris(pyrazolyl)methane ligands.[155] In the synthesis, $HC(Pz)_2Py$ is deprotonated at the apical carbon atom by potassium *t*-butoxid and reacts subsequently with paraformaldehyde resulting in **1** (Scheme 3.1). For purification, recrystallisation from hexane/ethylacetate was sufficient and gave a colourless solid product (yield: 66 %).

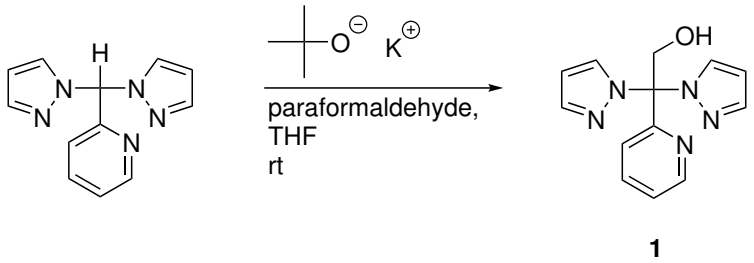

1

Scheme 3.1: Synthesis of ligand **1**.

3.2 Complexes of $HOCH_2C(Pz)_2Py$ (1) in the Solid State

Investigation of the coordination chemistry of ligand **1** towards different 3*d* transition metals revealed two different coordination modes. The first coordination mode is a tridentate $\{N_3\}$-coordination, which is the same as for other complexes with bis(pyrazolyl)methane ligands.[144,147] The second coordination mode is a bidentate {NO}-coordination with only one pyrazole/pyridine coordinating the metal centre and the deprotonated OH-group as the second donor. Because the theoretically four donors are arranged in opposite directions and are not intended to coordinate the same metal centre, a maximum of three can coordinate the same metal centre at the same time.
An overview of the complexes obtained with ligand **1** that were characterised by SCXRD are shown in Figure 3.2. A detailed discussion of the compounds will follow in separate sections. Unless otherwise noted, the complexation reactions with ligand **1** were performed under aerobic conditions.

3.2.1 Iron Complexes of $HOCH_2C(Pz)_2Py$ (1)

$[Fe(HOCH_2C(Pz)_2Py)_2]X$ (1a–1d, X = Br, $[FeBr_4]Br$, $[FeCl_4]Cl$, OTf)

Crystal structures of iron complexes with ligand **1** in this work are $[Fe(\mathbf{1})_2]Br_2 \cdot MeCN$ (**1a**), $[Fe(\mathbf{1})_2][FeBr_4]Br \cdot C_7H_8$ (**1b**), $[Fe(\mathbf{1})_2][FeCl_4]Cl \cdot 2\,MeCN$ (**1c**) and $[Fe(\mathbf{1})_2](OTf)_2 \cdot 2\,MeCN$ (**1d**). They all show the same complex cation $[Fe(HOCH_2C(Pz)_2Py)_2]^{2+}$ where iron(II) is coordinated by two molecules of **1** in a bisfacial fashion (Scheme 3.2). Figure 3.3 shows an exemplary structure of this cation in crystals of **1c**. Differences in the solid state structures of the four compounds which were characterised via SCXRD are the anions of the cationic complexes and crystal solvent molecules. The bisfacial coordination motif is typical for

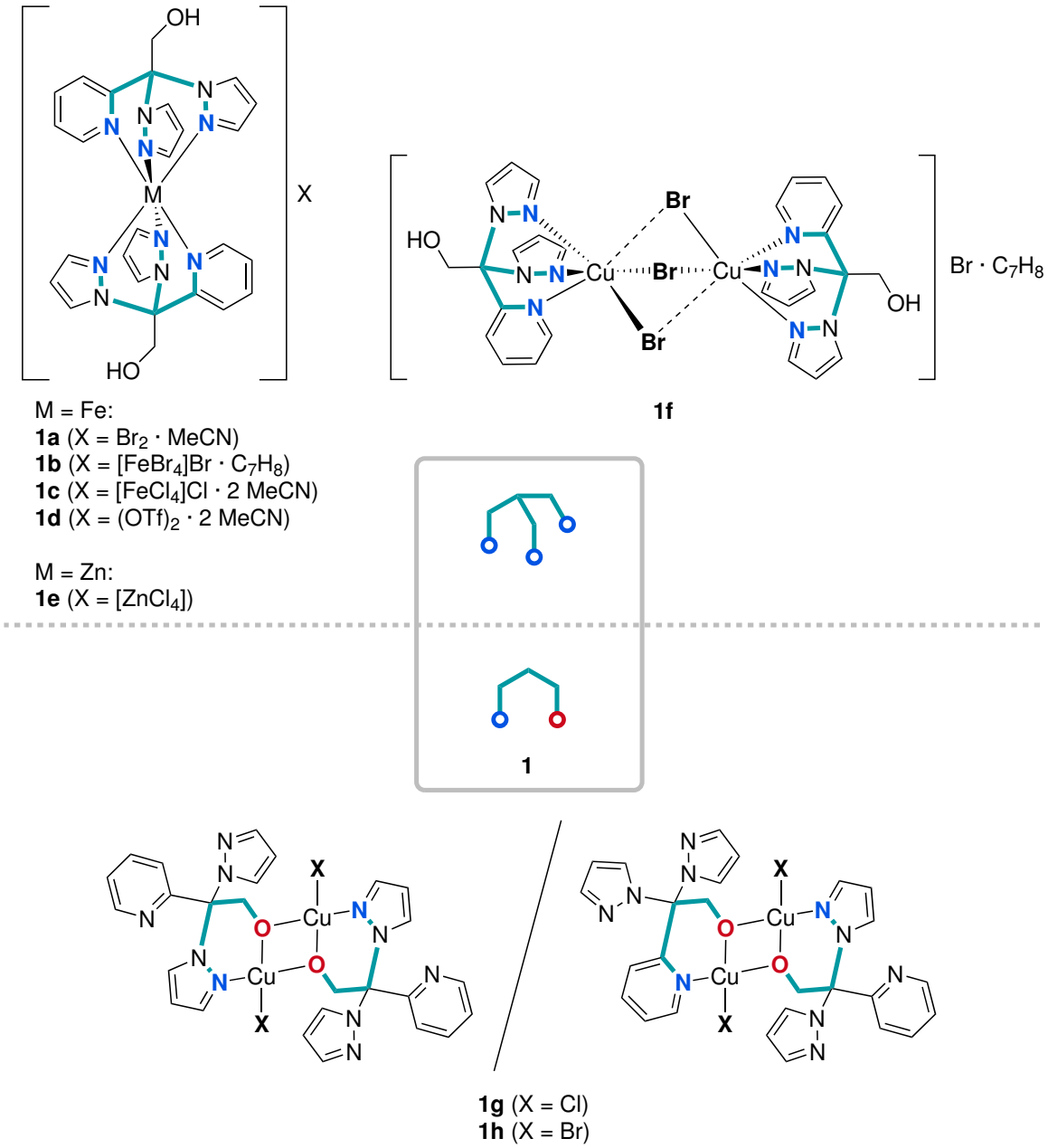

Figure 3.2: Overview of complexes with ligand **1**.

bis(pyrazolyl)methane ligands and their derivatives.[144,147]

Combination of $FeBr_3$ and ligand **1** resulted in the complex $[Fe(\mathbf{1})_2]Br_2 \cdot MeCN$ (**1a**, Scheme 3.2). Other than expected, the iron was reduced from iron(III) to iron(II) during synthesis. **1a** crystallises as acetonitrile solvate in the triclinic space group $P\bar{1}$ with $Z = 2$ and two half complex cations per asymmetric unit. Per complex, there are two bromide counterions and one disordered acetonitrile molecules co-crystallised. The reaction of $FeBr_2$ with **1** resulted in complex $[Fe(\mathbf{1})_2][FeBr_4]Br \cdot C_7H_8$ (**1b**, Scheme 3.2). **1b** crystallises as a toluene solvate in the monoclinic space group $P2_1/n$ with $Z = 4$ and two half complex cations per asymmetric unit. The charge of the iron centres is again iron(II). Additional to the anions, there was one toluene molecule found to be co-crystallising but

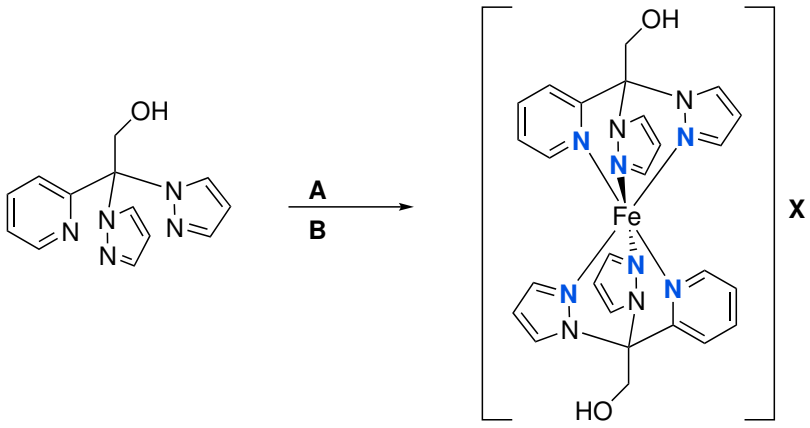

Complex	A	B	X
1a	$FeBr_3$	MeCN	$Br_2 \cdot$ MeCN
1b	$FeBr_2$	MeCN, diffusion with toluene	$[FeBr_4]Br \cdot C_7H_8$
1c	$FeCl_2$	MeCN	$[FeCl_4]Cl \cdot 2$ MeCN
1d	$Fe(OTf)_2 \cdot 2$ MeCN	MeCN, diffusion with Et_2O	$(OTf)_2 \cdot 2$ MeCN

Scheme 3.2: Synthesis of complexes **1a**, **1b**, **1c** and **1d**.

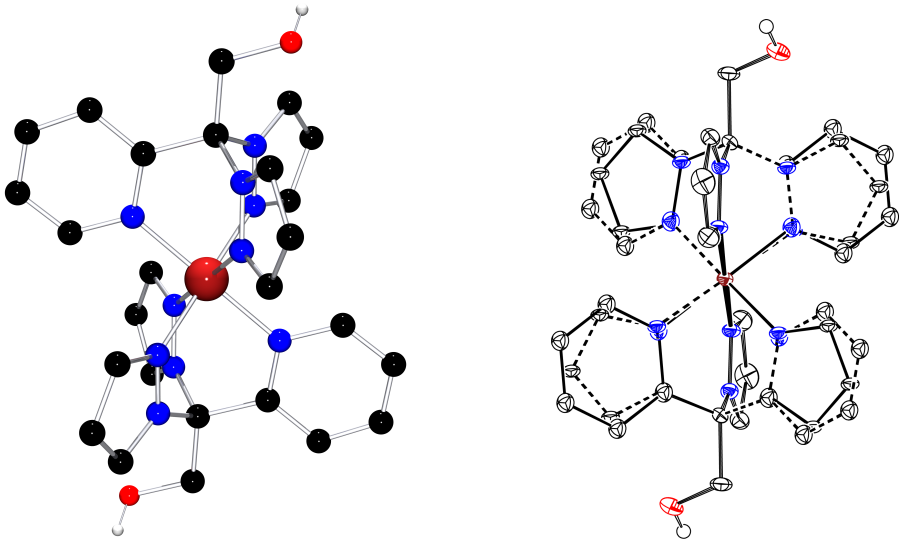

Figure 3.3: $[Fe(\mathbf{1})_2]^{2+}$ cation in crystals of **1c** (left) and Pz/Py-disorder in $[Fe(\mathbf{1})_2]^{2+}$ cation around Fe(2) in crystals of **1c** (minority component dashed, 50 % probability, right). C bonded hydrogen atoms, counterions and crystal solvent molecules are omitted for clarity. Colour code: black = carbon, blue = nitrogen, red = oxygen, scarlet = iron, white = hydrogen.

due to disorder that could not be modelled in an adequate manner it was treated using the BYPASS algorithm as implemented in PLATON/SQUEEZE.[156–158] Complex synthesis with $FeCl_2$ and **1** resulted in crystals of $[Fe(\mathbf{1})_2][FeCl_4]Cl \cdot 2$ MeCN (**1c**, Scheme 3.2). Besides the crystal solvent molecules, this complex is the chloride analogue to complex **1b**. The co-crystallised solvent for crystals of **1c** are two molecules of acetonitrile per complex cation. The compound crystallises as acetonitrile solvate in the triclinic space group $P\bar{1}$ with $Z = 2$ and two half complex cations per asymmetric unit. The reaction of $Fe(OTf)_2 \cdot 2$ MeCN

and **1** in absolute (abs.) acetonitrile with subsequent gas phase diffusion under aerobic conditions resulted in crystals of $[Fe(\mathbf{1})_2](OTf)_2 \cdot 2\,MeCN$ (**1d**, Scheme 3.2). **1d** crystallises as acetonitrile solvate in the triclinic space group $P\bar{1}$ with $Z = 2$ and two half complex cations per asymmetric unit.

The molecular structures of **1a**–**1d** have in common that the iron centres are positioned on crystallographic inversion centres. The two pyridinyl moieties are always arranged in a *trans* configuration. The Fe – N bond lengths are for all four complexes below 2.0 Å which is typical for an iron(II) LS species (Table 3.1).[119] The coordination geometry of all complex cations is very close to an ideal octahedron (CSM: S(OC-6) = 0.1).

In complexes **1b** and **1c**, the positive charge of the complex cation is balanced by a halide and a tetrahalidoferrate anion. The charge of the tetrahalidoferrate anion can be assigned via the iron halogen bond lengths.

For the Fe – Br bond lengths in **1b**, a CSD search on bond lengths in $[FeBr_4]^-$ and $[FeBr_4]^{2-}$ anions was performed.[58] The average Fe – Br bond length found for $[FeBr_4]^-$ anions is 2.35 Å (112 structures) and for $[FeBr_4]^{2-}$ anions 2.43 Å (20 structures). The Fe – Br bond lengths of the anion in crystals of **1b** is on average 2.305 Å and therefore the anion is assigned as $[FeBr_4]^-$ counterion. For crystals of **1c**, the charge of $[FeCl_4]^-$ was determined based on literature values for Fe – Cl bond lengths in $[FeCl_4]^-$ ($\approx$ 2.19 Å) and $[FeCl_4]^{2-}$ (2.28 – 2.34 Å) anions.[159] The averaged Fe – Cl bond length found for the anion in **1c** is 2.196 Å, which assigns the anion to be an $[FeCl_4]^-$ anion. This is another indication that the complex cations of **1b** and **1c** are iron(II) species.

In complexes **1a**, **1b** and **1c**, the halide ions are positioned close to the OH-groups of **1** and form H-bonds towards them (Figure 3.4). A search in the CSD for the distance between the oxygen atom of a carbon bonded OH-group and an unbonded bromide (O – H – Br angle: 150 – 180 °) shows that the values found in structures of the bromide containing complexes **1a** and **1b** are in a typical range (Figure 3.5). A CSD search for the corresponding O···Cl distance as found in crystals of **1c**, revealed that these H-bonds are in the typical range, too (Figure 3.5).[58]

In the structure solution of crystals of **1c**, a disorder between pyrazolyl and pyridinyl groups was modelled for the complex cation around Fe(2) (Figure 3.3, right). A comparable Pz/Py disorder was found for both complex cations in the asymmetric unit of crystals of **1d**. This disorder was also found in structure models of other bis(pyrazolyl)pyridinyl methane complexes.[142] Due to the high level of disorder and the amount of restraints and constraints used to model the pyrazolyl and pyridinyl moieties, the obtained bond lengths of **1d** must be taken with caution.

Additionally, in crystals of **1d** the alcohol groups were modelled with split positions for CH_2 – OH. The hydrogen atoms of the OH-groups were modelled to result in reasonable H-bonds towards H-bond acceptor atoms, if possible. For three of them, this was possible

Table 3.1: Selected bond lengths, atom distances, bond angles and structure parameters of **1a**, **1b**, **1c** and **1d**.

	1a $[Fe(HOCH_2C(Pz)_2Py)_2]$ $Br_2 \cdot MeCN$ Fe(1) / Fe(2)	**1b** $[Fe(HOCH_2C(Pz)_2Py)_2]$ $[FeBr_4]Br \cdot C_7H_8$ Fe(1) / Fe(2)	**1c** $[Fe(HOCH_2C(Pz)_2Py)_2]$ $[FeCl_4]Cl \cdot 2\,MeCN$ Fe(1) / Fe(2) | Fe(2)'	**1d** $[Fe(HOCH_2C(Pz)_2Py)_2]$ $(OTf)_2 \cdot 2\,MeCN$ Fe(1) | Fe(1)' / Fe(2) | Fe(2)'
Space group	$P\bar{1}$	$P2_1/n$	$P\bar{1}$	$P\bar{1}$
Bond lengths [Å]				
$Fe-N_{Pz}$	1.938(4)–1.951(5)	1.934(3)–1.961(3)	1.935(2)–1.951(2)	1.9418(16)–1.989(5)
$Fe-N_{Py}$	1.970(4)–1.975(4)	1.969(3)–1.982(3)	1.951(5)–1.982(1)	1.927(4)–1.961(3)
Ø Fe – N	1.950 / 1.956	1.957 / 1.955	1.958 / 1.948 | 1.949	1.946 | 1.963 / 1.963 | 1.943
Atom distances [Å]				
$C_{ap}\cdots Fe$	3.044(6) / 3.049(6)	3.059(4) / 3.065(4)	3.041(2) / 3.043(2)	3.0491(19) / 3.0500(19)
$O-H\cdots Br^-/Cl^-/O$	O(1) – H(1) ···Br(2) 3.154(5) O(2) – H(2) ···Br(1) 3.177(4)	O(1) – H(1) ···Br(1) 3.259(3) O(2) – H(2) ···Br(1) 3.190(3)	O(1) – H(1) ···Cl(1) 3.0344(19) O(2) – H(2) ···Cl(1) 3.006(2)	O(1A) – H(91A)···O(6A) 2.698(3) O(1B) – H(91B)···O(5B) 2.35(2) O(2A) – H(92A)···O(3A) 2.668(19)
Bond angles [°]				
$N_{Pz}-Fe-N_{Pz\text{-}trans}$	180.0	180.0	180.0	180.0
$N_{Py}-Fe-N_{Py\text{-}trans}$	180.0	180.0	180.0	180.0
Struct. param.				
CSM *S*(OC-6)	0.1 / 0.1	0.1 / 0.1	0.1 / 0.1 | 0.1	0.1 | 0.1 / 0.1 | 0.1
CSM *S*(TPR-6)	16.1 / 15.9	15.8 / 15.9	16.0 / 16.0 | 16.0	15.9 | 16.0 / 16.0 | 16.0
Pz/Py disorder	no	no	no / yes	yes / yes

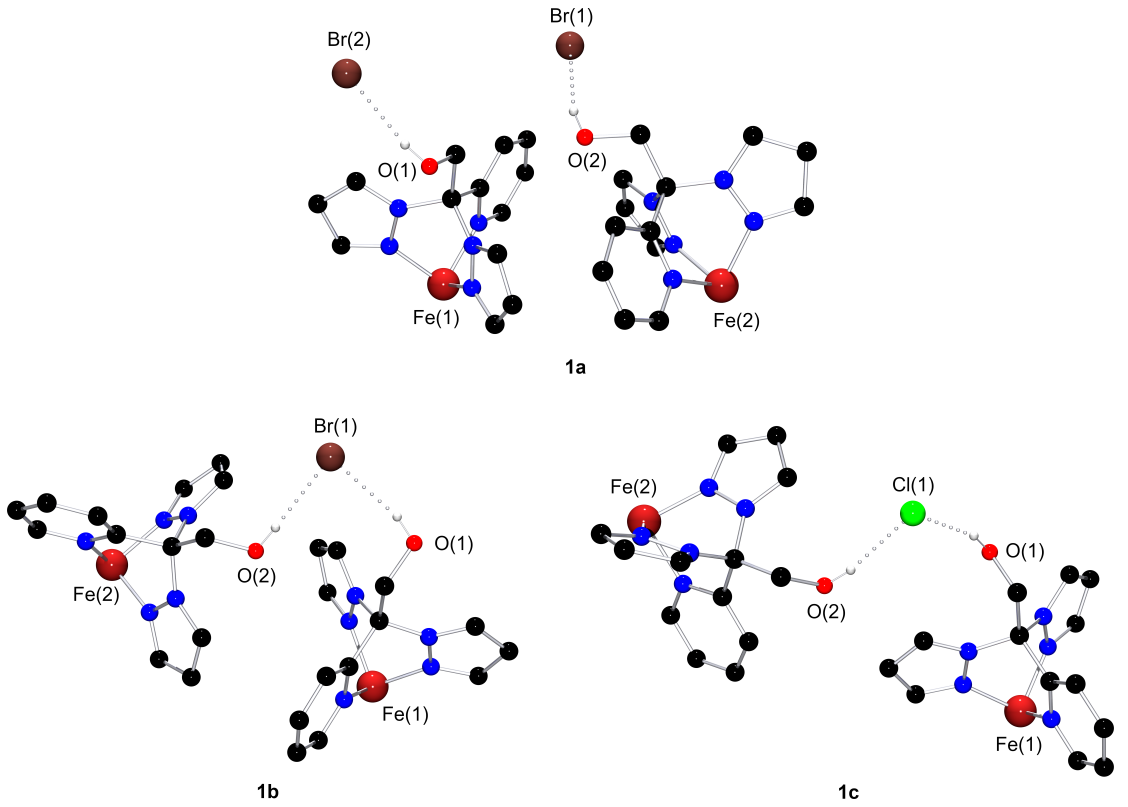

Figure 3.4: H-bonds in crystals of **1a**, **1b** and **1c**. C bonded hydrogen atoms, counterions not involved in H-bonds, crystal solvent molecules, Pz/Py-disorder and the second ligand of the complex cations are omitted for clarity. Colour code: black = carbon, blue = nitrogen, red = oxygen, scarlet = iron, green = chlorine, brown = bromine, white = hydrogen.

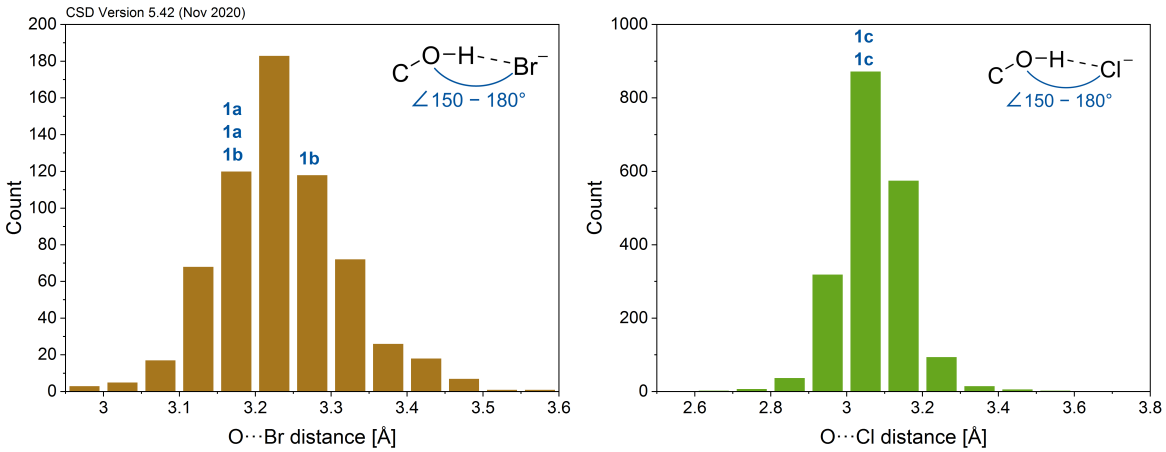

Figure 3.5: Histograms of hits for O···Br (left) and O···Cl distances in the CSD.[58] Searched fragments as shown in plot. The number of bonded atoms was set to 2 for oxygen and 0 for bromine/chlorine. The O – H – Br/O – H – Cl angle was restrained to 150 – 180 °.

so that H-bonds towards O-atoms of triflate anions were found (2.353(2)–2.698(3) Å). The triflate anions were also modelled on split positions. Overall, the bisfacial coordination of ligand **1** is consistent with the non-backbone functionalised bis(pyrazolyl)methane ligands.

3.2.2 Zinc Complex of $HOCH_2C(Pz)_2Py$ (1)

$[Zn(HOCH_2C(Pz)_2Py)_2][ZnCl_4]$ (1e)

The synthesis of zinc complexes gives the opportunity to test the coordination abilities of a ligand in absence of ligand field stabilisation. The combination of $ZnCl_2$ and ligand **1** in tetrahydrofurane resulted in the bisfacial zinc complex $[Zn(\mathbf{1})_2][ZnCl_4]$ (**1e**, Scheme 3.3).

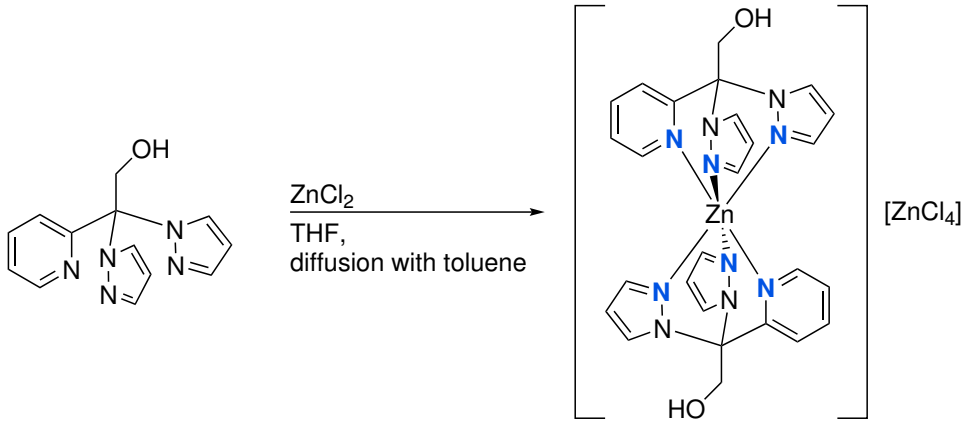

Scheme 3.3: Synthesis of complex **1e**.

Gas phase diffusion with the anti-solvent toluene led to suitable crystals for SCXRD (Figure 3.6, Table 3.2). Compound **1e** crystallises in the monoclinic space group $P2_1/c$ with $Z = 4$.

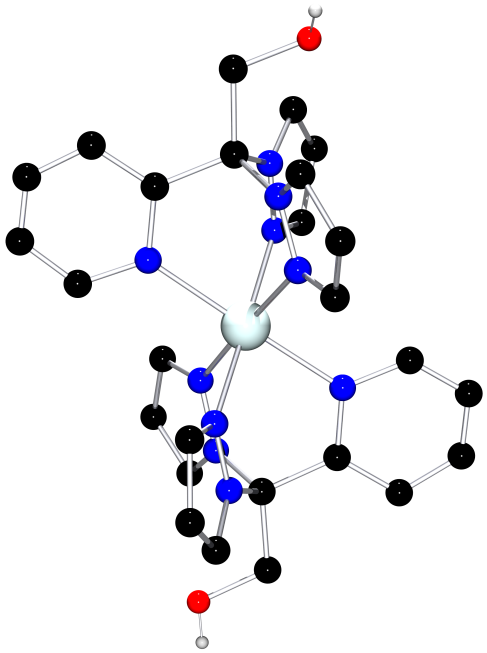

Figure 3.6: $[Zn(\mathbf{1})_2]^{2+}$ cation in crystals of **1e**. C bonded hydrogen atoms and counterions are omitted for clarity. Colour code: black = carbon, blue = nitrogen, red = oxygen, light blue = zinc, white = hydrogen.

Table 3.2: Selected bond lengths, atom distances, bond angles and structure parameters of **1e**.

	1e $[Zn(HOCH_2C(Pz)_2Py)_2][ZnCl_4]$
Space group	$P2_1/c$
Bond lengths [Å]	
$Zn-N_{Pz}$	2.107(4)–2.126(4)
$Zn-N_{Py}$	2.152(4)–2.169(4)
Ø Zn – N	2.131
Atom distances [Å]	
$C_{ap}\cdots Zn$	3.1887(5)–3.201(5)
Bond angles [°]	
$N_{Pz}-Zn-N_{Pz\text{-}trans}$	177.65(15)–179.08(15)
$N_{Py}-Zn-N_{Py\text{-}trans}$	178.07(14)
Struct. param.	
CSM *S*(OC-6)	0.6
CSM *S*(TPR-6)	14.5

In zinc complexes, this bisfacial coordination mode is typical for bis(pyrazolyl)methane ligands with unsubstituted pyrazolyl units and no additional available donor.[144,160] Similar to the bisfacial iron complexes the pyridinyl units of the two ligands are arranged *trans* to each other. The Zn – N bond lengths in **1e** are all above 2.1 Å (Figure 3.2), which is longer than for the LS iron(II) complexes **1a**–**1d**. The zinc centre of the cationic complex is not positioned on a crystallographic inversion centre as seen for the iron complexes. Also, the coordination sphere of the metal centre is slightly less octahedral (CSM: S(OC-6) = 0.6) compared to the iron complexes. This can be explained with the absent ligand field stabilisation energy for d^{10} metal cations like zinc(II). Therefore, the geometric restriction by the ligand is dominant here. The co-crystallisation of a $[ZnCl_4]^{2-}$ anion was also observed for bisfacial bis(pyrazolyl)methane ligands.[144,161]

3.2.3 Copper Complexes of $HOCH_2C(Pz)_2Py$ (1)

Copper is the only 3*d* metal used in this work which exhibits two different coordination modes of ligand **1**. One is a pure $\{N_3\}$-coordination and the other is a mixed $\{NO\}$-coordination.

$\{N_3\}$-Coordination of $HOCH_2C(Pz)_2Py$ (1)

Only one complex structure ($[Cu_2(\mu\text{-}Br)Br_2(\mathbf{1})_2]Br \cdot C_7H_8$ (**1f**)) was characterised successfully by SCXRD showing $\{N_3\}$-coordination mode.

$[Cu_2(\mu\text{–}Br)Br_2(HOCH_2C(Pz)_2Py)_2]Br \cdot C_7H_8$ (1f): The dinuclear copper complex $[Cu_2(\mu\text{-}Br)Br_2(\mathbf{1})_2]Br \cdot C_7H_8$ (**1f**) is a product of the reaction of $CuBr_2$ and **1** in acetonitrile and subsequent gas phase diffusion with toluene (Scheme 3.4). **1f** was obtained as

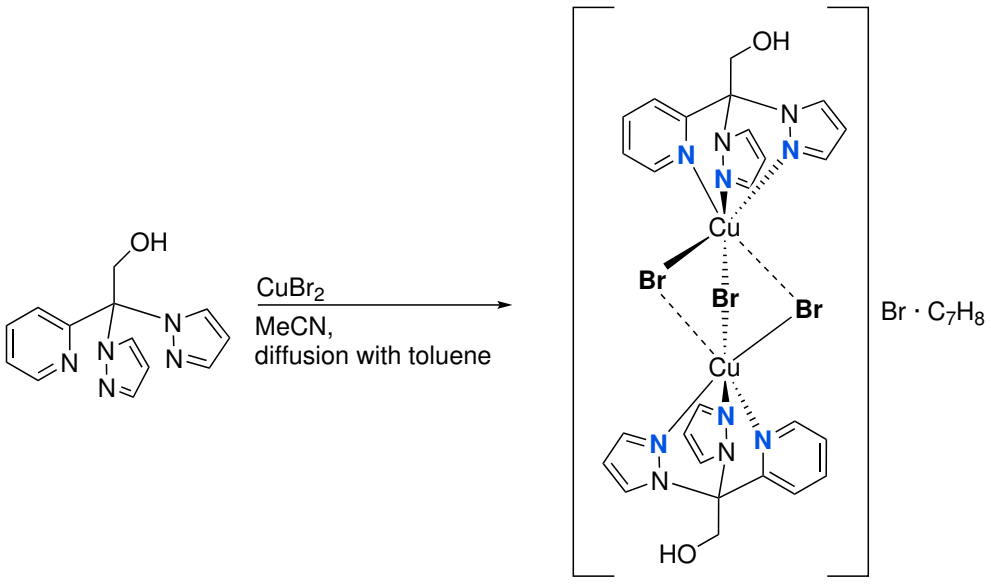

Scheme 3.4: Synthesis of complex **1f**.

yellow crystals that were suitable for SCXRD which crystallise as a toluene solvate in the monoclinic space group $P2_1/n$ with $Z = 4$. (Figure 3.7, Table 3.3).

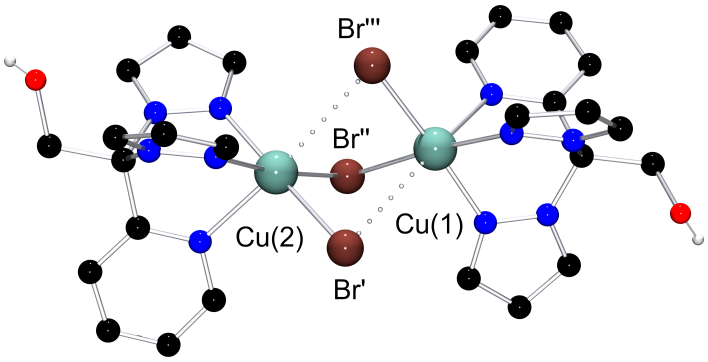

Figure 3.7: $[Cu_2(\mu\text{-}Br)Br_2(\mathbf{1})_2]^+$ cation in crystals of **1f**. Elongated Cu···Br contacts dashed. C bonded hydrogen atoms, counterions and crystal solvent molecules are omitted for clarity. Colour code: black = carbon, blue = nitrogen, red = oxygen, green copper = copper, brown = bromine, white = hydrogen.

Together with this yellow crystals blue crystals were obtained, but their quality was too poor for a sufficient SCXRD structure solution. To investigate whether the crystallising species depends on the amount of anti-solvent used in the crystallisation process, a series with varying amounts of toluene (1–4.5 mL; 20 mL of MeCN) was prepared. Photographs of the result under a light microscope can be seen in Figure 3.8. It was not observed that the two species could be obtained individually but an optimised ratio for the crystallisation of both varieties simultaneously was found to be 4 mL of toluene.

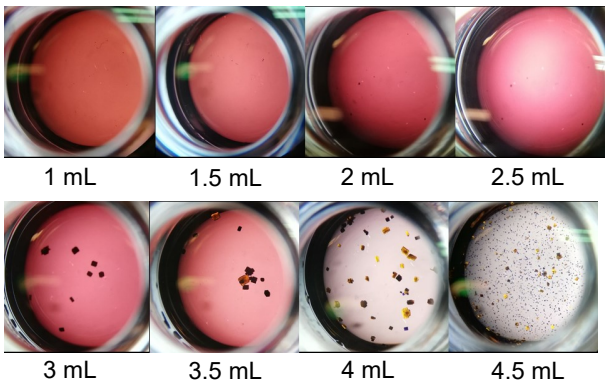

Figure 3.8: Crystallisation reactions of $CuBr_2$ and **1** in MeCN (2 mL) with varying amounts of toluene (anti-solvent, gas phase diffusion).

The coordination sphere around both copper(II) cations in **1f** is a distorted octahedron (CSM: S(OC-6)= 2.2 & 3.0, Table 3.3). Three facial coordination sites are occupied by the three N-donors of one molecule of **1** while the remaining sites are μ_2-bridging bromido ligands shared between the two copper(II) cations. The coordination sphere displays a pronounced tetragonal elongation corresponding to a Jahn-Teller distortion. The short contacts in the

Table 3.3: Selected bond lengths, atom distances, bond angles and structure parameters of **1f** and XESDUU.[162]

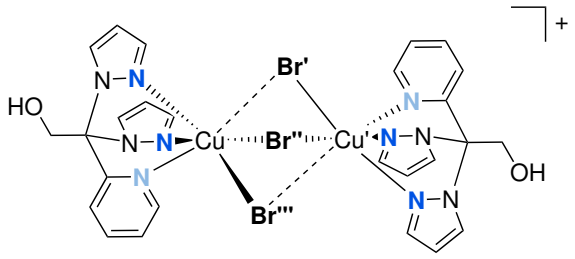

1f

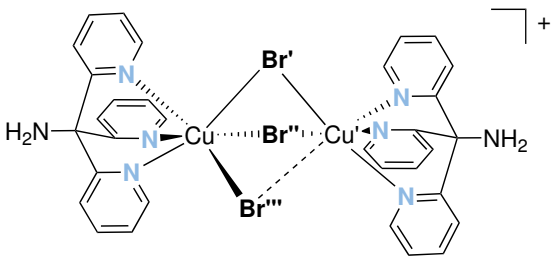

XESDUU

	1f $[Cu_2(\mu\text{-}Br)Br_2(HOCH_2C(Pz)_2Py)_2]$ $Br \cdot C_7H_8$ Cu(1) / Cu(2)	XESDUU[162] $[Cu_2(\mu\text{-}Br_2)Br(H_2NCPy_3)_2]$ $\cdot$ 3 MeOH Cu(2) / Cu(1)
Space group	$P2_1/n$	$Pnmm$
Bond lengths [Å]		
Cu – N_{Pz}	1.995(3)–2.015(3)	–
Cu – N_{Py}	2.250(3)	2.034(13)–2.134(13)
Cu – Br'	3.0187(8) / 2.3934(7)	2.738(2) / 2.508(2)
Cu – Br''	2.4575(8) / 2.4740(7)	2.738(2) / 2.508(2)
Cu – Br'''	2.4316(8) / 3.2093(9)	2.492(3) / 2.980(4)
Atom distances [Å]		
C_{ap}···Cu	3.145(3)–3.161(3)	3.102–3.109
Cu···Cu	3.3636(10)	3.321
Bond angles [°]		
Cu – Br – Cu	71.71(4)–86.01(3)	74.11–78.42
N_{Pz} – Cu – Br_{trans}	172.57(11)–176.22(11)	–
N_{Py} – Cu – Br_{trans}	169.61(10)–173.32(9)	174.37–179.06
Struct. param.		
CSM *S*(OC-6)	2.2 / 3.0	1.5 / 1.5
CSM *S*(TPR-6)	16.2 / 14.3	16.3 / 16.4

basal plane are to the pyrazolyl (1.995(3)–2.015(3) Å) and the two remaining bromide ligands (2.3934(7)–24740(7) Å), respectively. The elongated bonds are to the pyridinyl (2.250(3) Å) and a bromido ligand (3.0187(8) & 3.2093(9) Å, dashed) for both cations. Consequently, two of the bromido bridges are asymmetric while the in third bridge the bromide has short contacts to both copper(II) cations (2.4575(8) & 2.4740(7) Å).

The coordination mode with three *N*-donors per copper centre and three bromides between the two copper centres is quite unusual. There is one published structure with a similar coordination motif in which the tripodal *N*-donor ligand has three pyridine moieties (CDS refcode: XESDUU).[162] In this structure only one Cu – Br contact is elongated compared to the others (2.980(4) Å, Table 3.3). In terms of Cu – Br bond lengths the $\{Cu_2Br_3\}$-core of XESDUU is less symmetric than in **1f** although the ligand H_2NCPy_3 (tpm) offers three equal

N-donors instead of two different *N*-donor types as provided by ligand **1**. Nevertheless, the structural motif is very similar as shown by an overlay of both complex cations in Figure 3.9.

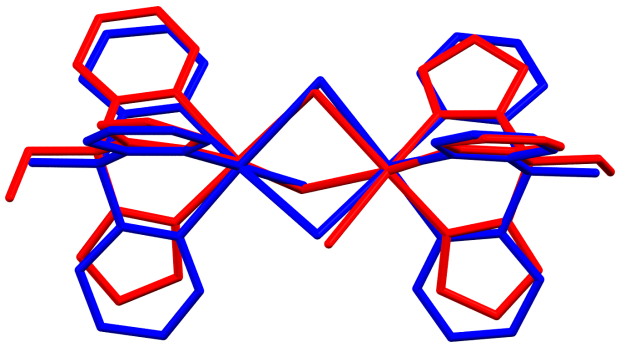

Figure 3.9: Structure overlay of **1f** (red) and XESDUU[162] (blue).

{NO}-Coordination of $OCH_2C(Pz)_2Py^-$ ($\mathbf{1}^-$)

The second coordination mode of ligand **1** found for copper complexes gave two structures ($[Cu_2(\mathbf{1}^-)_2Cl_2]$ (**1g**) and $[Cu_2(\mathbf{1}^-)_2Br_2]$ (**1h**)) which are isostructural (Scheme 3.5). In this coordination mode the OH-group of **1** is deprotonated resulting in $OCH_2C(Pz)_2Py^-$ ($\mathbf{1}^-$).

$[Cu_2(OCH_2C(Pz)_2Py)_2X_2]$ (1g & 1h): Complex **1g** is the result of a reaction of CuCl and **1** in acetonitrile (Scheme 3.5). It was possible to obtain crystals suitable for SCXRD (Figure 3.10). The combination of CuBr and **1** in acetonitrile leads to crystals of complex **1h** after slow evaporation of solvent (Scheme 3.5) (Figure 3.10).

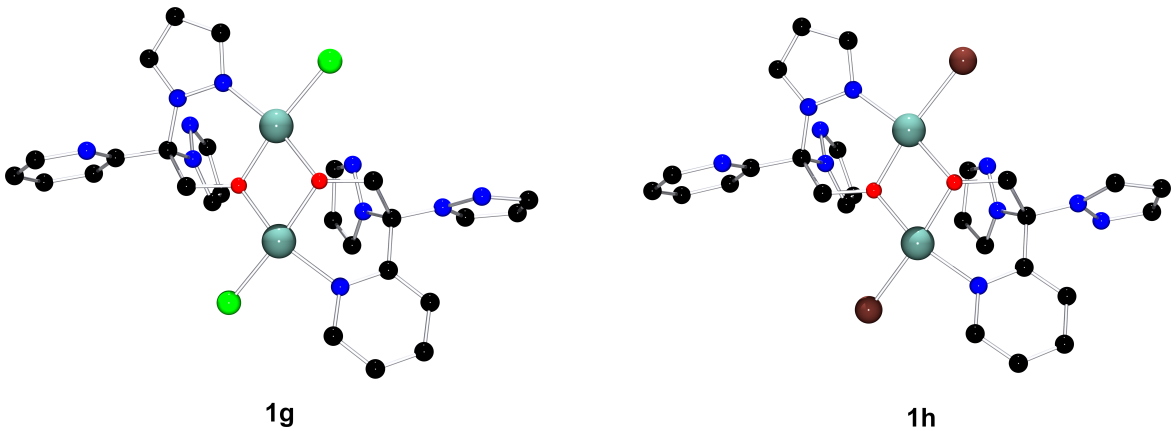

Figure 3.10: $[Cu_2(\mathbf{1}^-)_2Cl_2]$ unit in crystals of **1g** in majority configuration **1gαβ** (left) and $[Cu_2(\mathbf{1}^-)_2Br_2]$ unit in crystals of **1h** in majority configuration **1hαβ** (right). Hydrogen atoms are omitted for clarity. Colour code: black = carbon, blue = nitrogen, red = oxygen, green copper = copper, green = chlorine, brown = bromine.

The complexes **1g** and **1h** crystallise in the triclinic space group $P\bar{1}$ with one molecule $[Cu_2(\mathbf{1}^-)_2X_2]$ (X = Cl, Br) per asymmetric unit or two of them per unit cell ($Z = 1$ for $[Cu_4(\mathbf{1}^-)_4X_4]$). The synthesis of these compounds under aerobic conditions enabled the

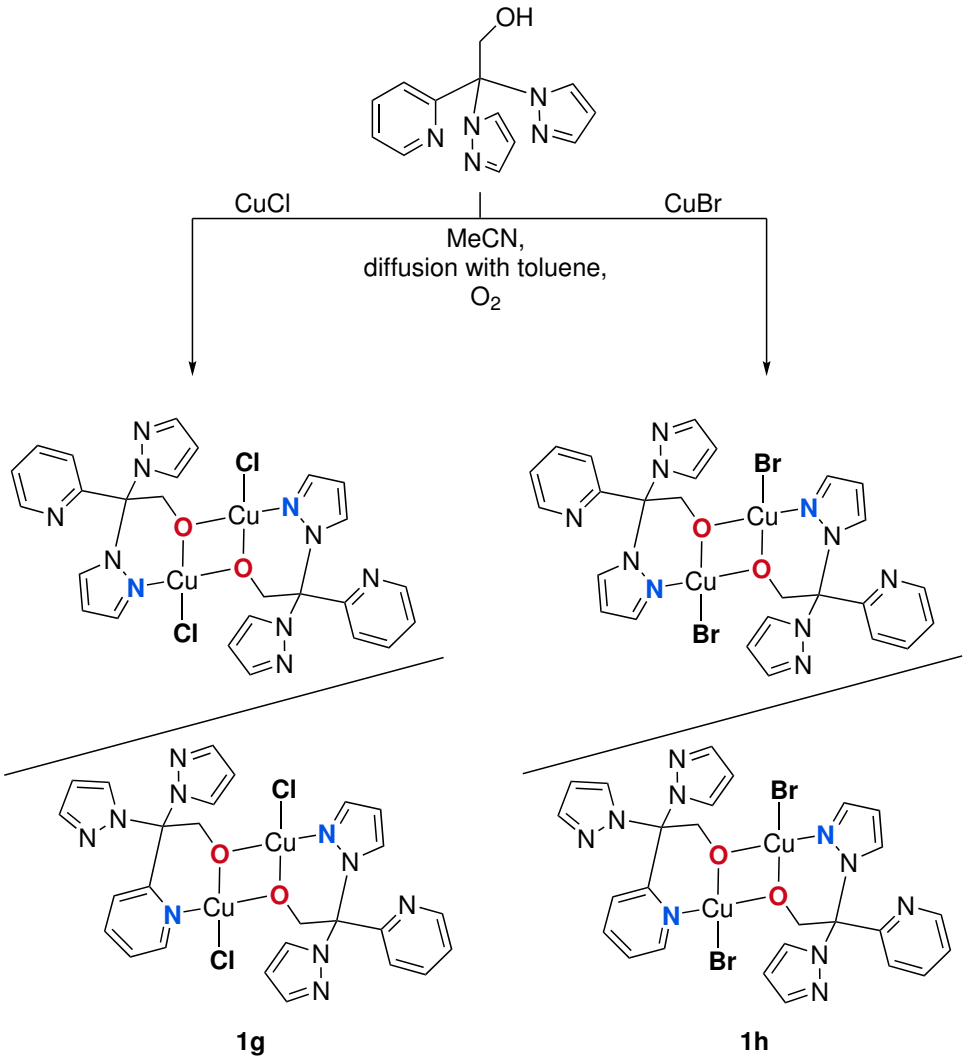

Scheme 3.5: Synthesis of complexes **1g** and **1h**.

oxidation from copper(I) in the used precursor salt to copper(II) in the resulting complex. There are several aspects that make these crystal structures interesting. The first aspect is the formation of dinuclear complexes with the deprotonated hydroxy group acting as a bridging ligand between the two copper centres (Figure 3.10). The copper centres in the dinuclear complex have a distance of 3.0503(11) and 3.0556(13) Å, respectively (Table 3.4). The Cu – O and Cu – N_{Pz} bond lengths are just below 2.0 Å and the Cu – N_{Py} bond lengths are slightly above 2.0 Å. For **1h**, the Cu – Br bond lengths are elongated about 0.14 Å compared to **1g**.

The second aspect is that there are two independent Pz/Py-disorders. Around Cu(1), the ligand has a Pz/Py-disorder of the two non-coordinating *N*-donors (**1g**: 72.3(5) % & 27.7(5) %, Figure 3.11; **1h**: 58.6(6) % & 41.4(6) %, Figure 3.12). At the second Cu centre Cu(2), the coordinating *N*-donor is disordered with one of the non-coordinating ones. The shares are in **1g** and **1h** almost equal: In 52.8(6) % and 50.3(7) % the pyridine and in 47.2(6) % and 49.7(7) % the pyrazolyl moiety is coordinating, respectively. Together, this results in four

Table 3.4: Selected bond lengths, atom distances, bond angles and structure parameters of **1g** and **1h**.

	1g $[Cu_2(OCH_2C(Pz)_2Py)_2Cl_2]$ Cu(1) / Cu(2)	**1h** $[Cu_2(OCH_2C(Pz)_2Py)_2Br_2]$ Cu(1) / Cu(2)
Space group	$P\bar{1}$	$P\bar{1}$
Bond lengths [Å]		
Cu – N_{Pz}	1.995(5) / 1.922(6)	1.991(6) / 1.923(8)
Cu – N_{Py}	– / 2.020(7)	– / 2.004(11)
Cu – $O_{trans\text{-}Cl/Br}$	1.921(3) / 1.986(3)	1.930(4) / 1.983(4)
Cu – $O_{trans\text{-}N}$	1.984(4) / 1.923(3)	1.966(5) / 1.926(5)
Cu – Cl/Br	2.2505(15) / 2.2479(16)	2.3892(12) / 2.3917(12)
Atom distances [Å]		
Cu···Cu	3.0503(11)	3.0556(13)
Cu···Cl/Br'	– / 2.7703(16)	– / 2.9328(12)
Cu···O'	2.570(3) / –	2.686(5)/ –
Bond angles [°]		
Cu – O – Cu	100.41(16)–105.02(17)	101.4(2)–104.8(2)
O – Cu – O	77.19(15)–77.32(15)	76.68(18)–76.97(19)
Cl/Br – Cu – $O_{trans\text{-}Cl/Br}$	172.65(11) / 174.43(11)	172.08(14) / 174.07(14)
N_{Pz} – Cu – $O_{trans\text{-}N}$	168.16(16) / 161.8(3)	167.9(2) / 163.5(4)
N_{Py} – Cu – $O_{trans\text{-}N}$	– / 159.5(4)	– / 162.7(6)
Struct. param.	Cu(1) / Cu(2)Pz | Cu(2)Py	
CSM *S*(SP-4)	1.2 / 1.5 | 1.6	1.6 / 1.8 | 1.8
CSM *S*(T-4)	30.7 / 28.6 | 27.8	30.5 / 30.3 | 29.7
CSM *S*(TBPY-5)*	6.6 / 4.8 | 4.6	6.9 / 5.7 | 5.5
CSM *S*(SPY-5)*	2.0 / 2.3 | 2.3	2.4 / 2.7 | 2.7

* Considering the borderline Cu···X as coordinating for the coordination geometry.

possible arrangements of the ligands in complexes **1g** (Figure 3.11) and **1h** (Figure 3.12). To distinguish the different isomers additional labelling was used. The label **α** means that a pyrazolyl moiety is coordinating and **β** denotes a coordinating pyridinyl moiety. With an apostrophe, the two different arrangements for the Pz/Py-disorder of the non-coordinating ligand arms at Cu(1) are marked. For the chlorido complex **1gαβ** is the majority component (38 %), followed by **1gαα** (34 %). The two minority components are **1gαβ'** (15 %) and **1gαα'** (13 %). For the bromido complex the majority configurations are **1gαβ** and **1gαα** with 29 %, while the two remaining configurations are present at 21 %, respectively (Figure 3.12).

If only the dinuclear complexes are considered, the coordination geometry is close to square planar for all copper centres (CSM: *S*(SP-4, Cl) = 1.2–1.6 & *S*(SP-4, Br) = 1.6–1.8). Furthermore, the whole $\{Cu_2O_2N_2X_2\}$-complex core is almost planar. Considering a least-squares plane (lspl) containing the $\{Cu_2O_2\}$-core, the distances from the other donor atoms towards this plane can be calculated (Table 3.5). The distances for the chlorido donors in **1g** are rather short (0.061 & 0.220 Å) which indicates them to be nearly in plane with

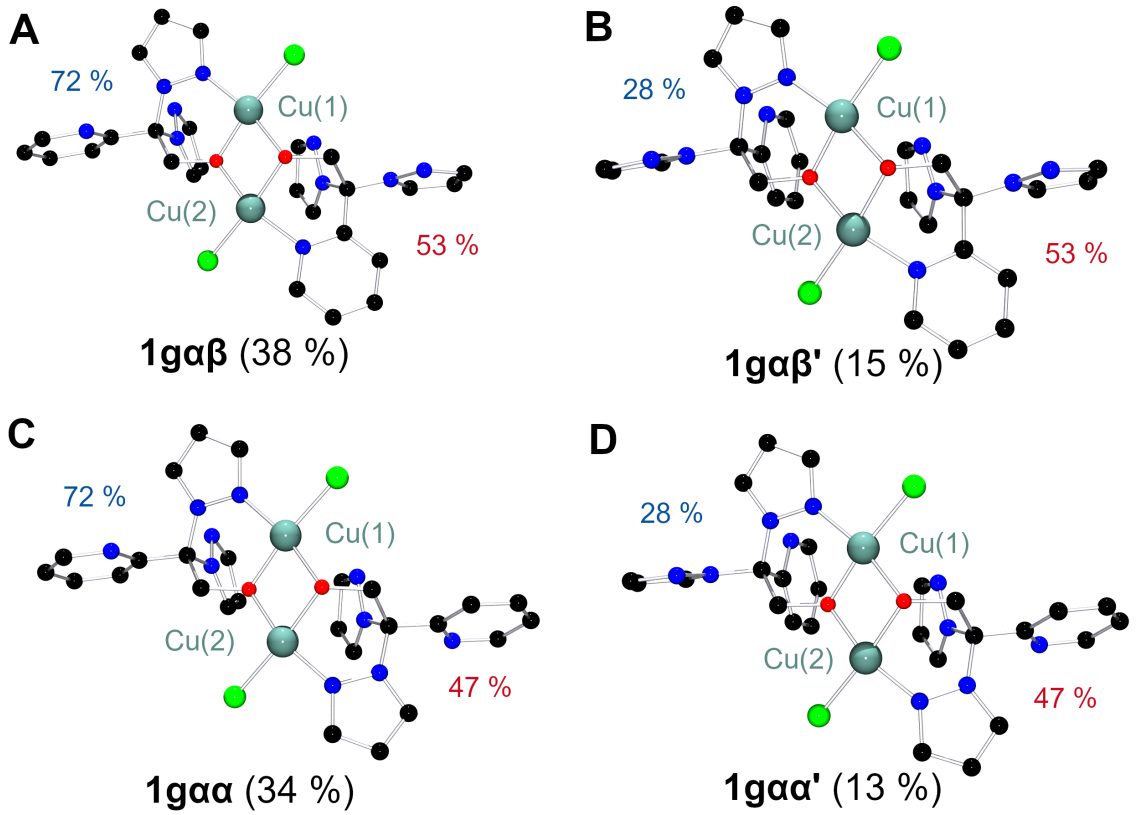

Figure 3.11: $[Cu_2(\mathbf{1}^-)_2Cl_2]$ unit in crystals of **1g** with all four possible ligand arrangements (A–D) due to Pz/Py-disorder. **α** denotes a Pz coordination and **β** a Py coordination. The different spatial arrangement of the non-coordinating Pz and Py of the ligand coordinating Cu(1) is denoted with **'**. Hydrogen atoms are omitted for clarity. Colour code: black = carbon, blue = nitrogen, red = oxygen, green copper = copper, green = chlorine.

Table 3.5: Distances (absolute values) of N and X (Cl or Br) towards a least-squares plane containing the $\{Cu_2O_2\}$-core.

Atoms	Distances to $\{Cu_2O_2\}$-lspl [Å]	
	1g	**1h**
$X_{Cu(1)}$	0.220	0.273
$X_{Cu(2)}$	0.061	0.122
$N_{Pz,Cu(1)}$	0.069	0.073
$N_{Pz,Cu(2)}$	0.529	0.434
$N_{Py,Cu(2)}$	0.621	0.500

the $\{Cu_2O_2\}$-core. The non-disordered *N*-donor ($N_{Pz,Cu(1)}$) can also be considered as in plane (0.069 Å) whereas the Pz/Py-disordered *N*-donors show lager distances to the plane (0.529 & 0.621 Å) when coordinating. For the $\{Cu_2O_2N_2Br_2\}$-core the largest distances to a least-squares plane of the $\{Cu_2O_2\}$-core feature again the (coordinating) Pz/Py-disordered *N*-donors (0.434 & 0.500 Å). The other donor atoms also show the same tendencies in the

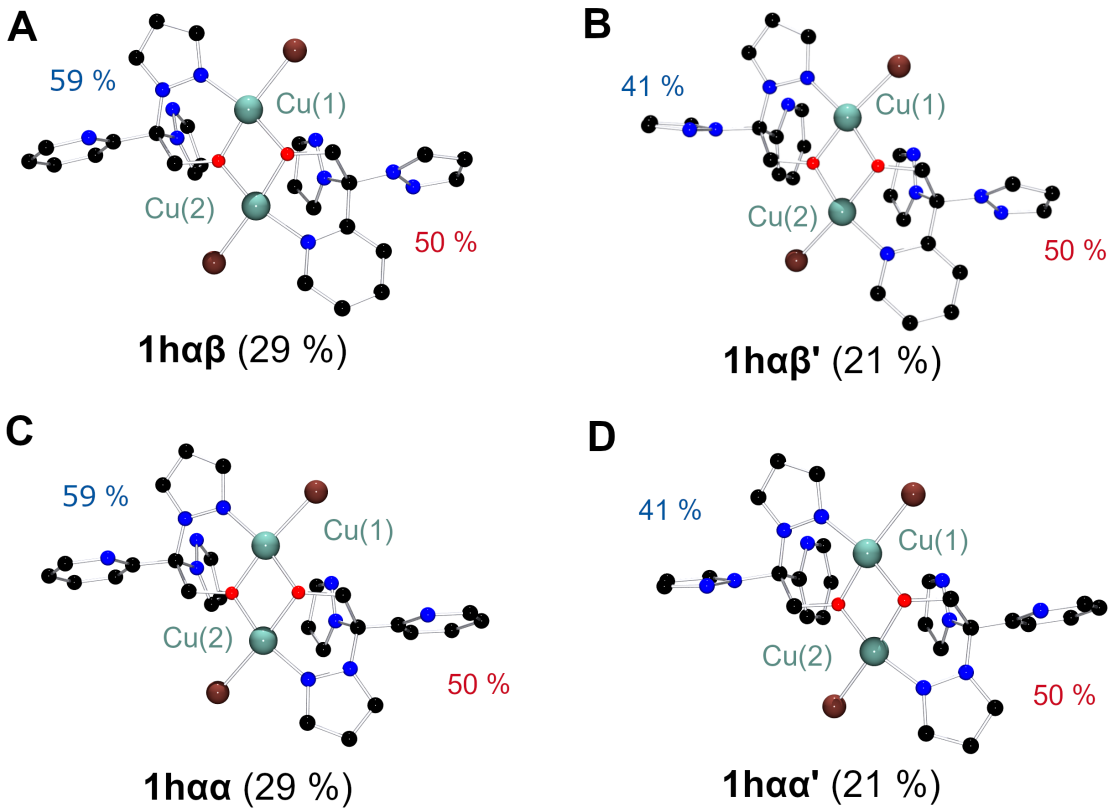

Figure 3.12: $[Cu_2(\mathbf{1}^-)_2Br_2]$ unit in crystals of **1h** with all four possible ligand arrangements (A–D) due to Pz/Py-disorder. **α** denotes a Pz coordination and **β** a Py coordination. The different spatial arrangement of the non-coordinating Pz and Py of the ligand coordinating Cu(1) is denoted with '. Hydrogen atoms are omitted for clarity. Colour code: black = carbon, blue = nitrogen, red = oxygen, green copper = copper, brown = bromine.

distance to the lspl with values in a comparable range as in the structure of **1g**. Similar alkoxide bridged dinuclear copper complexes are a common structural motif in coordination chemistry.[163–170]

Dinuclear copper complexes with a $\{Cu_2O_2N_2X_2\}$-core can form dimeric species. In general, there are three different ways in which these dimers can be formed (Figure 3.13). In the easiest arrangement, the cubane type (A), the two dinuclear complexes are sandwiched with the top half being rotated by 90° to enable four Cu – O contacts.[171–178] The second possible arrangement is the stepped cube type (B), in which the two dinuclear building blocks are aligned in the same way, but the upper half is shifted so that the right side of the upper half is connected to the left side of the lower half.[179] Again, Cu – O contacts connect this arrangement. The third type is a defect dicubane (C) which is enabled when the terminal halogen donors are incorporated in a stepped cubane arrangement. Again, the dinuclear complexes are orientated the same way but in the opposite direction than for the stepped cubane type.[166,180–182] The cubane type can be found more often than the two other arrangements.[166]

The dinuclear complexes $[Cu_2(\mathbf{1}^-)_2X_2]$ in crystals of **1g** and **1h** are arranged around a

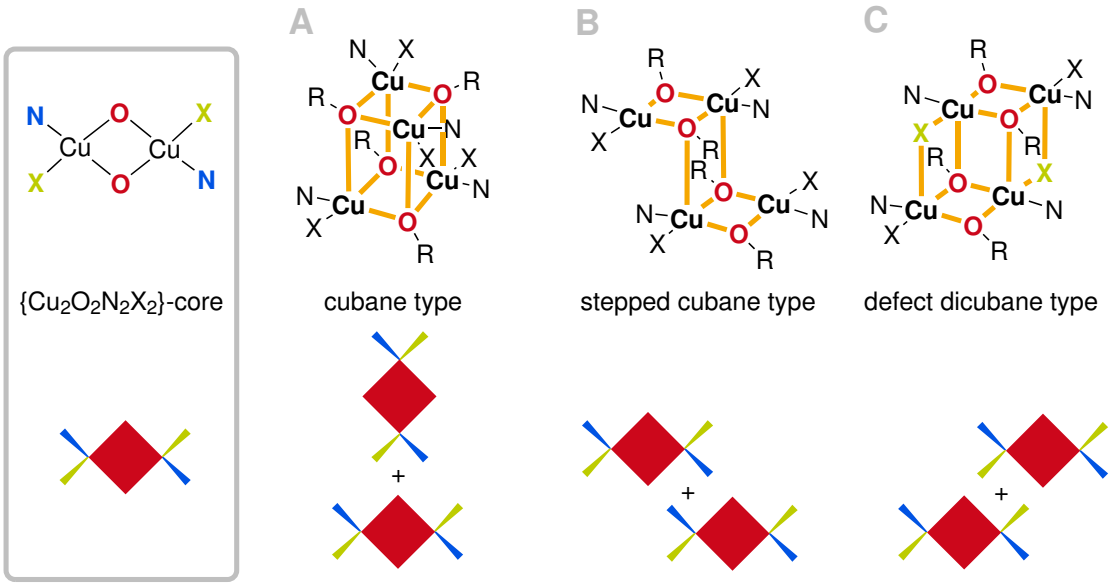

Figure 3.13: Schematic depiction of the $\{Cu_2O_2N_2X_2\}$-core (left, X = Cl, Br) and dimers arranged in cubane (A), stepped cubane (B) and defect dicubane fashion (C).

crystallographic inversion centre in very close contact in the solid state and form a defect dicubane dimer (Figure 3.14). Taking the dimeric structure into account the coordination number rises to five for each copper centre and the coordination geometry can be seen as a distorted square pyramid (CSM: S(SPY-5, Cl) = 2.0–2.3 & S(SPY-5, Br) = 2.4–2.7).
In crystals of **1g**, the distances between the two dinuclear complex molecules in the dimer are 2.570(3) Å (Cu···O') and 2.7703(16) Å (Cu···Cl'). Compared with defect dicubane structures from literature, the Cu···O' distance in **1g** are slightly longer and the Cu···Cl' distances are slightly shorter (Table 3.6).[166,180–182]

Table 3.6: Distances between dinuclear complexes in defect dicubane dimers of **1g** (top), **1h** (bottom) and literature compounds.

Compounds (CSD refcodes)	Atom distances [Å] Cu···Cl'	Cu···O'	References
1g	2.7703(11)	2.570(3)	this work
GANDAD	2.852–2.872	2.342–2.416	[180]
LETKIF	3.004	2.447	[166]
RIVBUW	2.948	2.477	[182]
TONPOE	2.813	2.428	[181]
	Cu···Br'	Cu···O'	
1h	2.9328(12)	2.686(5)	this work
LEWWEQ	3.110–3.167	2.511–2.537	[166]
RIVCAD	3.226	2.422	[182]

For **1h**, the main difference lies in the lager distances between the two parts of the dimer which are elongated by 0.12–0.16 Å (Table 3.4). In the CSD, two structures for the defect

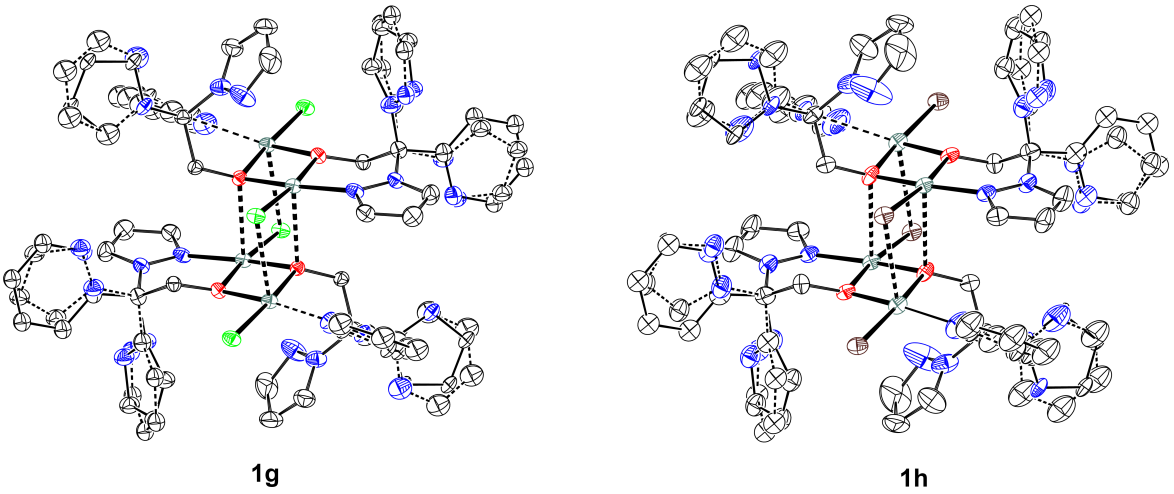

Figure 3.14: Two $[Cu_2(\mathbf{1}^-)_2X_2]$ units from crystals of **1g** (left) and **1h** (right) arranged in a dimeric fashion (dashed bold bonds) with Pz/Py-disorder (minority components dashed, 50 % probability). Hydrogen atoms are omitted for clarity. Colour code: black = carbon, blue = nitrogen, red = oxygen, green copper = copper, green = chlorine, brown = bromine.

dicubane variant with bromide can be found.[58,166,182] As already described for **1g**, the Cu···O' distances for **1h** are slightly longer (2.686(5) Å) than for the already known compounds and the Cu···Br' distances are slightly shorter (2.9328(12) Å, Table 3.6). Although the larger bromide ions in **1h** cause longer bond lengths, a molecular overlay of **1g** (green) and **1h** (brown) in Figure 3.15 visualises the high degree of similarity and that the structures are isomorphous. Besides structural chemistry, the defect dicubane structures are often investigated regarding their magnetic behaviour because of antiferromagnetic coupling of the four copper centres.[166,180]

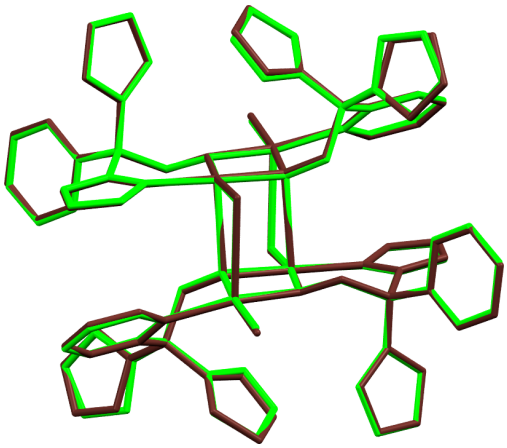

Figure 3.15: 1gαβ (green) and **1hαβ** (brown) as molecular overlay of the dimeric structures.

3.2.4 General Considerations of Complexes of $HOCH_2C(Pz)_2Py$ (1) in the Solid State

Complexes with ligand **1** in the $\{N_3\}$-coordination mode show a preferred orientation of the OH-group. If one assumes to view in direction of an axis from the CH_2-group over the apical carbon towards the metal centre, there are two different observed position of the OH-group (Figure 3.16). In the major configuration, the OH-group is positioned between the pyrazole moieties *trans* to the pyridine residue. In the minor configuration, the OH-group is positioned between a pyrazole and pyridine residue.

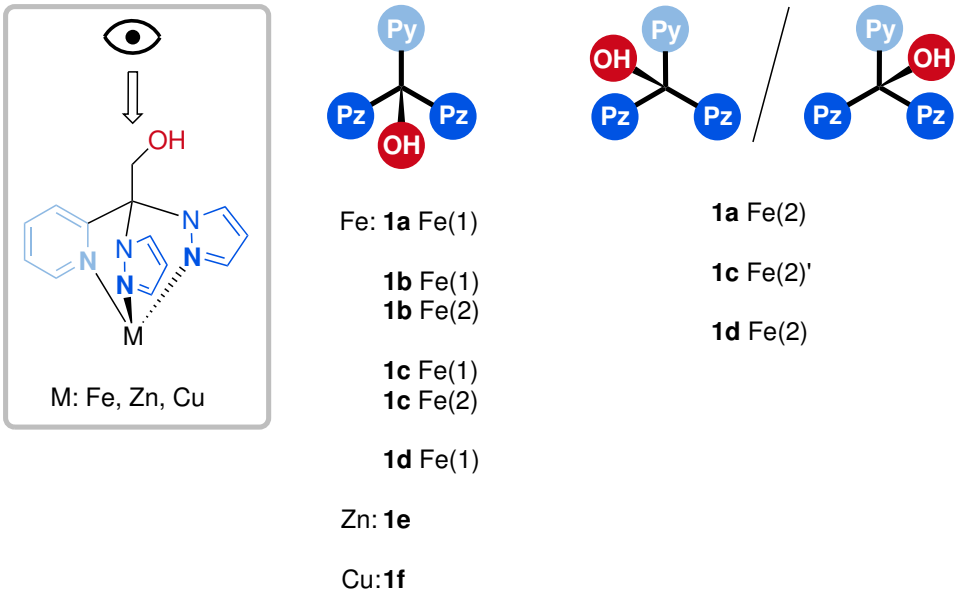

Figure 3.16: Schematic depiction of the position of the OH-group in relation to the pyrazolyl and pyridinyl donors in crystal structures of **1a** to **1f**.

Although the $\{N_3\}$-coordination mode of **1** obtained with iron, zinc and copper looks very similar, the fit of the metal ion in the coordinative cavity, provided by the pyrazolyl and pyridinyl donors, differs. To obtain a comparable value for these complexes, the distance between the apical carbon atom (C_{ap}) and the metal ion was determined (Figure 3.17).

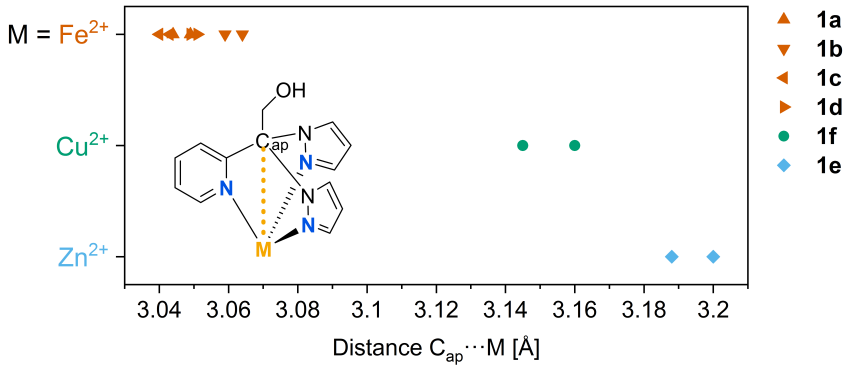

Figure 3.17: Distances $C_{ap}\cdots M$ ($M = Fe^{2+}, Cu^{2+}, Zn^{2+}$) for complexes of ligand **1**.

Iron(II) (LS) is closest to C_{ap} (3.04–3.06 Å). Copper (II) and zinc(II) show larger distances of 3.15–3.16 and 3.19–3.20 Å, respectively. This trend is in accordance with the Shannon-radii of these ions.[183] However, this correlation must be taken with caution since the influence of the ligand field stabilisation energy is not included. It would be interesting to investigate if this correlation continues for other 3*d* metal complexes with **1** in $\{N_3\}$-coordination mode.

3.3 Iron Complexes of $HOCH_2C(Pz)_2Py$ (1) in Solution

The complexes were synthesised to be potential homogeneous catalysts. Hence, the question arises if the bisfacial coordination mode that was found for the complexes in the solid state is maintained in solution or if 1 : 1 ratios of iron salt and ligand can result in monofacial solution species.

3.3.1 UV/Vis Titration Experiments

Titration experiments with different solutions of iron salts, where ligand **1** is added stepwise, delivered very different results. Note that these experiments were carried out under aerobic conditions and with non-dried solvent unless otherwise stated.
To a solution of $FeCl_2$ in acetonitrile, a solution of **1** was added stepwise (Figure 3.18, left).

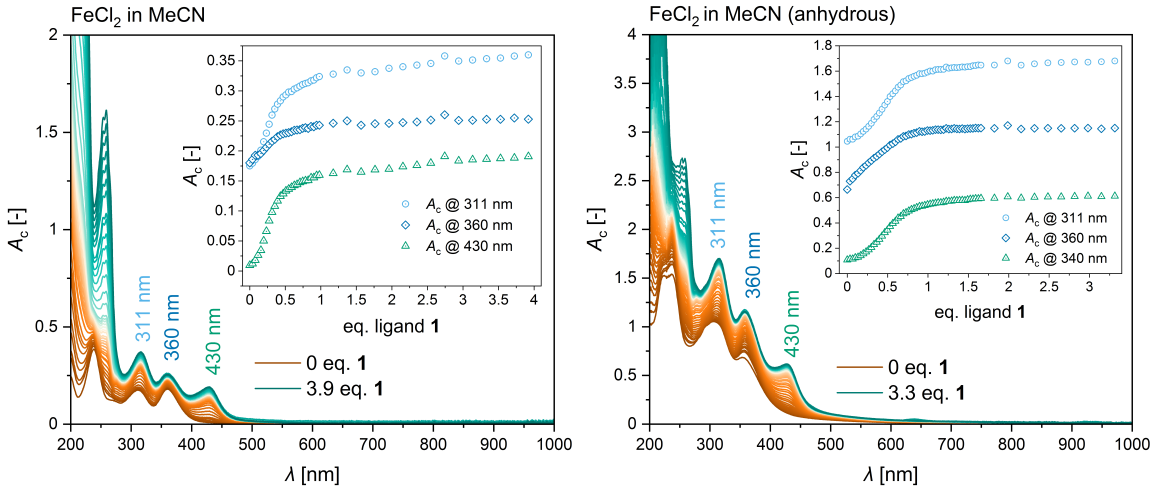

Figure 3.18: UV/Vis spectra with corrected absorption A_c of $FeCl_2$ in MeCN and titration with **1**. Left: 0.1 mM $FeCl_2$; Right: 0.1 mM anhydrous $FeCl_2$ in abs. MeCN.

To take into account the dilution of the UV/Vis sample upon adding ligand solution, the absorption A was corrected by a dilution factor to give a corrected absorption A_c (for details see subsection 9.1.4). The extinction coefficient was not calculated because the resulting species and their concentrations are unknown. The absorption of the bands at 311, 360 and 430 nm plotted against the added equivalents of **1** are shown in the inset. For all three bands a plateau is reached after around 1 eq. of **1** was added. In contrast to the bisfacial species

found in solid state (**1c**), this would correspond to a monofacial species. Notably, the bands at 311 and 360 nm are present from the beginning in the pure iron-salt solution without any ligand added, which is also shown in Figure 3.19. As comparison, the experiment was repeated with anhydrous $FeCl_2$ using abs. acetonitrile (Figure 3.18, right, aerobic conditions). Here, the same bands at 311 and 360 nm were observed in the pure salt solution. The addition of ligand **1** gave similar results with a plateau starting around 1 eq. of added ligand.

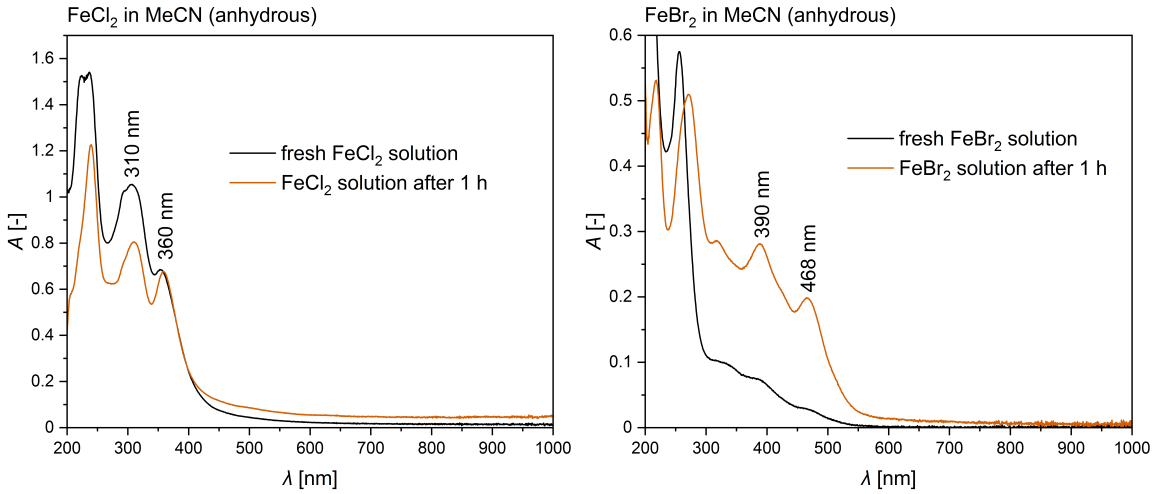

Figure 3.19: UV/Vis spectra of $FeCl_2$ in MeCN (0.1 mM, left) and $FeBr_2$ in MeCN (0.1 mM, right). Spectra at start of titration in black and similar solution prepared 1 h later in orange (aerobic conditions).

Since the bands at 311 and 360 nm are observed without addition of ligand **1**, it is obvious that it must be a species solely with iron and chloride. Thinkable is a tetrachloridoferrate anion as it was observed in the crystal structure of **1c**. Only the band at 430 nm can be assigned to the formed complex with **1**. Since more than one species is found – an iron complex with ligand **1** and a potential tetrachloridoferrate anion – it seems not reasonable to assign one equivalent of **1** to a monofacial species. This could lead to the following hypothesis: Parts of $FeCl_2$ form tetrachloridoferrate anions in the pure iron salt solution right at the beginning. After addition of the ligand, a complex forms which may be a monofacial species with additional coordination sites occupied by acetonitrile, which is known to be a coordinating solvent. This would generate free chloride ions which are available to form further tetrachloridoferrate anions with remaining $FeCl_2$. The formation of tetrachloridoferrate anions consumes iron from the 1 eq. of iron available for the complex formation with **1**, which would mean that at 1 eq. of added ligand there is more than one ligand molecule per available iron centre (not involved in tetrachloridoferrate anions). Considering that all chloride anions available form tetrachloridoferrate anions, this would theoretically lead to a bisfacial complex species at 1 eq. of ligand **1**:

$$2\,FeCl_2 + 2\,(\mathbf{1}) \longrightarrow [Fe(\mathbf{1})_2]^{2+} + [FeCl_4]^{2-}$$

Another possibility would be the formation of a monofacial complex of iron and **1** with chloride anions occupying the free coordination sites. However, this would not necessarily explain the simultaneous rise of the tetrachloridoferrate bands at 311 and 360 nm, unless such a chlorido complex would have the exact same UV/Vis bands. The amount of water seems to have an additional impact on the tetrachloridoferrate anion formation as indicated by the experiment conducted under anhydrous conditions.

Research in the literature about UV/Vis spectra of iron chloride compounds in acetonitrile revealed that the $[FeCl_4]^-$ anion shows characteristic absorption bands at 311 and 359 nm (314 and 364 nm in DCM) which matches the species observed in this work.[184,185] For $[FeCl_4]^{2-}$ no appropriate data for comparison could be found. If the observed species is $[FeCl_4]^-$ some redox process from iron(II) to iron(III) must have taken place. This could be due to the aerobic conditions under which these experiments were conducted. However, the observation of an iron(III) tetrachloridoferrate anion matches the $[FeCl_4]^-$ found in crystals of **1c**, which were also synthesised under aerobic conditions. In summary, the two bands present from the beginning at 311 and 360 nm are most likely from $[FeCl_4]^-$, but they also rise upon ligand addition.

The same ligand titration experiment was also performed with $FeCl_3$ as iron salt (Figure 3.20). In this case, the same bands at 311, 360 and 430 nm were observed. All three absorption maxima are stagnant at the addition of around 1 eq. of **1**, which is similar to the experiments with $FeCl_2$. This also indicates the formation of $[FeCl_4]^-$ anions, which expands with further ligand addition and seems more reasonable because iron(III) is used. A monofacial complex $[Fe(HOCH_2C(Pz)Py)Cl_3]$ as it could be characterised in the solid state via SCXRD during my Master's thesis is not very likely, as it would not explain the rise of the $[FeCl_4]^-$ band upon ligand addition.[140]

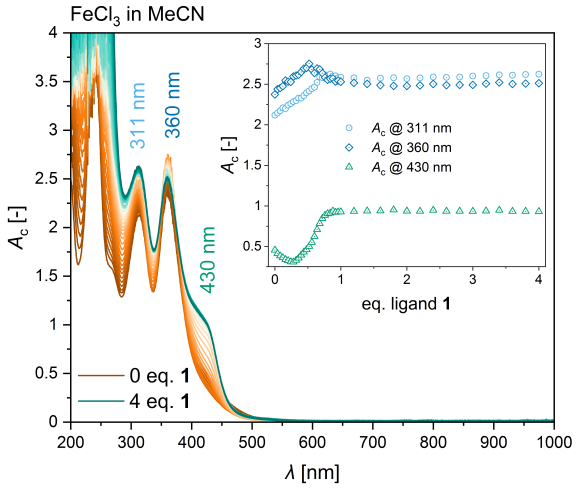

Figure 3.20: UV/Vis spectra with corrected absorption A_c of $FeCl_3$ in MeCN and titration with **1** (0.5 mM $FeCl_3$).

A possible species for the formation of $[FeCl_4]^-$ in the solution at the start of the titration, could be $[Fe^{III}Cl_2(MeCN)_4][Fe^{III}Cl_4]$ as Gao *et al.* observed for $FeCl_3$ in acetonitrile.[186]

Interestingly, the complex band at 430 nm first decreases and then rises until 1 eq. of **1** has been added.

The titration experiment was also performed with $FeBr_2$ in acetonitrile (Figure 3.21). The left spectrum shows the formation of two bands at 320 and 428 nm after addition of the ligand **1**, which stagnate at about 1 eq. of the **1**. At the start of the titration, different bands can be observed. The ones at 390 and 468 nm are the most interesting ones, as these indicate the formation of potential tetrabromidoferrate anions, analogous to the chloride experiments (Lit. $[FeBr_4]^-$: 391 and 469.5 nm in MeCN; 392 and 472 nm in DCM).[184,185] Analogous to the tetrachloridoferrate species, only literature values for an iron(III) anion could be found. However, this matches the $[FeBr_4]^-$ anion found in crystals of **1b**, which were also synthesised under aerobic conditions.

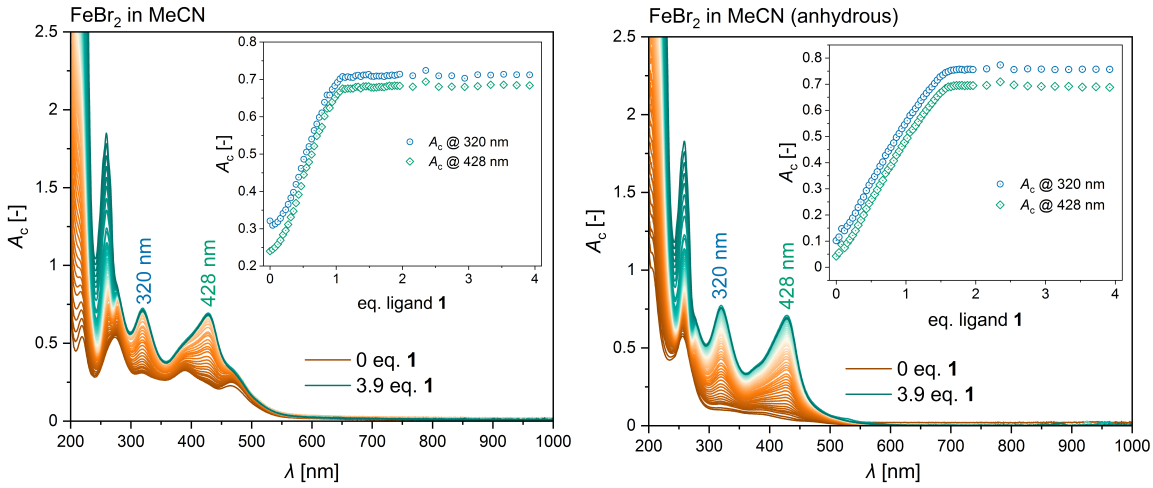

Figure 3.21: UV/Vis spectra with corrected absorption A_c of $FeBr_2$ in MeCN and titration with **1**. Left: 0.1 mM $FeBr_2$; Right: 0.1 mM anhydrous $FeBr_2$ in abs. MeCN.

The same experiment was repeated with anhydrous $FeBr_2$ and abs. acetonitrile (Figure 3.21, right, aerobic conditions). Here, the bands for tetrabromidoferrate anions are much lower. If such a solution is prepared from a 1 h old stock solution, which is exposed to oxygen, these bands are getting more intensive (Figure 3.19, right) and are similar to those of the non-anhydrous $FeBr_2$. So, the older the starting solution is, the more tetrabromidoferrate can be observed. For $FeCl_2$ (left), both spectra show nearly the same bands indicating that the tetrachloridoferrate formation is faster than formation of tetrabromidoferrate.

Different to the saturation of the maxima at 1 eq. of ligand for the left spectra in Figure 3.21, the right spectra for anhydrous $FeBr_2$ and abs. acetonitrile show a saturation at 1.6 eq. of ligand. Maybe the complex formation is promoted by the amount of tetrabromidoferrate anion and is therefore finished in the left spectrum earlier. Another problem with this spectrum is that the new formed bands (320 and 428 nm) are overlaid by the bands of the tetrabromidoferrate anions (390 and 468 nm).

To circumvent the issue with the tetrahalidoferrate anions, the titration experiment was also performed with $Fe(NO_3)_3 \cdot 9\,H_2O$ (Figure 3.22). In this experiment, a steep increase for

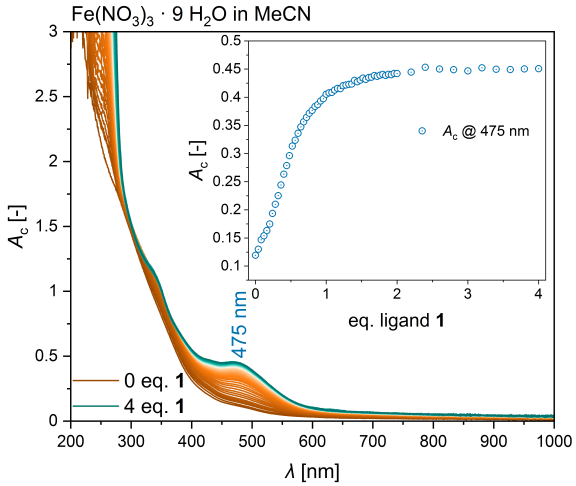

Figure 3.22: UV/Vis spectra with corrected absorption A_c of $Fe(NO_3)_3 \cdot 9\,H_2O$ (0.5 mM) in MeCN and titration with **1**.

the absorption at 475 nm was observed until addition of 1 eq. of **1**. Afterwards, the band is still rising but with a much flatter slope and is stagnant after 2 eq. of **1**. This would indicate a bisfacial rather than a monofacial species.

To investigate the influence of the solvent, some experiments were repeated in methanol (Figure 3.23). $FeCl_2$ in methanol shows bands at 320 and 428 nm that are rising upon addition of **1** (left). The absorptions rise until the addition of 2 eq. of ligand and can be considered stable afterwards although the measurements show some noise. The right plot shows the same experiment for $FeCl_3$. Bands with maxima at the same wavelengths (320 and 428 nm) are observed. The slope changes with the addition of 2 eq. of **1** and becomes flatter, but it does not reach a plateau. This suggests that more than one process is taking place.

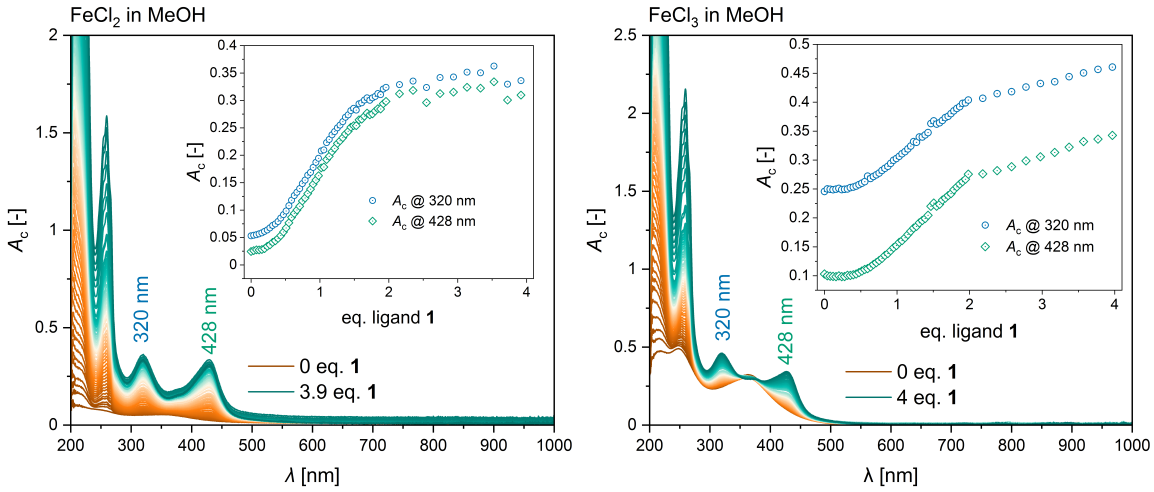

Figure 3.23: UV/Vis spectra with corrected absorption A_c of iron chloride salts in MeOH and titration with **1**. Left: 0.1 mM $FeCl_2$; Right: 0.09 mM $FeCl_3$.

A similar behaviour can be observed for the titration experiment with $FeBr_2$ in methanol (Figure 3.24). Again, bands are at 320 and 428 nm with a steeper slope up to 2 eq. of ligand

and a flatter slope for higher ligand amounts. For all measurements in methanol, bands at 320 and 428 nm were observed which correspond to the bands seen for $FeBr_2$ in acetonitrile (Table 3.7).

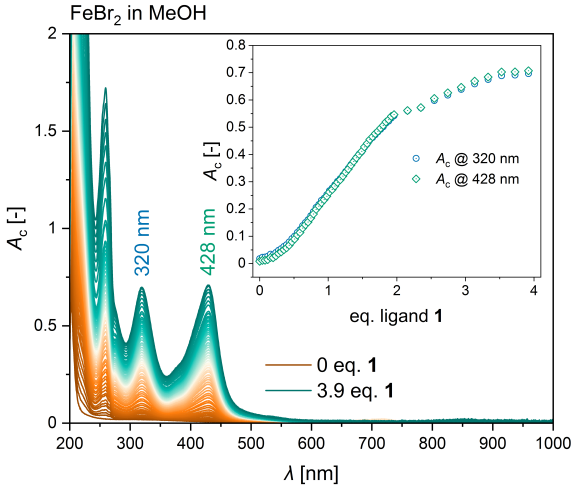

Figure 3.24: UV/Vis spectra with corrected absorption A_c of $FeBr_2$ (0.1 mM) in MeOH with and titration with **1**.

Table 3.7: UV/Vis bands observed at the end of the titration experiments.

Experiments	UV/Vis bands at the end of the titration [nm]						
in MeCN:							
$FeCl_2$	257	311		360	430		
$FeCl_2$ (anhydrous)	257	311		360	430		
$FeCl_3$		311		360	430		
$FeBr_2$	259		320		428		
$FeBr_2$ (anhydrous)	259		320		428		
$Fe(NO_3)_3 \cdot 9\,H_2O$							475
in MeOH:							
$FeCl_2$	259		320		428		
$FeCl_3$	259		320		428		
$FeBr_2$	259		320		428		
References in MeCN:	UV/Vis bands [nm]						
$[FeCl_4]^-$ [184]		311.5		360			
$[FeBr_4]^-$ [184]					391	469.5	

Experiments with chlorides in acetonitrile all show bands similar to those of the tetrachloridoferrate anion and one additional band at 430 nm. In the other experiments, the bands at 320 and 428 nm are dominating: nearly all have a band at 257 or 259 nm in common. The only measurement without halide anions but iron nitrate showed a completely different single band at 475 nm.

Considering all results, a bisfacial species is more likely than a monofacial species for all

UV/Vis spectroscopic experiments with iron and ligand **1**. Although some results with iron halide salts first indicate a monofacial species, the results are biased by the formation of an unknown amount of tetrahalidoferrate anions. Therefore, components are removed from the simple salt plus ligand equilibrium, making the interpretation much more complicated. Overall, the addition of ligand **1** seems to enable easier the formation of tetrahalidoferrate anions.

3.3.2 Cyclovoltammetric Experiments

*Results from the UV/Vis experiments with **1** and different iron salts led to reevaluation of cyclic voltammograms (CV) that were measured during my Master's thesis.[140] CVs with **1** and iron chloride and bromide salts were measured between May and November 2018, and these CV plots are respectively marked with *. The reference experiments and the new interpretation of the former results were performed during the work in this thesis (Scheme 3.6).*

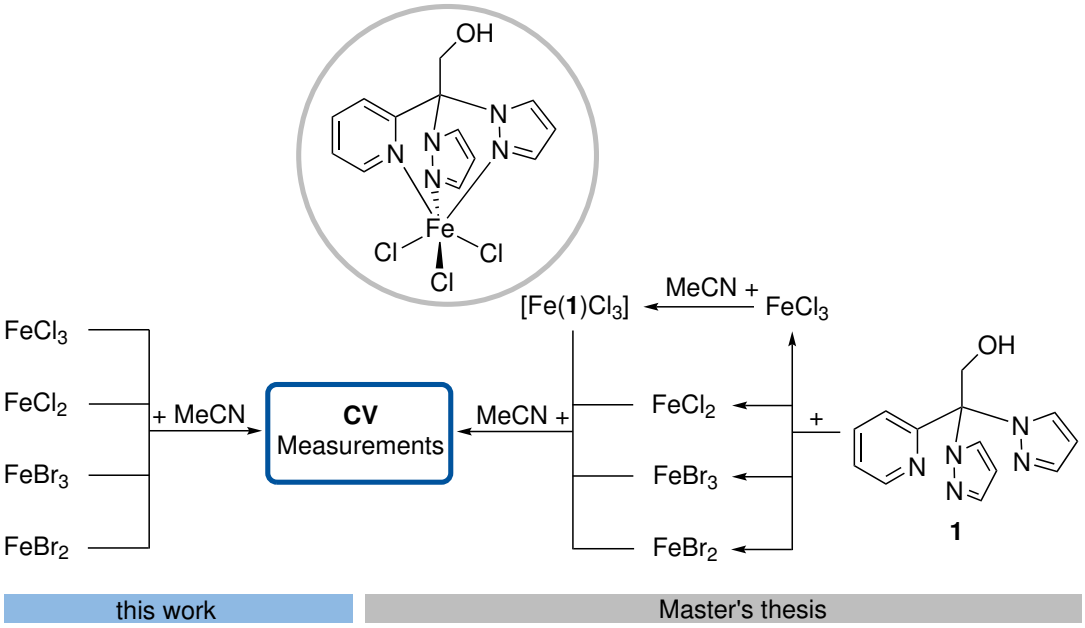

Scheme 3.6: CVs measured with iron chloride/bromide salts and **1** in MeCN and the point in time of experiment.

The aim of these experiments is to determine the redox potential of the bisfacial iron complexes with ligand **1**. Iron(II) and iron(III) species were chosen as starting points to investigate both variants for a potential redox-cycle. The experiments were performed under aerobic conditions at room temperature (for details see subsection 9.1.10). The measurement of CVs with different scan rates (20–200 mV/s) of only $FeCl_3$ in acetonitrile resulted in a reversible redox process (Figure 3.25) with a half-wave potential of $E_{1/2} = -0.395$ V against the ferrocene redox couple (Fc/Fc^+) (Table 3.8). The CVs that were measured 10 min later look very similar and show that the observed species is stable in this time range. Since $[FeCl_4]^-$ anions are easily formed by $FeCl_3$ in acetonitrile (see subsection 3.3.1), $[FeCl_4]^{-/2-}$ is a

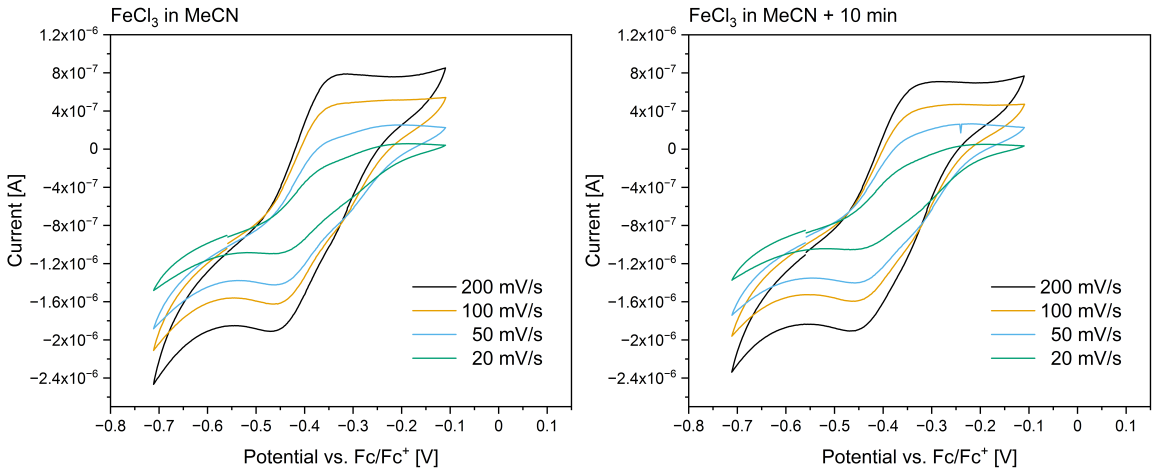

Figure 3.25: CVs observed for a solution of $FeCl_3$ in MeCN (left) and the same sample 10 min later (right).

Table 3.8: Half-wave potentials ($E_{1/2}$) and peak-to-peak separations (ΔE) obtained from the CVs.

Compound(s)	$E_{1/2}$ vs. Fc/Fc^+ [V]	ΔE [mV]
$FeCl_3$	−0.395	75
$FeCl_2$	not reversible	
$FeBr_3$	not determined	
$FeBr_2$	not reversible	
[Fe(**1**)Cl_3]	−0.390*	77*
$FeCl_2$ + **1**	−0.364*	85*
$FeBr_3$ + **1**	−0.217*	77*
$FeBr_2$ + **1**	−0.207*	89*

* Results obtained during Master's thesis.

reasonable redox couple for this experiment. Collomb *et al.* determined the redox potential of the $[FeCl_4]^{-/2-}$ pair in acetonitrile to be −0.32 V vs. $Ag/AgNO_3$ which corresponds to −0.40 V vs. Fc/Fc^+.[187] However, the CV measured in the Master's thesis for iron(III) and iron(III) species are very similar (Figure 3.26) and redox potentials in the same range (−0.390 & −0.364 V, respectively). It stands to reason that the species observed in the experiments with **1** are not a complex of **1** but $[FeCl_4]^{-/2-}$. This is also consistent with the observations in the UV/Vis spectra from the previous sections where these anions were observed.

Interestingly, the use of only $FeCl_2$ does not lead to a reversible redox potential that indicates the presence of $[FeCl_4]^{-/2-}$ anions (Figure 3.27). Again, the use of ligand **1** enables the formation of $[FeCl_4]^{-/2-}$ anions since the experiment with **1** shows a reversible redox potential in the corresponding region. Ligand **1** and $FeCl_2$ were used in equimolar amounts. The formation of $[FeCl_4]^{-/2-}$ anions suggests formation of a bisfacial complex cation. The observation that formation of complexes that "release" Cl^- enables the formation of $[FeCl_4]^{-/2-}$ was also made by Collomb *et al.*[187]

Similar observations for the CVs were made with bromide instead of chloride. A formation

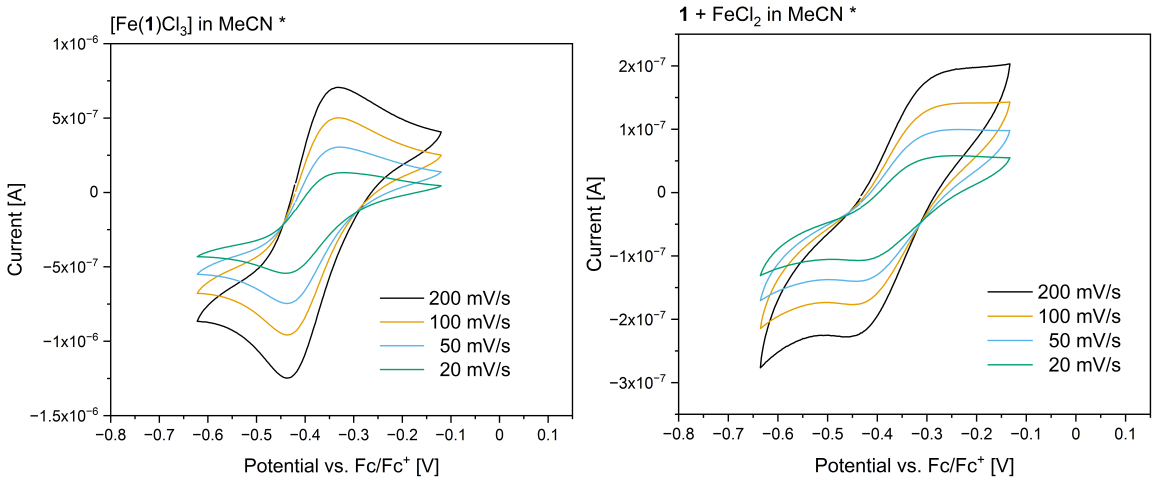

Figure 3.26: CVs observed for a solution of [Fe(**1**)Cl_3] (left) and $FeCl_2$ with **1** (right) in MeCN.

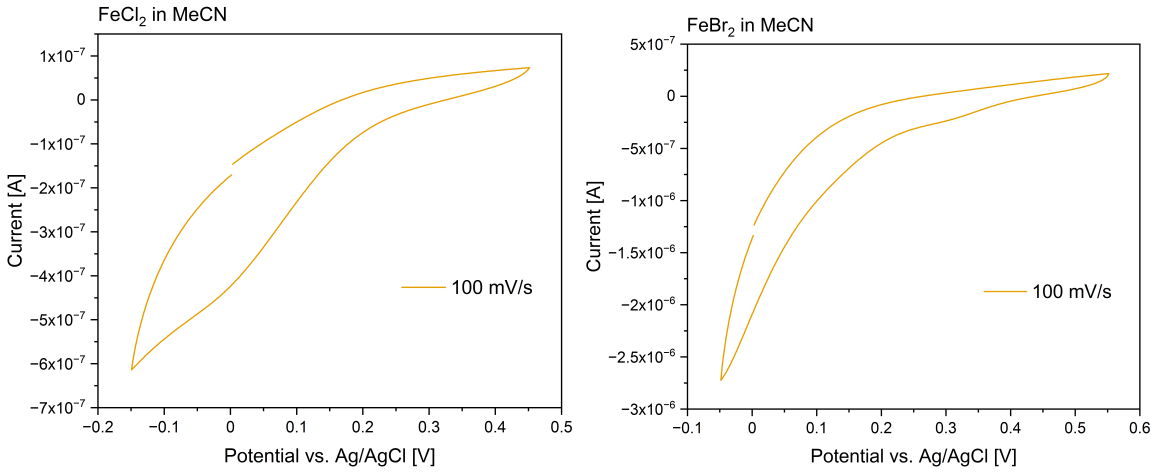

Figure 3.27: CVs observed for a solution of $FeCl_2$ (left) and $FeBr_2$ (right) in MeCN.

of a species with reversible redox potential was not possible when only $FeBr_2$ was added into acetonitrile (Figure 3.27). However, starting from $FeBr_3$ a quasi-reversible species could be observed, showing a poor stability since an additional measurement after 10 min showed a clear decrease in the observed species (Figure 3.28). No appropriate literature values could be found for comparison. Nevertheless, the spectra with addition of the ligand **1** showed reversible spectra for $FeBr_3$ and $FeBr_2$ with reduction potentials of −2.217 and −2.07 V, respectively (Figure 3.29). Although addition of ligand also enables the formation of most likely $[FeBr_4]^{-/2-}$ anions, the bromide variant is less stable than the chloride analogue as indicated by the CV measured after 13 min (Figure 3.29, top, right).

Taking all the CV results into account, starting from iron(II) halide salts, it is not possible to see the redox potential of the tetrahalidoferrate anions (Scheme 3.7). If the starting species is the corresponding iron(III) salt, the typical CV of the tetrahalidoferrate anion couple can be observed. Solutions with ligand **1** and the corresponding iron chloride/bromide salt lead to the observation of tetrahalidoferrate anions, regardless of whether the starting species was an iron(II) or iron(III) salt. Species with bromide are less stable than with chloride.

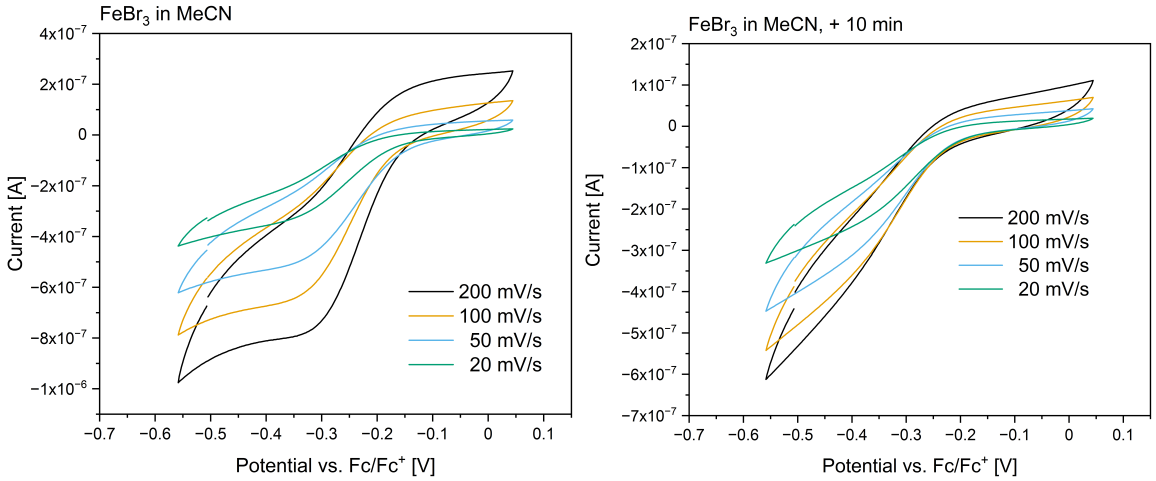

Figure 3.28: CVs observed for a solution of $FeBr_3$ in MeCN (left) and the same sample 10 min later (right).

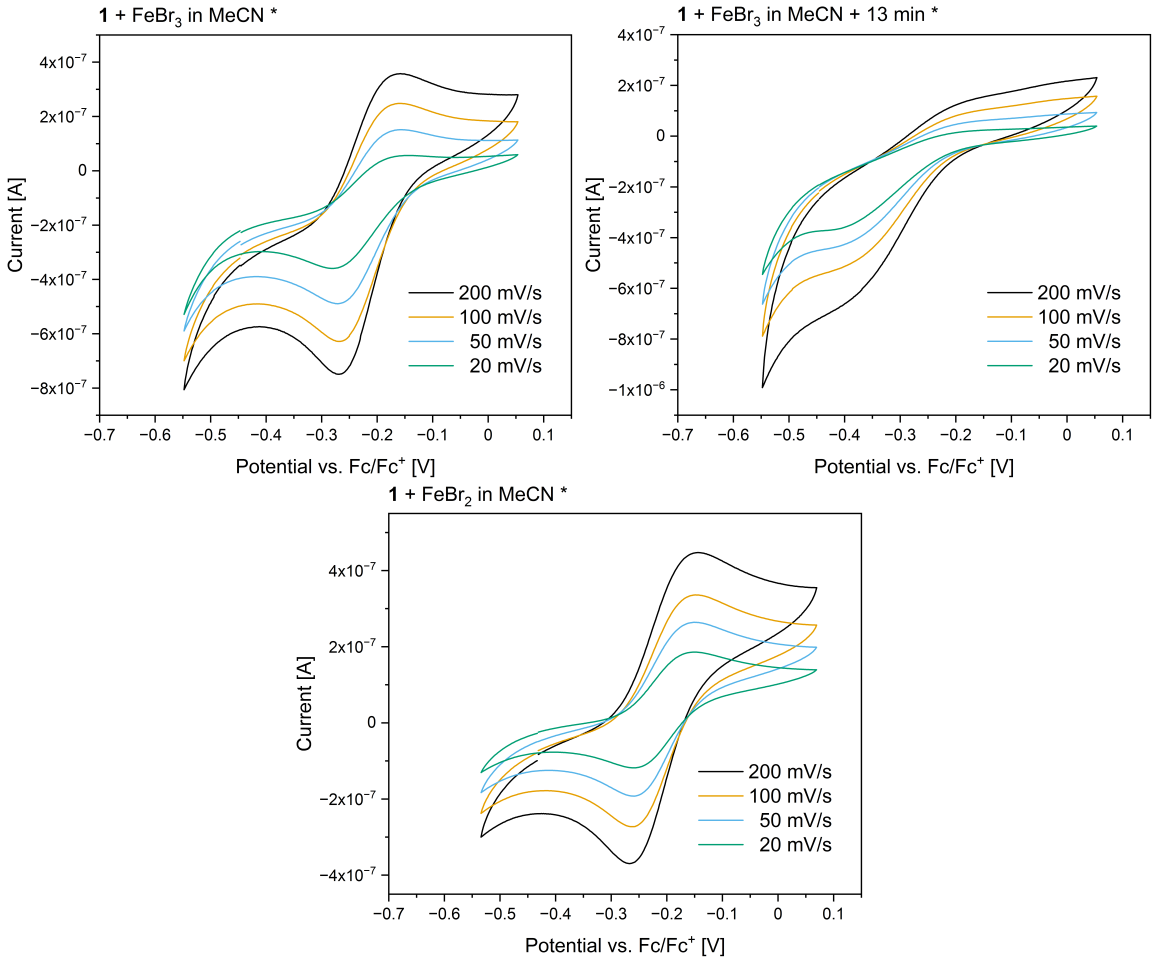

Figure 3.29: CVs observed for a solution of $FeBr_3$ with **1** (top, left), $FeBr_3$ with **1** after 13 min (top, right) and $FeBr_2$ with **1** (bottom, middle), all in MeCN.

3.3.3 General Considerations in Solution

The UV/Vis as well as the cyclic voltammetry experiment results point towards the same direction as tetrahalidoferrate anions were observed with both measurement techniques.

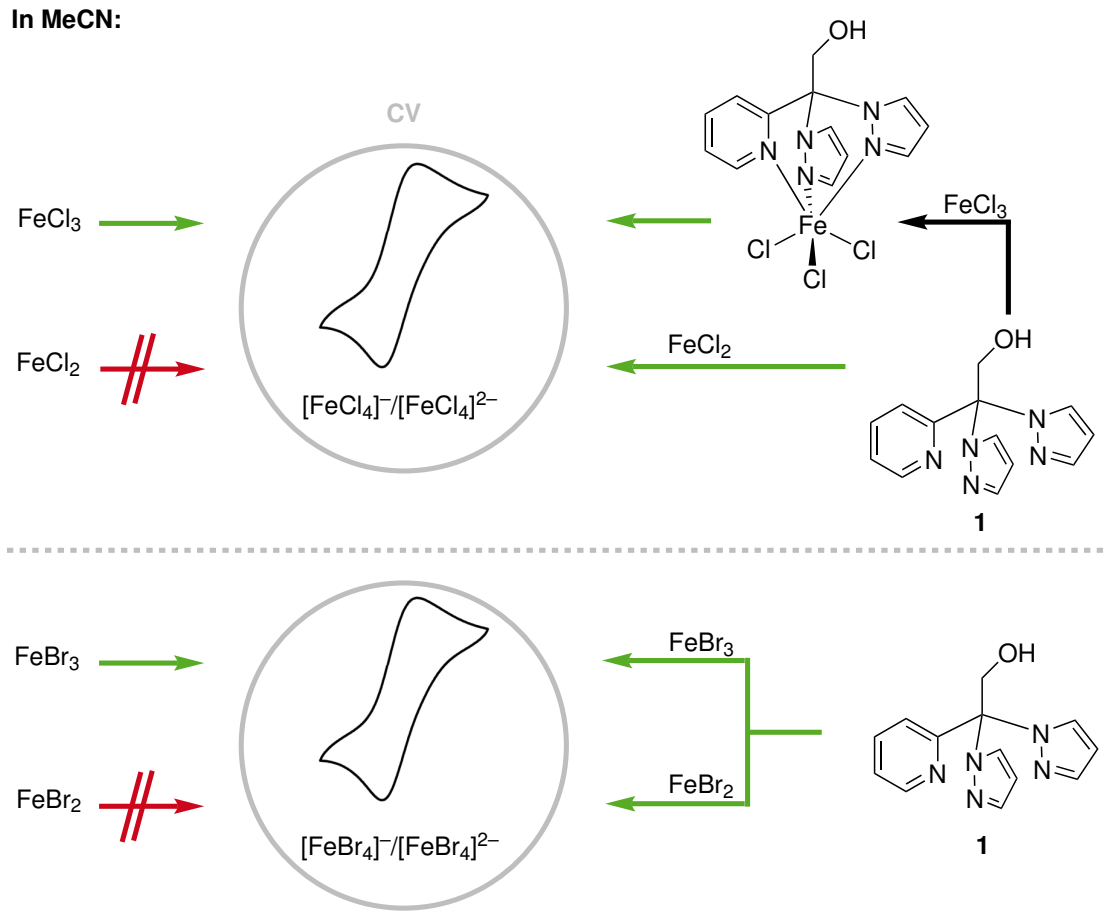

Scheme 3.7: Results of CVs in MeCN for combination of ligand **1** and iron chloride/bromide salts.

The tetrahalidoferrate anions were observed in solutions without added ligand where they form more easily from iron(III) than from iron(II) salts. Furthermore, the formation of tetrahalidoferrate anions is promoted by the presence of ligand **1**, most likely through the formation of a complex species without halogen donors. Due to the aerobic conditions of the experiments, the observed tetrahalidoferrate anions are rather an iron(III) species ($[FeX_4]^-$). Possible reaction pathways and species in solution are shown in Scheme 3.8. Note that this is only a rough sketch of assumed processes and the reality is most likely even more complicated. To reveal the full picture of processes happening here, more measurements are needed but investigations were stopped at this point since the synthesised complexes are no longer suitable as potential homogeneous catalysts. The main reason is that it would be very challenging to examine if the desired complex with ligand **1** is functioning as catalyst or if the tetrahalidoferrate anions are acting as catalyst. In case of bromide, these tetrabromidoferrate anions have been found to be active in the atom radical transfer polymerisation.[188] Furthermore, the structure of the complex formed by iron(II) and **1** is still not fully understood in solution. Additionally, the most likely bisfacial complex is expected to be not a very effective homogeneous catalyst since there are no vacant coordination sites available for substrates at the metal centre. Consequently, tetradentate

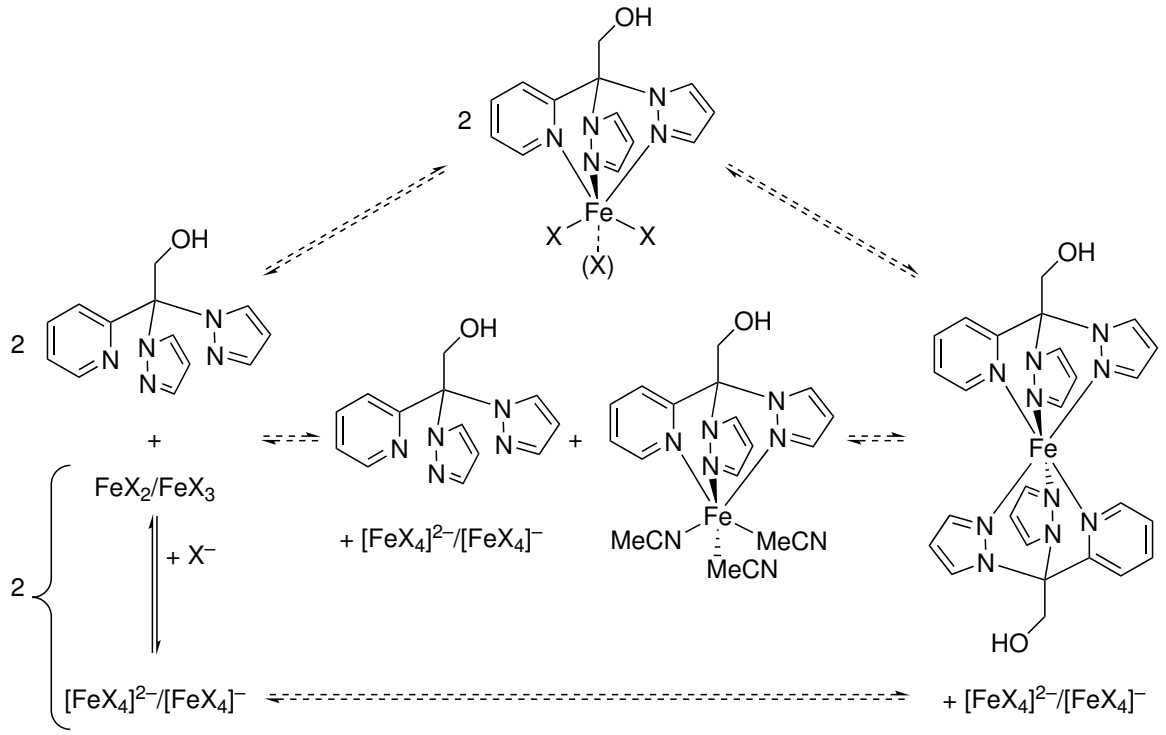

Scheme 3.8: Possible species present in MeCN for combination of ligand **1** and iron chloride/bromide salts.

ligands are needed to prevent bisfacial coordination and generating labile coordination sites for homogeneous catalysis.[126,148]

3.4 Concluding Remarks on Complexes of Ligand $HOCH_2C(Pz)_2Py$ (1)

The backbone functionalisation of **1** did reveal a similar coordination behaviour compared to the parent ligand $HC(Pz)_2Py$ since studies in the solid state and in solution mostly indicated bisfacial $\{N_6\}$-coordinated complexes. Exceptions to this are the obtained copper structures of **1f**, **1g** and **1h**.

However, the results point out that changing the 3*d* metal ion may lead to a variety of complexes depending on the different characters of the metal ions. Therefore, it is important to tailor each ligand to the metal ion in order to obtain the desired complex properties, rather than using one ligand for a variety of metal ions.

Regarding the iron compounds – which are the main focus of this thesis – the bisfacial coordination mode saturating the primary coordination sphere does not provide labile coordination sites which are key for metal mediated catalytic processes. Hence, the following chapters address the development of iron complexes with tetradentate ligands that prevent a bisfacial coordination mode and provide better protection of the metal ion while allowing *cis*-labile coordination sites.

4 Bis(pyridinyl)phenanthrolinylmethane – a Ligand with $\{N_4\}$-Coordination

*The ligand MeC(Py)$_2$Phen (**2**) was developed by Dr. Kristina Keisers during her PhD thesis together with the iron(II) complex [Fe(MeC(Py)$_2$Phen)(MeCN)$_2$](OTf)$_2$ (**2a**). First investigations towards an iron(IV)oxo species were performed by her.[136] The potential of this iron(IV)oxo complex as catalyst for C – H bond activation reactions is investigated in the present work. In the context of this thesis the tetrafluoridoborate analogue to **2a** [Fe(MeC(Py)$_2$Phen)(MeCN)$_2$](BF$_4$)$_2$ · MeCN (**2b**) could be structurally characterised. Combined results were published in "Catalytically Active Iron(IV)oxo Species Based on a Bis(pyridinyl)phenanthrolinylmethane".[189] Mößbauer measurements and fitting of data were performed by Dr. Linda Iffland-Mühlhaus in the group of Prof. Dr. Ulf-Peter Apfel at Ruhr-Universität Bochum, Germany. Femtosecond X-ray emission spectroscopy experiments (XES) were carried out at European XFEL (Hamburg/Schenefeld, Germany) at the femtosecond X-ray experiments (FXE) instrument in November 2021. The measurements were performed in cooperation with Dr. Mykola Biednov and support of the whole FXE group under supervision of Dr. Christopher Milne. XES data correction was performed by Dr. Mykola Biednov.*

4.1 Iron Complexes of MeC(Py)$_2$Phen (2) in the Solid State

Besides the known complex [Fe(MeC(Py)$_2$Phen)(MeCN)$_2$](OTf)$_2$ (**2a**), three other molecular structures of iron complexes of ligand **2** were characterised in this thesis (Figure 4.1).
In order to make the structures comparable among each other (e.g. bond lengths and angles) a labelling of the donors is used according to Figure 4.2. The free coordination sites are labelled Y and Z. Y is *trans* to the *N*-donor of one of the pyridinyl groups ($N_{Py\text{-}Y}$). Z is on the *trans*-position to the *N*-donor of the phenanthrolinyl group which is closest to the central quaternary carbon atom ($N_{Phen\text{-}Z}$).

[Fe(MeC(Py)$_2$Phen)(MeCN)$_2$](BF$_4$)$_2$ · MeCN (2b)

If the triflate iron salt in the synthesis of **2a** is substituted by [Fe(MeCN)$_6$](BF$_4$)$_2$, the same bis(acetonitrile) complex cation of [Fe(**2**)(MeCN)$_2$]$^{2+}$ can be obtained (Scheme 4.1). It was possible to obtain suitable crystals of [Fe(**2**)(MeCN)$_2$](BF$_4$)$_2$ · MeCN (**2b**) for SCXRD (Figure 4.3). **2b** crystallises as an acetonitrile solvate in the triclinic space group $P\bar{1}$ with $Z = 2$. The tetrafluoridoborate anions remain uncoordinated like the triflate anions in the

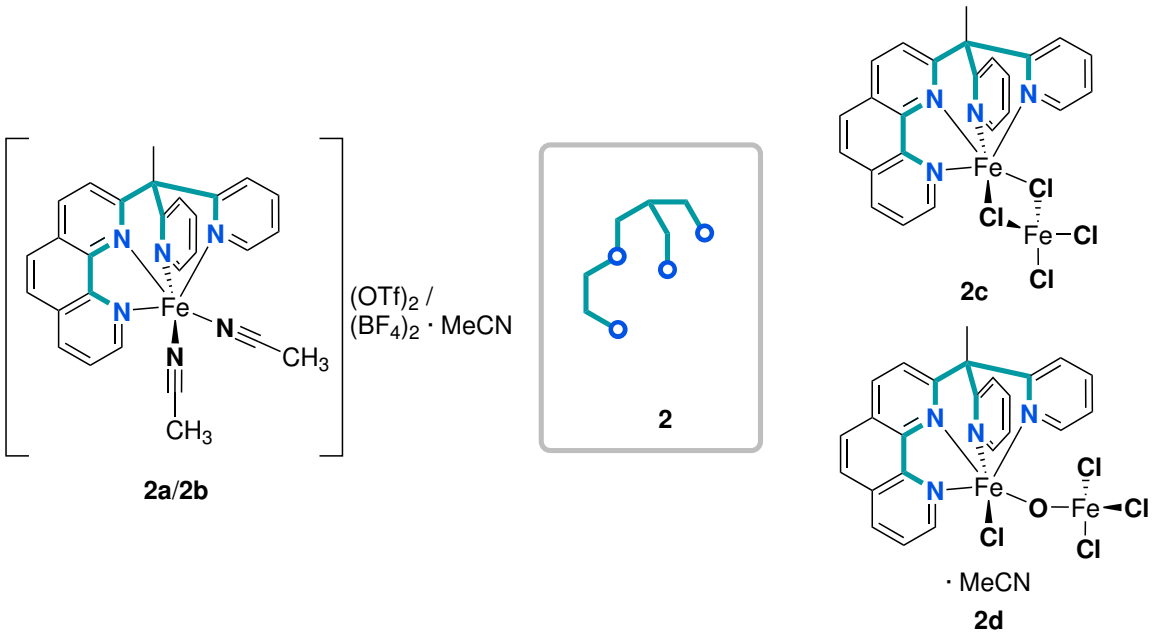

Figure 4.1: Overview of complexes with ligand **2**.

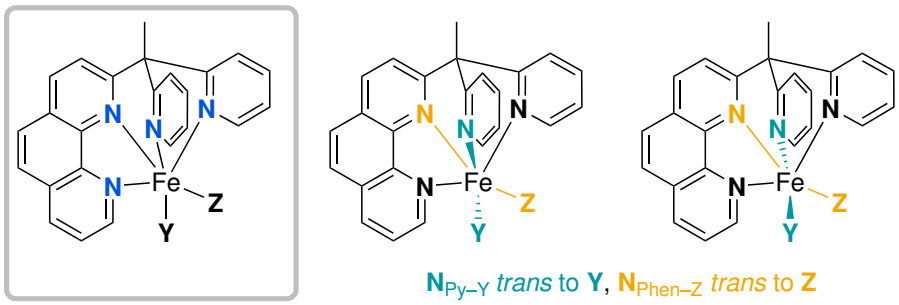

Figure 4.2: Donor atom positions and labelling of complexes with ligand **2**.

structure of **2a**. In addition, there is one non-coordinating acetonitrile molecule which is highly disordered so it could not be modelled properly and the data was treated with the BYPASS algorithm as implemented in PLATON/SQUEEZE.[156–158] The longest Fe – N bond can be found between the iron centre and the outer *N*-donor of the phenanthrolinyl unit Fe – N_{Phen} (2.0219(19) Å) whereas the shortest Fe – N bond is located between iron and the other phenanthrolinyl *N*-donor Fe – $N_{Phen\text{-}Z}$ (1.9087(17) Å, Table 4.1). The other Fe – N bond lengths are in a quite similar range of 1.944–1.967 Å. Since the average Fe – N bond length is below 2.0 Å, **2b** is presumably a LS species in the solid state. The unsymmetry of the Fe – N bonds of the two phenanthrolinyl donors may be caused by the LS iron(II) centre, which has a smaller radius than an iron(II) HS cation. Therefore, the iron can be wrapped more tightly by the ligand, which is also represented by a short distance from the iron centre to the apical carbon atom of about 3.05 Å. Since the phenanthrolinyl unit is very rigid, the outer N_{Phen}-donor cannot bend more inwards which results in a slightly longer Fe – N_{Phen} bond. For HS species with ligand **2** like complexes **2c** and **2d**, which will be discussed in the following sections, the unsymmetry of Fe – N_{Phen} and Fe – $N_{Phen\text{-}Z}$

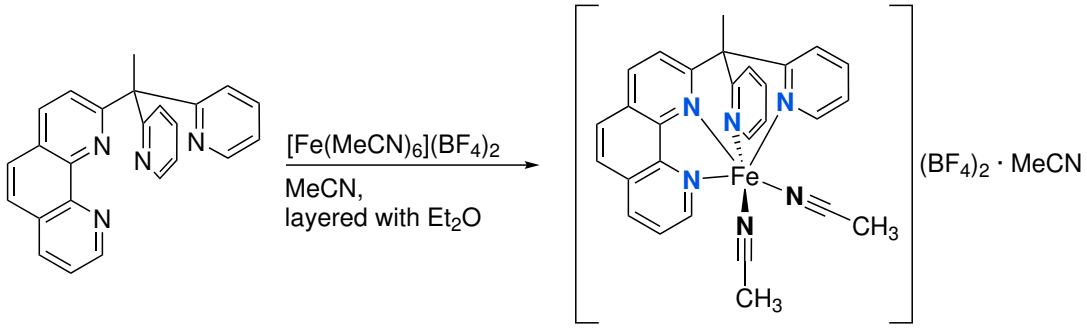

Scheme 4.1: Synthesis of complex **2b**.

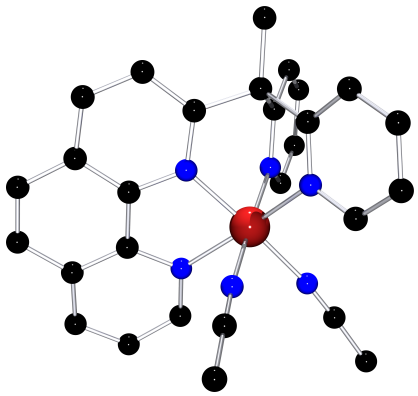

Figure 4.3: $[Fe(\mathbf{2})(MeCN)_2]^{2+}$ cation in crystals of **2b**. Hydrogen atoms, counterions and crystal solvent molecules are omitted for clarity. Colour code: black = carbon, blue = nitrogen, scarlet = iron.

bond lengths is significantly smaller. The acetonitrile co-ligands are only bent slightly (Fe – N – CMe: 172.27(18)–175.67(18)°). The coordination geometry is close to an ideal octahedron (CSM: S(OC-6) = 0.7). Looking at **2a** all the values are similar, but compared to $[Fe(MeC(Py)_2BiPy)(MeCN)_2](OTf)_2$ the unsymmetry of bonds between the iron centre and the N-donors of the bipyridinyl/phenanthrolinyl unit is stronger for the complex with the more rigid phenanthrolinyl backbone.[84,136,189] Nevertheless, the trends for the Fe – N bond lengths are the same as for the bipyridinyl based complex, but the more flexible ligand allows a slightly more octahedral and even coordination geometry.

$[Fe(MeC(Py)_2Phen)(\mu{-}Cl)_2FeCl_2]$ (2c)

The combination of $FeCl_2$ and **2** did not result in the expected species $[Fe(\mathbf{2})Cl_2]$ where the Y and Z position would be occupied by chloride ions. The species that could be obtained was $[Fe(MeC(Py)_2Phen)(\mu\text{-}Cl)_2FeCl_2]$ (**2c**) in sufficient quality for SCXRD (Scheme 4.2, Figure 4.4). Complex **2c** crystallises in the monoclinic space group $I2/a$ with $Z = 8$. Instead of two independent chloride ions, two chloride ions of an $[Fe^{II}Cl_4]^{2-}$ anion are coordinating the iron centre. The charge of −2 of this anion could be confirmed in two ways: first, the overall charge balance is fulfilled if one considers both iron centres to be iron(II); second, the average Fe – Cl bond length between the iron centre and the anion is 2.324 Å (Table 4.2).

Table 4.1: Selected bond lengths, atom distances, bond angles and structure parameters of **2b** and related complexes.

	2b SUTKAW[189] [Fe(MeC(Py)$_2$Phen)(MeCN)$_2$](BF$_4$)$_2$ · MeCN	**2a** SUTJUP[136,189] [Fe(MeC(Py)$_2$Phen)(MeCN)$_2$](OTf)$_2$	DIVROS[84] [Fe(MeC(Py)$_2$BiPy)(MeCN)$_2$](OTf)$_2$
Space group	$P\bar{1}$	$P\bar{1}$	$P2_1/c$
Bond lengths [Å]			
Fe – N_{Py}	1.967(2)	1.965(2)	1.969(2)
Fe – $N_{Py\text{-}Y}$	1.9552(18)	1.955(2)	1.951(2)
Fe – N_{Phen}	2.0219(19)	2.016(2)	1.995(2)[a]
Fe – $N_{Phen\text{-}Z}$	1.9087(17)	1.904(2)	1.905(2)[a]
Fe – N_Y	1.9569(18)	1.961(1)	1.950(2)
Fe – N_Z	1.9441(18)	1.944(1)	1.951(2)
Ø Fe – N	1.959	1.958	1.954
Atom distances [Å]			
$N_{Phen}\cdots N_{Phen\text{-}Z}$	2.573	2.564	2.530[a]
Bond angles [°]			
Fe – N_Y – CMe	175.67(18)	175.8(2)	176.2(2)
Fe – N_Z – CMe	172.27(18)	171.9(2)	173.9(2)
Struct. param.			
CSM *S*(OC-6)	0.7	0.8	0.6
CSM *S*(TPR-6)	12.1	12.6	13.1

[a] Phen denotes here BiPy.

These value would fit to the literature values of $[Fe^{II}Cl_4]^{2-}$ (2.28–2.34 Å) whereas the values for $[Fe^{III}Cl_4]^-$ (approx. 2.19 Å) are shorter.[159]

There is only a small number of similar examples of complexes with an iron centre coordinated at four sides by organic ligand molecules (with *N*- or *O*-donors) and on the two remaining coordination sites by an $[Fe^{II}Cl_4]^{2-}$ anion. In the CSD database[58] only three structures are listed.[190,191]

The Fe – N bond lengths towards the iron coordinated by **2** are all larger than 2.0 Å indicating this iron centre to be HS in the solid state. The Fe – N bonds in this complex are

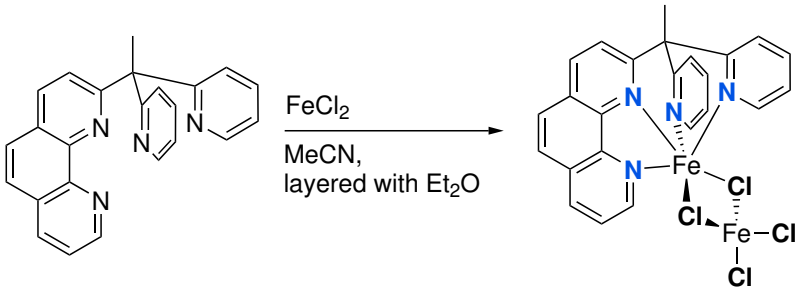

Scheme 4.2: Synthesis of complex **2c**.

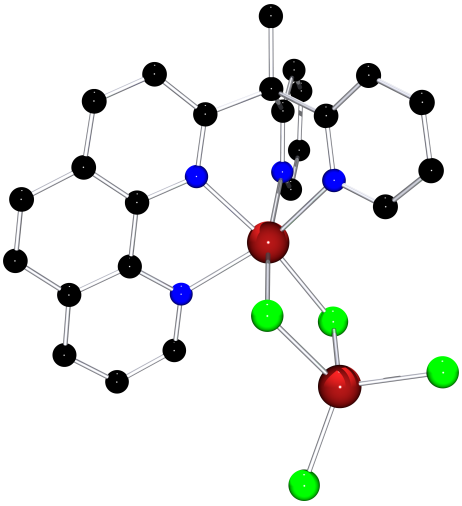

Figure 4.4: [Fe(**2**)(μ-$Cl)_2FeCl_2$] unit in crystals of **2c**. Hydrogen atoms are omitted for clarity. Colour code: black = carbon, blue = nitrogen, scarlet = iron, green = chlorine.

Table 4.2: Selected bond lengths, atom distances, bond angles and structure parameters of **2c**.

	2c [Fe(MeC$(Py)_2$Phen)(μ-$Cl)_2FeCl_2$]
Space group	*I*2/*a*
Bond lengths [Å]	
Fe – N_{Py}	2.173(3)
Fe – $N_{Py\text{-}Y}$	2.170(3)
Fe – N_{Phen}	2.186(3)
Fe – $N_{Phen\text{-}Z}$	2.118(3)
Ø Fe – N	2.162
Fe – Cl_Y	2.6345(10)
Fe – Cl_Z	2.4046(10)
Fe' – Cl_Y	2.3623(10)
Fe' – Cl_Z	2.4265(10)
Fe' – Cl_{term}	2.2365(12), 2.2711(11)
Atom distances [Å]	
$N_{Phen}\cdots N_{Phen\text{-}Z}$	2.669
Fe···Fe'	3.522
Bond angles [°]	
Fe – Cl_Y – Fe'	89.47(3)
Fe – Cl_Z – Fe'	93.62(3)
Struct. param.	
CSM *S*(OC-6, Fe)	3.0
CSM *S*(TPR-6, Fe)	9.0
CSM *S*(T-4, Fe')	0.8
CSM *S*(SP-4, Fe')	30.9

much more uniform (2.118(3)–2.186(3) Å) than in **2b**. The Fe – $N_{Phen\text{-}Z}$ bond length is the shortest (2.118(3) Å). The bond lengths towards the chloride atoms are longer (2.4046(10)–2.6345(10) Å). What was barely visible in **2b** becomes here a more significant trend: The bond from the six-fold coordinated iron centre to the Y position is elongated compared to the Z position. This is also in line with the HS species **2c** compared to the LS complexes **2a** and **2b**.

The three literature known complexes show bond lengths in the same range between the six-fold coordinated iron centre and the ligands (2.107–2.235 Å) and the bridging chloride ions (2.475–2.532 Å), as well as between the tetra-coordinated iron centre and the bridging chloride ions (2.406–2.423 Å). This is also true for the terminal chloride ions (2.228–2.259 Å).[190,191]

The coordination geometry of the iron coordinated by the ligand is a slightly distorted octahedron (CSM *S*(OC-6, Fe) = 3.0). The $[FeCl_4]^{2-}$ anion exhibits a slightly distorted tetrahedron (CSM *S*(T-4, Fe') = 0.8). The nature of the spin of the tetra-coordinated iron cannot be estimated by the Fe – Cl bond lengths, but since tetrahedral complexes are only in excep-

tional cases LS and chlorides are weak field ligands, a HS species would be expected.[192] To investigate this closer as well as possible magnetic coupling between the two iron centres, further magnetometry measurements would be necessary.

[Fe(MeC(Py)$_2$Phen)Cl(μ−O)FeCl$_3$] · MeCN (2d)

If the reaction giving **2c** is exposed to oxygen, the Fe(II) cations are oxidised to Fe(III) and a different dinuclear compound [Fe(MeC(Py)$_2$Phen)Cl(μ-O)FeCl$_3$] · MeCN (**2d**) crystallises as acetonitrile solvate in the triclinic space group $P\bar{1}$ with $Z = 2$ (Scheme 4.3, Figure 4.5).

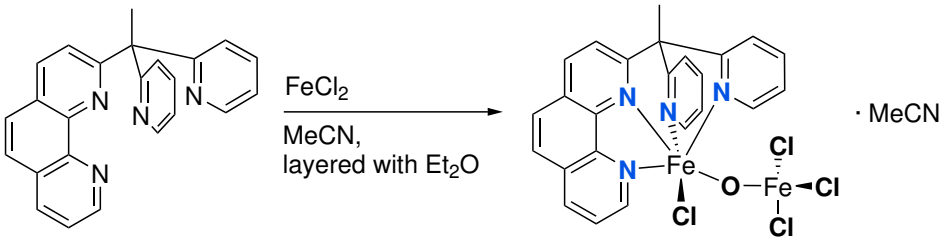

Scheme 4.3: Synthesis of complex **2d**.

In contrast to **2c**, the result is an interesting oxygen bridged diiron species. Charge neutrality implies both iron centres to be iron(III) bridged by an O^{2-}-ion. The O^{2-}-ion bridging $[Fe(\mathbf{2})Cl]^{2+}$ and $[FeCl_3]$ occupies the Z position. The single chloride anion of $[Fe(\mathbf{2})Cl]^{2+}$ is on the Y position. Such a motif of an unsymmetrical μ-oxodiiron(III) complex is a literature known oxidation product of $[FeLCl_2]$ complexes.[193–203]

The Fe – N bond lengths from ligand **2** towards the hexa-coordinated iron are in the same range (2.149(2)–2.202(2) Å) as for **2c** (Table 4.3). Different than in the other structures with ligand **2**, the Fe – $N_{Py\text{-}Y}$-bond is elongated (2.202(2) Å). This goes along with a shorter Fe – Cl_Y bond (2.3589(2) Å) than in complex **2c** (2.6345(10) Å). This phenomenon is known as structural *trans*-effect in octahedral complexes.[204] Furthermore **2d** is the only characterised iron(III) complex with ligand **2**, which also influences the coordination geometry. The bond lengths of the bridging μ-oxide are unsymmetrical. Towards the hexa-coordinated iron centre, the bond is longer (1.8056(17) Å) than the tetra-coordinated iron centre (1.7718(17) Å). The bond lengths of the terminal chloride ligands at the tetra-coordinated iron centre show bond lengths of Fe' – Cl_{term} = 2.2219(9)–2.2425(10) Å. The Fe – Fe' distance is 3.495 Å and the Fe – O_Z – Fe' angle is 155.32(11)°. The coordination geometries are a slightly distorted octahedron (CSM *S*(OC-6) = 2.1) and a tetrahedron (CSM *S*(T-4) = 0.5) which is comparable to complex **2c**. Bond lengths in literature known similar complexes are all in the same range. Also the Fe – Fe' distances (3.35–3.56 Å) and Fe – O_Z – Fe' angles (139.2–172.5°) in the literature are in a comparable range.[193–203] Such unsymmetrical μ-oxo diiron species are also investigated as catalysts to mimic the enzyme methane monooxygenase (MMO) in terms of C – H-bond oxidation reactions.[195,198,199]

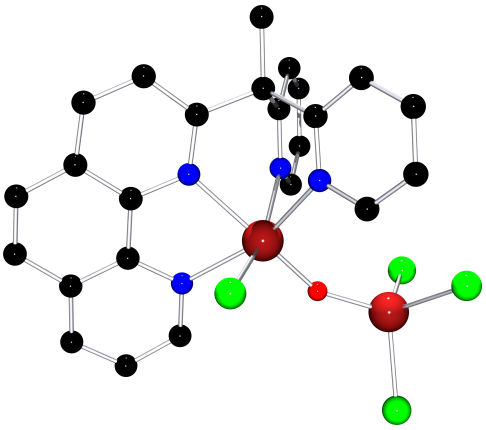

Figure 4.5: [Fe(**2**)Cl(μ-O)$FeCl_3$] unit in crystals of **2d**. Hydrogen atoms and crystal solvent molecules are omitted for clarity. Colour code: black = carbon, blue = nitrogen, red = oxygen, scarlet = iron, green = chlorine.

Table 4.3: Selected bond lengths, atom distances, bond angles and structure parameters of **2d**.

	2d [Fe(MeC(Py)$_2$Phen)(μ-O)$FeCl_3$] · MeCN
Space group	$P\bar{1}$
Bond lengths [Å]	
Fe – N_{Py}	2.128(2)
Fe – $N_{Py\text{-}Y}$	2.202(2)
Fe – N_{Phen}	2.184(2)
Fe – $N_{Phen\text{-}Z}$	2.149(2)
Ø Fe – N	2.166
Fe – Cl_Y	2.3589(10)
Fe – O_Z	1.8056(17)
Fe' – O_Z	1.7718(17)
Fe' – Cl_{term}	2.2219(9)–2.2425(10)
Atom distances [Å]	
$N_{Phen}\cdots N_{Phen\text{-}Z}$	2.640
Fe···Fe'	3.495
Bond angles [°]	
Fe – O_Z – Fe'	155.32(11)
Cl_Y – Fe – O_Z	105.25(6)
Struct. param.	
CSM *S*(OC-6, Fe)	2.1
CSM *S*(TPR-6, Fe)	12.0
CSM *S*(T-4, Fe')	0.5
CSM *S*(SP-4, Fe')	32.3

4.1.1 Summary of Iron Complexes of Ligand 2 in the Solid State

In terms of solid state structures of complexes with ligand **2**, the bis(acetonitrile) motif could be repeated with tetrafluoridoborate anions (**2b**). Attempts of crystallising a bis(chlorido) complex were not successful. Instead two different chloride based species were obtained. In the first one a $[FeCl_4]^{2-}$ anion is coordinating in a chelate fashion occupying both co-ligand sites (**2c**). The other one exhibits a known oxide bridged side product which is typically observed in context of iron chlorido complexes (**2d**).

4.2 Studies with [Fe(MeC(Py)$_2$Phen)(MeCN)$_2$](OTf)$_2$ (2a) as Precursor Complex for an Iron-Oxo Species

Based on the results of Dr. Kristina Keisers, *m*-chloroperoxybenzoic acid (mCPBA) is used as oxidation agent to obtain high-valent iron-oxo species from **2a** as precursor complex

(Scheme 4.4). For the further characterisation of the high-valent iron-oxo species, CSI-mass spectrometry, Mößbauer and UV/Vis experiments were used which will be discussed in the following sections. Furthermore, the ability for catalytic C – H bond oxidation was tested.

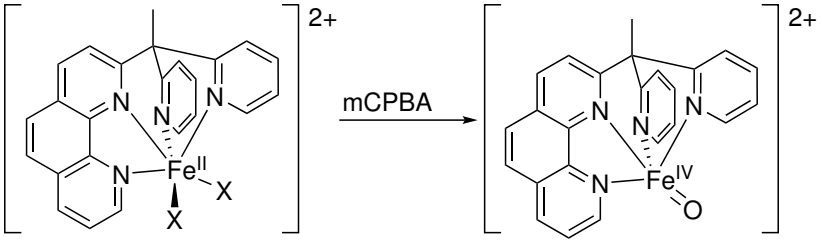

Scheme 4.4: Oxidation of an iron(II) complex with ligand **2** to an iron(IV)oxo species using mCPBA.

4.2.1 CSI-mass Spectrometry Experiment

To obtain more information about the nature of the oxidised iron complex species starting from $[Fe(MeC(Py)_2Phen)(MeCN)_2](OTf)_2$ (**2a**), high resolution cryospray-ionisation mass spectrometry (CSI-MS) at −20 °C in MeCN was measured after oxidation with mCPBA. The low temperatures were necessary as previous UV/Vis studies showed that the decay of the species can be slowed down at lower temperatures.[136] The measured isotope distribution pattern with the main signal centred at 217 m/z fits the calculated pattern of $[Fe^{IV}(\mathbf{2})O]^{2+}$ (Figure 4.6).

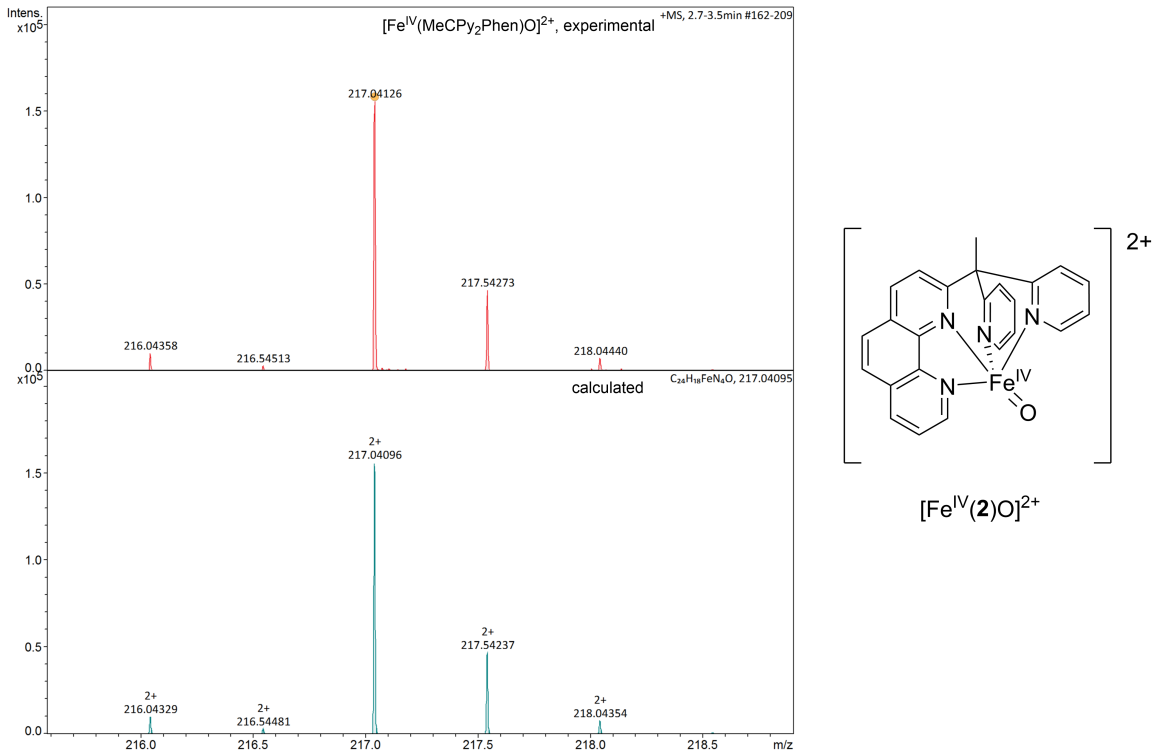

Figure 4.6: Experimental (top) and calculated (bottom) isotope distribution pattern for $[Fe^{IV}(\mathbf{2})O]^{2+}$.

This supports the hypothesis of **2a** being oxidised by mCPBA to an iron(IV)oxo species. Structures for two other species found in the spectra could be proposed: The first species has the sum formula of $[C_{31}H_{22}ClFeN_4O_3]^+$ which fits the isotope distribution pattern with the main signal at 589 m/z. This corresponds to an adduct of the iron-oxo complex and mCPBA (Figure 4.7). In the literature, similar species with peracids for iron(III)/iron(V) complexes were reported.[104,111]

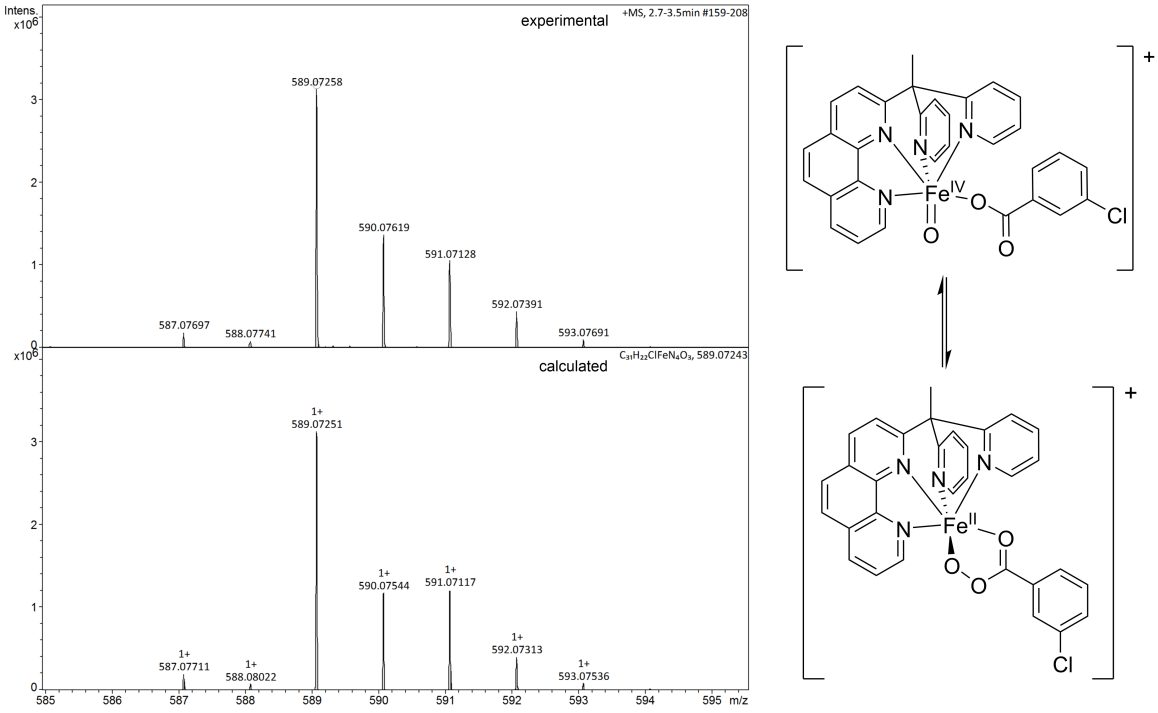

Figure 4.7: Experimental (top) and calculated (bottom) isotope distribution pattern and possible species (right) for $[C_{31}H_{22}ClFeN_4O_3]^+$.

The sum formula of the second species which fits to the isotope distribution pattern around 581 m/z is $[C_{62}H_{44}Cl_2Fe_2N_8O_{52}]^+$. Thinkable for this formula would be a mCPBA bridged species of an iron complex and an iron-oxo complex (Figure 4.8).

4.2.2 Mößbauer Experiments

The existence of the iron(IV)oxo species can also be confirmed with Mößbauer spectroscopy. Figure 4.9 shows the spectra of frozen solutions of the precursor complex **2a** and after oxidation with mCPBA both immediately and after 4h.

For the precursor complex, the signals correspond to the expected Fe(II) LS species with an isomer shift of 0.42 mm s^{-1} and a quadrupole splitting of 0.51 mm s^{-1} (Table 4.4). The addition of 2 eq. of mCPBA to the solution of **2a** at −20 °C and subsequent measurement of this as a frozen solution resulted in a different spectrum (Figure 4.9, middle), which can be modelled as two quadrupole doublets. The minor species (37 %, green fit) shows an isomer shift of 0.04 mm s^{-1} and a quadrupole splitting of 0.54 mm s^{-1}. This corresponds to

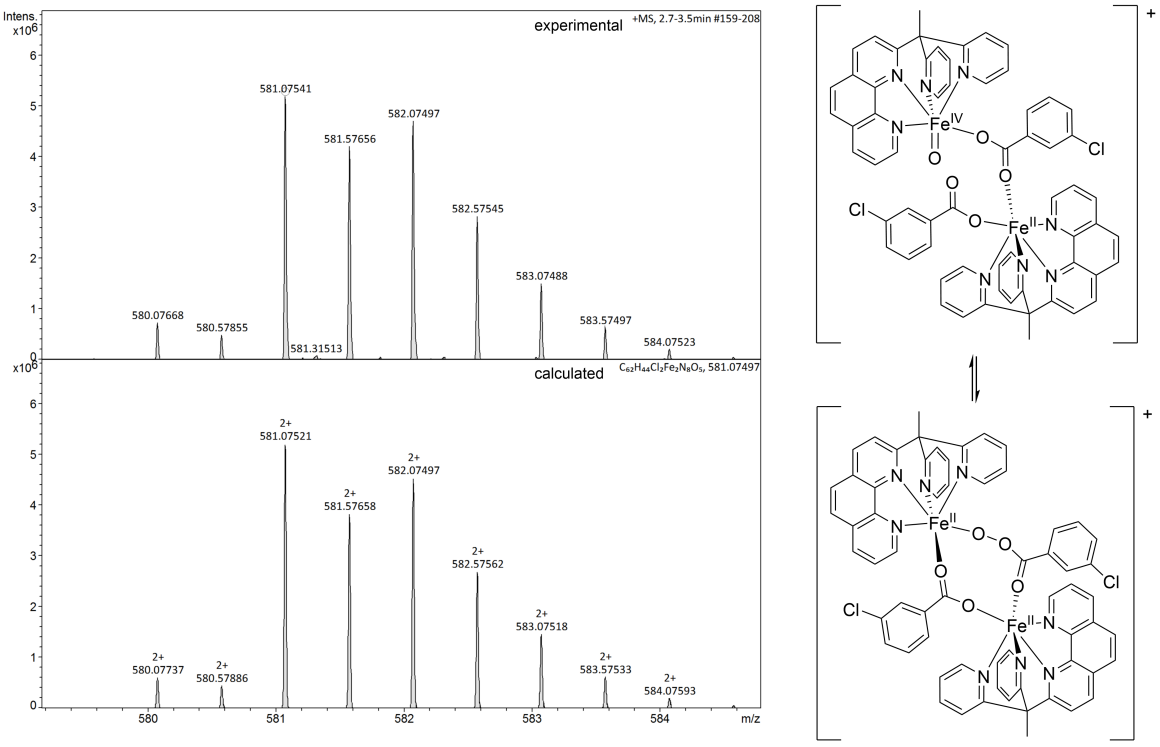

Figure 4.8: Experimental (top) and calculated (bottom) isotope distribution pattern and possible species (right) for $[C_{62}H_{44}Cl_2Fe_2N_8O_{52}]^+$.

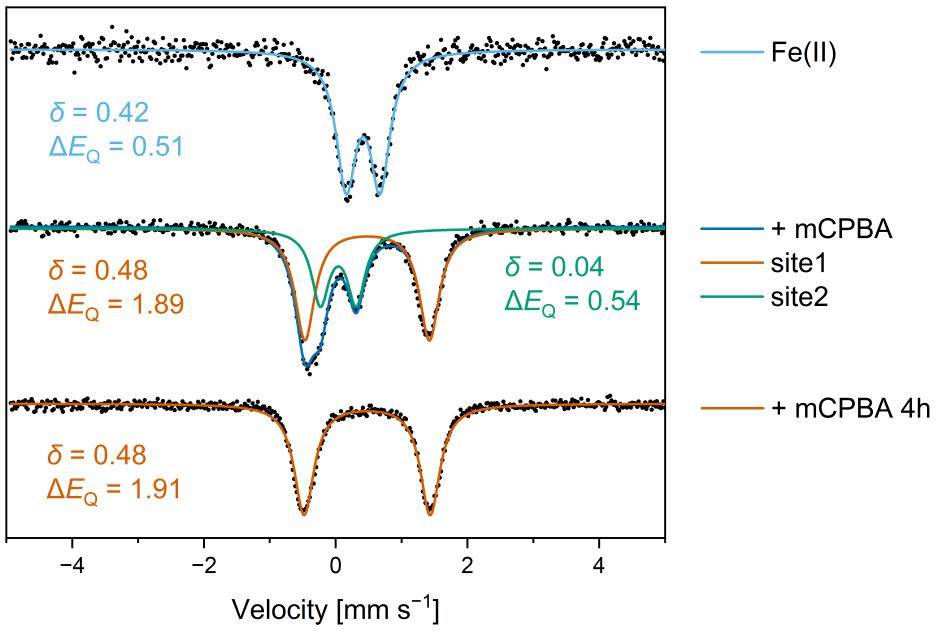

Figure 4.9: Mößbauer spectra of frozen MeCN solutions (80 K): top: **2a** (light blue), middle: reaction solution of **2a** with mCPBA directly after addition at −20 °C (blue) with $[Fe^{IV}(\mathbf{2})O]^+$ species (green) and decomposition product (orange) and bottom: reaction solution after 4 h at −20 °C showing decomposition product (orange).

a HS iron(IV)oxo species and is in the same range as comparable complexes reported in the literature. The iron-oxo species $[tpa^{Ph}Fe^{IV}O]^-$ with the tetradentate *N*-donor ligand tris(5-phenylpyrrole-2-ylmethyl)amine (tpa^{Ph}) shows an isomer shift of 0.09 mm s^{-1} and

Table 4.4: Mößbauer results of frozen MeCN solutions for **2a** and after addition of mCBPA.

Frozen solution	δ [mm s^{-1}]	ΔE_Q [mm s^{-1}]	Amount [%]	Assignment
2a	0.42	0.51		LS Fe(II)
2a + mCPBA	0.04	0.54	37	HS Fe(IV)
	0.48	1.89	63	Fe(III)
2a + mCPBA, 4 h	0.48	1.91		Fe(III)

a quadrupole splitting of 0.51 mm s^{-1}.[98] The major species after oxidation with mCPBA (δ = 0.48 mm s^{-1}, ΔE_Q = 1.89 mm s^{-1}) indicates an iron(III) species which is in line with values of oxide bridged iron(III) species observed by Nordlander *et al.*[205] It is very likely that this iron(III) species is a decomposition product of the iron(IV)oxo species, whose decay can be followed in the UV/Vis spectra.[136] In order to find more evidence for this assumption, the experiment was repeated. The conditions were identical, but after the addition of mCPBA the solution of **2a** in acetonitrile was stirred for 4 h at −20 °C. Afterwards, the solution was frozen in liquid nitrogen and the Mößbauer measurement was performed (80 K). This time only one quadrupole doublet (δ = 0.48 mm s^{-1}, ΔE_Q = 1.91 mm s^{-1}) is visible (Figure 4.9, bottom) which matches the iron(III) species from the previous experiment.
The results confirm the existence of an evanescent iron(IV)oxo species. It is evidently not stable for prolonged periods of time which is in line with UV/Vis spectroscopic measurements and also with the clearly visible changes in colour. The degradation product is an Fe(III) complex.

4.2.3 Recovery of the Iron-Oxo Species

Dr. Kristina Keisers showed in her work that complex **2a** can be oxidised with mCPBA to a species which shows in UV/Vis spectroscopic experiments a band at 752 nm typical for iron-oxo complexes. The half-life time of this species was determined to be 5 min at room temperature.[136]
To act as a catalyst, the decomposition product of the iron(IV)oxo needs to be able to react back to the iron(IV)oxo with more of the oxidation reagent. This is important for the metal complex to mediate the reaction in multiple catalytic cycles. To investigate this issue, UV/Vis spectroscopy was chosen with the strategy of adding fresh oxidation agent to the complex solution several times and follow the intensity of the iron-oxo species band for every addition. The set-up should also enable the solution to be stirred for good mixing of complex and oxidation agent as well as the possibility of fast scans. The experiment was performed under aerobic conditions. Every 15 min, 1 eq. of mCPBA was added to the solution of **2a** in a UV/Vis cuvette. An absorption band at 752 nm could be (re)obtained for every addition of oxidation agent (Figure 4.10). The rise and fall of this feature is getting

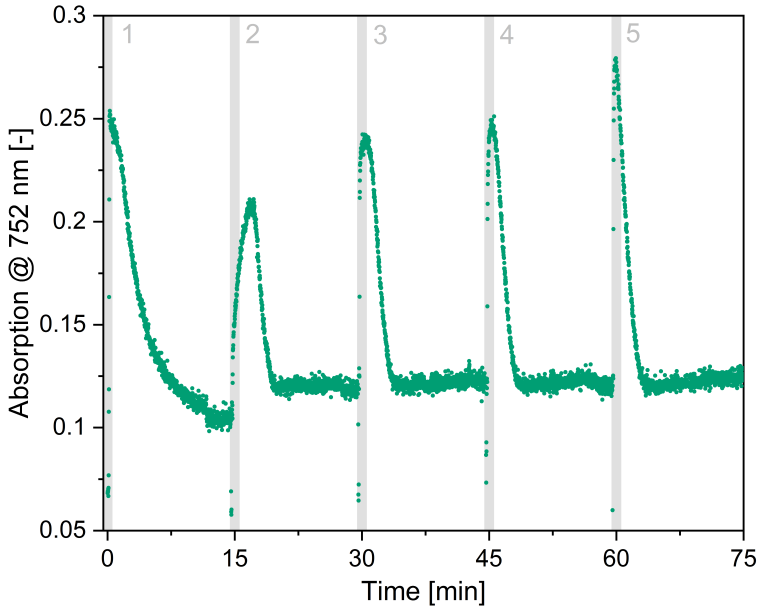

Figure 4.10: Time resolved development of the absorption at 752 nm with addition of 1 eq. mCPBA (in solution) at 0, 15, 30, 45 and 60 min (grey bars).

faster after every addition. The reached absorption maximum is high for the first and lower for the second addition. Afterwards, maximum intensity is getting higher again for every addition from the second to the fifth. The absorption of the Fe(III) decomposition products is not zero at 752 nm ($\approx$ 0.12) and overlaps with the intensity of the iron(IV)oxo band. Assuming that all of the **2a** precursor has been consumed after the first addition of the oxidant, all additions other than the first will form the iron(IV)oxo species from the decay product. Since mCPBA was added as a solution, the volume increases throughout the whole experiment (117 % of starting volume) and the concentrations decrease. It is not possible to make precise statements about the completeness of each formation of the oxo species as the absorption of the latter and the decay species overlap. Nevertheless, this experiment is an important hint that such an iron(IV)oxo species can be reobtained even from the decay product and therefore is capable of more than one turnover in a catalytic cycle.

4.2.4 Catalytic Oxidation of C – H Bonds

Based on all the promising results and the identification of an iron(IV)oxo species, the goal was to test if this species is also suitable as catalyst for C – H oxidation reactions. Cyclohexane, adamantane and cyclohexane-d_{12} were chosen as substrates for typical model reactions (Scheme 4.5).

For the catalytic oxidation of cyclohexane with **2a**, different ratios of the oxidation agent mCPBA (10 or 20 eq.) and substrate (100–1000 eq.) were used (Table 4.5). The reaction conditions were chosen to be similar to those of Chen *et al.*, to obtain comparable results to those obtained with the closely related bipyridine variant of the ligand **2**.[84] The amount

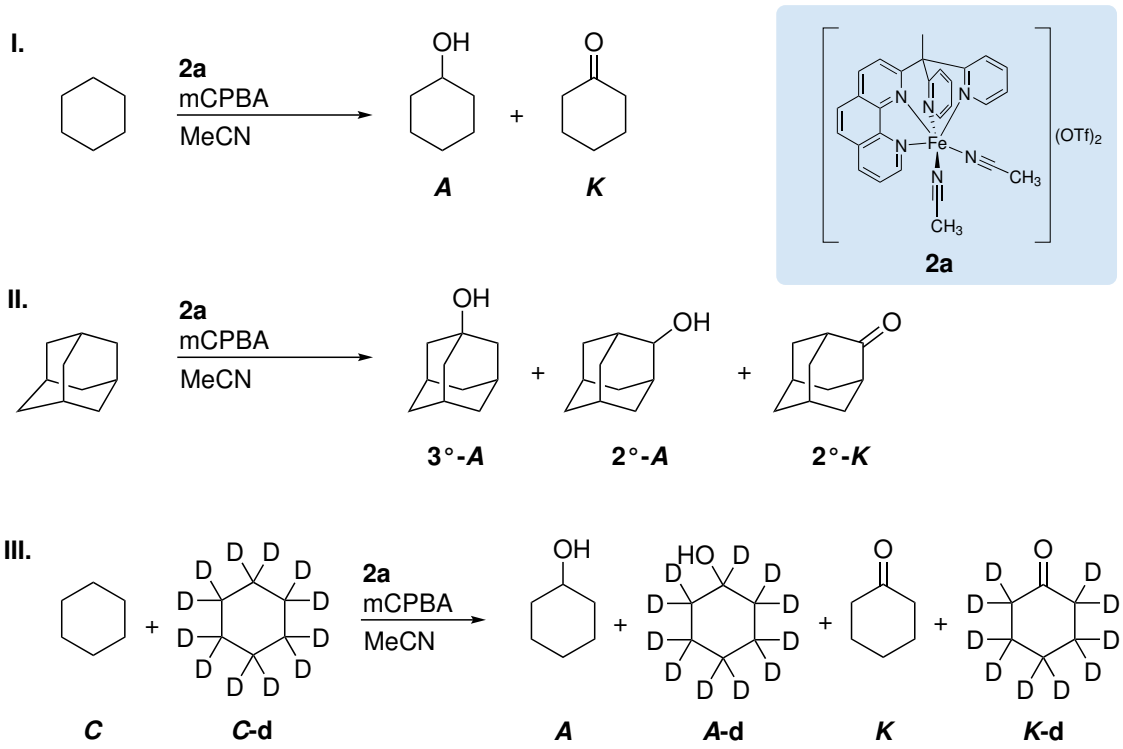

Scheme 4.5: Catalytic oxidation of: **I.** Cyclohexane to cyclohexanol (***A***) and cyclohexanone (***K***) (top); **II.** Adamantane to 1-adamantanol (3°-***A***), 2-adamantanol (2°-***A***) and 2-adamantanone (2°-***K***) (middle); **III.** Cyclohexane (***C***) and cyclohexane-d_{12} (***C*-d**) to cyclohexanol (***A***), cyclohexanol-d_{11} (***A*-d**), cyclohexanone (***K***) and cyclohexanone-d_{10} (***K*-d**) (bottom).

of obtained products for each reaction condition is shown in Figure 4.11 (left). One main information that can be gathered in this model reaction is the alcohol-to-ketone ratio (***A***/***K***). A higher ***A***/***K*** ratio (≫ 1) indicates a metal-based reaction as the alcohol is generated when a rapid rebound of the intermediate radical species to the metal centre takes place.[112] For high substrate amounts, high ***A***/***K*** ratios of 6.1 and 4.0 could be achieved, respectively (Figure 4.11, right). Since they are considerably larger than one, this is the first evidence for a metal-mediated reaction. In contrast, the ***A***/***K*** ratio is close to one for reactions with lower amounts of substrate because side reactions could take place. The ***A***/***K*** ratios for the higher amounts of oxidant (20 eq.) are systematically lower. A reason for this could be that more oxidation agent could lead to more side reactions, favouring the ketone product. Chen *et al.* published a closely related iron-oxo complex with a bipyridine instead of the phenanthroline unit in the ligand scaffold (MeC(Py)$_2$BiPy).[84] Their catalytic study showed ***A***/***K*** ratios of 7.5 and 4.8 for comparable conditions, respectively, which is slightly higher than the results obtained with **2a**.

To check if the incorporated oxygen originates from the oxidant and not from molecular dioxygen, it is important to repeat the reaction under aerobic conditions.[80] In this case, the ***A***/***K*** ratio of 4.7 is a little lower than under oxygen free conditions, indicating side reactions, but still in a similar range. It is known that incorporation of molecular oxygen

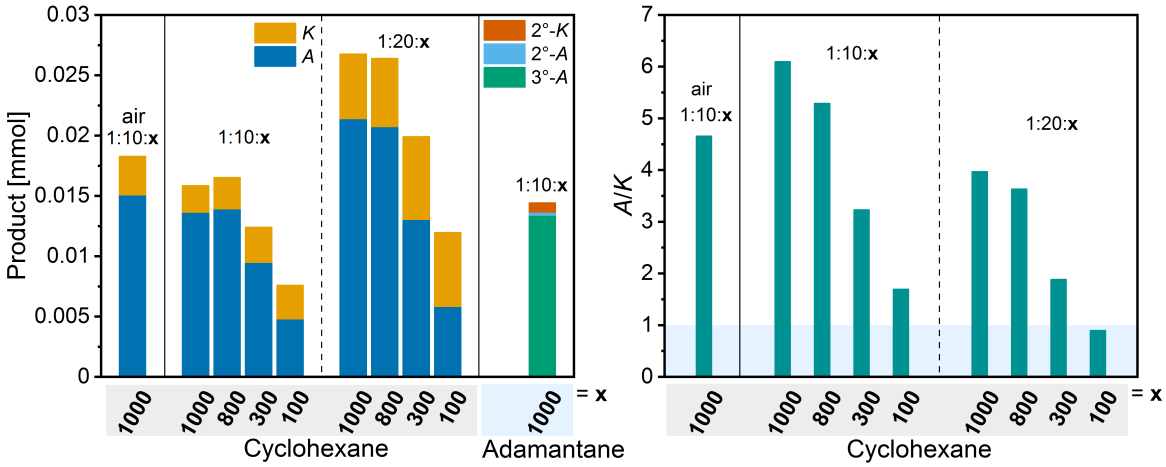

Figure 4.11: Molar amounts of cyclohexanol (***A***) & cyclohexanone (***K***) and 1-adamantanol (3°-***A***), 2-adamantanol (2°-***A***) & 2-adamantanone (2°-***K***) for different substrate ratios **x** (left) and alcohol-to-ketone ratios (***A***/***K***) of catalytic cyclohexane oxidations for different substrate ratios **x** (right).

leads to cyclohexanone as product by a non-metal-based reaction pathway.[80] This side reaction could have lowered the ***A***/***K*** ratio. In terms of the total product, the amount of reaction under nitrogen atmosphere and under aerobic conditions is very similar. This supports the hypothesis of a few additional side reactions with molecular oxygen besides the metal-mediated catalysis.

The yield of this reactions is limited by the amount of oxidant present in the reaction. Therefore, an oxidation agent based yield or in other words an efficiency of the oxidation agent has to be used. If the whole 10 or 20 eq. of oxidation agent in the reaction leads to oxidised product, the efficiency would be 100 %. The efficiency of the reactions here is in a range of 20–55 % (Table 4.5 & Figure 4.12), which is a medium range. For the reaction under aerobic conditions, the efficiency is slightly higher which again indicates side reactions. The bipyridine-based system of Chen *et al.* shows higher efficiencies of 48–90 %.[84] An explanation for these higher values could be that the room temperature half-life time of the

Table 4.5: Catalytic oxidation of cyclohexane with **2a**.

#	**2a** : mCPBA : cyclohexane	***A***/***K***[a]	Efficiency [%][b]	TON[c]
1	1 : 10 : 1000	6.1	53	5
2	1 : 10 : 800	5.3	55	6
3	1 : 10 : 300	3.2	41	4
4	1 : 10 : 100	1.7	25	3
5	1 : 20 : 1000	4.0	45	9
6	1 : 20 : 800	3.6	44	9
7	1 : 20 : 300	1.9	32	7
8	1 : 20 : 100	0.9	20	4
9	1 : 10 : 1000	4.7	61	6

[a] $A/K = \frac{A}{K}$, [b] efficiency = $\frac{A+K}{\text{mCPBA}} \cdot 100$, [c] TON = $\frac{A+K}{\mathbf{2a}}$, all in molar amounts.

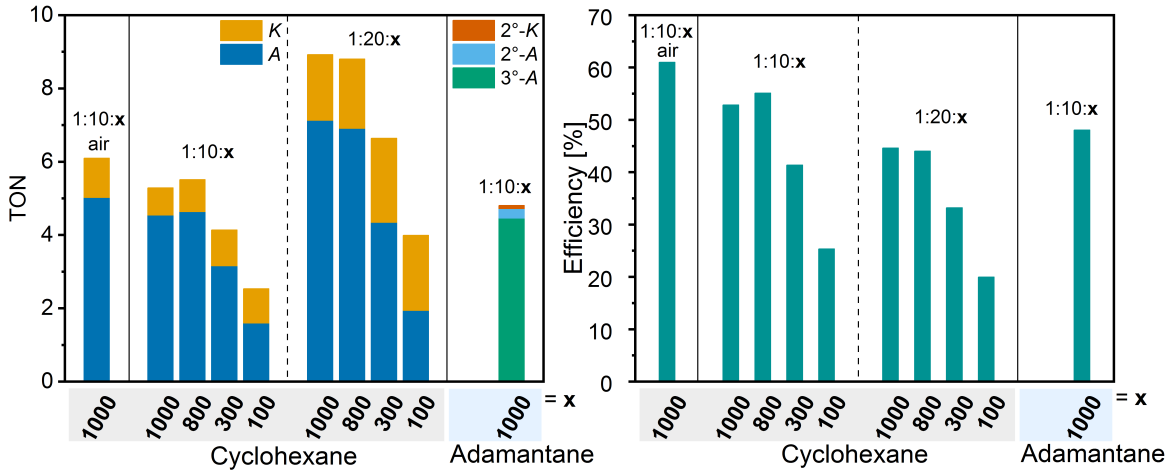

Figure 4.12: TONs of the formation of cyclohexanol (***A***) & cyclohexanone (***K***) and 1-adamantanol (3°-***A***), 2-adamantanol (2°-***A***) & 2-adamantanone (2°-***K***) for different substrate ratios **x** (left) and efficiencies of oxidation agent for different substrate ratios **x** (right).

iron(IV)oxo species of the bipyridine-based complex is 30 min, which is six times longer than that of $[Fe^{IV}(\mathbf{2})O]^{2+}$ (5 min).[84,136]

The turnover numbers (TON) of 3–5 (10 eq. mCPBA) or 4–9 (20 eq. mCPBA) indicate that the reactions are catalytic (Table 4.5 & Figure 4.12). Note, that the equivalents of mCPBA determine the maximum possible TON. For twice amount of oxidant, the TON is also almost twice as high. The fewer cyclohexane is used as substrate, the lower the efficiency and TON are. At least for reactions with higher substrate amounts, the catalysis seems to be mediated by a metal complex species rather than a long-lived radical.

The reactions under aerobic conditions show slightly higher efficiencies (61 vs. 53 %) and TONs (6 vs. 5) which again indicates a few more side reactions.

The second model reaction regarding the regioselectivity was performed with adamantane as substrate. For a metal-based oxidant, the attack of the C – H bond of tertiary carbon atoms should be preferred resulting in the tertiary alcohol product 1-adamantanol (3°-***A***). As opposed to this, less of the secondary carbon products 2-adamantanol (2°-***A***) and 2-adamantanone (2°-***K***) should be observed. For this experiments, the ratio of 1 : 10 : 1000 for **2a** : mCPBA : adamantane was chosen since this showed the most promising results in the cyclohexane reactions. The ratio of tertiary to secondary products (3°/2°) was found to be 38 (Table 4.6). This clearly shows that 1-adamantanol is the favoured product and is a further hint for a metal-based oxidant. With values of 48 % and 5 for efficiency and TON,

Table 4.6: Catalytic oxidation of adamantane with **2a**.

#	**2a** : mCPBA : adamantane	3°/2°[a]	Efficiency [%][b]	TON[c]
1	1 : 10 : 1000	38	48	5

[a] $3°/2° = 3 \cdot \frac{3°\text{-}A}{2°\text{-}A + 2°\text{-}K}$, [b] efficiency $= \frac{3°\text{-}A + 2°\text{-}A + 2°\text{-}K}{\text{mCPBA}} \cdot 100$, [c] TON $= \frac{3°\text{-}A + 2°\text{-}A + 2°\text{-}K}{\mathbf{2a}}$, all in molar amounts.

respectively, these numbers are comparable to the cyclohexane reactions. The bipyridine based complex of Chen *et al.* shows a higher 3°/2° ratio of 45 (efficiency 87 %).[84] Here, an explanation may also be the sixfold longer lifetime of the active species.

The third type of reaction was performed with different mixtures of cyclohexane and cyclohexane-d_{12} to determine the KIE. It is expected that the C – H bond is preferentially broken by a metal-based catalyst than the approx. 1.7 kcal/mol stronger C – D bond.[112] The ratios of cyclohexane : cyclohexane-d_{12} (***C*** : ***C*-d**) were varied from 1 : 3 up to 4 : 1 in six steps (Table 4.7) with the combined amount of cyclohexane and cyclohexane-d_{12} always being 1000 eq. As expected, lower amounts of deuterated substrate led to lower amounts of deuterated products (Table 4.7, Figure 4.13).

Table 4.7: Catalytic oxidation of cyclohexane vs. cyclohexane-d_{12} (***C*** : ***C*-d**) with **2a** for 1 : 10 : 1000.

#	***C*** : ***C*-d**	***A*/*A*-d**[a]	***K*/*K*-d**[b]	***A*/*K***[c]	Efficiency [%][d]	TON[e]
1	1 : 3	0.9	2.1	6.1	41	4
2	1 : 2	1.6	3.4	6.2	45	4
3	1 : 1	3.4	6.8	6.0	40	4
4	2 : 1	6.7	11.4	6.5	41	4
5	3 : 1	11.9	17.5	7.5	42	4
6	4 : 1	15.8	21.9	8.2	50	5

$C + C\text{-d} = 1000$ eq., [a] $A/A\text{-d} = \frac{A}{A\text{-d}}$, [b] $K/K\text{-d} = \frac{K}{K\text{-d}}$, [c] $A/K = \frac{A+A\text{-d}}{K+K\text{-d}}$, [d] efficiency = $\frac{A+A\text{-d}+K+K\text{-d}}{\text{mCPBA}}$, [e] TON = $\frac{A+A\text{-d}+K+K\text{-d}}{\mathbf{2a}}$, all in molar amounts.

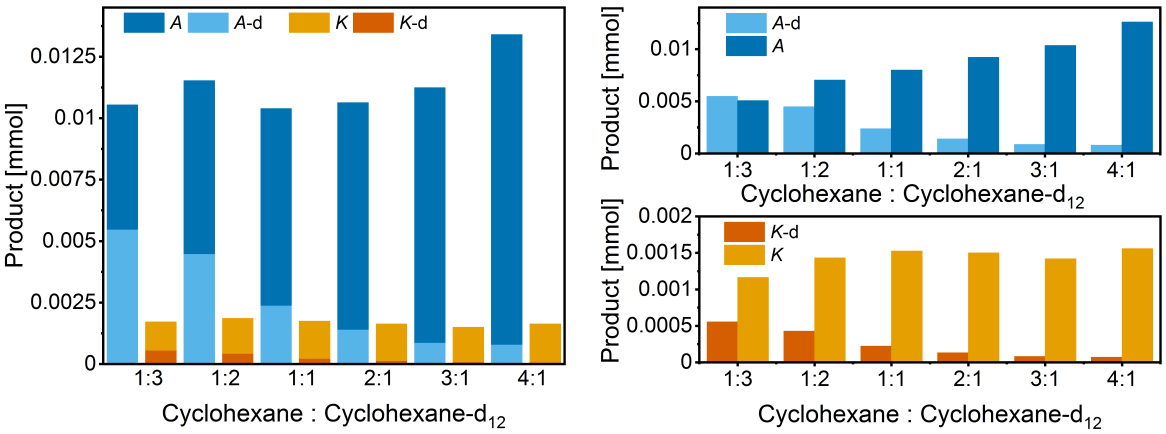

Figure 4.13: Molar amounts of cyclohexanol (***A***), cyclohexanol-d_{11} (***A*-d**), cyclohexanone (***K***) and cyclohexanone-d_{10} (***A*-d**) for different ratios of cyclohexane to cyclohexane-d_{12}. Left: all products. Right: alcohol products (top) and ketone products (bottom).

Important here is the correlation of the initial ratio of non-deuterated and deuterated substrate compared to the ratio of non-deuterated and deuterated product. For the generally favoured alcohol product (cyclohexanol), a plot of these two ratios can be fitted with a linear regression to obtain the kinetic isotope effect (Figure 4.14). In this case, the KIE is 3.8 which is higher than the one observed for the bipyridinyl based analogue by Chen *et al.* of 3.2.[84] For the 1 : 3 ratio of cyclohexane to cyclohexane-d_{12}, efficiency and TON are

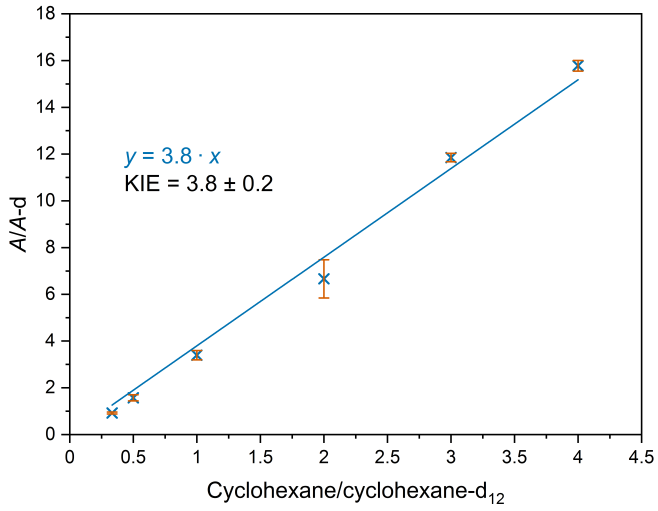

Figure 4.14: Ratio of cyclohexanol to cyclohexanol-d_{11} (***A***/***A*-d**) vs. ratio of cyclohexane to cyclohexane-d_{12} for determination of KIE by linear regression.

lower (41 % and 4) than for the 4 : 1 ratio (50 % and 5). The latter are almost on the level of the reaction with non-deuterated cyclohexane (53 % and 5). Surprisingly, ***A***/***K*** ratios for the reactions with cyclohexane-d_{12} are all similar or slightly higher (6.0–8.2) than for the reactions without (6.1). But the ***A***/***K*** ratios are getting higher for the reactions with less cyclohexane-d_{12} present.

Overall, this complex basically shows the same catalytic trends as the closely related bipyridine based complex by Chen *et al.* For oxidation catalysis of cyclohexane and adamantane, the catalytic performance for **2a** seems to be a bit lower but for the KIE experiments, the performance of **2a** is better than for the compared bipyridine-based complex.[84] To investigate the detailed differences between these two complexes, it would be necessary to repeat the catalytic experiments under the exact same conditions for both.

The more rigid backbone caused by the phenanthrolinyl unit in **2a** does not make this complex a better catalyst than the one with a $MeC(Py)_2BiPy$ ligand. Here, the main difference may be the shorter lifetime of the iron(IV)oxo species. With **2a**, reactions under aerobic conditions are possible and still deliver reasonable results although a small amount of side reactions that are most likely caused by the incorporation of molecular oxygen were observed.

4.2.5 Summary of Studies with 2a and the Iron-Oxo Complex

Further experiments with complex **2a** showed that it can act as a precursor of a high-valent iron-oxo species. The latter could be identified as an iron(IV)oxo species by CIS-MS and Mößbauer experiments. In a UV/Vis spectroscopic experiment, it was shown that the decay product of the iron(IV)oxo species can be reactivated with additional oxidant, causing the characteristic iron-oxo band in the UV/Vis spectrum to rise again. This kind of reactivation can also be seen in the results of the catalytic C – H oxidation reactions where the complex

showed activities comparable to similar already known complexes. However, the more rigid phenanthroline unit (MeC(Py)$_2$Phen) reduces the reactivity slightly compared to the ligand with the more flexible bipyridine based scaffold (MeC(Py)$_2$BiPy).

4.3 Femtosecond X-ray Emission Spectroscopy Experiments

4.3.1 X-ray Emission Spectroscopy (XES)

X-ray Emission Spectroscopy (XES) is a method to obtain information about spin and oxidation state of a metal complex, among other things.[206] If a core electron is removed by X-ray radiation (ionisation), the vacancy is filled by electrons of higher energy levels in a fluorescence process. (Figure 4.15).[207] Thereby photons are emitted depending on the energy difference of the levels. In the Kα emission line (Kα$_1$, Kα$_2$), a vacancy in the 1*s* orbital is filled with an electron of a 2*p* level, which is the most likely event. The Kβ emission (Kβ$_{1,3}$, Kβ′), which is one order of magnitude less likely, is observed when the electron gap is filled by an electron of a 3*p* level.[207]

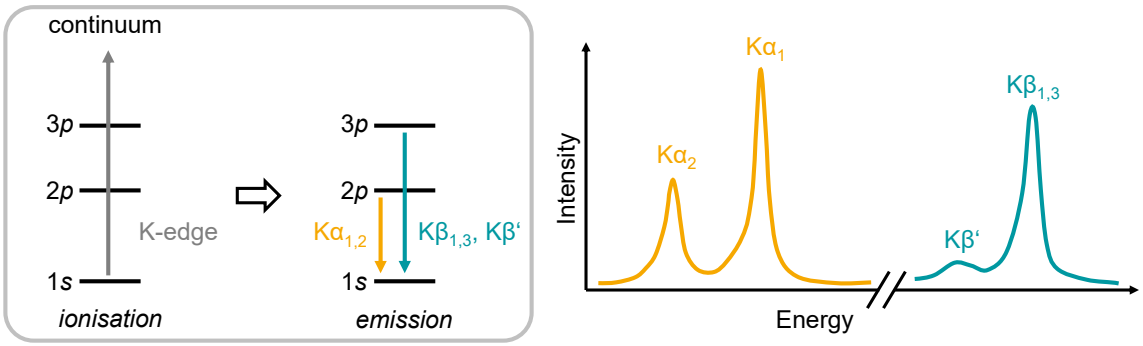

Figure 4.15: Ionisation of a 1*s* electron to the continuum and subsequent emission lines (left) and schematic XES spectra with Kα and Kβ bands (right). Line shape for Kα and Kβ are idealised, Kα$_1$ is usually about 10× more intensive than Kβ. Figure cumulated from Kowalska *et al.* and Bergmann & Glatzel.[206,207]

4.3.2 XES Pump-Probe Experiments

The line shape of the Kβ emission provides information about the spin state of the system. Therefore, the line shape of a new iron complex can be compared to the line shape of a well characterised iron complex with a known spin state (Figure 4.16, left).[208] While static XES spectra provide information about the ground state, pump-probe experiments give information about the excited state. For example, the complex can be excited with an optical laser and the obtained spectra of the ground state (laser OFF) and the excited state (laser ON), which is a combination of optically excited and ground state, can be used to calculate

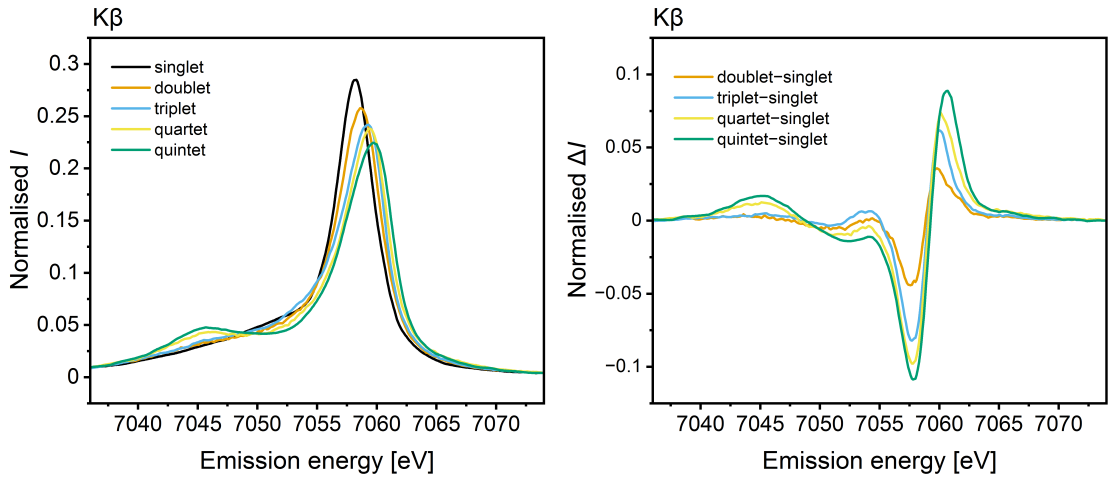

Figure 4.16: Intensity (I) of Kβ bands in fluorescence spectra of reference compounds with different spin states (left): singlet $[Fe(BiPy)_3]^{2+}$ (black), doublet $[Fe(BiPy)_3]^{3+}$ (orange), triplet iron(II) phthalocyanine (blue), quartet iron(III) phthalocyanine chloride (yellow), quintet $Fe(Phen)_2(NCS)_2$ (green). Plotted with data taken from Zhang *et al.*[208] Constructed model complex intensity difference (ΔI) spectra for exited states calculated with data shown in the left spectrum (right): doublet−singlet (orange), triplet−singlet (blue), quartet−singlet (yellow), quintet−singlet (green).

a difference spectrum.[209] The difference spectrum is used to obtain information about the spin state of the exited states. The needed reference difference spectra in Figure 4.16 (right) can be constructed using the fluorescence bands of the model complexes in Figure 4.16 (left).[208] Since it is possible that more than one exited state is reached by the complex in a cascade, the time between the excitation with the optical laser and the measurement of the emission spectra is important. Powerful short pulsed X-ray free-electron laser (XFEL) sources allow to observe very short-lived exited states in the femtosecond range.[209] One of the best characterised iron complexes in XES pump-probe experiments is $[Fe(BiPy)_3]^{2+}$.[208–211] Studies in water suggest that the photocycle after excitation with an optical laser involves a singlet to triplet metal to ligand charge transfer state (^{1,3}MLCT), which is converted within a few hundreds of femtoseconds to an intermediate short-lived triplet state ($S = 1$, ^{3}MC) and subsequently to a longer-lived (660 ps) quintet HS state ($S = 2$, ^{5}MC).[209,211] Studies suggest that the maximum population of the ^{3}MC is reached after about 100 fs and after about 600 fs for the ^{5}MC.[208,211]

The iron complex $[Fe(BiPy)_3]^{2+}$ offers a homoleptic ligand set-up with three bidentate ligands (Figure 4.17). In this work two different complexes were investigated. Complex $[Fe(HC(3,5\text{-}MePz)_2Py)_2](CF_3CO_2)_2$ (**5a**) also provides a homoleptic ligand set-up, but there are two tridentate ligands coordinating in a bisfacial fashion. This is different to other intensively studied tridentate ligands like terpyridines coordinating the metal centre meridional.[212,213] Additionally, ligand **5** offers two kinds of *N*-donors: one pyridine and two pyrazoles. This mixed *N*-donor set-up of complex **5a** was analysed in comparison with the ligand $HC(3,5\text{-}MePz)_2Py$ in previous N K-edge X-ray absorption spectroscopy (XAS) experiments where distinct features for coordinating pyridinyl, the coordinating N atom in

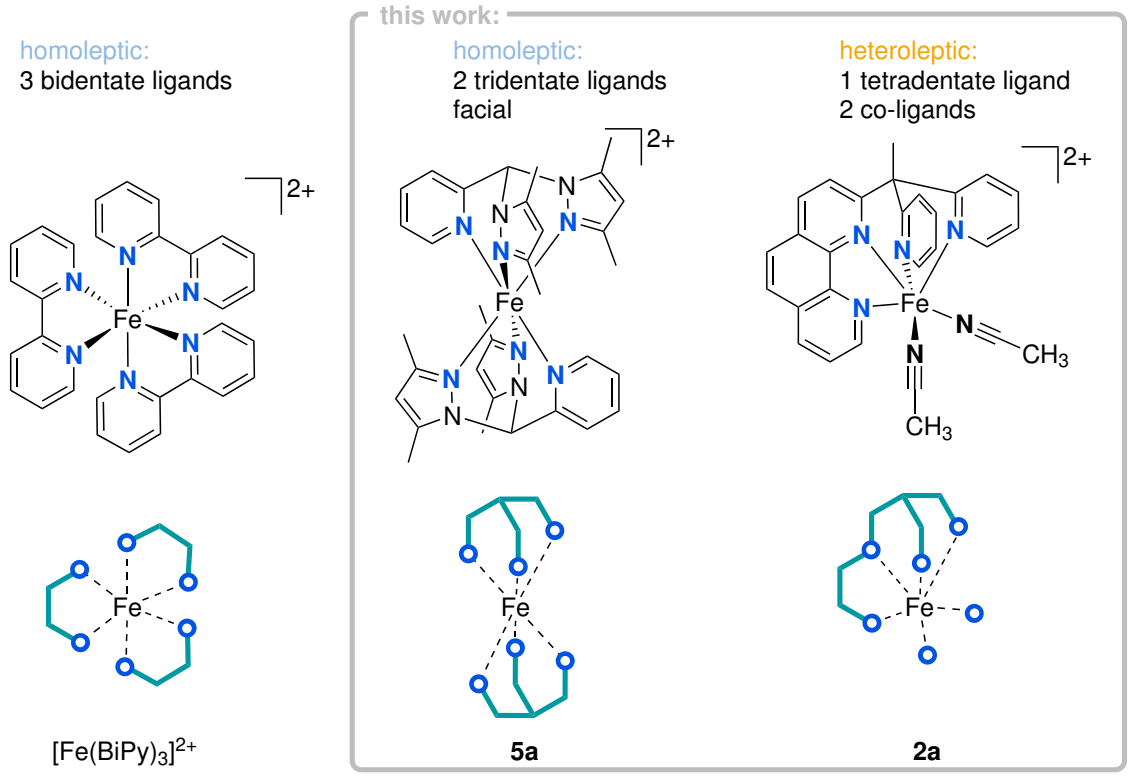

Figure 4.17: Comparison of ligand set-up in $[Fe(BiPy)_3]^{2+}$, **5a** and **2a**.

the pyrazolyl and the non-coordinating N atom in the pyrazolyl moiety could be identified. Furthermore, pump-probe iron(II) K-edge XAS allowed the analysis of the LS ground state compared to the exited state.[161]

A third different coordination sphere is found in complex **2a** where one tetradentate ligand and two co-ligands in *cis*-position are responsible for a heteroleptic ligand set-up. The tetradentate ligand provides a more rigid set-up of the four *N*-donors, while the two monodentate acetonitrile co-ligands are considered to be more flexible.

The complexes **2a** and **5a** were chosen to investigate if the denticity of the ligands and the different *N*-donors have an influence on the nature of the excited states and their lifetime. Since a lot of investigations were focused on bipyridine and terpyridine complexes, systems with mixed *N*-donors or heteroleptic ligand set-up such as the complex **2a** with two *cis*-labile co-ligands were less studied. However, such complexes with *cis*-labile coordination sites were commonly used in homogeneous catalysis and, therefore, it is of large interest to obtain more information about their excited states.

4.3.3 Femtosecond XES Pump-Probe Experiments of 5a & 2a

Solutions of complexes **5a** and **2a** were measured at the FXE (femtosecond X-ray experiments) instrument at European XFEL in Hamburg/Schenefeld (Germany). The FXE instrument provides the opportunity to perform XES pump-probe experiments in a sub

100 fs timescale. The use of a von Hamos spectrometer in combination with a Jungfrau 500k detector enabled simultaneous recording of Kα and Kβ spectra. For more experimental details see subsection 9.1.11.

XES Results of 5a

The static Kα and Kβ X-ray emission lines without optical excitation (laser OFF) of complex **5a** in water are shown in Figure 4.18 (top).

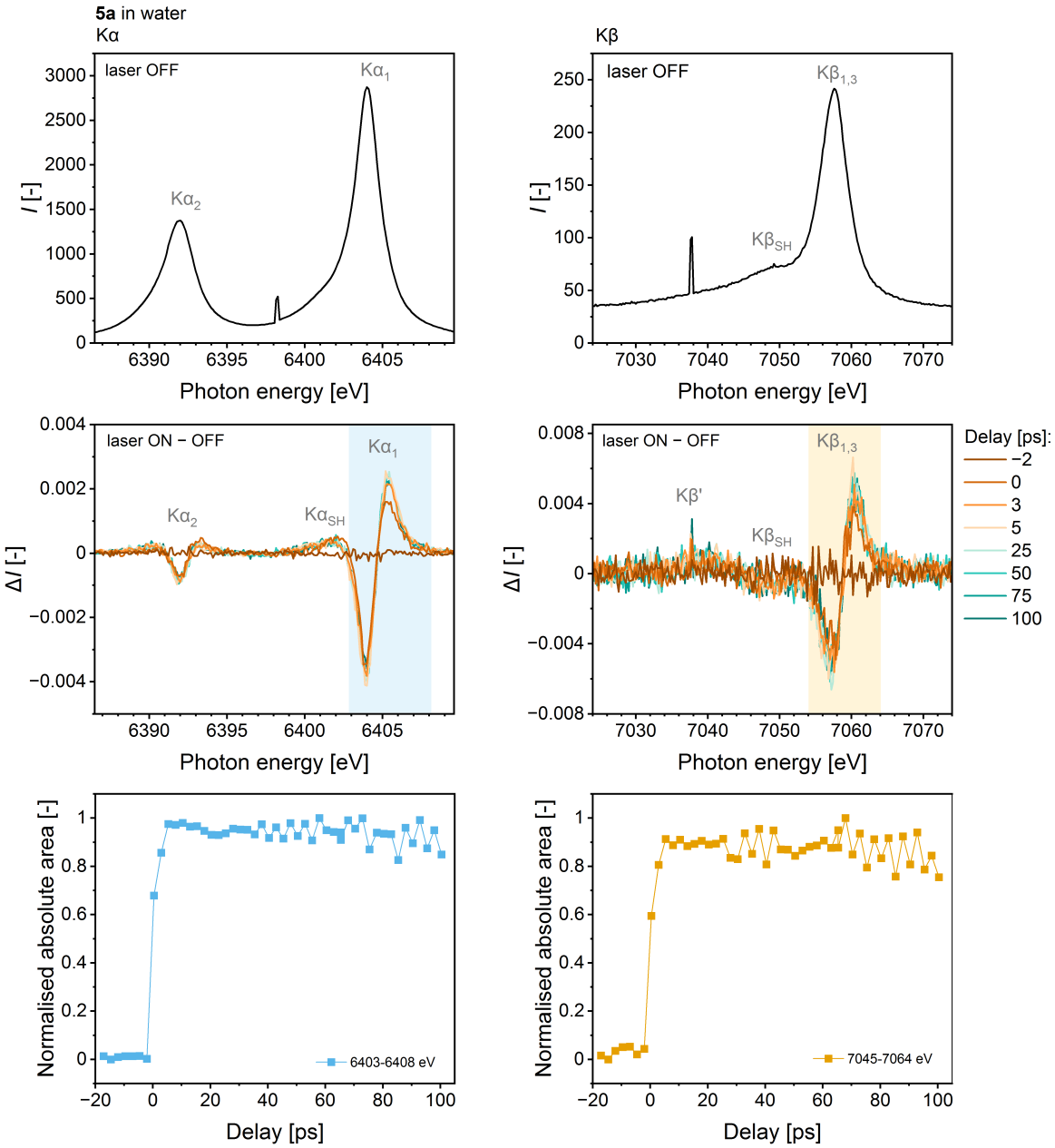

Figure 4.18: Unpumped (laser OFF) static Kα and Kβ spectra of **5a** in H_2O (top) and corresponding difference traces (laser ON − OFF) of selected pump-probe time delays (middle) and kinetic traces of normalised absolute integrals of $K\alpha_1$ (6403–6408 eV) and $K\beta_{1,3}$ (7054–7064 eV) difference traces vs. delay times (−17 to 100 ps; bottom). The integration ranges are visualised by the coloured areas in the plots in the middle.

The $K\alpha_1$ and $K\alpha_2$ occur at 6404 and 6392 eV, respectively. From the Kβ emission, the $K\beta_{1,3}$ emission line (7058 eV) with a shoulder ($K\beta_{SH}$) at 7049 eV can be identified. For the pump-probe experiments, different delay times were measured between excitation with an optical laser and probing with the XFEL X-ray beam. For clarity, only spectra at selected delay times are shown in Figure 4.18 (middle). For Kα and Kβ, the most prominent spectral changes occur within 1 ps after excitation with the optical laser. This effect can also be seen in the kinetic traces (Figure 4.18, bottom) where the absolute integral of the $K\alpha_1$ and $K\beta_{1,3}$ difference traces is plotted against all measured delay times in a range of −17 up to 100 ps. The difference traces show a very fast process that for the spectral changes and the new species remains stable up to 100 ps. It becomes evident that this large range of delay times is not suitable to study the evolution of the long-lived species in more detail, as the change occurs within four data points. Therefore, the measurement was repeated with a series of shorter delay times. The spectral changes for Kα and Kβ with delay times between −500 fs up to 2000 fs are shown in Figure 4.19.

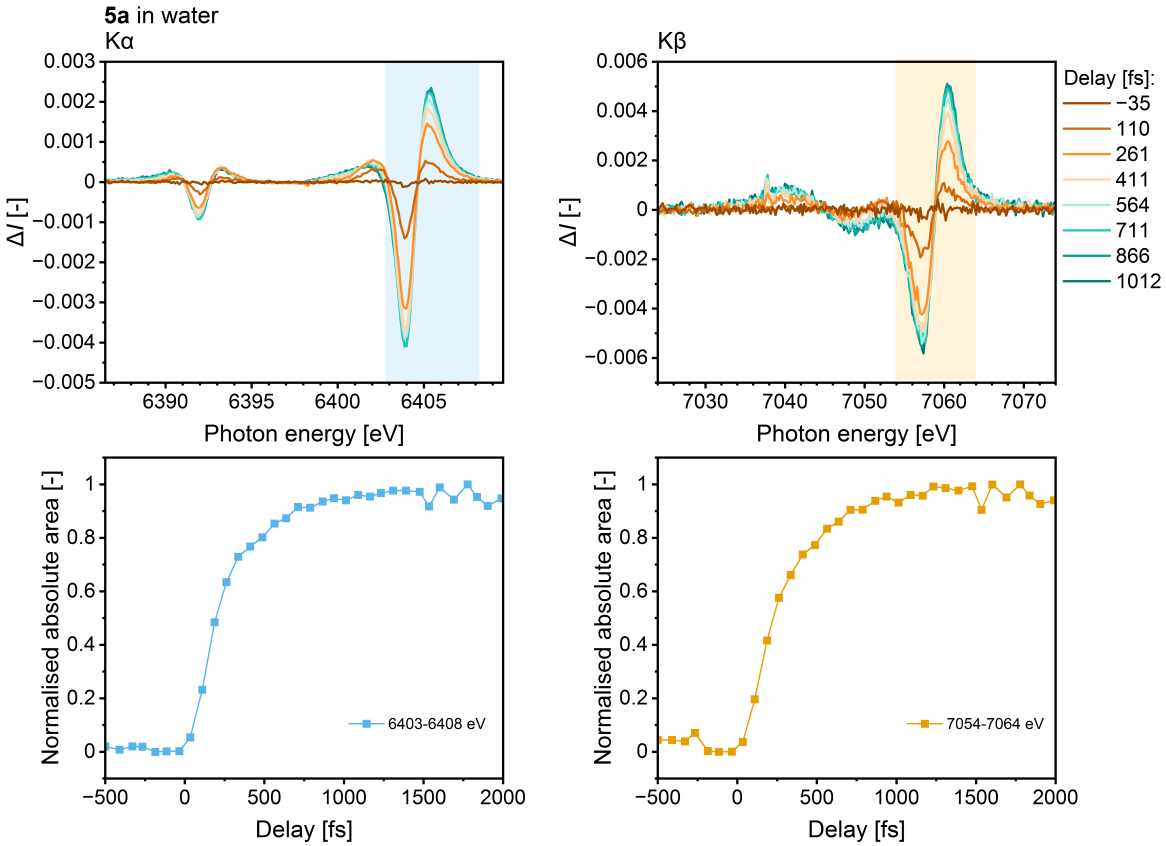

Figure 4.19: Kα and Kβ difference traces (laser ON − OFF) of **5a** for selected short pump-probe time delays (top) and kinetic plots of normalised absolute integrals of $K\alpha_1$ (6403–6408 eV) and $K\beta_{1,3}$ (7054–7064 eV) difference traces vs. delay times (−500 to 2000 fs; bottom). The integration ranges are visualised by the coloured areas in the upper plots.

The delay times in the femtosecond range are suitable to see the evolution of the spectral changes in the difference traces.

There are two hints for a process involving two different species in the Kα spectra. The

first is that the two components (negative and positive) of the Kα_1 line are increasing asymmetrically. Second, the rise time of the whole Kα_1 difference trace and its shoulder (Kβ_{SH}) are different (Figure 4.20). This is visualised with a plot of the normalised integrated absolute integral of the Kα_1 and Kα_{SH} difference trace vs. the delay times. The grey triangles in Figure 4.20 (right) show the difference of the two features (Kβ_{SH}–Kα_1). This shape indicates that an intermediate state is populated within 200 fs and a final state is reached after about 1 ps.

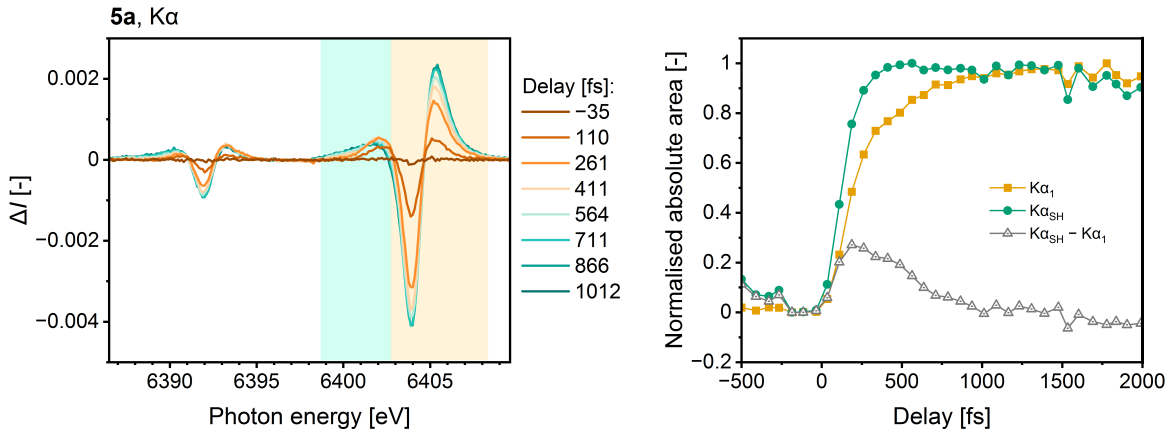

Figure 4.20: Selected difference traces (laser ON − OFF) of Kα of **5a** in H_2O (left) and kinetic traces of normalised absolute integrals of Kα_1 (6403–6408 eV) and Kα_{SH} (6399–6403 eV) difference traces vs. delay times of −500 to 2000 fs and the difference of both (Kα_{SH}–Kα_1, right). The integration ranges are visualised by the coloured areas in the left plot.

The K$\beta_{1,3}$ and Kβ′ difference traces show a similar rise if the absolute integral of the difference traces is normalised (Figure 4.21). The most interesting information can be obtained from the shoulder of the K$\beta_{1,3}$ difference trace (Kβ_{SH}). As shown in Figure 4.16, this shoulder is sensitive to the spin multiplicity of the excited state. Therefore, the mathematical integral of Kβ_{SH} is compared to K$\beta_{1,3}$ (positive half) and Kβ′ against the delay times (Figure 4.22). For better visibility the mathematical integral of the Kβ′ difference traces is multiplied by 2 and for Kβ_{SH} by 5. The integral of the shoulder difference trace rises for the first 150–200 fs and afterwards at 250 fs gets negative until a stable state is reached after 1 ps. A positive shoulder may indicate a MLCT or ^{3}MC (triplet) state, whereas negative values indicate a ^{5}MC (quintet) state. Taking all these information into account, the following photocycle can be proposed: (MLCT + ^{3}MC) ⟶ 1 ps ⟶ ^{5}MC.

XES Results of 2a

Similar XES measurements were performed for complex **2a** in MeCN. The Kα and Kβ lines of the unpumped (laser OFF) measurement are shown in Figure 4.23 (top). Spectral changes are observed within 1 ps and the optically excited species has a lifetime of at least 15 ps. Again, different delay times in the picosecond range are too wide and the spectral changes occur

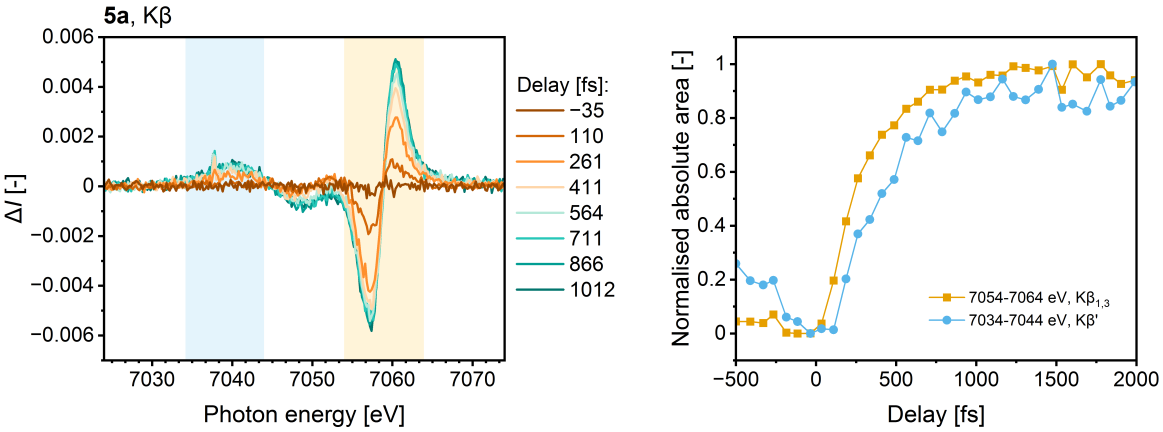

Figure 4.21: Selected difference traces (laser ON − OFF) of Kβ of **5a** in H_2O (left) and kinetic traces of normalised absolute integrals of $K\beta_{1,3}$ (7054–7064 eV) and Kβ′ (7034–7044 eV) difference traces vs. delay times of −500 to 2000 fs (right). The integration ranges are visualised by the coloured areas in the left plot.

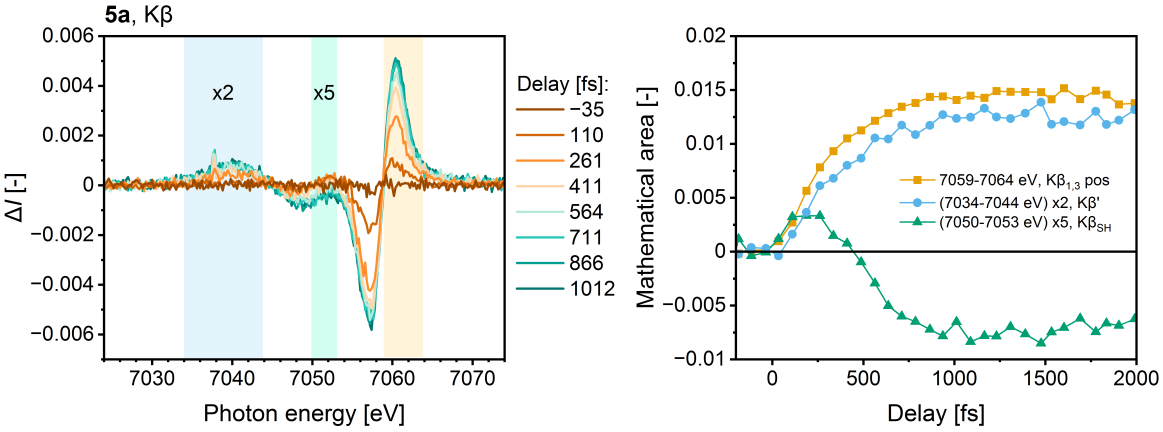

Figure 4.22: Selected difference traces (laser ON − OFF) of Kβ of **5a** in H_2O (left) and kinetic traces of mathematical integrals of $K\beta_{1,3}$ (positive half, 7059–7064 eV), $K\beta_{SH}$ (×5, 7050–7053 eV) and Kβ′ (×2, 7034–7044 eV) difference traces vs. delay times of −200 to 2000 fs (right). The integration ranges are visualised by the coloured areas in the left plot.

within two data points. Delay times in the femtosecond range allow a closer investigation of the spectral changes (Figure 4.24). The difference spectra for the pump-probe measurements are similar to those obtained for **5a**. The two components of the $K\alpha_1$ difference traces show a similar asymmetry, too. Again, the negative part of the $K\alpha_1$ difference traces grows larger. The full growth of the difference trace is reached after about 700 fs.

Furthermore, the $K\alpha_1$ difference traces reveal a short-lived intermediate state when the kinetics of the normalised integral of the whole $K\alpha_1$ difference traces is compared to the $K\alpha_1$ shoulder ($K\alpha_{SH}$, Figure 4.25). The rise of $K\alpha_{SH}$ is faster indicating a potential short-lived intermediate state which rises up to 150 fs and decays afterwards at 300 fs. After about 300 fs, the $K\alpha_{SH}$ and after 820 fs, $K\alpha_1$ integrals reached their maximum, respectively. Overall, the Kα line shows a similar trend as in the experiment with **5a**.

More information can be obtained from the Kβ spectra. The $K\beta_{1,3}$ and Kβ′ difference traces

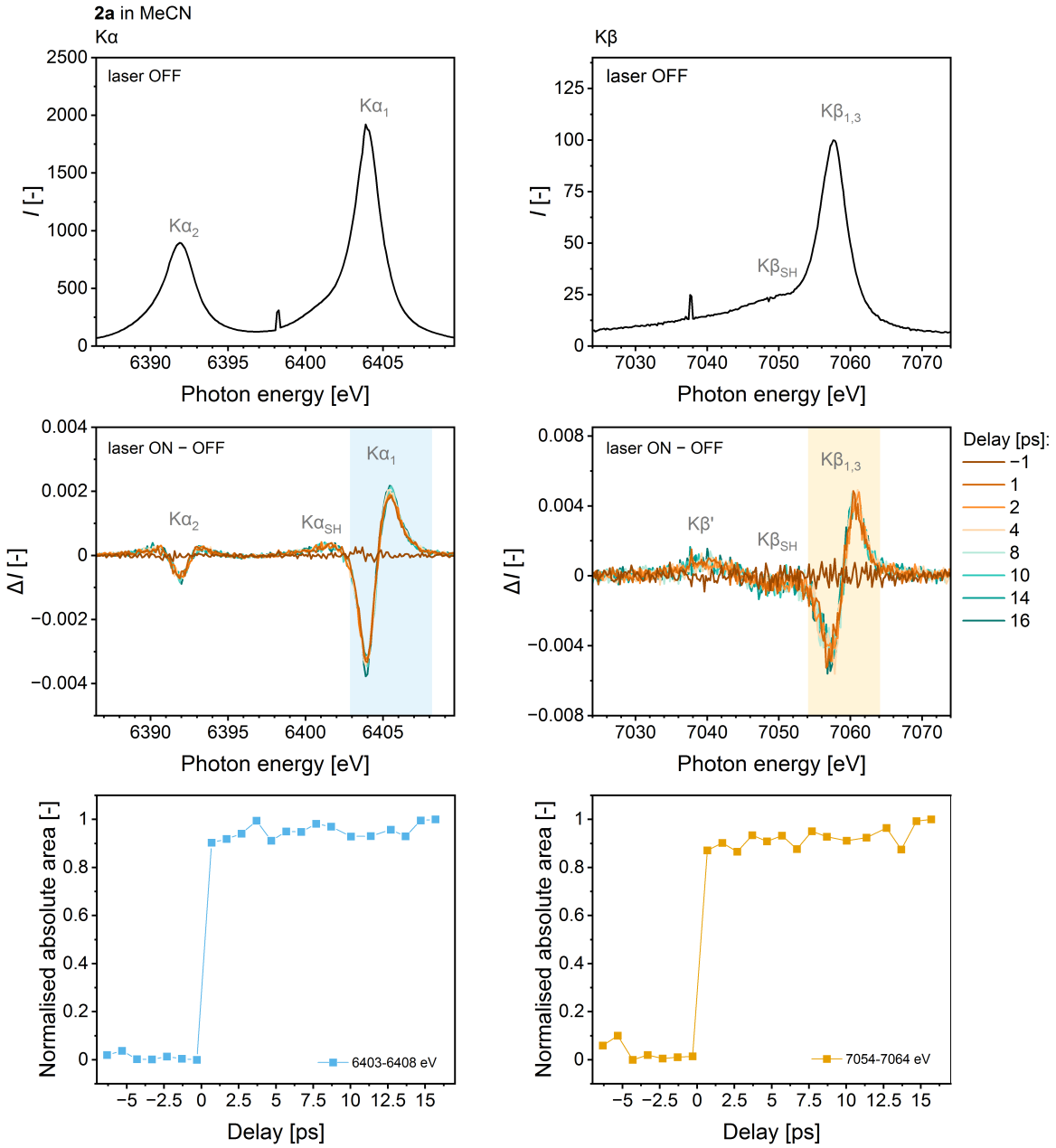

Figure 4.23: Unpumped (laser OFF) static Kα and Kβ spectra of **2a** in MeCN (top) and corresponding difference traces (laser ON − OFF) of selected pump-probe time delays (middle) and kinetic traces of normalised absolute integrals of $K\alpha_1$ (6403–6408 eV) and $K\beta_{1,3}$ (7054–7064 eV) difference traces vs. delay times (−6 to 16 ps; bottom). The integration ranges are visualised by the coloured areas in the plots in the middle.

grow in a similar way (Figure 4.26). To overcome the intensity differences between $K\beta_{1,3}$ and Kβ′ difference signals the normalised absolute integrals are plotted vs. the delay. At about 680 fs, both integrals have reached their maximum.

The most valuable information extracted from the Kβ difference traces can be obtained by comparing the mathematical integral of the $K\beta_{1,3}$ (positive half), $K\beta_{SH}$ and Kβ′ for different delay times (Figure 4.27). For better visibility, the kinetics of $K\beta_{SH}$ were multiplied by two and for Kβ′ by five. The mathematical integral of $K\beta_{SH}$ first has positive values, which

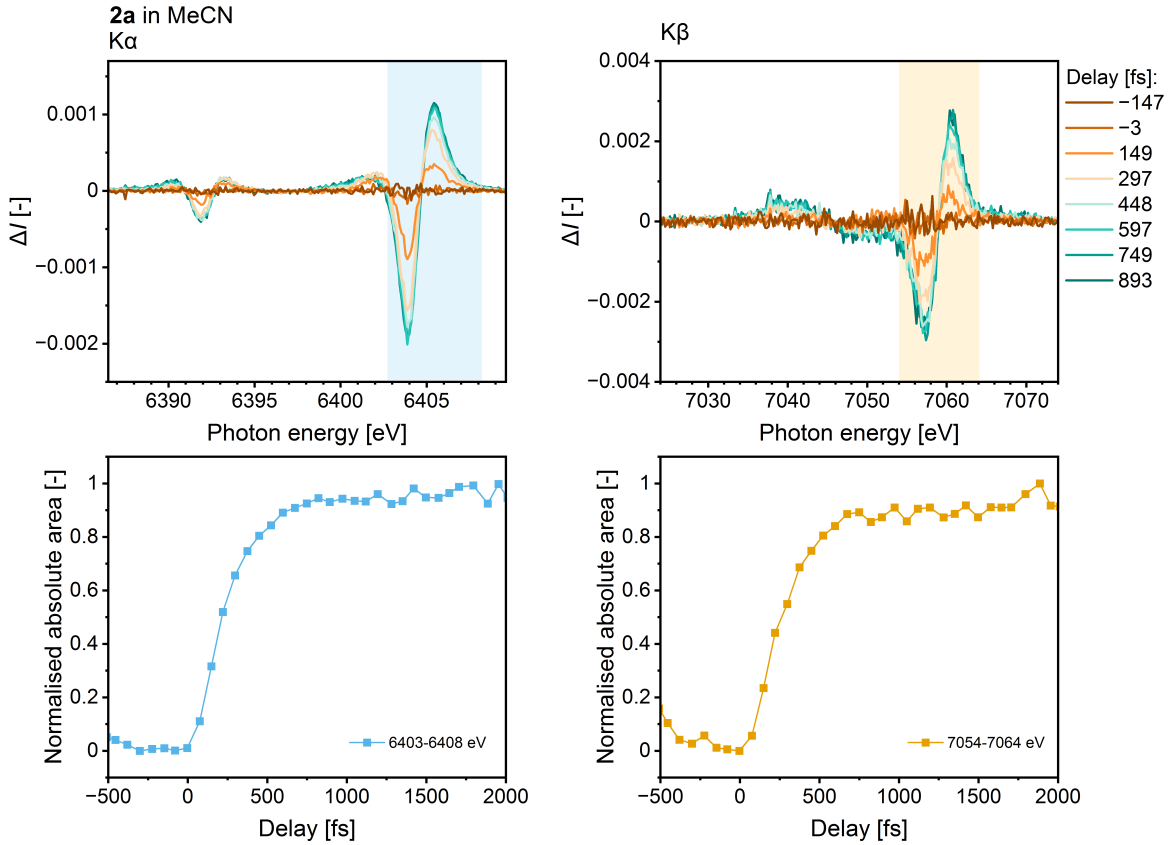

Figure 4.24: Kα and Kβ difference traces (laser ON − OFF) of **2a** for selected short pump-probe time delays (top) and kinetic traces of normalised absolute integrals of $K\alpha_1$ (6403–6408 eV) and $K\beta_{1,3}$ (7054–7064 eV) difference traces vs. delay times (bottom). The integration ranges are visualised by the coloured areas in the upper plots.

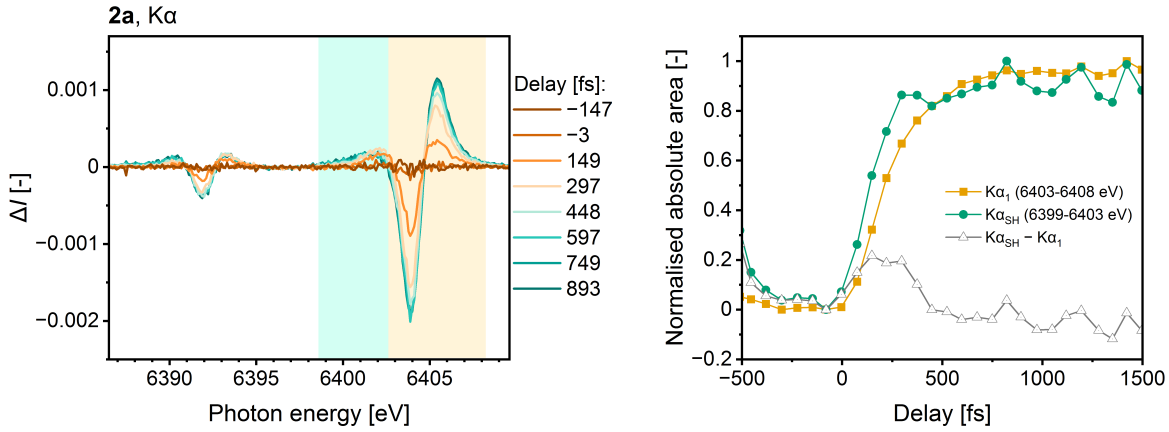

Figure 4.25: Selected difference traces (laser ON − OFF) of Kα of **2a** in MeCN (left) and kinetic traces of normalised absolute integrals of $K\alpha_1$ (6403–6408 eV) and $K\alpha_{SH}$ (6399–6403 eV) difference traces vs. delay times of −500 to 2000 fs and the difference of both ($K\alpha_{SH}$–$K\alpha_1$, right). The integration ranges are visualised by the coloured areas in the left plot.

would be typical for a triplet state (^{3}MC). This short-lived species reaches its maximum at 150 fs and the decays until the integral gets negative (300 fs). The latter is typical for a quintet state (^{5}MC), which is longer-lived and fully established after 600 fs.

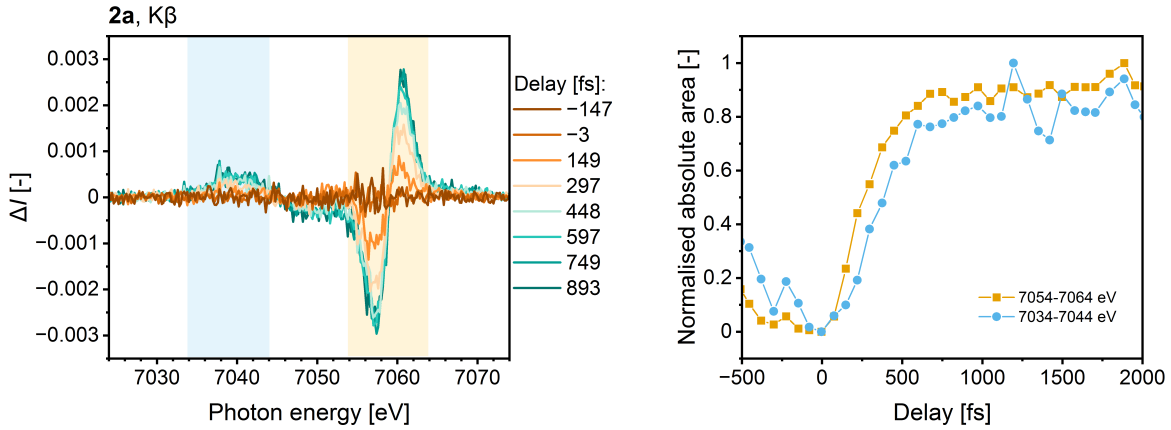

Figure 4.26: Selected difference traces (laser ON − OFF) of Kβ of **2a** in MeCN (left) and kinetic traces of normalised absolute integrals of $K\beta_{1,3}$ (7054–7064 eV) and Kβ′ (7034–7044 eV) difference traces vs. delay times of −500 to 2000 fs (right). The integration ranges are visualised by the coloured areas in the left plot.

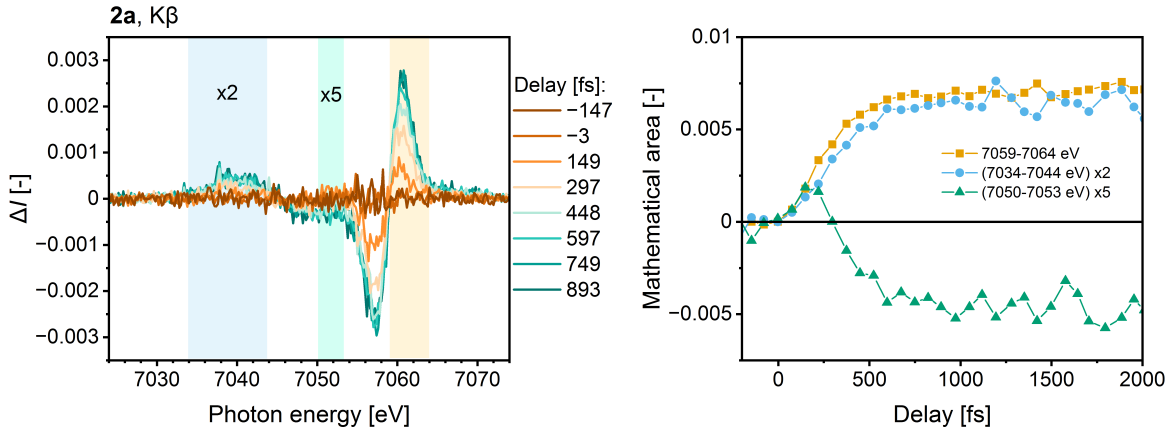

Figure 4.27: Selected difference traces (laser ON − OFF) of Kβ of **5a** in H_2O (left) and kinetic traces of mathematical integrals of $K\beta_{1,3}$ (positive half, 7059–7064 eV), $K\beta_{SH}$ (×5, 7050–7053 eV) and Kβ′ (×2, 7034–7044 eV) difference traces vs. delay times of −200 to 2000 fs (right). The integration ranges are visualised by the coloured areas in the left plot.

Taking all theses information into account, the following photocycle can be proposed for **2a**: (MLCT + ^{3}MC) ⟶ 600 fs ⟶ ^{5}MC.

Comparison of XES Results of 5a and 2a

Altogether, the results for complexes **2a** and **5a** are in close accordance and the proposed photocycles contain the same (intermediate) species. The overall $K\alpha_1$ and $K\beta_{1,3}$ kinetics are almost identical (Figure 4.28). Differences occur for the lifetime of intermediate triplet species and reaching the long-lived quintet state. The comparison of the rise between the $K\alpha_{SH}$ and $K\alpha_1$ difference traces (Figure 4.29, left) as well as the rise of the $K\beta_{SH}$ difference trace (right) shows that the reaching of the short-lived intermediate is similar for both complexes. However, the decay to the long-lived species is faster for complex **2a**. For **2a** the long-lived quintet is established after about 600 fs whereas for **5a** this process needs 1 ps.

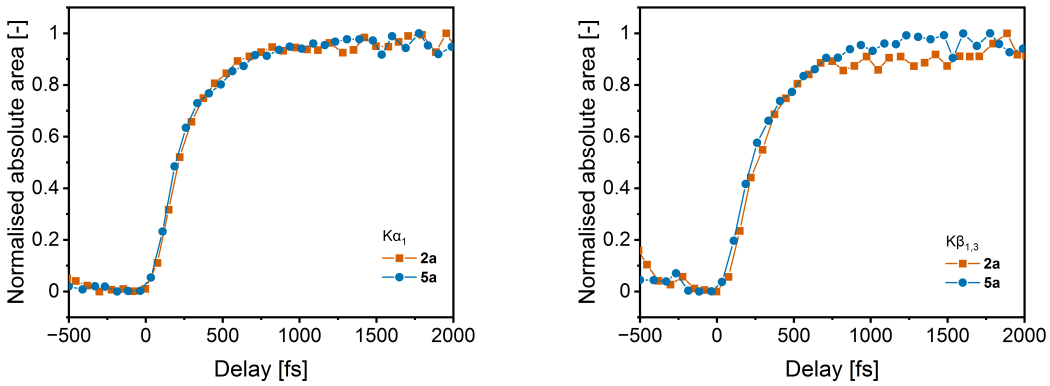

Figure 4.28: $K\alpha_1$ (left) and $K\beta_{1,3}$ (right) kinetic traces obtained from normalised absolute integrals vs. delay times of **2a** and **5a**. The integration ranges in the corresponding difference spectra were 6403–6408 eV and 7054–7064 eV, respectively.

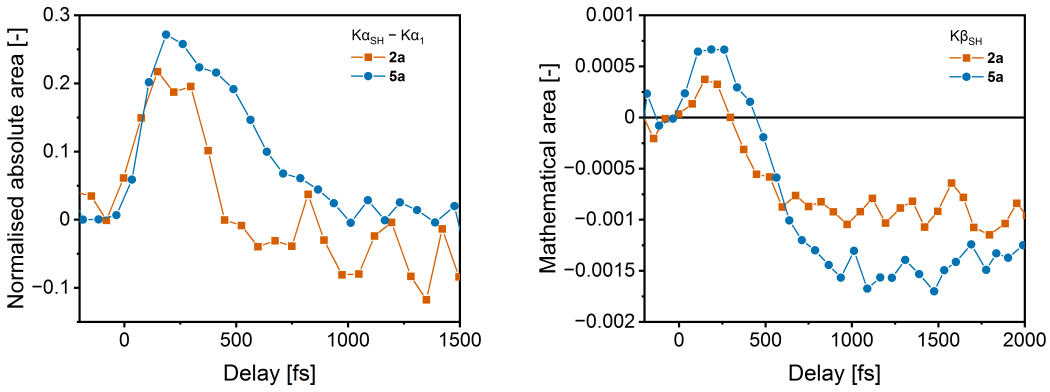

Figure 4.29: Comparison of difference $K\alpha_{SH}-K\alpha_1$ of normalised absolute integrals of difference traces vs. delay times (left) and comparison of mathematical integrals of $K\beta_{SH}$ difference traces vs. delay times (right) of **2a** and **5a**. The integration ranges in the corresponding difference spectra were 6403–6408 eV, 6399–6403 eV and 7050–7053 eV, respectively.

The timescale of complex **2a** is closer to the well known $[Fe(BiPy)_3]^{2+}$ system. A reason may be that the octahedral coordination sphere of $[Fe(BiPy)_3]^{2+}$ and **2a** both consists of three individual ligands, whereas the octahedral coordination sphere of **5a** is provided by two ligands. Further, the measurement of $[Fe(BiPy)_3]^{2+}$ and **5a** were carried out in water and those of **2a** in acetonitrile, which could have an influence on the comparability of the results. On the other hand, the nature of the *N*-donors itself may have the bigger influence. The multidentate ligands in $[Fe(BiPy)_3]^{2+}$ and **2a** consist only of pyridine and pyridine-like donors, whereas complex **5a** also is coordinated by four pyrazolyl moieties. To investigate the reasons for the molecular dynamics of the excited states of these complexes in the femtosecond range, a closer evaluation of the data and further measurements are needed. For example time-resolved wide-angle X-ray scattering (WAXS) could deliver information about the Fe – N bond elongation processes for the switch from the LS ground state to the exited HS state in solution.[209]

However, it was possible to identify short-lived exited states in the femtosecond range for **2a** and **5a**. Features that are indicative for a quintet state could not only be identified in the

Kβ spectra, what the usual procedure is, but also in the Kα spectra. This was only possible through the truly simultaneous recording of both emission lines enabled by the set-up of the FXE instrument.

Excluding X-ray Damage

If metal complexes are irradiated with hard X-rays, there is the possibility of X-ray damage. Both complexes survived the measurements without severe X-ray damage as the UV/Vis spectra before and after the measurement show the same absorption bands (Figure A.3 & Figure A.4 in the Appendix). The spectra were normalised to account for different concentrations due to dilution during the measurement (e.g. dead volume in pump system) or solvent evaporation.

4.4 Concluding Remarks on Complexes of $MeC(Py)_2Phen$ (2)

In addition to three new molecular structures, the experiments started by Dr. Kristina Keisers towards a biomimetic iron-oxo complex were successfully continued. Overall, these results comprise new bits of useful information for the continuously growing number of functional *N*-donor ligand based iron-oxo model complexes.
The femtosecond XES pump-probe experiments revealed a proposed photocycle, that is very similar to the one of the well characterised $[Fe(BiPy)_3]^{2+}$ complex. Mixed *N*-donors or a heteroleptic ligand set-up in the complexes **5a** and **2a** provide a further degree of complexity in the *N*-donor arrangement compared to the bi- and terpyridine complexes form previous studies. For complex **5a** the femtosecond XES experiments are an important addition to the former iron(II) and N K-edge XAS experiments.[161] Since these are the first photophysical measurements for the heteroleptic complex **2a**, it is an interesting candidate for potential further photophysical measurements in the femtosecond range.

5 Bis(pyridinyl)methylpicolinate – a Ligand with {N_3O}-Coordination

Mößbauer measurements and fitting of data were performed by Dr. Linda Iffland-Mühlhaus in the group of Prof. Dr. Ulf-Peter Apfel at Ruhr-Universität Bochum, Germany.

5.1 Ligand Development of MeC(Py)$_2$PicMe (3)

The ligand methyl 6-(1,1-di(pyridin-2-yl)ethyl)picolinate (MeC(Py)$_2$PicMe, **3**) was developed as a new variant of the ligands MeC(Py)$_2$BiPy[161,214–217] and MeC(Py)$_2$Phen[136,189] where one *N*-donor is substituted by an *O*-donor (Figure 5.1). This enables a donor set one step closer to the 2H1C facial triad found in natural enzymes with high-valent iron-oxo species. McDonald *et al.* presented a ligand system where the substitution of *N*-donors by *O*-donors in tetradentate ligands resulted in higher reactivities in C – H bond oxidation reactions.[52]

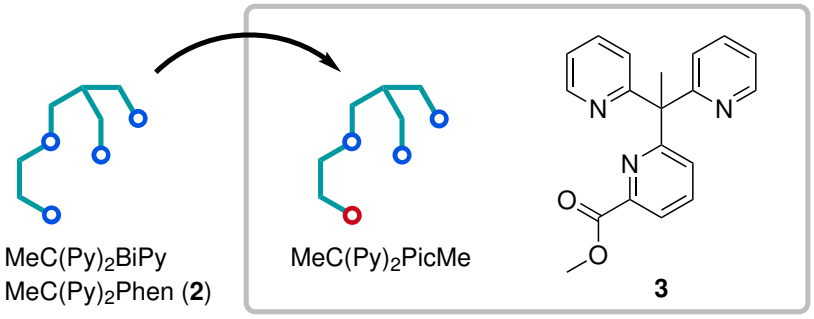

Figure 5.1: Idea for development of ligand MeC(Py)$_2$PicMe (**3**). Colour code: blue = *N*-donor, red = *O*-donor.

The synthesis of **3** is a lithiation reaction (Scheme 5.1). 2,2'-(Ethane-1,1-diyl)dipyridine is deprotonated with *n*-butyllithium (*n*-BuLi) and reacts in a second step with the halogenated building block methyl-6-brompyridine-2-carboxylate (or methyl-6-bromopicolinate) in a nucleophilic substitution reaction. Efficient purification was possible by dissolving the crude product in warm hexane and subsequent filtration and recrystallisation (yield: 28 %).

5.2 Iron Complexes of MeC(Py)$_2$PicMe (3) in the Solid State

Figure 5.2 presents an overview of all complexes with ligand **3** that could be characterised by SCXRD. The detailed discussion of all these structures will follow in individual sections.

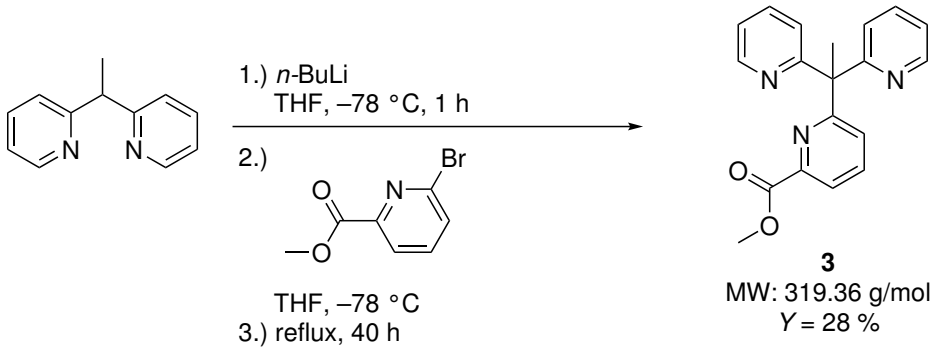

Scheme 5.1: Synthesis of ligand **3**.

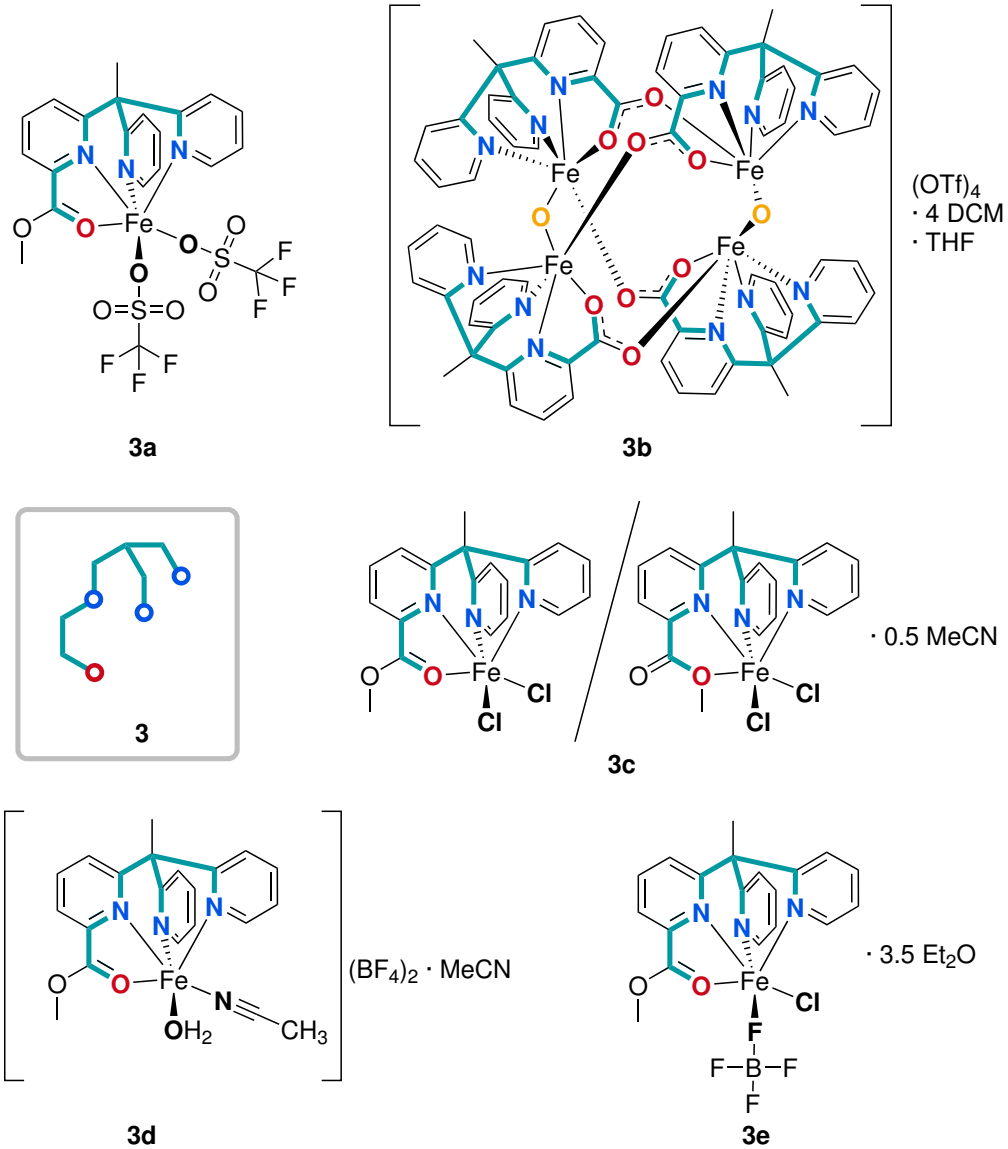

Figure 5.2: Overview of complexes with ligand **3**.

In order to make the structures comparable among each other (e.g. bond lengths and angles), a labelling of the donors is used according to Figure 5.3. The free coordination sites are labelled Y and Z. Y is *trans* to the *N*-donor of one of the pyridinyl groups ($N_{Py\text{-}Y}$). Z is in

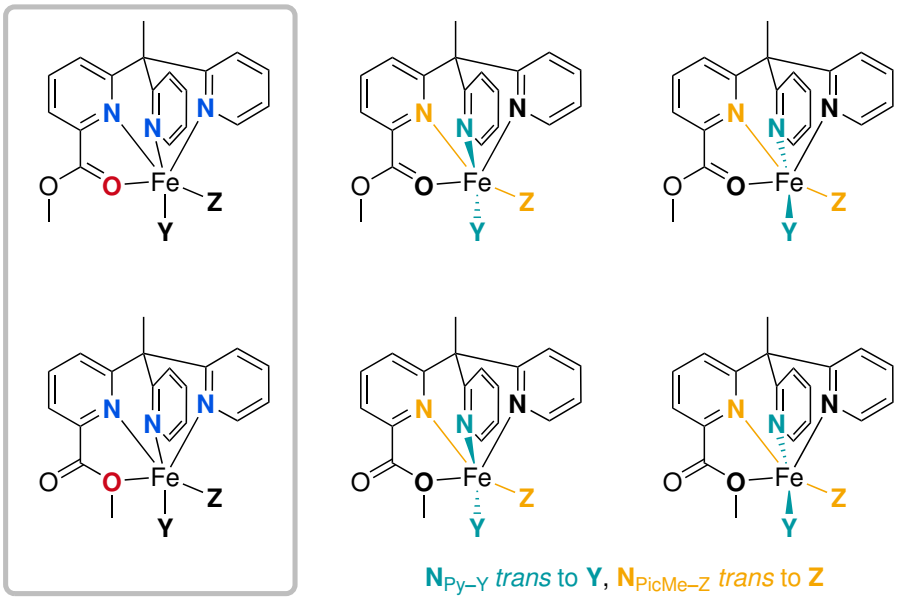

Figure 5.3: Donor atom positions and labeling of complexes with ligand **3**.

the *trans*-position to the *N*-donor of the methyl picolinate group ($N_{PicMe\text{-}Z}$).

[Fe(MeC(Py)$_2$PicMe)(OTf)$_2$] (3a)

With the iron triflate salt Fe(OTf)$_2$ · 2 MeCN and the ligand **3**, complex [Fe(**3**)(OTf)$_2$] (**3a**) was obtained as a crystalline solid from the synthesis in acetonitrile and subsequent layering with diethyl ether (Scheme 5.2).

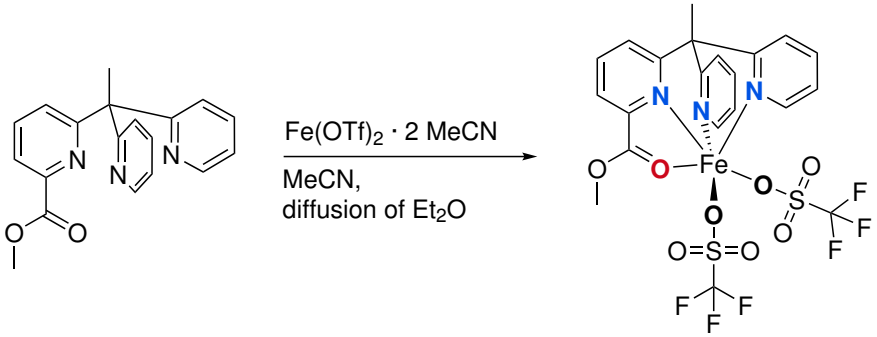

Scheme 5.2: Synthesis of complex **3a**.

Since it is nearly impossible to foresee whether the bis(acetonitrile) or the bis(triflato) species is favoured in the solid state, SCXRD is the method of choice to investigate this issue. Complex **3a** crystallises in the triclinic space group $P\bar{1}$ with $Z = 2$ and is present as a bis(triflato) structure (Figure 5.4). One facial side of the distorted coordination octahedron (CSM, S(OC-6) = 3.8) is purely *N*-donor coordinated and the opposite facial side purely *O*-donor coordinated.

The Fe – N bond lengths are longer than 2.0 Å (Table 5.1). This indicates **3a** to be a HS species in the solid state. The metal-donor bond lengths are all in a very similar range. The

Fe – O_{PicMe} bond is slightly elongated (2.2166(12) Å) and Fe – O_Z bond is slightly shortened (2.0621(15) Å).

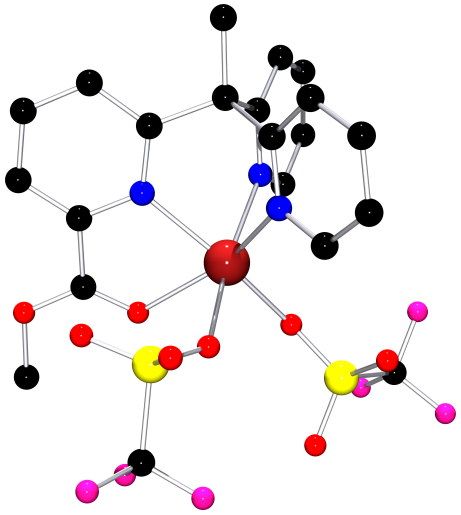

Figure 5.4: [Fe(**3**)$(OTf)_2$] unit in crystals of **3a**. Hydrogen atoms are omitted for clarity. Colour code: black = carbon, blue = nitrogen, red = oxygen, scarlet = iron, yellow = sulphur, pink = fluorine.

Table 5.1: Selected bond lengths, atom distances and structure parameters of **3a**.

	3a [Fe(MeC$(Py)_2$PicMe)$(OTf)_2$]
Space group	$P\bar{1}$
Bond lengths [Å]	
Fe – N_{Py}	2.1319(14)
Fe – $N_{Py\text{-}Y}$	2.1930(14)
Fe – $N_{PicMe\text{-}Z}$	2.1329(16)
Ø Fe – N	2.153
Fe – O_{PicMe}	2.2166(12)
Fe – O_Y	2.1635(12)
Fe – O_Z	2.0621(15)
Atom distances [Å]	
$O_{PicMe}\cdots N_{PicMe\text{-}Z}$	2.6428(19)
Struct. param.	
CSM *S*(OC-6)	3.8
CSM *S*(TPR-6)	5.8

$[Fe_4(\mu\text{–}O)_2(MeC(Py)_2Pic)_4](OTf)_4 \cdot 4\,DCM \cdot THF$ (3b)

Iron-triflate species with ligand **3** are oxygen sensitive. A different solvent combination and a procedure that was only partly performed under inert conditions resulted in the tetrameric species $[Fe_4(\mu\text{-}O)_2(\mathbf{3'})_4](OTf)_4 \cdot 4\,DCM \cdot THF$ (**3b**) which contains two bridging oxygen atoms (Scheme 5.3). This structure was characterised by SCXRD and crystallises as dichloromethane and tetrahydrofuran solvate in the triclinic space group $P\bar{1}$ with $Z = 2$

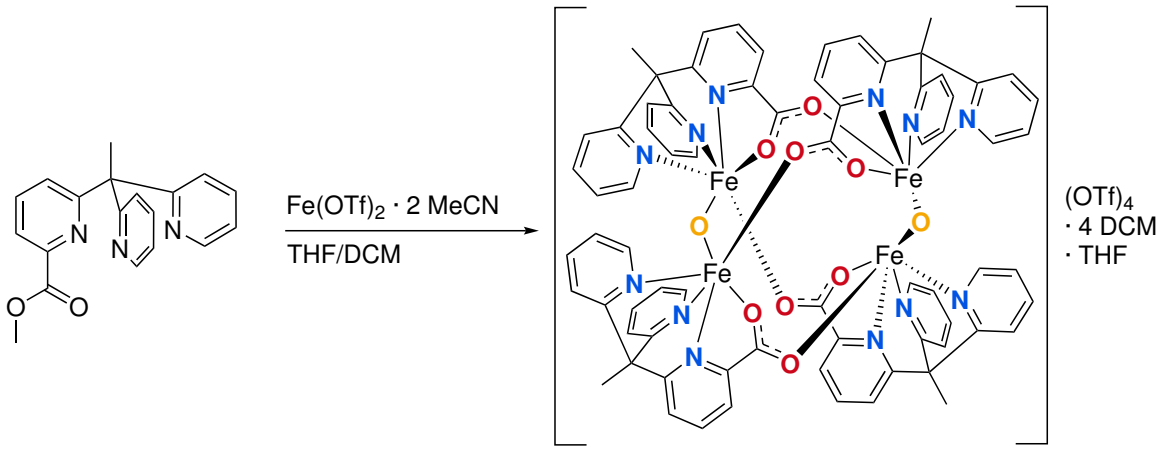

Scheme 5.3: Synthesis of complex **3b**.

(Figure 5.5). The methyl ester of ligand **3** (MeC(Py)$_2$PicMe) is hydrolysed in this crystal structure (MeC(Py)$_2$Pic$^-$, **3'**). The resulting carboxylate group fulfils two functions. First, one oxygen atom coordinates together with the tree *N*-donors one iron centre. Second, the other oxygen of the carboxylic group is a bridging ligand to the next iron centre. Two additional O^{2-} anions act also as bridging ligands. The iron centres are in the oxidation state +3. Together with the negatively charged ligands and the two bridging oxide anions the complex cation has a charge of +4 ([Fe$_4$(μ-O)$_2$(MeC(Py)$_2$Pic)$_4$]$^{4+}$). This charge is balanced by four non-coordinating triflate counterions.

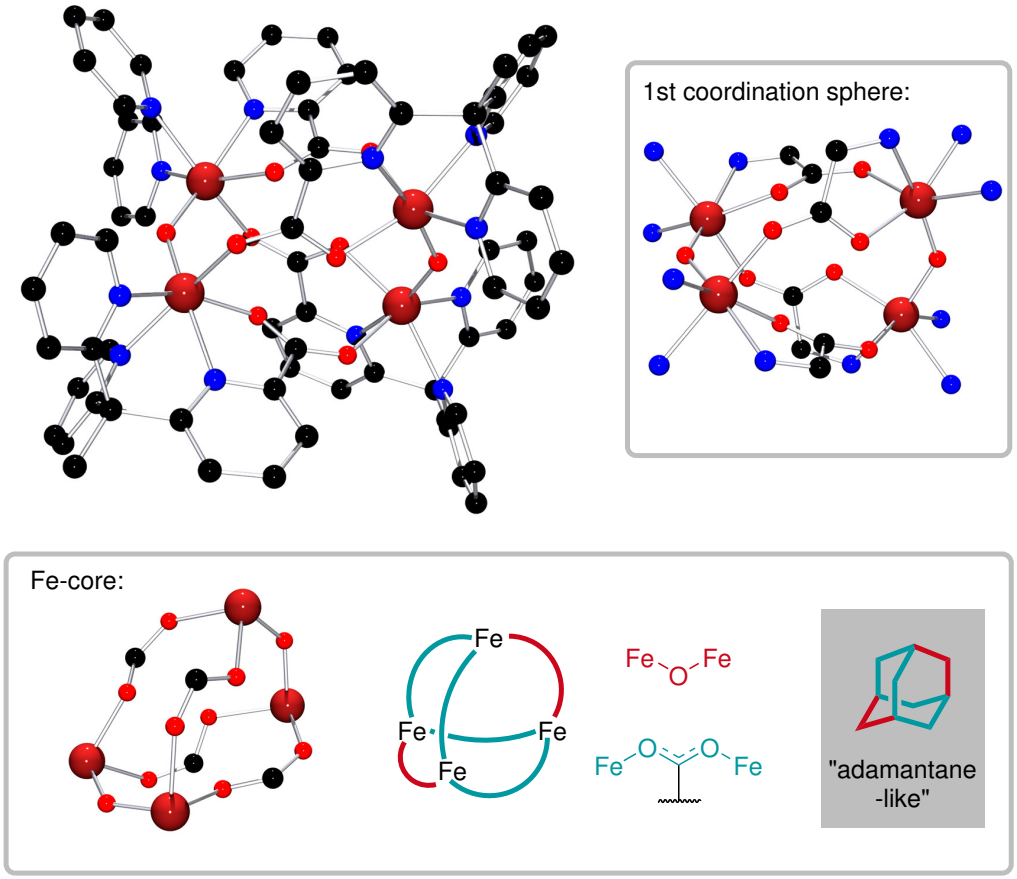

Figure 5.5: Complex cation (top, left), first coordination sphere (top, right) and arrangement & connectivity of iron centres in [Fe$_4$(μ-O)$_2$(**3'**)$_4$]$^{4+}$ cation (bottom) in crystals of **3b**. Hydrogen atoms, counterions and crystal solvent molecules are omitted for clarity. Colour code: black = carbon, blue = nitrogen, red = oxygen, scarlet = iron.

The coordination sphere of all four iron centres is octahedrally distorted (CSM: *S*(OC-6) = 2.0–2.4) and has the same donor set-up. Besides the {N$_3$O}-coordination by MeC(Py)$_2$Pic$^-$ the second oxygen atom of a carboxylate of the next ligand is coordinating on the Y position which bridges two iron + MeC(Py)$_2$Pic$^-$ building blocks (Table 5.2). The Z position is occupied by a O^{2-} anion bridging the iron centre to a different iron centre in the structure. This creates a complex core in which all four iron atoms are connected to each other in two different ways. The arrangement of all four iron centres is reminiscent of an adamantane

Table 5.2: Selected bond lengths, atom distances, bond angles and structure parameters of **3b**.

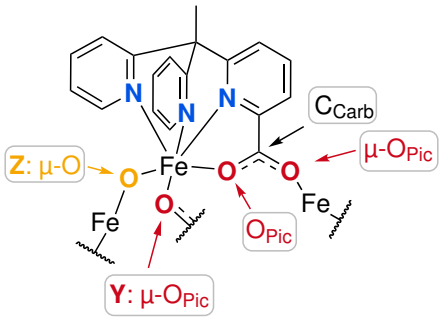

	3b $[Fe_4(\mu\text{-}O)_2(MeC(Py)_2Pic)_4](OTf)_4 \cdot 4\,DCM \cdot THF$ Fe(1) / Fe(2) / Fe(3) / Fe(4)
Space group	$P\bar{1}$
Bond lengths [Å]	
Fe – N_{Py}	2.168(6) / 2.163(6) / 2.168(6) / 2.173(6)
Fe – $N_{Py\text{-}Y}$	2.160(6) / 2.168(6) / 2.173(6) / 2.162(6)
Fe – N_{Pic-Z}	2.137(6) / 2.182(6) / 2.182(6) / 2.174(6)
Ø Fe – N	2.168
Fe – O_{Pic}	2.057(5) / 2.047(5) / 2.045(5) / 2.050(5)
Fe – O_Y, (μ-O_{Pic})	2.064(5) / 2.078(5) / 2.065(5) / 2.067(5)
Fe – O_Z, (μ-O)	1.811(5) / 1.804(5) / 1.821(5) / 1.810(5)
C_{Carb} – O_{Pic}	1.269(9) / 1.247(8) / 1.251(8) / 1.252(8)
C_{Carb} – μ-O_{Pic}	1.255(9) / 1.246(8) / 1.254(8) / 1.258(8)
Atom distances [Å]	
$O_{Pic}\cdots N_{Pic-Z}$	2.550(7) / 2.535(7) / 2.558(7) / 2.540(7)
Fe(1) ⋯Fe(2)	5.423(2)
Fe(1) ⋯Fe(3)	3.3528(17)
Fe(1) ⋯Fe(4)	5.375(2)
Fe(2) ⋯Fe(3)	5.410(2)
Fe(2) ⋯Fe(4)	3.3588(18)
Fe(3) ⋯Fe(4)	5.419(2)
Bond angles [°]	
Fe(1) – μ-O – Fe(3)	134.8(3)
Fe(2) – μ-O – Fe(4)	136.7(3)
Fe – O_{Pic} – C_{Carb}	116.7(5) / 118.0(5) / 118.4(4) / 116.9(5)
Fe – μ-O_{Pic} – C_{Carb}	133.1(5) / 134.4(5) / 134.2(5) / 134.9(5)
Struct. param.	
CSM *S*(OC-6)	2.1 / 2.0 / 2.4 / 2.1
CSM *S*(TPR-6)	11.6 / 9.8 / 10.4 / 9.4

like structure with two short (oxo) and four long (carboxylate) bonds (Figure 5.5). From a different perspective this complex can also be seen as dimer of μ-O-bridged dimers which are arranged in a perpendicular fashion (Figure 5.6). This tetrameric (or dimer of dimers) structure with two O^{2-} and four carboxylate bridging ligands connecting four iron(III) centres was already observed by other groups with other tetradentate ligands.[218–222]

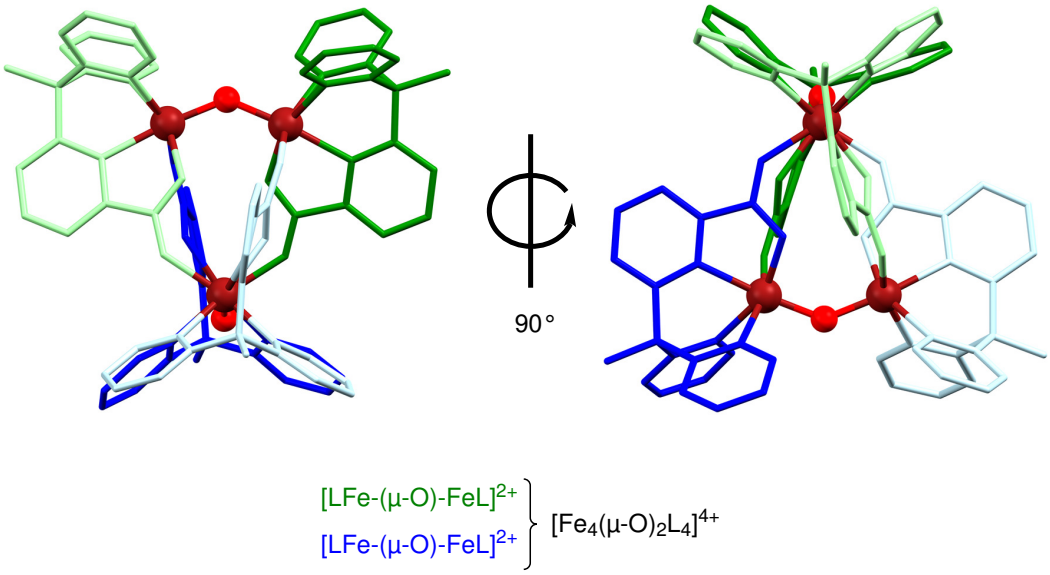

Figure 5.6: Tetrameric structure of $[Fe_4(\mu\text{-}O)_2(\mathbf{3'})_4]^{4+}$ cation in crystals of **3b** consisting of two perpendicular μ-oxo dimeric sub-units (one green (top), one blue (bottom)). Colour code: red = oxygen, scarlet = iron, (light) blue/green = ligand scaffold.

The Fe – N bond lengths (2.137(6)–2.182(6) Å) in **3b** are all slightly higher as those of the carboxylate Fe – O bond lengths (2.045(5)–2.078(5) Å). Notably shorter are the Fe – O bond lengths with the bridging μ-O (1.804(5)–1.821(5) Å). The bridging oxygen atom of the carboxylate group $\mu\text{-}O_{Pic}$ coordinates always to the Y position (*trans* to pyridine) of the next iron centre. In all coordinations in the Z position the bridging O^{2-} anions (μ-O) are involved.

The distances of the iron centres can be sorted in two categories. The iron centres directly bridged by μ-O are closer together (3.3528(17)–3.3588(18) Å) than the iron centres bridged by $\mu\text{-}O_{Pic} - C_{Carb} - O_{Pic}$ (5.375(2)–5.423(2) Å). Fe – μ-O – Fe bond angles are in a range of 134.8(3)–136.7(3)°. The angles of $Fe - O_{Pic} - C$ (116.7(5)–118.4(4)°) are sharper than those of $Fe - \mu\text{-}O_{Pic} - C_{Carb}$ (133.1(5)–134.9(5)°).

The tetrameric structures in the literature are very similar in terms of distances, bond lengths and angles. The Fe···Fe distances are in a range of 3.287–3.433 Å or 5.149–5.339 Å, respectively. The Fe – μ-O – Fe bond angles are in a range of 132.0–147.5°. Most of these structures were found in the context of synthesising dimeric iron complexes as biomimetic model compounds for the enzyme methane monooxygenase (MMO).[218–222]

[Fe(MeC(Py)$_2$PicMe)Cl$_2$] · 0.5 MeCN (3c)

The combination of ligand **3** and $FeCl_2$ resulted in the expected bis(chlorido) iron complex [Fe(**3**)Cl$_2$] · 0.5 MeCN (**3c**, Scheme 5.4). It was possible to obtain suitable crystals for SCXRD, which proved to be the bis(chlorido) species (Figure 5.7). Complex **3c** crystallises as an acetonitrile solvate in the monoclinic space group $C2/c$ with $Z = 8$. A disorder was found

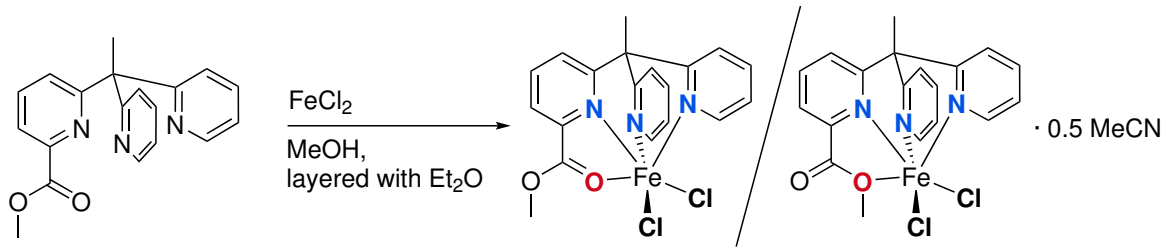

Scheme 5.4: Synthesis of complex **3c**.

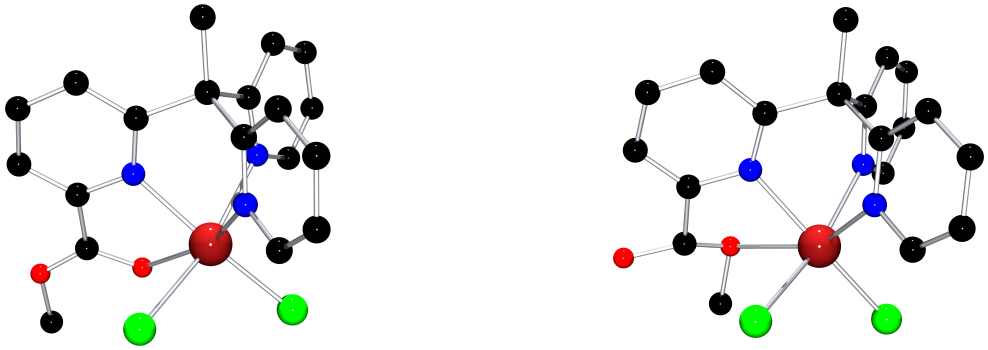

Figure 5.7: [Fe(**3**)Cl_2] unit in both coordination modes in crystals of **3c**. Hydrogen atoms and crystal solvent molecules are omitted for clarity. Colour code: black = carbon, blue = nitrogen, red = oxygen, scarlet = iron, green = chlorine.

showing both oxygen atoms of the ester group being able coordinating the iron centre. With an occupancy of 0.750(12) the C = O atom is coordinating (like in all other mononuclear complexes with **3**) and with an occupancy of 0.250(12) the other oxygen of the ester group is coordinating (**3c'**). The latter shows a weaker coordination since the Fe – O bond is quite elongated (2.42(3) Å, Table 5.3). It also gives the impression that the ester group is rotated a little more than necessary making the Fe – O bond longer (Figure 5.8). The reason for this may be that in this coordination mode the methyl group needs additional space and can not get too close to the two chlorido ligands. The Fe – N bond lengths Fe – N_{Py} and Fe – $N_{PicMe\text{-}Z}$

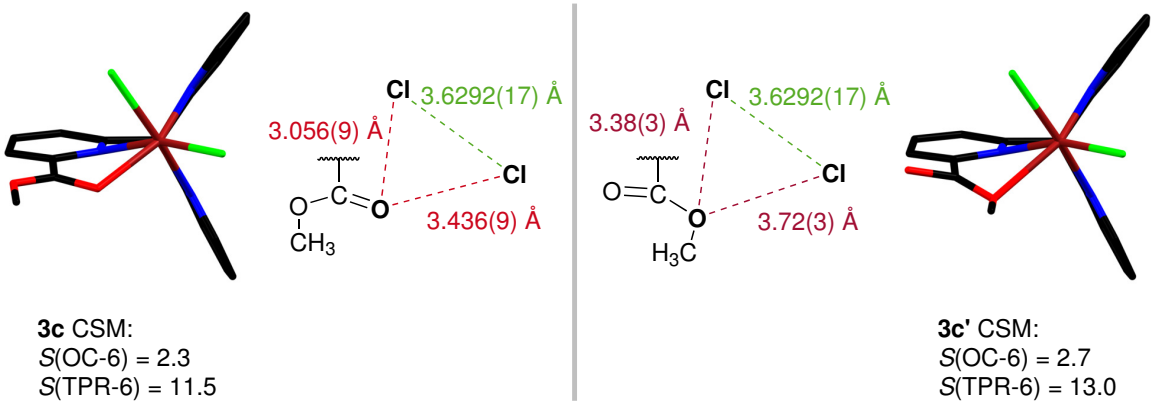

3c CSM:
S(OC-6) = 2.3
S(TPR-6) = 11.5

3c' CSM:
S(OC-6) = 2.7
S(TPR-6) = 13.0

Figure 5.8: View in direction of the Fe – C – Me-axis and Fe···Cl distances in crystals of **3c** for both coordination modes. Hydrogen atoms and crystal solvent molecules are omitted for clarity. Colour code: black = carbon, blue = nitrogen, red = oxygen, scarlet = iron, green = chlorine.

Table 5.3: Selected bond lengths, atom distances and structure parameters of **3c**.

	3c [Fe(MeC(Py)$_2$PicMe)Cl$_2$] · 0.5 MeCN	
	3c, $O_{PicMe=O}$	**3c'**, $O_{PicMe-OMe}$
Space group	$C2/c$	
Bond lengths [Å]		
Fe – N_{Py}	2.150(3)	
Fe – N_{Py-Y}	2.221(3)	
Fe – $N_{PicMe-Z}$	2.140(4)	
Ø Fe – N	2.170	
Fe – O	2.312(10)	2.42(3)
Fe – Cl_Y	2.4527(12)	
Fe – Cl_Z	2.3107(13)	
Atom distances [Å]		
$O_{PicMe}\cdots N_{PicMe-Z}$	2.671(9)	2.45(3)
$Cl_Y\cdots Cl_Z$	3.6292(17)	
$Cl_Y\cdots O$	3.056(9)	3.38(3)
$Cl_Z\cdots O$	3.436(9)	3.72(3)
Struct. param.		
CSM *S*(OC-6)	2.3	2.7
CSM *S*(TPR-6)	11.5	13.0

are very similar to each other with 2.120(3) and 2.140(4) Å, respectively. Contrasting to this the Fe – N_{Py-Y} bond length is elongated to 2.221(3) Å. The Fe – Cl bond lengths are in a range of 2.3107(13)–2.4527(12) Å, with the Y position being the elongated bond. Since the Fe – N bond lengths are longer than 2.0 Å this is a hint for a HS species in the solid state. The coordination geometry is a distorted octahedron where the major variant **3c** (CSM: *S*(OC-6) = 2.3) is slightly less distorted than the minor variant **3c'** (CSM: *S*(OC-6) = 2.7).

[Fe(MeC(Py)$_2$PicMe)(H$_2$O)(MeCN)](BF$_4$)$_2$ · MeCN (3d)

The expected species from the complexation reaction between **3** and [Fe(MeCN)$_6$](BF$_4$)$_2$ in acetonitrile would be [Fe(**3**)(MeCN)$_2$](BF$_4$)$_2$. Nevertheless, the compound [Fe(**3**)(H$_2$O)(MeCN)](BF$_4$)$_2$ · MeCN (**3d**) was obtained in SCXRD quality crystals (Scheme 5.5, Figure 5.9). Instead of a second acetonitrile co-ligand, the Y position is occupied by a water molecule as co-ligand. This indicates that water is a competing co-ligand for these complexes and this is the result of exposure to moisture over a longer crystallisation time. Complex **3d** crystallises as acetonitrile solvate in the monoclinic space group $P2_1/c$ with $Z = 4$. The iron-donor bond lengths are all above 2.0 Å (Ø Fe – N = 2.116 Å, Table 5.4), which indicates **3d** to be a HS species in the solid state. The Fe – O_{PicMe} is the most elongated bond length (2.2266(11) Å) whereas the shortest one is Fe – $N_{PicMe-Z}$ (2.0983(12) Å). The coordination sphere is a distorted octahedron (CSM: *S*(OC-6) = 2.8).

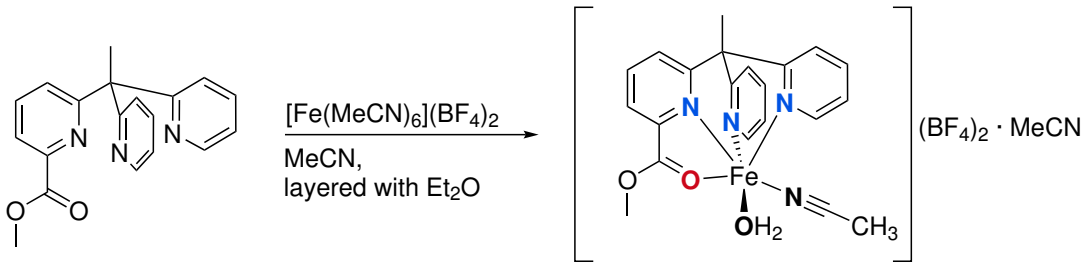

Scheme 5.5: Synthesis of complex **3d**.

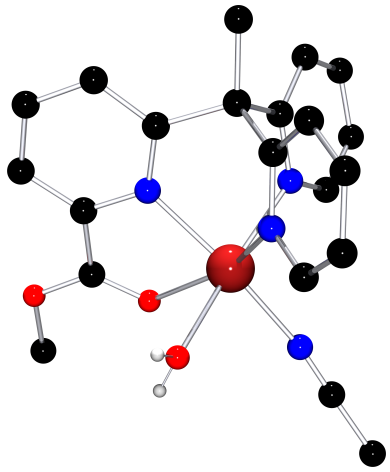

Figure 5.9: $[Fe(\mathbf{3})(H_2O)(MeCN)]^{2+}$ cation in crystals of **3d**. C bonded hydrogen atoms, counterions and crystal solvent molecules are omitted for clarity. Colour code: black = carbon, blue = nitrogen, red = oxygen, scarlet = iron, white = hydrogen.

Table 5.4: Selected bond lengths, atom distances and structure parameters of **3d**.

	3d $[Fe(MeC(Py)_2PicMe)(H_2O)(MeCN)](BF_4)_2 \cdot MeCN$
Space group	$P2_1/c$
Bond lengths [Å]	
$Fe-N_{Py}$	2.1207(13)
$Fe-N_{Py\text{-}Y}$	2.1432(12)
$Fe-N_{PicMe\text{-}Z}$	2.0983(12)
$Fe-N_Z$	2.1033(13)
Ø Fe – N	2.116
$Fe-O_{PicMe}$	2.2266(11)
$Fe-O_Y$	2.1435(12)
Atom distances [Å]	
$O_{PicMe}\cdots N_{PicMe\text{-}Z}$	2.6111(16)
Struct. param.	
CSM *S*(OC-6)	2.8
CSM *S*(TPR-6)	7.5

$[Fe(MeC(Py)_2PicMe)(BF_4)Cl] \cdot 3.5\,Et_2O$ (3e)

The use of $FeCl_2$ and $[Fe(MeCN)_6](BF_4)_2$ in equal amounts with one equivalent of ligand **3** in methanol resulted in a rare mixed co-ligand species $[Fe(\mathbf{3})(BF_4)Cl] \cdot 3.5\,Et_2O$ (**3e**) which could be characterised by SCXRD (Scheme 5.6, Figure 5.10). Complex **3e** crystallises as a diethyl ether solvate in the monoclinic space group $P2_1/c$ with $Z = 4$. 3.5 diethyl ether molecules per complex could not be modelled in an appropriate manner and were masked using the BYPASS algorithm as implemented in PLATON/SQUEEZE.[156–158]
Since tetrafluoridoborate is a weak coordinating anion, it is not expected to coordinate easily. In the CSD (12.05.2023) only eleven structures are listed with iron coordinated by a tetrafluoridoborate anion.[58,223–232] Only in one of the structures an iron centre is coordinated by two tetrafluoridoborate anions at the same time in a *trans* configuration.[224] Alvarez made a data analysis of complexes available in the CSD database about i.a. anions and solvents and their coordination ability.[233] For 12872 structures containing tetrafluoridoborate it

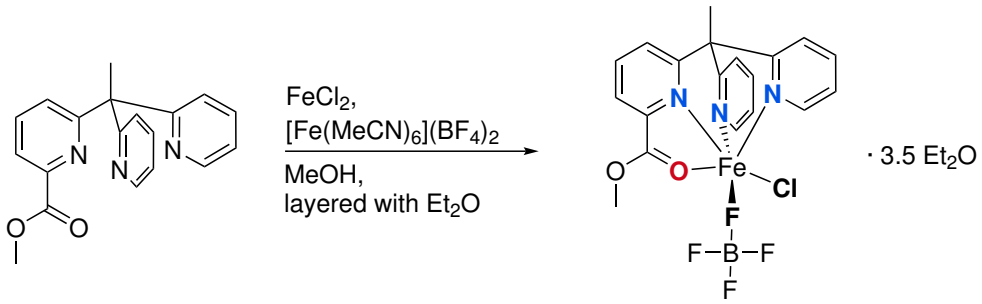

Scheme 5.6: Synthesis of complex **3e**.

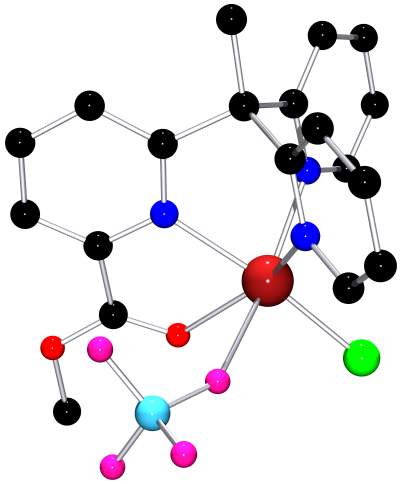

Figure 5.10: [Fe(**3**)(BF$_4$)Cl] unit in crystals of **3e**. Hydrogen atoms and crystal solvent molecules are omitted for clarity. Colour code: black = carbon, blue = nitrogen, red = oxygen, scarlet = iron, pink = fluorine, green = chlorine, sky blue = boron.

Table 5.5: Selected bond lengths, atom distances and structure parameters of **3e**.

	3e [Fe(MeC(Py)$_2$PicMe)(BF$_4$)Cl]
Space group	$P2_1/c$
Bond lengths [Å]	
Fe – N_{Py}	2.1432(17)
Fe – $N_{Py\text{-}Y}$	2.1487(17)
Fe – $N_{PicMe\text{-}Z}$	2.1390(16)
Ø Fe – N	2.144
Fe – O_{PicMe}	2.2028(15)
Fe – F_Y	2.3226(14)
Fe – Cl_Z	2.2872(8)
Atom distances [Å]	
$O_{PicMe}\cdots N_{PicMe\text{-}Z}$	2.627(2)
Struct. param.	
CSM *S*(OC-6)	3.6
CSM *S*(TPR-6)	8.7

was only found to be coordinating (or semi-coordinating) in 8 % of them. For comparison, triflate was coordinating in 30 % (10043 structures) and chloride in 92 % (72048 structures) of the cases. The Fe – F_{BF4} bond in crystals of **3e** is about 0.04 Å longer than those that can be found in the CSD (Table 5.6).[58] In general, the Fe – F_{BF4} bonds show a great variety in lengths (1.987–2.284 Å). Within the structure of **3e**, the Fe – F_{BF4} bond is also the most elongated followed by the Fe – Cl_Z bond (2.2872(8) Å, Table 5.5). The Fe – N_{Py} bond lengths are nearly identical (2.1432(17) & 2.1487(17) Å). The Fe – $N_{PicMe\text{-}Z}$ bond length is the shortest (2.1390(16) Å) and the *O*-donor iron bond length is the longest between **3** and the iron centre (2.2028(15) Å). The coordination geometry is a distorted octahedron (CSM: *S*(OC-6) = 3.6) which matches the observation of a coordinating tetrafluoridoborate.

Table 5.6: Fe – F_{BF4} bond lengths found in the CSD.[58]

Compounds	Bond lengths Fe – F_{BF4} [Å]	References
3e	2.3226(14)	this work
(CSD refcode)		
BALDOK	2.284	[223]
BALDUQ	2.234	[223]
KISPIM	2.263	[224]
LEWYOD	2.057	[225]
MAKJIR	2.077–2.10	[226]
MARFET	2.008	[227]
MOYTUP	1.966	[228]
NASKIC	2.067	[229]
TIWQAU	1.987	[230]
TUWHIF	2.050	[231]
VADSEC	2.283–2.303	[232]

5.2.1 Summary of Iron Complexes of Ligand 3 in the Solid State

The obtained structures show that iron complexes with ligand **3** are oxygen sensitive and presence of moisture results in a competing water co-ligand. The tetrameric species **3b** is a decomposition product of complex **3a** when synthesis is carried out under aerobic conditions. Crystals were not red as the ones of **3a** but they were brown. The brown crystals of **3b** were obtained after 6 weeks instead of one week as for **3a**. In the case of a synthesis with $[Fe(MeCN)_6](BF_4)_2$, a long crystallisation time (8 months) resulted in a species with an aqua ligand, although the solution was prepared under inert conditions in abs. solvents. Therefore, these complexes are vulnerable to small amounts of moisture or oxygen over long periods of time.

5.3 Iron Complexes of $MeC(Py)_2PicMe$ (3) in Solution

5.3.1 Triflate-Acetonirile Equilibria in Solution

Although no bis(acetonitrile) iron complex with ligand **3** could be characterised by SCXRD, studies in solution suggest that such species exist, since it is typical for acetonitrile to displace weakly or moderately coordinating co-ligands (e.g. triflate) in acetonitrilic solutions.[90,121,126,234–236]

In addition, a clear colour change from orange to red takes place in acetonitrile during cooling in solutions of dissolved crystals of **3a** (Figure 5.11). This is a first hint for a spin crossover behaviour. In the following, it will be discussed if this behaviour is an SCO or CISSS process and which species are present in acetonitrile and other solvent. Used methods are NMR and UV/Vis spectroscopy.

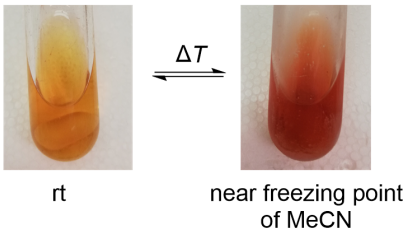

Figure 5.11: MeCN Solution of crystals of **3a** at high (left, ~ rt) and low temperature (right).

NMR Studies

The first question is if acetonitrile is coordinating when it is used as solvent. Since either acetonitrile or triflate anions are possible co-ligands, the triflate anions can be used to indirectly determine whether acetonitrile coordinates. In the ^{19}F-NMR spectrum, coordinating and free triflate anions have clearly different chemical shifts.
Crystals of [Fe(MeC(Py)$_2$PicMe)(OTf)$_2$] (**3a**) were dissolved in acetonitrile-d$_3$ and KPF_6 was added as internal standard. The ^{19}F-NMR spectrum shows a sharp doublet at −72.9 ppm for KPF_6 and a broad singlet at −71.0 ppm (Figure 5.12, top).

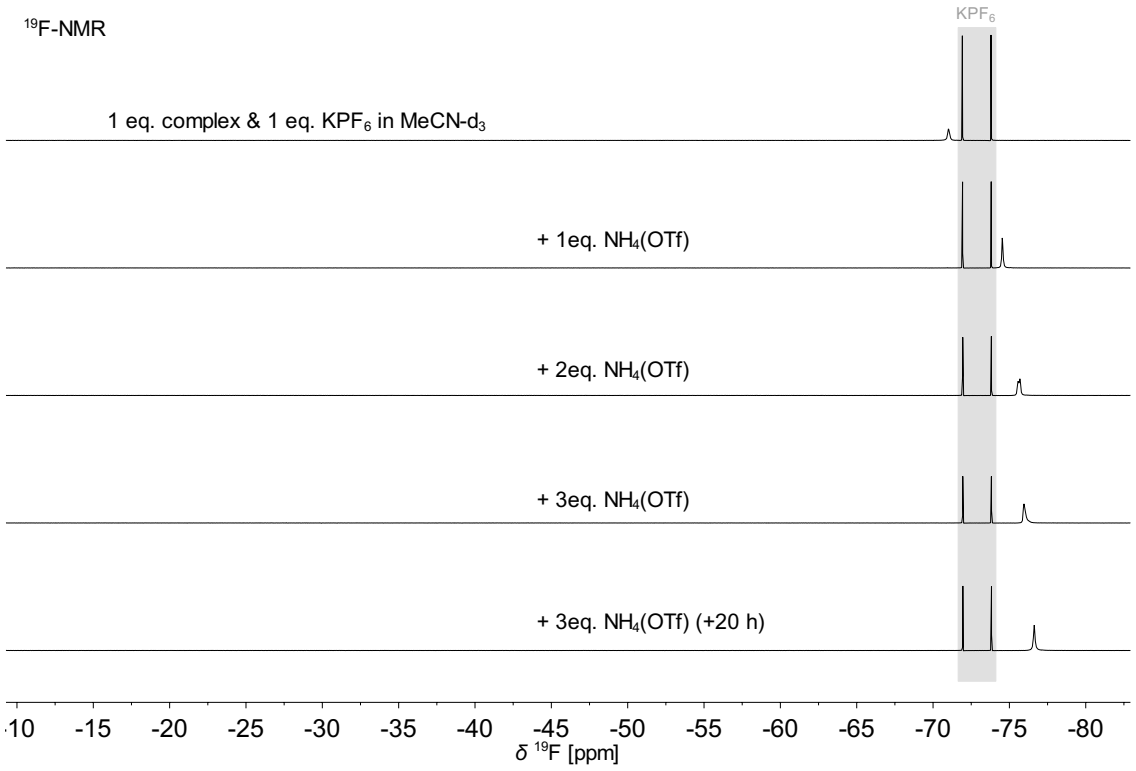

Figure 5.12: ^{19}F-NMR spectra of complex **3a** in MeCN-d$_3$ and KPF_6 as internal standard (top). Addition of up to 3 eq. of $NH_4(OTf)$ (total) below.

Typical values for the chemical shift for terminally bound triflate would be approx. −10 ppm and free triflate −80 ppm.[236,237] Since there is no peak at −10 ppm but a peak in the region of −80 ppm most of the triflate anions seem to be unbound triflate. This would match the

observation that triflate complexes in acetonitrile tend to swap triflate for acetonitrile as labile co-ligands.[90,121,126,234–236] The addition of further triflate anions in form of $NH_4(OTf)$ to up to 3 eq. shows a shift of the signal towards the expected value of approx. −80 ppm. This could be a hint, that the signal observed at −71 ppm is the result of a very fast exchange of bound and free triflate with most of the triflate being dissociated. By implication, this means that the main species of the iron complex in solution is most likely a bis(acetonitrile-d_3) species.

As the nature of the main species at room temperature is assigned a bis(acetonitrile) species, it is of interest to investigate what happens to the species upon temperature change which changes the complex colour in solution. The ^{1}H-NMR spectrum of crystals of **3a** in acetonitrile-d_3 at different temperatures (VT, variable temperature) is shown in Figure 5.13 and Figure 5.14.

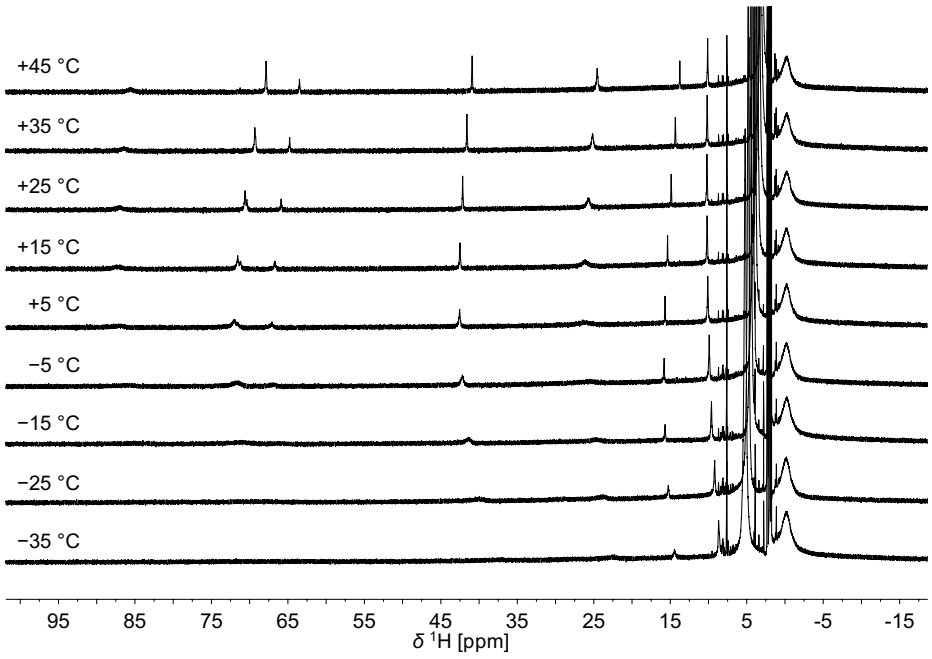

Figure 5.13: VT-^{1}H-NMR spectra of **3a** in MeCN-d_3 in a range of +45 to −35 °C.

The spectra at higher temperatures show signals shifted downfield to up to 87 ppm. At lower temperatures these signals get broader and finally disappear. This behaviour is typical for compounds with a large fraction of HS species at higher temperatures which have a paramagnetic character. The higher fraction of diamagnetic LS species at lower temperatures typically has less downfield shifted signals. This behaviour is known for iron(II) complexes showing spin state switching processes in solution.[138]

Although a capillary containing pure acetonitrile-d_3 was added, it was not possible to obtain reasonable results with the Evans method in the analysis of the shift of the two acetonitrile signals. With the VT-^{1}H-NMR spectra, it is not possible to say if the acetonitrile co-ligands also coordinate at low temperatures. Therefore, VT-^{19}F-NMR would be needed or other

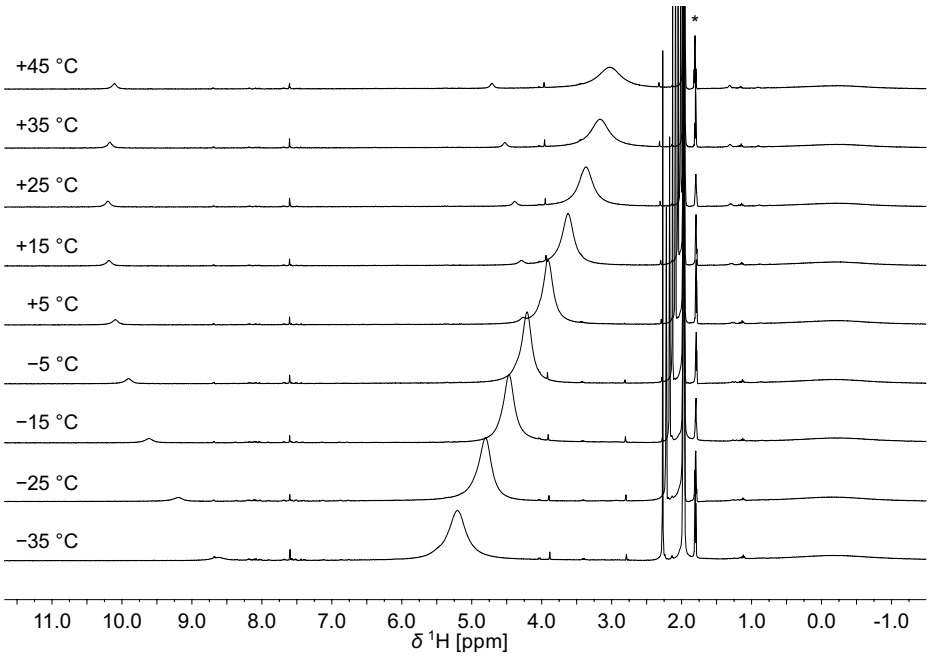

Figure 5.14: Magnification of the VT-^{1}H-NMR Spectra of **3a** in MeCN-d_3 in a temperature range of +45 to −35 °C. Signal of pure MeCN-d_3 in capillary marked with *.

measurement methods like UV/Vis spectroscopy could provide further information about the low temperature species.

UV/Vis Spectroscopic Measurements

In a non-coordinating solvent, it is typical that the triflates that are coordinating in the solid state structure are also coordinating in solution.[121,138,235,236] Consequently, triflate coordination is expected to be maintained when the bis(triflate) species with ligand **3**, as found in crystals of **3a**, is dissolved in a weakly or non-coordinating solvent. However, the dissociation of one triflate molecule to a penta-coordinated mono(triflato) species is also conceivable.[121,236]

UV/Vis spectroscopic measurements of crystals of **3a** in the weakly coordinating solvent tetrahydrofuran show a species with two shoulders at 345 and 465 nm (Figure 5.15). There are no major changes in absorption for a temperature range of −40 to +25 °C.

The situation is totally different for the complex in acetonitrile since there is a change in colour upon cooling. This first visual observation can be followed more precisely in a UV/Vis spectroscopic set-up (Figure 5.16). At 25 °C, two absorptions at 345 and 420 nm can be observed. Lowering the temperature leads to an increase of intensity and the emerging of a new band at 480 nm. More intensive absorptions at lower temperatures are a typical behaviour of spin crossover compounds as the LS species at lower temperatures exhibit a larger ligand field strength and shorter iron-donor bond lengths.[16]

The change in absorption at 480 nm can be plotted against the temperatures (Figure 5.16,

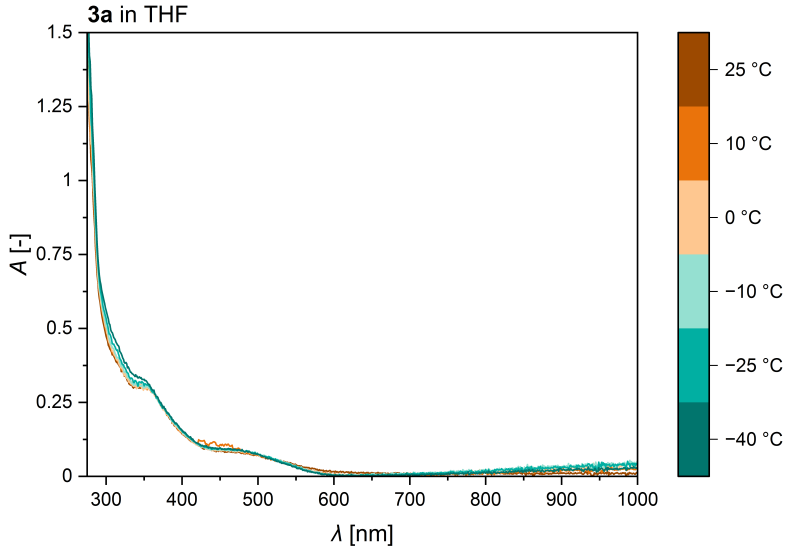

Figure 5.15: UV/Vis spectra of **3a** in THF at different temperatures. (Change in absorption due to temperature-dependent solvent density change not taken into account.)

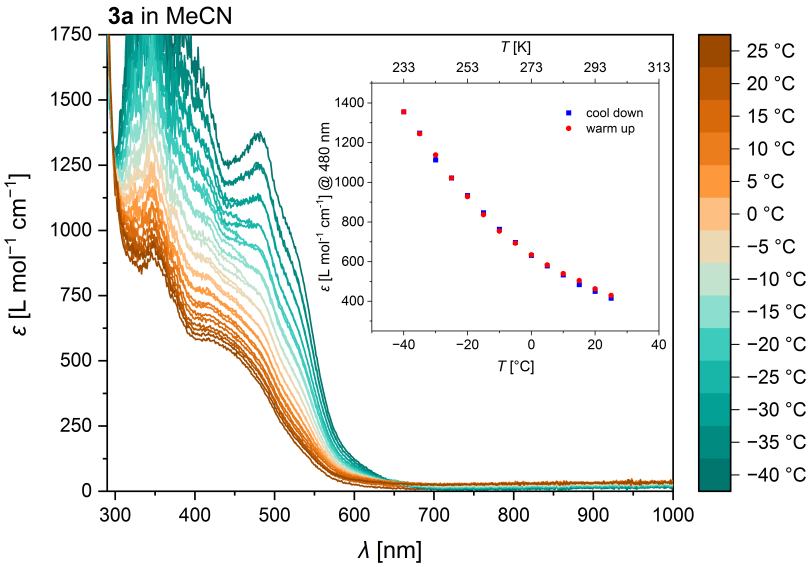

Figure 5.16: UV/Vis spectra of **3a** in MeCN at different temperatures. Inset: temperature-dependent change of absorption at 480 nm.

inset). Due to the lack of cooperativity, the SCO phenomena usually proceed gradually in solution according to a Boltzmann distribution, which is in contrast to the solid state. This is represented by the inverse S-shaped curve of the change in absorption. Although the liquid range of acetonitrile reveals only a part of this inverse S-shaped curve, the fitting of these data enables the calculation of thermodynamic parameters of the spin switch like ΔH, ΔS and the SCO temperature $T_{1/2}$ (Table 5.7). Calculation details are given in the subsection 9.1.4. The values of $\Delta H = 19 \pm 2\,\mathrm{kJ\,mol^{-1}}$ and $\Delta S = 81 \pm 8\,\mathrm{J\,mol^{-1}\,K^{-1}}$ are in line with typical thermodynamic parameters for SCO behaviour in solution ($\Delta H < 30\,\mathrm{kJ\,mol^{-1}}$, $\Delta S < 130\,\mathrm{J\,mol^{-1}\,K^{-1}}$) without dissociation or association processes involved in the spin switching event. A CISSS would result in larger thermodynamic values ($\Delta H > 30\,\mathrm{kJ\,mol^{-1}}$,

Table 5.7: Overview of thermodynamic parameters ΔH, ΔS and $T_{1/2}$ obtained through fitting experimental data from the temperature-dependent UV/Vis spectroscopic measurements of **3a** in MeCN.

UV/Vis	ε_{LS} [L mol^{-1} cm^{-1}]	ε_{HS} [L mol^{-1} cm^{-1}]	ΔH [kJ mol^{-1}]	ΔS [J mol^{-1} K^{-1}]	$T_{1/2}$ [K]
OTf^-	2496 ± 242	169 ± 44	19 ± 2	81 ± 8	234

$\Delta S > 120\,\mathrm{J\,mol^{-1}\,K^{-1}}$).[238,239] The $T_{1/2}$ is 234 K which implies that shortly before the freezing point of acetonitrile there is approx. a 50 : 50 mixture of HS and LS species.
The fraction of the complex molecules being in HS state γ_{HS} at a given temperature can be calculated via Equation 5.1.

$$\gamma_{HS} = \frac{1}{1 + \exp(\frac{\Delta H}{RT} - \frac{\Delta S}{R})} \tag{5.1}$$

The obtained γ_{HS} values for **3a** in acetonitrile are plotted in Figure 5.17.

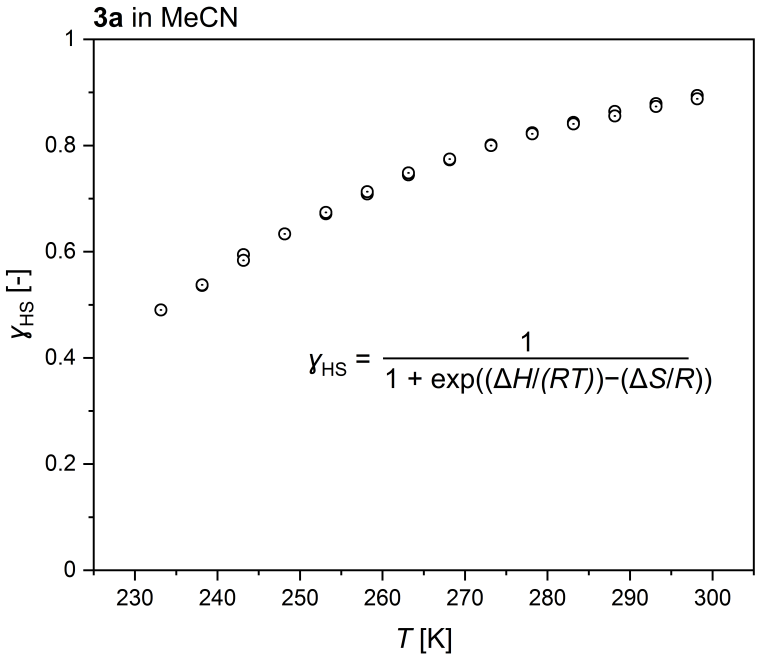

Figure 5.17: High-spin fraction γ_{HS} of dissolved **3a** in MeCN at different temperatures for UV/Vis data calculated from fitted parameters.

To support the hypothesis that a triflate-independent acetonitrile species is present in acetonitrile solution, an "OTf^--free" reference experiment with $[Fe(MeCN)_6](BF_4)_2$ as iron salt can provide further insights. Tetrafluoridoborate is considered to be a very weakly-coordinating anion, so that a bis(acetonitrile) species is expected. The UV/Vis spectrum of the species obtained in acetonitrile using $[Fe(MeCN)_6](BF_4)_2$ is plotted in Figure 5.18. The absorption bands are in good accordance with the one obtained for **3a** in acetonitrile. A reason that they are not exactly the same may be that the tetrafluoridoborate based species was generated *in situ*. In contrast to these two species is the species in tetrahydrofuran

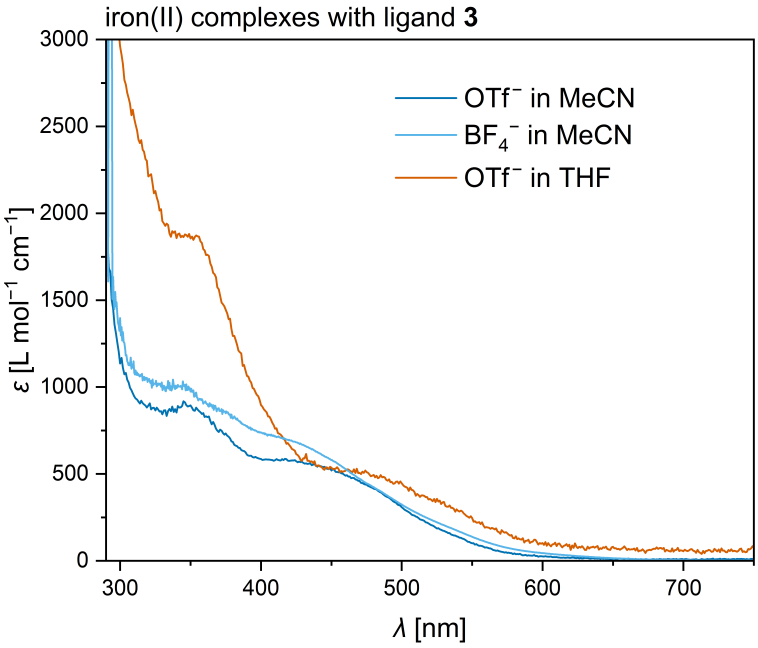

Figure 5.18: UV/Vis spectra of iron(II) complexes with OTf^- or $BF_4{}^-$ anions and ligand **3** in MeCN or THF at rt (~ 25 °C).

which has the same absorption at 345 nm as the two others, but the shoulder at 420 nm is in tetrahydrofurane shifted to 465 nm. All spectra were recorded at room temperature (~ 25 °C). This is a further hint that the same bis(acetonitrile) species is present in acetonitrile.
Taking all the results of the UV/Vis spectroscopic measurements together, a bis(triflato) species as in the solid state structure **3a** is most likely in non-coordinating solvents. In more coordinating acetonitrile, a bis(acetonitrile) species may be present which shows a temperature-dependent SCO.
The quantitative analysis of the SCO in solution was possible for the UV/Vis spectroscopic data. For the NMR spectra, only a qualitative analysis of the spin state switching process could be performed. Since no solid state structure of the bis(acetonitrile) species with triflate or tetrafluoridoborate anions could be obtained, it could not be investigated if an SCO behaviour is also present in the solid state. Nevertheless, the results in solution are consistent with a bis(acetonitrile) main species and there are hints for a very fast exchange of acetonitrile and triflate co-ligands in solution. Overall, the solution behaviour is in line with similar iron(II) complexes.[90,121,126,234,236]

5.3.2 Attempts of Generating Iron-Oxo Species from Bis(acetonitrile) Species using mCPBA

Analogous to the experiments with complexes of ligand **2**, mCPBA was chosen as oxidation agent to obtain potential high-valent iron-oxo species of complexes with ligand **3** (Scheme 5.7). For the iron(II) precursor species, two different routes were chosen: dis-

solving crystals of the bis(triflato) complex **3a** or generating of an *in situ* species with **3** and $[Fe(MeCN)_6](BF_4)_2$. The tetrafluoridoborate based precursor complex could only be prepared *in situ* as no defined solid of this complex is available. According to the results from the previously described solution behaviour, the species in acetonitrile solution should be a bis(acetonitrile) complex for both precursor routes. The chosen methods to identify a potential high-valent iron-oxo species were UV/Vis spectroscopy, CSI-mass spectrometry and Mößbauer spectroscopy.

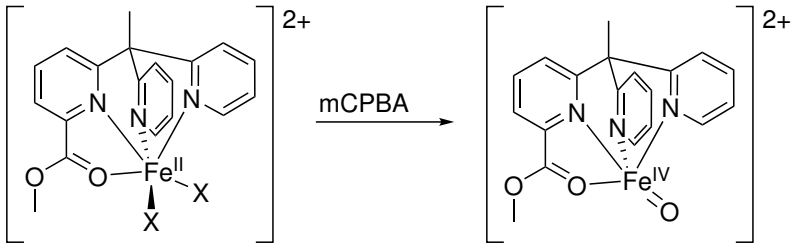

Scheme 5.7: Oxidation of an iron(II) complex with ligand **3** to an iron(IV)oxo species using mCPBA.

UV/Vis Spectroscopy

High-valent iron-oxo species often have characteristic UV/Vis spectroscopic features, which are typically weak absorption bands (ε = 260–290 L mol^{-1} cm^{-1}) at higher wavelengths (λ = 803–900 nm) for an iron(IV)oxo species (S = 2) .[47]

An acetonitrile solution of crystals of **3a** was treated with 1.3 eq. of mCPBA. The colour of the orange solution changed to greenish, which is often observed for high-valent iron-oxo species.[61] The resulting UV/Vis spectrum is shown in Figure 5.19. In the range of approx. 600–750 nm, an increase in absorbance is visible, but not in a defined band but rather in a broad shoulder.

To minimise the influence of the rapid triflate-acetonitrile co-ligand exchange, which results in the acetonitrile species being the main species, the experiment was repeated with the less coordinating tetrafluoridoborate as counterion (Figure 5.20). In this spectrum, a more defined band at 704 nm is visible directly after mCPBA addition (1.2 eq.) which shows a decay process in the following minutes. The formation process was too fast to be monitored with this UV/Vis spectroscopic set-up.

This fast formation process can be monitored more properly in a stopped-flow UV/Vis spectroscopic set-up. The corresponding measurement for the first 120 s at −20 °C is shown in Figure 5.21. The formation of the band at 704 nm is finished after approx. 5 s. A comparison for the band formation at 704 nm for different temperatures is plotted in Figure 5.22. For higher temperatures, the formation of this band is even faster. The absorption values in this spectra have to be taken with care as the baseline with pure acetonitrile was measured at −34 °C and the absorption is not corrected for the temperature dependent change in solvent density. This leads to negative starting values at the higher temperature measurements.

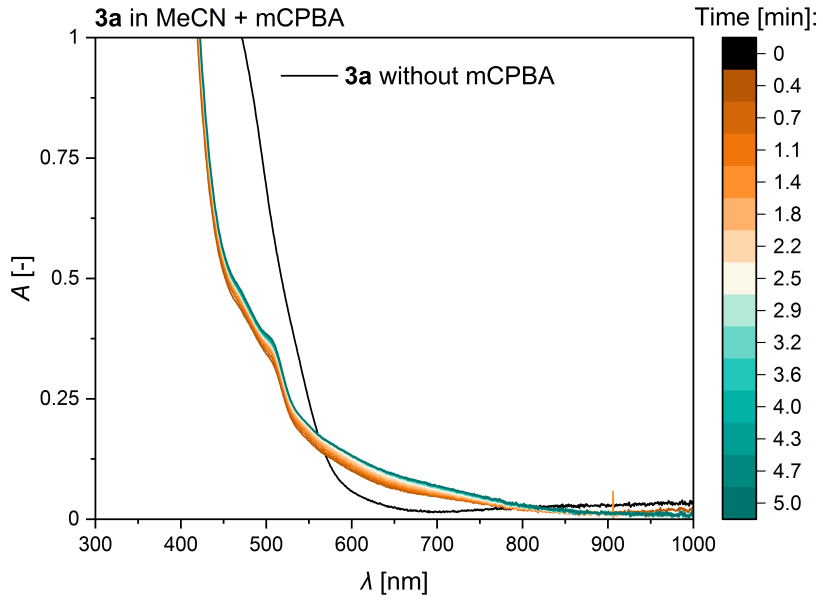

Figure 5.19: UV/Vis spectra of **3a** in MeCN and subsequent addition of mCPBA.

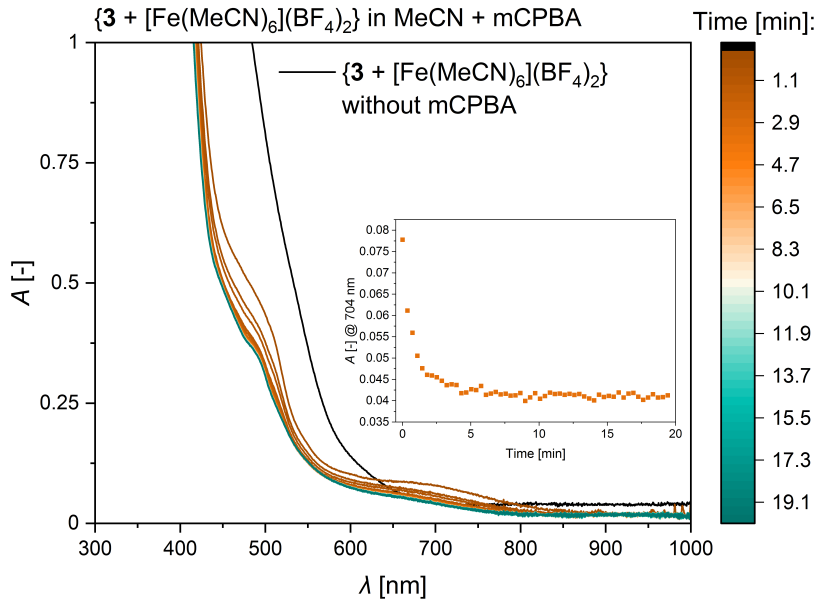

Figure 5.20: UV/Vis spectra of **3** and $[Fe(MeCN)_6](BF_4)_2$ in MeCN and subsequent addition of mCPBA. Inset: absorption at 704 nm vs. time.

Additionally, it is very likely that at higher temperatures the formation of the band at 704 nm is not complete.

Compared to the formation measurements of the iron(IV)oxo species with the $MeC(Py)_2Phen$ (**2**) ligand by Kristina Keisers, the formation of the band for the complex with ligand **3** is less temperature-dependent and overall much faster.[136,189] For the complex with the ligand $MeC(Py)_2Phen$ (**2**), formation times of 0.4 min (20 °C) up to 6 min (−20 °C) were observed.[136,189]

In terms of stability, the species with ligand **3** also has a faster decay at room temperature (Figure 5.20). After approx. 5 min, the band at 704 nm disappears and the half-life time is

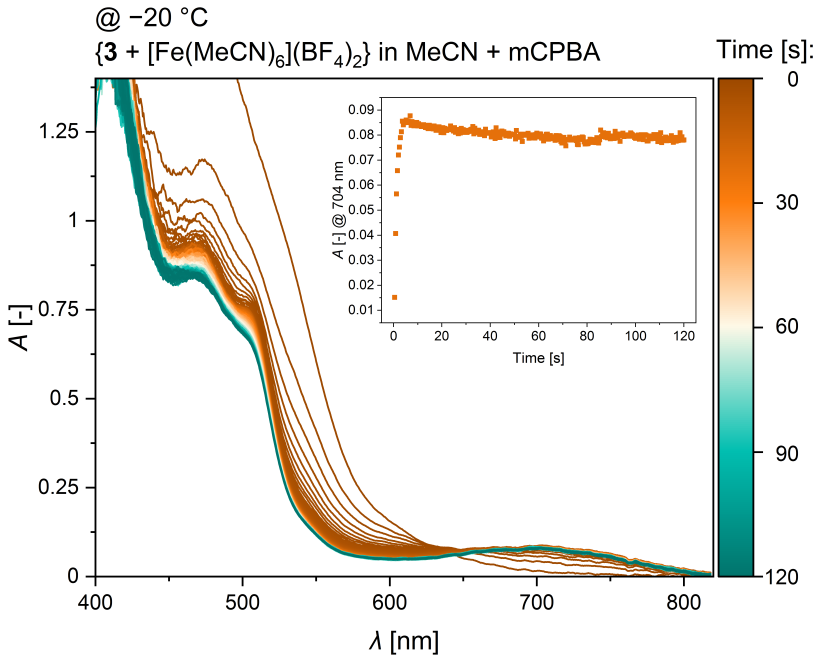

Figure 5.21: Stopped-flow UV/Vis spectra of **3** and $[Fe(MeCN)_6](BF_4)_2$ in MeCN and subsequent addition of mCPBA. Inset: absorption at 704 nm vs. time.

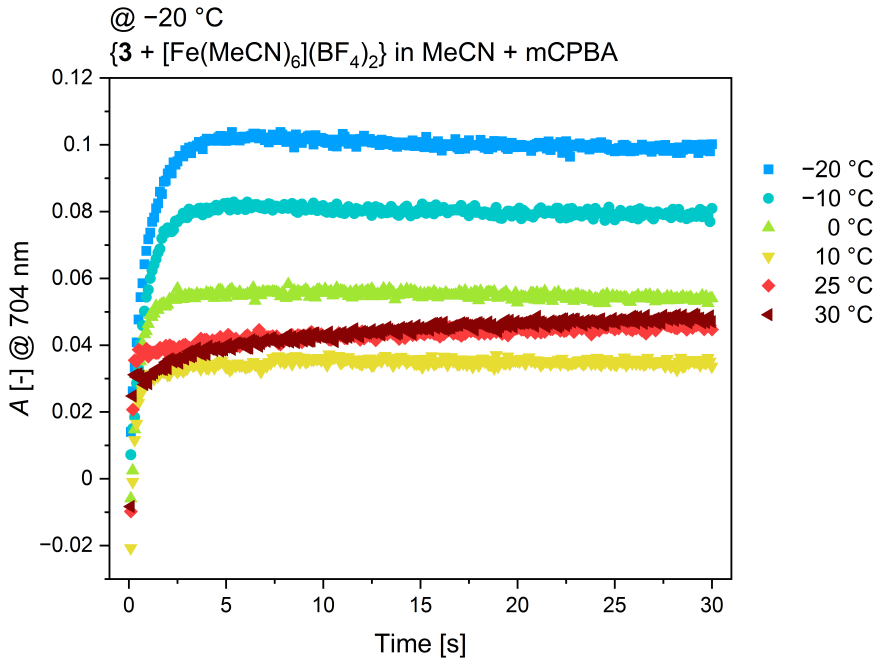

Figure 5.22: Stopped-flow UV/Vis absorption at 704 nm of **3** and $[Fe(MeCN)_6](BF_4)_2$ in MeCN and subsequent addition of mCPBA at different temperatures in the first 30 s.

approx. 1 min. For the complex with ligand **2**, the half-life time is longer (5 min).[136,189] This could indicate a more reactive species with ligand **3**.

This weak absorption band at 704 nm observed in the UV/Vis experiments is a first hint for a high-valent iron-oxo species. Complexes with similar ligands show also absorptions in the 700 nm range for their high-valent iron(IV)oxo intermediates: MeC(Py)$_2$BiPy at 739 nm,[84] and MeC(Py)$_2$Phen (**2**) at 752 nm.[136,189]

CSI-Mass Spectrometry Experiment

A high resolution cryospray-ionisation mass spectrometry (CSI-MS) at −20 °C in acetonitrile was performed to identify the species found in the UV/Vis spectra. Therefore, complex **3a** was dissolved in acetonitrile and cooled to −20 °C. Then, an acetonitrile solution of mCPBA was added at −20 °C and the CIS-MS measurement was performed subsequently. The CSI-MS spectrum (Figure 5.23) shows the expected peak at 196 m/z which corresponds to the iron(IV)oxo species $[Fe^{IV}(\mathbf{3})O]^{2+}$.

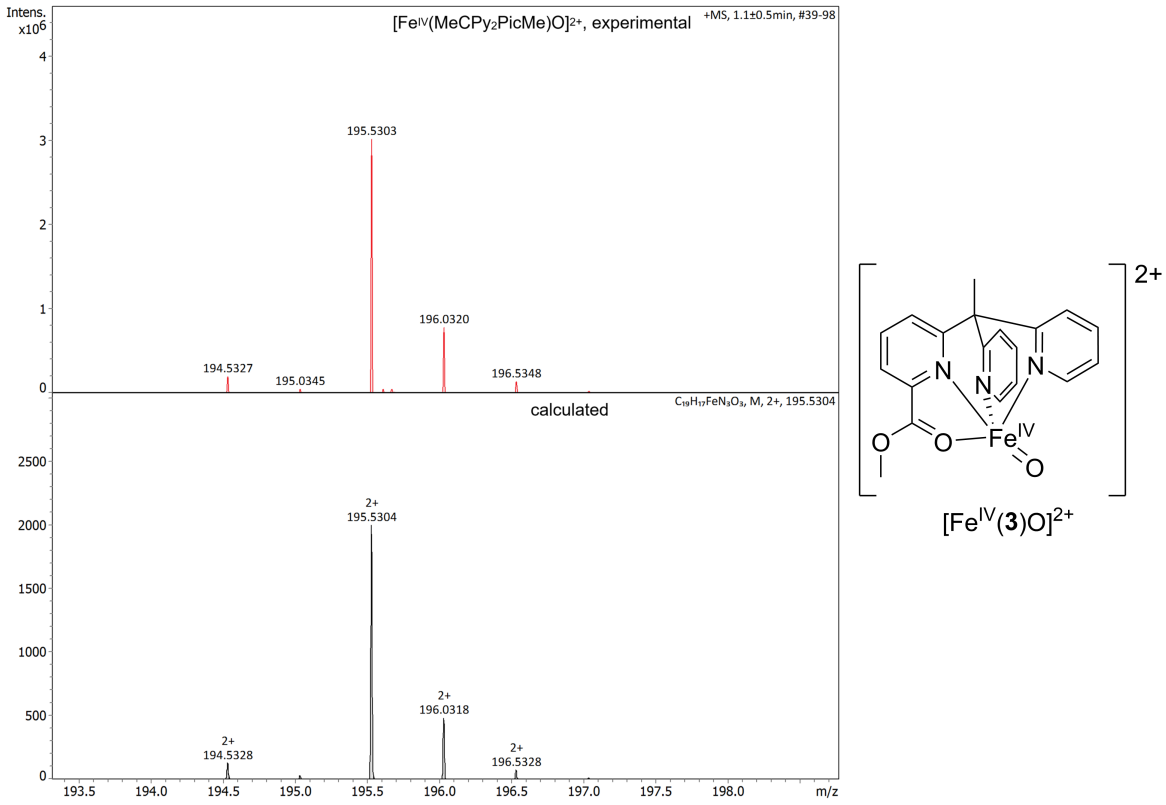

Figure 5.23: Experimental (top) and calculated (bottom) isotope distribution pattern for $[Fe^{IV}(\mathbf{3})O]^{2+}$.

The corresponding experiment with the tetrafluoridoborate-based complex was not successful because the formation of the precursor complex *in situ* was not sufficient. However, as already mentioned, both precursor routes should lead to the same bis(acetonitrile) precursor complex.

The measurement with **3a** shows that an iron(IV)oxo species can be observed after oxidation with mCPBA. This suggests that the species visible in the UV/Vis spectrum with a band at 704 nm is caused by the iron(IV)oxo complex.

Mößbauer Experiments

Mößbauer measurements were performed with frozen acetonitrile solutions of the precursor complex (**3** + $[Fe(MeCN)_6](BF_4)_2$, *in situ*) and the mCPBA treated complex solution (Figure 5.24, Table 5.8). The *in situ* complex formation did not give the expected result, as

three different species were identified in the spectrum instead of the expected one. The addition of mCBPA to this mixture resulted in two different species. However, it could not be assigned which of the three precursor species was oxidised and these oxidation products could not be further identified.

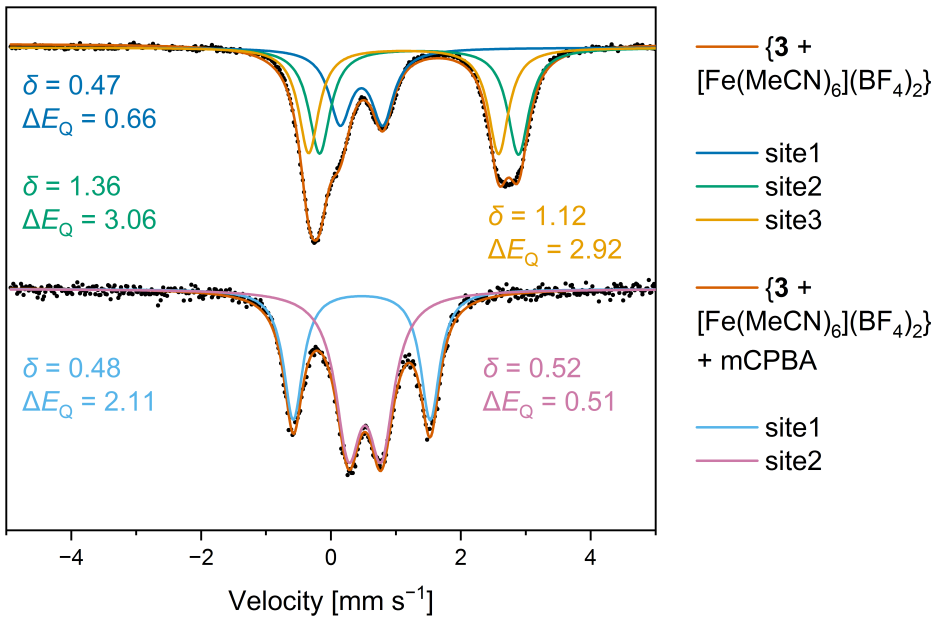

Figure 5.24: Mößbauer spectra of frozen MeCN solutions (80 K): top: $[Fe(MeCN)_6](BF_4)_2$ + **3**, bottom: reaction of solution of $[Fe(MeCN)_6](BF_4)_2$ + **3** with mCPBA directly after addition at −20 °C.

Table 5.8: Mößbauer parameters of frozen MeCN solutions (80 K): top: $[Fe(MeCN)_6](BF_4)_2$ + **3**, bottom: reaction of solution of $[Fe(MeCN)_6](BF_4)_2$ + **3** with mCPBA directly after addition at −20 °C.

Frozen solution	δ [mm s^{-1}]	ΔE_Q [mm s^{-1}]	Assignment
{$[Fe(MeCN)_6](BF_4)_2$ + **3**}	0.47	0.66	site1
	1.36	3.06	site2
	1.12	2.92	site3
{$[Fe(MeCN)_6](BF_4)_2$ + **3**} + mCPBA	0.48	2.11	site1
	0.52	0.51	site2

For future experiments, the use of crystals of **3a** as precursor species is more preferable as this is a defined species and the CSI-MS measurements were successful with this route. All these results are only first indicators that a high-valent iron-oxo species is accessible from iron(II) complexes of ligand **3**. To truly confirm the nature of the absorption band at 704 nm in the UV/Vis spectrum, a repetition of the Mößbauer experiments and basic catalytic tests analogous to complex **2a** are required.

5.3.3 Attempts of Generating Iron-Oxo Species from Chlorido Species using mCPBA

The chlorido complex with ligand **3** ([Fe(**3**)Cl_2]), generated (*in situ* or by dissolving crystals of **3c**) in acetonitrile, is not suitable as precursor complex for high-valent iron-oxo species generated by mCPBA as oxidant. The corresponding UV/Vis spectra did not indicate the formation of such a high-valent species upon mCPBA addition.
More promising results were obtained by dissolving crystals of the mixed co-ligand species [Fe(**3**)(BF_4)Cl] · 3.5 Et_2O (**3e**) in acetonitrile and subsequent treatment with mCPBA. Upon addition of mCPBA, a visible change in colour can be observed (Figure 5.25). Before the mCPBA addition, the solution is bright orange (Figure 5.25, left). Very rapidly after the addition of a mCPBA solution in acetonitrile, the colour of the solution changes to green. A green colour is often observed for high-valent iron-oxo species.[61] After approx. 10 s later, the solution is already yellow. However, further mCBPA addition does not lead to a green solution again and the solution remains yellow.

Figure 5.25: MeCN solution of crystals of **3e** (left, orange solution) and subsequent addition of mCPBA (2. left, green solution) and further colour change of solution (2x right, yellow solution).

To get more quantifiable results, the experiment was repeated and followed by UV/Vis spectroscopy (Figure 5.26). The addition of 1.4 eq. mCPBA leads to the formation of a new absorption band at 588 nm which decays within one minute. For an iron(IV)oxo species, this would be a quite low wavelength. However, the rather loosely coordinating tetrafluoridoborate anion in the structure of **3e** (2.3226(14) Å) may enable a more facile co-ligand exchange than a [Fe(**3**)Cl_2] species, that is necessary for the formation of a high-valent iron-oxo species with one chloride ion in *cis*-position. Since the observed band has a different wavelength than for the complex with only tetrafluoridoborate anions, an involvement of the chloride anion at the oxidised species is very likely. Such a chlorido-iron-oxo intermediate species is e.g. proposed to take part in halogenation reactions of C – H bonds with halogen based high-valent iron-oxo compounds.[240] To identify the species causing the absorption band at 588 nm, further experiments are needed.

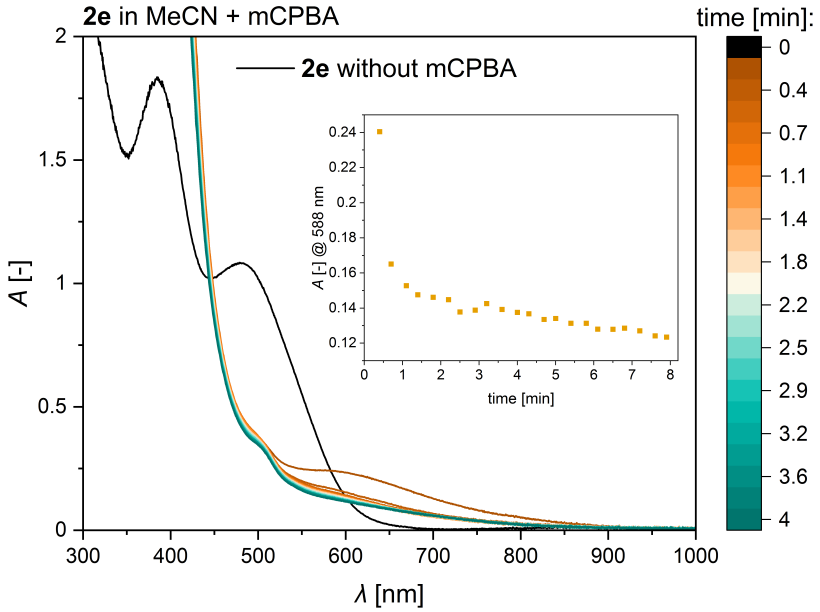

Figure 5.26: UV/Vis spectra of **3e** in MeCN and subsequent addition of mCPBA. Inset: absorption at 588 nm vs. time.

5.3.4 Summary of Iron Complexes of Ligand 3 in Solution

The results suggest that for triflate and tetrafluoridoborate anions, the main species in acetonitrile solution is a bis(acetonitrile) species. This species can undergo a temperature-dependent SCO. There are first hints that this species can be transformed to a high-valent iron-oxo species in the UV/Vis spectra and an iron(IV)oxo species was observed by CSI-MS. The Mößbauer results are inconclusive du to issues with a single defined precursor species, and additional measurements are required. Further, first promising results towards high-valent iron-oxo complexes were obtained using the mixed co-ligand complex with chloride and tetrafluoridoborate. Both potential iron-oxo species require further experiments for detailed characterisation. An additional problem could be that side products like the oxo-bridged tetramer found in crystals of **3b** may form easily during oxidation processes and be a dead-end for potential catalytic applications.

5.4 Concluding Remarks on Iron Complexes of MeC(Py)$_2$PicMe (3)

In the solid state, a bis(triflato) species is easily accessible (**3a**), whereas a bis(acetonitrile) species could not be crystallised. However, this is the main species assumed to be present in solution and it displays a temperature-dependent SCO behaviour. Since the matching SCXRD structure was not available, this behaviour could not be investigated in the solid state. Long crystallisation times resulted in side products like the oxo-bridged tetramer **3b** or the mixed co-ligand species with water and acetonitrile (**3d**). The bis(chlorido) species

(**3c**) was also available in the solid state as well as a chloride tetrafluoridoborate mixed co-ligand species. The attempts of generating high-valent iron-oxo complexes from iron(II) complexes of ligand **3** revealed the existence of an iron(IV)oxo species in the mass spectrum. Furthermore, the introduction of the oxygen donor in ligand **3** brought the additional risk of obtaining oxygen-bridged complexes. In the solid state structures, this was only observed in one crystal structure after saponification of the ester donor. On the other hand, this offered the formation of an additional structural motif which is the tetranuclear complex (**3b**).
However, this ligand variation provided new insights into the coordination chemistry of precursor complexes for potential biomimetic complexes. In terms of donor set, the ligand **3** providing one *O*-donor instead of a pure *N*-donor set is also closer to the 2H1C facial triad observed in natural enzymes than its pure *N*-donor relatives.

6 Tri(quinolin-8-yl)amine – a Ligand with {N_4}-Coordination

*The synthesis protocol for the ligand NQu_3 (**4**) was developed by Dr. Joshua Heck during his doctoral studies.[241] Since **4** one of the is missing members in the family of tripodal tetradentate ligands wildly used in the field of biomimetic iron(oxo) model complexes, the potential of **4** as ligand for biomimetic iron complexes was investigated in this work. Mößbauer measurements and fitting of data were performed by Dr. Linda Iffland-Mühlhaus in the group of Prof. Dr. Ulf-Peter Apfel at Ruhr-Universität Bochum, Germany. SQUID magnetometry measurements in solution and data correction were performed by Dr. Sophie Schönfeld and Andreas Dürrmann in the group of Prof. Dr. Birgit Weber at University of Bayreuth, Germany. SQUID magnetometry measurements of single crystals and data correction were performed by Hend Shahed and Dr. Neetika Sharma from the Jülich Centre for Neutron Science-2, Forschungszentrum Jülich, Germany. Parts of this chapter are already published.[242]*

6.1 Choice of NQu_3 (4) as Ligand

The triquinolinyl ligand NQu_3 (**4**) is one of the missing pieces in the family of tripodal tetradentate ligands in iron coordination chemistry. During the work of this dissertation, the synthesis protocol for **4** was developed within the Herres-Pawlis group.[241] Simultaneously, Chaibuth *et al.* developed the same ligand **4**, whose copper complexes are active in photoredox catalysis.[243]

The parent TPA ligand was one of the early ligand systems studied intensively in the field of non-heme iron-oxo model complexes (Figure 6.1).[42,61] The introduction of quinoline moieties was also investigated using the TQA ligand system, which is particularly active in C – H bond oxidation catalysis due to the $S = 2$ ground state of the oxo species. The

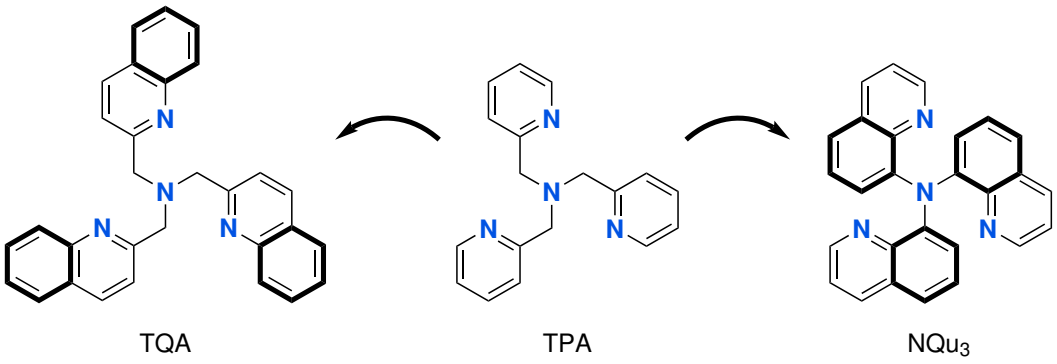

Figure 6.1: TPA ligand and the corresponding quinoline variants TQA and NQu_3 (**4**).

explanation given by the Que group for reaching an $S = 2$ state is the overall weaker ligand field of the TQA compared to the TPA ligand due to the quinolines, which at the same time makes the α-position next to the *N*-donor sterically more demanding.[51,97]
The ligand NQu_3 (**4**) is a different quinoline variant of TPA with the second aromatic ring being part of the ligand backbone instead of pointing outwards like in TQA. This creates a more rigid ligand scaffold while the α-position stays unsubstituted like in the parent TPA. Together, this gives the opportunity for a deeper insight in the steric and electronic effects of these ligands by comparing complexes of the new **4** ligand to the well characterised complexes with TPA and TQA ligands.

6.2 Iron Complexes of NQu_3 (4) in the Solid State

The reaction of ligand **4** with different iron salts led to a plethora of complex species which were characterised by SCXRD in the solid state. These species can be sorted into three different categories (Figure 6.2): **I. Complexes Obtained from the Acetonitrile/Triflate Equilibrium**. The majority of the crystalline compounds presented here emerged from the reaction of **4** with $[Fe(OTf)_2] \cdot 2\,MeCN$ in acetonitrile. As triflate is a moderately coordinating anion, acetonitrile can displace it from the coordination sphere as discussed in the previous chapter for ligand **3**. All three possible combinations of anion/solvent coordination were observed. The second category **II. Complexes Obtained with Different Solvents** contains complexes that were synthesised with $[Fe(OTf)_2] \cdot 2\,MeCN$ as well but in solvents different than acetonitrile. Here, coordinating solvents like propionitrile and methanol were used as well as non-coordinating solvents like dichloromethane. For the last category **III. Complexes Obtained with Different Counterions** iron salts with different anions than triflate were used. This includes (pseudo-)halides and weakly coordinating anions.
The aim of this entire complex series was to find a reproducible metal complex species that can be used as a solid state precursor complex for the generation of high-valent iron-oxo species or for catalytic experiments. Furthermore, a deeper understanding of which species can be obtained under which conditions should be gained.

6.2.1 Complexes Related to the MeCN/OTf^- Equilibrium

Ligands with similar backbone to **4**, designed for coordinating in a tripodal fashion forming 5-membered chelate rings, usually provide two *cis*-labile coordination sites when coordinating iron(II). Selected ligands with similar backbones are shown in Figure 6.3. When a triflate salt is used in acetonitrile, the question is whether the solvent or the anion occupies the vacant coordination sites: acetonitrile is a weak *N*-donor ligand and triflate is a moderately coordinating anion. There are two issues in this co-ligand competition: one is which complex species is the main species in solution and the other is which complex species is most likely

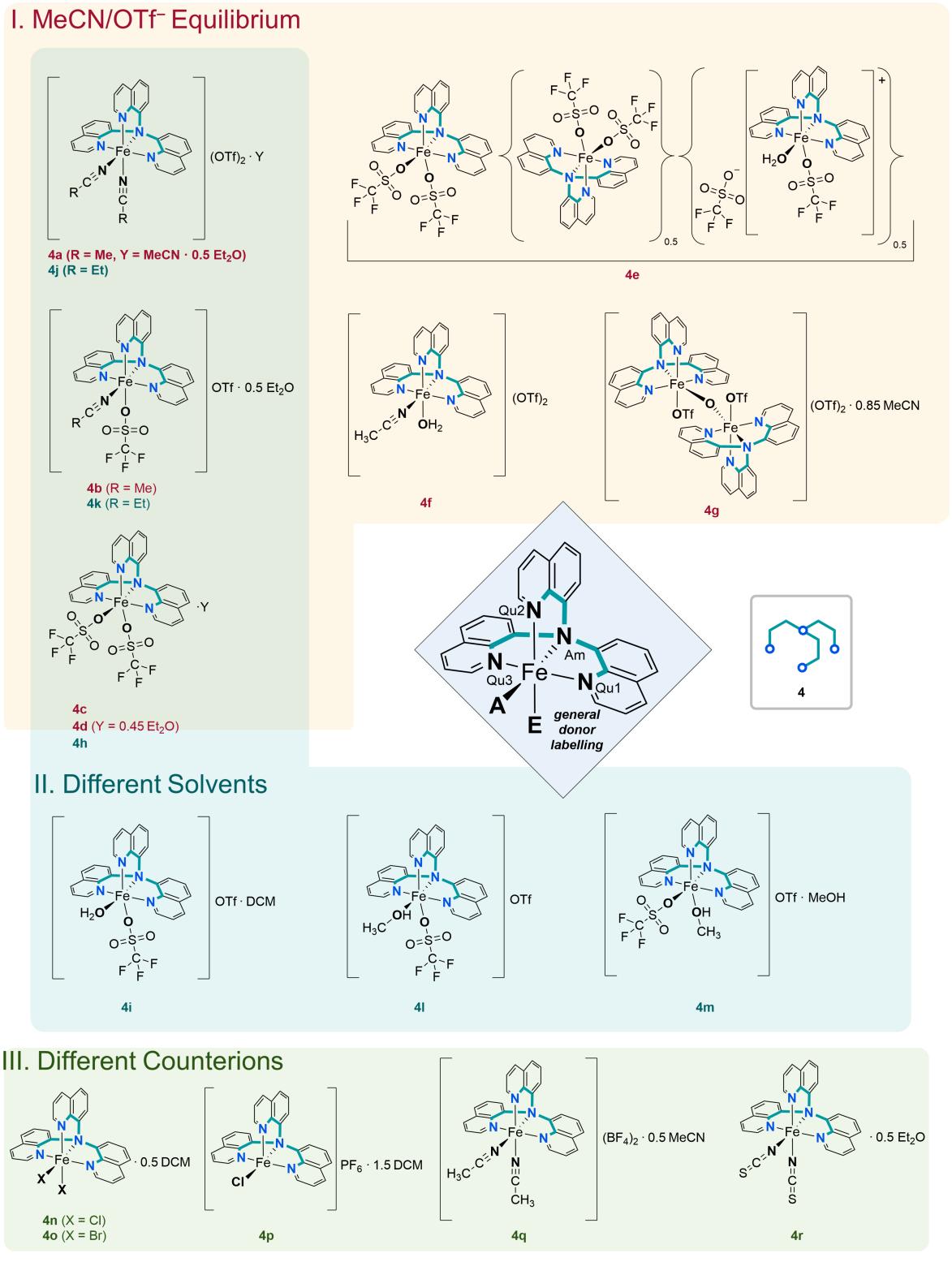

Figure 6.2: Overview of complexes with ligand **4** sorted by three different categories: I. Complexes from the MeCN/OTf$^-$ equilibrium (red), II. Complexes obtained with different solvents (blue) and III. Complexes obtained with different counterions (green). The rhombus in the middle shows the general labelling of donors for tables with bond lengths and angles of the complexes. Ligand scaffold highlighted in bold.

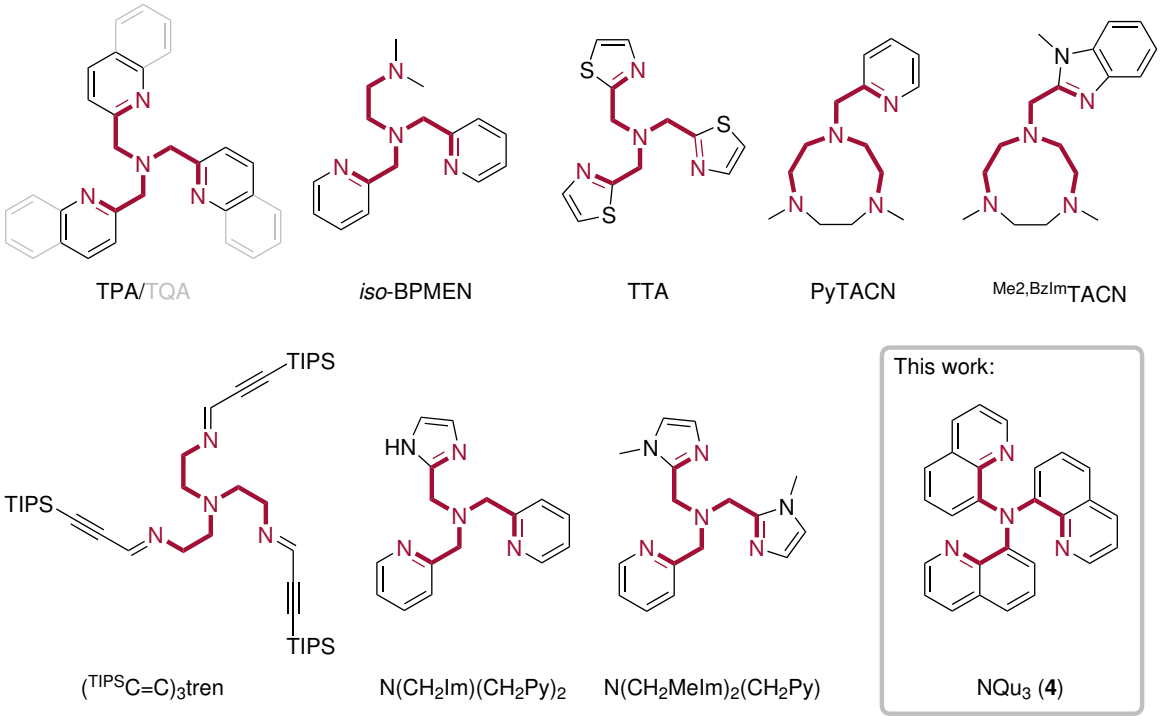

Figure 6.3: Examples for tetradentate *N*-donor ligands designed for coordinating iron in a tripodal fashion forming 5-membered chelate rings with two vacant coordination sites for their octahedral complexes. Ligand structures adapted from the following references: TPA,[138,244,245] TQA,[97] *iso*-BPMEN,[236] TTA,[246] PyTACN,[247,248] ^{Me2,BzIm}TACN,[249] (^{TIPS}C=C)$_3$tren,[121] N(CH$_2$Im)(CH$_2$Py)$_2$,[250] N(CH$_2$MeIm)$_2$(CH$_2$Py),[250] NQu$_3$.[241,243]

to crystallise.

For ligands with a similar backbone (tetradentate, coordinating in a tripodal fashion and forming 5-membered chelate rings), 24 bis(triflato), ten bis(acetonitrile) and two mixed co-ligand species are listed in the CSD (03.05.2023).[58] There are only three ligands for which a bis(acetonitrile) and a bis(triflato) species could be crystallised (TPA,[138,244,245] PyTACN[247,248] and 6-Me-PyTACN[90,251]). The different species with the same ligand were obtained under different reaction conditions. Also, among all the complexes of the three different co-ligand variants, there are only a small number of examples where both co-ligands were present during crystallisation (5 x bis(triflato), 3 x bis(acetonitrile)). Due to the small number of examples and the lack of a systematic study, it is not statistically relevant which isomer is preferred in the solid state.

Ligand **4** is the first ligand with this donor arrangement where all three possible coordination isomers – bis(acetonitrile), bis(triflato) and mixed co-ligand species – could be crystallised and characterised by SCXRD (Figure 6.4). Of the two conceivable mixed co-ligand species, only one variant was observed in the solid state. Moreover, the three coordination isomers were crystallised under the same reaction conditions: **4** and Fe(OTf)$_2 \cdot 2$ MeCN (1 : 1) in acetonitrile with diethyl ether as anti-solvent. This indicates an equilibrium between the coordinating co-ligands. Some species crystallised concomitantly in the same reaction

vessel. Also, two by-products could be crystallised and characterised with SCXRD. An overview of all these species and their synthesis is given in Scheme 6.1.

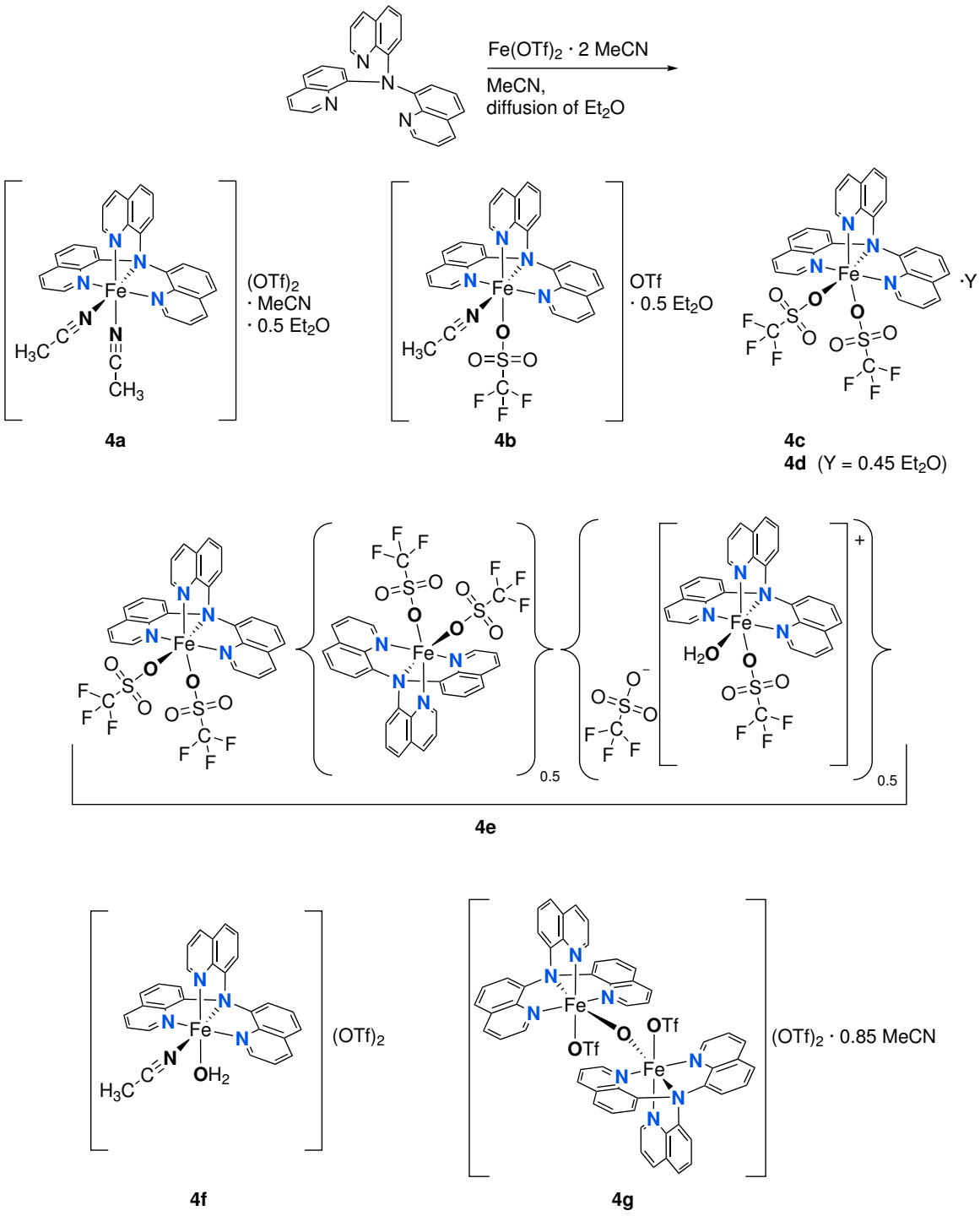

Scheme 6.1: Synthesis of complexes **4a**, **4b**, **4c**, **4d**, **4e**, **4f** and **4g**.

$[Fe(NQu_3)(MeCN)_2](OTf)_2 \cdot MeCN \cdot 0.5\,Et_2O$ (4a)

The bis(acetonitrile) motif $[Fe(\mathbf{4})(MeCN)_2]^{2+}$ (Figure 6.4, left) was obtained as crystals of the mixed solvate $[Fe(\mathbf{4})(MeCN)_2](OTf)_2 \cdot MeCN \cdot 0.5\,Et_2O$ (**4a**). The complex **4a** crystallises in

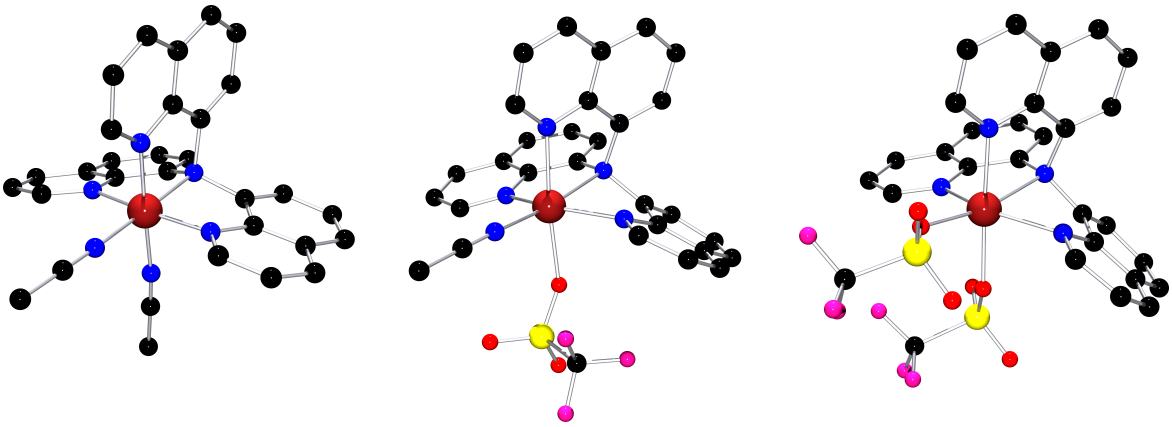

Figure 6.4: $[Fe(\mathbf{4})(MeCN)_2]^{2+}$ cation in crystals of **4a** (left), $[Fe(\mathbf{4})(OTf)(MeCN)]^{+}$ cation in crystals of **4b** (middle) and $[Fe(\mathbf{4})(OTf)_2]$ unit in crystals of **4d** (right). Hydrogen atoms, counterions and crystal solvent molecules are omitted for clarity. Colour code: black = carbon, blue = nitrogen, red = oxygen, scarlet = iron, yellow = sulphur, pink = fluorine.

the monoclinic space group $P2_1/c$ with $Z = 2$. The Fe – N_{Qu} bond lengths are in the range of 1.946(2)–1.950(2) Å (Table 6.1). The acetonitrile in the A position (*trans* to N_{Am}, Figure 6.2) has a shorter bond length (1.924(2) Å) than the acetonitrile ligand on the E position (*trans* to N_{Qu2}, 1.959(2) Å). Compared to the other Fe – N bonds, the Fe – N_{Am} bond is elongated the most (2.027(2) Å). On average, the Fe – N bond lengths are below 2.0 Å, which is typical for a LS species.[119,138] Although the bond lengths of the different *N*-donors vary, the coordination geometry is close to an ideal octahedron (CSM: *S*(OC-6) = 0.3).

Table 6.1: Selected bond lengths, bond angles and structure parameters of **4a**.

	4a $[Fe(NQu_3)(MeCN)_2](OTf)_2 \cdot MeCN \cdot 0.5\,Et_2O$
Space group	$P2_1/c$
Bond lengths [Å]	
Fe – N_{Am}	2.027(2)
Fe – N_{Qu}	1.946(2)–1.950(2)
Fe – N_A	1.924(2)
Fe – N_E	1.959(2)
Ø Fe – N	1.959
Bond angles [°]	
N_{Qu} – Fe – N_{Am}	84.39(8)–85.67(8)
N_A – Fe – N_E	90.04(9)
N_{Am} – Fe – N_E	91.03(8)
N_{Am} – Fe – N_A	178.91(8)
N_{Qu2} – Fe – N_E	176.63(9)
N_{Qu1} – Fe – N_{Qu3}	167.50(9)
Struct. param.	
CSM *S*(OC-6)	0.3
CSM *S*(TPR-6)	14.5

[Fe(NQu_3)(OTf)(MeCN)](OTf) · 0.5 Et_2O (4b)

The mixed co-ligand species [Fe(**4**)(OTf)(MeCN)]$^+$ (Figure 6.4, middle) crystallises as diethyl ether solvate [Fe(**4**)(OTf)(MeCN)](OTf) · 0.5 Et_2O (**4b**) in the monoclinic space group $P2_1/c$ with $Z = 2$. Half of a diethyl ether molecule per complex could not be modelled appropriately and was masked using the BYPASS algorithm as implemented in PLATON/SQUEEZE.[156–158] In contrast to the bis(acetonitrile) species, all Fe – N bond lengths are longer than 2.0 Å (Table 6.2). This is in line with a HS species in the solid state,[119] which is caused by the weaker ligand field of triflate compared to acetonitrile. The trend in bond lengths is again similar to those observed in the bis(acetonitrile) structure with the shortest iron-donor bond of the donor in the A position (2.0925(16) Å) and the longest iron-donor bond of the central amine (2.2971(14) Å). The E position is occupied by the triflate ligand (2.2413(13) Å). The two literature-known mixed co-ligand species of Mandon and coworkers (ligand: F_2TPA) and the Fiedler group (ligand: $N(CH_2MeIm)_2(CH_2Py)$) show the same arrangement.[235,250] A mixed co-ligand species of triflate and acetonitrile with inverted co-ligand occupations was not observed in the solid state. This is also in line with a structural *trans*-effect, which favours the stronger field acetonitrile ligand in *trans* position to the elongated Fe – N_{Am} bond.[204] The coordination geometry of the mixed co-ligand species shows a higher deviation from an ideal octahedron (S(OC-6) = 2.0) than that of the bis(acetonitrile) species.

Table 6.2: Selected bond lengths, bond angles and structure parameters of **4b**.

	4b [Fe(NQu_3)(OTf)(MeCN)](OTf) · 0.5 Et_2O
Space group	$P2_1/c$
Bond lengths [Å]	
Fe – N_{Am}	2.2971(14)
Fe – N_{Qu}	2.1111(17)–2.1492(16)
Fe – N_A	2.0925(16)
Ø Fe – N	2.158
Fe – O_E	2.2413(13)
Bond angles [°]	
N_{Qu} – Fe – N_{Am}	73.85(6)–77.75(6)
N_A – Fe – O_E	89.82(5)
N_{Am} – Fe – O_E	97.68(5)
N_{Am} – Fe – N_A	172.47(6)
N_{Qu2} – Fe – N_E	174.36(5)
N_{Qu1} – Fe – N_{Qu3}	148.03(6)
Struct. param.	
CSM S(OC-6)	2.0
CSM S(TPR-6)	11.0

[Fe(NQu$_3$)(OTf)$_2$] Complexes

The bis(triflato) complex motif [Fe(**4**)(OTf)$_2$] could be observed in three different crystal structures: [Fe(**4**)(OTf)$_2$] (**4c**), [Fe(**4**)(OTf)$_2$] · 0.45 Et$_2$O (**4d**) and [Fe(**4**)(OTf)$_2$][Fe(**4**)(OTf)$_2$]$_{0.5}${[Fe(**4**)(OTf)(H$_2$O)](OTf)}$_{0.5}$ (**4e**). As an example, the complex molecule of **4d** is shown in Figure 6.4. The bis(triflato) complexes have the same chemical formula for the complex molecule, but the spatial arrangement of the triflate ions is different in each of the crystal structures. It also differs within one crystal structure when more than one independent complex molecule present. To illustrate these different arrangements, Figure 6.5 shows overlays of the individual complex molecules with a complex molecule in the structure of **4c**.

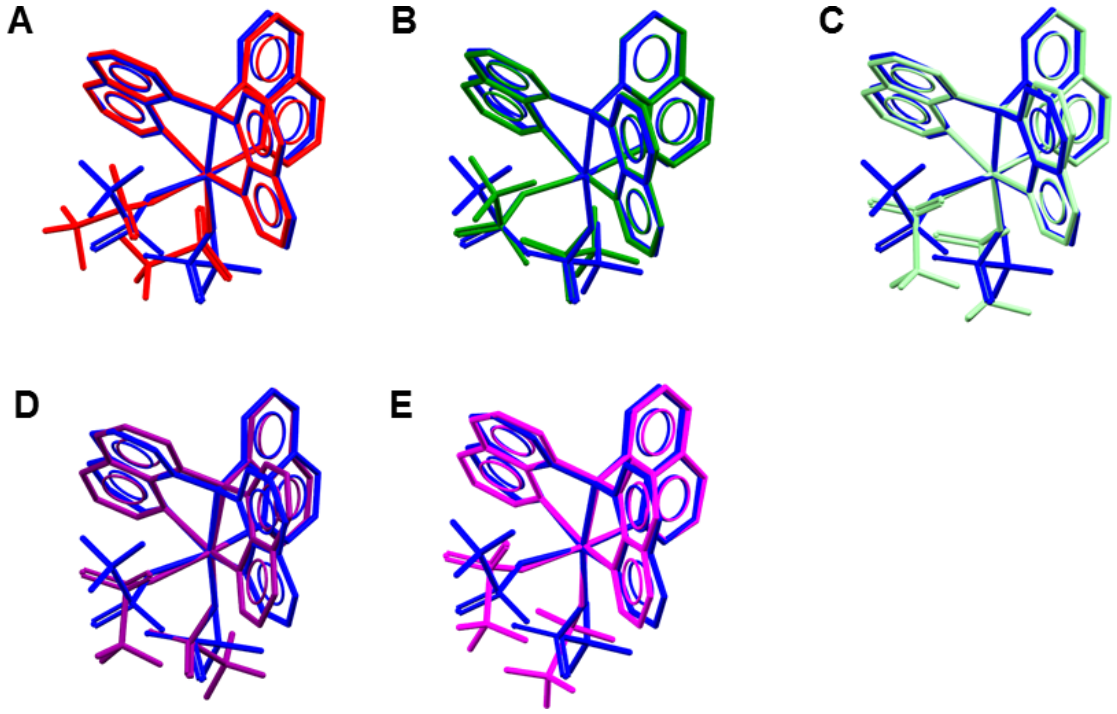

Figure 6.5: Comparison of the arrangement of the triflate ligands in the different molecular structures in the solid state of triflate species as overlay. Hydrogen atoms omitted for clarity. Colour code: blue = **4c**/Fe(1) (all), red = **4c**/Fe(2) (A), green = **4d**/Fe(1) (B), mint = **4d**/Fe(2) (C), purple = **4e**/Fe(1) (D), magenta = **4e**/Fe(2) (E). If more than one iron centre is present in the asymmetric unit the number in parentheses denotes which iron centre is shown with the same labelling as in the SCXRD data files.

The pure bis(triflato) compound [Fe(**4**)(OTf)$_2$] (**4c**) crystallises in the triclinic space group $P\bar{1}$ with $Z = 2$ (for $C_{58}H_{36.36}F_{12}Fe_2N_8O_{12.18}S_4$) with two bis(triflato) complex molecules in the asymmetric unit. A minority species (17.8 %) has an H$_2$O co-ligand in the A position at Fe(2) and the triflate that used to coordinate Fe(2) in the A position is located non-coordinating nearby. The other triflate co-ligand of the Fe(2) in the E position is modelled disordered as well as the triflate in the A position at Fe(1). The diethyl ether solvate [Fe(**4**)(OTf)$_2$] · 0.45 Et$_2$O (**4d**) crystallises in the triclinic space group $P\bar{1}$ as well with a total of four complex molecules in the unit cell but $Z = 2$ since the formula was defined

as two complex molecules with 0.9 diethylether molecules ($[Fe(\mathbf{4})(OTf)_2]_2 \cdot 0.9\,Et_2O$). The diethyl ether molecules in **4d** are positioned on all corners of the unit cell and on two face-centred positions. Since these positions are on inversion centres, the diethyl ether molecules are disordered by symmetry. The diethyl ether molecules on the face-centred positions could not be modelled in an adequate manner and were treated with the BYPASS algorithm as implemented in Platon/SQUEEZE.[156–158] To visualise the differences in the packing between the bis(trilfato) complexes in **4c** and **4d**, the unit cells of both are shown in Figure 6.6.

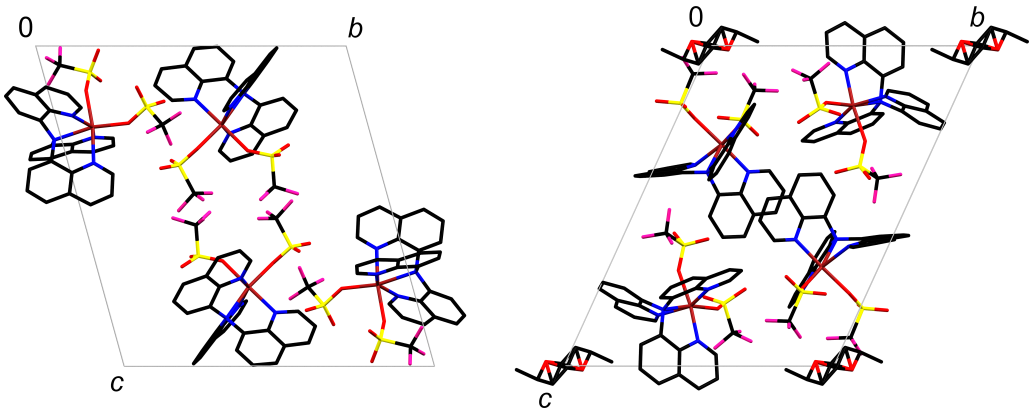

Figure 6.6: Unit cells of **4c** (left) and **4d** (right). Hydrogen atoms and disorder of triflate co-ligands in **4c** omitted for clarity.

The third crystal structure was obtained after synthesis in acetonitrile containing the bis(triflato) complex $[Fe(\mathbf{4})(OTf)_2][Fe(\mathbf{4})(OTf)_2]_{0.5}\{[Fe(\mathbf{4})(OTf)(H_2O)](OTf)\}_{0.5}$ (**4e**). **4e** crystallises in the triclinic space group $P\bar{1}$ with $Z = 1$ (for $[Fe(\mathbf{4})(OTf)_2]_2[Fe(\mathbf{4})(OTf)_2]\{[Fe(\mathbf{4})(OTf)(H_2O)](OTf)\}$ as formula). Z was defined this way to avoid fractional numbers for atoms in the sum formula. In the structure, a cooperative triflate-water disorder was found for the complex of iron centre Fe(2) (Figure 6.7) whereas the complex of Fe(1) shows no disorder. The complex with Fe(2) as central atom is either coordinated by two triflate molecules ($[Fe(\mathbf{4})(OTf)_2]$) or by one triflate molecule and a water molecule with a non-coordinating triflate anion nearby ($[Fe(\mathbf{4})(OTf)(H_2O)](OTf)$). The co-ligand in the A position (OTf^- or H_2O) is close to an inversion centre and both isomers have an occupation of 0.5 by necessity. Deviations from this would lead to a defective charge balance and an inappropriately short distances between the atoms. In addition, the water molecule forms hydrogen bonds with the neighbouring triflate anions ($O_{H2O}-H\cdots O_{OTf\text{-}coord}$: 2.82(5)–3.35(5) Å and $O_{H2O}-H\cdots O_{OTf\text{-}non\text{-}coord}$: 2.82(5) Å, Figure 6.7).

In **4c**, **4d** and **4e**, all Fe – N bond lengths are longer than 2.0 Å, which is typical for iron(II) HS species (Table 6.3 & Table 6.4).[119,138,252] The $Fe-O_E$ bond lengths with the E positioned co-ligand are always elongated compared to the $Fe-O_A$ bond lengths with the A positioned co-ligand. The same asymmetric co-ligand bonds were also found in the TPA based bis(triflato) complex.[138] Distorted octahedral coordination geometries were found

Table 6.3: Selected bond lengths, bond angles and structure parameters of **4c** and **4d**.

	4c $[Fe(NQu_3)(OTf)_2]$	**4d** $[Fe(NQu_3)(OTf)_2] \cdot 0.45\,Et_2O$
Space group	$P\bar{1}$	$P\bar{1}$
Bond lengths [Å]		
Fe – N_{Am}	2.307(3)–2.325(3)	2.2868(17)–2.2870(17)
Fe – N_{Qu}	2.103(3)–2.162(3)	2.1029(17)–2.1992(18)
Ø Fe – N	2.176/2.185	2.175/2.191
Fe – O_A	2.005(11)–2.092(4)	2.0232(16)–2.0543(15)
Fe – O_E	2.142(3)–2.212(19)	2.1312(18)–2.1988(18)
Bond angles [°]		
N_{Qu} – Fe – N_{Am}	73.58(11)–77.85(10)	73.07(6)–78.20(6)
O_A – Fe – O_E	85.17(15)–95.3(3)	87.55(7)–97.15(7)
N_{Am} – Fe – O_E	90.0(6)–103.52(11)	94.49(7)–103.99(7)
N_{Am} – Fe – O_A	161.6(4)–170.50(19)	167.95(6)–168.28(6)
N_{Qu2} – Fe – O_E	167.8(6)–178.31(13)	171.23(6)–175.20(6)
N_{Qu1} – Fe – N_{Qu3}	147.50(12)–149.58(11)	147.44(7)–148.86(7)
Struct. param.		
CSM *S*(OC-6)	2.1/2.0/2.6	1.9/2.8
CSM *S*(TPR-6)	9.7/10.1/10.0	11.4/9.0

Table 6.4: Selected bond lengths, bond angles and structure parameters of **4e**.

	4e $[Fe(NQu_3)(OTf)_2][Fe(NQu_3)(OTf)_2]_{0.5}\{[Fe(NQu_3)(OTf)(H_2O)](OTf)\}_{0.5}$
Space group	$P\bar{1}$
Bond lengths [Å]	
Fe – N_{Am}	2.314(2)–2.342(2)
Fe – N_{Qu}	2.086(2)–2.149(2)
Ø Fe – N	2.174/2.175/{2.175}
Fe – O_A	2.037(2)–2.15(4), {1.98(4)}
Fe – O_E	2.218(2)–2.238(2)
Bond angles [°]	
N_{Qu} – Fe – N_{Am}	73.83(8)–78.01(9)
O_A – Fe – O_E	82.8(15)–85.84(8), {81.2(14)}
N_{Am} – Fe – O_E	103.91(8)–109.49(8)
N_{Am} – Fe – O_A	164.66(9)–173.3(14), {174.7(15)}
N_{Qu2} – Fe – O_E	164.66(9)–175.47(8)
N_{Qu1} – Fe – N_{Qu3}	139.77(10)–145.44(10)
Struct. param.	
CSM *S*(OC-6)	4.6/2.9/{2.8}
CSM *S*(TPR-6)	6.8/9.3/{9.6}

Values for H_2O coordination in curly brackets.

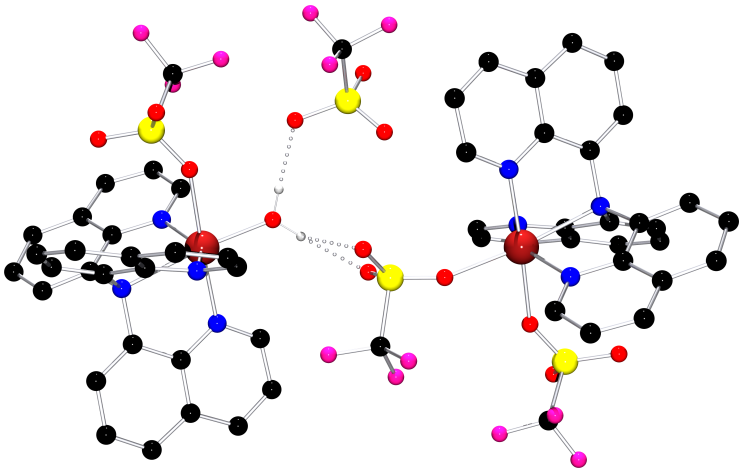

Figure 6.7: Cooperative triflate-water disorder of the complexes $[Fe(\mathbf{4})(OTf)_2]_{0.5}\{[Fe(\mathbf{4})(OTf)(H_2O)](OTf)\}_{0.5}$ found in crystals of **4e** around an inversion centre. Hydrogen atoms not involved in H-bonds are omitted for clarity. Colour code: black = carbon, blue = nitrogen, red = oxygen, scarlet = iron, yellow = sulphur, pink = fluorine, white = hydrogen.

for **4c**, **4d** and **4e** with equal or slightly stronger distortions than in the mixed co-ligand species **4b**. The coordination geometry around Fe(1) in **4e**, on the other hand, can be considered as diffuse distorted, since the *S*(OC-6) and *S*(TPR-6) values are both larger than the intermediate value of 4.42 between those two geometries.[132]

Since all three co-ligand variants – bis(acetonitrile), bis(triflato) and mixed – could be crystallised, this suggests that none of the co-ligand variants is significantly thermodynamically preferred. None of the co-ligand isomers has a crystal packing that is significantly more favourable than the others, so that the equilibrium would be shifted to this species. Also for the bis(trilato) complexes various packing options were found. This could be caused by the geometry of the ligand framework with the three rigid quinoline groups and the resulting gaps, which does not seem to pack well on its own. This leads to the availability of all crystal structures (**4a**–**4e**) from crystallisation experiments at room temperature under similar conditions.

$[Fe(NQu_3)(H_2O)(MeCN)](OTf)_2$ (4f)

The complex $[Fe(\mathbf{4})(H_2O)(MeCN)](OTf)_2$ (**4f**) is a side product of the triflate-based complexes obtained from acetonitrile solution where a water molecule is incorporated as one of the co-ligands (Figure 6.8). **4f** crystallises in the triclinic space group $P\bar{1}$ with $Z = 4$. Comparable to the mixed co-ligand species **4b**, the acetonitrile ligand occupies the A position. Consequently, the water co-ligand is located on the E position and forms H-bonds towards neighbouring non-coordinating triflate anions. Together with the next iron centre (Fe(1) & Fe(1)' or Fe(2) & Fe(2)') a twelve-membered ring is formed (Figure 6.9). Similar to the other complexes with *N*- and *O*-donors, the Fe – N bond lengths are all longer than 2.0 Å (Table 6.5). Like the other structures, this indicates **4f** being a HS species in the solid state.[119,138,252] The

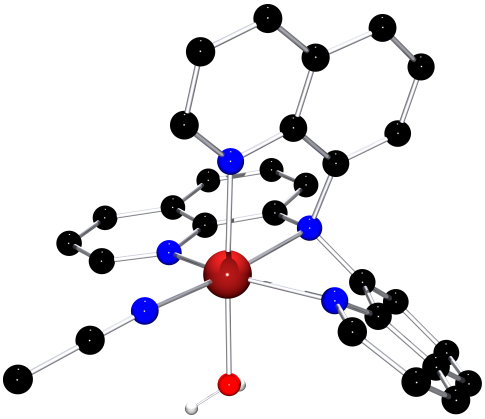

Figure 6.8: $[Fe(\mathbf{4})(H_2O)(MeCN)]^{2+}$ cation in crystals of **4f**. C bonded hydrogen atoms and counterions are omitted for clarity. Colour code: black = carbon, blue = nitrogen, red = oxygen, scarlet = iron, white = hydrogen.

Table 6.5: Selected bond lengths, bond angles and structure parameters of **4f**.

	4f $[Fe(NQu_3)(H_2O)(MeCN)](OTf)_2$
Space group	$P\bar{1}$
Bond lengths [Å]	
$Fe-N_{Am}$	2.2981(17)–2.3063(16)
$Fe-N_{Qu}$	2.1202(17)–2.1640(18)
$Fe-N_A$	2.0998(18)–2.1010(18)
Ø Fe – N	2.163/2.166
$Fe-O_E$	2.1397(16)–2.1459(15)
Bond angles [°]	
$N_{Qu}-Fe-N_{Am}$	73.35(6)–77.70(6)
N_A-Fe-O_E	83.66(7)–83.77(7)
$N_{Am}-Fe-O_E$	101.55(6)–102.94(6)
$N_{Am}-Fe-N_A$	172.98(6)–174.80(6)
$N_{Qu2}-Fe-N_E$	177.78(7)–178.16(7)
$N_{Qu1}-Fe-N_{Qu3}$	147.87(7)–147.87(7)
Struct. param.	
CSM *S*(OC-6)	2.4/2.3
CSM *S*(TPR-6)	10.7/10.8

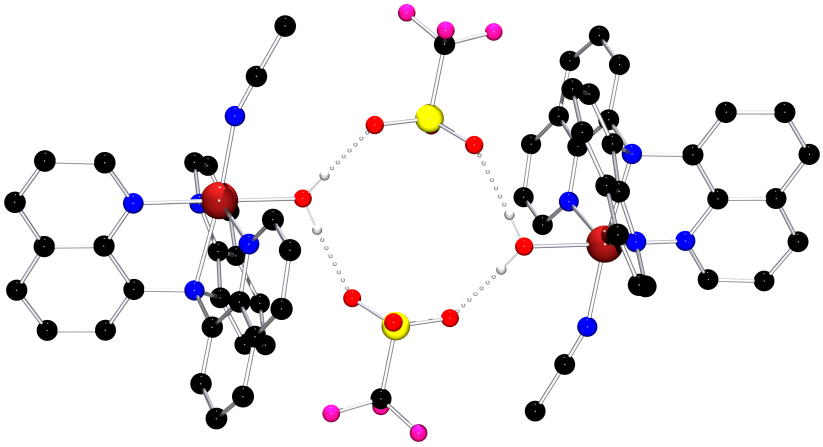

Figure 6.9: H-bonds (dotted) in crystals of **4f** between Fe(1) and Fe(1)'. C bonded hydrogen atoms and counterions are omitted for clarity. Colour code: black = carbon, blue = nitrogen, red = oxygen, scarlet = iron, yellow = sulphur, pink = fluorine, white = hydrogen.

CSM *S*(OC-6) value of 2.4 and 2.3, respectively, is in a similar range as the other mixed donor complexes and indicates a distorted octahedral coordination geometry. The use of freshly distilled solvents stored over molecular sieves prevented further observation of the **4f** complexes.

Selectivity for Complexes obtained from $Fe(OTf)_2 \cdot 2\,MeCN$

4a–**4f** were all obtained in acetonitrile solutions of **4** and $Fe(OTf)_2 \cdot 2\,MeCN$ at room temperature under inert conditions with diethyl ether as anti-solvent for crystallisation. To identify the complexes, either a full structure determination or a short cell determination (for repeated experiments) was performed using SCXRD. Complex **4a** is the only complex of this series with a $\{N_6\}$-coordination sphere and the short Fe – N bond lengths in this complex are in line with a LS species. All other complexes have either an $\{N_5O\}$- or $\{N_4O_2\}$-coordination environment and longer Fe – N bond lengths typical for HS species. The influences that determine which of these six species is obtained in an experiment seem to be too small to reproduce experimentally. Notably, the frequent simultaneous crystallisation of several of these phases underlines that they are in principle thermodynamically equivalent.

The situation changes if the crystallisation temperature is altered. A lower crystallisation temperature (e.g. 6 °C) selectively enables the crystallisation of complex **4a**. The complex species was identified by cell determinations of multiple single crystals of each sample to ensure a sufficient analysis of the bulk material. Phase purity could not be confirmed by powder X-ray diffraction (PXRD), which will be discussed in the following section. The dependence of the species on the crystallisation temperature is visualised in Figure 6.10.

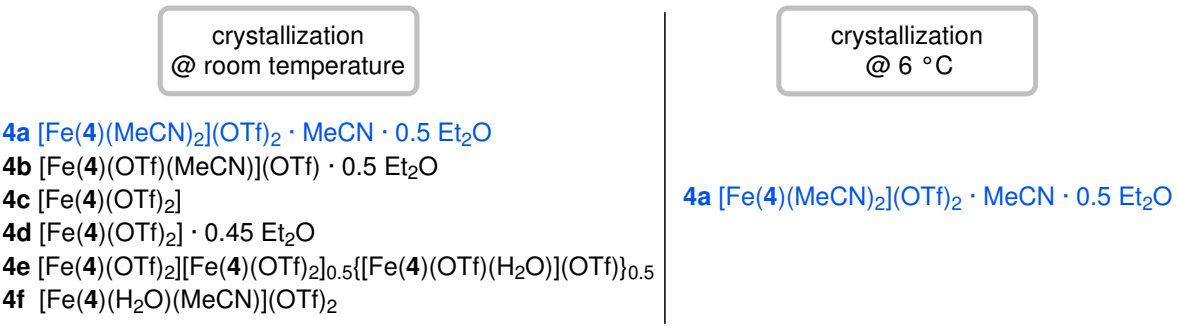

Figure 6.10: Crystallisation results of reactions of **4** and $Fe(OTf)_2 \cdot 2\,MeCN$ in MeCN with Et_2O as anti-solvent at different crystallisation temperatures.

Since **4a** was the only complex that could be selectively prepared, these crystals were used for further analyses in the solid state and are referred to as compound **C** since they do not maintain the exact composition of **4a**.

Mößbauer & PXRD Studies

The Mößbauer spectrum of crystals of **C** (isolated compound **4a**, see above) was measured under inert conditions. However, it does not show the expected signal for a LS iron(II) species, but a mixture of three different iron species, which can be assigned as iron(II) HS (Figure 6.11 & Table 6.6).[126,250] This is a first hint, that the crystals are maybe not stable when isolated from their mother liquor. Moreover, the experimental PXRD of crystals

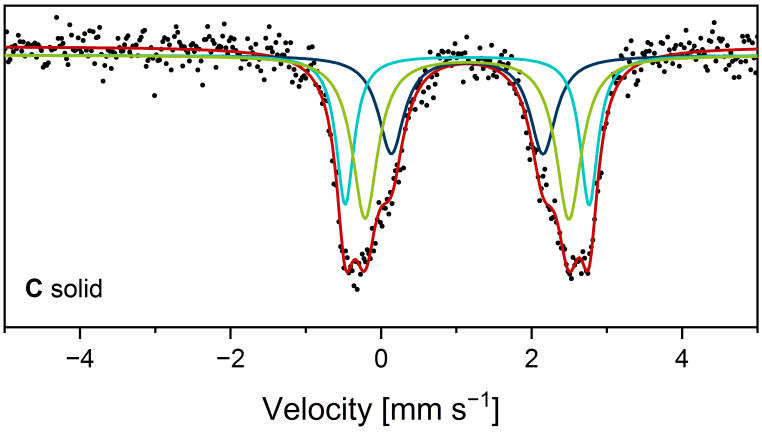

Figure 6.11: Mößbauer spectrum of compound **C** as solid sample measured at 80 K. Experimental data are shown in black, overall fit in red and fit for three different iron(II) HS species in blue, turquoise and green.

Table 6.6: Mößbauer parameters for solid crystals of **C**.

Solid	δ [mm s^{-1}]	ΔE_Q [mm s^{-1}]	Amount [%]	Assignment
C	1.14	2.02	27	HS Fe(II)
	1.14	3.24	29	HS Fe(II)
	1.14	2.71	44	HS Fe(II)

of **C** under inert conditions does not match the simulated PXRD pattern of crystals of **4a**, supporting this assumption (Figure 6.12, left). However, the experimental PXRD pattern has high similarities with the simulated PXRD patterns of the two species with triflate co-ligands **4c** and **4d** (Figure 6.12, right). Accordingly, the crystals of **C** quickly loose the acetonitrile co-ligands when removed from the mother liquor and no protection by perfluorinated oil like for SCXRD measurements is offered. This would also match the Mößbauer data interpretation of an iron(II) HS species. The mixed co-ligand species **4b** has a simulated PXRD pattern with reflections that do not fit well the experimental data for compound **C** (see Figure A.16 in the Appendix). This indicates that both acetonitrile co-ligands are lost during isolation. Consequently, crystals of **4a** are rather sensitive towards solvent changes. The removal of the mother liquor and drying of the crystals of **4a** leads to a conversion to compound **C**, which can best be described as a mixture of {Fe(NQu$_3$)(OTf)$_2$} solvates. Small changes in solvation influence the nature of the coordination sphere and result in different Mößbauer spectra. Ekanayake *et al.* reported a structurally similar bis(acetonitrile) complex (SCXRD) which gave three different species (2x HS, 1x LS) in the Mößbauer spectra of the solid isolated complex.[250] It is very likely that they also observed a (partial) loss of acetonitrile co-ligands.

Different results were obtained for active manipulation of the solvation of compound **C**. The Mößbauer data of a frozen solution of compound **C** in acetonitrile is in line with a single defined iron(II) LS species (δ = 0.44 mm s^{-1} & ΔE_Q = 0.43 mm s^{-1}; Figure 6.13 & Table 6.7).

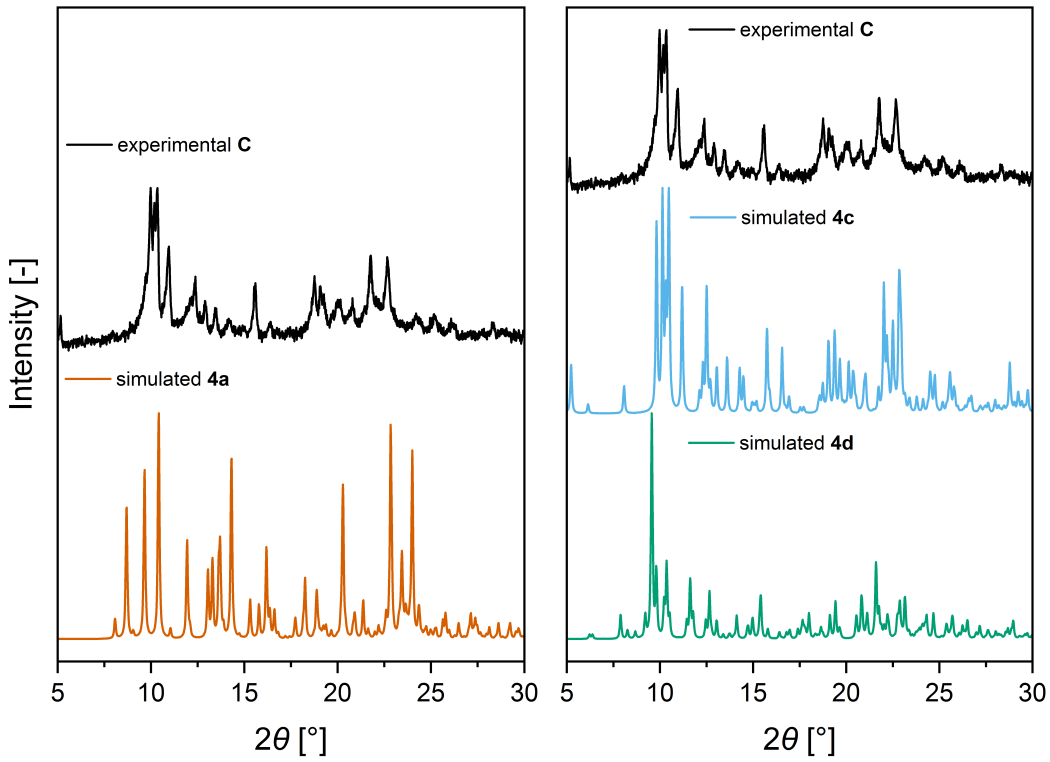

Figure 6.12: Experimental PXRD of compound **C** (black) in comparison with the simulated patterns of **4a** (orange, left) and **4c** (blue) & **4d** (green, right).

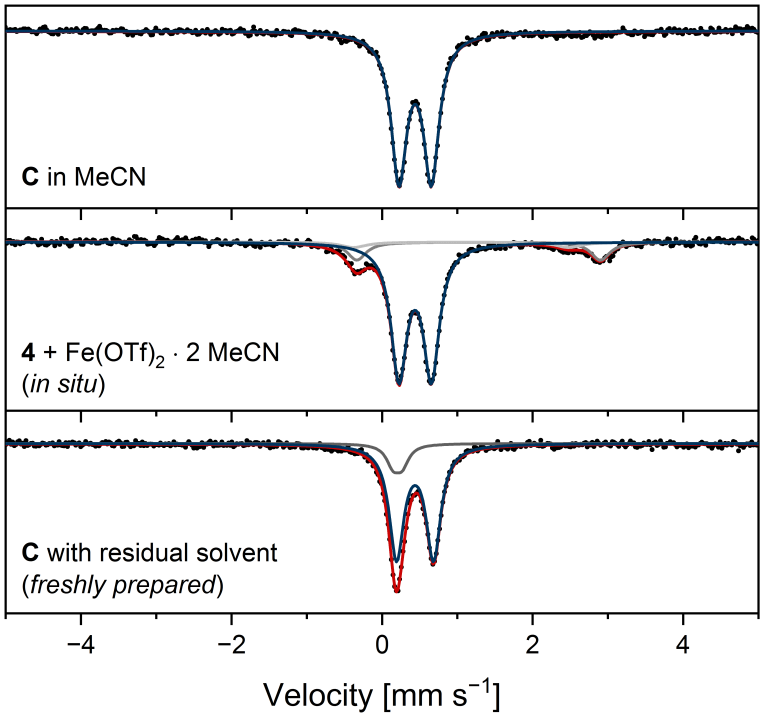

Figure 6.13: Mößbauer spectra of frozen MeCN solutions (80 K) of **C** (top), *in situ* reaction of **4** and $Fe(OTf)_2 \cdot 2\,MeCN$ (middle) and freshly prepared crystals **C** with residual solvent (bottom). Experimental data are shown in black, overall fit in red, fit of LS species in blue and minor impurities in grey.

Table 6.7: Mößbauer parameters for **C** in MeCN, the *in situ* reaction of **4** and $Fe(OTf)_2 \cdot 2\,MeCN$ and freshly prepared crystals **C** with residual solvent.

Frozen solution	δ [mm s^{-1}]	ΔE_Q [mm s^{-1}]	Amount [%]	Assignment
C in MeCN	0.44	0.43	100	LS Fe(II)
4 + $Fe(OTf)_2 \cdot 2\,MeCN$ in MeCN	0.44	0.43	81	LS Fe(II)
	1.28	3.24	13	impurity
	1.05	2.86	5	impurity
C with residual solvent	0.44	0.49	86	LS Fe(II)
	0.21	0.12	14	impurity

The same species is observed as major species (81 %) when ligand **4** and $Fe(OTf)_2 \cdot 2\,MeCN$ are combined *in situ* in acetonitrile and the resulting solution is subsequently frozen for the Mößbauer measurement. Since it is very challenging to perfectly measure ligand and salt on a 1 : 1 ratio in a small scale, two minor signals ($\delta = 1,28\,mm\,s^{-1}$ & $\Delta E_Q = 3.24\,mm\,s^{-1}$ and $\delta = 1.05\,mm\,s^{-1}$ & $\Delta E_Q = 2.86\,mm\,s^{-1}$, respectively) occur which cannot be assigned to a defined species.

The data of the two species assigned as iron(II) LS are in line with values reported for iron(II) LS complexes with {N_6}-coordination sphere.[250,253,254] This is a hint for the bis(acetonitrile) species being dominant in acetonitrile solution.

Taking into account the solvation sensitivity of crystals of **4a**, crystals **C** were prepared and measured in the presence of residual solvent with Mößbauer spectroscopy. The resulting spectrum shows a major species (86 %, $\delta = 0.44\,mm\,s^{-1}$ & $\Delta E_Q = 0.49\,mm\,s^{-1}$) in line with the former iron(II) LS species observed in frozen solution. In addition, an unknown impurity (14 %) was observed. Overall, this confirms the existence of an LS bis(acetonitrile) complex as in the SCXRD structure of **4a** which is very sensitive towards changes in the solvation and cannot be isolated while maintaining the {N_6}-coordination sphere.

$[Fe_2(\mu{-}O)(NQu_3)_2(OTf)_2](OTf)_2 \cdot 0.85\,MeCN$ (4g)

Complex $[Fe_2(\mu\text{-}O)(\mathbf{4})_2(OTf)_2](OTf)_2 \cdot 0.85\,MeCN$ (**4g**) was observed as an oxidation side product of the triflate based complexes with ligand **4** in acetonitrile (Figure 6.14). It was first obtained in reactions with an additional triflate source ($NH_4(OTf)$) intended to result selectively in a bis(triflato) complex species. However, this did not work, but after exposure of the reaction solution to air and further crystallisation time, crystals of **4g** were received. Crystals of **4g** were also observed in reactions without $NH_4(OTf)$ addition that had been in short contact with air. An oxide-bridged iron(III) dimer complex with similar structure was reported e.g. by Ward *et al.*[255] **4g** crystallises in the monoclinic space group $P2_1/c$ with $Z = 4$. The Fe – N bond lengths of this iron(III) dimer are all larger than 2.0 Å, which is in line with an iron(III) HS species (Table 6.8).[252,255] The Fe – O – Fe angle (164.7(3)°) is about 10°

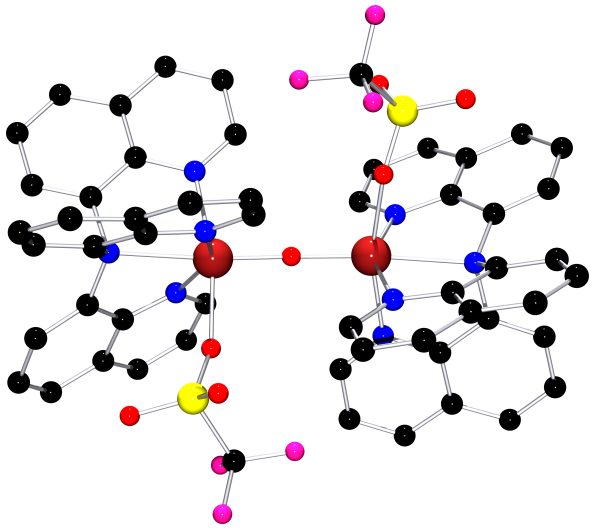

Figure 6.14: $[Fe_2(\mu\text{-}O)(\mathbf{4})_2(OTf)_2]^{2+}$ cation in crystals of **4g**. Hydrogen atoms, counterions and crystal solvent molecules are omitted for clarity. Colour code: black = carbon, blue = nitrogen, red = oxygen, scarlet = iron, yellow = sulphur, pink = fluorine.

Table 6.8: Selected bond lengths, atom distances, bond angles and structure parameters of **4g**.

	4g $[Fe_2(\mu\text{-}O)(NQu_3)_2(OTf)_2](OTf)_2 \cdot 0.85\,MeCN$
Space group	$P2_1/c$
Bond lengths [Å]	
Fe – N_{Am}	2.318(5)–2.322(5)
Fe – N_{Qu}	2.075(6)–2.103(5)
Ø Fe – N	2.145
Fe – O_A	1.785(4)–1.789(4)
Fe – O_E	1.92(3)–2.094(6)
Atom distances [Å]	
Fe···Fe	3.5420(15)
Bond angles [°]	
N_{Qu} – Fe – N_{Am}	74.62(19)–78.68(18)
O_A – Fe – O_E	91.3(16)–98.1(2)
N_{Am} – Fe – O_E	86.4(2)–93.3(16)
N_{Am} – Fe – O_A	174.29(18)–175.37(18)
N_{Qu2} – Fe – O_E	165.0(3)–171.6(17)
N_{Qu1} – Fe – N_{Qu3}	150.6(2)–151.5(2)
Struct. param.	
CSM *S*(OC-6)	1.0/0.8/1.1
CSM *S*(TPR-6)	13.0/14.5/13.0

smaller than the dimer reported by Ward *et al.* (174.6(2)°).[255] The coordination geometries of the iron centres are in line with a slightly distorted octahedron (*S*(OC-6) = 0.8–1.1).

Another hint that the complexes **4a** to **4g** are not stable when isolated, are the corresponding IR spectra (Figure A.17 & Figure A.18 in the Appendix). Under aerobic conditions, all spectra

show basically the same bands which should not be the case for such different complex structures in the solid state. Although the crystals in samples with concomitantly crystallised species were sorted manually before measurement, it could not be ensured that only one species was measured.

6.2.2 Complexes Obtained with Different Solvents

Complexes Obtained in DCM

$[Fe(NQu_3)(OTf)_2] \cdot 1.3\,DCM \cdot Z$ (4h)

To selectively crystallise the bis(triflato) species, complexes with **4** and $Fe(OTf)_2 \cdot 2\,MeCN$ were prepared in dichloromethane, which is a non-coordinating solvent (Scheme 6.2). With diethyl ether as anti-solvent, orange crystals suitable for SCXRD were obtained.

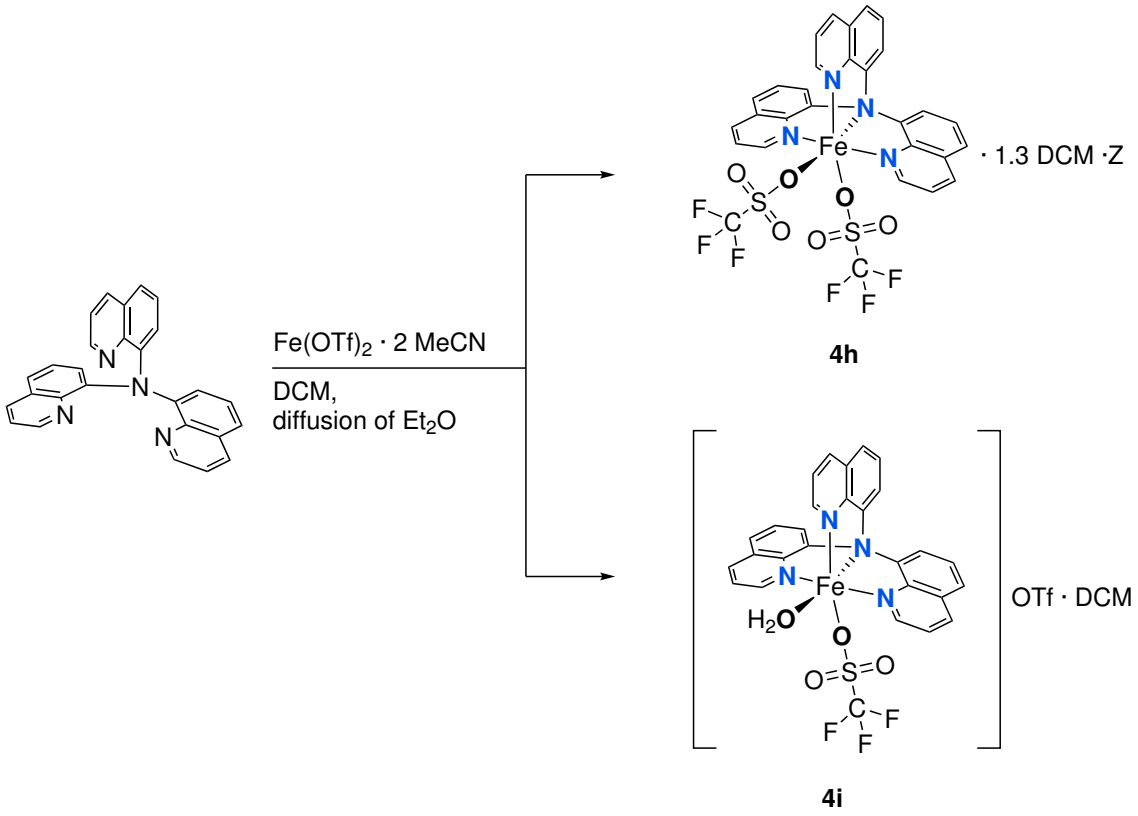

Scheme 6.2: Synthesis of complexes **4h** and **4i**.

The obtained dataset had reduced quality, which only allowed the identification of the bis(triflato) complex molecule with co-crystallised dichloromethane and further highly disordered solvent molecules (Z), which could not be assigned further. This leads to a preliminary formula of $[Fe(\mathbf{4})(OTf)_2] \cdot 1.3\,DCM \cdot Z$ (**4h**) for the complex species obtained from dichloromethane. Bond lengths and angles for **4h** will not be discussed in detail due to the poor quality of the dataset. Rapid loss of crystal solvent molecules and the unclear composition also make this species unsuitable for most further experiments.

Despite the unclear composition, it was possible to measure Mößbauer spectra of this species. Therefore, crystals of **4h** were isolate analogous to compound **C**. This so-called compound **D** has a Mößbauer spectrum where three different iron(II) HS species could be identified (Figure 6.15 & Table 6.9). The obtained values are similar to those of solid compound **C** and these are probably also bis(triflato) species that are very sensitive to solvent residues.

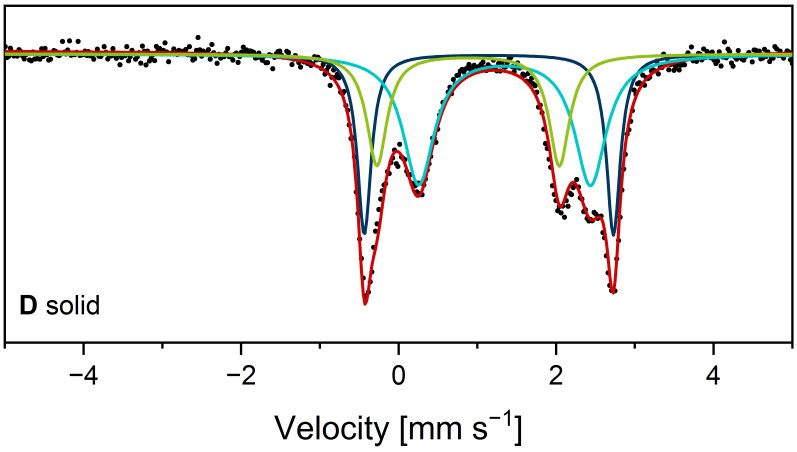

Figure 6.15: Mößbauer spectrum of compound **D** as solid sample measured at 80 K. Experimental data are shown in black, overall fit in red and fits for three different iron(II) HS species in blue, turquoise and green.

Table 6.9: Mößbauer parameters for solid crystals of **D**.

Solid	δ [mm s^{-1}]	ΔE_Q [mm s^{-1}]	Amount [%]	Assignment
D	1.15	3.17	28	HS Fe(II)
	1.35	2.18	29	HS Fe(II)
	0.88	2.32	44	HS Fe(II)

[Fe(NQu$_3$)(OTf)(H$_2$O)](OTf) · DCM (4i)

In dichloromethane, a side product could be crystallised where water is incorporated as one of the co-ligands. The complex [Fe(**4**)(OTf)(H$_2$O)](OTf) · DCM (**4i**) crystallises in the monoclinic space group $C2/c$ with $Z = 8$ as a dichloromethane solvate (Figure 6.16). The arrangement of the co-ligands (A: H$_2$O, E: OTf$^-$) is inverse to the other structure with water and acetonitrile as co-ligands (**4f**; A: MeCN, E: H$_2$O). Both complexes underline that water is a strong competitor in the co-ligand equilibria and small mistakes with working under inert conditions can lead to structural motifs with water as co-ligand. In agreement with the other *N*/*O*-mixed donor species discussed previously, the bond lengths of Fe – N are above 2.0 Å, which is in line with an HS species (Table 6.10).[119,138,252] The coordination geometry is octahedral distorted (CSM: S(OC-6) = 2.3).

Table 6.10: Selected bond lengths, bond angles and structure parameters of **4i**.

	4i $[Fe(NQu_3)(OTf)(H_2O)](OTf) \cdot DCM$
Space group	$C2/c$
Bond lengths [Å]	
$Fe-N_{Am}$	2.300(2)
$Fe-N_{Qu}$	2.107(2)–2.164(2)
Ø Fe – N	2.176
$Fe-O_A$	2.074(2)
$Fe-O_E$	2.1743(19)
Bond angles [°]	
$N_{Qu}-Fe-N_{Am}$	73.77(9)–78.49(9)
O_A-Fe-O_E	82.15(8)
$N_{Am}-Fe-O_E$	101.38(8)
$N_{Am}-Fe-O_A$	176.29(9)
$N_{Qu2}-Fe-O_E$	170.61(8)
$N_{Qu1}-Fe-N_{Qu3}$	149.38(10)
Struct. param.	
CSM *S*(OC-6)	2.3
CSM *S*(TPR-6)	9.7

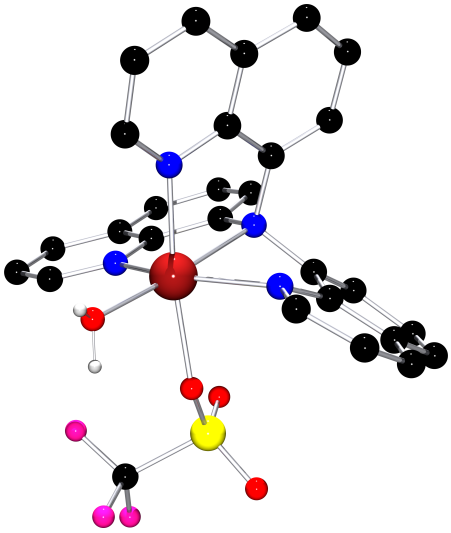

Figure 6.16: $[Fe(\mathbf{4})(OTf)(H_2O)]^+$ cation in crystals of **4i**. C bonded hydrogen atoms, counterions and crystal solvent molecules are omitted for clarity. Colour code: black = carbon, blue = nitrogen, red = oxygen, scarlet = iron, yellow = sulphur, pink = fluorine, white = hydrogen.

Complexes Obtained in EtCN

To obtain a purely {N_6}-coordinated complex cation via a different synthesis, acetonitrile was replaced by propionitrile as solvent in the complex synthesis. However, this did not enhance the selectivity towards a single species, but it led to both variants of complexes with propionitrile as co-ligands: One of them being the bis(propionitrile) $[Fe(\mathbf{4})(EtCN)_2](OTf)_2$ (**4j**) species and the other one being the mixed co-ligand variant $[Fe(\mathbf{4})(OTf)(EtCN)](OTf) \cdot 0.5\,Et_2O$ (**4k**) (Figure 6.17, Scheme 6.3).

Even though acetonitrile was present in stoichiometric amounts in the $Fe(OTf)_2 \cdot 2\,MeCN$, only propionitrile species were observed. This is reasonable since propionitrile was present in excess and it has a higher tendency for coordination than acetonitrile.[233] The complex cations **4j** and **4k** are analogue to the acetonitrile variants **4a** and **4b**, respectively. Contrasting the results in acetonitrile, synthesis at 6 °C did not lead to selective crystallisation of one species.

$[Fe(NQu_3)(EtCN)_2](OTf)_2$ (4j)

The complex $[Fe(\mathbf{4})(EtCN)_2](OTf)_2$ (**4j**) crystallises in the monoclinic space group $P2_1/c$ with $Z = 4$. Overall the complex geometry is similar to the bis(acetonitrile) complex **4a**. The $Fe-N_{Qu}$ and $Fe-N_{MeCN}$ bond lengths are shorter than 2.0 Å while the $Fe-N_{Am}$ bond is longer (2.024(2) Å, Table 6.11). The average Fe – N bond length of 1.957 Å is in line with a

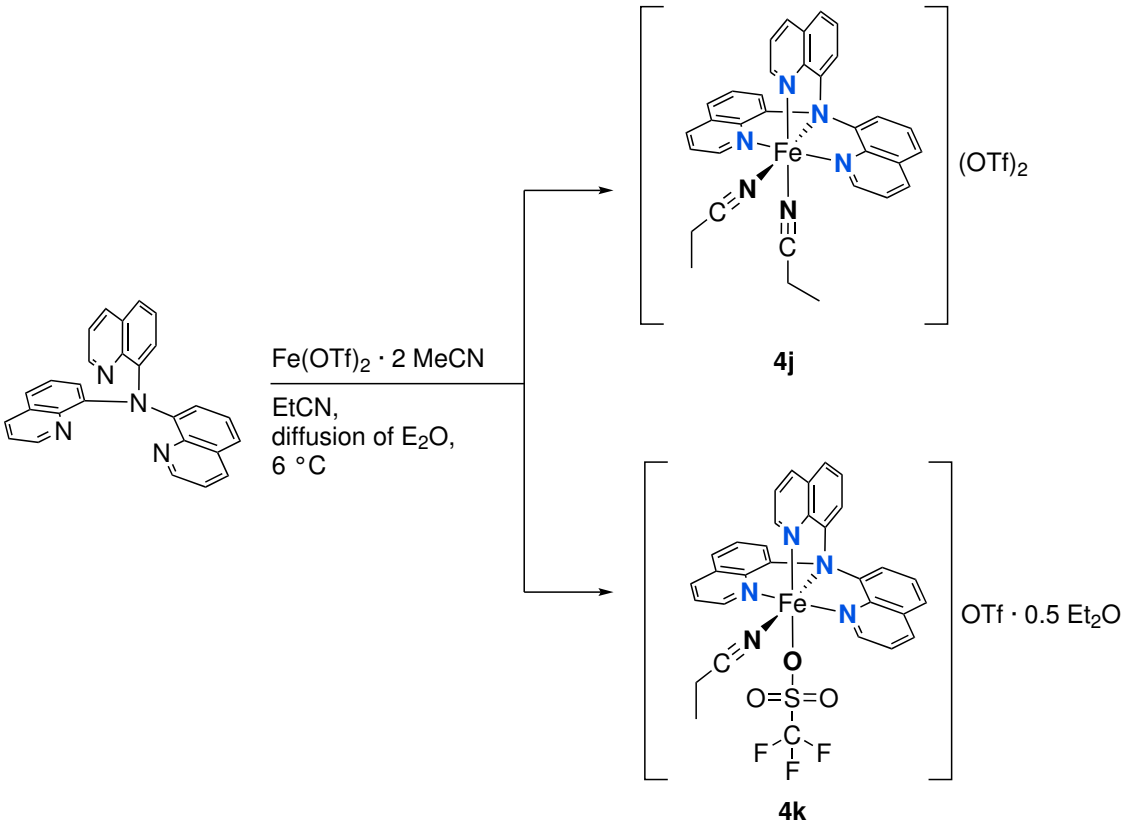

Scheme 6.3: Synthesis of complexes **4j** and **4k**.

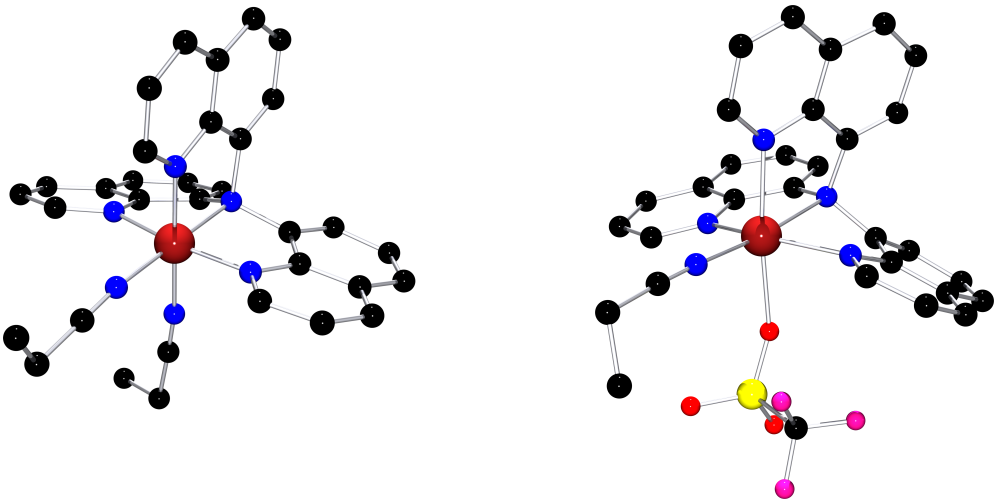

Figure 6.17: $[Fe(\mathbf{4})(EtCN)_2]^{2+}$ cation in crystals of **4j** (left) and $[Fe(\mathbf{4})(OTf)(EtCN)]^{+}$ cation in crystals of **4k** (right). Hydrogen atoms, counterions and crystal solvent molecules are omitted for clarity. Colour code: black = carbon, blue = nitrogen, red = oxygen, scarlet = iron, yellow = sulphur, pink = fluorine.

LS species.[119,138] The coordination geometry is close to an ideal octahedron with a CSM value of S(OC-6) = 0.3.

Table 6.11: Selected bond lengths, bond angles and structure parameters of **4j** and **4k**.

	4j $[Fe(NQu_3)(EtCN)_2](OTf)_2$	**4k** $[Fe(NQu_3)(OTf)(EtCN)](OTf) \cdot 0.5\,Et_2O$
Space group	$P2_1/c$	$P\bar{1}$
Bond lengths [Å]		
$Fe-N_{Am}$	2.024(2)	2.2929(17)
$Fe-N_{Qu}$	1.937(2)–1.956(2)	2.0985(19)–2.162(2)
$Fe-N_A$	1.928(2)	2.087(2)
$Fe-N_E/O_E$	1.950(2)	2.2765(17)
Ø Fe – N	1.957	2.152
Bond angles [°]		
$N_{Qu}-Fe-N_{Am}$	83.84(8)–86.09(9)	75.13(7)–78.33(7)
N_A-Fe-N/O_E	87.30(9)	90.72(7)
$N_{Am}-Fe-N/O_E$	91.51(9)	95.30(6)
$N_{Am}-Fe-N_A$	178.78(9)	173.96(7)
$N_{Qu2}-Fe-N_E$	177.15(9)	172.64(6)
$N_{Qu1}-Fe-N_{Qu3}$	168.00(8)	149.18(7)
Struct. param.		
CSM *S*(OC-6)	0.3	1.7
CSM *S*(TPR-6)	14.9	11.4

$[Fe(NQu_3)(OTf)(EtCN)](OTf) \cdot 0.5\,Et_2O$ (4k)

The mixed co-ligand propionitrile species $[Fe(\mathbf{4})(OTf)(EtCN)](OTf) \cdot 0.5\,Et_2O$ (**4k**) crystallises as diethyl ether solvate in the triclinic space group $P\bar{1}$ with $Z = 1$ with a formula of $[Fe(\mathbf{4})(OTf)(EtCN)]_2(OTf)_2 \cdot Et_2O$. Z was defined this way to avoid fractional numbers in the sum formula. The propionitrile mixed co-ligand species **4k** has the same co-ligand arrangement (A: nitrile-donor, E: OTf^-) as the acetonitrile analogue (**4b**). The bond lengths are in a similar range (Fe – N > 2.0Å) and show the same trends for both mixed co-ligand species (Table 6.11, Table 6.2). Like all *N*/*O*-mixed donor species with ligand **4**, this is in line with a HS species that has a distorted octahedral coordination geometry (CSM: *S*(OC-6) = 1.7).[119,126,235] The investigation of these complexes was stopped at this point because the use of propionitrile did not selectively lead to one species but to the same coordination isomers as in acetonitrile and due to the toxicity of propionitrile.

Complexes Obtained in MeOH

Two coordination isomers could be crystallised from methanol. No bis(methanol) species was obtained, although it would be expected as the main species in solution, but the two different variants of mixed co-ligand species with methanol and triflate could be crystallised (Scheme 6.4, Figure 6.18).[121] The isomer with methanol in the A and triflate in the E position is complex $[Fe(\mathbf{4})(OTf)(MeOH)](OTf)$ (**4l**) whereas the isomer with triflate in the A and methanol in the E position is complex $[Fe(\mathbf{4})(OTf)(MeOH)](OTf) \cdot MeOH$ (**4m**).

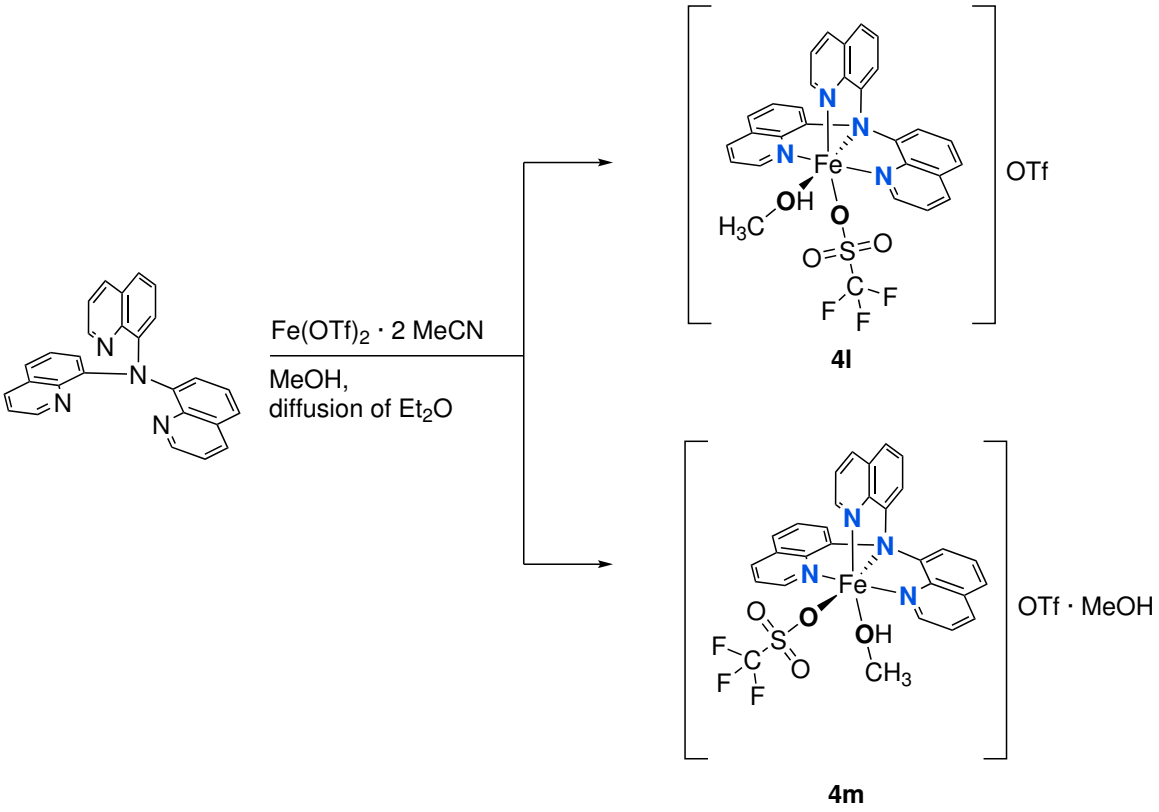

Scheme 6.4: Synthesis of complexes **4l** and **4m**.

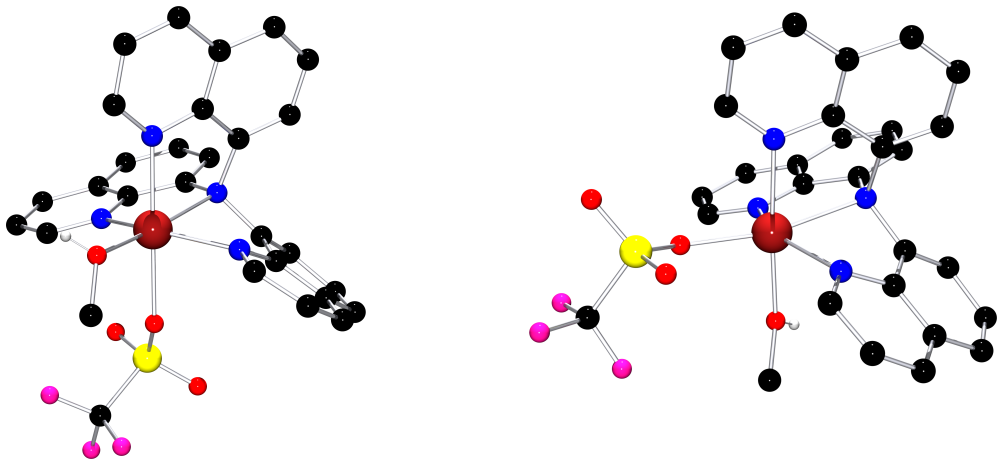

Figure 6.18: [Fe(**4**)(OTf)(MeOH)]$^+$ cation in crystals of **4l** (left) and [Fe(**4**)(OTf)(MeOH)]$^+$ cation in crystals of **4m** (right). C bonded hydrogen atoms, counterions and crystal solvent molecules are omitted for clarity. Colour code: black = carbon, blue = nitrogen, red = oxygen, scarlet = iron, yellow = sulphur, pink = fluorine, white = hydrogen.

[Fe(NQu_3)(OTf)(MeOH)](OTf) (4l)

The complex [Fe(**4**)(OTf)(MeOH)](OTf) (**4l**) crystallises in the monoclinic space group $P2_1/c$ with $Z = 4$. Like in all other N/O-mixed donor complexes with **4**, the Fe – N bond lengths are in the range of a HS species (Table 6.12).[138,252] The Fe – O_A bond to the methanol co-ligand (2.0657(9) Å) is shorter than the Fe – O_E bond to the triflate (2.2355(9) Å). The coordination

Table 6.12: Selected bond lengths, bond angles and structure parameters of **4l** and **4m**.

	4l [Fe(NQu$_3$)(OTf)(MeOH)](OTf)	**4m** [Fe(NQu$_3$)(OTf)(MeOH)](OTf) · MeOH
Space group	$P2_1/c$	$P\bar{1}$
Bond lengths [Å]		
Fe – N_{Am}	2.2778(9)	2.301(2)
Fe – N_{Qu}	2.0888(9)–2.1597(10)	2.126(2)–2.190(2)
Ø Fe – N	2.167	2.193
Fe – O_A	2.0657(9)	2.0422(18)
Fe – O_E	2.2355(9)	2.1371(19)
Bond angles [°]		
N_{Qu} – Fe – N_{Am}	74.57(3)–78.81(3)	72.87(7)–77.65(7)
O_A – Fe – O_E	86.21(4)	90.19(8)
N_{Am} – Fe – O_E	101.04(3)	99.53(8)
N_{Am} – Fe – O_A	170.92(4)	167.47(7)
N_{Qu2} – Fe – O_E	177.80(3)	176.50(8)
N_{Qu1} – Fe – N_{Qu3}	148.44(4)	144.90(8)
Struct. param.		
CSM *S*(OC-6)	2.3	2.8
CSM *S*(TPR-6)	9.7	8.7

geometry can be described as distorted octahedron (CSM: *S*(OC-6) = 2.3). In this structure, a H-bond between the coordinating methanol molecule towards the non-coordinating triflate anion was found (O_{MeOH} – H···O_{OTf} 2.6498(13) Å, Figure 6.19).

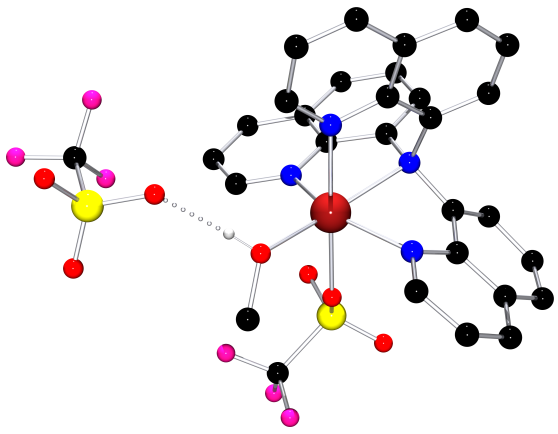

Figure 6.19: H-bond (dotted) in crystal structure of **4l**. C bonded hydrogen atoms and counterions are omitted for clarity. Colour code: black = carbon, blue = nitrogen, red = oxygen, scarlet = iron, yellow = sulphur, pink = fluorine, white = hydrogen.

[Fe(NQu$_3$)(OTf)(MeOH)](OTf) · MeOH (4m)

The complex [Fe(**4**)(OTf)(MeOH)](OTf) · MeOH (**4m**) crystallises as a methanol solvate in the triclinic space group $P\bar{1}$ with $Z = 2$. The Fe – N bonds in **4m** are slightly elongated

(Ø Fe – N 2.193 Å) compared to the ones in **4l** (2.167 Å). Like in the other isomer, the Fe – O_A bond length is shorter (2.0422(18) Å, OTf^-) than the Fe – O_E bond (2.1371(19) Å, MeOH). This shows that the Fe – O bond lengths depend more on the position (A/E) than on the type of O donor as co-ligand. This asymmetry of the A and E position was observed for all complexes with ligand **4** but with the comparison of complexes **4l** and **4m**, which have both options of co-ligands with different steric demand, this asymmetry is most likely caused by a structural *trans*-effect. The long Fe – N_{Am} bond goes along with a shortened Fe – O_A bond in *trans* position. Such structural *trans*-effects are known in octahedral complexes.[204] The coordination geometry of **4m** is slightly more distorted (CSM: S(OC-6) = 2.8) than for the other isomer **4l**. This may be caused by a partial steric influence on the coordination geometry besides the electronic effects when the bulkier triflate is in the A position. Differently from the complex **4l**, the complex **4m** has the additional non-coordinating methanol molecule involved in the H-bonds. There is an H-bond between the coordinating methanol molecule and the non-coordination one (O_{MeOH_coord} – H···$O_{MeOH\_non\text{-}coord}$ 2.639(3) Å) and an H-bond between the non-coordinating methanol molecule and the non-coordinating triflate anion ($O_{MeOH\_non\text{-}coord}$ – H···O_{OTf} 2.768(3) Å, Figure 6.20).

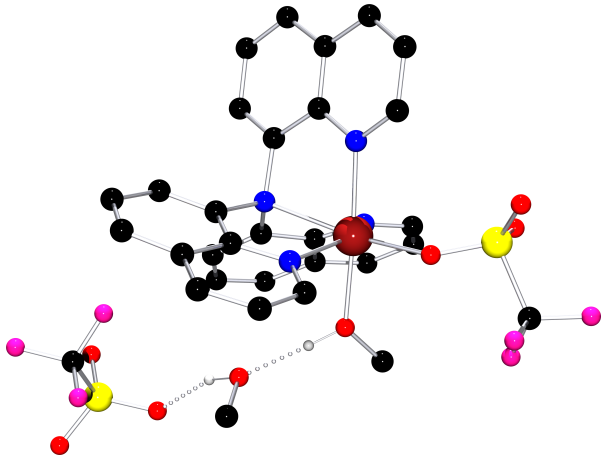

Figure 6.20: H-bonds (dotted) in crystal structures of **4m**. C bonded hydrogen atoms, counterions and crystal solvent molecules are omitted for clarity. Colour code: black = carbon, blue = nitrogen, red = oxygen, scarlet = iron, yellow = sulphur, pink = fluorine, white = hydrogen.

6.2.3 Complexes Obtained with Different Counterions

$[Fe(NQu_3)Cl_2] \cdot 0.5\,DCM$ (4n)

An iron(II) bis(chlorido) species is obtained with $FeCl_2$ (Scheme 6.5). The resulting complex is $[Fe(\mathbf{4})Cl_2] \cdot 0.5\,DCM$ (**4n**), a dichloromethane solvate crystallising in the triclinic space group $P\bar{1}$ with $Z = 2$ (Figure 6.21). Half of a dichloromethane molecule per complex could not be modelled in an appropriate manner and was masked using the BYPASS algorithm as implemented in PLATON/SQUEEZE.[156–158] The Fe – N bond lengths in the structure

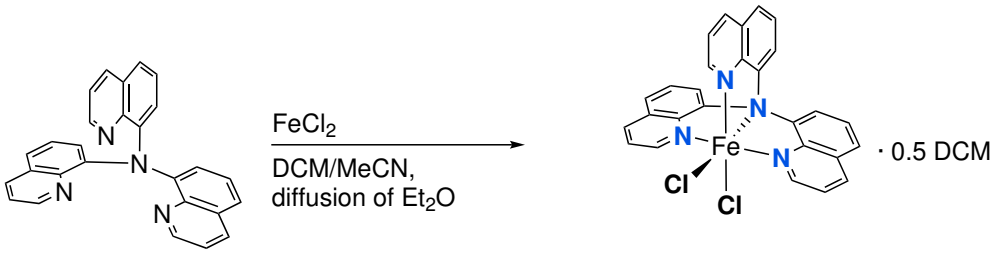

Scheme 6.5: Synthesis of complex **4n**.

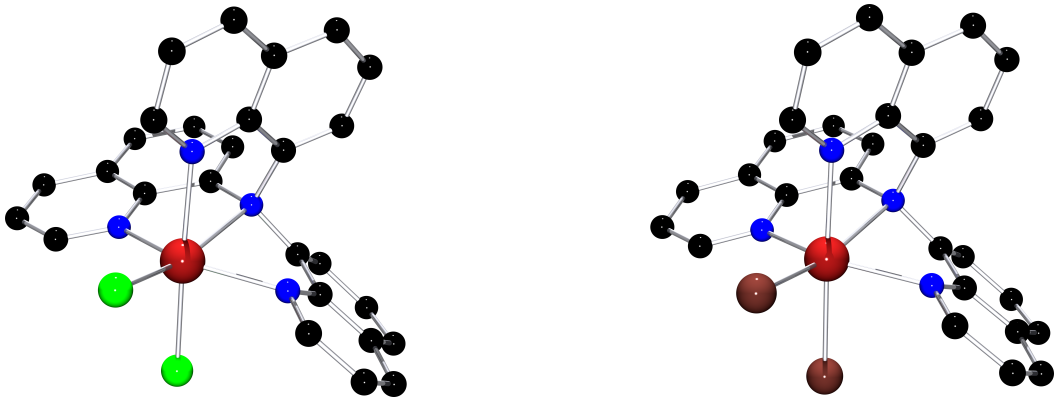

Figure 6.21: [Fe(**4**)Cl_2] unit in crystals of **4n** (left) and [Fe(**4**)Br_2] unit in crystals of **4o** (right). Hydrogen atoms and crystal solvent molecules are omitted for clarity. Colour code: black = carbon, blue = nitrogen, scarlet = iron, green = chlorine, brown = bromine.

of **4n** are in the range of 2.1259(16)–2.3924(15) Å (Table 6.13). This is consistent with a HS species, which is in line with expectations, as halides are generally weak field ligands causing less ligand field splitting than acetonitrile.[235] Like in all other structures, the bond to the co-ligand in A position is shorter (2.3181(7) Å) than to the co-ligand in E position (2.4758(10) Å). The coordination geometry is a distorted octahedron (CSM: *S*(OC-6) = 3.4).

[Fe(NQu$_3$)Br$_2$] · 0.5 DCM (4o)

The use of $FeBr_2$ results in the complex [Fe(**4**)Br_2] · 0.5 DCM (**4o**) which is isomorphous to **4n** (Scheme 6.6, Figure 6.21). Again, half of a dichloromethane molecule per complex could not be modelled appropriately and was masked using the BYPASS algorithm as implemented in PLATON/SQUEEZE.[156–158] The structure of **4o** has a slightly larger unit cell volume,

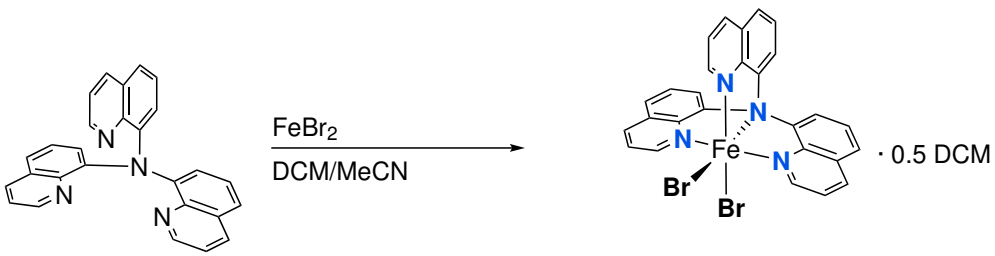

Scheme 6.6: Synthesis of complex **4o**.

Table 6.13: Selected bond lengths, bond angles and structure parameters of **4n** and **4o**.

	4n $[Fe(NQu_3)Cl_2] \cdot 0.5\,DCM$	**4o** $[Fe(NQu_3)Br_2] \cdot 0.5\,DCM$
Space group	$P\bar{1}$	$P\bar{1}$
Bond lengths [Å]		
$Fe - N_{Am}$	2.3924(12)	2.373(6)
$Fe - N_{Qu}$	2.1264(12)–2.2482(11)	2.130(6)–2.226(6)
Ø Fe – N	2.234	2.223
$Fe - Cl_A/Br_A$	2.3178(4)	2.4290(16)
$Fe - Cl_E/Br_E$	2.4753(4)	2.6378(16)
Bond angles [°]		
$N_{Qu} - Fe - N_{Am}$	71.52(4)–75.57(4)	71.7(2)–75.9(2)
$Cl_A/Br_A - Fe - Cl_E/Br_E$	96.519(15)	95.02(5)
$N_{Am} - Fe - Cl_E/Br_E$	101.03(3)	101.91(14)
$N_{Am} - Fe - Cl_A/Br_A$	162.07(3)	162.78(15)
$N_{Qu2} - Fe - Cl_E/Br_E$	173.37(3)	173.69(17)
$N_{Qu1} - Fe - N_{Qu3}$	143.27(5)	142.9(2)
Struct. param.		
CSM *S*(OC-6)	3.4	3.9
CSM *S*(TPR-6)	10.1	10.5

which is associated with the larger bromido ligands. The overlay of the unit cells of both structures indicates the high degree of similarity of the isomorphous structures **4n** and **4o** (Figure 6.22). The bond lengths are similar to complex **4n** or slightly larger and the coordination geometry is octahedral with a higher distortion (CSM: *S*(OC-6) = 3.9). All this matches the expectations for the larger sized bromido co-ligands.

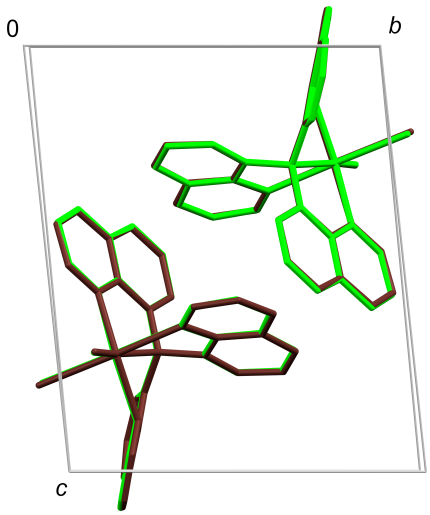

Figure 6.22: Overlay of the unit cells of **4n** (green) and **4o** (brown).

[Fe(NQu$_3$)Cl]PF$_6$ · 1.5 DCM (4p)

Complex [Fe(**4**)Cl]PF$_6$ · 1.5 DCM (**4p**) was found after a reaction with the intention to introduce hexafluorophosphate anions to an iron(II) complex with ligand **4** (Figure 6.23).

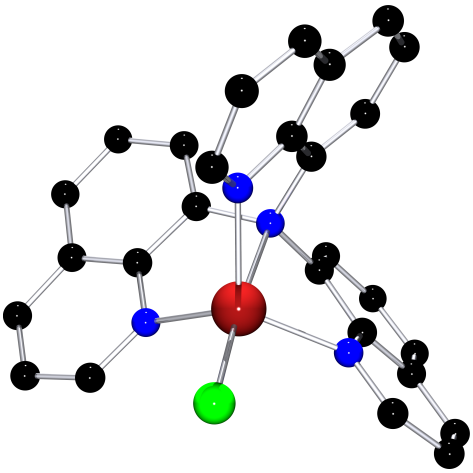

Figure 6.23: [Fe(**4**)Cl]$^+$ cation in crystals of **4p**. Hydrogen atoms, counterions and crystal solvent molecules are omitted for clarity. Colour code: black = carbon, blue = nitrogen, scarlet = iron, green = chlorine.

Table 6.14: Selected bond lengths, bond angles and structure parameters of **4p**.

	4p [Fe(NQu$_3$)Cl]PF$_6$ · 1.5 DCM
Space group	*Pbcn*
Bond lengths [Å]	
Fe – N_{Am}	2.339(4)
Fe – N_{Qu}	2.080(4)–2.109(4)
Ø Fe – N	2.156
Fe – Cl	2.2768(17)
Bond angles [°]	
N_{Qu} – Fe – N_{Am}	74.88(16)–76.36(16)
N_{Am} – Fe – Cl	176.11(12)
N_{Qu} – Fe – Cl	100.02(13)–105.93(13)
N_{Qu} – Fe – N_{Qu}	111.42(17)–117.64(17)
Struct. param.	
CSM *S*(TBPY-5)	2.1
CSM *S*(SPY-5)	6.2

Therefore, a salt metathesis in dichloromethane starting with an iron(II) chlorido complex was performed (Scheme 6.7). To remove the chloride ions, AgPF$_6$ salt was used subsequently. To investigate whether the halides can be substituted stepwise and enforce an intermediate species with one chlorido ligand, FeCl$_2$ and AgPF$_6$ were used in a 1 : 1 ratio. Diethyl ether as anti-solvent resulted in a large amount of orange poor quality crystals and a few yellow crystals suitable for SCXRD. The yellow crystals (**4p**) are a dichloromethane solvate in the orthorhombic space group *Pbcn* with $Z = 8$. This complex is the only penta-coordinated complex for ligand **4** with iron. This five-fold coordination was observed for other transition metals with preferences for lower coordination numbers such as copper.[241]

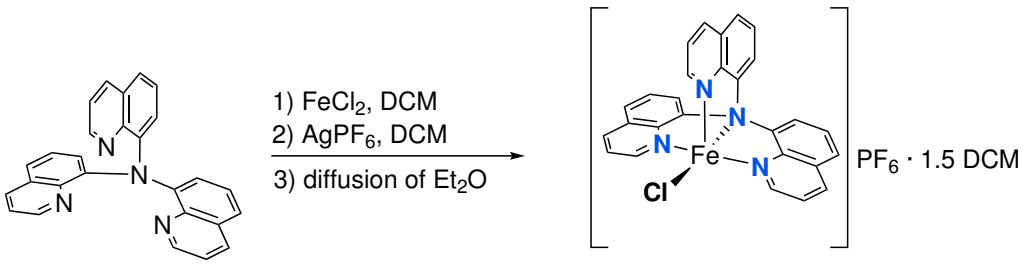

Scheme 6.7: Synthesis of complex **4p**.

The coordination geometry is a slightly distorted trigonal bipyramid (CSM: S(TBPY-5) = 2.1, Figure 6.14). The trigonal bipyramidal coordination fits better the threefold symmetry of the pure ligands as the three quinoline arms can now distribute equally around the metal centre. The length of the Fe – N bonds is in line with other reported penta-coordinate iron mono-chlorido complexes that have been assigned as HS complexes.[256–258] No further bulk analyses could be carried out with this compound as only a few crystals could be obtained.

$[Fe(NQu_3)(MeCN)_2](BF_4)_2 \cdot 0.5\,MeCN$ (4q)

$[Fe(MeCN)_6](BF_4)_2$ can be used to obtain an isostructural bis(acetonitrile) complex cation to the one in crystals of **4a** (Scheme 6.8).

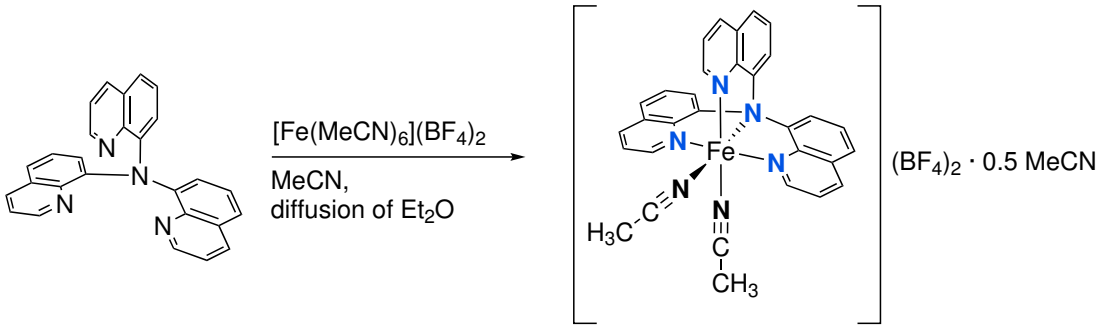

Scheme 6.8: Synthesis of complex **4q**.

This was expected since tetrafluoridoborate is less coordinating than triflate and thus there is less competition between solvent and anion for the co-ligand positions.[233] The high degree of similarity between the complex cations of $[Fe(\mathbf{4})(MeCN)_2](BF_4)_2 \cdot 0.5\,MeCN$ (**4q**) and **4a** is depicted in Figure 6.24. Complex **4q** crystallises in the triclinic space group $P\bar{1}$ with $Z = 2$. The bond lengths, angles and the coordination geometry are similar to those of **4a** (Table 6.15). The Fe – N bond lengths are in line with a LS species.[119,138] Especially, $\{N_6\}$-coordinated complexes are good candidates for SCO complexes.[119] This complex was exemplarily chosen to investigate a potential SCO behaviour in the solid state. A temperature-dependent series of measurements on one crystal was performed to investigate whether the species is still LS at higher temperatures (> 100 K) or whether longer Fe – N bond lengths indicate the transition to a HS species. The values for bond lengths and angles obtained from structures at 100 K, 250 K and 273 K show no significant changes with the temperature (Table 6.16). At least for this crystal structure, the $[Fe(\mathbf{4})(MeCN)_2]^{2+}$ complex shows no spin crossover behaviour between 100 and 273 K in the solid state. At higher temperatures, the degree of crystallinity of the crystal most likely decreased due to solvent loss, so that no sufficient diffraction data could be obtained. Note, that SCO behaviour in the solid state is sensitive to the crystal packing and lattice effects so the choice of a different crystal structure (e.g. **4a**) could lead to a different result.[117,118]

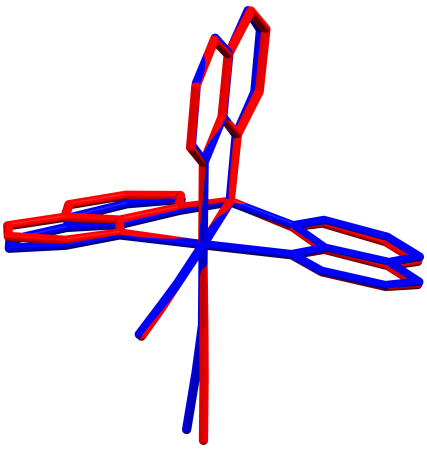

Figure 6.24: Overlay of the $[Fe(\mathbf{4})(MeCN)_2]^{2+}$ cation in crystals of **4a** (blue) and **4q** (red).

Table 6.15: Selected bond lengths, bond angles and structure parameters of **4q**.

	4q $[Fe(NQu_3)(MeCN)_2](BF_4)_2 \cdot 0.5\,MeCN$
Space group	$P\bar{1}$
Bond lengths [Å]	
$Fe-N_{Am}$	2.0208(15)
$Fe-N_{Qu}$	1.9402(14)–1.9521(14)
$Fe-N_A$	1.9191(16)
$Fe-N_E$	1.9560(15)
Ø Fe – N	1.955
Bond angles [°]	
$N_{Qu}-Fe-N_{Am}$	84.09(6)–85.73(6)
N_A-Fe-N_E	88.48(6)
$N_{Am}-Fe-N_E$	92.72(6)
$N_{Am}-Fe-N_A$	178.80(6)
$N_{Qu2}-Fe-N_E$	178.34(6)
$N_{Qu1}-Fe-N_{Qu3}$	168.00(6)
Struct. param.	
CSM *S*(OC-6)	0.3
CSM *S*(TPR-6)	14.3

Table 6.16: Selected bond lengths, bond angles of **4q** at 100 K, 250 K and 273 K.

Temperature	100 K	250 K	273 K
Bond lengths [Å]			
$Fe-N_{Am}$	2.021(4)	2.025(3)	2.024(4)
$Fe-N_{Qu1}$	1.948(4)	1.947(3)	1.949(4)
$Fe-N_{Qu2}$	1.942(4)	1.939(4)	1.939(4)
$Fe-N_{Qu3}$	1.944(4)	1.946(3)	1.943(3)
$Fe-N_A$	1.908(4)	1.928(3)	1.919(4)
$Fe-N_E$	1.952(5)	1.958(4)	1.957(5)
Ø Fe – N	1.953	1.957	1.955
Bond angles [°]			
$N_{Qu1}-Fe-N_{Am}$	84.16(15)	84.05(13)	84.06(15)
$N_{Qu2}-Fe-N_{Am}$	85.68(16)	85.38(14)	85.20(16)
$N_{Qu3}-Fe-N_{Am}$	84.93(15)	84.80(13)	84.86(14)
N_A-Fe-N_E	88.56(17)	88.08(15)	88.26(18)
$N_{Am}-Fe-N_E$	92.70(16)	93.13(14)	93.22(17)
$N_{Am}-Fe-N_A$	178.74(19)	178.78(16)	178.52(19)
$N_{Qu2}-Fe-N_E$	178.36(16)	178.41(14)	178.27(17)
$N_{Qu1}-Fe-N_{Qu3}$	168.18(16)	167.70(13)	167.84(15)

$[Fe(NQu_3)(NCS)_2] \cdot 0.5\,Et_2O$ (4r)

Iron complexes with thiocyanate co-ligands are good candidates for SCO complexes, but they do not necessarily have to show SCO behaviour.[117,118,259] Additionally, they offer

the opportunity of a pure *N*-donor coordination sphere and charge neutral complexes as thiocyanate is an anionic co-ligand. This eliminates co-ligand equilibria between counterions and coordinating solvents. To obtain such a charge neutral complex with ligand **4**, the ligand was combined with $[Fe(NCS)_2(Py)_4]$ (Scheme 6.9). Complex **4r** crystallises in the monoclinic space group $C2/c$ with $Z = 8$ (Figure 6.25).

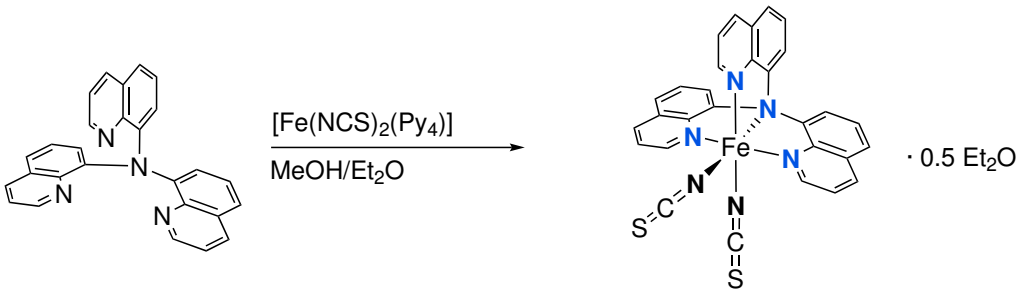

Scheme 6.9: Synthesis of complex **4r**.

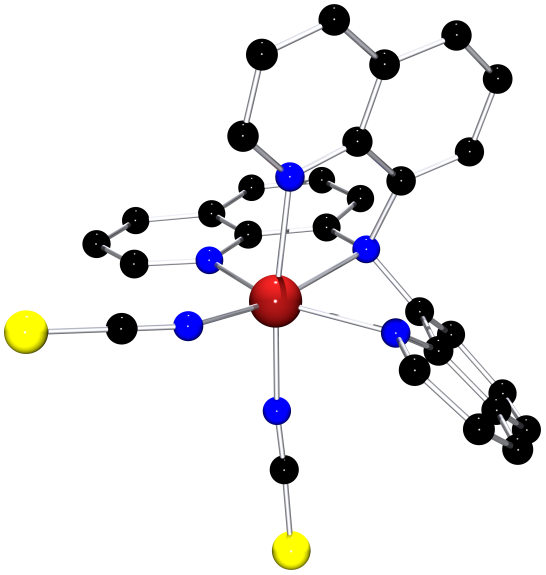

Figure 6.25: $[Fe(\mathbf{4})(NCS)_2]$ unit in crystals of **4r**. Hydrogen atoms and crystal solvent molecules are omitted for clarity. Colour code: black = carbon, blue = nitrogen, scarlet = iron, yellow = sulphur.

Table 6.17: Selected bond lengths, bond angles and structure parameters of **4r**.

	4r $[Fe(NQu_3)(NCS)_2] \cdot 0.5\,Et_2O$
Space group	$C2/c$
Bond lengths [Å]	
$Fe-N_{Am}$	2.328(3)
$Fe-N_{Qu}$	2.125(3)–2.199
$Fe-N_A$	2.034(4)
$Fe-N_E$	2.095(3)
Ø Fe – N	2.162
Bond angles [°]	
$N_{Qu}-Fe-N_{Am}$	72.22(11)–76.76(10)
N_A-Fe-N_E	96.50(13)
$N_{Am}-Fe-N_E$	95.23(11)
$N_{Am}-Fe-N_A$	168.22(12)
$N_{Qu2}-Fe-N_E$	170.51(12)
$N_{Qu1}-Fe-N_{Qu3}$	147.97(11)
Struct. param.	
CSM *S*(OC-6)	1.8
CSM *S*(TPR-6)	11.8

Different to the other crystal structures in this work, the SCXRD data collection was performed at 200 K. At lower temperatures the crystal quality was deteriorated. Only with slow cooling of the crystal, data at 100 K could be collected but the quality was still deteriorated. Besides $C2/c$, the data at 100 K could be solved reasonably in the triclinic space group $P\bar{1}$. This could be a first hint for a temperature phase transition which may be induced by a SCO. The lower temperature dataset revealed the same complex structure with slightly

shorter bond lengths. Due to the poor quality of the 100 K data only the 200 K data will be discussed further.

The co-crystallised solvent in the 200 K crystal structure was highly disordered and could not be modelled in an adequate manner and the solvent was masked with the BYPASS algorithm as implemented in PLATON/SQUEEZE.[156–158]

The Fe – N bond lengths are longer than 2.0 Å indicating a HS species at 200 K (Table 6.17). The distorted octahedral coordination sphere (CSM: S(OC-6) = 1.8) is also more in line with the geometry of the HS complexes observed with ligand **4**.

To investigate a potential SCO behaviour in the solid state in more detail, magnetic susceptibility measurements on a single crystal were performed (Figure 6.26). For the zero field cooled (ZFC) data (in black), the sample was cooled prior to the measurement from 300 to 5 K without applying an external field. The data were measured under application of an external field of 2 T while the sample was warmed up to 300 K again. A cooling down while an external field of 2 T is applied and measuring of the magnetisation (field cooled cooling, FCC) is represented by the blue curve and the corresponding measurement during warming up with an external field of 2 T (field cooled warming, FCW) resulted in the red data points. The magnetisation data show a SCO behaviour of **4r** with a hysteresis, which is typical behaviour for solid SCO phenomena.[118] The SCO temperature for cooling down is 124 K while it is 155 K for warming up. Furthermore, the results confirm that the crystal structure of **4r** measured at 200 K is a HS complex.

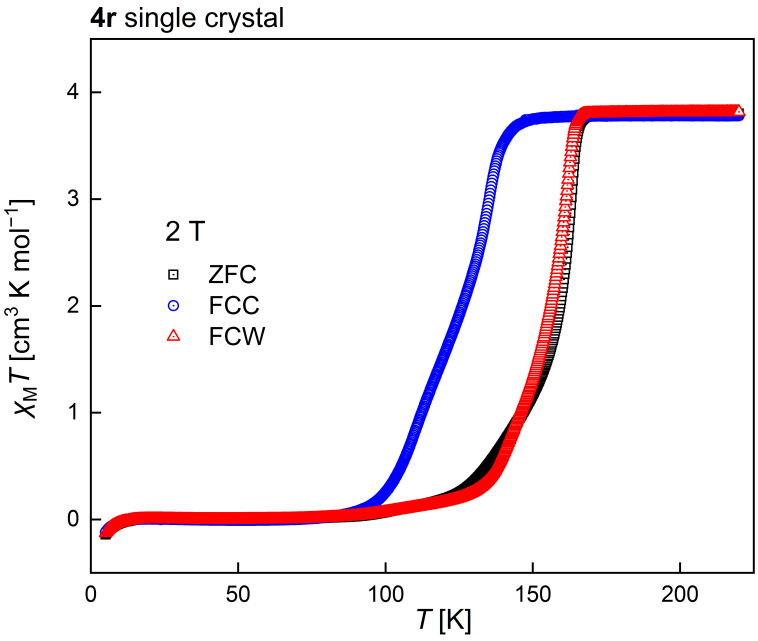

Figure 6.26: Molar susceptibility vs. temperature data obtained by magnetic susceptibility measurement of a single crystal of **4r**.

6.2.4 Trends & Context for Complexes of NQu_3 (4) in the Solid State

As far as the spin state of the solid complexes is concerned, a general trend is discernible. Complexes with nitrile co-ligands (**4a**, **4j** & **4q**), which have a $\{N_6\}$-coordination sphere, have overall shorter Fe – N bond lengths (< 2 Å) consistent with a LS species. In this work, only three structures of this type were obtained. All thirteen complexes with mixed donor set-ups ($\{N_5X\}$, $\{N_4X_2\}$ & $\{N_4X\}$) go along with elongated Fe – N bond lengths (> 2 Å) and were assigned as HS species. For the bis(acetonitrile) complex **4q**, no temperature-dependent change in the Fe – N bond lengths could be measured but for the bis(thiocyanato) complex **4r**, the magnetisation data shows a temperature-dependent SCO behaviour, which is usually associated with a change in Fe – N bond lengths.

Overall, these results are in line with other reported complexes that have tetradentate *N*-donor ligands coordinating in a tripodal fashion forming 5-membered chelate rings (Table 6.18). For bis(triflato) species, 24 structures are listed in the CSD, and they all have average bond lengths longer than 2.0 Å.[58] This is the typical range for HS species and consistent with the complexes synthesised in this work. The only two mixed co-ligand species reported with acetonitrile and triflate show Fe – N bond lengths over 2.0 Å indicating HS species, which was also found in this work for **4b**. Most of the reported bis(acetonitrile) complexes have shorter Fe – N bond lengths (< 2 Å) like the three complexes with two nitrilic co-ligands in this work. The only deviation in the reported complexes are complexes with ligands that have sterically demanding substituents in the alpha position to the pyridine donor: ^{Me}PyTACN, 6-Me$_3$TPA & 6-Ph-TPA. These substituents hinder shorter Fe – N bond lengths and the average bond lengths are longer than 2.0 Å. In addition, a temperature dependent SCO behaviour was reported for the complex with the ^{Me}PyTACN ligand (CSD refcode: MIPMEF, MIPMEF01).[90]

The detailed study on the coordination behaviour of iron(II) complexes with TPA by Diebold and Hagen reported bis(triflato) and bis(acetonitrile) complexes which is in line with the results obtained in this work.[138] However, they crystallised two complexes which were coordinated by two TPA ligands each ($\{N_6\}$ and $\{N_8\}$). For **4**, such species were not observed. One reason for this could be the much more rigid backbone of **4** compared to TPA, which may not be flexible enough to allow the coordination of two ligands of **4** with four donors each or outward rotation of two donors and coordination of three donors per ligand. In contrast, Diebold and Hagen did not observe any mixed co-ligand species. These species were only crystallised by Mandon and co-workers and the Fiedler group.[235,250]

A major difference between the study of Diebold and Hagen and this work is that they obtained different complex species selectively by changing parameters such as solvent, counterion or stoichiometry. This is contrasting the high number of coordination isomers obtained with ligand **4** for similar or identical reaction conditions. Especially, in coordinating solvents such as acetonitrile, propionitrile ot methanol two or more coordination isomers

Table 6.18: List of Fe – N bond lengths from bis(acetonitrile), bis(triflato) and mixed co-ligand complex crystal structures. The data was taken from the CSD[58] (03.05.2023).

Complex Cation/Molecule	Compounds (CSD Refcode)	T [K]	Ø Fe – N [Å]	References
$[FeL(MeCN)_2]^{2+}$	EBORIW	173	1.974	[86]
	EBOROC	173	1.957	[86]
	EFEWES	100	1.979	[247]
	IBEPUD	296	1.966, 1.960	[244]
	NELGUG	173	1.955	[138]
	NELGUG01	100	1.958	[260]
	RUFYOG	172	1.947	[245]
	RUFYOG01	173	1.965	[138]
	WAKNAB	100	1.960	[250]
	LAMGEL	173	2.182	[261]
	MIPMEF	300	2.196*	[90]
	MIPMEF01	100	2.009*	[90]
	RUFYUM	172	2.196	[245]
$[FeL(OTf)(MeCN)]^{+}$	TEKWUD	173	2.178	[235]
	WAKNEF	100	2.168	[250]
$[FeL(OTf)_2]$	CIRTOO	298	2.194	[249]
	DAGJOO	100	2.155	[121]
	EBORUI	293	2.202	[86]
	ECIZIC	130	2.183	[262]
	EFEWAO	100	2.252	[247]
	FISNIG	150	2.229	[251]
	FOXROB	173	2.204	[97]
	MIPKIH	100	2.213	[90]
	MIPKON	150	2.194	[90]
	MIPKUT	100	2.202	[90]
	MIPLAA	300	2.198	[90]
	MIPLEE	300	2.198	[90]
	MIPLII	100	2.200	[90]
	MIPLOO	100	2.206	[90]
	MIPLUU	298	2.224	[90]
	MIPMAB	100	2.213	[90]
	NELGAM	173	2.178	[138]
	PEPXAL	120	2.176	[263]
	PERVUF	173	2.217	[246]
	PIVCED	100	2.213	[248]
	TEKXAK	173	2.213	[235]
	TEKXEO	173	2.194	[235]
	TUVLEB	173	2.219	[264]
	VAVMOV	203	2.204	[236]

*SCO phenomenon in solid state.

were observed. The change of the counterion had the biggest impact on the crystallising species, as most coordination isomers were observed in syntheses involving triflate salts.

6.2.5 Summary of Complexes of Ligand 4 in the Solid State

A variety of complexes of ligand **4** and iron triflate could be crystallised from acetonitrile solutions. However, the synthesis is neither very selective (coordination isomers) nor are the crystals stable when removed from their mother liquor. Although crystallisation at lower temperatures resulted in a reproducible species, this is very sensitive to residual solvent after removal of the mother liquor. The use of different solvents than acetonitrile enabled the crystallisation of even more complex species. Overall, more different species with ligand **4** could be crystallised than with previous ligands from the TPA family. In contrast to the multitude of species in the solid state, the Mößbauer data showed a single defined species in acetonitrile solution, so the behaviour of these complexes in solution is discussed in detail in the following section.

6.3 Iron Complexes of NQu_3 (4) in Solution

In solution, the issue regarding the co-ligands depends strongly on the solvent choice. If the solvent is weak to non-coordinating like dichloromethane, species with triflate anions as co-ligands are expected. Acetonitrile instead is a moderately coordinating solvent. Weaker coordinating anions such as triflate, exhibiting a weak ligand field, are replaced by stronger field acetonitrile ligands if it is the main solvent.[90,121,126,235–237]

6.3.1 Solution Behaviour in Acetonitrile

UV/Vis Spectroscopic Measurements

UV/Vis spectroscopic measurements of 1 : 1 mixtures of $Fe(OTf)_2 \cdot 2\,MeCN$ and ligand **4** show a main species with absorption bands at 295 and 460 nm formed within seconds. This indicates a rapid complex formation. The species formed is stable under inert conditions, as the UV/Vis spectra show no significant changes within 16 h (Figure 6.27).
Lowering the temperature leads to a gradual change of the UV/Vis spectrum. In the range between 250–600 nm, three isosbestic points (265, 305 and 370 nm) occur which indicates the shift of an equilibrium between two species (Figure 6.28). Since LS species usually show more intense absorptions than the HS counterparts, this temperature-dependent absorption behaviour is typical for spin switching behaviour in solution.[90,126]
The species in solution is presumably a bis(acetonitrile) species. This was confirmed by repeating the series of UV/Vis spectroscopic measurements at the same temperature intervals with $[Fe(MeCN)_6](BF_4)_2$ and **4**. The series of spectra are identical within the accuracy of the method (Figure 6.29). A coordination of the counteranion would drastically change the absorption. This can be forced by using a non-coordinating solvent like DCM resulting in spectrum that misses the absorption at 460 nm completely (Figure 6.36, discussed in

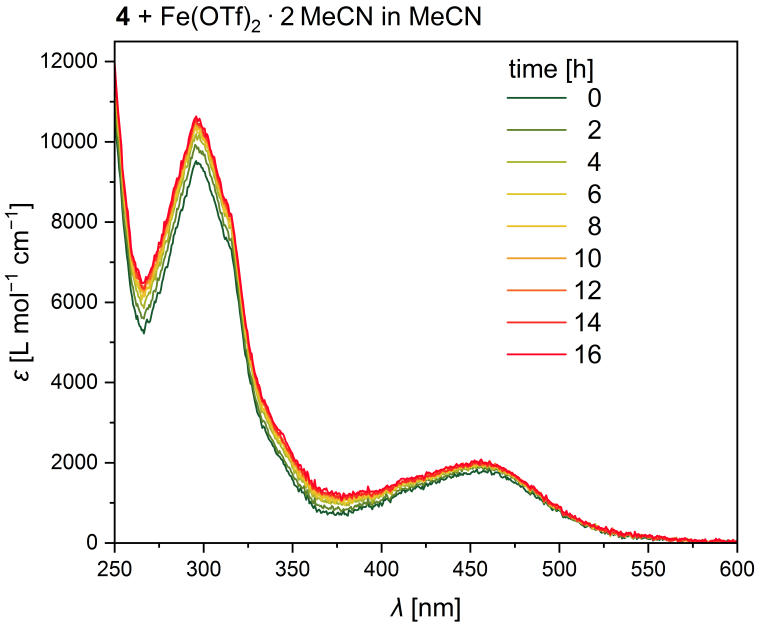

Figure 6.27: UV/Vis spectra of **4** and $Fe(OTf)_2 \cdot 2\,MeCN$ in MeCN (*in situ* complex formation) from 0 up to 16 h.

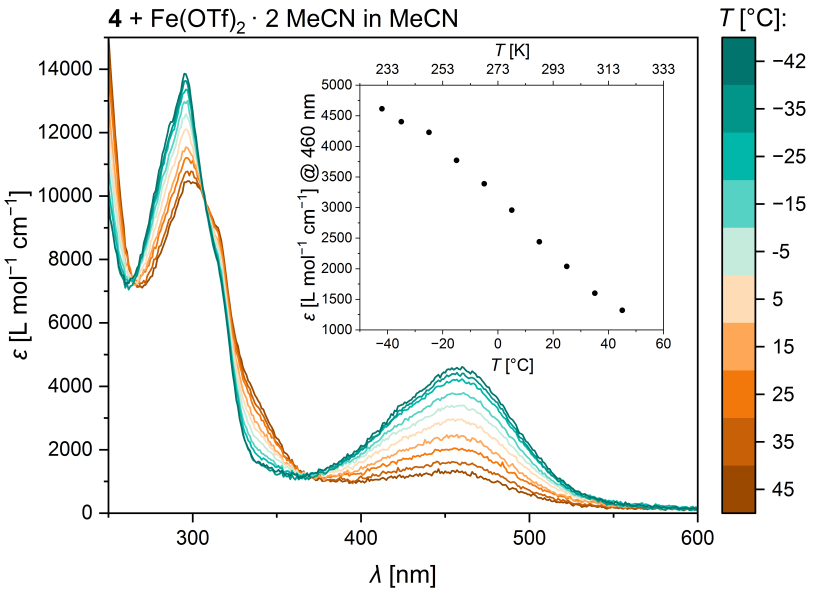

Figure 6.28: UV/Vis spectra of **4** and $Fe(OTf)_2 \cdot 2\,MeCN$ in MeCN at different temperatures. Inset: temperature-dependent change of absorption at 460 nm.

subsection 6.3.2 below). Thus, the dominant species in an acetonitrile solution has to be the bis(acetonitrile) complex.

This is consistent with previous results for similar complexes in acetonitrile solution in contrast to the solid state results, which revealed all three possibilities regarding the co-ligands.[90,121,235,236] In addition, the reversibility of the absorption changes was also verified during this measurement series (Figure 6.30). Under ideal circumstances, a complete series of measurements should show saturation of the absorption at both low and high temperatures in the form of an inverse S-shape curve, indicating full conversion between the two

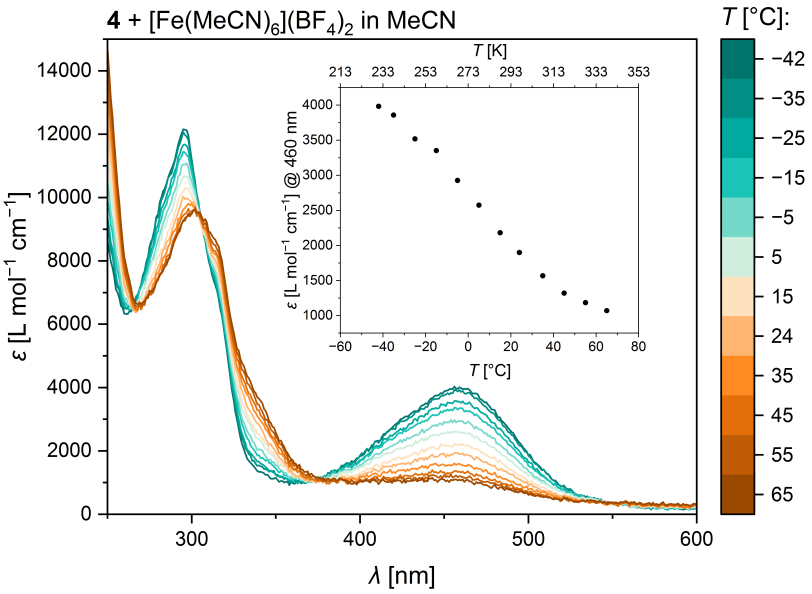

Figure 6.29: UV/Vis spectra of **4** and $[Fe(MeCN)_6](BF_4)_2$ in MeCN at different temperatures. Inset: temperature-dependent change of absorption at 460 nm.

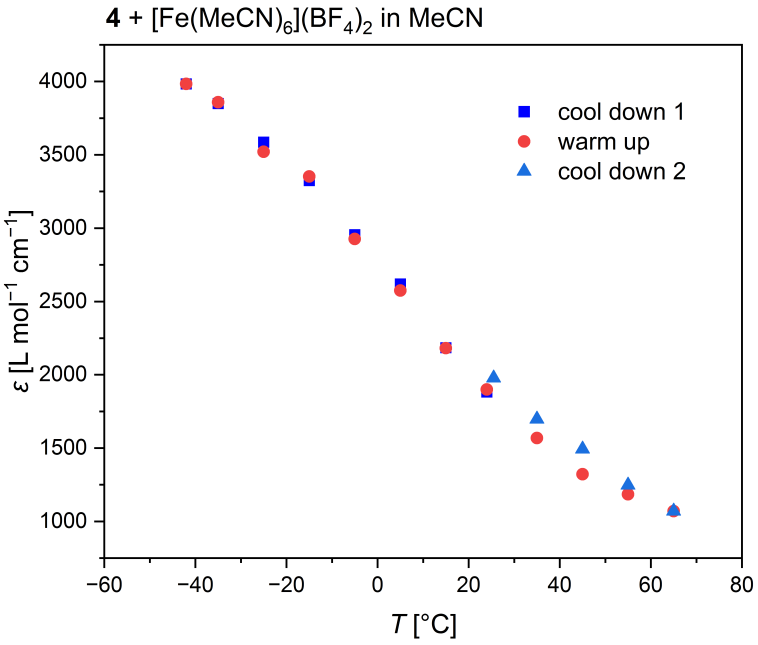

Figure 6.30: Extinction coefficient vs. temperature extracted from UV/Vis spectra of **4** and $[Fe(MeCN)_6](BF_4)_2$ in MeCN at different temperatures; "OTf-free"-conditions.

species. In the measurements which were carried out, these plateaus could not be reached due to the limited temperature range of liquid acetonitrile.

The temperature-dependent absorption changes can be fitted analogously to the variable temperature data obtained in section 5.3 for **3a** in MeCN. For the performed temperature-dependent UV/Vis measurements with complexes of ligand **4**, the thermodynamic parameters can only be estimated roughly because only the straight middle part of the inverse S-shaped curve could be measured. Calculation details can be found in subsection 9.1.4 and

the plotted fits are shown in Figure A.11 and Figure A.12 in the Appendix. The fit of both temperature-dependent UV/Vis spectroscopic measurements in acetonitrile delivers values for the thermodynamic parameters ΔH and ΔS in the same range ($\Delta H \approx 25 - 26\,\mathrm{kJ\,mol^{-1}}$, $\Delta S \approx 89\,\mathrm{J\,mol^{-1}\,K^{-1}}$, Table 6.19), respectively.

Table 6.19: Overview of thermodynamic parameters ΔH, ΔS and $T_{1/2}$ obtained through fitting experimental data from the temperature-dependent UV/Vis spectroscopic measurements "with OTf" and "without OTf" of the $[LFe(MeCN)_2]^{2+}$ species in MeCN and temperature-dependent magnetic measurement data of **C** in MeCN.

UV/Vis	ε_{LS} [$\mathrm{L\,mol^{-1}\,cm^{-1}}$]	ε_{HS} [$\mathrm{L\,mol^{-1}\,cm^{-1}}$]	ΔH [$\mathrm{kJ\,mol^{-1}}$]	ΔS [$\mathrm{J\,mol^{-1}\,K^{-1}}$]	$T_{1/2}$ [K]
OTf^-	4923 ± 126	0 ± 414*	26 ± 4	89 ± 16	288
$BF_4{}^-$	4283 ± 118	522 ± 189	25 ± 4	89 ± 13	284
SQUID	$(\chi_M T)_{LS}$ [$\mathrm{cm^3\,K\,mol^{-1}}$]	$(\chi_M T)_{HS}$ [$\mathrm{cm^3\,K\,mol^{-1}}$]	ΔH [$\mathrm{kJ\,mol^{-1}}$]	ΔS [$\mathrm{J\,mol^{-1}\,K^{-1}}$]	$T_{1/2}$ [K]
cool-down (345–204 K)	1.79 ± 0.01	5.25 ± 0.04	20.5 ± 0.4	71 ± 2	289
warm-up (235–345 K)	1.82 ± 0.03	5.12 ± 0.05	21.1 ± 0.8	73 ± 3	290

*ε_{HS} was constrained to ≥ 0. Please note that the absolute values of $(\chi_M T)_{LS}$ and $(\chi_M T)_{HS}$ are imprecise due to difficulties with the diamagnetic correction and the potential presence of additional iron(III) HS impurities.

This is in line with typical values for SCO behaviour in solution ($\Delta H < 30\,\mathrm{kJ\,mol^{-1}}$, $\Delta S < 130\,\mathrm{J\,mol^{-1}\,K^{-1}}$) without dissociation and association. The latter would result in higher values ($\Delta H > 30\,\mathrm{kJ\,mol^{-1}}$, $\Delta S > 120\,\mathrm{J\,mol^{-1}\,K^{-1}}$).[238,239] This is another indication that no further (co-)ligand exchange takes place (CISSS) when the temperature is varied and that the $[L(Fe)(MeCN)_2]^{2+}$ species is responsible for the temperature dependent SCO in acetonitrile. The SCO temperature $T_{1/2}$ provides information about the point at which there is a 50 : 50 mixture of HS and LS species. With 284–288 K the SCO temperature is just below room temperature. This is relatively close to the target SCO temperature centred at room temperature, which is discussed as ideal for possible applications of SCO compounds.[116,265] However, the SCO should also be fully observable within a reasonable range.[266] This is not the case for the species with **4** in solution.

Magnetic Susceptibility Measurements

For the magnetic susceptibility measurement of a complex in acetonitrile solution compound **C** was dissolved and kept in a sealed quartz glass tube to maintain inert conditions. The measured magnetic moment and the molar susceptibility ($\chi_M T$) in a temperature range of 150–345 K are plotted in Figure 6.31.

The first indication that the species is undergoing a gradual spin crossover is seen in the raw data obtained directly from the instrument, as measured. The molar susceptibility was

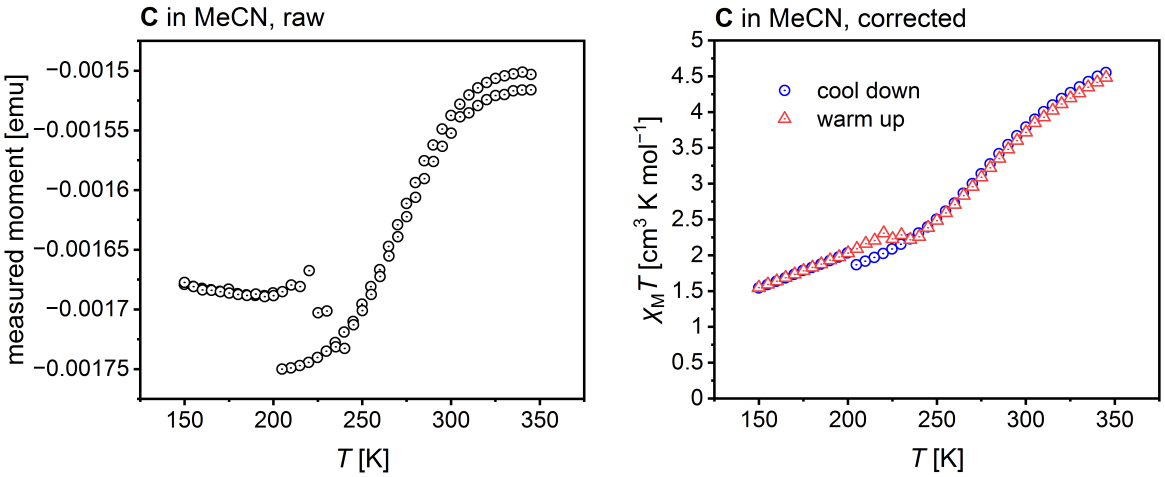

Figure 6.31: Measured moment vs. temperature data obtained by magnetic susceptibility measurement of **C** in MeCN under inert conditions (left) and molar susceptibility vs. temperature data obtained due to diamagnetic correction (see subsection 9.1.5) of data shown left (right).

calculated from this data which was corrected for the diamagnetism of the solvent and ligand (details see subsection 9.1.5). The susceptibility data show discontinuities for the cooling process at 204 K and for the warming at 220–250 K, respectively. It is crucial to note that the apparent hysteresis is not a direct result of the SCO process, but rather reflects the solidification and melting of the solvent. At 345 K, the $\chi_M T$ value of 4.6 $cm^3\,K\,mol^{-1}$ is too high for an iron(II) HS complex ($S = 2$, spin-only value 3.0 $cm^3\,K\,mol^{-1}$).[267] For the interpretation of the data, it must be kept in mind that the solution measurements are extremely sensitive to the slightest changes in diamagnetic correction and therefore no absolute statements can be made about the completeness or incompleteness of the SCO. Various ways of correcting for the diamagnetic contribution of the solvent were tried, and the details are given in subsection 9.1.5. The lowest $\chi_M T$ value of 1.54 $cm^3\,K\,mol^{-1}$ reached at 150 K is not in line with a pure LS state. For this, lower temperatures would be needed like in the Mößbauer spectroscopy at 80 K which revealed a pure LS compound in frozen acetonitrile solution. Besides the discontinuities (204–235 K), the cooling and warming process have the same behaviour. The data is consistent with a SCO behaviour where no complete transformation into LS or HS species can be observed in the investigated temperature range, which would be consistent with the data from optical spectroscopy. Due to the iron(III)-HS contamination in the Mößbauer spectrum (Figure 6.13), it cannot be excluded that some iron(III) species is present in the magnetic measurements of the solution.

By fitting the data analogously to the UV/Vis data, the thermodynamic parameters of the SCO can be calculated. The fitting of the data was only performed for the liquid solution (cool-down 345–204 K; warm-up 235–345 K) and delivers results similar to the optical spectroscopy ($\Delta H = 20.5 \pm 0.4,\ 21.1 \pm 0.8$ kJ mol^{-1} & $\Delta S = 71 \pm 2,\ 73 \pm 3$ J mol^{-1} K^{-1}, respectively). The SCO temperatures of 289 K and 290 K are also in a similar range.

High-Spin Fraction in Acetonitrile

The thermodynamic parameters of the SCO can be used to calculate the fraction of HS species (γ_{HS}) at different temperatures (Equation 5.1 in subsection 5.3.1). γ_{HS} values obtained from UV/Vis spectroscopy and magnetic measurement data are shown in Figure 6.32.

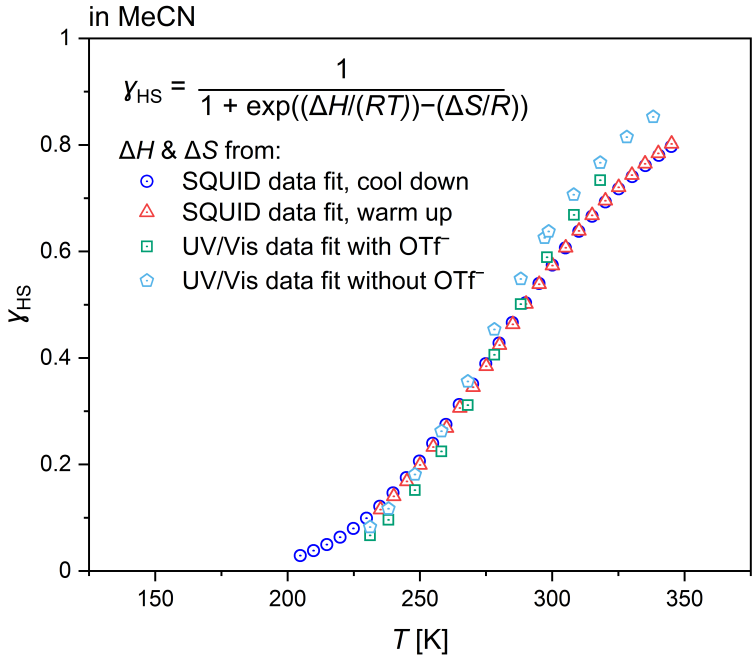

Figure 6.32: High-spin fraction γ_{HS} in MeCN at different temperatures for UV/Vis and magnetometry data calculated from fitted parameters.

The γ_{HS} value is similar for both methods with the largest deviations towards higher temperatures. Taking into account the possible measurement errors, a good agreement is achieved between the different methods. Although a pure LS state was not achieved in the probed temperature range, the Mößbauer spectra of compound **C** in frozen acetonitrile (Figure 6.13) discussed earlier indicate that further cooling to 80 K would ultimately lead to a complete conversion to the LS state.

VT-NMR in Acetonitrile

The temperature-dependent change of a species in solution can be followed by NMR spectroscopy at variable temperature (VT), especially if a change from a diamagnetic (iron(II), LS) to a paramagnetic species (iron(II), HS) is expected. For the experiment, compound **C** was dissolved under inert conditions in deuterated acetonitrile and spectra were recorded in a temperature range between +30 °C and −40 °C. Signals with a chemical shift up to 36 ppm are present in the ^{1}H-NMR spectrum at +30 °C (Figure 6.33, left). In the spectrum at −40 °C the signals are upfield shifted. To investigate if these signals are the same as in the spectrum at +30 °C, a gradient measurement from −40 °C and +30 °C (2 °C/min, spectra every 30 s) was performed, so that the temperature dependent development of the signals

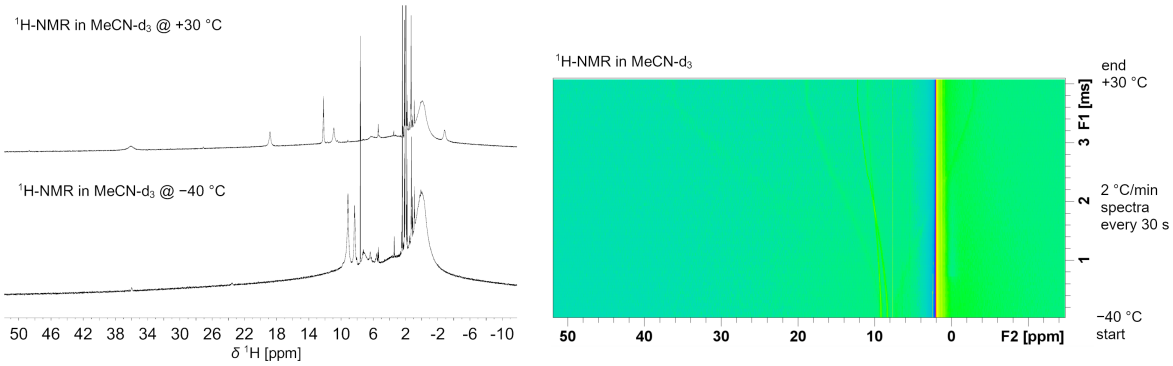

Figure 6.33: ^{1}H-NMR spectra of **C** in MeCN-d$_3$ at −40 °C (bottom, left) and +30 °C (top, left). Gradual ^{1}H-NMR measurement between −40 °C and +30 °C (2 °C/min, spectra every 30 s; right).

can be followed (Figure 6.33, right). This also shows that two signals in the range of 10 ppm change position with temperature changes. The difference in signal positions at high and low temperatures match a species with a smaller fraction of HS species. The crossing of signals during the temperature change was observed for iron(II) complexes with SCO behaviour before.[138] Overall, the ^{1}H-NMR spectra are in line with optical spectroscopy and magnetic susceptibility data.

To follow the temperature-dependent magnetic changes in the sample with the Evans method, the NMR tube contained a capillary with pure deuterated acetonitrile. It was not possible to clearly identify the second acetonitrile signal, which is needed for this method. ^{19}F-NMR spectroscopy can be used to identify coordinated or uncoordinated triflate ions as triflate has only one signal in the ^{19}F-NMR spectrum and the chemical shift is significantly different for both variants. Uncoordinated or free triflate is expected to show signals in the area of −80 ppm and coordinating triflate around −20 ppm.[235,237] Single peaks with chemical shifts of −78 ppm (room temperature) and −80 ppm (−40 °C) were obtained, which indicate a bis(acetonitrile) with non-coordinating triflate anions as the main species in acetonitrile at the probed temperatures (Figure 6.34).

6.3.2 Solution Behaviour in Dichloromethane

The solution behaviour in non-coordinating dichloromethane is expected to be different than in coordinating acetonitrile. Although small amounts of acetonitrile may be present during synthesis because of the $Fe(OTf)_2 \cdot 2\,MeCN$ salt, it is expected that a bis(triflato) species dominates. Unlike in acetonitrile, the formation of a complex species with NQu_3 and $Fe(OTf)_2 \cdot 2\,MeCN$ in dichloromethane is quite slow. The process can be followed by UV/Vis spectroscopy (Figure 6.35) and the spectra show a prominent absorption of the ligand at 380 nm in the beginning. In advance, the mixture of NQu_3 and $Fe(OTf)_2 \cdot 2\,MeCN$ in dichloromethane was stirred for 4 h to give a clear stock solution. The formation of the complex band at 305 nm and parallel decay of the ligand band at 380 nm takes approx. one day for full conversion.

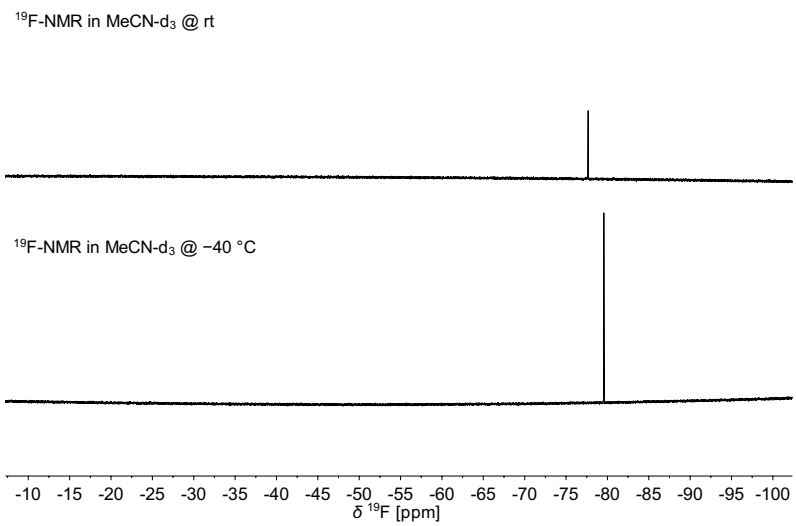

Figure 6.34: ^{19}F-NMR spectra of **C** in MeCN-d$_3$ at rt (top) and −40 °C (bottom).

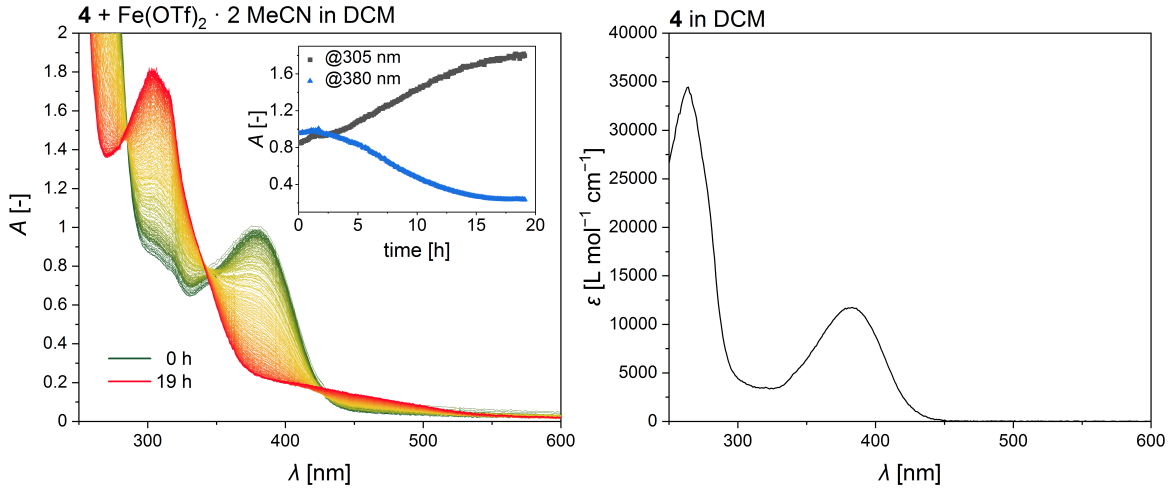

Figure 6.35: UV/Vis spectra of **4** and Fe(OTf)$_2$ · 2 MeCN in DCM over 19 h (0 h, green–19 h, red) showing the slow complex formation in DCM (+4 h stirring before UV/Vis; left). The absorption at 380 nm is identical to the one of the free ligand **4**. UV/Vis spectrum of **4** in DCM (right).

To exclude an influence of the acetonitrile in the Fe(OTf)$_2$ · 2 MeCN salt on the species formed in dichloromethane, an experiment with exclusion of acetonitrile was performed. Therefore, a salt metathesis was chosen as reaction route, where from an *in situ* formed chlorido complex the anions were exchanged with Ag(OTf). After removal of the AgCl precipitate, the solution contained a species with identical UV/Vis spectroscopic features as the species starting from Fe(OTf)$_2$ · 2 MeCN after one day (Figure 6.36). The UV/Vis spectra of this species were measured at different temperatures, but after correction for density, no significant changes in absorbance were visible. Since the species appears to be independent of acetonitrile, a bis(triflato) species is most likely. This is also in line with the expectations and results of other groups for similar complexes, as well as with the solid state results of triflate species obtained in dichloromethane.[235]

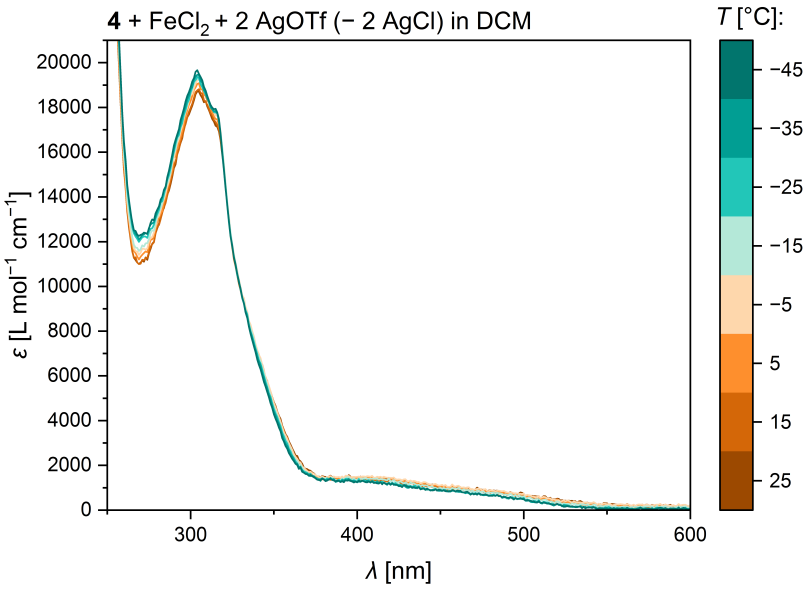

Figure 6.36: UV/Vis spectra of complex formed from **4** and $FeCl_2$ via salt metathesis with Ag(OTf) in DCM at different temperatures.

VT-NMR in Dichloromethane

^{1}H-NMR spectra in deuterated dichloromethane were measured of dissolved compound **C**. At room temperature, peaks show chemical shifts of e.g. 48 or 25 ppm (Figure 6.37).

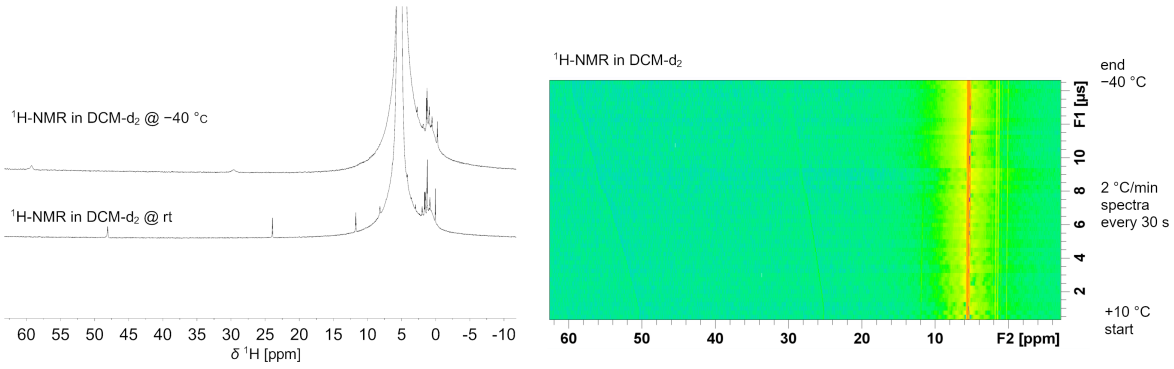

Figure 6.37: ^{1}H-NMR spectra of **C** in DCM-d_2 at rt (bottom, left) and −40 °C (top, left). Gradual ^{1}H-NMR measurement between +10 °C and −40 °C (−2 °C/min, spectra every 30 s; right).

At −40 °C, these signals show line broadening and further downfield shift to 59 and 30 ppm, respectively. This behaviour is common for paramagnetic complexes where the paramagnetic shift follows the Curie law and indicates a HS species to be present over the probed temperature range. Moreover, this is in line with the results obtained from optical spectroscopy.

The ^{19}F-NMR spectra of the species in dichloromethane at different temperatures show a peak in the range of −23 up to −12 ppm which shows line broadening for the lower temperatures (Figure 6.38). This range of chemical shifts is typical for coordinating triflate anions further supporting the hypothesis of a bis(triflato) species in dichloromethane.[234,237]

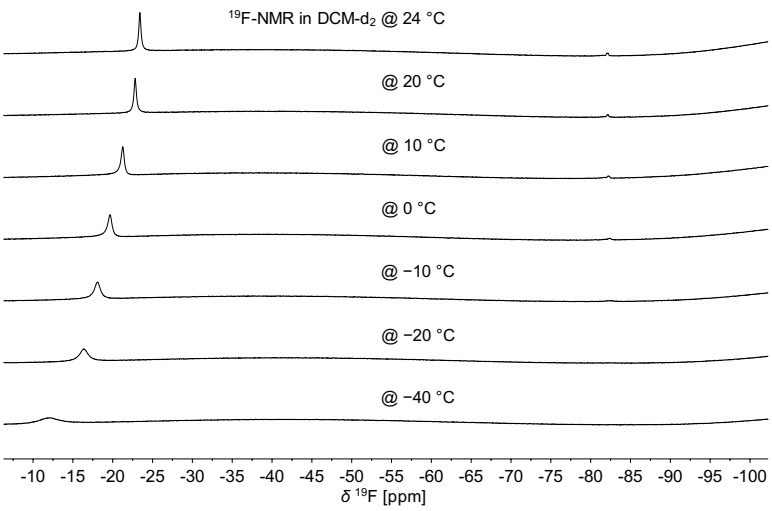

Figure 6.38: ^{19}F-NMR spectra of **C** in DCM-d$_2$ at different temperatures.

6.3.3 UV/Vis Spectroscopic Measurements of Dissolved Complexes

Compound **C** was dissolved in acetonitrile or dichloromethane, respectively, and the resulting spectra were compared to the *in situ* variants of the species in the corresponding solvent (Figure 6.39).

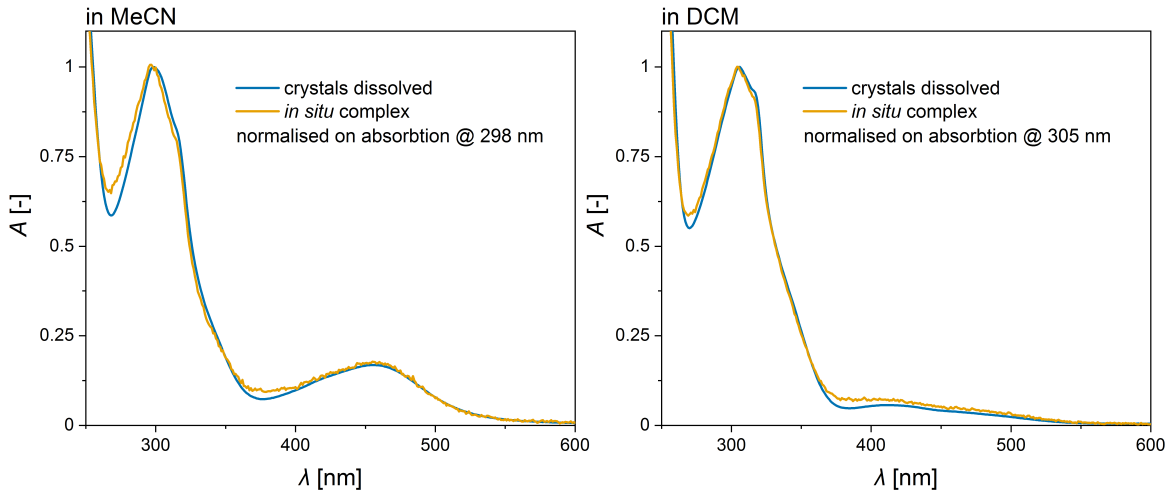

Figure 6.39: Crystals of **C** dissolved in MeCN (lef) and in DCM (right) compared to the corresponding *in situ* experiments normalised on absorption at 298 nm for MeCN and 305 nm for DCM.

The spectra were normalised for better comparison. Although compound **C** is most likely a triflate based species "[Fe(NQu$_3$)(OTf$_2$)]", the spectra of the dissolved crystals are almost identical with the *in situ* species. This indicates that there is a solvent-depending exchange of co-ligands in solution regardless which co-ligand variant was present in the solid state. The preference for the nature of co-ligands for each solvent is the same for dissolved compound and *in situ* experiment, respectively. Similar solvent-dependent co-ligand exchange is documented in literature.[138]

6.3.4 Solution Behaviour with Changing Solvent

The difference between the species in acetonitrile and dichloromethane are the (non-)coordinating triflate anions. Since their coordination behaviour can be easily followed by ^{19}F-NMR spectroscopy, the question arises whether the species can be converted into each other in solution by changing the solvent composition. To a solution of compound **C** in deuterated dichloromethane, deuterated acetonitrile was added stepwise and fluorobenzene was used as an internal reference. The corresponding spectra are shown in Figure 6.40.

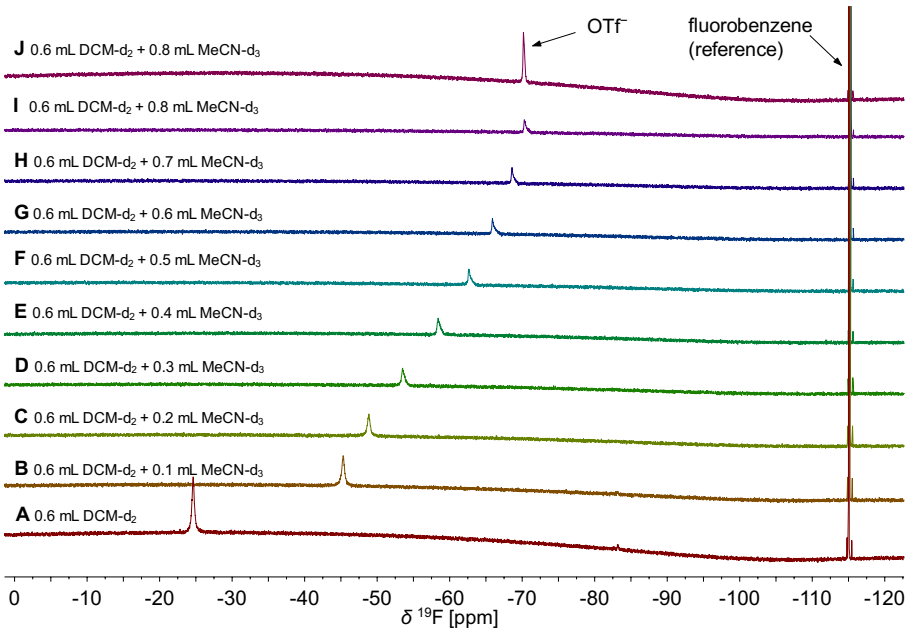

Figure 6.40: ^{19}F-NMR spectra of A: compound **C** in DCM-d_2 with fluorobenzene as internal reference. B–I: stepwise addition of 0.1 mL of MeCN-d_3. J: same sample composition as I, but measurement with locking and shimming.

With each addition, the signal in the ^{19}F-NMR spectrum is shifted from values for coordinating triflate (approx. −25 ppm) towards the region of non-coordinating triflate (approx. −70 ppm). The value for solely free triflate (−78 ppm in MeCN-d_3) is not reached. For this, possibly further equivalents of deuterated acetonitrile would be needed. The spectra only exhibit one signal, which indicates the triflate exchange process timescale to be faster than the observable of the NMR experiment. The paramagnetic nature of the species at the beginning (A) made proper locking and shimming of the sample impossible. The increasing amount of acetonitrile and the therefore increasing amount of diamagnetic LS complex enabled a proper lock and shim for the last measurement (J). This is expressed in the sharper and more symmetric signal compared to measurement I, which had the same solution composition. Overall, this shows that an interconversion of the two solution species is possible. However, acetonitrile has to be added in a large excess and not stoichiometrically to enable the change of co-ligands. This was also observed for experiments with the $[Fe(OTf)_2] \cdot 2\,MeCN$ salt, as the two acetonitrile molecules per iron showed no effect in non-coordinating solvents.

6.3.5 Summary of the Solution Analyses

The results for the solution studies of triflate-based complexes with ligand **4** are visually summarised in Scheme 6.10.

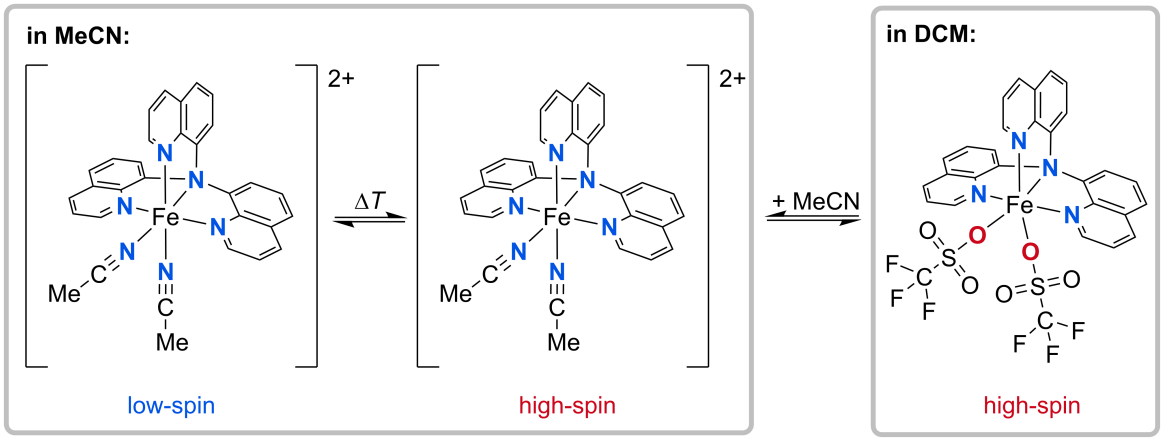

Scheme 6.10: Overview of main species assumed to be present in solution.

Altogether, the solution experiments show a high dependency of the main species on the solvent. In acetonitrile, all results are consistent with a bis(acetonitrile) main species. The bis(acetonitrile) species shows a temperature-dependent SCO, which is incomplete in the temperature range of liquid acetonitrile. Contrary, in dichloromethane the results indicate a bis(triflato) species which is HS for all temperatures. Additionally, the formation of the complex species is fast in acetonitrile and slow in dichloromethane. It is possible to interconvert these species with changing the solvent composition which results in very fast co-ligand exchange equilibria for solvent mixtures. An overlay of UV/Vis spectra of the species in acetonitrile and dichloromethane at 25 °C is shown in Figure A.13 in the Appendix.
SCO behaviour for the {N_6}-coordinated species in acetonitrile is in line with the large number of examples for iron(II) SCO compounds with {N_6}-coordination in the literature.[119,123,127]
Comparable solution behaviour data were obtained for triflate-based iron(II) complexes with TPA as ligand. In acetonitrile, the species was described as a bis(acetonitrile) species showing a temperature-dependent spin-switching behaviour. Consistent with the present work, the use of a non-coordinating solvent leads to a temperature-independent bis(triflato) HS species.[138]

6.4 Attempts of Generating High-Valent Iron-Oxo Species of Complexes of NQu_3 (4)

The strategies for generation of a high-valent iron-oxo species from iron(II) complexes with ligand **4** was different than for the two previous complex systems (Scheme 6.11).

Analogous to literature results with TPA and TQA ligands, the oxidants (2-*t*-butylsulfonyl)iodosylbenzene (sPhIO) and H_2O_2 were additionally tested besides mCPBA.[61,97,236]

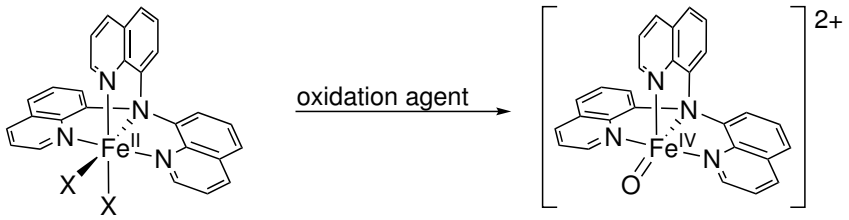

Scheme 6.11: Oxidation of an iron(II) complex with ligand **4** to an iron(IV)oxo species.

6.4.1 UV/Vis Spectroscopy

Oxidation with mCPBA

The addition of mCPBA under aerobic conditions, comparable to complexes with ligands **2** and **3**, results in UV/Vis spectra with a shoulder in the region of 700–750 nm (Figure 6.41).

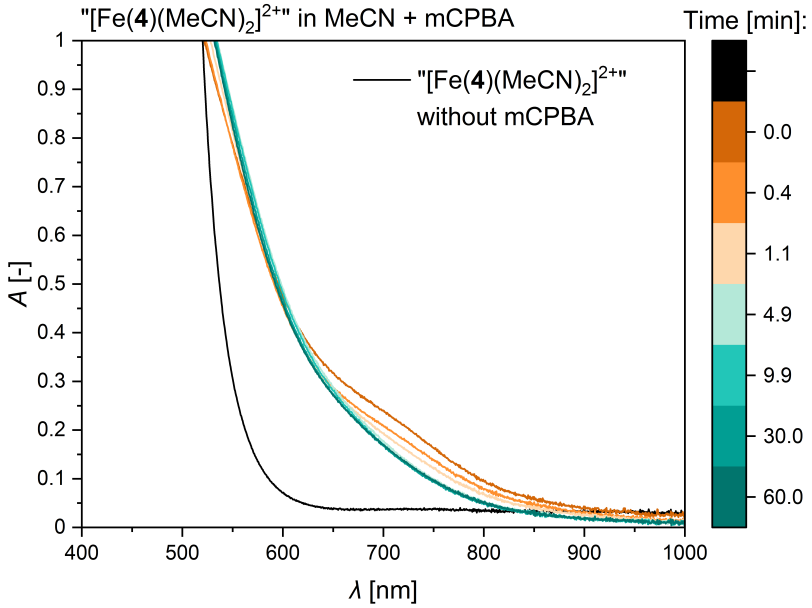

Figure 6.41: Selected UV/Vis spectra of compound **C** in MeCN and subsequent addition of mCPBA.

The shoulder is not very distinct and gets weaker within the first minutes (< 9 min). It is obvious that some oxidation takes place when mCPBA is added, but not much can be said about the species because of the shoulder character of the band. Oxidation with the two other oxidation agents sPhIO and H_2O_2 gave more promising results.

Oxidation with sPhIO

The oxidation with sPhIO under the same conditions resulted in a more distinct UV/Vis band at 708 nm (Figure 6.42). Immediately after the formation of the band, a decay can be observed, which reaches a plateau after about 25 min. This band is a more promising hint for a potential high-valent iron-oxo species. The UV/Vis band of the iron(IV)oxo species of the comparable complex with TPA as ligand shows after oxidation with peroxo acetic acid a band at 724 nm.[61] The TQA complex derivative exhibits bands at 400 (shoulder), 650 and 900 nm after oxidation with sPhIO.[97]

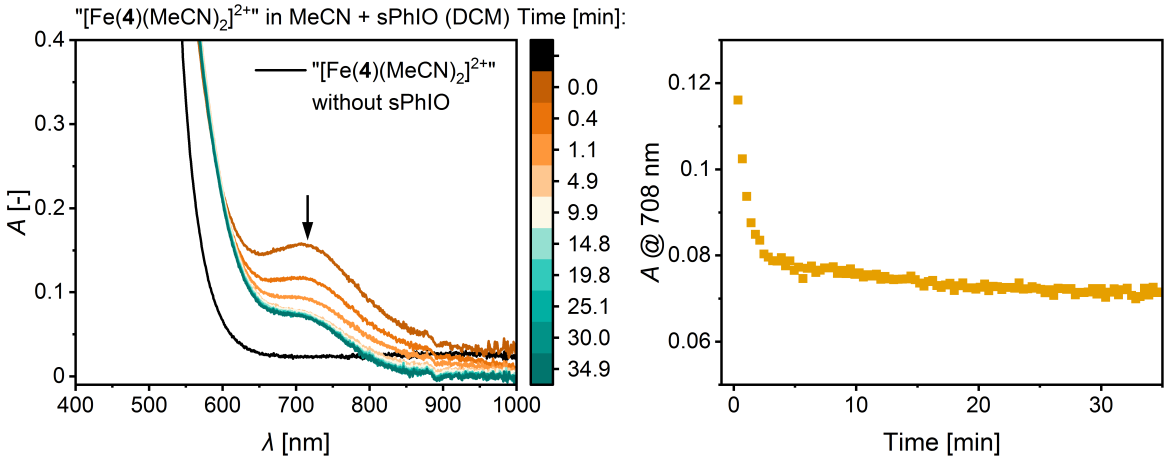

Figure 6.42: UV/Vis spectra of compound **C** in MeCN and subsequent addition of sPhIO in DCM (selected spectra, left). Absorption at 708 nm vs. time (right).

Oxidation with H_2O_2

The second promising UV/Vis spectroscopic result in terms of a high-valent iron-oxo species was obtained with H_2O_2 as oxidation agent. An experiment with compound **C** dissolved in acetonitrile at room temperature shows the formation of a band at 708 nm, which grows within four minutes and with a slight shift to 720 nm (Figure 6.43, left). However, this band shows a more drastic shift to 760 nm within the next 28 minutes (Figure 6.43, right). Afterwards, the band at 760 nm is rising slightly (Figure 6.44). The bands at 720 nm and 760 nm are overlapping so that a separate analysis of the bands is not possible. It is conceivable that a high-valent iron-oxo species is formed first, followed by the formation of a decay species. It is unlikely that the latter is a μ-oxo-bridged dimer as found in crystals of **4g**. Such linear $Fe^{III}-O-Fe^{III}$-dimers show usually no distinct UV/Vis spectroscopic features and the bands are blue shifted for larger $Fe^{III}-O-Fe^{III}$ angles.[268,269] For the related $[Fe^{II}(TPA)(MeCN)]^{2+}$ complex in acetonitrile, the addition of H_2O_2 at −40 °C results in an $[Fe^{III}(TPA)(OOH)]^{2+}$ species (λ_{max} = 538 nm) which decays at room temperature to a proposed $[Fe^{III}_2(\mu\text{-}O)(TPA)_2(OH_2)_2]^{4+}$ species.[270] To identify the two species at 708–720 nm and 760 nm observed in this work, further experiments like ESI-MS are needed.

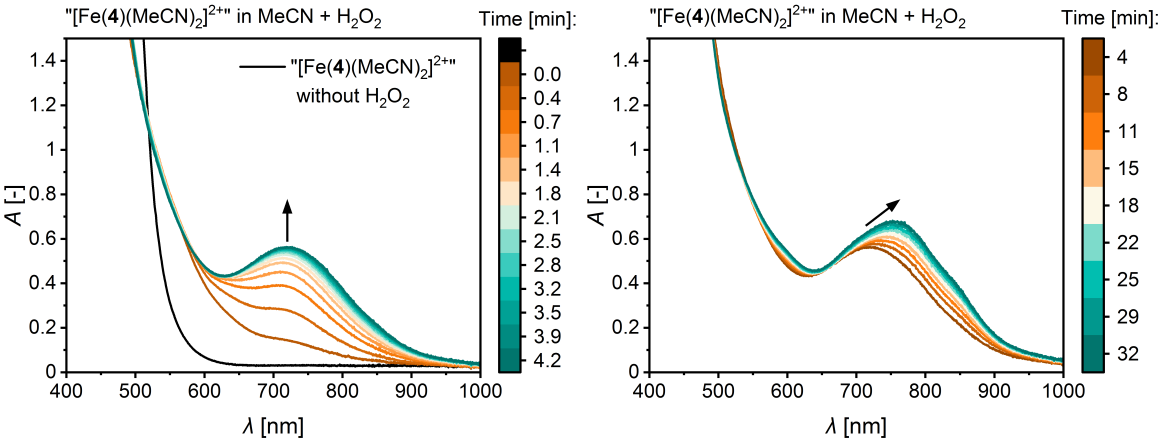

Figure 6.43: UV/Vis spectra of compound **C** in MeCN and subsequent addition of H_2O_2. Rise of absorption band at 708–720 nm in the first 0–4 min (left). Shift of absorption band from 720 to 760 nm between 4 min and 32 min (right).

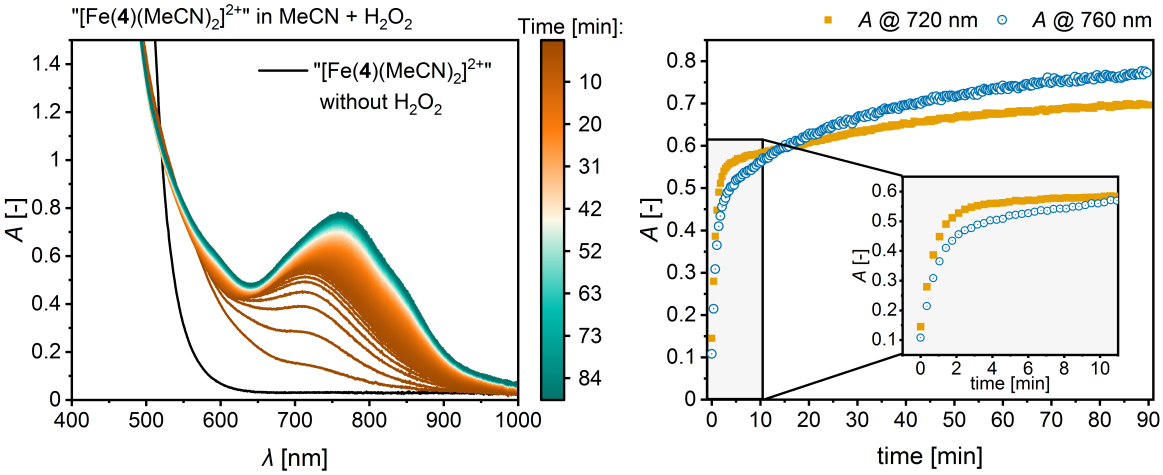

Figure 6.44: UV/Vis spectra of compound **C** in MeCN and subsequent addition of H_2O_2 (total measurement, left). Absorption at 720 nm and 760 nm vs. time (right).

Comparison of Species

Different to the species that was observed after sPhIO addition, which shows a direct decay, the formation of the species obtained from H_2O_2 addition can be observed, before it converts to a second species. This is a indication that the mechanism of oxidation is different for both oxidation agents. It is known that sPhIO as single oxygen donor has a different reaction mechanism as H_2O_2 (see Figure 1.11 in the Introduction).[92]

However, the bands that are occurring shortly (0.4 min) after oxidation with H_2O_2 (first species) or sPhIO are both at 708 nm. For the overlay in Figure 6.45, the absorption of the band from the oxidation with sPhIO had to be multiplied with 2.5. A reason for the much weaker band in the sPhIO experiment could be that the mechanisms seem to be different which could result in different yield for the oxidation reaction. Nevertheless, the quite similar position of the bands could be a hint for the same oxidised species.

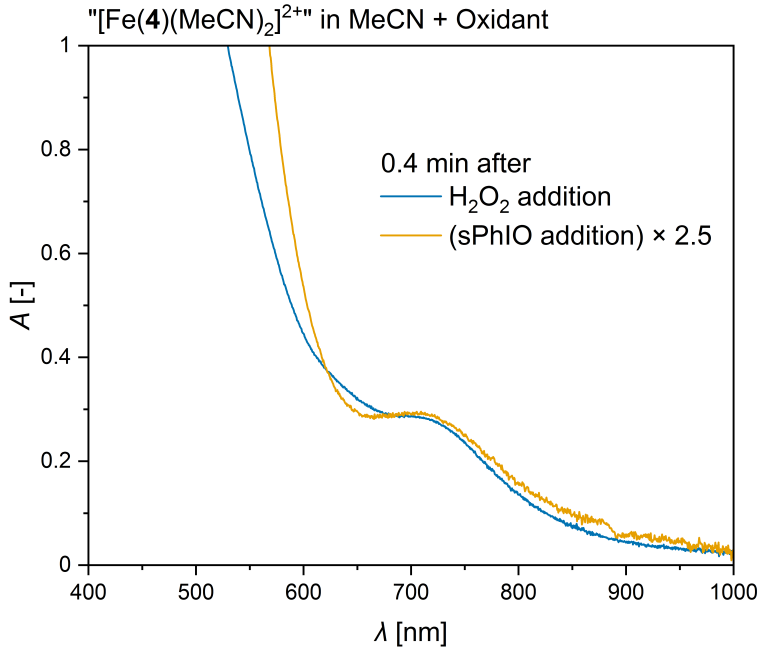

Figure 6.45: Overlay of UV/Vis spectra of compound **C** in MeCN after addition of H_2O_2 (blue, 0.4 min) and sPhIO (orange, 0.4 min).

6.4.2 CSI- & ESI-Mass Spectrometry

To obtain more information about the species seen in the UV/Vis spectroscopic experiments with sPhIO and H_2O_2, these oxidation agents were used in mass spectrometry experiments.

Oxidation with sPhIO

A high resolution CSI-MS at −30 °C in acetonitrile was performed to identify the species found in the UV/Vis spectra. The low temperature was chosen as high-valent iron-oxo species are usually more stable at lower temperatures and there was an immediate decay visible in the UV/Vis spectra. For the measurement, compound **C** was dissolved in acetonitrile and cooled to −30 °C. Then, an acetonitrile suspension of sPhIO was added at −30 °C and the CIS-MS measurement was performed subsequently. The CSI-MS spectrum (Figure 6.46) shows the expected peak for an iron(IV)oxo species at 235 m/z which corresponds to $[Fe^{IV}(\mathbf{4})O]^{2+}$.

Oxidation with H_2O_2

To obtain more information about the two bands identified in the UV/Vis spectra after the addition of H_2O_2, ESI-MS spectra were recorded at room temperature at different times after the H_2O_2 addition. Similar to the development of the bands in the UV/Vis spectra, two time points below 5 min and one time point of 30 min were chosen for the measurement of the spectra (Figure 6.47). All three spectra show signals at similar m/z positions and in all of them a signal at 235 m/z can be identified, which corresponds to $[Fe^{IV}(\mathbf{4})O]^{2+}$.

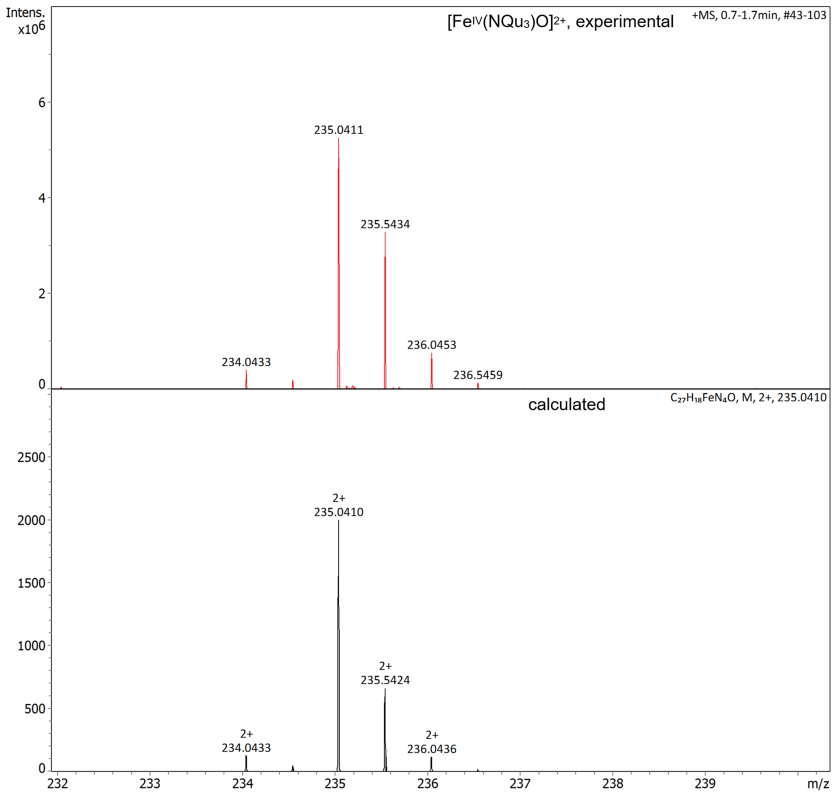

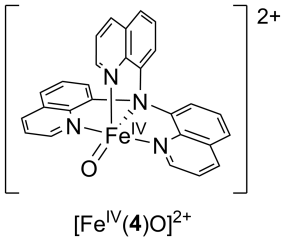

$[Fe^{IV}(\mathbf{4})O]^{2+}$

Figure 6.46: Experimental (top) and calculated (bottom) isotope distribution pattern for $[Fe^{IV}(\mathbf{4})O]^{2+}$ after oxidation with sPhIO.

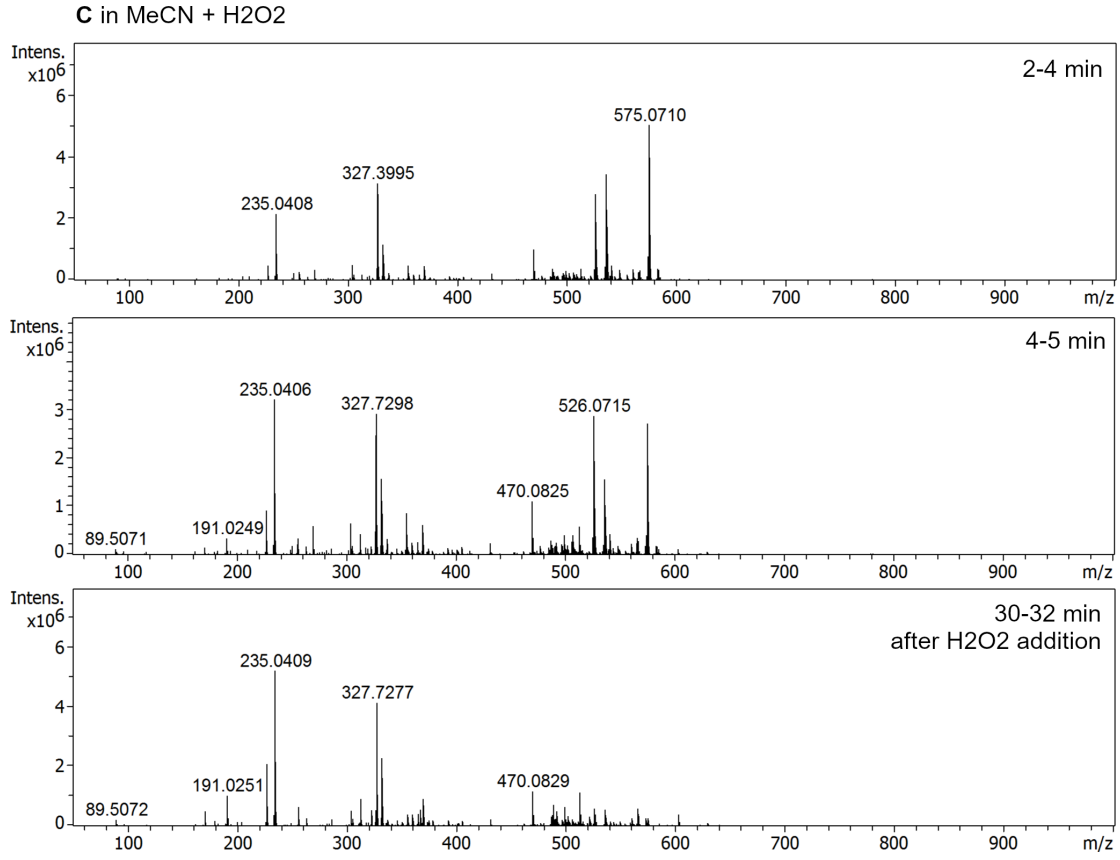

Figure 6.47: Experimental isotope distribution pattern for oxidation of dissolved compound **C** with H_2O_2 at different times after H_2O_2 addition, respectively.

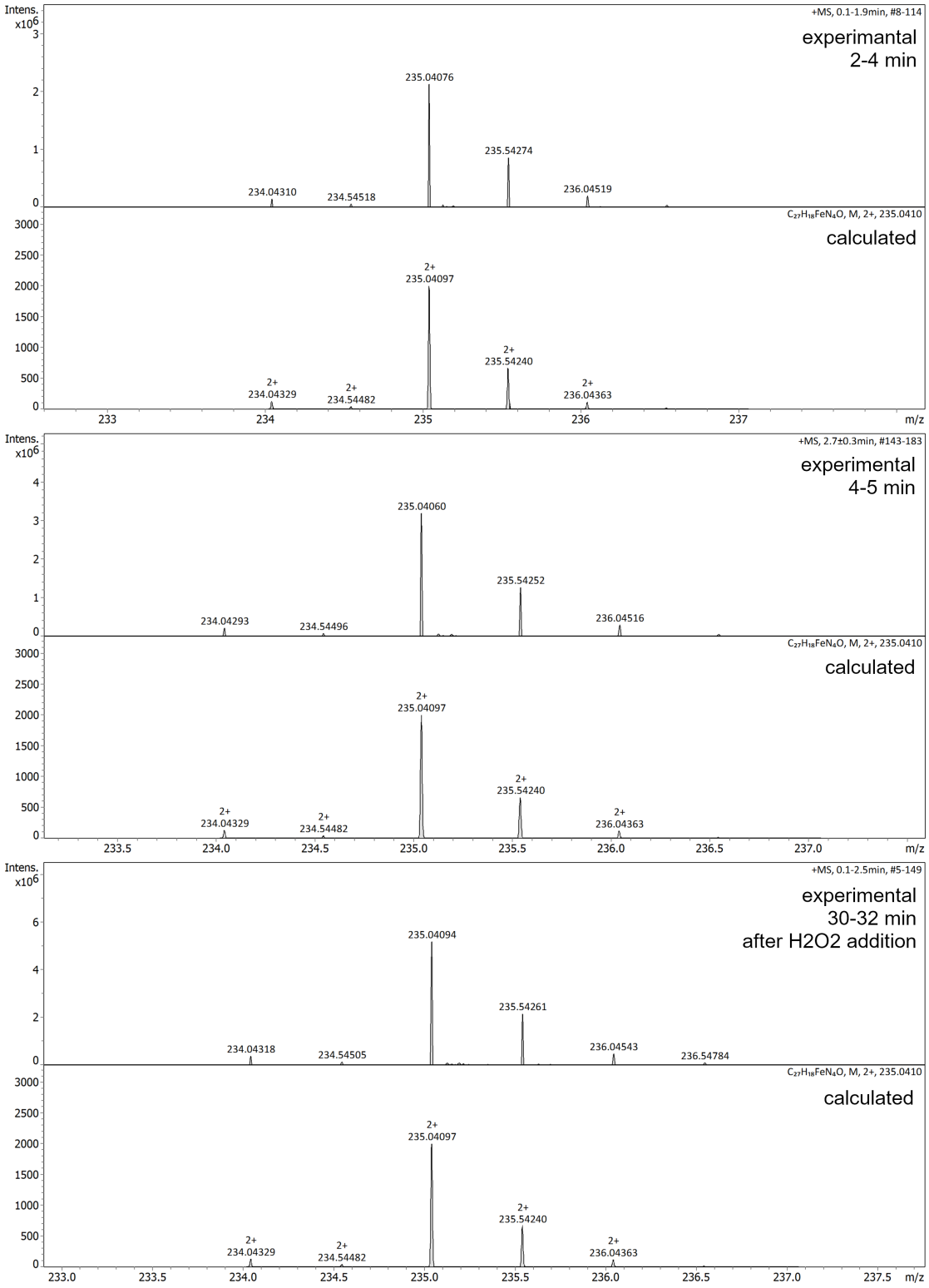

Figure 6.48: Experimental (top) and calculated (bottom) isotope distribution pattern around 235 m/z for $[Fe^{IV}(\mathbf{4})O]^{2+}$ at different times after H_2O_2 addition, respectively.

The isotopic patterns of all three in comparison to the calculated isotopic pattern are shown in Figure 6.48. Taken together, this means that with H_2O_2 as well as with sPhIO the same iron(IV)oxo species can be generated from $[Fe(\mathbf{4})(MeCN)_2]^{2+}$. Furthermore, this indicates that the UV/Vis bands at 720 nm most likely correspond to the $[Fe^{IV}(\mathbf{4})O]^{2+}$ species.

6.5 Catalytic Oxidation Experiments of C – H Bonds of Complexes of NQu_3 (4)

In order to investigate the reactivity of the high-valent iron-oxo species for iron(II) complexes of **4**, a series of experiments on the oxidation of C – H bonds with iron(II) complexes of **4** as potential catalysts for C – H oxidation reactions was performed. Therefore, a solution-based complex species with $[Fe(OTf)_2] \cdot 2\,MeCN$ was chosen as precursor, because the data in solution indicate a defined main species in terms of co-ligands for each solvent and there were several challenges with solid complexes of **4** (see section 6.2). It has to be mentioned that it may would have been more beneficial to use solutions of compound **C** as more predefined precursor species than in solution generated complexes but since the absolute composition of compound **C** could not be clarified, the solution generated complexes were the better option for quantitative experiments.
As a model substrate, cyclohexane was chosen analogously to the catalytic experiments with complex **2a**. Screened parameters for the reactions were solvent, temperature and oxidation agent. Since different solvents lead to different species in solution, experiments in acetonitrile ($[Fe(\mathbf{4})(MeCN)_2]^{2+}$) and dichloromethane ($[Fe(\mathbf{4})(OTf)_2]$) were performed. It was taken into account that solution species in dichloromethane needed a formation time of one day. Three different temperatures (0 °C, rt & 50 °C) were investigated. As oxidation agents three typical oxidants were tested: mCPBA, sPhIO and H_2O_2.
All reactions in dichloromethane showed very low selective conversions of substrate (Table A.3 in the Appendix). The results in acetonitrile were slightly more promising with the best results for H_2O_2 as oxidation agent at room temperature (***A***/***K***: 5.3, efficiency 10 %, TON: 1.0; Table A.4). Although the highest TON was obtained here, the value of 1.0 only indicates a stoichiometric instead of a catalytic reaction. The stepwise addition of H_2O_2 in 10 steps (to mimic a syringe pump) did not increase the results significantly (***A***/***K***: 6.5, efficiency 11 %, TON: 1.1). Of even greater concern is that the blank reaction with $Fe(OTf)_2 \cdot 2\,MeCN$ without ligand **4** delivers similar results (***A***/***K***: 4.9, efficiency 14 %, TON: 1.4) as the ones with the complex of ligand **4** and $Fe(OTf)_2 \cdot 2\,MeCN$.
For a better comparison to other reported similar complexes, four examples are listed in Table 6.20. This shows the poor reactivity of the complex with ligand **4**.
One reason could be that ligand NQu_3 with its backbone-oriented quinolines does not sufficiently shield the iron centres from the formation of iron(III) μ-oxo-dimers, which are known to be catalytically inactive, compared to the TQA ligand with outwards pointing quinolines.[42,271] Such a species was found in the solid state studies in crystals of **4g**. If a high-valent iron-oxo species is formed from iron(II) complexes with **4**, catalytically inactive dimers may be formed so rapidly that the TON is hardly greater than one. On the contrary, the mass spectrometric results where an iron(IV)-oxo species generated by H_2O_2 could

Table 6.20: Oxidation of cyclohexane with H_2O_2 in MeCN starting from iron(II) complexes with triflate as anions (iron complex : H_2O_2 : cyclohexane, 1 : 10 : 1000).

Ligand	A/K	Efficiency [%]	Syringe pump	Literature
4	5.3	10	no[a]	this work
TPA	12.0	32	yes[b]	[236]
BPQA	10	–	yes[b]	[86]
PyTACN	12	65	yes[b]	[248]
^{Me2,BzIM}TACN	10.6	93	yes[b]	[249]

[a] Complex solution and catalysis prepared under inert conditions, H_2O_2 solution under aerobic conditions.
[b] Catalysis under aerobic conditions.

still be identified after 30 min at ambient conditions. However, the solutions for the mass spectrometry experiments were quite diluted, so the conditions may not be comparable. The other reason could be that the iron-oxo species are comparably stable and, therefore, less reactive.

6.6 Protonated NQu_3 (4) in the Solid State

A threefold protonated ligand structure H_3(**4**)$(OTf)_3 \cdot$ DCM was obtained as side product of an UV/Vis spectroscopic experiment with *in situ* generated bis(triflato) complex {**4** + $Fe(OTf)_2 \cdot 2$ MeCN} in dichloromethane and oxidation with sPhIO on the next day. The solution of the experiment was kept in a capped vial under aerobic conditions and colourless crystals, which were suitable for SCXRD, were obtained together with an orange powder after about two months. H_3(**4**)$(OTf)_3 \cdot$ DCM crystallises in the triclinic space group $P\bar{1}$ as dichloromethane solvate with $Z = 2$ (Figure 6.49). The triflate anions in crystals of H_3(**4**)$(OTf)_3 \cdot$ DCM are connected *via* H-bonds (2.766(4), 2.774(5) & 2.807(4) Å) to protonated

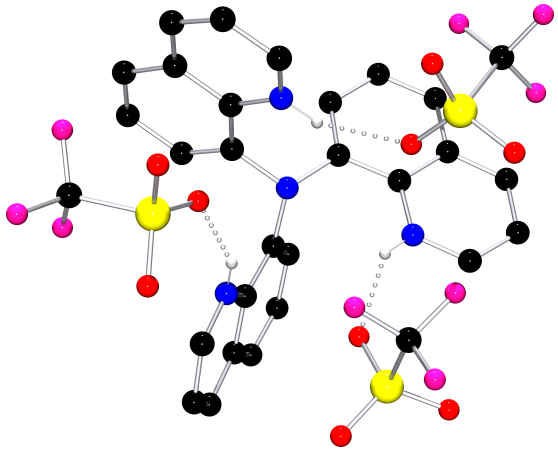

Figure 6.49: H-bonds towards $H_3(\mathbf{4})^{3+}$ from OTf^- anions found in crystals of H_3(**4**)$(OTf)_3 \cdot$ DCM. Hydrogen atoms not involved in H-bonds (dotted) and crystal solvent are omitted for clarity. Colour code: black = carbon, blue = nitrogen, red = oxygen, scarlet = iron, yellow = sulphur, pink = fluorine, white = hydrogen.

quinoline *N*-atoms, respectively (Figure 6.49). Similar "coordination" of anions via H-bonds is also reported for protonated version of the closely related TPA ligand.[272–274]

Table 6.21: Selected bond lengths, atom distances, bond and torsion angles of $H_3(\mathbf{4})(OTf)_3 \cdot DCM$.

	$H_3(NQu_3)(OTf)_3 \cdot DCM$
Space group	$P\bar{1}$
Bond lengths [Å]	
$N_{Am} - C_{8\text{-}Qu}$	1.441(4)–1.458(4)
Atom distances [Å]	
$N_{Am} \cdots N_{Qu}$	2.856(4)–2.875(4)
Bond angles [°]	
$C_{8\text{-}Qu} - N_{Am} - C_{8\text{-}Qu'}$	113.0(3)–114.0(3)
$N_{Am} - C_{8\text{-}Qu} - C_{9\text{-}Qu}$	119.3(3)–119.5(3)
Torsion angles [°]	
$N_{Am} - C_{8\text{-}Qu} - C_{9\text{-}Qu} - N_{Qu}$	−2.8(5)–2.0(5)

6.7 Concluding Remarks on Complexes of NQu_3 (4)

The plethora of complexes available as crystal structures in the solid state enable a deeper insight into the coordination chemistry of this ligand. Especially, the change in ligand conformation for different spin states give valuable information. Moreover, the three solid-state structures of the triflate-acetonitrile equilibrium – bis(acetonitrile), bis(triflato) and mixed co-ligand species – form a new aspect in this co-ligand competition. However, most of the species cannot be synthesised selectively and isolation of crystals may result in a different species.

In mass spectroscopic experiments, a high-valent iron(IV)oxo species $[Fe^{IV}(\mathbf{4})O]^{2+}$ was successfully identified for oxidation with both sPhIO and H_2O_2. The mild and ambient reaction conditions under which the iron-oxo species could still be observed in the mass spectra 30 min after the addition of the oxidant H_2O_2 should be emphasised. The UV/Vis spectroscopic experiments suggest different reaction pathways for both oxidants.

However, the use of these complexes in C – H oxidation catalysis was not successful as the best result was a stoichiometric conversion of cyclohexane. Although the complexes cannot be used as precursors for high-valent catalytically active iron-oxo species, the closer study of the $[Fe^{IV}(\mathbf{4})O]^{2+}$ species and the involved mechanisms remains of interest. Mößbauer spectroscopy experiments could provide information about the spin state of the complex.

All these complexes with ligand **4** provided a particularly detailed insight into the coordination chemistry of this type of complex. This is due to the combination of a variety of characterised structural motifs in the solid state alongside studies of different species in solution.

7 General Coordination Geometry Considerations for Iron Complexes

The four ligands used in this thesis gave rise to thirty new crystal structures of iron complexes. To investigate the influences of the different ligand backbones and donor set-ups on the resulting complexes, it is worth comparing the geometry of the coordination spheres. Since the iron metal ion can exist in HS or LS state, it is also interesting how the ligand framework can adapt to the change in ion radii for the different spin states. The discussion will be divided into ligands with a quaternary carbon backbone and with a tertiary amine backbone.

7.1 Quaternary Carbon Backbone Ligands for Iron Complexes

Ligands $HOCH_2C(Pz)_2Py$ (**1**), $MeC(Py)_2Phen$ (**2**) and $MeC(Py)_2PicMe$ (**3**) have different numbers and types of donors, but they each have three *N*-donors, arranged with the same number of bonds to a quaternary carbon atom. Therefore, it is useful to compare the ligands and their coordination geometries in iron complexes to investigate the effects of the different ligand scaffolds (Figure 7.1).

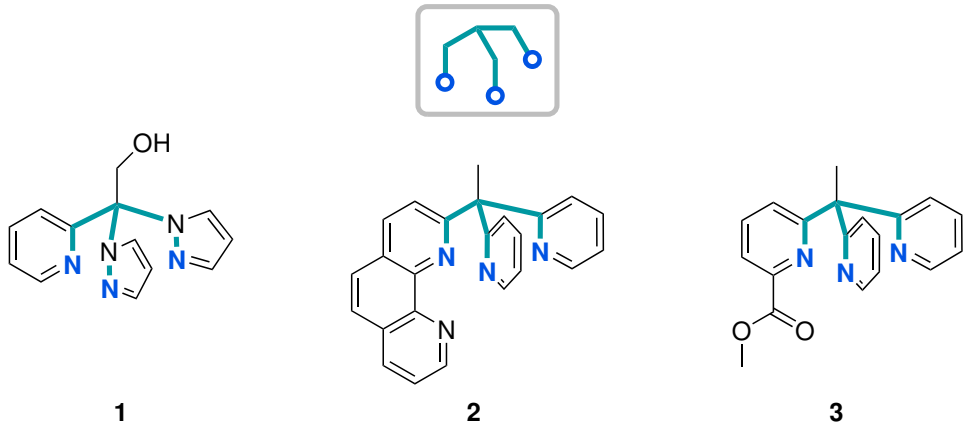

Figure 7.1: Structural similarities of ligands **1**, **2** and **3**.

7.1.1 Distance Between the Iron Centre and the Quaternary Carbon Atom

Iron cations with different spin states also have different ionic radii. The size of an iron cation is important when it comes to how well it fits into the coordinative cavity spanned by the donors of multidentate ligands. This is along the same lines as how well a multidentate ligand wraps around a bare metal centre. A very basic approach to this question for ligands **1**, **2** and **3** is to determine the distance from the iron centre to the quaternary carbon, since this limits the coordination cavity in one direction and at the same time lies relatively centrally between the three facial coordinating *N*-donors (Figure 7.2).

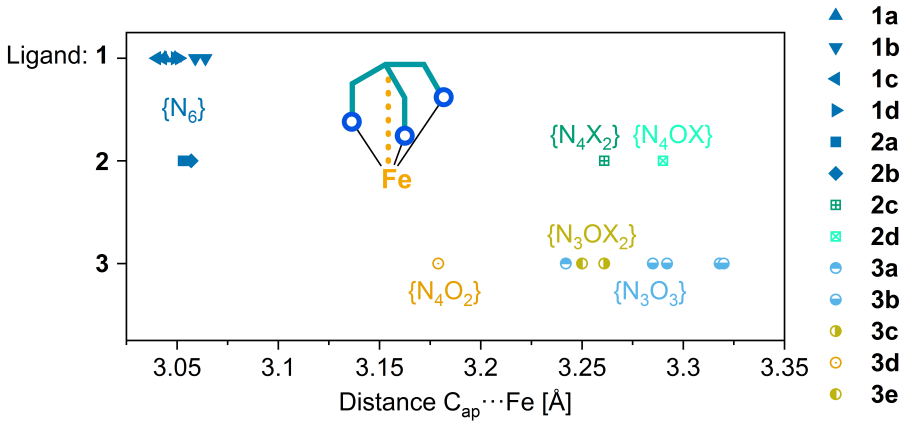

Figure 7.2: Distances C_{ap}···Fe for complexes with ligands **1**, **2** and **3** in Å.

The shortest C_{ap}···Fe distance (approx. 3.05 Å) occurs for complexes of ligands **1** and **2** with a $\{N_6\}$-coordination sphere. This matches the spin state of these complexes as they were assigned as LS species in the solid state and iron(II) LS cations have smaller radii than iron(II) HS cations. The $\{N_3O_3\}$-, $\{N_3OX_2\}$-, $\{N_4X_2\}$-, $\{N_4OX\}$-mixed donor species show larger C_{ap}···Fe distances (approx. 3.24–3.32 Å) which is in line with the assignment of HS species. For the mixed $\{N_4O_2\}$-species, it is impossible to say if they show in general intermediate C_{ap}···Fe distances (3.18 Å) as only one of these species was observed. This is also the only species with one *N*-donor and one *O*-donor as co-ligand. The overall trend of a larger C_{ap}···Fe distance for this HS complex than for the LS $\{N_6\}$-complexes is still valid. For the data obtained in this work, no significant influence of the ligands **1**, **2** and **3** themselves can be deduced, although it must be taken into account that only a limited number of complexes are available for comparison.

7.1.2 Spatial Ligand Arrangement Comparison of Ligands 2 & 3

The ligands **2** and **3** differ only in the nature of the fourth donor, but the number of bonds between the donors is identical. Therefore, the spatial arrangement in the coordination of iron cations and the resulting coordination geometry can also be compared. It should

be noted that the coordination geometry can be determined not only by the tetradentate ligand but also by the nature and steric requirement of the two co-ligands that complete the coordination sphere.

The complexes with ligands **2** and **3** can be compared by viewing along the Fe – C_{ap} axis (Figure 7.3). The three similar *N*-donor show very similar arrangements around the iron centre. Also, the fourth donors (*O*-donor of ester group or second *N*-donor in phenanthrolinyl unit) occupy similar positions. The ester group has two ways to enable a more octahedral coordination sphere: One is rotating the carbonyl group and the second is the tilt of the whole picoline methylester unit. For the rigid phenanthrolinyl unit of ligand **2**, only tilting is possible. More precisely, the coordination geometries at the iron centres can be compared by plotting the CSM *S*(OC-6) vs. *S*(TPR-6) values in a scatter plot (Figure 7.4). Closest to an octahedral coordination geometry are the purely *N*-coordinated complexes **2a** and **2b**. This is in line with d^6 LS species showing a high ligand field stabilisation energy. All other complexes of **2** and **3** with oxygen or halide based donors show higher distortion from an ideal octahedral coordination geometry. As there are only a small number of complexes, no trend can be identified. Complicating matters further, no species with exactly the same co-ligands could be observed for both ligands.

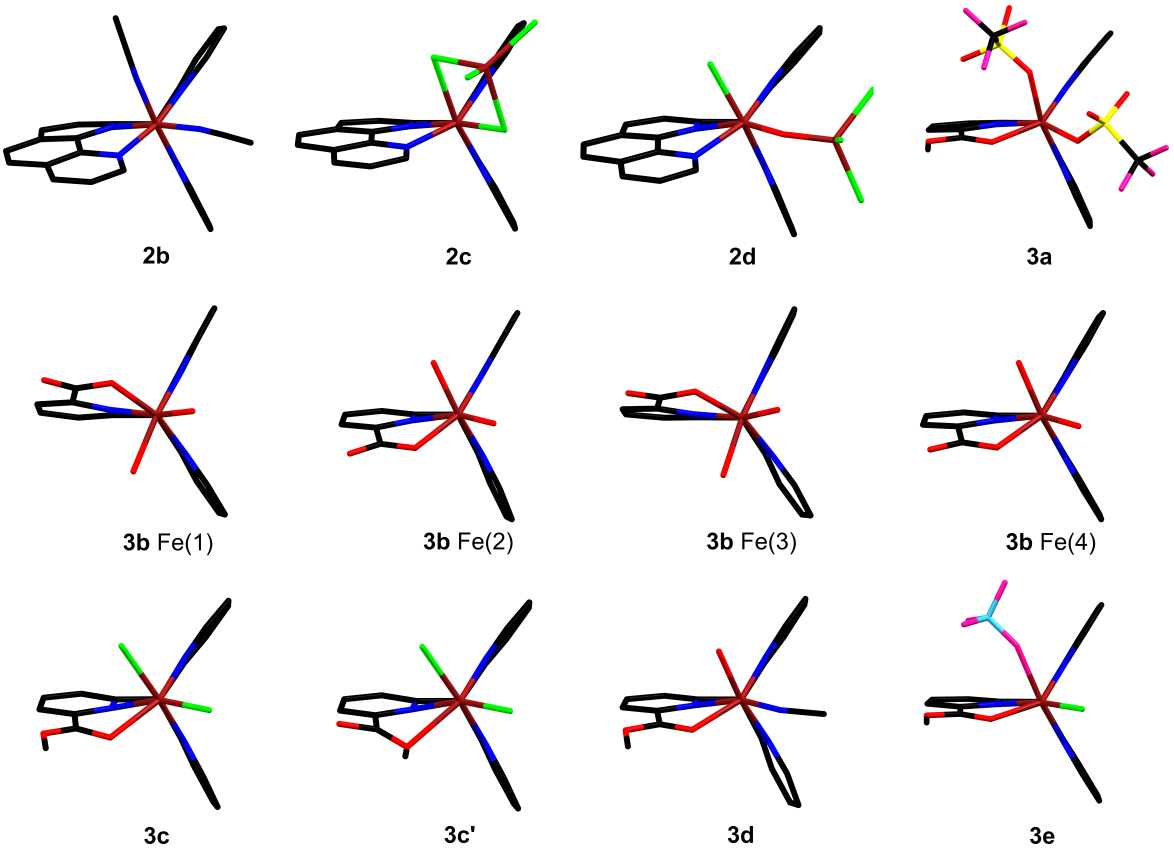

Figure 7.3: View in the direction of the Fe – C – Me-axis for complexes of **2** and **3**. Structure of **3b** split up in 1st coordination sphere (with complete tetradentate ligand) for each iron centre. Colour code: black = carbon, blue = nitrogen, red = oxygen, scarlet = iron, yellow = sulphur, pink = fluorine, green = chlorine, sky blue = boron.

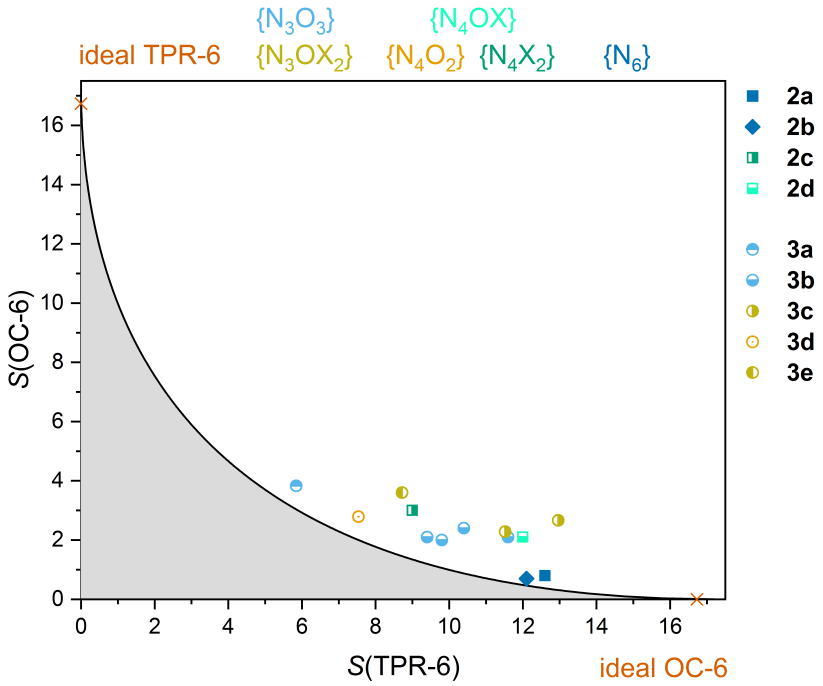

Figure 7.4: Scatter plot of CSM *S*(OC-6) vs. *S*(TPR-6) values for six-fold coordinated iron complexes with ligands **2** and **3**.

7.2 Tertiary Amine Backbone Ligands for Iron Complexes

7.2.1 Geometric Considerations for Complexes with NQu_3 (4)

Since a large number of structures of complexes with ligand **4** could be crystallised, some geometrical observations can be derived from this. First, the asymmetry of the co-ligand bonds will be discussed. In Figure 7.5, the Fe – A and Fe – E bond lengths for the mononuclear complexes with ligand **4** are plotted (only for 100 K SCXRD data). It can be derived that all Fe – E bond lengths are longer than the corresponding Fe – A bond lengths. For the complexes with two *N*-donor co-ligands ($\{N_6\}$-coordination sphere) the difference between the Fe – A and Fe – E bond lengths is smaller whereas for all mixed donor complexes ($\{N_5O\}$, $\{N_4O_2\}$ & $\{N_4X_2\}$-coordination sphere), the difference is larger. This co-ligand bond asymmetry may be caused by electronic effects as discussed with the example of the two methanol-triflate complexes **4l** and **4m**. The central amine *trans* to the A position is a weak donor and has always the longest Fe – N bond length. For octahedral complexes, structural *trans*-effects are known, where one shortened bond length is *trans* to an elongated bond length.[204] This explains the systematic shorter Fe – A bond lengths *trans* to the tertiary amine in complexes with **4**. But also steric effects caused by the three rigid quinolines may have an influence on the coordination geometry.

Second, the Fe – N_{Am} bond lengths correlate with the spin state of the complexes (Figure 7.6). The LS complexes exhibit Fe – N_{Am} bond lengths slightly longer than 2.00 Å and all have a $\{N_6\}$-coordination sphere. All other mononuclear complexes that were assigned as HS

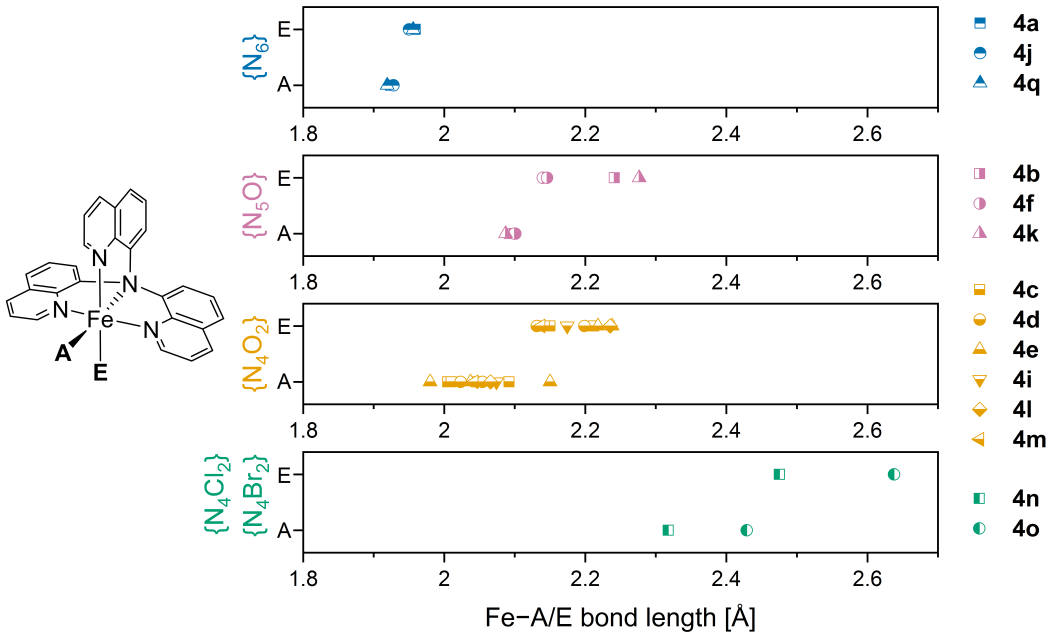

Figure 7.5: Bond lengths from iron to co-ligands at A or E position of mononuclear complexes with ligand **4**. Only structures with SCXRD data collected at 100 K are shown.

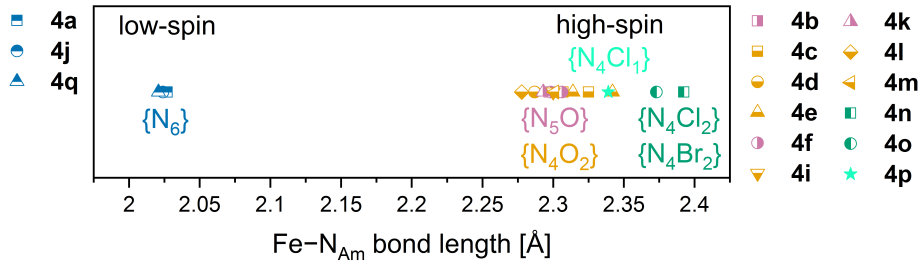

Figure 7.6: Bond lengths from iron to central amine (N_{Am}) of mononuclear complexes with ligand **4**. Only structures with SCXRD data collected at 100 K are shown.

species have Fe – N_{Am} bond lengths around 2.3-2.4 Å. This is in line with the larger radii of iron(II) HS cations compared to iron(II) LS.[183]

The size of the metal ion and the number of coordinating co-ligands have further influence on the spatial arrangement of the ligand. Due to the rather unflexible backbone with the three rigid quinolinyl moieties, the iron-donor distance can only be varied by the tilt of the quinolines. The result is that basically three different conformations of the ligand **4** were found among all the SCXRD structures (Figure 7.7). The three conformations are most evident when the complex structures are viewed along the N_{Am} – Fe-axis. The only complex with a five-fold coordinated metal centre in this work **4p** has a conformation reminiscent of a "windmill". The quinolines are tilted all in the same direction. Note, that all complexes with ligand **4** crystallised in centrosymmetric space groups so an inverted conformation to the one described here is always present, too. The "windmill" conformation is reminiscent of a C_3 symmetry. Together with the single co-ligand, a trigonal bipyramidal coordination geometry around the iron centre is formed. Complexes in which such "windmill-like" orientations,

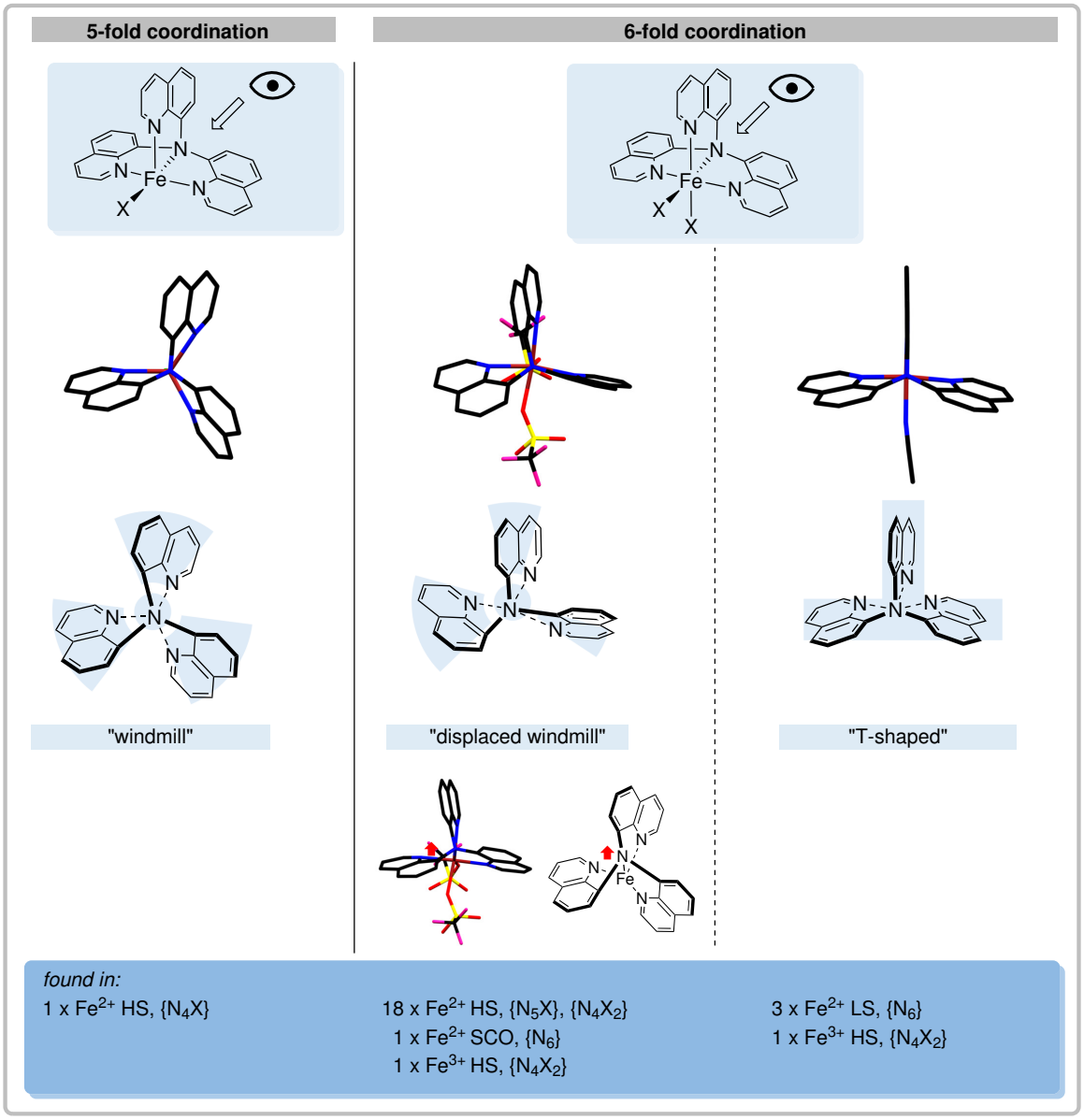

Figure 7.7: Arrangements of **4** for five-fold coordination: "windmill", and six-fold coordination: "displaced windmill" and "T-shaped". View along the N_{Am} – Fe-axis. Examples of complexes from crystals of **4p** (left), **4c** (middle) and **4a** (right).

with the arms of a ligand twisted in the same direction or oriented "propeller-like", have been observed, for example, in complexes with tris(pyrazolyl)borate ligands that have naphthalene or two phenyl substituents.[275–277] However, a five-fold coordination mode is very unusual for TPA-based ligands when coordinating iron(II). Nevertheless, other tetradentate ligands such as TMG_3tren (1,1,1-tris{2-[N^2-(1,1,3,3-tetramethylguanidino)]ethyl}amine) favour this coordination mode.[19]

A six-fold coordination, often present in combination with TPA-based ligands for coordination of iron, induces two different conformations for ligand **4**. Therein, the tilt of the quinoline moieties leads either to a "displaced windmill" or "T-shaped" conformation. The "T-shaped" conformation can be seen as extreme opposite of the "windmill" conformation

and was found mainly for the $\{N_6\}$-coordinated LS species. The smaller iron(II) LS ions are surrounded by coordination spheres close to an ideal octahedron. As shown in Figure 7.6, the Fe – N_{Am} bond lengths of the $\{N_6\}$-complexes are shorter compared to the other complexes with ligand **4**. The Qu2 quinoline is not tilted and the other two are slightly tilted in opposing directions.

The "displaced windmill" conformation can be seen as intermediate conformation between "windmill" and "T-shaped". If the viewing position is slightly shifted from the N_{Am} – Fe-axis (Figure 7.7) a more "windmill"-like conformation can be seen in the structures with "displaced windmill" conformation. However, viewed along the N_{Am} – Fe-axis the tilt of the quinolines is increasing in anti-clockwise direction. This conformation was found mainly for the $\{N_5X\}$- and $\{N_4X_2\}$-coordinated complexes which were assigned as HS species and exhibit more distorted octahedral coordination geometries. This conformation was found most often in this work. Overviews with all complexes shown in the direction of view along the N_{Am} – Fe axis are presented in Figure 7.8 and Figure 7.9. Two complexes show deviations from the conformational trends described above. One is the dinuclear iron(III) complex **4g**. Around Fe(1), the conformation is best described as "displaced windmill" whereas around Fe(2) the orientation is "T-shaped". The other deviation is found within the SCO complex **4r**. Since it was measured at 200 K and not at 100 K, it is somewhere between a true LS or HS geometry with a tendency more towards HS ($T_{1/2}$ approx. 160 K). Therefore, it does not show a "T-shaped" conformation like the other $\{N_6\}$-coordinated complexes but a "displaced windmill" conformation like the other HS complexes (Figure 7.9). This indicates that the complex is more likely a HS than LS species in terms of ligand geometry at this temperature.

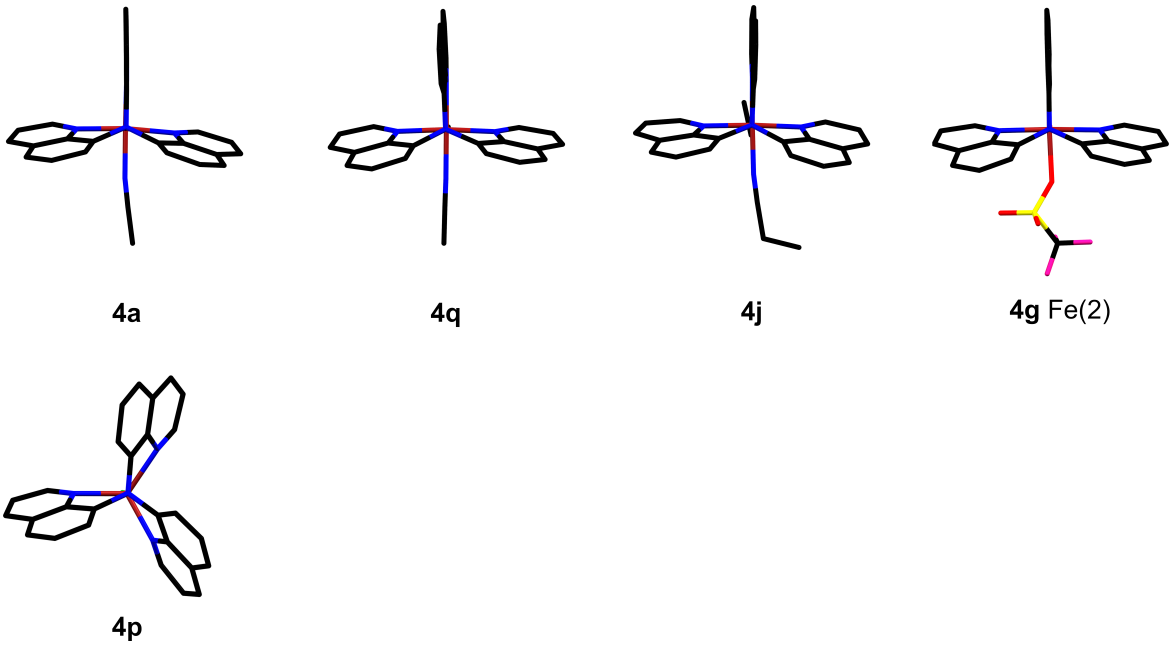

Figure 7.8: View on complex cations in direction of the central amine-iron axis in molecular structures in the solid state with "T-shaped" (top) or "windmill" (bottom) conformation.

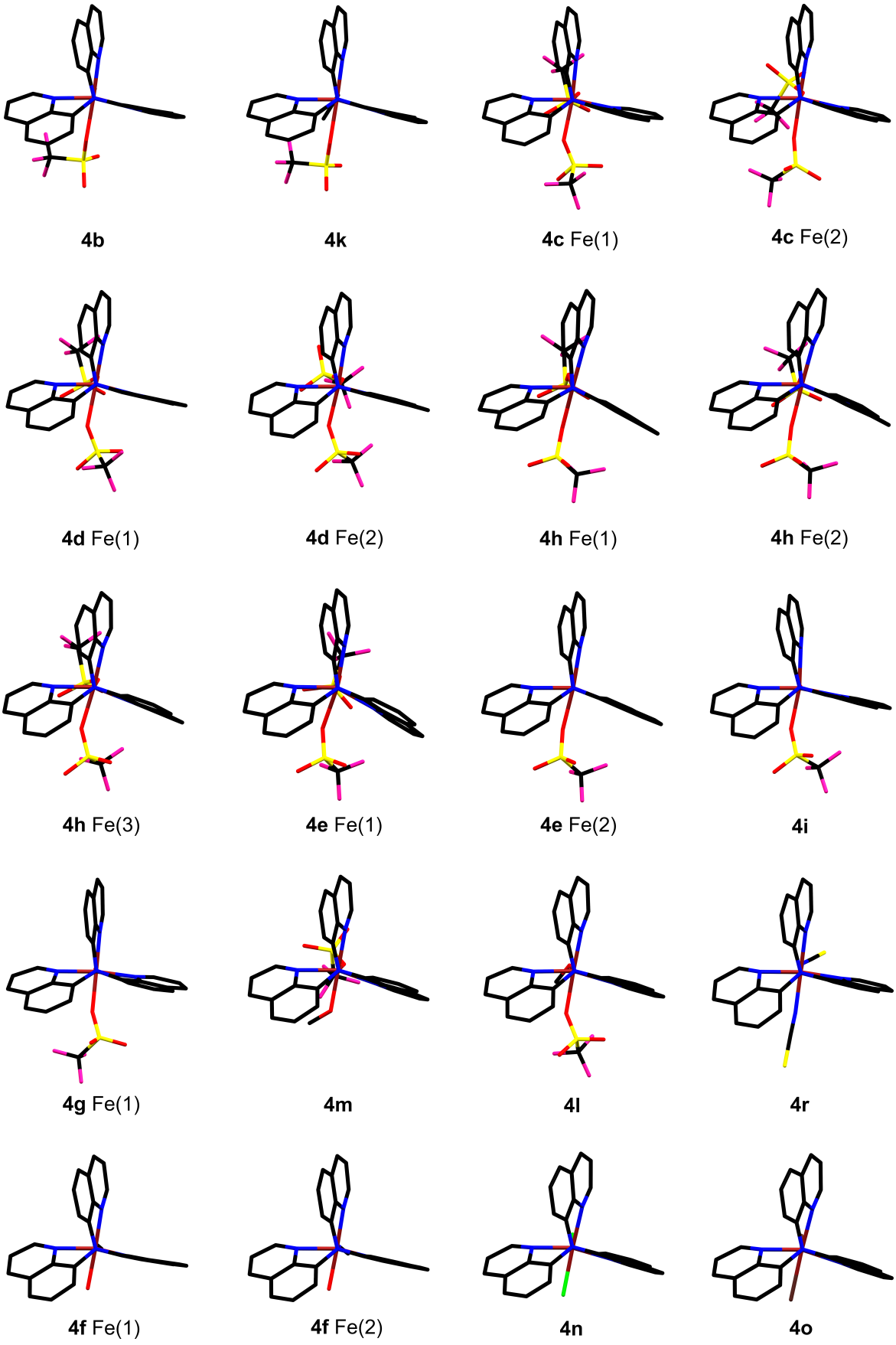

Figure 7.9: View on (cationic) complexes in direction of the central amine-iron axis in molecular structures in the solid state with displaced windmill conformation.

This phenomenon with different ligand conformations is difficult to compare with other reported complexes with TPA-related ligands as the tripodal ligands with aliphatic backbones are much more flexible and allow for different conformations (see Figure 6.3). For the other fully quinoline-based ligand (TQA), only one iron crystal structure is known ([Fe(TQA)$(OTf)_2$], CSD reference code: FOXROB), which makes it difficult to determine whether the spatial quinoline arrangement in the structure is a general phenomenon or a packing effect.[97] Therefore, a comparison to the complexes obtained in this work would not be meaningful.

7.3 Coordination Geometry Comparison of Iron Complexes of Ligands 1–4

All coordination geometries of six-fold coordinated iron complexes in this work can be visualised in a scatter plot of CSM *S*(OC-6) vs. *S*(TPR-6) values for ligands **1**, **2**, **3** and **4** (Figure 7.10). Closest to an ideal octahedral coordination geometry are the $\{N_6\}$-coordinated complexes with ligand **1**. Slightly higher distortions are observed for $\{N_6\}$-complexes with ligands **2** and **4**. All mixed donor species show higher distortions but still octahedral-like coordination geometries. An exception is the oxo-dimer iron(III) complex **4g** which shows a comparable distortion to some of the $\{N_6\}$-complexes. Overall, no distortion tendencies of the complexes for a specific tetradentate ligand are discernible, but rather for the general set of donors (pure *N*- vs. mixed-donor complexes).

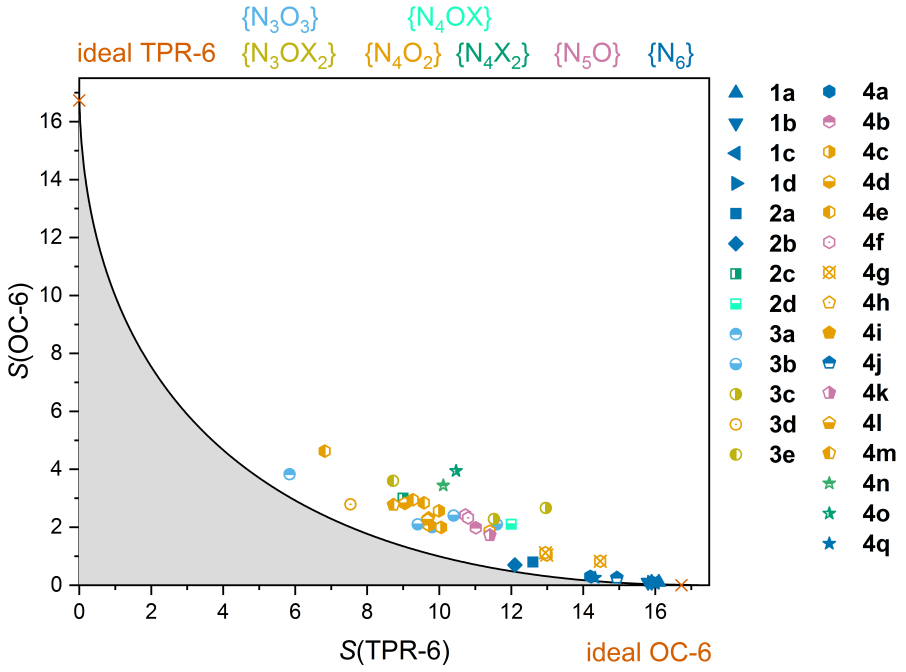

Figure 7.10: Scatter plot of CSM *S*(OC-6) vs. *S*(TPR-6) values for six-fold coordinated iron complexes of ligands **1**, **2**, **3** and **4**.

8 Conclusions & Outlook

In this thesis, four ligands were successfully used in the synthesis of new bioinspired iron complexes. The number of donor groups and their nature resulted in different complexes (Figure 8.1).

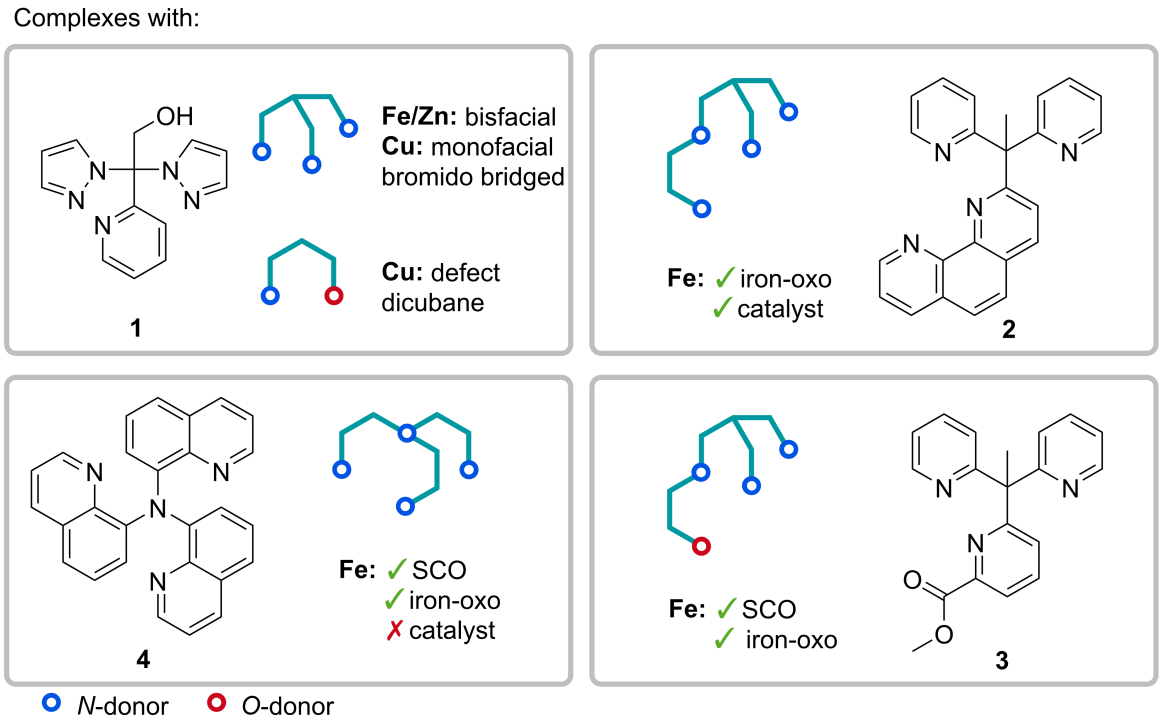

Figure 8.1: Overview of ligands used in this thesis for new complexes and main results.

In chapter 3, the use of the bis(pyrazolyl)ethanol ligand **1** led to the same bisfacial complex cation $[Fe(\mathbf{1})_2]^{2+}$ in four different compounds in the solid state structures (**1a**–**1d**). The obtained zinc complex SCXRD structure (**1e**) revealed the same coordination mode. For copper, two different coordination modes were observed. One was the bromide bridged dimer of two monofacial copper complexes. The only coordination involving the alcohol function of **1** was the {NO}-coordination in complexes **1g** and **1h** enabling a defect dicubane arrangement. For complexes with $\{N_3\}$-coordination of ligand **1**, the distance between the apical carbon and the metal ion seems to correlate with the ion radius of the metal centre. A series of experiments were performed to evaluate the suitability of iron complexes of **1** as biomimetic catalysts. These revealed, that the predominant species in solution is the bisfacial $[Fe(\mathbf{1})_2]^{2+}$ complex. The saturated coordination sphere with no labile coordination sites limits the use as potential biomimetic homogeneous catalysts. Furthermore, solutions with stoichiometric quantities of iron halide salt and ligand display the formation of tetrahalidoferrate anions which would interfere with the catalysis. Hence, in the remainder

of this thesis tetradentate ligands were used that provide two *cis*-labile coordination sites which can enable catalysis at the metal centre through co-ligand exchange processes.
Three new solid state structures of iron complexes with ligand **2** were discussed in chapter 4. Complex **2b** is the tetrafluoridoborate variant of the already known bis(acetonitrile) complex **2a**. For syntheses with iron chloride two dinuclear complexes **2c** and **2d** where two iron centres are bridged by chloride or oxygen, respectively, were found instead of a bis(chlorido) species. In these asymmetric complexes only one of the iron centres is coordinated by ligand **2** and the other iron centre is saturated with additional chloride co-ligands. The further characterisation of an iron(IV)oxo species generated from the bis(acetonitrile) precursor complex **2a** with CSI-MS and Mößbauer experiments was successful. Tests towards the catalytic C – H oxidation of (deuterated) cyclohexane and adamantane suggest that the metal-based species is involved in the catalytic process rather than unwanted side reactions. Femtosecond XES measurements of **2a** and **5a** revealed a similar photocycle compared to the photophysical well-characterised $[Fe(BiPy)_3]^{2+}$ complex. For both complexes, evidence for a quintet state (after ≤ 1 ps) was found in the Kβ and Kα emission lines, which was only possible through the truly simultaneous acquisition of both emission lines.
In chapter 5, crystal structures of four different mononuclear and one tetranuclear iron complexes with ligand **3** were presented. Species that meet the expectations for this kind of complexes are a bis(triflato) (**3a**) and bis(chlorido) (**3c**) species. A bis(acetonitrile) complex could not be crystallised but an acetonitrile water mixed co-ligand by-product (**3d**) was successfully characterised in the solid state. Another solid state by-product is the tetrameric structure of **3b**, where the ester group of the ligand underwent a saponification process. The maybe most interesting and unusual co-ligand combination for iron complexes with ligand **3** was found in crystals of **3e**. The simultaneous presence of a stronger coordinating chloride co-ligand which stands *cis* to a weakly coordinating tetrafluoridoborate may enable different and more directed catalytic pathways than a bis(chlorido) complex. In solution, the bis(triflato) species of **3a** undergoes a co-ligand exchange in acetonitrile to a bis(acetonitrile) species. The latter shows a temperature dependent SCO behaviour with an SCO temperature of approx. 234 K. Attempts to generate and characterise an iron-oxo species were successful in the UV/Vis spectroscopic and mass spectrometric experiments. In the latter, the species could be identified as $[Fe^{IV}(\mathbf{3})O]^{2+}$. The chloride-tetraflouroborate mixed co-ligand species **3e** showed also promising UV/Vis spectroscopic bands in terms of high-valent iron-oxo species.
By far the most solid state structures were obtained with the ligand **4** in chapter 6. For this ligand geometry for the first time, all three variant of a triflate acetonitrile equilibrium could be characterised as solid state structures by SCXRD: bis(acetonitrile) (**4a**), bis(triflato) (**4c**, **4d**, **4e**) and a mixed co-ligand species (**4b**). Besides, by-products with a water co-ligand (**4f**) or a μ-oxo-bridged dimer (**4g**) were found. Only the synthesis of the bis(acetonitrile) species is selectively available via a low temperature route, but the crystals are not isolateable due

to loss of co-crystallised solvents and change of co-ligands.
These triflate acetonitrile equilibria could be investigated closer in solution. In an acetonitrile solution the bis(acetonitrile) species was identified as the main species, which undergoes a temperature dependent SCO in solution ($T_{1/2}$ approx. 284–290 K). Using a non-coordinating solvent (DCM) gave the bis(triflato) species as main species. This was also seen for crystals grown from dichloromethane solution, but reduced quality of crystals only gave preliminary information about these species (**4h**). A water triflate species (**4i**) was also characterised by SCXRD as a by-product in dichloromethane.
The change to other coordinating solvents provided the same coordination motifs for propionitrile as for acetonitrile: the bis(propionitrile) (**4j**) and the mixed co-ligand species (**4k**). While for the nitrilic solvents only one arrangement of the mixed co-ligand species was observed, crystallisation from methanol solution gave both variants of the co-ligand arrangement for methanol and triflate (**4l**, **4m**). A bis(methanol) or bis(triflato) species could not be crystallised from methanol.
Besides the solvents, also the anions were varied in complex synthesis with ligand **4**. Syntheses with halide salts (Cl, Br) gave the corresponding bis(halogenido) complexes (**4n**, **4o**). It was also possible to obtain the only penta-coordinated structure with ligand **4**, which has only one chlorido co-ligand (**4p**). Change to a more weakly coordinating anion (BF_4^-) resulted in a bis(acetonitrile) complex (**4q**). A charge neutral complex with full $\{N_6\}$-coordination sphere was achieved for a bis(thiocyanato) species (**4r**), which shows a SCO in the solid state ($T_{1/2}$ = 124–155 K).
The change of spin state of the iron centre also influences the conformation of ligand **4** in the complexes. While for LS iron(II) complexes the ligand is arranged in a "T-shape", the conformation changes to a "displaced windmill" for HS complexes. A "windmill" conformation was observed for the only penta-coordinated complex (HS). The $Fe-N_{Am}$ bond length also correlates very well with the spin state of the complexes.
A high-valent iron(IV)oxo species was generated successfully with both sPhIO and H_2O_2. The species shows typical band in the UV/Vis spectra and was identified as $[Fe^{IV}(\mathbf{4})O]^{2+}$ in mass spectrometric experiments. However, the experiments on the catalytic activity in C–H oxidation of the iron-oxo species showed a maximum stoichiometric reaction using H_2O_2 as oxidant.
Overall, iron complexes with $\{N_6\}$-coordination sphere in this work were all assigned to be LS in the solid state structures. An exception is the complex **4r** ($[Fe(NQu_3)(NCS)_2] \cdot 0.5\,Et_2O$) which shows a temperature dependent SCO in the solid state. All other complexes characterised by SCXRD with mixed-donor coordination spheres were assigned as HS compounds in the solid state.
However, this subdivision is no longer strict in solution. The $\{N_6\}$-coordinated species $[Fe(NQu_3)(MeCN)_2]^{2+}$ shows SCO behaviour as well as the $\{N_5O\}$-coordinated species $[Fe(MeC(Py)_2PicMe)(MeCN)_2]^{2+}$. They have in common that at least the co-ligands are

N-donors, whereas the *O*-donor of the latter is incorporated into the tetradentate ligand scaffold. The SCO of $[Fe(MeC(Py)_2PicMe)(MeCN)_2]^{2+}$ in solution is interesting as most of the literature known iron SCO complexes are coordinated by a $\{N_6\}$-coordination sphere. For the tetradentate ligands comprising two *cis*-labile coordination sites, a more general trend for acetonitrile triflate equilibria can be observed (Figure 8.2).

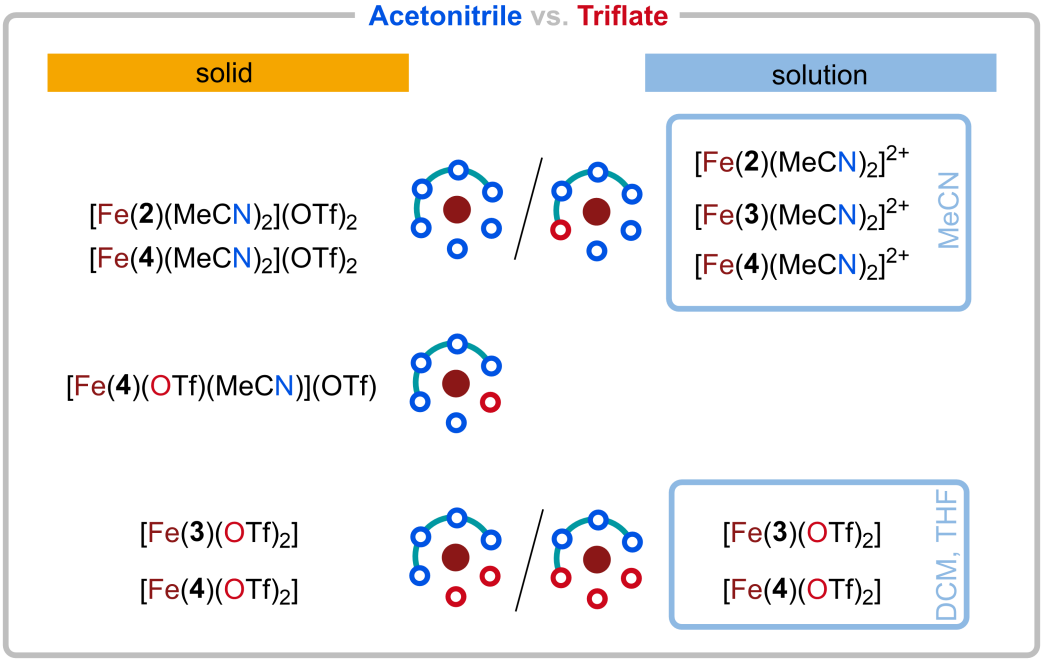

Figure 8.2: Acetonitrile vs. triflate: overview of complexes in solid state (left) and species in solution (right) observed in this work. Crystal solvent molecules omitted for clarity.

The results suggest the tendency for a bis(acetonitrile) species to be the main species in acetonitrile. For less coordinating solvents, bis(triflato) species were observed as main species. However, the results underline, especially for triflate-based complexes, that the solid state structures and the solution species do not necessarily have to be identical. For these species, the choice of solvent has proven to be crucial.

To build on the first promising results of complexes with ligand **3** in terms of high-valent iron-oxo complexes, it would make sense to conduct further experiments. Although, the UV/Vis spectra of the dissolved triflate-based complex **3a** looked not as promising as the *in situ* generated tetrafluoridoborate-based complexes, it may be worth taking a closer look. Especially as the Mößbauer results were not consistent with the expectations, starting with a more defined crystallisable species may be more efficient. However, both *in situ* and dissolved complexes should lead to the identical complex cations in acetonitrile solution. The mixed co-ligand species **3e** (Cl^-/BF_4^-) is worth of further investigations as the two co-ligands may have different exchange rates. This may enable more tailored catalytic pathways compared to a bis(chlorido) species as precursor complex.

After the identification of the $[Fe^{IV}(\mathbf{4})O]^{2+}$ species in the mass spectrometric experiment, the next research question would be the spin state of this species. Mößbauer or electron paramagnetic resonance (EPR) spectroscopy would be appropriate methods. Furthermore, the different reaction mechanisms of the sPhIO and H_2O_2 oxidation remain a field of interest. For the further development of the NQu_3-based complexes, a better steric shielding of the metal ion could be beneficial in terms of generating high-valent iron-oxo species to prevent the formation of oxygen-bridged dimers like observed in crystals of **4g**. Methylation in the 2-position of each quinoline moiety resulting in a tris(2-methylquinolin-8-yl)amine ligand ($N(2MeQu)_3$) would be one option for increased steric demand (Figure 8.3).

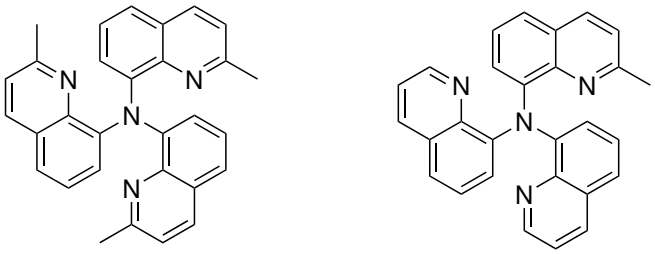

Figure 8.3: Structures of potential ligands $N(2MeQu)_3$ and $N(2MeQu)(Qu)_2$.

This ligand was already synthesised by Dr. Joshua Heck in his PhD thesis and was not used for iron complexes yet.[241] However, it has to be considered that a CH_3-group in very close proximity to an iron centre designed for C – H oxidation reactions may result in some challenges like unwanted oxidation of the ligand itself. Investigations with 6 -Me_3-TPA, which is a TPA derivate with methyl groups in each α-position of the pyridine moieties, showed poor catalytic results in C – H oxidation reactions compared to a TPA variant with only one α-methyl substituent.[86] Thus, $N(2MeQu)(Qu)_2$, a single methylated NQu_3 derivate, may be more interesting than the $N(2MeQu)_3$ ligand. Furthermore, α-methylation is expected to lead to a HS bis(acetonitrile) precursor iron(II) complexes instead of LS.[86] Another interesting point would be the use of the tetradentate ligands discussed in this work for complexes with other transition metals than iron, as biomimetic high-valent metal-oxo or metal-dioxygen species are also known for copper and manganese, for instance.[14] Biomimetic manganese complexes show similar reactivities to their iron paragons.[42] Therefore, it would be attractive to synthesise the corresponding manganese complexes of the ligands studied in this work as well as to compare and even improve their reactivity.
A different aspect that could be addressed in future investigations is the SCO complex in the solid state **4r**. If a series of temperature-dependent SCXRD data can be measured, it would be interesting to see whether the conformational change between "displaced windmill" and "T-shaped" of ligand **4** observed for pure HS or LS state complexes in the solid state is prevented by lattice effects or can also be observed for a SCO complex in the solid state. This would mean that the ligand in complex **4r** changes to "T-shaped" conformation for the

low temperature LS state.

The photophysical measurements in the femtosecond range are also a promising topic that should be pursued further. These measurements deliver valuable information about possible excited states and their lifetime. This information could be useful for designing new iron-based molecular catalysts. In particular, the approach of using ligand structures that deviate from the usual bi- and tridentate ligands studied in photophysical experiments provides new insights for species that also structurally have more in common with catalytically active complexes. Especially the results obtained in this thesis about the spin state and co-ligands of species in solution are valuable information for the selection of new complexes for these experiments.

Overall, this work provides new insights into the coordination behaviour of iron complexes with tri- and tetradentate ligands with *N*- and *O*-donors. Since biomimetic complexes are usually utilised in homogeneous catalysis, not only the structure in the solid state but also the structure in solution was investigated, which is more important for this type of application. These findings can be used for the development of further tailor-made ligands and corresponding complexes, which will enable more advanced biomimetic model systems that are intended to increasingly approximate natural archetypes in terms of structure and function.

Experimental

9 Methods & Procedures

9.1 Instrumentation & Measurement Details

9.1.1 Nuclear Magnetic Resonance (NMR) Spectroscopy

NMR spectra were recorded on a Bruker Avance II 400 or Bruker Avance III HD 400 nuclear resonance spectrometer at 25 °C. ^{1}H-, ^{13}C- and ^{19}F-NMR spectra were given relative to the residue signal of the solvent as an internal standard (for measurements at rt).[278] Chemical shifts were assigned with the use of two-dimensional NMR experiments (COSY, HSQC, HMBC). For the Bruker Avance III HD 400, the software TopSpin (version 3.5 pl 7) from Bruker and for the Bruker Avance II 400, the software TopSpin (version 2.1) from Bruker were used for data acquisition. For visualisation and examination of the NMR spectra, the software MestReNova (version 12.0.1-20560) from Mestrelab Research was used.

Special NMR Measurements of Species with Ligand 3

^{19}F-NMR of 3a in MeCN-d_3 with Addition of Triflate: Crystals of **3a** (4.4 mg, 0.0065 mmol, 1 eq.) and KPF_6 (1.2 mg, 0.0065 mmol, 1 eq., internal reference) were combined with MeCN-d_3 (0.6 mL). Triflate was added in form of a NH_4(OTf) solution (c = 65 mM) in MeCN-d_3 in 1 eq. steps (0.1 mL).
Plotted spectra: Figure 5.12.

VT-NMR in MeCN-d_3: Crystals of **3a** (2.1 mg, 0.003 mmol) was dissolved in MeCN-d_3 (0.6 mL). The solution was transferred into a Young NMR tube together with a sealed capillary with pure MeCN-d_3.
Plotted spectra: Figure 5.13 & Figure 5.14.

Special NMR Measurements of Species with Ligand 4

VT-NMR in MeCN-d_3: 4.1 mg of compound **C** were dissolved in 4 mL of abs. MeCN-d_3. 0.6 mL of this solution were transferred into a Young NMR tube together with a sealed capillary with pure MeCN-d_3.
Plotted spectra: Figure 6.33 & Figure 6.34.

VT-NMR in DCM-d_2: 4.0 mg of compound **C** were dissolved in 4 mL of abs. DCM-d_2. 0.6 mL of this solution were transferred into a Young NMR tube.
Plotted spectra: Figure 6.37 & Figure 6.38.

Changing Solvent from DCM-d_2 to DCM-d_2/MeCN-d_3 Mixture: 4.1 mg of compound **C** were dissolved in 4 mL of abs. DCM-d_2. A few crystals of Na(OTf) and 2 drops of fluorobenzene were added as reference. Na(OTf) was not dissolved and remained as a solid. 0.6 mL of this solution were transferred into a Young NMR tube. After each measurement, 0.1 mL of abs. MeCN-d_3 were added (total 0.8 mL of MeCN-d_3).
Plotted spectra: Figure 6.40.

9.1.2 Infrared Spectroscopy (IR)

FT-IR spectra were recorded on a Shimadzu IRTracer 100 using a CsI beam splitter in combination with an ATR unit (Quest model from Specac utilising a robust monolithic crystalline diamond) with a resolution of 2 cm^{-1}. For data acquisition, the software LabSolution IR (version 2.15) from Shimadzu was used.

9.1.3 Mass Spectrometry (MS)

Mass spectrometry was carried out by Brigitte Pütz at the Institute of Inorganic Chemistry at or by mass spectrometry team at the Institute of Organic Chemistry at RWTH Aachen University, Germany.

ESI-MS

Electrospray ionisation mass spectrometry (ESI-MS) measurements were performed with an UHR-TOF Bruker Daltonik maXis II (source voltage: 4.50 kV) or LTQ-Orbitrap XL of ThermoFisher Chemicals (source voltage: 4.49 kV, capillary temperature: 299.54 °C and tube lens voltage: between 110 and 130 V).

Oxidation of Iron Complex of Ligand 4 with H_2O_2: To dissolved compound **C** (2.3 mg, 0.003 mmol for assumption of [Fe(NQu$_3$)(OTf)$_2$]) in MeCN (2.9 mL), 200 µL of a solution of H_2O_2 (30 %, 15 µL, 0.15 mmol) in MeCN (5.1 mL) were added (1.9 eq.). After short stirring (> 30 s), 100 µL of this solution were diluted in 2.9 mL of MeCN. An ESI-MS measurement at rt was performed 1.5 and 30 min after H_2O_2-addition.

CSI-MS

Cryospray-ionisation mass spectrometry (CSI-MS) measurements were performed on an UHR-TOF Bruker Daltonik maXis II, an ESI-quadrupole time-of-flight (qToF) mass spectrometer capable of a resolution of at least 80.000 FWHM, which was coupled to a Bruker Daltonik Cryospray unit. Detection was in positive ion mode; the source voltage was 3.5 kV. The drying gas (N_2), to achieve solvent removal was held at 0 °C and the spray gas was held at −20 or −30 °C. The mass spectrometer was calibrated subsequently to every experiment

via direct infusion of a L-proline sodium salt solution, which provided a m/z range of singly charged peaks up to 3000 Da in positive ion modes.

Oxidation of Iron Complex of Ligand 2 with mCPBA: To dissolved crystals of **2a** (2.4 mg, 0.0030 mmol) in MeCN (2.9 mL), 200 µL of a solution of mCPBA (77 %, 34.5 mg, 0.15 mmol) in MeCN (5.1 mL) were added at −20 °C (2 eq.). After stirring for 5 min, 100 µL of this solution were diluted in 2.9 mL of MeCN (at −20 °C). A CSI-MS measurement at −20 °C was performed as soon as possible (∼ 10 min).

Oxidation of Iron Complex of Ligand 3 with mCPBA: To dissolved crystals of **3a** (2.4 mg, 0.0036 mmol) in MeCN (3.5 mL), 200 µL of a solution of mCPBA (77 %, 41.3 mg, 0.18 mmol) in MeCN (6.3 mL) were added at −20 °C (2.8 eq.). After short stirring (> 1 min), 100 µL of this solution were diluted in 2.9 mL of MeCN (at −20 °C). A CSI-MS measurement at −20 °C was performed as soon as possible (∼ 10 min).

Oxidation of Iron Complex of Ligand 4 with sPHIO: To dissolved compound **C** (3.8 mg, 0.0051 mmol for assumption of $[Fe(NQu_3)(OTf)_2]$) in MeCN (4.8 mL), 400 µL of a suspension of sPhIO (93 %, 52.9 mg, 0.14 mmol) in MeCN (9.4 mL) were added at −30 °C (1.2 eq.). After short stirring (> 1 min), 100 µL of this solution were diluted in 2.9 mL of MeCN (at −20 °C). A CSI-MS measurement at −50 °C was performed ∼ 25 min later.

9.1.4 UV/Vis Spectroscopy

Baselines were recoded with pure solvent at rt, unless otherwise noted. In this thesis different UV/Vis spectroscopic set-ups were used:

A–Cary Cuvette: UV/Vis spectra were recorded at ambient conditions with a Cary 60 UV/Vis spectrometer from Agilent Technologies using quartz cuvettes (Hellma, QS, 1 cm). For data acquisition, the software Cary WinUV (version 4.10 or 5.1.3) from Agilent Technologies was used.

B–Cary Immersion Probe: UV/Vis spectra were recorded with a Cary 60 UV/Vis spectrometer from Agilent Technologies in combination with a fiber-optic quartz glass immersion probe (Hellma, 1 mm) in a customised Schlenk measurement cell with magnetic stirring bar under inert conditions. To control the temperature of the solution, a Lauda Master cryostat adapted with a Proline RP890 control unit was used if necessary. Temperature was controlled by an external traceable thermocouple by VWR International GmbH. For data acquisition, the software Cary WinUV (version 4.10 or 5.1.3) from Agilent Technologies was used.

C–Jasco Cuvette: UV/Vis spectra were recorded at ambient conditions with a Jasco V-770 UV/Vis spectrometer using quartz cuvettes (Hellma, QS, 1 cm). For data acquisition, the software Spectra Manager (version 2.13.000) was used.

D–Avantes Cuvette: UV/Vis spectra were recorded at ambient conditions with an Avantes AvaSpec-ULS2048 CCD-Spectrometer and an Avantes AvaLight-DH-SBAL light source. The measurements were done in Hellma QS screw-cap cuvettes with an optical path length of 1 cm and a magnetic stirring bar. The cuvette holder was connected to lamp and spectrometer via Avantes FC-UV200-2 optical fibres.

E–Stopped Flow: The stopped-flow measurements were performed with a HI-TECH Scientific SF-61SX2 device with a charge-coupled device (CCD) photodiode array detector. The analyses were carried out with the TgK Scientific program Kinetic Studio 4.0.8.18533. The optical path length of the quartz glass cuvette was 1 cm and the mixing time of the two initial solutions was 2 ms. A xenon arc lamp was used as light source. Solutions were transferred in gas-tight Luer Lock syringes and mixed equimolar during the measurement. Measurements were carried out in a wavelength range of 400–818 nm with 2.5 up to 10 scans/s for 120 or 30 s, respectively.

F–Shimadzu Cuvette: UV/Vis spectra were recorded at ambient conditions with a Shimadzu UV-3600 spectrometer using quartz cuvettes (1 mm).

UV/Vis Spectroscopic Measurements of Species with Ligand 1

Titration of Iron Salt Solutions with 1: All experiments were performed with UV/Vis spectroscopic **Set-up A**. The used solvents and irons salts as well as the concentrations of the corresponding iron salt (c_{salt}) and ligand (c_{ligand}) stock solutions are given in Table 9.1. For every titration experiment, a baseline was measured with 1.8 mL of pure solvent. Afterwards, 200 µL of the iron salt solution were added. Subsequently, ligand solution was added in smaller portions (usually 10 or 50 µL) until 1 mL of ligand solution was added in total. The solution was stirred briefly between the addition of the ligand and the measurement.

Dilution Factor of Titrations: The absorptions A measured for the titration experiments were corrected (A_{c}) by a dilution factor. Therefore the ratio of the total volume for each titration step to the volume before the titration is used.

$$A_{\mathrm{c}} = \frac{A \cdot V_0}{V_{\mathrm{total}}} \tag{9.1}$$

A:	absorption	V_0:	volume before titration
A_{c}:	corrected absorption	V_{total}:	total volume

Table 9.1: Composition of iron salt (c_{salt}) and ligand (c_{ligand}) stock solutions for titration experiments with ligand **1**.

Salt, solvent	c_{salt} [mM]	c_{ligand} [mM]	Plotted spectra
$FeCl_2$, MeCN	1	0.8	Figure 3.18
$FeCl_2$, MeCN (anhydrous)*	1	0.8	Figure 3.18
$FeCl_3$, MeCN	5	4	Figure 3.20
$FeBr_2$, MeCN	1	0.8	Figure 3.21
$FeBr_2$, MeCN (anhydrous)*	1	0.8	Figure 3.21
$Fe(NO_3)_3 \cdot 9\,H_2O$, MeCN	5	4	Figure 3.22
$FeCl_2$, MeOH	1	0.8	Figure 3.23
$FeCl_3$, MeOH	1	0.8	Figure 3.23
$FeBr_2$, MeOH	1	0.8	Figure 3.24

* Use of abs. solvents and anhydrous iron salts that were stored under inert conditions. Measurements were performed under aerobic conditions.

UV/Vis Spectroscopic Measurements of Species with Ligand 2

Recovery of Iron-oxo Species (Set-up D): 1.5 mL of a solution of **2a** (c = 3.5 mM) in MeCN (abs.) were used. Addition of 1 eq. of mCPBA solution in MeCN (50 µL, c = 0.105 M) after 0, 15, 30, 45 and 60 min.
Plotted absorption: Figure 4.10.

UV/Vis Spectroscopic Measurements of Species with Ligand 3

Temperature Resolved Spectra of 3a in THF (Set-up B): Crystals of **3a** (14.5 mg, 0.08 mmol) were dissolved in THF (7.5 mL). A baseline was measured with 6 mL of THF and the complex solution was added subsequently for the measurement (c = 1.6 mM).
Plotted spectra: Figure 5.15.

Temperature Resolved Spectra of 3a in MeCN (Set-up B): Crystals of **3a** (54 mg, 0.08 mmol) were dissolved in MeCN (2.5 mL). A baseline was measured with 6 mL of MeCN and the complex solution was added subsequently for the measurement (c = 9.4 mM).
Plotted spectra: Figure 5.16.

Spectra of 3a + mCPBA in MeCN (Set-up A): Crystals of complex **3a** (7.2 mg, 0.011 mmol) were dissolved in abs. MeCN (5 mL). 2.5 mL of this solution were measured in a cuvette under aerobic conditions. Afterwards, 500 µL of a mCPBA solution (77 %, 9.4 mg, 0.042 mmol in 3 mL of abs. MeCN) were added (1.3 eq.).
Plotted spectra: Figure 5.19.

Spectra of {3 + $[Fe(MeCN)_6](BF_4)_2$} + mCPBA in MeCN (Set-up A): **3** (37.3 mg, 0.12 mmol, 1 eq.) in abs. MeCN (2 mL) was combined with $[Fe(MeCN)_6](BF_4)_2$ (55.0 mg,

0.12 mmol, 1 eq.) in abs. MeCN (2 mL). In a cuvette with nitrogen atmosphere 210 µL of this complex solution were diluted in abs. MeCN (2.3 mL). Afterwards, 500 µL of a mCPBA solution (77 %, 9.4 mg, 0.042 mmol in 3 mL of abs. MeCN) were added (1.2 eq.).
Plotted spectra: Figure 5.20.

Spectra of {3 + [Fe(MeCN)$_6$](BF$_4$)$_2$} + mCPBA in MeCN (Set-up E): Two solutions were prepared for this measurement. The first solution was obtained by combining a solution of [Fe(MeCN)$_6$](BF$_4$)$_2$ (19.0 mg, 0.04 mmol, 1 eq.) in abs. MeCN (5 mL) with a solution of **3** (12.8 mg, 0.04 mmol, 1 eq.) in abs. MeCN (5 mL). For the second solution, mCPBA (77 %, 8.7 mg, 0.02 mmol) was dissolved in abs. MeCN (10 mL). Prior to the measurements a baseline with pure MeCN was measured at −34 °C. For the measurements, the two solutions were mixed (2 ms) in equimolar amounts.
Plotted spectra: Figure 5.21.

Spectra of 3e + mCPBA (Set-up A): Crystals of complex **3e** (5.5 mg, 0.007 mmol) were dissolved in abs. MeCN (5 mL). 2.5 mL of this solution were measured in a cuvette under aerobic conditions. Afterwards, 500 µL of a mCPBA solution (77 %, 13.3 mg, 0.059 mmol in 5.7 mL of abs. MeCN) were added (1.4 eq.).
Plotted spectra: Figure 5.26.

UV/Vis Spectroscopic Measurements of Species with Ligand 4

Time Resolved Spectra in MeCN (Set-up B): **4** (2.2 mg, 0.006 mmol, 1 eq.) was dissolved in 1 mL and Fe(OTf)$_2 \cdot 2$ MeCN (2.6 mg, 0.006 mmol, 1 eq.) in 3 mL of MeCN. A baseline was measured with 6.0 mL of MeCN and both solutions were added for the measurements (c = 0.5 mM). Spectra were taken every 5 min for 16 h.
Plotted spectra: Figure 6.27.

Temperature Resolved Spectra in MeCN (Set-up B): **4** (10.0 mg, 0.025 mmol, 1.1 eq.) and Fe(OTf)$_2 \cdot 2$ MeCN (10.6 mg, 0.024 mmol, 1 eq.) were dissolved in 2.0 mL of MeCN. A baseline was measured with 9.6 mL of MeCN and 400 µL of the solution were added for the measurements (c = 0.5 mM). Spectra were taken from 45 °C to −42 °C in approx. 10 °C steps.
Plotted spectra: Figure 6.28.

Temperature Resolved Spectra in MeCN "OTf-free Conditions" (Set-up B): **4** (10.3 mg, 0.026 mmol, 1.1 eq.) and [Fe(MeCN)$_6$](BF$_4$)$_2$ (11.9 mg, 0.025 mmol, 1 eq.) were dissolved in 2.0 mL of MeCN. A baseline was measured with 9.6 mL of MeCN and 400 µL of the solution were added for the measurements (c = 0.5 mM). Spectra were taken from rt to

−42 °C to 65 °C to rt in ~ 10 °C steps.
Plotted spectra: Figure 6.29 & Figure 6.30.

Time Resolved Spectra in DCM (Set-up B): **4** (13.8 mg, 0.035 mmol, 1 eq.) and $Fe(OTf)_2 \cdot 2\,MeCN$ (15.1 mg, 0.035 mmol, 1 eq.) were combined with 13.5 mL of DCM and stirred for 4 h. A baseline was measured with 6.0 mL of DCM and 6.0 mL of the solution were added for the measurements (c = 1.3 mM). Spectra were taken every 5 min for 19 h.
Plotted spectra: Figure 6.35.

Temperature Resolved Spectra in DCM (Set-up B): **4** (20.0 mg, 0.05 mmol, 1 eq.) and $FeCl_2$ (15.1 mg, 0.05 mmol, 1 eq.) were combined with 4.0 mL of DCM and stirred for 30 min. Ag(OTf) (25.9 mg, 0.1 mmol, 2 eq.) was dissolved in a mixture of DCM (2 mL) and Et_2O (2 mL). The colourless Ag(OTf) solution was added to the dark purple complex solution. AgCl precipitated as a colourless solid and the solution was filtered. A baseline was measured with 9.4 mL of DCM and 600 µL of the filtered complex solution were added for the measurement (c = 0.4 mM). Spectra were taken from to 25 °C to −45 °C in ~ 10 °C steps.
Plotted spectra: Figure 6.36.

Spectrum of 4 in DCM (Set-up B): **4** (2.0 mg, 0.005 mmol) was dissolved in 1.0 mL of DCM. A baseline was measured with 9.0 mL of DCM. The ligand solution was added for the measurement (c = 0.5 mM).
Plotted spectrum: Figure 6.35.

Spectrum of 4 in MeCN (Set-up B): **4** (2.0 mg, 0.005 mmol) was dissolved in 1.0 mL of MeCN. A baseline was measured with 9.0 mL of MeCN. The ligand solution was added for the measurement (c = 0.5 mM).
Plotted spectrum: Figure A.10.

Spectrum of Compound C Dissolved in MeCN or DCM (Set-up C): A few crystals of compund C were dissolved in MeCN or DCM, respectively.
Plotted spectra: Figure 6.39.

Spectra of Compound C + mCPBA in MeCN (Set-up A): Compound **C** (5.7 mg, 0.0075 mmol for assumption of $[Fe(NQu_3)(OTf)_2]$) was dissolved in abs. MeCN (3.5 mL). 2.5 mL of this solution (c = 5 mM) were transferred into the cuvette. 0.5 mL of a solution of mCPBA (77 %, 9.0 mg, 0.04 mmol) in MeCN (3.8 mL) were added (0.005 mmol, 1 eq.).
Plotted spectra: Figure 6.41.

Spectra of Compound C + sPhIO in MeCN (Set-up A): Compound **C** (4.7 mg, 0.0062 mmol for assumption of $[Fe(NQu_3)(OTf)_2]$) was dissolved in abs. MeCN (2.9 mL). 2.5 mL of this solution (c = 5 mM) were transferred into the cuvette. 0.5 mL of a solution of sPhIO (93 %, 9.9 mg, 0.027 mmol) in DCM (1.4 mL) were added (0.01 mmol, 2 eq.).
Plotted spectra: Figure 6.42.

Spectra of Compound C + H_2O_2 in MeCN (Set-up A): Compound **C** (8.1 mg, 0.01 mmol for assumption of $[Fe(NQu_3)(OTf)_2]$) was dissolved in abs. MeCN (5 mL). 2.5 mL of this solution (c = 5 mM) were transferred into the cuvette. 0.5 mL of a solution of H_2O_2 (30 %, 30.5 µL, 0.3 mmol) in MeCN (3 mL) were added (0.05 mmol, 10 eq.).
Plotted spectra: Figure 6.43 & Figure 6.44.

Data Analysis: For time and temperature resolved measurements an occurring baseline shift was corrected by subtracting a baseline (minimum of spectrum). The extinction in temperature resolved spectra was calculated for all wavelengths (Lambert-Beer law, Equation 9.2)

$$\varepsilon = \frac{A}{d \cdot c} \tag{9.2}$$

and corrected due to temperature induced changes in volume and density of the solvent considering $c = \frac{n}{V}$ and $\rho(T) = \frac{m}{V}$ (Equation 9.3):

$$\varepsilon = \frac{A \cdot m}{d \cdot n \cdot \rho(T)} \tag{9.3}$$

ε:	extinction coefficient [$L\,mol^{-1}\,cm^{-1}$]	A:	absorption [-]
m:	mass of solvent [g]	d:	layer thickness [cm]
n:	amount of substance [mol]	$\rho(T)$:	density at temperature T [$g\,L^{-1}$]
c:	concentration [$mol\,L^{-1}$]	V:	Volume [L]

Temperature Dependent Density for Acetonitrile:[279]

$$\rho(T) = 0.80307 - 0.0010542 \cdot T \tag{9.4}$$

$\rho(T)$: density at temperature T [$g\,mL^{-1}$] T: temperature [°C]

Temperature Dependent Density for Dichloromethane: Densities were calculated using the modified Rackett equation and values from literature as described by Spencer and Adler:[280]

$$\frac{1}{\rho_s} = \left[\frac{R \cdot T_c}{p_c}\right] \cdot Z_{RA}^{\left[1+\left(1-\frac{T}{T_c}\right)^{\frac{2}{7}}\right]} \tag{9.5}$$

$$\rho = \rho_s \cdot M \tag{9.6}$$

ρ:	density [g/mL]	ρ_s:	saturated liquid density [mol/cm^3]
T:	temperature [K]	T_c	critical temperature [K], DCM: 510.0 K
p_c:	critical pressure [atm], DCM: 60.0 atm	M:	molar mass [g/mol]
Z_{RA}:	constant of the modified Rackett equation, DCM: 0.26184		
R:	universal gas constant, 82.06 atm cm^3 mol^{-1} K^{-1}		

Fitting of the Extinction Coefficients in the UV/Vis Spectra: Since SCO phenomena in solution are usually gradual and follow a Boltzmann distribution values of the extinction coefficients at certain temperatures can be fitted to calculate thermodynamic data using the following equations:[238]

$$\gamma_{HS} = \frac{\varepsilon - \varepsilon_{LS}}{\varepsilon_{HS} - \varepsilon_{LS}} \tag{9.7}$$

$$\gamma_{HS} = \frac{1}{1 + e^{\frac{\Delta H}{RT} - \frac{\Delta S}{R}}} \tag{9.8}$$

$$\varepsilon = \varepsilon_{LS} + \left(\frac{1}{1 + e^{\frac{\Delta H}{RT} - \frac{\Delta S}{R}}}\right) \cdot (\varepsilon_{HS} - \varepsilon_{LS}) \tag{9.9}$$

$$T_{1/2} = \frac{\Delta H}{\Delta S} \tag{9.10}$$

T:	temperature [K]	ε_{LS}:	extinction coefficient of pure low-spin state [L mol^{-1}cm^{-1}]
$T_{1/2}$:	SCO temperature [K]	ε_{HS}:	extinction coefficient of pure high-spin state [L mol^{-1}cm^{-1}]
ΔH:	enthalpy [J mol^{-1}]	γ_{HS}:	molar fraction of molecules in high-spin state
ΔS:	entropy [J mol^{-1} K^{-1}]	R:	universal gas constant, 8.31446 kg cm^2 s^{-2} mol^{-1} K^{-1}
ε:	extinction coefficient [L mol^{-1}cm^{-1}]		

9.1.5 SQUID Magnetometry

SQUID Magnetometry of Solid Samples

The magnetic susceptibility measurements in the solid state and the data correction were performed by Hend Shahed and Dr. Neetika Sharma at Jülich Centre for Neutron Science-2, Forschungszentrum Jülich, Germany. Measurements were performed on the crystals (taped with scotch on drinking straws used as sample holders) using the RSO (reciprocating sample option) option of a SQUID (superconducting quantum interference device) magnetometer from Quantum Design (model MPMS XL) applying a constant field of $\mu_0 H = 2$ T.

SQUID Magnetometry of Liquid Samples

SQUID magnetometry measurements in solution and data correction were performed by Dr. Sophie Schönfeld, Andreas Dürrmann in the group of Prof. Dr. Birgit Weber at University of Bayreuth, Germany. The magnetic measurements were carried out using a SQUID MPMS-XL5 magnetometer from Quantum Design, interfaced by MPMS MultiVu. A magnetic field of 5000 or 15000 Oe was applied, and the samples were measured in the range from 345 to 150 K in sweep mode (5 K min^{-1}). The quartz glass tubes were held in a plastic straw.

Sample Preparation: Crystals **C** were prepared via the low temperature route as described in synthesis the of **4a**. The solvent was removed and the crystals were washed with Et_2O (3×2 mL) and dried under reduced pressure. 9.5 mg of the crystals were dissolved in 250 µL of MeCN and 80 µL of this solution were transferred to a quartz glass tube. It was assumed that the solid complex has the composition $[Fe(NQu_3)(OTf)_2]$ (752.44 g mol^{-1}; see subsection 6.2.1). The solution was frozen in liquid nitrogen and the tube was evacuated. Afterwards, the tube was sealed by melting in an open flame, while the sample was tried to be kept frozen in liquid nitrogen at the same time. For diamagnetic correction, 80 µL of MeCN were put in a sealed quartz glass tube the same way as the sample and also measured. Two further samples were prepared for the diamagnetic correction using 80 µL of MeCN, where the quartz glass tube was sealed using Pattex®power clay to avoid sealing in the open flame and evaporation of the solvent, however the best correction results were obtained with the first sample (see below).

Data Correction: The raw data was corrected for the diamagnetism of the sample holder and solvent using an analogously prepared sample without iron complex. The obtained values for the diamagnetism of the solvent (see sample preparation above) were −0.00228 emu, −0.00168 emu and −0.00139 emu. The most reasonable result for the $\chi_M T$ plot was obtained for a correction with −0.00228 emu, which corresponds to the diamagnetic correction sample prepared via sealing by melting. The corresponding plot of the molar susceptibility temperature product is shown in Figure 6.31, although the molar susceptibility temperature product is significantly higher than expected for a HS iron(II) species. A diamagnetic solvent correction of −0.00168 emu delivered values which are much lower than expected (Figure A.14 in the Appendix). To avoid overparameterisation of the results, it was actively decided against using the average values of the two corrections while excluding the other options (see below), which would have resulted in "better" results. For the correction value of −0.00139 emu and further attempts to use literature values for acetonitrile resulted in negative molar susceptibility temperature products over the whole temperature range. Note that a small change in the correction for the diamagnetism of the solvent leads to drastic changes in the molar susceptibility temperature product. Potential reasons for the fluctu-

ations of the measured diamagnetic values of the acetonitrile solution are first of all the sample preparation (evaporation of the solvent during the sealing procedure). Furthermore, it cannot be ruled out, that for the different samples the inner diameter of the quartz glass tube is slightly different leading to differences in the sample shape. The diamagnetism of the organic ligand was corrected using tabulated Pascal's constants.[281]

Fitting of $\chi_M T$ Obtained in the SQUID Measurement: Simulation of the $\chi_M T$ curve can be performed similar to the extinction coefficients obtained from the UV/Vis spectroscopic data.[238] For the obtained values $(\chi_M T)_{LS}$ and $(\chi_M T)_{HS}$ it has to be kept in mind that the absolute values are erroneous due to difficulties with the diamagnetic correction and the potential presence of additional HS iron(III) impurities that do not show spin crossover:

$$\gamma_{HS} = \frac{\chi_M T - (\chi_M T)_{LS}}{(\chi_M T)_{HS} - (\chi_M T)_{LS}} \tag{9.11}$$

$$\gamma_{HS} = \frac{1}{1 + e^{\frac{\Delta H}{RT} - \frac{\Delta S}{R}}} \tag{9.12}$$

$$\chi_M T = (\chi_M T)_{LS} + \left(\frac{1}{1 + e^{\frac{\Delta H}{RT} - \frac{\Delta S}{R}}}\right) \cdot ((\chi_M T)_{HS} - (\chi_M T)_{LS}) \tag{9.13}$$

$$T_{1/2} = \frac{\Delta H}{\Delta S} \tag{9.14}$$

T:	temperature [K]	$(\chi_M T)_{LS}$:	molar susceptibility of pure low-spin state [$cm^3\,K\,mol^{-1}$]
$T_{1/2}$:	SCO temperature [K]	$(\chi_M T)_{HS}$:	molar susceptibility of pure high-spin state [$cm^3\,K\,mol^{-1}$]
ΔH:	enthalpy [$J\,mol^{-1}$]	γ_{HS}:	molar fraction of molecules in high-spin state
ΔS:	entropy [$J\,mol^{-1}\,K^{-1}$]	R:	universal gas constant, 8.31446 $kg\,cm^2\,s^{-2}\,mol^{-1}\,K^{-1}$
$\chi_M T$:	molar susceptibility [$cm^3\,K\,mol^{-1}$]		

9.1.6 Single Crystal X-ray Diffraction (SCXRD)

Data Collection

Two different diffractometers were used for intensity data collection. Full crystallographic data of selected SCXRD structures have been deposited with the Cambridge Crystallographic Data Centre as supplementary. The corresponding CCDC deposition numbers can be found in the crystallographic details in the appendix along with information about the diffractometer used for each crystal structure (Table A.5–Table A.17 in the Appendix).

STOE: Data were collected on a Stadivari diffractometer of STOE with an Eulerian cradle and Dectris Pilatus3 R 200K hybrid-pixel detector with GeniX 3D high flux Mo ($\lambda = 0.71073$ Å) or Cu radiation ($\lambda = 1.54186$ Å). The temperature was controlled with an Oxford Cryostream 800. Data were collected with X-Area Pilatus[282,283] and integrated with X-Area Integrate[284,285] and X-Area Recipe.[286,287] A spherical absorption correction was performed with STOE X-Red32 followed by a multi-scan absorption correction and scaling of reflections

with X-Area LANA.[288,289]

Bruker: Data were collected with a Bruker D8 goniometer with APEX CCD using an Incoatec microsource with Mo-Kα radiation (λ = 0.71073 Å) and temperature control was achieved with an Oxford Cryostream 700. Data were collected at 100 K in ω-scan mode, unless otherwise noted. Data were collected with SMART,[290] integrated with SAINT[291] and corrected for absorption by multi-scan methods with SADABS.[292]

Structure Solution & Refinement

The structures were solved by intrinsic phasing (ShelXT[293]) and refined with ShelXL[294] against F^2 with the full-matrix least-square method using ShelXle.[295] Non-hydrogen atoms were refined with anisotropic displacement parameters. All hydrogen atoms, except acidic protons, were calculated at idealised positions and refined with isotropic displacement parameters.

Special refinement details:

1b: In **1b** it was not possible to model the disordered toluene solvent molecules in an adequate manner, and the data set was treated with the BYPASS algorithm as implemented in PLATON/SQUEEZE.[156–158] The algorithm found a total volume of 400 Å^3 with 117 electrons in each unit cell. This approx. corresponds to one C_7H_8 molecule per complex molecule.

1f: In **1f** it was not possible to model the disordered toluene solvent molecules in an adequate manner, and the data set was treated with the BYPASS algorithm as implemented in PLATON/SQUEEZE.[156–158] The algorithm found a total volume of 964 Å^3 with 275 electrons in each unit cell. This approx. corresponds to one C_7H_8 molecule per complex molecule.

2b: In **2b** it was not possible to model the disordered acetonitrile solvent molecules in an adequate manner, and the data set was treated with the BYPASS algorithm as implemented in PLATON/SQUEEZE.[156–158] The algorithm found a total volume of 178 Å^3 with 45 electrons in each unit cell. This approx. corresponds to one C_2H_3N molecule per unit complex molecule.

3c: In **3c** it was not possible to model the disordered acetonitrile solvent molecules in an adequate manner, and the data set was treated with the BYPASS algorithm as implemented in PLATON/SQUEEZE.[156–158] The algorithm found a total volume of 231 Å^3 with 60 electrons in each unit cell. This approx. corresponds to 0.5 C_2H_3N molecules per complex molecule.

3e: In **3e** it was not possible to model the disordered diethyl ether solvent molecules in an adequate manner, and the data set was treated with the BYPASS algorithm as implemented in PLATON/SQUEEZE.[156–158] The algorithm found a total volume of 575 Å^3 with 148 electrons in each unit cell. This approx. corresponds to 3.5 $C_4H_{10}O$ molecules per complex molecule.

4b: In **4b** it was not possible to model the disordered solvent molecules in an adequate

manner, and the data set was treated with the BYPASS algorithm as implemented in PLATON/SQUEEZE.[156–158] The algorithm found two voids of 240 Å^3 with 59 electrons, respectively, in each unit cell. Considered the solvent used, this approx. corresponds to two molecules of $C_4H_{10}O$.

4c: In crystals of **4c** a minority species for the complex with Fe(2) was found to be present where the triflate anion in A position is replaced by a water co-ligand and the triflate anion that used to be at the A position is non-coordinating (17.8 %). In the structure model the Fe(2) – O_{H2O} distance was restrained to 2.01(1) Å and is thus not used for bond length or angle discussions.

4d: In **4d** it was not possible to model the disordered solvent molecules in an adequate manner, and the data set was treated with the BYPASS algorithm as implemented in PLATON/SQUEEZE.[156–158] The algorithm found a void of 175 Å^3 with 36 electrons in each unit cell. This approx. corresponds to 0.45 $C_4H_{10}O$ molecules per complex molecule.

4h: The crystals of **4h** tended to lose co-crystallised solvent (Z) rapidly, which reduced the quality of the crystals. Additionally, the poor packing of the molecules left space for larger amounts of non-coordinated solvent, which showed a high disorder so that not all electron density could be assigned properly. 1.3 molecules of dichloromethane per complex molecule could be assigned but 56 electrons per complex molecule were treated with the BYPASS algorithm as implemented in PLATON/SQUEEZE.[156–158] This could either be highly disordered dichloromethane or diethyl ether (Z). Furthermore, multiple twinning also influenced the quality of the solution of this crystal structure.

4n & 4o: In **4n** and **4o** it was not possible to model the disordered solvent molecules in an adequate manner, and the data set was treated with the BYPASS algorithm as implemented in PLATON/SQUEEZE.[156–158] The algorithm found a void of 211 Å^3 with 55 electrons in **4n** and a void of 229 Å^3 with 42 electrons in **4o**, respectively, in each unit cell. Considered the solvent used, this approx. corresponds to one molecules of CH_2Cl_2 per unit cell.

4r: In **4r** it was not possible to model the disordered diethyl ether solvent molecules in an adequate manner, and the data set was treated with the BYPASS algorithm as implemented in PLATON/SQUEEZE.[156–158] The algorithm found a total volume of 815 Å^3 with 174 electrons in each unit cell. This approx. corresponds to 0.5 $C_4H_{10}O$ molecules per complex molecule.

9.1.7 Powder X-ray Diffraction (PXRD)

PXRD experiments were performed at ambient conditions using 0.7 mm capillaries measured on a STOE STADI P ESSENTIALS diffractometer with Debye-Scherrer geometry (Cu-Kα_1, λ = 1.540598 Å, Dectris Mythen 1K detector). The crystalline powder was filled into the capillary under inert conditions and the capillary was sealed with plastic modelling clay.

9.1.8 Mößbauer Spectroscopy

The Mößbauer measurements and fitting of the data was performed by Dr. Linda Iffland-Mühlhaus in the group of Prof. Dr. Ulf-Peter Apfel at Ruhr-Universität Bochum, Germany. Mößbauer spectra were recorded at 80 K under N_2 atmosphere by using a SeeCo constant acceleration spectrometer equipped with a temperature controller maintaining temperatures within ±0.1 K and a ^{57}Co radiation source in a Rh matrix. Isomer shifts are referred to a α-Fe metal foil at room temperature. Data were fitted with a sum of Lorentzian quadrupole doublets by using a least-square routine with the WMOSS program.[296]

Sample Preparation

All samples were prepared under inert conditions. General, samples were transferred in liquid N_2, inserted in a He counter-stream and measured under N_2 atmosphere.

Species with Ligand 2: Crystals of **2a** (40 mg, 0.05 mmol) were dissolved in abs. MeCN (0.8 mL). For the precursor species approx. 0.3–0.4 mL of this solution were transferred into the measurement cell and frozen. For the oxidised species a mCPBA solution (77 %, 30 mg, mmol, dissolved in 0.96 mL of MeCN) was added to 0.4 mL of the complex solution. The mixture was frozen immediately or after 4 h stirring for subsequent measurement.

Species with Ligand 3: A solution with **3** (16.0 mg, 0.05 mmol, 1 eq.) and $[Fe(MeCN)_6](BF_4)_2$ (23.8 mg, 0.05 mmol, 1 eq.) in abs. MeCN (0.8 mL) was prepared. For the precursor species approx. 0.3–0.4 mL of this solution were transferred into the measurement cell and frozen. For the oxidised species, a mCPBA solution (77 %, 30 mg, mmol, dissolved in 0.96 mL of MeCN) was added to 0.4 mL of the complex solution. The mixture was frozen immediately for subsequent measurement.

Species with Ligand 4: Crystals **C** were prepared via the low temperature route as described in the synthesis of **4a**. The solvent was removed and the crystals were washed with Et_2O (3 × 2 mL) and dried under reduced pressure. Solid sample was prepared under Ar. For the dissolved crystal samples in solution, **4a** (21.9 mg) was dissolved under Ar in 0.4 mL of abs. MeCN and stirred for 10 min at rt. For the *in situ* prepared complex sample in solution, **4** (10.0 mg, 0.025 mmol, 1 eq.) and $Fe(OTf)_2 \cdot 2\,MeCN$ (10.9 mg, 0.025 mmol, 1 eq.) were dissolved under Ar in 0.4 mL of abs. MeCN and stirred for 30 min at rt. The freshly prepared crystals of **4a** (crystals **C**) were dissolved in MeCN. Et_2O was added and the mixture was stored at −35°C for crystallisation. After 3 days, mother liquor was decantated off and crystals were washed with Et_2O once, wetted with solvent and frozen. Samples of the solutions were prepared under inert conditions and freeze-quenched in liquid N_2. Compound **D** was synthesised as described in the synthesis of $[Fe(NQu_3)(OTf)_2] \cdot 1.3\,DCM \cdot Z$. The

crystals were washed with Et_2O (3 × 2 mL) and dried under reduced pressure. Solid sample was prepared under Ar.

9.1.9 Gas Chromatography (GC)

Gas chromatographic measurements were performed on a Shimadzu GC2010plus with a flame ionisation detector. Capillary column used for experiment with complex **2a** (substrates: cyclohexane and adamantane): FS-Supreme 5mS; 5 % phenylmethylpolysiloxane, length: 30 m, diameter: 0.32 mm, film thickness: 0.25 µm. Capillary column used for experiment with complex **2a** (substrates: cyclohexane-d_{12} vs. cyclohexane) and complexes with ligand **4**: FS-OV-1701-CB-0.25, 86 % methyl-, 7 % cyanopropyl- und 7 % phenylsilicone, length: 30 m, diameter: 0.32 mm, film thickness: 0.25 µm. For quantifying the products, calibration curves were recorded using nitrobenzene as internal standard. For all peaks, the retention times were compared to authentic samples.

9.1.10 Cyclic Voltammetry

Cyclic voltammetry measurements were performed at ambient conditions with a Metrohm Autolab Potentiostat PGSTAT 101 using a three-electrode arrangement with a Pt disc working electrode (1 mm diameter), a Pt wire as counter electrode and an Ag/AgCl reference electrode (in saturated ethanolic LiCl). The measurements were performed in MeCN containing 0.1 mol L^{-1} NBu_4PF_6. Ferrocene was added as an internal standard after the measurements of the sample and all potentials are referenced relative to the Fc/Fc^+ couple. Cyclic voltammograms were measured with 200 mV/s, 100 mV/s, 50 mV/s and 20 mV/s. For data acquisition and analysis, the NOVA 2.1 (Build 5763) software from Metrohm Autolab was used.

9.1.11 Femtosecond X-ray Emission Spectroscopy (XES) Pump-Probe Experiments

Femtosecond X-ray emission spectroscopy experiments (XES) were carried out at European XFEL (Hamburg/Schenefeld, Germany) at the femtosecond X-ray experiments (FXE) instrument in November 2021. The measurements were performed in cooperation with Dr. Mykola Biednov and support of the whole FXE group under supervision of Dr. Christopher Milne.

Femtosecond XES Sample Preparation

Complex 5a. 507 mg of solid complex **5a** were dissolved in water (60 mL, Milli-Q®, 10 mM). The sample was handled under aerobic conditions. For UV/Vis spectroscopic measurements

(Set-up **F**) before and after X-ray radiation 1 mL of the sample solution was diluted with 9 mL of pure solvent.

Complex 2a. 480 mg of solid complex **2a** were dissolved in acetonitrile (60 mL, hypergrade for LC-MS LiChrosolv®, 10 mM). The sample was handled under aerobic conditions. For UV/Vis spectroscopic measurements (Set-up **F**) before and after X-ray radiation 1 mL of the sample solution was diluted with 9 mL of pure solvent.

Femtosecond XES Set-up

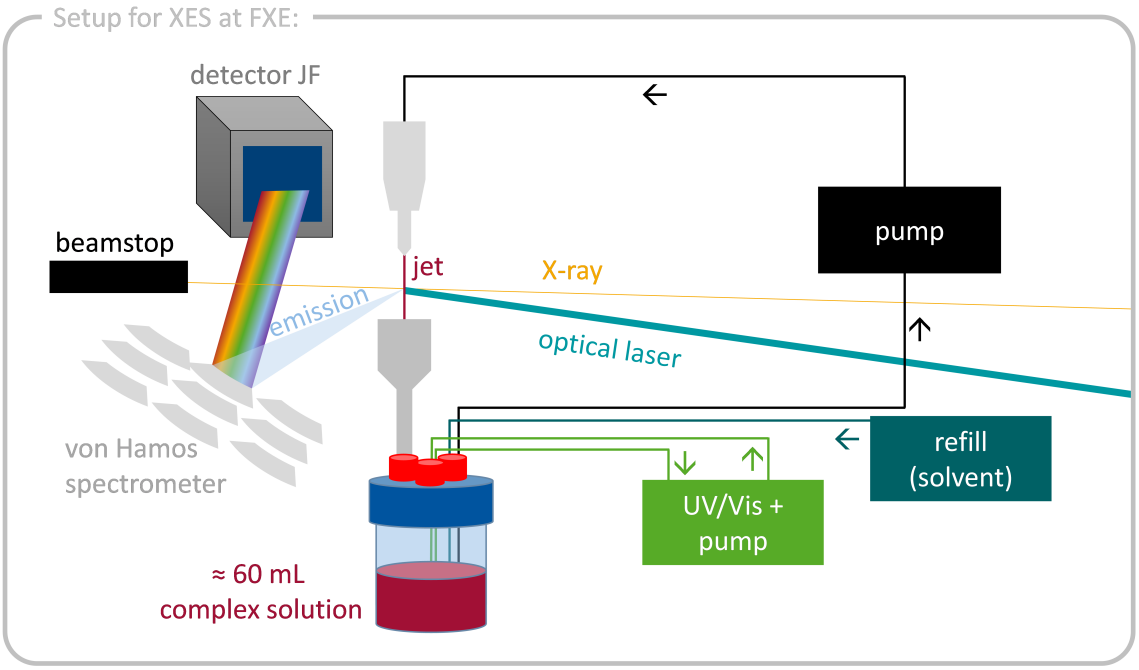

Figure 9.1: Schematic depiction of measurement set-up used for XES pump-probe experiments with complexes **5a** and **2a** at FXE (European XFEL).

The jet speed for both samples was 30 mL/min delivered by a Shimadzu HPLC LC-20AP pump. The optical excitation of **5a** was performed using pulses with central wavelength of 400 nm, generated as a second harmonic of the fundamental wavelength of the pump-probe laser system 1 of European XFEL.[209] The **2a** sample was excited using 510 nm laser pulses, produced using the optical parametric amplifier TOPAS Prime, pumped by the pump-probe laser system 1 of European XFEL.[209] Samples were probed by X-ray pulses at 9.3 keV. The pulse energy was 1.6 mJ for **5a** and 1.8 mJ for **2a**. The intra-train repetition rate was 0.564 MHz with 150 for **5a** or 180 pulses per train for **2a**. The laser spot at both wavelengths had diameter of 50 µm FWHM. The intra-train of the laser was equal to the intra-train repetition rate of X-rays, each second X-ray train was optically pumped (5 Hz pumping). The jet diameter was 100 µm (round jet). A von Hamos dispersive-type spectrometer in combination with a Jungfrau 500k detector was used for simultaneous recording of Kα and

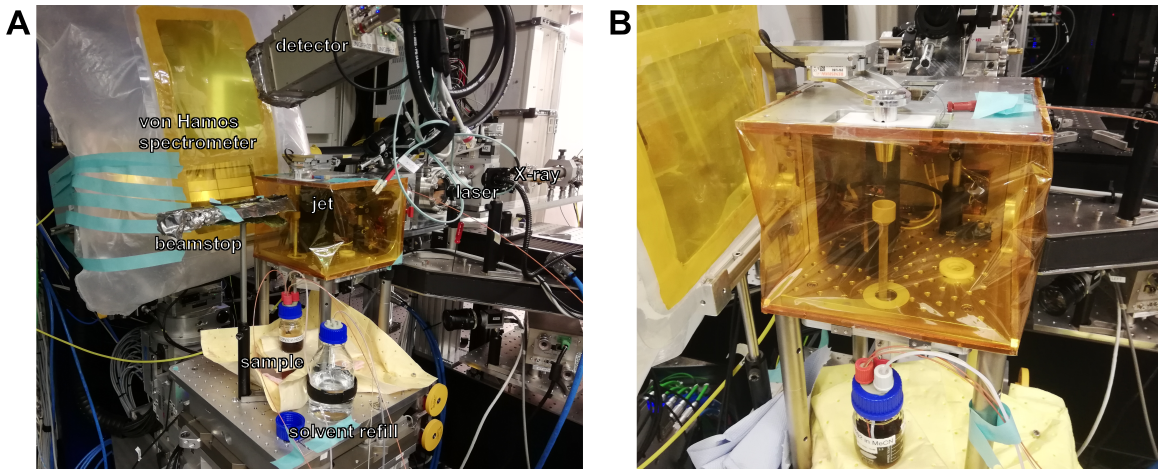

Figure 9.2: Photographs of measurement set-up used for XES pump-probe experiments with complexes **5a** and **2a** at FXE (European XFEL). Overview of the set-up (left, A) and close-up of the measurement chamber around the jet (right, B).

Kβ emission lines. Several pump-probe delays were measured with an exposure of 30 s for each delay point with each delay scan repeated up to 5 times to reach the desired signal to noise ratio.
A region of interest containing the Kα or Kβ spectrum was selected for analysis and the corresponding rows were summed. To obtain the background, lines that did not contain a spectrum were summed and subtracted from the spectra. Each spectrum was area normalised for further processing after additional subtraction of the linear background. The transient signals were obtained by subtracting the laser OFF (unpumped, without laser excitation) from the laser ON (pumped, with laser excitation) spectra. The spectra were normalised to the area under the curve.

9.2 Software

9.2.1 Figures

Measurement data was plotted with OriginPro 2021b (version 9.8.5.212) from OriginLab. Figures with chemical structure formulas were created with ChemDraw (version 20.1.1). Ball and stick representations of SCXRD structures were created with ORTEP3 and rendered with POV-Ray (version 3.7). Capped stick representations of SCXRD structures were crated with Mercury (version 2020.3.0)[297] and rendered with POV-Ray (version 3.7). Displacement ellipsoid plots of SCXRD structures were created with PLATON.[157,158] Figures showing protein SCXRD structures were created with Mol* as implemented in the website of the PDB.[23,31]

10 Substances & Synthesis of Compounds

10.1 Substances Obtained from Commercial Vendors

Table 10.1: List of chemicals obtained from commercial vendors.

Substance	Vendor
acetonitrile (≥ 99.8 %)	Fisher Chemical
acetonitrile-d_3 (≥ 99.8 %)	Sigma-Aldrich
adamantane (≥ 99 %)	Aldrich Chemistry
adamantanol (99 %)	Acros Organics
adamantanone (98 %)	Alfa Aesar
ammonium trifluoromethanesulfonate (99 %)	Acros Organics
chloroform-d (99.8 atom % D)	Sigma-Aldrich
copper(I) bromide (99 %)	Sigma-Aldrich
copper(II) bromide (99 %)	abcr
copper(I) chloride (99 %)	Alfa Aesar
cyclohexane (99.5 atom % D)	Aldrich Chemistry
cyclohexane (99.5 %)	Acros Organics
cyclohexanol (98 %)	Acros Organics
cyclohexanol-d_{12} (98 atom % D)	Aldrich Chemistry
cyclohexanone (99 %)	abcr
cyclohexanone-d_{10} (98 atom % D)	Camebridge Isotope Laboratries
dichloromethane (≥ 99.8 %)	Fisher Chemical
dichloromethane-d_2 (≥ 99.8 %)	Euriostop
diethyl ether (≥ 99.8 %)	Fisher Chemical
dimethyl sulfoxide-d_6 (99.8 atom % D)	Sigma-Aldrich
ethyl acetate (≥ 99.8 %)	Fisher Chemical
hydrogen peroxide (30 %)	Chemsolute
Geduran®Si 60 (SiO_2)	Merck
iron(II) bromide (98 %)	Thermo Scientific
iron(II) bromide (anhydrous, 99,99 %)	Alfa Aesar
iron(II) chloride (99.5 %)	Alfa Aesar
iron(II) chloride (anhydrous, 99.5 %)	Alfa Aesar
iron(III) bromide (99 %)	abcr
iron(III) bromide (anhydrous, 99 %)	abcr
iron(III) chloride (> 98 %)	Riedel de Haën
iron(III) chloride (anhydrous, 99.9 %)	Sigma-Aldrich
iron(III) nitrate nonahydrate (≥ 98 %)	Sigma-Aldrich
magnesium sulfate (99 %)	Grüssing
m-chloroperoxybenzoic acid (77 %)	Sigma-Aldrich
methanol (≥ 99.9 %)	Fisher Chemical
methyl-6-brompyridine-2-carboxylate (≥ 95 %)	abcr
n-butyllithium (2.5 mM in hexane)	Acros Organics
n-hexane (95 %)	Fisher Chemical

Substance	Vendor
nitrobenzene (99 %)	Sigma-Aldrich
paraformaldehyde (> 95 %)	Merck Schuchardt
potassium iodide (> 99.5 %)	VWR
potassium *t*-butoxide (98 %)	Sigma-Aldrich
propionitrile (≥ 99 %)	Sigma-Aldrich
silver chloride	Riedel de Haën
silver hexafluorophosphate (99 %)	abcr
silver trifluoromethanesulfonate (≥ 99 %)	Sigma-Aldrich
tetrabutylammonium hexafluoridophosphate (≥ 99.0 %)	Sigma-Aldrich
tetrahydrofuran (≥ 99.8 %)	Fisher Chemical
triphenylphosphine (99 %)	Sigma-Aldrich
toluene (≥ 99.8 %)	Fisher Chemical
zinc(II) chloride (99 %)	Alfa Aesar

For experiments with exclusion of water, solvents were dried according to the literature.[298] For very sensitive compounds, the dried solvents were additionally stored over molecular sieves.

10.2 Substances Synthesised According to Literature Protocols

Following substances were resynthesised according to literature or previous reports by the Herres-Pawlis group: $Fe(OTf)_2 \cdot 2\,MeCN$,[299] $[Fe(MeCN)_6](BF_4)_2$,[300] $[Fe(NSC)_2(Py)_4]$,[301] 2-(pyridinyl)bis(pyrazolyl)methane,[141] 2,2'-(ethane-1,1-diyl)dipyridine,[302] $MeC(Py)_2Phen$ (**2**),[136,189] $[Fe(MeC(Py)_2Phen)(MeCN)_2](OTf)_2$ (**2a**),[136,189] sPhIO,[93]* NQu_3 (**4**)[241] and $[Fe(HC(3,5-MePz)_2Py)_2](CF_3CO_2)_2$ (**5a**).[135]

10.3 Synthesis of Ligands

10.3.1 Synthesis of $HOCH_2C(Pz)_2Py$ (1)

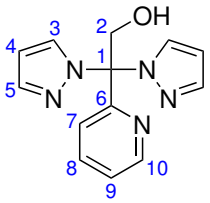

1
$C_{13}H_{13}N_5O$
MW: 255.28 g/mol

In a Schlenk flask with abs. THF (100 mL), 2-(pyridinyl)bis(pyrazolyl)methane (2.04 g, 9.06 mmol, 1.0 eq.) was added under a nitrogen stream followed by potassium *t*-butoxide (2.60 g, 23.2 mmol, 2.6 eq.) and paraformaldehyde (689 mg, 22.9 mmol, 2.5 eq.). This mixture was stirred overnight. The reaction was stopped by adding water (100 mL). The product was extracted with diethyl ether (3 × 60 mL) and dried over $MgSO_4$. After filtration, the solvent was removed under reduced pressure and the product was recrystallised from ethyl acetate. The colourless slightly yellowish solid was collected and dried (yield: 1.76 g, 6.89 mmol, 76 %).

^{1}H-NMR (400 MHz, $CDCl_3$, 25 °C): δ = 8.63 (ddd, J = 4.8, 1.8, 0.9 Hz, 1H, H-10), 7.71 (td, J = 8.0, 4.0 Hz, 1H, H-8), 7.67 (dd, J = 1.8, 0.7 Hz, 2H, H-5), 7.35 (dd, J = 2.6, 0.7 Hz, 2H, H-3), 7.33 (ddd, J = 7.6, 4.8, 1.1 Hz, 1H, H-9), 6.53 (dt, J = 8.0, 1.0 Hz, 1H, H-7), 6.36 (dd, J = 2.6, 1.8 Hz, 2H, H-4), 4.98 (s, 2H, H-2) ppm.

^{13}C-NMR (101 MHz, $CDCl_3$, 25 °C): δ = 157.8 (1C, C-6), 149.1 (1C, C-10), 140.5 (2C, C-5), 137.4 (1C, C-8), 130.6 (2C, C-3), 124.0 (1C, C-9), 122.4 (1C, C-7), 106.2 (2C, C-4), 83.0 (1C, C-1), 68.5 (1C, C-2) ppm.

IR (ATR), $\tilde{\nu}$ [cm^{-1}]: 3246 (w), 3158 (w), 3131 (w), 3118 (w), 3066 (vw), 2959 (vw), 2935 (vw), 1587 (m), 1573 (w), 1517 (w), 1461 (m), 1453 (w), 1436 (m), 1421 (m), 1392 (m), 1354 (vw), 1331 (m), 1299 (m), 1277 (m), 1261 (w), 1245 (m), 1225 (w), 1214 (w), 1202 (m), 1112 (m), 1104 (m), 1084 (vs), 1065 (m), 1052 (m), 1044 (m), 1034 (m), 994 (m), 964 (w), 951 (m), 925 (s), 915 (m), 896 (w), 889 (w), 864 (w), 846 (vw), 788 (w), 770 (s), 754 (vs), 742 (s), 694 (m), 658 (m), 627 (m), 618 (s), 613 (m), 604 (s), 519 (w), 515 (vw), 408 (m).

*Caution: synthesis route contains explosive intermediates! The purity of sPhIO was determined by iodometric titration to 93 %.

HRMS (ESI$^+$, in MeCN, *m/z* [%]): Calc.: 278.10123 (100) $[NaC_{13}H_{13}N_5O]^+$, 279.10459 (14) $[Na^{12}C_{12}{}^{13}C_1H_{13}N_5O]^+$. Found: 278.10053 (100), 279.10340 (15).

10.3.2 Synthesis of MeC(Py)$_2$PicMe (3)

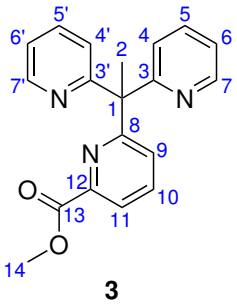

3
$C_{19}H_{17}N_3O_2$
MW: 319.36 g/mol

At −78 °C, *n*-BuLi (4 mL, 2.5 mM in hexane, 1.2 eq.) was added dropwise to a solution of 2,2'-(ethane-1,1-diyl)dipyridine (1.9 g, 10.0 mmol, 1.2 eq.) in THF (50 mL). After stirring for 1 h at −78 °C, methyl-6-bromopyridine-2-carboxylate (1.8 g, 8.3 mmol, 1 eq.) dissolved in THF (10 mL) and was added to the solution. The mixture was gently warmed to ambient temperature and afterwards refluxed for 40 h. After quenching with water (50 mL), the mixture was extracted with DCM (3 × 50 mL). The combined organic phases were washed with brine (100 mL) and dried over $MgSO_4$. The solvent was removed under reduced pressure and the crude product was obtained as a brown oil. The product was dissolved in warm hexane (≈ 200 mL, 50 °C) and the solution filtered resulting in a bright yellow solution. At lower temperatures the product precipitated in hexane and yellow solid of **3** could be separated (yield: 0.74 g, 2.3 mmol, 28 %).

^{1}H-NMR (400 MHz, $CDCl_3$, 25 °C): δ = 8.59–8.53 (m, 2H, H-7), 7.94 (dd, J = 7.6, 1.0 Hz, 1H, H-11), 7.68 (t, J = 7.8 Hz, 1H, H-10), 7.59 (td, J = 7.8, 1.9 Hz, 2H, H-5), 7.36 (dd, J = 8.0, 1.0 Hz, 1H, H-9), 7.12 (ddd, J = 8.0, 5.6, 1.1 Hz, 4H, H-4 & H-6), 3.91 (s, 3H, H-14), 2.37 (s, 3H, H-2) ppm.

^{1}H-NMR (400 MHz, DMSO-d_6, 25 °C): δ = 8.51–8.46 (m, 2H, H-7), 7.89 (dd, J = 7.7, 1.2 Hz, 1H, H-11), 7.83 (t, J = 7.8 Hz, 1H, H-10), 7.70 (td, J = 7.8, 1.9 Hz, 2H, H-5), 7.27–7.19 (m, 3H, H-6 & H-9), 7.05 (d, J = 7.9 Hz, 2H, H-4), 3.82 (s, 3H, H-14), 2.21 (s, 3H, H-2) ppm.

^{13}C-NMR (101 MHz, $CDCl_3$, 25 °C): δ = 166.3 (1C, C-13), 165.9 (2C, C-3), 165.7 (1C, C-8), 148.9 (2C, C-7), 147.0 (1C, C-12), 136.4, (1C, C-10), 136.3 (2C, C-5), 127.9 (1C, C-9), 123.4 (2C, C-4), 123.0 (1C, C-11), 121.4 (2C, C-6), 60.4 (1C, C-1), 52.6 (1C, C-14), 27.2 (1C, C-2) ppm.

^{13}C-NMR (101 MHz, DMSO-d_6, 25 °C): δ = 165.7 (1C, C-8), 165.5 (1C, C-13), 165.3 (2C, C-3), 148.7 (2C, C-7), 146.4 (1C, C-12), 137.1 (1C, C-10), 136.6 (2C, C-5), 127.9 (1C, C-9), 123.3 (2C, C-4), 122.8 (1C, C-11), 121.8 (2C, C-6), 60.1 (1C, C-1), 52.6 (1C, C-14), 27.1 (1C, C-2) ppm.

IR (ATR), $\tilde{\nu}$ [cm^{-1}]: 2986 (vw), 2956 (vw), 1739 (vs), 1586 (s), 1565 (m), 1470 (w), 1459 (m), 1447 (m), 1372 (w), 1298 (m), 1255 (m), 1242 (m), 1215 (w), 1195 (m), 1170 (w), 1142 (m), 1109 (w), 1101 (w), 1093 (w), 1084 (w), 1060 (w), 1048 (w), 991 (m), 984 (m), 900 (vw), 879 (w), 869 (w), 825 (w), 790 (m), 775 (m), 763 (s), 749 (vs), 739 (w), 677 (m), 654 (m), 639 (m), 617 (m), 581 (m), 403 (m).

HRMS (ESI$^+$, in MeCN, *m/z* [%]): Calc.: 320.13935 (100) $[C_{19}H_{18}N_3O_2]^+$, 321.14271 (21) $[^{12}C_{18}{}^{13}C_1H_{18}N_3O_2]^+$, 322.14606 (2) $[^{12}C_{17}{}^{13}C_2H_{18}N_3O_2]^+$. 342.12130 (100) $[NaC_{19}H_{17}N_3O_2]^+$, 343.12465 (21) $[Na^{12}C_{18}{}^{13}C_1H_{17}N_3O_2]^+$, 344.12801 (2) $[Na^{12}C_{17}{}^{13}C_2H_{17}N_3O_2]^+$. Found:

320.13868 (100), 321.14188 (21), 322.14482 (3). 342.12072 (100), 343.12380 (22), 344.12672 (3).

10.3.3 Synthesis of $H_3(NQu_3)(OTf)_3 \cdot DCM$

A threefold protonated ligand structure $H_3(NQu_3)(OTf)_3 \cdot DCM$ was obtained under aerobic conditions as side product of a reaction mixture used for a UV/Vis spectroscopic experiment. 6 mL of a solution of $Fe(OTf)_2 \cdot 2\,MeCN$ (14.7 mg, 0.034 mmol 1 eq.) and **4** (14.1 mg, 0.035 mmol, 1.1 eq.) in DCM (9 mL, 15 min stirring) were diluted in DCM (6 mL). This solution was stirred overnight and 1 mL of a solution of sPhIO (12.8 mg, 0.038 mmol, 1.1 eq.) in DCM (1.5 mL) was added the next day. After a few hours of stirring the mixture was stored in a capped vial at aerobic conditions. Two months later, an orange powder and colourless crystals which were suitable for SCXRD could be obtained. A selective bulk analysis could not be performed because the crystals could not be separated selectively from the orange powder in an appropriate amount.

10.4 Synthesis of Complexes

Complexes with ligand **1** were synthesised under aerobic conditions with non-dried solvents. Complexes with ligands **2**, **3** and **4** were synthesised under inert conditions (Schlenk-technique or glove box) with abs. solvents, unless otherwise noted.

10.4.1 Synthesis of Complexes with Ligand 1

Synthesis of $[Fe(HOCH_2C(Pz)_2Py)_2]Br_2 \cdot MeCN$ (1a)

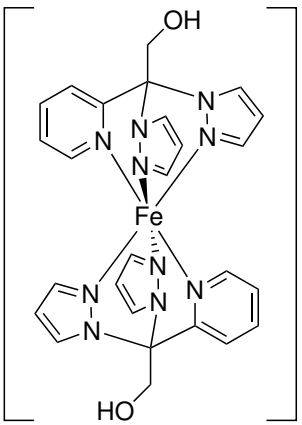

$Br_2 \cdot MeCN$

1a
$C_{28}H_{29}Br_2FeN_{11}O_2$
MW: 767.29 g/mol

To $FeBr_3$ (29.9 mg, 0.1 mmol, 1 eq.) in MeCN (6 mL) **1** (25.5 mg, 0.1 mmol, 1 eq.) was added. The resulting dark brown mixture was filtrated and stored at rt in a capped vial. Orange to yellow crystals could be obtained.

IR (ATR), $\tilde{\nu}$ [cm^{-1}]: 3110 (m), 3065 (m), 2899 (vw), 2843 (vw), 1602 (w), 1508 (w), 1478 (m), 1449 (w), 1413 (s), 1399 (m), 1373 (w), 1336 (m), 1313 (w), 1264 (w), 1225 (m), 1150 (m), 1106 (m), 1091 (s), 1077 (s), 1060 (m), 981 (w), 935 (m), 925 (m), 913 (m), 878 (m), 812 (w), 791 (m), 768 (s), 751 (vs), 718 (m), 694 (m), 664 (m), 651 (m), 630 (m), 597 (s), 522 (w), 481 (w), 450 (w), 409 (w).

HRMS (ESI^+, in MeCN, *m/z* [%]): Calc.: 282.08127 (6) $[C_{26}H_{26}N_{10}O_2{}^{54}Fe]^{2+}$, 282.58295 (2) $[^{12}C_{25}{}^{13}C_1H_{26}N_{10}O_2{}^{54}Fe]^{2+}$, 283.07893 (100) $[C_{26}H_{26}N_{10}O_2{}^{56}Fe]^{2+}$, 283.58061 (28)

$[^{12}C_{25}{}^{13}C_1H_{26}N_{10}O_2{}^{56}Fe]^{2+}$, 284.08229 (4) $[^{12}C_{24}{}^{13}C_2H_{26}N_{10}O_2{}^{56}Fe]^{2+}$. Found: 282.08038 (6), 282.58172 (2), 283.07804 (100), 283.57935 (33), 284.08019 (7).

Synthesis of $[Fe(HOCH_2C(Pz)_2Py)_2][FeBr_4]Br \cdot C_7H_8$ (1b)

To $FeBr_2$ (17.6 mg, 0.08 mmol, 1.1 eq.) and **1** (19.5 mg, 0.075 mmol, 1 eq.), MeCN (15 mL) was added. The mixture was filtrated and 2 mL of the resulting solution were taken. After gas phase diffusion with toluene (first at 6 °C, afterwards rt), brown crystals were obtained.

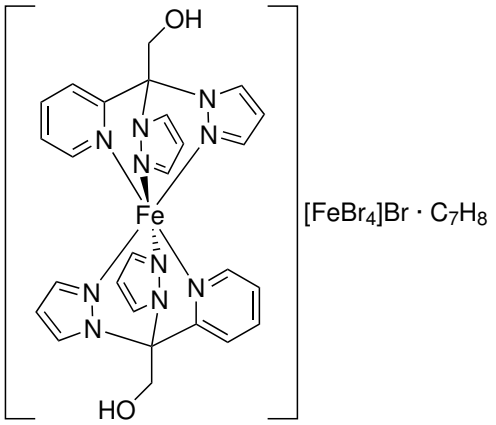

1b
$C_{33}H_{34}Br_5Fe_2N_{10}O_2$
MW: 1113.19 g/mol

IR (ATR), $\tilde{\nu}$ [cm^{-1}]: 3206 (w), 3156 (w), 3137 (w), 3106 (w), 2247 (w), 1602 (w), 1508 (w), 1471 (w), 1449 (w), 1410 (m), 1396 (m), 1337 (m), 1310 (w), 1262 (w), 1227 (m), 1159 (w), 1145 (w), 1106 (m), 1071 (m), 1058 (m), 980 (w), 935 (m), 912 (m), 876 (m), 754 (vs), 716 (m), 695 (m), 650 (w), 622 (m), 599 (m), 521 (w), 473 (w), 444 (w), 426 (w).

HRMS (ESI$^+$, in MeCN, *m*/*z* [%]): Calc.: 282.08127 (6) $[C_{26}H_{26}N_{10}O_2{}^{54}Fe]^{2+}$, 282.58295 (2) $[^{12}C_{25}{}^{13}C_1H_{26}N_{10}O_2{}^{54}Fe]^{2+}$, 283.07893 (100) $[C_{26}H_{26}N_{10}O_2{}^{56}Fe]^{2+}$, 283.58061 (28) $[^{12}C_{25}{}^{13}C_1H_{26}N_{10}O_2{}^{56}Fe]^{2+}$, 284.08229 (4) $[^{12}C_{24}{}^{13}C_2H_{26}N_{10}O_2{}^{56}Fe]^{2+}$. Found: 282.08038 (7), 282.58177 (2), 283.07811 (100), 283.57930 (36), 284.08025 (7).

Synthesis of $[Fe(HOCH_2C(Pz)_2Py)_2][FeCl_4]Cl \cdot 2\,MeCN$ (1c)

To $FeCl_2$ (12.2 mg, 0.1 mmol, 1 eq.) and **1** (25.1 mg, 0.1 mmol, 1 eq.), MeCN (5 mL) was added. The resulting orange solution was filtrated and the solution was stored in a capped vial at rt. Brown crystals could be obtained.

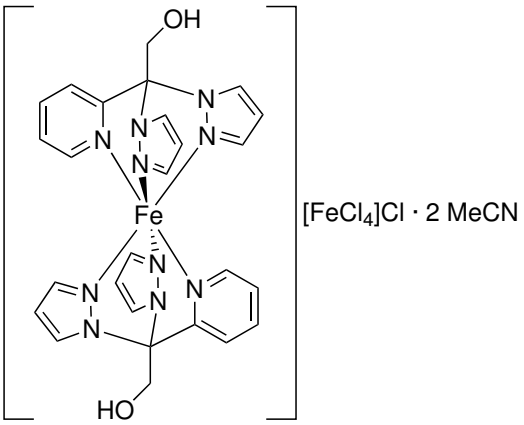

1c
$C_{30}H_{32}Cl_5Fe_2N_{12}O_2$
MW: 881.61 g/mol

IR (ATR), $\tilde{\nu}$ [cm^{-1}]: 3228 (w), 3120 (m), 2906 (vw), 2860 (vw), 2833 (vw), 2254 (vw), 1604 (w), 1513 (w), 1513 (w), 1473 (w), 1450 (w), 1412 (m), 1400 (m), 1370 (w), 1329 (m), 1312 (m), 1312 (m), 1265 (m), 1229 (s), 1213 (m), 1159 (m), 1148 (m), 1110 (m), 1090 (s), 1075 (m), 1063 (m), 983 (m), 936 (m), 929 (w), 913 (m), 898 (w), 898 (w), 877 (m), 813 (w), 813 (w), 762 (vs), 752 (vs), 725 (m), 695 (m), 666 (m), 666 (m), 649 (m), 630 (m), 613 (m), 599 (m), 555 (w), 523 (w), 480 (w), 455 (vw), 420 (vw).

HRMS (ESI$^+$, in MeCN, *m*/*z* [%]): Calc.: 282.08127 (6) $[C_{26}H_{26}N_{10}O_2{}^{54}Fe]^{2+}$, 282.58295

(2) $[^{12}C_{25}{}^{13}C_1H_{26}N_{10}O_2{}^{54}Fe]^{2+}$, 283.07893 (100) $[C_{26}H_{26}N_{10}O_2{}^{56}Fe]^{2+}$, 283.58061 (28) $[^{12}C_{25}{}^{13}C_1H_{26}N_{10}O_2{}^{56}Fe]^{2+}$, 284.08229 (4) $[^{12}C_{24}{}^{13}C_2H_{26}N_{10}O_2{}^{56}Fe]^{2+}$. Found: 282.08032 (6), 282.58169 (2), 283.07794 (100), 283.57924 (33), 284.08011 (7).

Synthesis of $[Fe(HOCH_2C(Pz)_2Py)_2](OTf)_2 \cdot 2\,MeCN$ (1d)

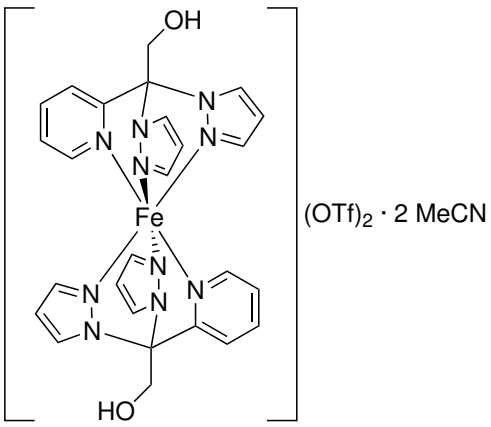

1d
$C_{32}H_{32}F_6FeN_{12}O_8S_2$
MW: 946.66 g/mol

To $Fe(OTf)_2 \cdot 2\,MeCN$ (21.0 mg, 0.05 mmol, 1 eq.) and **1** (25 mg, 0.1 mmol, 2 eq.), abs. MeCN (1 mL) was added and the mixture was stirred overnight. The resulting orange solution was placed in a second vial for gas phase diffusion with Et_2O. A red to orange powder precipitated which was discarded by filtration. From the remaining solution orange crystals could be obtained.

IR (ATR, $\tilde{\nu}$ [cm^{-1}]: 3360 (w, br), 3166 (vw), 3141 (vw), 3104 (vw), 2920 (vw), 2619 (vw), 2559 (vw), 2209 (w), 2020 (w), 1701 (w), 1654 (w), 1477 (w), 1414 (w), 1337 (w), 1290 (m), 1236 (m), 1222 (s), 1179 (m), 1149 (m), 1105 (w), 1082 (m), 1070 (w), 1025 (vs), 982 (w), 935 (w), 913 (w), 878 (w), 812 (vw), 748 (s), 722 (m), 696 (w), 637 (vs), 601 (m), 575 (w), 513 (m).

HRMS (ESI$^+$, in MeCN, *m/z* [%]): Calc.: 713.11511 (6) $[F_3C_{27}H_{26}N_{10}O_5{}^{54}Fe^{32}S]^+$, 714.11773 (2) $[F_3{}^{12}C_{26}{}^{13}C_1H_{26}N_{10}O_5{}^{54}Fe^{32}S]^+$, 715.11048 (100) $[F_3C_{27}H_{26}N_{10}O_5{}^{56}Fe^{32}S]^+$, 716.11293 (36) $[F_3{}^{12}C_{26}{}^{13}C_1H_{26}N_{10}O_5{}^{56}Fe^{32}S]^+$, 717.11182 (12) $[F_3C_{27}H_{26}N_{10}O_5{}^{56}Fe^{34}S]^+$ & $[F_3{}^{12}C_{25}{}^{13}C_2H_{26}N_{10}O_5{}^{56}Fe^{32}S]^+$, 718.11233 (3) $[F_3{}^{12}C_{26}{}^{13}C_1H_{26}N_{10}O_5{}^{56}Fe^{34}S]^+$. Found: 713.11428 (15), 714.11699 (5), 715.11204 (100), 716.11259 (82), 717.11132 (23), 718.11143 (5).

Synthesis of $[Zn(HOCH_2C(Pz)_2Py)_2][ZnCl_4]$ (1e)

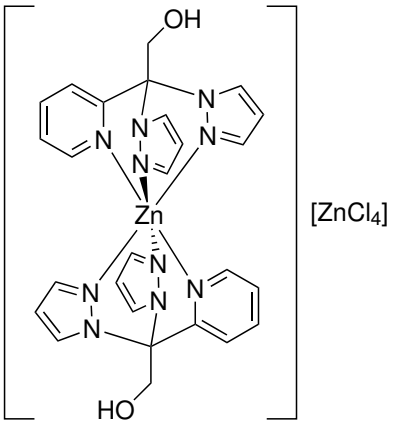

1e
$C_{26}H_{26}Cl_4N_{10}O_2Zn_2$
MW: 783.11 g/mol

To $ZnCl_2$ (14.2 mg, 0.1 mmol, 1 eq.) and **1** (25.2 mg, 0.1 mmol, 1 eq.), THF (20 mL) was added. The colourless solution was filtrated and 2 mL of the filtrate were taken for gas phase diffusion with toluene (2.5 mL) as anti-solvent. Colourless crystals were obtained.

IR (ATR, $\tilde{\nu}$ [cm^{-1}]: 3375 (vw, br), 3132 (vw), 2926 (vw), 2852 (vw), 2322 (vw), 1659 (vw), 1636 (vw), 1520 (w), 1474 (w), 1443 (m), 1400 (m), 1330 (m), 1258 (m), 1226 (m), 1203 (w), 1165 (w), 1140 (w), 1107 (m), 1085 (s), 1056 (m), 1016 (m), 972 (m), 929 (m), 912 (m), 878 (w), 768 (m), 753 (vs), 721 (m), 693 (m), 655 (m), 641 (w), 615 (s), 598 (m), 512 (w), 415 (m).

In ESI-HRMS spectra of **1e** no zinc complex but $[\mathbf{1} + Na]^+$ and $[(\mathbf{1})_2 + Na]^+$ species could be identified.

Synthesis of $[Cu_2(\mu{-}Br)Br_2(HOCH_2C(Pz)_2Py)_2]Br \cdot C_7H_8$ (1f)

To $CuBr_2$ (23.3 mg, 0.1 mmol, 1 eq.) and **1** (26.0 mg, 0.1 mmol, 1 eq.), MeCN (20 mL) was added. The resulting mixture was filtered and 2 mL of the filtrate were taken for gas phase diffusion with toluene (2.5 mL) as anti-solvent. From the dark red solution besides blue also yellow crystals were obtained. This are the yellow crystals, which correspond to the structure depicted on the side.

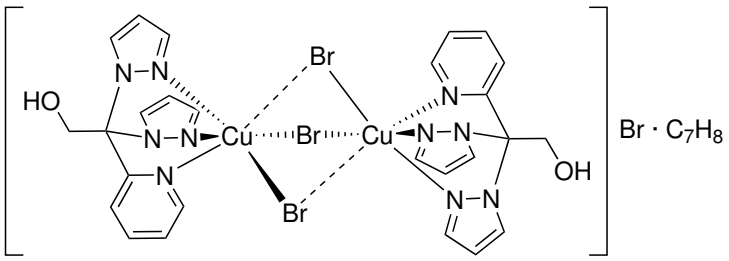

1f
$C_{33}H_{34}Br_4Cu_2N_{10}O_2$
MW: 1049.41 g/mol

IR (ATR), $\tilde{\nu}$ [cm^{-1}]: 3376 (w, br), 3157 (w), 3110 (m), 3021 (vw), 2903 (vw), 2330 (vw), 1593 (m), 1508 (w), 1473 (w), 1443 (m), 1403 (m), 1388 (m), 1334 (m), 1258 (m), 1223 (s), 1166 (w), 1141 (w), 1104 (m), 1075 (m), 1013 (m), 972 (m), 932 (m), 923 (w), 913 (m), 879 (m), 815 (vw), 755 (vs), 718 (m), 693 (m), 688 (m), 655 (w), 636 (w), 614 (m), 601 (m), 510 (w), 409 (w).

HRMS (ESI$^+$, in MeCN, *m/z* [%]): Calc.: 872.83768 (17) $[C_{26}H_{26}{}^{79}Br_3{}^{63}Cu_2N_{10}O_2]^+$, 873.84035 (5) $[{}^{12}C_{25}{}^{13}C_1H_{26}{}^{79}Br_3{}^{63}Cu_2N_{10}O_2]^+$, 874.83579 (66) $[C_{26}H_{26}{}^{79}Br_2{}^{81}Br_1{}^{63}Cu_2N_{10}O_2]^+$, 875.83839 (21) $[{}^{12}C_{25}{}^{13}C_1H_{26}{}^{79}Br_2{}^{81}Br_1{}^{63}Cu_2N_{10}O_2]^+$, 876.83397 (100) $[C_{26}H_{26}{}^{79}Br_1{}^{81}Br_2{}^{63}Cu_2N_{10}O_2]^+$ & $[C_{26}H_{26}{}^{79}Br_2{}^{81}Br_1{}^{63}Cu_1{}^{65}Cu_1N_{10}O_2]^+$, 877.83647 (31) $[{}^{12}C_{25}{}^{13}C_1H_{26}{}^{79}Br_1{}^{81}Br_2{}^{63}Cu_2N_{10}O_2]^+$ & $[{}^{12}C_{25}{}^{13}C_1H_{26}{}^{79}Br_2{}^{81}Br_1{}^{63}Cu_1{}^{65}Cu_1N_{10}O_2]^+$, 878.83227 (74) $[C_{26}H_{26}{}^{79}Br_1{}^{81}Br_2{}^{63}Cu_1{}^{65}Cu_1N_{10}O_2]^+$, 879.83461 (23) $[{}^{12}C_{25}{}^{13}C_1H_{26}{}^{79}Br_1{}^{81}Br_2{}^{63}Cu_1{}^{65}Cu_1N_{10}O_2]^+$, 880.83082 (28) $[C_{26}H_{26}{}^{81}Br_3{}^{63}Cu_1{}^{65}Cu_1N_{10}O_2]^+$, 881.83286 (8) $[{}^{12}C_{25}{}^{13}C_1H_{26}{}^{81}Br_3{}^{63}Cu_1{}^{65}Cu_1N_{10}O_2]^+$, 882.83005 (4) $[C_{26}H_{26}{}^{81}Br_3{}^{65}Cu_2N_{10}O_2]^+$, 883.83147 (1) $[{}^{12}C_{25}{}^{13}C_1H_{26}{}^{81}Br_3{}^{65}Cu_2N_{10}O_2]^+$. Found: 872.83801 (16), 873.84023 (5), 874.83605 (66), 875.83875 (19), 876.83427 (100), 877.83711 (29), 878.83240 (72), 879.83491 (20), 880.83095 (23), 881.83326 (6), 882.83083 (3), 883.83215 (1).

Synthesis of $[Cu_2(OCH_2C(Pz)_2Py)_2Cl_2]$ (1g)

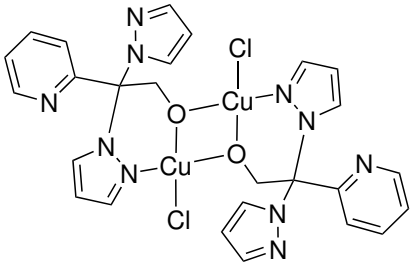

1g
$C_{26}H_{24}Cl_2Cu_2N_{10}O_2$
MW: 706.54 g/mol

To CuCl (9.9 mg, 0.1 mmol, 1 eq.) and **1** (25.5 mg, 0.1 mmol, 1 eq.), MeCN (15 mL) was added. From the resulting colourless solution 2.5 mL were taken for gas phase diffusion with toluene (2.5 mL) as anti-solvent where green crystals could be obtained.

IR (ATR), $\tilde{\nu}$ [cm^{-1}]: 3108 (vw), 2885 (vw), 2376 (vw), 2319 (vw), 1604 (w), 1588 (w), 1576 (vw), 1512 (w), 1476 (w), 1466 (w), 1436 (m), 1424 (w), 1404 (w), 1391 (m), 1329 (m), 1295 (w), 1277 (w), 1237 (m), 1198 (m), 1130 (m), 1118 (w), 1070 (m), 1057 (m), 994 (w), 979 (w), 962 (w), 935 (w), 914 (m), 882 (m), 860 (w), 831 (w), 800 (vw), 759 (vs), 748 (s), 700 (m), 691 (m), 672 (m), 661 (m), 655 (m), 633 (m), 621 (m), 615 (m), 610 (m), 547 (w), 513 (w), 444 (w), 425 (w), 403 (vw).

HRMS (ESI$^+$, in MeCN, *m/z* [%]): Calc.: 669.03587 (79) $[C_{26}H_{24}{}^{35}Cl^{63}Cu_2N_{10}O_2]^+$, 670.03853 (25) $[^{12}C_{25}{}^{13}C_1H_{24}{}^{35}Cl^{63}Cu_2N_{10}O_2]^+$, 671.03407 (100) $[C_{26}H_{24}{}^{35}Cl^{63}Cu_1{}^{65}Cu_1N_{10}O_2]^+$, 672.03654 (31) $[^{12}C_{25}{}^{13}C_1H_{24}{}^{35}Cl^{63}Cu_1{}^{65}Cu_1N_{10}O_2]^+$, 673.03247 (44) $[C_{26}H_{24}{}^{37}Cl^{63}Cu_1{}^{65}Cu_1N_{10}O_2]^+$ & $[C_{26}H_{24}{}^{35}Cl^{65}Cu_2N_{10}O_2]^+$, 674.03457 (13) $[^{12}C_{25}{}^{13}C_1H_{24}{}^{37}Cl^{63}Cu_1{}^{65}Cu_1N_{10}O_2]^+$ & $[^{12}C_{25}{}^{13}C_1H_{24}{}^{35}Cl^{65}Cu_2N_{10}O_2]^+$, 675.03154 (7) $[C_{26}H_{24}{}^{37}Cl^{65}Cu_2N_{10}O_2]^+$. Found: 669.03560 (75), 670.03895 (24), 671.03364 (100), 672.03636 (30), 673.03223 (37), 674.03460 (11), 675.03297 (6).

Synthesis of $[Cu_2(OCH_2C(Pz)_2Py)_2Br_2]$ (1h)

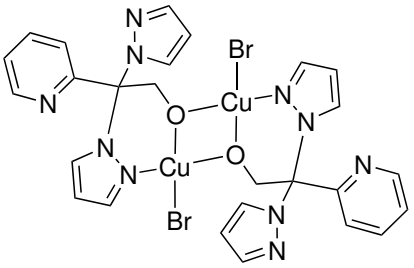

1h
$C_{26}H_{24}Br_2Cu_2N_{10}O_2$
MW: 795.45 g/mol

To CuBr (13.5 mg, 0.1 mol, 1 eq.) and **1** (25.0 mg, 0.1 mmol, 1 eq.), MeCN (10 mL) was added. The colourless solution was stored at ambient condition in a capped vial. Green crystals could be obtained.

IR (ATR), $\tilde{\nu}$ [cm^{-1}]: 3110 (vw), 2881 (vw), 2377 (vw), 2316 (vw), 1604 (w), 1587 (w), 1575 (w), 1516 (w), 1473 (w), 1436 (m), 1423 (w), 1404 (w), 1390 (m), 1326 (m), 1295 (w), 1236 (m), 1198 (m), 1119 (m), 1083 (m), 1070 (m), 1056 (m), 994 (w), 979 (m), 961 (w), 935 (w), 914 (m), 898 (w), 882 (m), 860 (vw), 832 (w), 800 (vw), 758 (vs), 747 (vs), 699 (m), 690 (m), 672 (m), 656 (m), 633 (m), 621 (m), 615 (m), 591 (w), 538 (w), 509 (w), 453 (vw), 436 (w), 420 (w), 406 (vw), 403 (vw).

HRMS (ESI$^+$, in MeCN, *m/z* [%]): Calc.: 712.98535 (52) $[C_{26}H_{24}{}^{79}Br^{63}Cu_2N_{10}O_2]^+$, 713.98802 (17) $[^{12}C_{25}{}^{13}C_1H_{24}{}^{79}Br^{63}Cu_2N_{10}O_2]^+$, 714.98362 (100) $[C_{26}H_{24}{}^{81}Br^{63}Cu_2N_{10}O_2]^+$ & $[C_{26}H_{24}{}^{79}Br^{63}Cu_1{}^{65}Cu_1N_{10}O_2]^+$, 715.98616 (32) $[^{12}C_{25}{}^{13}C_1H_{24}{}^{81}Br^{63}Cu_2N_{10}O_2]^+$ & $[^{12}C_{25}{}^{13}C_1H_{24}{}^{79}Br^{63}Cu_1{}^{65}Cu_1N_{10}O_2]^+$, 716.98216 (61) $[C_{26}H_{24}{}^{81}Br^{63}Cu_1{}^{65}Cu_1N_{10}O_2]^+$,

717.98443 (19) $[^{12}C_{25}{}^{13}C_1H_{24}{}^{81}Br^{63}Cu_1{}^{65}Cu_1N_{10}O_2]^+$, 718.98136 (13) $[C_{26}H_{24}{}^{81}Br^{65}Cu_2N_{10}O_2]^+$, 719.98301 (4) $[^{12}C_{25}{}^{13}C_1H_{24}{}^{81}Br^{65}Cu_2N_{10}O_2]^+$. Found: 712.98346 (52), 713.98712 (16), 714.98151 (100), 715.98499 (25), 716.97949 (56), 717.98303 (14), 718.97687 (8), 719.98096 (2).

10.4.2 Synthesis of Complexes with Ligand 2

Synthesis of $[Fe(MeC(Py)_2Phen)(MeCN)_2](BF_4)_2 \cdot MeCN$ (2b)

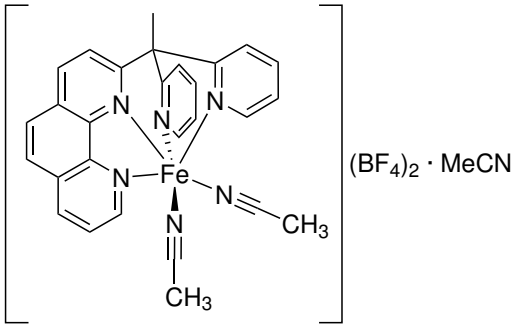

2b
$C_{30}H_{27}B_2F_8FeN_7$
MW: 715.05 g/mol

To a suspension of $[Fe(MeCN)_6](BF_4)_2$ (24.0 mg, 0.05 mmol, 1.0 eq.) in abs. MeCN (1 mL), was added a solution of **2** (18.2 mg, 0.05 mmol, 1.0 eq.) in abs. MeCN (1 mL). Red crystals suitable for SCXRD were obtained by addition of Et_2O (18 mg, 0.03 mmol, 54 %).

IR (ATR), $\tilde{\nu}$ [cm^{-1}]: 1597 (vw), 1474 (w), 1463 (w), 1441 (w), 1398 (w), 1287 (vw), 1263 (vw), 1047 (vs), 1027 (vs), 867 (w), 846 (w), 809 (w), 779 (w), 763 (m), 738 (w), 730 (w), 680 (w), 666 (m), 577 (vw), 558 (vw), 532 (w), 521 (m), 497 (vw), 478 (vw), 419 (w).

HRMS (ESI$^+$, in MeCN, *m*/*z* [%]): Calc.: 208.04583 (6) $[C_{24}H_{18}N_4{}^{54}Fe]^{2+}$, 208.54751 (2) $[^{12}C_{23}{}^{13}C_1H_{18}N_4{}^{54}Fe]^{2+}$, 209.04340 (100) $[C_{24}H_{18}N_4{}^{56}Fe]^{2+}$, 209.54517 (26) $[^{12}C_{23}{}^{13}C_1H_{18}N_4{}^{56}Fe]_2{}^{+}$, 210.04685 (3) $[^{12}C_{22}{}^{13}C_2H_{18}N_4{}^{56}Fe]^{2+}$. Found: 208.04577 (7), 208.54726 (2), 209.04340 (100), 209.54489 (29), 210.04607 (4).

Synthesis of $[Fe(MeC(Py)_2Phen)(\mu\text{-}Cl)_2FeCl_2]$ (2c)

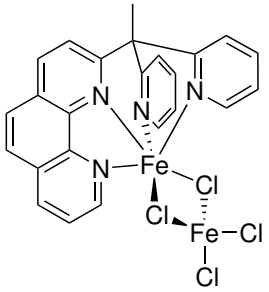

2c
$C_{24}H_{18}Cl_4Fe_2N_4$
MW: 615.92 g/mol

To $FeCl_2$ (6.0 mg, 0.05 mmol, 1.0 eq.) abs. MeCN (1 mL) was added and stirred for a short period of time. Subsequently, **2** (18 mg, 0.05 mmol, 1.0 eq.) was added. The mixture turned immediately red and a black solid started to precipitate. Again, abs. MeCN (3 mL) was added and the mixture was kept stirred overnight. The red liquid was separated from the dark solid and layered with abs. Et_2O (5 mL). Red crystals suitable for SCXRD were obtained after 3 days.

IR (ATR), $\tilde{\nu}$ [cm^{-1}]: 3093 (vw), 3061 (vw), 2323 (vw), 2198 (vw), 2177 (w), 2160 (vw), 1993 (vw), 1961 (vw), 1939 (vw), 1619 (w), 1577 (m), 1506 (w), 1490 (m), 1474 (m), 1460 (m), 1438 (m), 1432 (m), 1394 (m), 1308 (w), 1295 (w), 1245 (vw), 1218 (w), 1203 (vw), 1162 (w), 1145 (w), 1108 (w), 1072 (w), 1062 (w), 1054 (m), 1021 (m), 987 (w), 908 (w), 891 (w), 868 (s), 848 (m), 839 (w), 805 (vw), 770 (s), 762 (s), 756 (s), 748 (m), 738 (m), 730 (m), 680 (m), 668 (vs), 650 (m), 650 (m), 593 (m), 555 (m), 529 (w), 491 (m), 426 (m).

HRMS (ESI$^+$, in MeCN, *m*/*z* [%]): Calc.: 451.06107 (6) $[C_{24}H_{18}{}^{35}ClN_4{}^{54}Fe]^+$, 452.06442 (2) $[^{12}C_{23}{}^{13}C_1H_{18}{}^{35}ClN_4{}^{54}Fe]^+$, 453.05639 (100) $[C_{24}H_{18}{}^{35}ClN_4{}^{56}Fe]^+$, 454.05975 (26) $[^{12}C_{23}{}^{13}C_1H_{18}{}^{35}ClN_4{}^{56}Fe]^+$, 455.05344 (32) $[C_{24}H_{18}{}^{37}ClN_4{}^{56}Fe]^+$ 456.05680 (8) $[^{12}C_{23}{}^{13}C_1H_{18}{}^{37}ClN_4{}^{56}Fe]^+$. Found: 451.06127 (11), 452.06443 (3), 453.05754 (100), 454.05971

(52), 455.05432 (59), 456.05682 (17).

Synthesis of [Fe(MeC(Py)$_2$Phen)(μ−O)FeCl$_3$] · MeCN (2d)

To $FeCl_2$ (6.0 mg, 0.05 mmol, 1.0 eq.) a solution of abs. MeCN (2 mL) and **2** (18 mg, 0.05 mmol, 1.0 eq.) was added. The mixture turned black and additional abs. MeCN (5 mL) was added. The mixture was stirred for 1 h with no change in colour. 3 days later a red to orange solution was separated from the dark solid and layered with Et_2O (2.5 mL). Red to orange crystals were observed after 6 months, suitable for SCXRD were obtained after 1 year and 7 months.

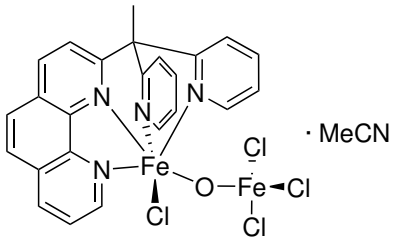

2d
$C_{26}H_{21}Cl_4Fe_2N_5O$
MW: 672.98 g/mol

IR (ATR), $\tilde{\nu}$ [cm^{-1}]: 3123 (vw), 3063 (vw), 3051 (wv), 2927 (vw), 2289 (vw), 2249 (w), 2189 (vw), 2038 (vw), 2008 (vw), 1982 (vw), 1620 (vw), 1597 (m), 1579 (m), 1571 (w), 1502 (m), 1493 (m), 1462 (m), 1433 (m), 1396 (m), 1373 (w), 1311 (w), 1298 (w), 1218 (w), 1204 (w), 1164 (w), 1110 (w), 1098 (w), 1073 (w), 1056 (w), 1027 (m), 1017 (m), 968 (w), 910 (w), 899 (w), 876 (m), 843 (vs), 830 (vs), 812 (s), 775 (m), 766 (s), 759 (m), 749 (m), 738 (m), 729 (m), 681 (m), 666 (m), 653 (m), 641 (w), 610 (w), 596 (m), 571 (w), 556 (w), 532 (w), 515 (vw), 488 (w), 451 (w), 440 (w), 432 (m), 412 (w).

HRMS (ESI$^+$, in MeOH, *m/z* [%]): Calc.: 451.06107 (6) [$C_{24}H_{18}{}^{35}ClN_4{}^{54}Fe]^+$, 453.05639 (100) [$C_{24}H_{18}{}^{35}ClN_4{}^{56}Fe]^+$, 454.05975 (26) [$^{12}C_{23}{}^{13}C_1H_{18}{}^{35}ClN_4{}^{56}Fe]^+$, 455.05344 (32) [$C_{24}H_{18}{}^{37}ClN_4{}^{56}Fe]^+$ 456.05680 (8) [$^{12}C_{23}{}^{13}C_1H_{18}{}^{37}ClN_4{}^{56}Fe]^+$. Found: 451.05938 (7), 453.05469 (100), 454.05769 (30), 455.05217 (34), 456.05482 (9).[†]

[†]No reasonable Fe(III) species could be identified in the spectrum.

10.4.3 Synthesis of Complexes with Ligand 3

Synthesis of [Fe(MeC(Py)$_2$PicMe)(OTf)$_2$] (3a)

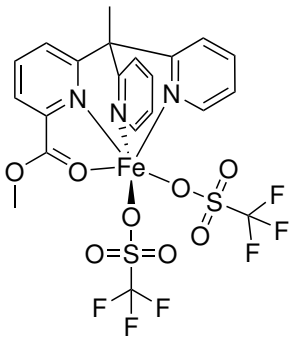

3a
$C_{21}H_{17}F_6FeN_3O_8S_2$
MW: 673.34 g/mol

To $Fe(OTf)_2 \cdot 2\,MeCN$ (22 mg, 0.05 mmol, 1 eq.) and **3** (16 mg, 0.05 mmol, 1 eq.) abs. MeCN (1 mL) was added. The mixture was stirred overnight resulting in a red solution. After gas phase diffusion with abs. Et_2O (total: 7.5 mL), orange crystals were obtained.

IR (ATR), $\tilde{\nu}$ [cm^{-1}]: 3745 (vw), 2968 (vw), 2227 (vw), 2159 (w), 2006 (w), 1973 (w), 1679 (m), 1592 (m), 1464 (w), 1440 (w), 1349 (m), 1349 (m), 1333 (m), 1319 (m), 1303 (m), 1278 (m), 1236 (m), 1206 (s), 1160 (m), 1054 (w), 1019 (s), 977 (w), 879 (w), 857 (w), 835 (w), 773 (w), 759 (m), 682 (w), 630 (vs), 572 (m), 540 (w), 514 (m), 486 (w), 450 (w), 443 (w), 415 (w).

HRMS (ESI$^+$, in MeCN, *m/z* [%]): Calc.: 522.02317 (6) $[F_3C_{20}H_{17}N_3O_5{}^{54}Fe^{32}S]^+$, 523.02652 (1) $[F_3{}^{12}C_{19}{}^{13}C_1H_{17}N_3O_5{}^{54}Fe^{32}S]^+$, 524.01849 (100) $[F_3C_{20}H_{17}N_3O_5{}^{56}Fe^{32}S]^+$, 525.02185 (22) $[F_3{}^{12}C_{19}{}^{13}C_1H_{17}N_3O_5{}^{56}Fe^{32}S]^+$, 526.01429 (4) $[F_3C_{20}H_{17}N_3O_5{}^{56}Fe^{34}S]^+$. Found: 522.02223 (6), 523.02514 (1), 524.01755 (100), 525.02039 (25), 526.01820 (6).

Synthesis of [Fe$_4$(μ−O)$_2$(MeC(Py)$_2$Pic)$_4$](OTf)$_4 \cdot$ 4 DCM $\cdot$ THF (3b)

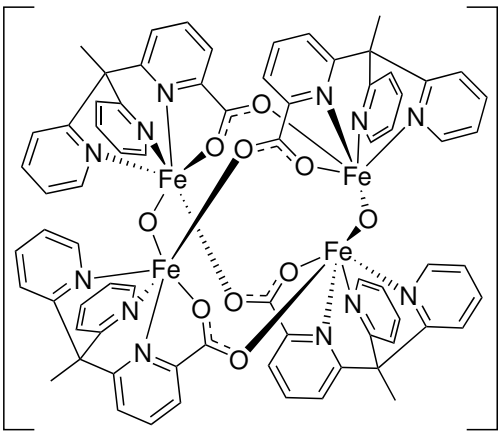

$(OTf)_4 \cdot 4\,DCM \cdot THF$

3b
$C_{84}H_{72}Cl_8F_{12}Fe_4N_{12}O_{23}S_4$
MW: 2480.77 g/mol

To $Fe(OTf)_2 \cdot 2\,MeCN$ (21.8 mg, 0.05 mmol, 1 eq.) abs. THF (1.5 mL) was added in a Schlenk flask. In a vial **3** (16.0 mg, 0.05 mmol, 1 eq.) was dissolved in abs. DCM (2 mL) under aerobic conditions. The ligand solution was added under stirring to the metal salt resulting in a red solution. Brown crystals were obtained.

IR (ATR), $\tilde{\nu}$ [cm^{-1}]: 3355 (w, br), 2978 (vw), 2879 (vw), 1749 (w), 1667 (m), 1639 (w), 1595 (m), 1579 (w), 1482 (w), 1465 (m), 1443 (w), 1397 (w), 1342 (w), 1282 (m), 1237 (s), 1225 (s), 1162 (s), 1028 (vs), 839 (m), 773 (w), 759 (m), 683 (w), 635 (s), 515 (m), 444 (w), 432 (w).

HRMS (ESI$^+$, in MeCN, *m/z* [%]): Calc.: 367.04279 (13) $[C_{36}H_{28}N_6O_5{}^{56}Fe_1{}^{54}Fe_1]^{2+}$, 367.54447 (5) $[{}^{12}C_{35}{}^{13}C_1H_{28}N_6O_5{}^{56}Fe_1{}^{54}Fe_1]^{2+}$, 368.04045 (100) $[C_{36}H_{28}N_6O_5{}^{56}Fe_2]^2$, 368.54213 (39) $[{}^{12}C_{35}{}^{13}C_1H_{28}N_6O_5{}^{56}Fe_2]^{2+}$, 369.04381 (7) $[{}^{12}C_{34}{}^{13}C_2H_{28}N_6O_5{}^{56}Fe_2]^{2+}$. Found:

367.04120 (14), 367.54349 (5), 368.03973 (100), 368.54111 (44), 369.04186 (12).

Synthesis of [Fe(MeC(Py)$_2$PicMe)Cl$_2$] · 0.5 MeCN (3c)

To $FeCl_2$ (10 mg, 0.08 mmol, 1 eq.) abs. MeCN (2 mL) was added. **3** (36.2 mg, 0.11 mmol, 1.4 eq.) was dissolved in abs. MeCN (2 mL). The iron-salt solution was added dropwise to the solution of **3** resulting in a dark red to brown solution which was layered with Et_2O (2 mL). Orange brown crystals suitable for SCXRD were obtained after 3 days.

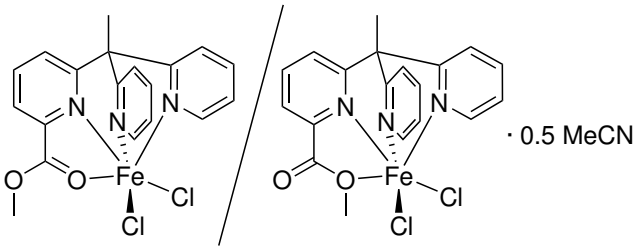

3c
$C_{20}H_{18.5}Cl_2FeN_{3.5}O_2$
MW: 466.64 g/mol

IR (ATR), $\tilde{\nu}$ [cm^{-1}]: 3083 (vw), 3074 (vw), 2985 (vw), 2955 (vw), 2914 (vw), 2253 (vw), 2237 (vw), 2167 (w), 2047 (vw), 1979 (vw), 1769 (m), 1685 (m), 1589 (m), 1474 (m), 1458 (s), 1433 (s), 1335 (m), 1272 (m), 1209 (w), 1165 (m), 1114 (m), 1078 (w), 1052 (m), 1018 (m), 961 (m), 875 (w), 858 (w), 827 (m), 759 (vs), 679 (m), 646 (s), 633 (vs), 572 (m), 507 (w), 423 (m).
HRMS (ESI$^+$, in MeCN, *m*/*z* [%]): Calc.: 408.04054 (6) $[C_{19}H_{17}{}^{35}ClN_3O_2{}^{54}Fe]^+$, 409.04390 (1) $[^{12}C_{18}{}^{13}C_1H_{17}{}^{35}ClN_3O_2{}^{54}Fe]^+$, 410.03587 (100) $[C_{19}H_{17}{}^{35}ClN_3O_2{}^{56}Fe]^+$, 411.03923 (21) $[^{12}C_{18}{}^{13}C_1H_{17}{}^{35}ClN_3O_2{}^{56}Fe]^+$, 412.03292 (32) $[C_{19}H_{17}{}^{37}ClN_3O_2{}^{56}Fe]^+$, 413.03628 (7) $[^{12}C_{18}{}^{13}C_1H_{17}{}^{37}ClN_3O_2{}^{56}Fe]^+$, 414.03963 (1) $[^{12}C_{17}{}^{13}C_2H_{17}{}^{37}ClN_3O_2{}^{56}Fe]^+$. Found: 408.03910 (17), 409.04228 (4), 410.03629 (100), 411.03751 (62), 412.03206 (88), 413.03461 (20), 414.03625 (3).

Synthesis of [Fe(MeC(Py)$_2$PicMe)(H$_2$O)(MeCN)](BF$_4$)$_2$ · MeCN (3d)

To $[Fe(MeCN)_6](BF_4)_2$ (55.0 mg, 0.12 mmol, 1 eq.) in MeCN (2 mL), a solution of **3** (37.3 mg, 0.12 mmol, 1 eq.) in MeCN (2 mL) was added. From the resulting solution 1.5 mL were taken and used for gas phase diffusion with Et_2O. No precipitation occurred within a reasonable timescale, so all solvents were removed and the residue was diluted in 1 mL of MeCN and layered with Et_2O (8 mL). After a long time (approx. 6 months), orange crystals were obtained besides a uncharacterised green powder.

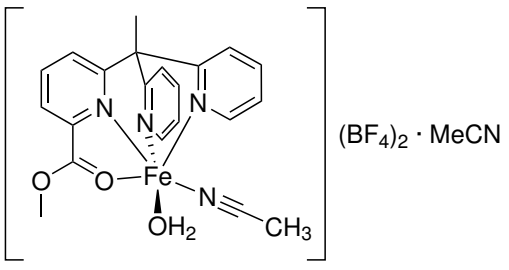

3d
$C_{23}H_{25}B_2F_8FeN_5O_3$
MW: 648.95 g/mol

IR (ATR), $\tilde{\nu}$ [cm^{-1}]: 3745 (w), 3476 (w, br), 3007 (vw), 2284 (vw), 2171 (vw), 2023 (w), 1965 (vw), 1674 (m), 1591 (m), 1464 (m), 1443 (m), 1391 (w), 1352 (m), 1300 (vw), 1282 (m), 1219 (vw), 1163 (w), 1072 (vs), 1052 (vs), 1018 (vs), 992 (vs), 879 (w), 859 (m), 838 (w), 764 (s), 682 (w), 650 (w), 638 (m), 572 (w), 520 (m), 442 (w), 422 (m).

HRMS (ESI$^+$, in MeCN, *m/z* [%]): Calc.: 320.13935 (100) $[C_{19}H_{18}N_3O_2]^+$, 321.14271 (21) $[^{12}C_{18}{}^{13}C_1H_{18}N_3O_2]^+$, 322.14606 (2) $[^{12}C_{17}{}^{13}C_2H_{18}N_3O_2]^+$. 342.12130 (100) $[NaC_{19}H_{17}N_3O_2]^+$, 343.12465 (21) $[Na^{12}C_{18}{}^{13}C_1H_{17}N_3O_2]^+$, 344.12801 (2) $[Na^{12}C_{17}{}^{13}C_2H_{17}N_3O_2]^+$. Found: 320.13956 (100), 321.14258 (26), 322.14543 (3). 342.12146 (100), 343.12447 (25), 344.12735 (3).

Synthesis of $[Fe(MeC(Py)_2PicMe)(BF_4)Cl] \cdot 3.5\,Et_2O$ (3e)

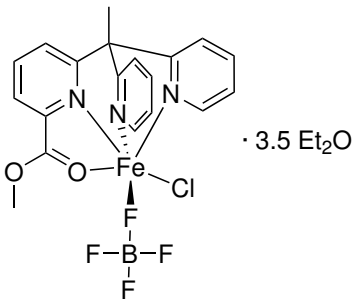

3e
$C_{33}H_{52}BClF_4FeN_3O_{5.5}$
MW: 756.89 g/mol

To $[Fe(MeCN)_6](BF_4)_2$ (24.0 mg, 0.05 mmol, 1 eq.), $FeCl_2$ (6.0 mg, 0.05 mmol, 1 eq.) and **3** (18.3 mg, 0.06 mmol, 1.2 eq.), abs. MeOH (2 mL) was added. The resulting dark red solution was layered with abs. Et_2O (8 mL). Red crystals suitable for SCXRD were obtained after 9 days.

IR (ATR), $\tilde{\nu}$ [cm^{-1}]: 3465 (w, br), 3095 (vw), 2968 (vw), 1678 (m), 1592 (s), 1463 (m), 1445 (m), 1394 (w), 1348 (s), 1281 (m), 1216 (w), 1163 (w), 1053 (vs), 1017 (vs), 976 (s), 881 (w), 863 (w), 837 (w), 780 (m), 772 (m), 761 (m), 681 (w), 648 (m), 636 (s), 575 (w), 520 (m), 482 (w), 472 (w), 450 (w), 424 (m).

HRMS (ESI$^+$, in MeCN, *m/z* [%]): Calc.: 408.04054 (6) $[C_{19}H_{17}{}^{35}ClN_3O_2{}^{54}Fe]^+$ 409.04390 (1) $[^{12}C_{18}{}^{13}C_1H_{17}{}^{35}ClN_3O_2{}^{54}Fe]^+$ 410.03587 (100) $[C_{19}H_{17}{}^{35}ClN_3O_2{}^{56}Fe]^+$ 411.03923 (21) $[^{12}C_{18}{}^{13}C_1H_{17}{}^{35}ClN_3O_2{}^{56}Fe]^+$ 412.03292 (32) $[C_{19}H_{17}{}^{37}ClN_3O_2{}^{56}Fe]^+$ 413.03628 (7) $[^{12}C_{18}{}^{13}C_1H_{17}{}^{37}ClN_3O_2{}^{56}Fe]^+$ 414.03963 (1) $[^{12}C_{17}{}^{13}C_2H_{17}{}^{37}ClN_3O_2{}^{56}Fe]^+$. Found: 408.03938 (7), 409.04246 (1), 410.03492 (100), 411.03766 (25), 412.03217 (35), 413.03477 (8), 414.03666 (1).

10.4.4 Synthesis of Complexes with Ligand 4

Synthesis of Complexes in Acetonitrile with Iron Triflate

Species identified were:
$[Fe(NQu_3)(MeCN)_2](OTf)_2 \cdot MeCN \cdot 0.5\,Et_2O$ (**4a**),
$[Fe(NQu_3)(OTf)(MeCN)](OTf) \cdot 0.5\,Et_2O$ (**4b**),
$[Fe(NQu_3)(OTf)_2]$ (**4c**),
$[Fe(NQu_3)(OTf)_2] \cdot 0.45\,Et_2O$ (**4d**),
$[Fe(NQu_3)(OTf)_2][Fe(NQu_3)(OTf)_2]_{0.5}\{[Fe(NQu_3)(OTf)(H_2O)](OTf)\}_{0.5}$ (**4e**),
$[Fe(NQu_3)(H_2O)(MeCN)](OTf)_2$ (**4f**),
$[Fe_2(\mu\text{-}O)(NQu_3)_2(OTf)_2](OTf)_2 \cdot 0.85\,MeCN$ (**4g**).
General reaction: To $Fe(OTf)_2 \cdot 2\,MeCN$ (21.8 mg, 0.05 mmol, 1 eq.) and **4** (19,9 mg, 0.05 mmol, 1 eq.) MeCN (1 mL) was added. The mixture was stirred for at least 30 min (up to two days) until it was a clear red to orange solution. Afterwards, the solution was layered with Et_2O (8 mL). Some of the crystal structures could be obtained by several reaction routes. If already identified products were obtained only a cell determination of additional single crystals via SCXRD was performed. In many reactions with $Fe(OTf)_2 \cdot 2\,MeCN$ and **4** in MeCN at rt, more than one complex species was found to be present. For bulk analytics, they were sorted manually if possible but phase purity could not always be confirmed.

Synthesis of $[Fe(NQu_3)(MeCN)_2](OTf)_2 \cdot MeCN \cdot 0.5\,Et_2O$ (4a):

Suitable red crystals for SCXRD were obtained after about three weeks. Also, short heating of the reaction mixture and reactions without Schlenk conditions led in some cases to this complex. For selective synthesis of this species, the solution layered with Et_2O must be stored at 6 °C, resulting in the same red crystals (crystals **C**). Satisfactory elemental analysis could not be performed since the crystals differ in their composition when removed from mother liquor and are very sensitive towards residual solvent (see subsection 6.2.1).

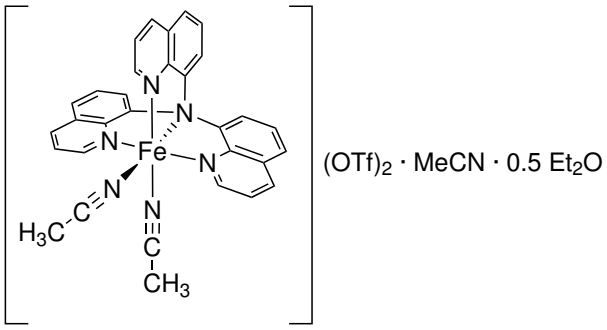

4a
$C_{37}H_{32}F_6FeN_7O_{6.5}S_2$
MW: 912.66 g/mol

IR (ATR), $\tilde{\nu}$ [cm^{-1}]: 3479 (w, br), 3370 (w, br), 3076 (vw), 1620 (vw), 1596 (w), 1502 (m), 1473 (w), 1385 (w), 1315 (w), 1285 (m), 1239 (s), 1224 (s), 1152 (s), 1109 (m), 1088 (w), 1027 (vs), 934 (vw), 866 (w), 836 (m), 810 (w), 800 (m), 787 (m), 765 (s), 717 (w), 671 (m), 664 (m), 635 (vs), 619 (m), 614 (m), 572 (m), 515 (m), 447 (w), 423 (w).
HRMS (ESI$^+$, in MeCN, *m*/*z* [%]): Calc.: 226.04583 (6) $[C_{27}H_{18}N_4{}^{54}Fe]^{2+}$, 226.54737 (2)

$[^{12}C_{26}{}^{13}C_1H_{18}N_4{}^{54}Fe]^{2+}$, 227.04351 (100) $[C_{27}H_{18}N_4{}^{56}Fe]^{2+}$, 227.54495 (33) $[^{12}C_{26}{}^{13}C_1H_{18}N_4{}^{56}Fe]^{2+}$, 228.04619 (6) $[^{12}C_{25}{}^{13}C_2H_{18}N_4{}^{56}Fe]^{2+}$, 228.54738 (1) $[^{12}C_{24}{}^{13}C_3H_{18}N_4{}^{56}Fe]^{2+}$. 601.04424 (6) $[F_3C_{28}H_{18}N_4O_3{}^{54}Fe{}^{32}S]^+$, 602.04723 (2) $[F_3{}^{12}C_{27}{}^{13}C_1H_{18}N_4O_3{}^{54}Fe{}^{32}S]^+$, 603.03960 (100) $[F_3C_{28}H_{18}N_4O_3{}^{56}Fe{}^{32}S]^+$, 604.04241 (35) $[F_3{}^{12}C_{27}{}^{13}C_1H_{18}N_4O_3{}^{56}Fe{}^{32}S]^+$, 605.04108 (11) $[F_3C_{28}H_{18}N_4O_3{}^{56}Fe{}^{34}S]^+$ & $[F_3{}^{12}C_{26}{}^{13}C_2H_{18}N_4O_3{}^{56}Fe{}^{32}S]^+$, 606.04161 (2) $[F_3{}^{12}C_{27}{}^{13}C_1H_{18}N_4O_3{}^{56}Fe{}^{34}S]^+$. Found: 226.04602 (16), 226.54748 (5), 227.04441 (100), 227.54210 (80), 228.04765 (13), 228.54765 (1). 601.04532 (11), 602.04841(4), 603.04197 (100), 604.04378 (63), 605.04289 (17), 606.04256 (4).

Synthesis of $[Fe(NQu_3)(OTf)(MeCN)](OTf) \cdot 0.5\,Et_2O$ (4b):

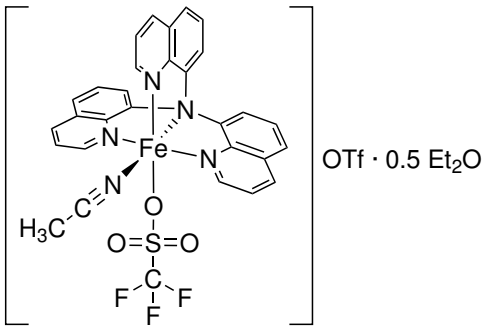

4b
$C_{33}H_{26}F_6FeN_5O_{6.5}S_2$
MW: 830.55 g/mol

Suitable yellow crystals for SCXRD were obtained after about one week.

IR (ATR), $\tilde{\nu}$ [cm^{-1}]: 3353 (w, br), 3251 (w, br), 3068 (vw), 2281 (vw), 1617 (w), 1596 (w), 1508 (m), 1500 (m), 1474 (w), 1425 (vw), 1386 (w), 1315 (w), 1283 (m), 1236 (s), 1223 (s), 1156 (s), 1108 (m), 1091 (w), 1025 (vs), 934 (vw), 867 (vw), 837 (m), 799 (m), 788 (w), 766 (m), 664 (w), 636 (s), 614 (m), 572 (m), 516 (m), 473 (w), 464 (w), 447 (vw), 424 (w), 406 (w).

HRMS (ESI$^+$, in MeCN, *m*/*z* [%]): Calc.: 226.04583 (6) $[C_{27}H_{18}N_4{}^{54}Fe]^{2+}$, 226.54737 (2) $[^{12}C_{26}{}^{13}C_1H_{18}N_4{}^{54}Fe]^{2+}$, 227.04351 (100) $[C_{27}H_{18}N_4{}^{56}Fe]^{2+}$, 227.54495 (33) $[^{12}C_{26}{}^{13}C_1H_{18}N_4{}^{56}Fe]^{2+}$, 228.04619 (6) $[^{12}C_{25}{}^{13}C_2H_{18}N_4{}^{56}Fe]^{2+}$, 228.54738 (1) $[^{12}C_{24}{}^{13}C_3H_{18}N_4{}^{56}Fe]^{2+}$. 601.04424 (6) $[F_3C_{28}H_{18}N_4O_3{}^{54}Fe{}^{32}S]^+$, 602.04723 (2) $[F_3{}^{12}C_{27}{}^{13}C_1H_{18}N_4O_3{}^{54}Fe{}^{32}S]^+$, 603.03960 (100) $[F_3C_{28}H_{18}N_4O_3{}^{56}Fe{}^{32}S]^+$, 604.04241 (35) $[F_3{}^{12}C_{27}{}^{13}C_1H_{18}N_4O_3{}^{56}Fe{}^{32}S]^+$, 605.04108 (11) $[F_3C_{28}H_{18}N_4O_3{}^{56}Fe{}^{34}S]^+$ & $[F_3{}^{12}C_{26}{}^{13}C_2H_{18}N_4O_3{}^{56}Fe{}^{32}S]^+$, 606.04161 (2) $[F_3{}^{12}C_{27}{}^{13}C_1H_{18}N_4O_3{}^{56}Fe{}^{34}S]^+$. Found: 226.04597 (9), 226.54745 (3), 227.04388 (100), 227.54512 (44), 228.04645 (7), 228.54757 (1). 601.04483 (6), 602.04792 (2), 603.04048 (100), 604.04317 (34), 605.04238 (9), 606.04215 (2).

Synthesis of $[Fe(NQu_3)(OTf)_2]$ (4c):

Suitable orange crystals for SCXRD were obtained after about one week.

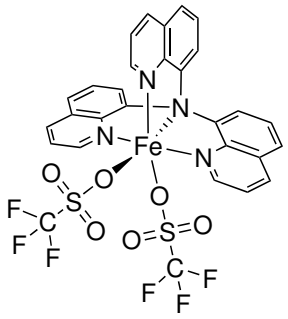

4c
$C_{29}H_{18}F_6FeN_4O_6S_2$
MW: 752.44 g/mol

IR (ATR), $\tilde{\nu}$ [cm^{-1}]: 3371 (w, br), 3070 (vw, br), 1597 (w), 1508 (m), 1502 (m), 1470 (w), 1385 (w), 1315 (w), 1286 (m), 1236 (s), 1224 (vs), 1155 (s), 1108 (m), 1089 (w), 1026 (vs), 931 (vw), 866 (w), 836 (m), 800 (m), 787 (m), 765 (m), 671 (w), 635 (s), 573 (m), 516 (m), 426 (w).

HRMS (ESI$^+$, in MeCN, *m*/*z* [%]): Calc.: 601.04424 (6) $[F_3C_{28}H_{18}N_4O_3{}^{54}Fe^{32}S]^+$, 602.04723 (2) $[F_3{}^{12}C_{27}{}^{13}C_1H_{18}N_4O_3{}^{54}Fe^{32}S]^+$, 603.03960 (100) $[F_3C_{28}H_{18}N_4O_3{}^{56}Fe^{32}S]^+$, 604.04241 (35) $[F_3{}^{12}C_{27}{}^{13}C_1H_{18}N_4O_3{}^{56}Fe^{32}S]^+$, 605.04108 (11) $[F_3C_{28}H_{18}N_4O_3{}^{56}Fe^{34}S]^+$ & $[F_3{}^{12}C_{26}{}^{13}C_2H_{18}N_4O_3{}^{56}Fe^{32}S]^+$, 606.04161 (2) $[F_3{}^{12}C_{27}{}^{13}C_1H_{18}N_4O_3{}^{56}Fe^{34}S]^+$. Found: 601.04485 (6), 602.04790 (2), 603.04039 (100), 604.04323 (35), 605.04247 (9) 606.04217 (2).

Synthesis of $[Fe(NQu_3)(OTf)_2] \cdot 0.45\,Et_2O$ (4d):

Suitable red crystals for SCXRD were obtained after about one week. Note that these crystals could also be observed in reactions with only half the amount of iron salt. Also, in a reaction with additional triflate anions due to the addition of 1 eq. of $NH_4(OTf)$ this complex was observed.

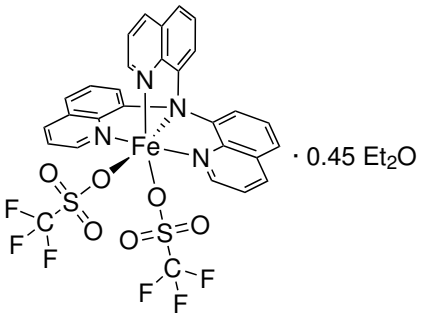

4d
$C_{30.8}H_{22.5}F_6FeN_4O_{6.45}S_2$
MW: 785.80 g/mol

IR (ATR), $\tilde{\nu}$ [cm^{-1}]: 3302 (w, br), 2198 (vw), 1616 (w), 1597 (w), 1510 (m), 1501 (m), 1471 (w), 1426 (vw), 1384 (w), 1315 (w), 1288 (s), 1223 (vs), 1163 (s), 1106 (m), 1089 (w), 1067 (w), 1026 (vs), 930 (vw), 867 (w), 835 (m), 811 (m), 800 (s), 765 (s), 721 (w), 671 (m), 632 (vs), 614 (s), 574 (m), 517 (s), 462 (m), 423 (m).

HRMS (ESI$^+$, in MeCN, *m*/*z* [%]): Calc.: 226.04583 (6) $[C_{27}H_{18}N_4{}^{54}Fe]^{2+}$, 227.04351 (100) $[C_{27}H_{18}N_4{}^{56}Fe]^{2+}$, 227.54495 (33) $[{}^{12}C_{26}{}^{13}C_1H_{18}N_4{}^{56}Fe]^{2+}$, 228.04619 (6) $[{}^{12}C_{25}{}^{13}C_2H_{18}N_4{}^{56}Fe]^{2+}$, 228.54738 (1) $[{}^{12}C_{24}{}^{13}C_3H_{18}N_4{}^{56}Fe]^{2+}$. 601.04424 (6) $[F_3C_{28}H_{18}N_4O_3{}^{54}Fe^{32}S]^+$, 602.04723 (2) $[F_3{}^{12}C_{27}{}^{13}C_1H_{18}N_4O_3{}^{54}Fe^{32}S]^+$, 603.03960 (100) $[F_3C_{28}H_{18}N_4O_3{}^{56}Fe^{32}S]^+$, 604.04241 (35) $[F_3{}^{12}C_{27}{}^{13}C_1H_{18}N_4O_3{}^{56}Fe^{32}S]^+$, 605.04108 (11) $[F_3C_{28}H_{18}N_4O_3{}^{56}Fe^{34}S]^+$ & $[F_3{}^{12}C_{26}{}^{13}C_2H_{18}N_4O_3{}^{56}Fe^{32}S]^+$. Found: 226.04517 (6), 227.04294 (100), 227.54442 (30), 228.04370 (18), 228.54489 (5). 601.05032 (19), 602.05139 (7), 603.03900 (100), 604.04188 (35), 605.04097 (10).

Synthesis of $[Fe(NQu_3)(OTf)_2][Fe(NQu_3)(OTf)_2]_{0.5}\{[Fe(NQu_3)(OTf)(H_2O)](OTf)\}_{0.5}$ (4e):

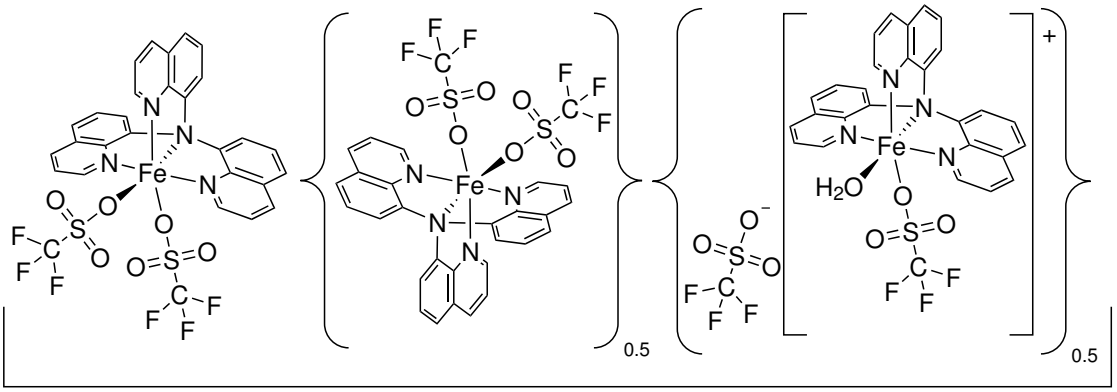

4e
$C_{58}H_{37}F_{12}Fe_2N_8O_{12.5}S_4$
MW: 1513.90 g/mol

Suitable orange crystals for SCXRD were obtained after about one week. Note that these crystals could also be obtained with short heating of the reaction.

IR (ATR), $\tilde{\nu}$ [cm^{-1}]: 3370 (w, br), 1596 (w), 1508 (m), 1473 (w), 1391 (w), 1315 (w), 1282 (m), 1234 (s), 1223 (s), 1160 (s), 1108 (m), 1094 (w), 1025 (vs), 867 (w), 837 (m), 799 (m), 788 (m), 767 (m), 664 (m), 636 (vs), 575 (m), 516 (m), 447 (w), 423 (m), 423 (m).

HRMS (ESI$^+$, in MeCN, *m*/*z* [%]): Calc.: 226.04583 (6) $[C_{27}H_{18}N_4{}^{54}Fe]^{2+}$, 226.54737 (2) $[{}^{12}C_{26}{}^{13}C_1H_{18}N_4{}^{54}Fe]^{2+}$, 227.04351 (100) $[C_{27}H_{18}N_4{}^{56}Fe]^{2+}$, 227.54495 (33) $[{}^{12}C_{26}{}^{13}C_1H_{18}N_4{}^{56}Fe]^{2+}$, 228.04619 (6) $[{}^{12}C_{25}{}^{13}C_2H_{18}N_4{}^{56}Fe]^{2+}$, 228.54738 (1) $[{}^{12}C_{24}{}^{13}C_3H_{18}N_4{}^{56}Fe]^{2+}$. 601.04424 (6) $[F_3C_{28}H_{18}N_4O_3{}^{54}Fe{}^{32}S]^+$, 602.04723 (2) $[F_3{}^{12}C_{27}{}^{13}C_1H_{18}N_4O_3{}^{54}Fe{}^{32}S]^+$, 603.03960 (100) $[F_3C_{28}H_{18}N_4O_3{}^{56}Fe{}^{32}S]^+$, 604.04241 (35) $[F_3{}^{12}C_{27}{}^{13}C_1H_{18}N_4O_3{}^{56}Fe{}^{32}S]^+$, 605.04108 (11) $[F_3C_{28}H_{18}N_4O_3{}^{56}Fe{}^{34}S]^+$ & $[F_3{}^{12}C_{26}{}^{13}C_2H_{18}N_4O_3{}^{56}Fe{}^{32}S]^+$, 606.04161 (2) $[F_3{}^{12}C_{27}{}^{13}C_1H_{18}N_4O_3{}^{56}Fe{}^{34}S]^+$. Found: 226.04556 (7), 226.54687 (2), 227.04322 (100), 227.54466 (32), 228.04597 (5), 228.54694 (1). 601.04450 (5), 602.04665 (2), 603.03987 (100), 604.04283 (35), 605.04253 (9), 606.04212 (2).

Synthesis of $[Fe(NQu_3)(H_2O)(MeCN)](OTf)_2$ (4f):

Suitable yellow-orange crystals for SCXRD were obtained after about four weeks.

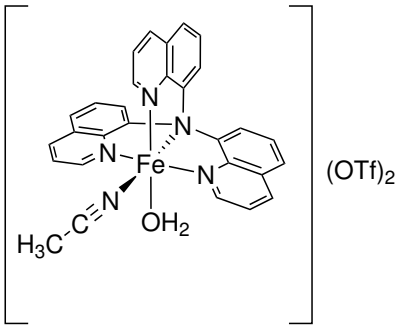

4f
$C_{31}H_{23}F_6FeN_5O_7S_2$
MW: 811.51 g/mol

IR (ATR), $\tilde{\nu}$ [cm^{-1}]: 3355 (w, br), 3071 (vw, br), 2282 (w), 1657 (vw), 1616 (vw), 1597 (w), 1508 (m), 1500 (m), 1473 (w), 1387 (w), 1315 (w), 1247 (s), 1224 (s), 1153 (s), 1140 (s), 1109 (m), 1066 (w), 1028 (vs), 924 (w), 865 (w), 836 (m), 787 (m), 779 (m), 765 (m), 755 (m), 672 (m), 636 (vs), 614 (s), 573 (m), 515 (m), 474 (w), 464 (w), 449 (w), 401 (w), 395 (w), 391 (w), 375 (w), 354 (vw), 349 (w), 343 (w), 338 (w), 322 (w), 317 (w), 290 (w), 285 (w), 281 (m), 276 (w), 266 (m), 259 (m), 255 (m), 253 (m).

HRMS (ESI$^+$, in MeOH, m/z [%]): Calc.: 226.04583 (6) $[C_{27}H_{18}N_4{}^{54}Fe]^{2+}$, 226.54737 (2) $[{}^{12}C_{26}{}^{13}C_1H_{18}N_4{}^{54}Fe]^{2+}$, 227.04351 (100) $[C_{27}H_{18}N_4{}^{56}Fe]^{2+}$, 227.54495 (33) $[{}^{12}C_{26}{}^{13}C_1H_{18}N_4{}^{56}Fe]^{2+}$, 228.04619 (6) $[{}^{12}C_{25}{}^{13}C_2H_{18}N_4{}^{56}Fe]^{2+}$, 228.54738 (1) $[12\,C_{24}{}^{13}C_3H_{18}N_4{}^{56}Fe]^{2+}$. 601.04424 (6) $[F_3C_{28}H_{18}N_4O_3{}^{54}Fe{}^{32}S]^+$, 602.04723 (2) $[F_3{}^{12}C_{27}{}^{13}C_1H_{18}N_4O_3{}^{54}Fe{}^{32}S]^+$, 603.03960 (100) $[F_3C_{28}H_{18}N_4O_3{}^{56}Fe{}^{32}S]^+$, 604.04241 (35) $[F_3{}^{12}C_{27}{}^{13}C_1H_{18}N_4O_3{}^{56}Fe{}^{32}S]^+$, 605.04108 (11) $[F_3C_{28}H_{18}N_4O_3{}^{56}Fe{}^{34}S]^+$ & $[F_3{}^{12}C_{26}{}^{13}C_2H_{18}N_4O_3{}^{56}Fe{}^{32}S]^+$, 606.04161 (2) $[F_3{}^{12}C_{27}{}^{13}C_1H_{18}N_4O_3{}^{56}Fe{}^{34}S]^+$. Found: 226.04559 (9), 226.54694 (3), 227.04352 (100), 227.54475 (46), 228.04606 (8), 228.54720 (1). 601.04386 (6), 602.04686 (2), 603.03947(100), 604.04219 (34), 605.04141 (9), 606.04118 (2).

Synthesis of $[Fe_2(\mu{-}O)(NQu_3)_2(OTf)_2](OTf)_2 \cdot 0.85\,MeCN$ (4g):

In this reaction, $NH_4(OTf)$ (8.4 mg, 0.05 mmol, 1 eq.) was additionally added to the general reaction procedure. At first, orange crystals of poor quality grew. After exposure to air, red crystals were formed within four months which were suitable for SCXRD. This species was also found in reactions without $NH_4(OTf)$ that were exposed to air for a short time.

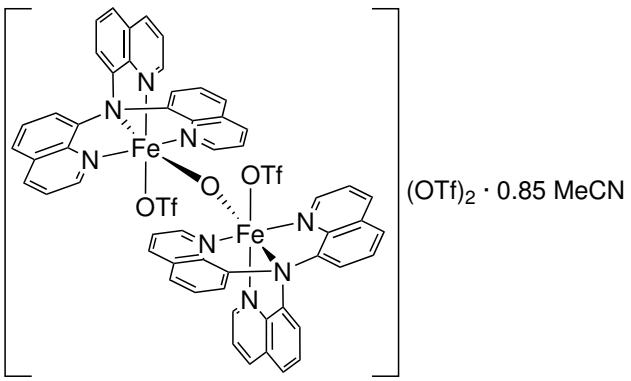

4g
$C_{59.69}H_{38.53}F_{12}Fe_2N_{8.85}O_{13}S_4$
MW: 1555.63 g/mol

IR (ATR), $\tilde{\nu}$ [cm^{-1}]: 3361 (w, br), 3238 (w, br), 3105 (w, br), 3075 (w, br), 2315 (vw), 2283 (vw), 1645 (vw), 1597 (w), 1509 (m), 1500 (m), 1472 (w), 1387 (w), 1315 (w), 1239 (vs), 1224 (vs), 1153 (s), 1109 (m), 1083 (m), 1067 (w), 1027 (vs), 934 (w), 925 (w), 866 (vw), 836 (m), 832 (m), 810 (w), 800 (m), 788 (w), 765 (m), 755

(m), 717 (vw), 672 (w), 635 (m), 614 (m), 574 (w), 516 (m), 474 (w), 463 (w), 448 (w), 422 (w). **HRMS (ESI$^+$, in MeCN, *m*/*z* [%]):** Calc.: 227.04351 (100) $[C_{27}H_{18}N_4{}^{56}Fe]^{2+}$, 227.54495 (33) $[{}^{12}C_{26}{}^{13}C_1H_{18}N_4{}^{56}Fe]^{2+}$. 399.16042 (100) $[C_{27}H_{19}N_4]^+$, 400.16350 (31) $[{}^{12}C_{26}{}^{13}C_1H_{19}N_4]^+$, 401.16659 (5) $[{}^{12}C_{25}{}^{13}C_2H_{19}N_4]^+$. 421.14237 (100) $[C_{27}H_{18}N_4Na]^+$, 422.14544 (31) $[{}^{12}C_{26}{}^{13}C_1H_{18}N_4Na]^+$, 423.14904 (4) $[{}^{12}C_{25}{}^{13}C_2H_{18}N_4Na]^+$. 497.06393 (6) $[Na_2C_{27}H_{17}N_4{}^{54}Fe]^+$, 498.06700 (2) $[Na_2{}^{12}C_{26}{}^{13}C_1H_{17}N_4{}^{54}Fe]^+$, 499.05929 (100) $[Na_2C_{27}H_{17}N_4{}^{56}Fe]^+$, 500.06215 (33) $[Na_2{}^{12}C_{26}{}^{13}C_1H_{17}N_4{}^{56}Fe]^+$, 501.06465 (6) $[Na_2{}^{12}C_{25}{}^{13}C_2H_{17}N_4{}^{56}Fe]^+$. Found: 227.02794 (100), 227.52938 (25). 399.13256 (100), 400.13572 (30), 401.13892 (4). 421.11314 (100), 422.11615 (33), 423.11925 (5). 497.05497 (14), 498.05807 (5), 499.05105 (100), 500.05318 (70), 501.05566 (12).

Synthesis of Complexes in Dichloromethane

Species identified in different runs of the reaction were: $[Fe(NQu_3)(OTf)_2] \cdot 1.3\,DCM \cdot Z$ (**4h**) and $[Fe(NQu_3)(OTf)(H_2O)](OTf) \cdot DCM$ (**4i**). To $Fe(OTf)_2 \cdot 2\,MeCN$ (21.8 mg, 0.05 mmol, 1 eq.) and **4** (19.9 mg, 0.05 mmol, 1 eq.) DCM (4 mL) was added. The mixture was stirred for a few hours.

$[Fe(NQu_3)(OTf)_2] \cdot 1.3\,DCM \cdot Z$ (4h):

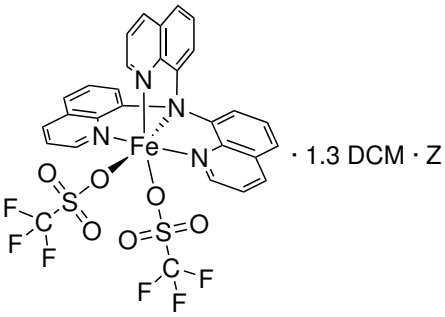

· 1.3 DCM · Z

4h

The solution was layered with Et_2O (8 mL). Suitable orange crystals for SCXRD were obtained after about four days.

IR (ATR), $\tilde{\nu}$ [cm^{-1}]: 3463 (vw, br), 3069 (vw), 1598 (vw), 1509 (w), 1473 (w), 1390 (w), 1333 (w), 1287 (m), 1229 (vs), 1201 (s), 1160 (s), 1151 (s), 1104 (m), 1030 (s), 983 (m), 868 (w), 839 (m), 788 (m), 764 (m), 665 (w), 631 (vs), 572 (m), 516 (s), 475 (m).

HRMS (ESI$^+$, in DCM-MeOH, *m*/*z* [%]): Calc.: 226.04583 (6) $[C_{27}H_{18}N_4{}^{54}Fe]^{2+}$, 226.54737 (2) $[12\,C_{26}{}^{13}C_1H_{18}N_4{}^{54}Fe]^{2+}$, 227.04351 (100) $[C_{27}H_{18}N_4{}^{56}Fe]^{2+}$, 227.54495 (33) $[{}^{12}C_{26}{}^{13}C_1H_{18}N_4{}^{56}Fe]^{2+}$, 228.04619 (6) $[{}^{12}C_{25}{}^{13}C_2H_{18}N_4{}^{56}Fe]^{2+}$, 228.54738 (1) $[{}^{12}C_{24}{}^{13}C_3H_{18}N_4{}^{56}Fe]^{2+}$. 601.04424 (6) $[F_3C_{28}H_{18}N_4O_3{}^{54}Fe{}^{32}S]^+$, 602.04723 (2) $[F_3{}^{12}C_{27}{}^{13}C_1H_{18}N_4O_3{}^{54}Fe{}^{32}S]^+$, 603.03960 (100) $[F_3C_{28}H_{18}N_4O_3{}^{56}Fe{}^{32}S]^+$, 604.04241 (35) $[F_3{}^{12}C_{27}{}^{13}C_1H_{18}N_4O_3{}^{56}Fe{}^{32}S]^+$, 605.04108 (11) $[F_3C_{28}H_{18}N_4O_3{}^{56}Fe{}^{34}S]^+$ & $[F_3{}^{12}C_{26}{}^{13}C_2H_{18}N_4O_3{}^{56}Fe{}^{32}S]^+$, 606.04161 (2) $[F_3{}^{12}C_{27}{}^{13}C_1H_{18}N_4O_3{}^{56}Fe{}^{34}S]^+$. Found: 226.04578 (8), 226.54688 (3), 227.04353 (100), 227.54491 (39), 228.04621 (6), 228.54722 (1). 601.04366 (6), 602.04598 (2), 603.03897 (100), 604.04189 (34), 605.04093 (8), 606.04079 (2).

[Fe(NQu$_3$)(OTf)(H$_2$O)](OTf) · DCM (4i):

Moisture and oxygen were not excluded completely in this reaction. The reaction mixture (see above) was filtered, resulting in a red brownish solution. The solution was layered with pentane (8 mL). Suitable yellow-orange crystals for SCXRD were obtained after about four weeks.

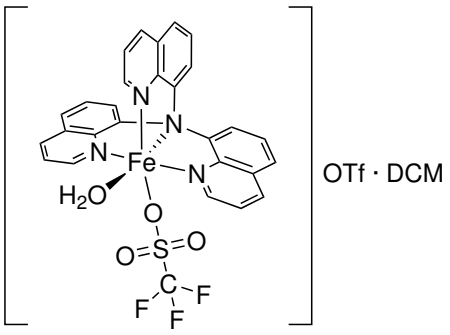

4i
$C_{30}H_{22}F_6Cl_2FeN_4O_7S_2$
MW: 588.38 g/mol

IR (ATR), $\tilde{\nu}$ [cm^{-1}]: 3321 (w, br), 1507 (m), 1500 (m), 1385 (w), 1282 (m), 1233 (s), 1224 (s), 1160 (s), 1108 (m), 1094 (m), 1025 (vs), 931 (vw), 838 (m), 788 (m), 767 (m), 664 (w), 636 (s), 613 (m), 572 (w), 516 (m).

HRMS (ESI$^+$, in MeOH, *m*/*z* [%]): Calc.: 226.04583 (6) $[C_{27}H_{18}N_4{}^{54}Fe]^{2+}$, 226.54737 (2) $[{}^{12}C_{26}{}^{13}C_1H_{18}N_4{}^{54}Fe]^{2+}$, 227.04351 (100) $[C_{27}H_{18}N_4{}^{56}Fe]^{2+}$, 227.54495 (33) $[{}^{12}C_{26}{}^{13}C_1H_{18}N_4{}^{56}Fe]^{2+}$, 228.04619 (6) $[{}^{12}C_{25}{}^{13}C_2H_{18}N_4{}^{56}Fe]^{2+}$, 228.54738 (1) $[{}^{12}C_{24}{}^{13}C_3H_{18}N_4{}^{56}Fe]^{2+}$. 601.04424 (6) $[F_3C_{28}H_{18}N_4O_3{}^{54}Fe{}^{32}S]^+$, 602.04723 (2) $[F_3{}^{12}C_{27}{}^{13}C_1H_{18}N_4O_3{}^{54}Fe{}^{32}S]^+$, 603.03960 (100) $[F_3C_{28}H_{18}N_4O_3{}^{56}Fe{}^{32}S]^+$, 604.04241 (35) $[F_3{}^{12}C_{27}{}^{13}C_1H_{18}N_4O_3{}^{56}Fe{}^{32}S]^+$, 605.04108 (11) $[F_3C_{28}H_{18}N_4O_3{}^{56}Fe{}^{34}S]^+$ & $[F_3{}^{12}C_{26}{}^{13}C_2H_{18}N_4O_3{}^{56}Fe{}^{32}S]^+$, 606.04161 (2) $[F_3{}^{12}C_{27}{}^{13}C_1H_{18}N_4O_3{}^{56}Fe{}^{34}S]^+$. Found: 226.04589 (6), 226.54721 (2), 227.04360 (100), 227.54500 (33), 228.04637 (5), 228.54752 (1). 601.04454 (7), 602.04749 (2), 603.04020 (100), 604.04291 (37), 605.04212 (10), 606.04181 (2).

Synthesis of [Fe(NQu$_3$)(EtCN)$_2$](OTf)$_2$ (4j)

To Fe(OTf)$_2$ · 2 MeCN (10.9 mg, 0.024 mmol, 1 eq.) and **4** (10.0 mg, 0.025 mmol, 1 eq.) EtCN (2 mL) was added. The mixture was stirred for 30 min until it became a clear purple solution. Afterwards, 1.6 mL of the solution were layered with Et$_2$O (6 mL) and stored at 6 °C. Suitable red-orange crystals for SCXRD were obtained after about two weeks.

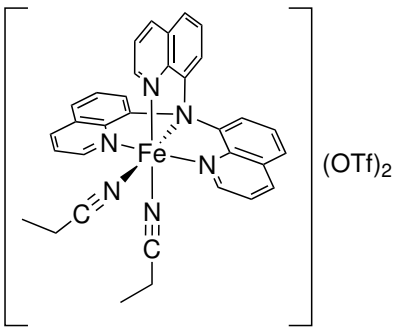

4j
$C_{35}H_{28}F_6FeN_6O_6S_2$
MW: 862.60 g/mol

IR (ATR), $\tilde{\nu}$ [cm^{-1}]: 3364 (vw, br), 3067 (vw), 1595 (w), 1504 (m), 1473 (w), 1427 (vw), 1388 (w), 1315 (w), 1277 (m), 1235 (s), 1222 (s), 1157 (s), 1149 (s), 1107 (m), 1026 (vs), 866 (vw), 837 (m), 810 (m), 767 (m), 671 (w), 635 (vs), 573 (m), 515 (m), 467 (w), 447 (w), 423 (w).

HRMS (ESI$^+$, in MeCN, *m*/*z* [%]): Calc.: 226.04583 (6) $[C_{27}H_{18}N_4{}^{54}Fe]^{2+}$, 226.54737 (2) $[{}^{12}C_{26}{}^{13}C_1H_{18}N_4{}^{54}Fe]^{2+}$, 227.04351 (100) $[C_{27}H_{18}N_4{}^{56}Fe]^{2+}$, 227.54495 (33) $[{}^{12}C_{26}{}^{13}C_1H_{18}N_4{}^{56}Fe]^{2+}$, 228.04619 (6) $[{}^{12}C_{25}{}^{13}C_2H_{18}N_4{}^{56}Fe]^{2+}$, 228.54738 (1) $[{}^{12}C_{24}{}^{13}C_3H_{18}N_4{}^{56}Fe]^{2+}$. Found: 226.03147 (6), 226.53298 (2), 227.02911 (100), 227.53054 (31) 228.03176 (4), 228.53281 (1).

Synthesis of [Fe(NQu$_3$)(OTf)(EtCN)](OTf) · 0.5 Et$_2$O (4k)

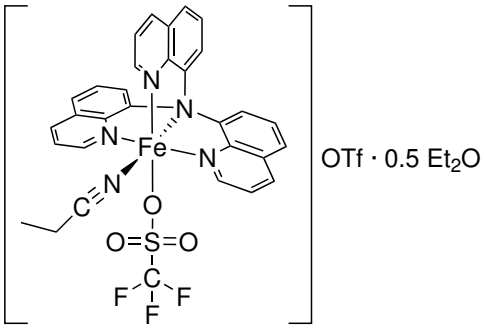

4k
$C_{34}H_{28}F_6FeN_5O_{6.5}S_2$
MW: 844.58 g/mol

To Fe(OTf)$_2$ · 2 MeCN (21.8 mg, 0.05 mmol, 1 eq.) and **4** (19.9 mg, 0.05 mmol, 1 eq.), EtCN (1 mL) was added. The mixture was stirred for 30 min until it became a clear dark red solution. Afterwards, the solution was layered with Et$_2$O (6 mL) and stored at 6 °C. Suitable orange crystals for SCXRD were obtained after about one week.

IR (ATR), $\tilde{\nu}$ [cm^{-1}]: 3364 (w), 3233 (w), 3068 (w), 1664 (vw), 1617 (vw), 1596 (w), 1508 (m), 1501 (m), 1473 (w), 1424 (vw), 1392 (w), 1315 (m), 1281 (m), 1234 (s), 1222 (vs), 1159 (s), 1136 (m), 1108 (m), 1094 (m), 1080 (m), 1024 (vs), 933 (w), 866 (w), 837 (m), 810 (w), 799 (m), 788 (m), 767 (m), 664 (m), 635 (vs), 614 (m), 574 (m), 516 (s), 473 (m), 466 (m), 423 (m).

HRMS (ESI$^+$, in MeCN, *m/z* [%]): Calc.: 399.16042 (100) $[C_{27}H_{19}N_4]^+$, 400.16350 (31) $[^{12}C_{26}{}^{13}C_1H_{19}N_4]^+$, 401.16659 (5) $[^{12}C_{25}{}^{13}C_2H_{19}N_4]^+$. 421.14237 (100) $[C_{27}H_{19}N_4Na]^+$, 422.14544 (31) $[^{12}C_{26}{}^{13}C_1H_{19}N_4Na]^+$, 423.14904 (4) $[^{12}C_{25}{}^{13}C_2H_{19}N_4Na]^+$. Found: 399.14714 (100), 400.15037 (31), 401.15357 (5). 421.12869 (100), 422.13155 (44), 423.13470 (7).

Synthesis of Complexes in Methanol

Species identified in different runs of the reaction were: [[Fe(NQu$_3$)(OTf)(MeOH)](OTf) (**4l**) and [Fe(NQu$_3$)(OTf)(MeOH)](OTf) · MeOH (**4m**). To Fe(OTf)$_2$ · 2 MeCN (21.8 mg, 0.05 mmol, 1 eq.) and **4** (19.9 mg, 0.05 mmol, 1 eq.), MeOH (1 mL) was added. The mixture was stirred for two days until it became a clear brown solution. Afterwards, the solution was layered with Et$_2$O (8 mL).

[Fe(NQu$_3$)(OTf)(MeOH)](OTf) (4l):

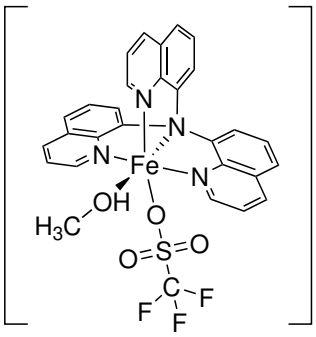

4l
$C_{30}H_{22}F_6FeN_4O_7S_2$
MW: 784.48 g/mol

Suitable red crystals for SCXRD were obtained after about one week.

IR (ATR), $\tilde{\nu}$ [cm^{-1}]: 1617 (vw), 1595 (vw), 1510 (w), 1502 (w), 1473 (w), 1388 (w), 1376 (w), 1318 (vw), 1293 (m), 1235 (w), 1213 (m), 1157 (m), 1137 (w), 1110 (w), 1080 (w), 1021 (vs), 867 (vw), 840 (m), 784 (w), 766 (m), 757 (m), 634 (vs), 574 (w), 518 (m), 418 (w).

HRMS (ESI$^+$, in MeOH, *m*/*z* [%]): Calc.: 226.04583 (6) $[C_{27}H_{18}N_4{}^{54}Fe]^{2+}$, 226.54737 (2) $[{}^{12}C_{26}{}^{13}C_1H_{18}N_4{}^{54}Fe]^{2+}$, 227.04351 (100) $[C_{27}H_{18}N_4{}^{56}Fe]^{2+}$, 227.54495 (33) $[{}^{12}C_{26}{}^{13}C_1H_{18}N_4{}^{56}Fe]^{2+}$, 228.04619 (6) $[{}^{12}C_{25}{}^{13}C_2H_{18}N_4{}^{56}Fe]^{2+}$, 228.54738 (1) $[{}^{12}C_{24}{}^{13}C_3H_{18}N_4{}^{56}Fe]^{2+}$. 601.04424 (6) $[F_3C_{28}H_{18}N_4O_3{}^{54}Fe^{32}S]^+$, 602.04723 (2) $[F_3{}^{12}C_{27}{}^{13}C_1H_{18}N_4O_{354}Fe^{32}S]^+$, 603.03960 (100) $[F_3C_{28}H_{18}N_4O_3{}^{56}Fe^{32}S]^+$, 604.04241 (35) $[F_3{}^{12}C_{27}{}^{13}C_1H_{18}N_4O_3{}^{56}Fe^{32}S]^+$, 605.04108 (11) $[F_3C_{28}H_{18}N_4O_3{}^{56}Fe^{34}S]^+$ & $[F_3{}^{12}C_{26}{}^{13}C_2H_{18}N_4O_3{}^{56}Fe^{32}S]^+$. 632.06263 (6) $[F_3C_{29}H_{21}N_4O_4{}^{54}Fe^{32}S]^+$, 633.06598 (2) $[F_3{}^{12}C_{28}{}^{13}C_1H_{21}N_4O_4{}^{54}Fe^{32}S]^+$, 634.05795 (100) $[F_3C_{29}H_{21}N_4O_4{}^{56}Fe^{32}S]^+$, 635.06131 (31) $[F_3{}^{12}C_{28}{}^{13}C_1H_{21}N_4O_4{}^{56}Fe^{32}S]^+$, 636.05968 (12) $[F_3C_{29}H_{21}N_4O_4{}^{56}Fe^{34}S]^+$ & $[F_3{}^{12}C_{27}{}^{13}C_2H_{21}N_4O_4{}^{56}Fe^{32}S]^+$, 637.05710 (1) $[F_3{}^{12}C_{28}{}^{13}C_1H_{21}N_4O_4{}^{56}Fe^{34}S]^+$. Found: 226.04569 (7), 226.54711 (2), 227.04349 (100), 227.54487 (36), 228.04616 (6), 228.54737 (1). 601.04421 (6), 602.04726 (2), 603.03977 (100), 604.04257 (34), 605.04176 (9), 606.04148 (2). 632.06283 (8), 633.06520 (2), 634.05797 (100), 635.06086 (33), 636.06068 (8), 637.05993 (2).

[Fe(NQu$_3$)(OTf)(MeOH)](OTf) · MeOH (4m):

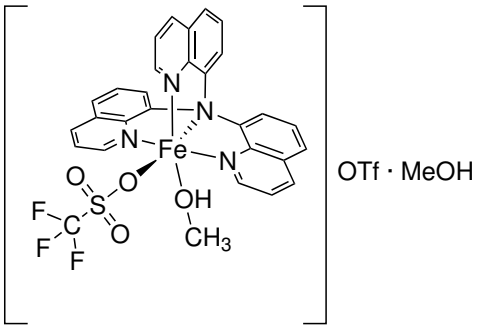

4m
$C_{31}H_{26}F_6FeN_4O_8S_2$
MW: 816.53 g/mol

Suitable orange crystals for SCXRD were obtained after about one week.

IR (ATR), $\tilde{\nu}$ [cm^{-1}]: 3211 (w, br), 2162 (vw), 1664 (vw), 1599 (vw), 1502 (m), 1474 (w), 1423 (vw), 1390 (w), 1316 (w), 1283 (m), 1234 (vs), 1223 (vs), 1158 (s), 1109 (m), 1065 (w), 1026 (vs), 1014 (m), 980 (w), 932 (vw), 866 (vw), 836 (m), 832 (m), 809 (w), 799 (m), 789 (m), 773 (w), 763 (m), 716 (vw), 670 (w), 636 (s), 617 (m), 572 (m), 544 (vw), 515 (m), 473 (w), 467 (w), 445 (vw), 424 (w).

HRMS (ESI$^+$, in MeOH, *m*/*z* [%]): Calc.: 226.04583 (6) $[C_{27}H_{18}N_4{}^{54}Fe]^{2+}$, 226.54737 (2) $[{}^{12}C_{26}{}^{13}C_1H_{18}N_4{}^{54}Fe]^{2+}$, 227.04351 (100) $[C_{27}H_{18}N_4{}^{56}Fe]^{2+}$, 227.54495 (33)

$[^{12}C_{26}{}^{13}C_1H_{18}N_4{}^{56}Fe]^{2+}$, 228.04619 (6) $[^{12}C_{25}{}^{13}C_2H_{18}N_4{}^{56}Fe]^{2+}$. 601.04424 (6) $[F_3C_{28}H_{18}N_4O_3{}^{54}Fe{}^{32}S]^+$, 603.03960 (100) $[F_3C_{28}H_{18}N_4O_3{}^{56}Fe{}^{32}S]^+$, 604.04241 (35) $[F_3{}^{12}C_{27}{}^{13}C_1H_{18}N_4O_3{}^{56}Fe{}^{32}S]^+$, 605.04108 (11) $[F_3C_{28}H_{18}N_4O_3{}^{56}Fe{}^{34}S]^+$ & $[F_3{}^{12}C_{26}{}^{13}C_2H_{18}N_4O_3{}^{56}Fe{}^{32}S]^+$. 632.06263 (6) $[F_3C_{29}H_{21}N_4O_4{}^{54}Fe{}^{32}S]^+$, 634.05795 (100) $[F_3C_{29}H_{21}N_4O_4{}^{56}Fe{}^{32}S]^+$, 635.06131 (31) $[F_3{}^{12}C_{28}{}^{13}C_1H_{21}N_4O_4{}^{56}Fe{}^{32}S]^+$, 636.05968 (12) $[F_3C_{29}H_{21}N_4O_4{}^{56}Fe{}^{34}S]^+$ & $[F_3{}^{12}C_{27}{}^{13}C_2H_{21}N_4O_4{}^{56}Fe{}^{32}S]^+$. Found: 226.04510 (6), 226.54657 (2), 227.04277 (100), 227.54425 (33), 228.04556 (6). 601.04240 (6), 603.03757 (100), 604.04061 (33), 605.04027 (11). 632.06041 (8), 634.05585 (100), 635.05880 (36), 636.05834 (8).

Synthesis of $[Fe(NQu_3)Cl_2] \cdot 0.5\,DCM$ (4n)

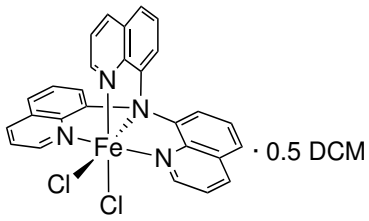

4n
$C_{27.5}H_{19}Cl_3FeN_4$
MW: 567.67 g/mol

To $FeCl_2$ (6.3 mg, 0.05 mmol, 1 eq.) and **4** (19.9 mg, 0.05 mmol, 1 eq.), DCM (1 mL) was added. The mixture was stirred for one day resulting in a purple suspension to which MeCN (3 mL) was added. Afterwards, the solution was stirred for another day, filtered and layered with Et_2O (8 mL). Suitable red crystals for SCXRD were obtained after about four weeks.
IR (ATR), $\tilde{\nu}$ [cm^{-1}]: 3065 (w), 3043 (w), 3009 (vw), 2972 (vw), 2860 (vw), 1613 (w), 1591 (w), 1577 (w), 1504 (m), 1466 (m), 1428 (w), 1380 (m), 1371 (m), 1314 (m), 1240 (m), 1213 (w), 1177 (w), 1160 (w), 1137 (w), 1111 (m), 1092 (m), 1075 (m), 1034 (w), 1005 (vw), 981 (w), 933 (vw), 862 (w), 837 (vs), 813 (m), 806 (s), 789 (s), 768 (vs), 736 (w), 709 (w), 669 (w), 660 (m), 613 (m), 572 (w), 556 (w), 544 (w), 519 (m), 511 (m), 475 (w), 467 (w), 441 (vw), 432 (w).
HRMS (ESI$^+$, in MeCN, *m*/*z* [%]): Calc.: 487.06107 (6) $[C_{27}H_{18}{}^{35}ClN_4{}^{54}Fe]^+$, 488.06414 (2) $[^{12}C_{26}{}^{13}C_1H_{18}{}^{35}ClN_4{}^{54}Fe]^+$, 489.05646 (100) $[C_{27}H_{18}{}^{35}ClN_4{}^{56}Fe]^+$, 490.05933 (33) $[^{12}C_{26}{}^{13}C_1H_{18}{}^{35}ClN_4{}^{56}Fe]^+$, 491.05471 (37) $[C_{27}H_{18}{}^{37}ClN_4{}^{56}Fe]^+$, 492.05676 (11) $[^{12}C_{26}{}^{13}C_1H_{18}{}^{37}ClN_4{}^{54}Fe]^+$, 493.05900 (2) $[^{12}C_{25}{}^{13}C_2H_{18}{}^{37}ClN_4{}^{54}Fe]^+$. Found: 487.05286 (6), 488.05631 (2), 489.04822 (100), 490.05116 (32), 491.04597 (34), 429.04842 (11), 493.05087 (2).

Synthesis of $[Fe(NQu_3)Br_2] \cdot 0.5\,DCM$ (4o)

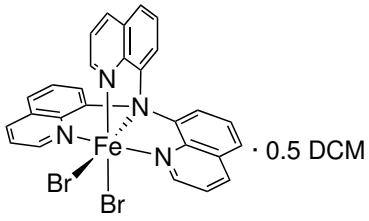

4o
$C_{27.5}H_{19}Br_2ClFeN_4$
MW: 656.59 g/mol

To $FeBr_2$ (9.7 mg, 0.04 mmol, 0.9 eq.) and **4** (20.7 mg, 0.05 mmol, 1 eq.), MeCN (4 mL) and DCM (4 mL) were added. The mixture was stirred for a few hours resulting in a clear red solution. Suitable red crystals for SCXRD were obtained after about four weeks.
IR (ATR), $\tilde{\nu}$ [cm^{-1}]: 3053 (w), 1614 (w), 1592 (w), 1581 (w), 1500 (s), 1467 (m), 1427 (w), 1375 (m), 1313 (m), 1240 (m), 1213 (w), 1177 (w), 1167 (w), 1138 (m), 1107 (m), 1088 (m), 1078 (m), 1035 (w), 990 (w), 936 (w), 930 (w), 862 (m), 836 (vs), 806 (m), 796 (s), 761 (vs), 736

(m), 714 (m), 670 (m), 613 (m), 522 (w), 511 (w), 447 (w), 426 (w).

HRMS (ESI$^+$, in MeCN, *m/z* [%]): Calc.: 531.01055 (6) $[C_{27}H_{18}{}^{79}BrN_4{}^{54}Fe]^+$, 532.01363 (2) $[{}^{12}C_{26}{}^{13}C_1H_{18}{}^{79}BrN_4{}^{54}Fe]^+$, 533.00606 (100) $[C_{27}H_{18}{}^{79}BrN_4{}^{56}Fe]^+$, 534.00893 (33) $[{}^{12}C_{26}{}^{13}C_1H_{18}{}^{79}BrN_4{}^{56}Fe]^+$, 535.00426 (97) $[C_{27}H_{18}{}^{81}BrN_4{}^{56}Fe]^+$, 536.00686 (31) $[{}^{12}C_{26}{}^{13}C_1H_{18}{}^{81}BrN_4{}^{56}Fe]^+$, 537.00928 (5) $[{}^{12}C_{25}{}^{13}C_2H_{18}{}^{81}BrN_4{}^{56}Fe]^+$. Found: 531.00148 (5), 532.00486 (1), 532.99706 (100), 534.00008 (32), 534.99515 (93), 535.99789 (29), 537.00081 (4).

Synthesis of $[Fe(NQu_3)Cl]PF_6 \cdot 1.5\,DCM$ (4p)

To $FeCl_2$ (6.3 mg, 0.05 mmol, 1 eq.) and **4** (19.9 mg, 0.05 mmol, 1 eq.), DCM (4 mL) was added. The mixture was stirred 10 min. A solution of $AgPF_6$ (12.9 mg, 0.05 mmol, 1 eq.) in DCM (2 mL) was added, resulting in a bright orange solution with yellow solid. The solution was filtered and layered with Et_2O. After one week, two kinds of crystals had grown. The majority were orange crystals with too poor quality for SCXRD (not investigated further). Besides this, a few yellow crystals could be obtained which were suitable for SCXRD. Since this was a side product instead of the intended one, there were too few yellow crystals to perform further bulk characterisation.

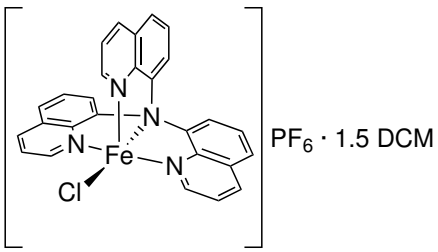

4p
$C_{28.5}H_{21}Cl_4F_6FeN_4P$
MW: 762.11 g/mol

Synthesis of $[Fe(NQu_3)(MeCN)_2](BF_4)_2 \cdot 0.5\,MeCN$ (4q)

To $[Fe(MeCN)_6](BF_4)_2$ (23.8 mg, 0.05 mmol, 1 eq.) and **4** (19.9 mg, 0.05 mmol, 1 eq.), MeCN (2 mL) was added. The mixture was stirred for one day until it was a clear orange solution. Afterwards, the solution was layered with Et_2O (10 mL). Suitable red crystals for SCXRD were obtained after about three weeks.

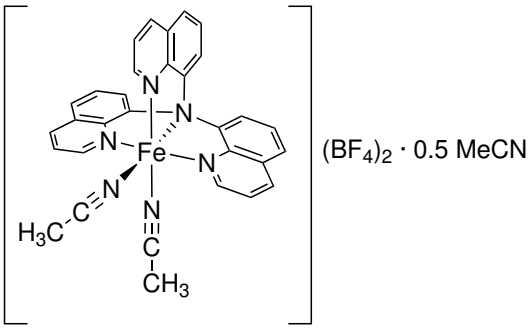

4q
$C_{32}H_{25.5}B_2F_8FeN_{6.5}$
MW: 730.56 g/mol

IR (ATR), $\tilde{\nu}$ [cm^{-1}]: 3555 (w, br), 1614 (w), 1504 (w), 1466 (w), 1421 (vw), 1375 (w), 1315 (w), 1286 (vw), 1234 (vw), 1221 (vw), 1045 (vs), 1013 (vs), 993 (s), 842 (m), 836 (m), 808 (w), 800 (m), 791 (m), 682 (w), 670 (w), 616 (vw), 582 (vw), 551 (vw), 519 (w), 465 (vw), 413 (vw).

HRMS (ESI$^+$, in MeCN, *m/z* [%]): Calc.: 226.04583 (6) $[C_{27}H_{18}N_4{}^{54}Fe]^{2+}$, 226.54737 (2) $[{}^{12}C_{26}{}^{13}C_1H_{18}N_4{}^{54}Fe]^{2+}$, 227.04351 (100) $[C_{27}H_{18}N_4{}^{56}Fe]^{2+}$, 227.54495 (33) $[{}^{12}C_{26}{}^{13}CH_{18}N_4{}^{56}Fe]^{2+}$, 228.04619 (6) $[{}^{12}C_{25}{}^{13}C_2H_{18}N_4{}^{56}Fe]^{2+}$. Found: 226.04589 (6),

226.54766 (2), 227.04372 (100), 227.54518 (31), 228.04648 (5).

Synthesis of $[Fe(NQu_3)(NCS)_2] \cdot 0.5\,Et_2O$ (4r)

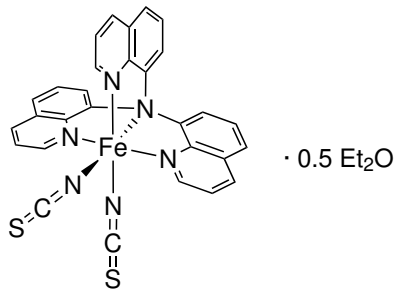

4r
$C_{31}H_{23}FeN_6O_{0.5}S_2$
MW: 607.53 g/mol

In a Schlenk tube, $[Fe(NSC)_2(Py)_4]$ (24.4 mg, 0.05 mmol, 1 eq.) was layered with MeOH (1 mL). In a second Schlenk tube, **4** (19.9 mg, 0.05 mmol, 1 eq.) was dissolved in MeOH (6 mL) and Et_2O (10 mL). The ligand solution was stirred for 10 min until it was yellow and clear. A mixture of MeOH (1.5 mL) and Et_2O (1.5 mL) was layered on top of the iron salt solution in the first tube. Afterwards, the ligand solution was layered carefully on top of this. Suitable dark crystals with red and green pleochroism for SCXRD were observed in the mixing layer of the solutions after one week.

IR (ATR), $\tilde{\nu}$ [cm^{-1}]: 3515 (vw), 3053 (vw), 2963 (w), 2053 (s), 1654 (vw), 1613 (vw), 1592 (w), 1581 (w), 1496 (m), 1466 (w), 1422 (vw), 1379 (w), 1311 (w), 1260 (m), 1208 (w), 1104 (m), 1088 (m), 1017 (m), 925 (w), 863 (w), 794 (vs), 762 (vs), 712 (w), 670 (m), 659 (w), 613 (w), 570 (vw), 444 (vw).

HRMS (ESI$^+$, in MeCN, *m/z* [%]): Calc.: 510.06736 (6) $[C_{28}H_{18}N_5{}^{54}Fe^{32}S]^+$, 511.07071 (2) $[{}^{12}C_{27}{}^{13}C_1H_{18}N_5{}^{54}Fe^{32}S]^+$, 512.06268 (100) $[C_{28}H_{18}N_5{}^{56}Fe^{32}S]^+$, 513.06604 (30) $[{}^{12}C_{27}{}^{13}C_1H_{18}N_5{}^{56}Fe^{32}S]^+$, 514.06401 (11) $[C_{28}H_{18}N_5{}^{56}Fe^{34}S]^+$ & $[{}^{12}C_{26}{}^{13}C_2H_{18}N_5{}^{56}Fe^{32}S]^+$, 515.06184 (1) $[{}^{12}C_{27}{}^{13}C_1H_{18}N_5{}^{56}Fe^{34}S]^+$. Found: 510.06625 (8), 511.07125 (3), 512.06344 (100), 513.06648 (35), 514.07095 (17), 515.07035 (2).

11 Oxidation Reactions

11.1 C – H Oxidation Reactions with 2a

11.1.1 C – H Bond Oxidation Reactions of Cyclohexane

In a typical reaction, **2a** (2.4 mg, 0.003 mmol, 1 eq.) and cyclohexane (325 µL, 3 mmol, 1000 eq.) were combined with a solution of nitrobenzene (0.015 mmol, internal standard) in abs. acetonitrile (2 mL). To start the reaction, a solution of mCPBA (0.03 mmol, 10 eq.) in abs. acetonitrile (1 mL) was added. It was taken into account that the mCPBA used contained 77 % mCPBA. The reaction mixture was stirred for 2 h at rt and stopped with the addition of minimum 25 eq. of PPh_3. To analyse the products, 1 mL of the reaction mixture was passed through a small silica column and then submitted to GC analysis. Reactions were carried out at least triplicate. Values shown in this work are averaged. Reactions at aerobic conditions were performed analogously. Blank reactions were performed without iron complex as well as $Fe(OTf)_2 \cdot 2\,MeCN$ instead of **2a**. Without iron complex, no products were observed in the GC analysis and use of $Fe(OTf)_2 \cdot 2\,MeCN$ leads to poorer results as the reactions with **2a** (Table A.1 in the Appendix).

11.1.2 C – H Bond Oxidation Reactions of Cyclohexane-d_{12}

Reaction with mixtures of cyclohexane and cyclohexane-d_{12} were carried out identical to the ones with non-deuterated cyclohexane but the 1000 eq. of substrate were combinations of deuterated and non-deuterated cyclohexane at certain ratios (1 : 3 up to 4 : 1 of ***C*** : ***C*-d**).

11.1.3 C – H Bond Oxidation Reactions of Adamantane

In a typical reaction, **2a** (2.4 mg, 0.003 mmol, 1 eq.) and adamantane (409 mg, 3 mmol, 1000 eq.) were combined with a solution of nitrobenzene (0.015 mmol, internal standard) in abs. acetonitrile (2 mL). To start the reaction, a solution of mCPBA (0.03 mmol, 10 eq.) in abs. acetonitrile (1 mL) was added. It was taken into account that the mCPBA used contained only 77 % mCPBA. The reaction mixture was stirred for 2 h at rt and stopped with the addition of minimum 25 eq. of PPh_3. To analyse the products 1 mL of the reaction mixture was passed through a small silica column and then submitted to GC analysis. Reactions were carried out at least triplicate. Values shown in this work are averaged. Blank reactions were performed without iron complex as well as $Fe(OTf)_2 \cdot 2\,MeCN$ instead of **2a**. Both leads to poorer results as the reactions with **2a** (Table A.2 in the Appendix).

11.2 C – H Bond Oxidation Reactions with NQu_3-Based Complexes

11.2.1 C – H Bond Oxidation Reactions of Cyclohexane in MeCN

The reactions were carried out at 0 °C, rt and 50 °C, with a complex : oxidant : substrate ratio of 1 : 10 : 1000. For the complex solution, **4** (6.0 mg, 0.015 mmol) and $Fe(OTf)_2 \cdot 2\,MeCN$ (6.5 mg, 0.015 mmol) were dissolved in anhydrous MeCN (10 mL) and stirred for approx. 30 min. As standard for the GC, nitrobenzene (15.5 µL, 0.151 mmol) was added after complex formation. For catalysis, 2 mL of the complex solution (0.003 mmol, 1 eq., with 0.03 mmol nitrobenzene) were mixed with 0.325 mL cyclohexane (0.253 mg, 3.00 mmol, 1000 eq.) and the mixture was stirred for 10 min at reaction temperature. The oxidant stock solution (0.03 mmol, 10 eq., see Table 11.1) was added. The reaction mixture was stirred for 2 h at rt and stopped with the addition of minimum 25 eq. of PPh_3. To analyse the products, 1 mL of the reaction mixture was passed through a small silica column (see subsection 11.2.3) and then submitted to GC analysis.

Table 11.1: Details for oxidant solutions for experiments in MeCN.

Oxidant	*m*(oxidant) [mg]	*V*(solvent) [mL]	Used *V*(solution) [mL]
sPhIO (93 %)	50.8	5 (MeCN)	1
H_2O_2 (30 %)	16.7	5 (MeCN)	1
mCPBA (77 %)	33.5	5 (MeCN)	1

11.2.2 C – H Bond Oxidation Reactions of Cyclohexane in DCM

The reactions were carried out at 0 °C, rt and 50 °C, with a complex : oxidant : substrate ratio of 1 : 10 : 1000. For the complex solution, **4** (6.0 mg, 0.015 mmol) and $Fe(OTf)_2 \cdot 2\,MeCN$ (6.5 mg, 0.015 mmol) were dissolved in anhydrous DCM (10 mL) and stirred for approx. 22 h. As standard for the GC, 15.5 µL (0.151 mmol) nitrobenzene was added after complex formation. For catalysis, 2 mL of the complex solution (0.003 mmol, 1 eq., with 0.03 mmol nitrobenzene) were mixed with 0.325 mL cyclohexane (0.253 mg, 3.00 mmol, 1000 eq.) and the mixture was stirred for 10 min at reaction temperature. The oxidant stock solution (0.03 mmol, 10 eq., see Table 11.2) was added. The reaction mixture was stirred for 2 h at rt and stopped with the addition of minimum 25 eq. of PPh_3. To analyse the products, 1 mL of the reaction mixture was passed through a small silica column (see subsection 11.2.3) and then submitted to GC analysis.

Table 11.2: Details for oxidant solutions for experiments in DCM.

Oxidant	*m*(oxidant) [mg]	*V*(solvent) [mL]	Used *V*(solution) [mL]
sPhIO (93 %)	50.8	5 (DCM) + 5 (MeCN)	2
H_2O_2 (30 %)	16.7	5 (DCM)	1
mCPBA (77 %)	33.5	5 (DCM)	1

11.2.3 Workup Procedures

A1: 1 mL of the reaction solution was added to a long silica column (see Figure 11.1) and rinsed with MeCN until the GC vial was full.
A2: 1 mL of the reaction solution was added to a long silica column (see Figure 11.1) and rinsed with DCM until the GC vial was full.
A3: 1 mL of the reaction solution was added to a short silica column (see Figure 11.1) and rinsed with MeCN until the GC vial was full.
A4: 1 mL of the reaction solution was added to a short silica column (see Figure 11.1) and rinsed with EtOH until the GC vial was full.

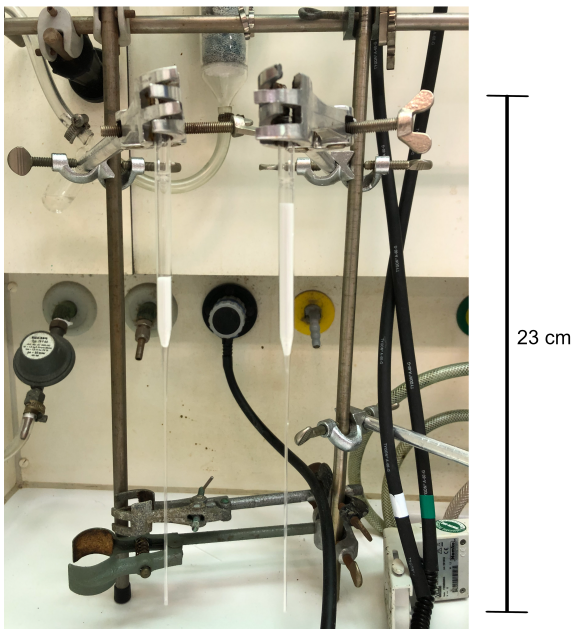

Figure 11.1: Photograph of short (left) and long (right) silica column used for workup of reactions.

References

[1] S. Herres-Pawlis, P. Klüfers, *Bioanorganische Chemie: Metalloproteine, Methoden und Modelle*, Wiley-VCH Verlag GmbH & Co. KGaA, Weinheim, 1st. edition **2017**.

[2] S. C. Andrews, P. Arosio, W. Bottke, J. F. Briat, M. von Darl, P. M. Harrison, J. P. Laulhère, S. Levi, S. Lobreaux, S. J. Yewdall, *J. Inorg. Biochem.* **1992**, *47*, 161–174, doi:10.1016/0162-0134(92)84062-R.

[3] K. Matthes, *Naunyn Schmiedebergs Arch. Exp. Pathol. Pharmakol.* **1935**, *179*, 698–711, doi:10.1007/BF01862691.

[4] G. A. Millikan, *Rev. Sci. Instrum.* **1942**, *13*, 434–444, doi:10.1063/1.1769941.

[5] S. M. Lopez Silva, M. L. Dotor Castilla, J. P. Silveira Martin, *J. Biomed. Opt.* **2003**, *8*, 525–533, doi:10.1117/1.1578495.

[6] A. M. Luks, E. R. Swenson, *Ann. Am. Thorac. Soc.* **2020**, *17*, 1040–1046, doi:10.1513/AnnalsATS.202005-418FR.

[7] J. R. Feiner, M. D. Rollins, J. W. Sall, H. Eilers, P. Au, P. E. Bickler, *Anesth. Analg.* **2013**, *117*, 847–858, doi:10.1213/ANE.0b013e31828610a0.

[8] J. Haldane, *J. Physiol.* **1895**, *18*, 430–462, doi:10.1113/jphysiol.1895.sp000578.

[9] X. Engelmann, I. Monte-Pérez, K. Ray, *Angew. Chem. Int. Ed.* **2016**, *55*, 7632–7649, doi:10.1002/anie.201600507, *Angew. Chem.* **2016**, *128*, 7760–7778, doi:10.1002/ange.201600507.

[10] G. Olivo, O. Cussó, M. Borrell, M. Costas, *J. Biol. Inorg. Chem.* **2017**, *22*, 425–452, doi:10.1007/s00775-016-1434-z.

[11] V. Dantignana, A. Company, M. Costas, *Isr. J. Chem.* **2020**, *60*, 1004–1018, doi:10.1002/ijch.201900161.

[12] E. I. Solomon, T. C. Brunold, M. I. Davis, J. N. Kemsley, S. K. Lee, N. Lehnert, F. Neese, A. J. Skulan, Y. S. Yang, J. Zhou, *Chem. Rev.* **2000**, *100*, 235–350, doi:10.1021/cr9900275.

[13] L. Que, W. B. Tolman, *Nature* **2008**, *455*, 333–340, doi:10.1038/nature07371.

[14] K. Ray, F. F. Pfaff, B. Wang, W. Nam, *J. Am. Chem. Soc.* **2014**, *136*, 13942–13958, doi:10.1021/ja507807v.

[15] A. F. Hollemann, E. Wieberg, N. Wieberg, *Lehrbuch der Anorganischen Chemie*, de Gruyter, Berlin, 91.-100. edition **1985**.

[16] B. Weber, *Koordinationschemie: Grundlagen und aktuelle Trends*, Springer, Berlin, 2nd. edition **2021**, doi:10.1007/978-3-662-63819-4.

[17] J. Hohenberger, K. Ray, K. Meyer, *Nat. Commun.* **2012**, *3*, 720, doi:10.1038/ncomms1718.

[18] M. Sono, M. P. Roach, E. D. Coulter, J. H. Dawson, *Chem. Rev.* **1996**, *96*, 2841–2888, doi:10.1021/cr9500500.

[19] H. Park, D. Lee, *Chem. Eur. J.* **2020**, *26*, 5916–5926, doi:10.1002/chem.201904975.

[20] S. Kal, L. Que, *J. Biol. Inorg. Chem.* **2017**, *22*, 339–365, doi:10.1007/s00775-016-1431-2.

[21] E. L. Hegg, L. Que, *Eur. J. Biochem.* **1997**, *250*, 625–629, doi:10.1111/j.1432-1033.1997.t01-1-00625.x.

[22] D. Buongiorno, G. D. Straganz, *Coord. Chem. Rev.* **2013**, *257*, 541–563, doi:10.1016/j.ccr.2012.04.028.

[23] H. M. Berman, J. Westbrook, Z. Feng, G. Gilliland, T. N. Bhat, H. Weissig, I. N. Shindyalov, P. E. Bourne, *Nucleic Acids Res.* **2000**, *28*, 235–242, doi:10.1093/nar/28.1.235.

[24] S. Han, L. D. Eltis, K. N. Timmis, S. W. Muchmore, J. T. Bolin, *Science* **1995**, *270*, 976–980, doi:10.1126/science.270.5238.976.

[25] T. Senda, K. Sugiyama, H. Narita, T. Yamamoto, K. Kimbara, M. Fukuda, M. Sato, K. Yano, Y. Mitsui, *J. Mol. Biol.* **1996**, *255*, 735–752, doi:10.1006/jmbi.1996.0060.

[26] K. E. Goodwill, C. Sabatier, C. Marks, R. Raag, P. F. Fitzpatrick, R. C. Stevens, *Nat. Struct. Mol. Biol.* **1997**, *4*, 578–585, doi:10.1038/nsb0797-578.

[27] P. L. Roach, I. J. Clifton, C. M. Hensgens, N. Shibata, C. J. Schofield, J. Hajdu, J. E. Baldwin, *Nature* **1997**, *387*, 827–830, doi:10.1038/42990.
[28] M. S. Lah, M. M. Dixon, K. A. Pattridge, W. C. Stallings, J. A. Fee, M. L. Ludwig, *Biochemistry* **1995**, *34*, 1646–1660, doi:10.1021/bi00005a021.
[29] W. Minor, J. Steczko, B. Stec, Z. Otwinowski, J. T. Bolin, R. Walter, B. Axelrod, *Biochemistry* **1996**, *35*, 10687–10701, doi:10.1021/bi960576u.
[30] K. D. Koehntop, J. P. Emerson, L. Que, *J. Biol. Inorg. Chem.* **2005**, *10*, 87–93, doi:10.1007/s00775-005-0624-x.
[31] D. Sehnal, S. Bittrich, M. Deshpande, R. Svobodová, K. Berka, V. Bazgier, S. Velankar, S. K. Burley, J. Koča, A. S. Rose, *Nucleic Acids Res.* **2021**, *49*, W431–W437, doi:10.1093/nar/gkab314.
[32] M. H. Stipanuk, C. R. Simmons, P. A. Karplus, J. E. Dominy, *Amino Acids* **2011**, *41*, 91–102, doi:10.1007/s00726-010-0518-2.
[33] D. M. Gunawardana, K. C. Heathcote, E. Flashman, *FEBS J.* **2021**, doi:10.1111/febs.16147.
[34] M. Sallmann, C. Limberg, *Acc. Chem. Res.* **2015**, *48*, 2734–2743, doi:10.1021/acs.accounts.5b00148.
[35] E. C. Monkcom, D. de Bruin, A. J. de Vries, M. Lutz, S. Ye, R. J. M. Klein Gebbink, *Chem. Eur. J.* **2021**, *27*, 5191–5204, doi:10.1002/chem.202004633.
[36] S. Ye, X. Wu, L. Wei, D. Tang, P. Sun, M. Bartlam, Z. Rao, *J. Biol. Chem.* **2007**, *282*, 3391–3402, doi:10.1074/jbc.M609337200.
[37] J. G. McCoy, L. J. Bailey, E. Bitto, C. A. Bingman, D. J. Aceti, B. G. Fox, G. N. Phillips, *Proc. Natl. Acad. Sci. U. S. A.* **2006**, *103*, 3084–3089, doi:10.1073/pnas.0509262103.
[38] C. R. Simmons, Q. Liu, Q. Huang, Q. Hao, T. P. Begley, P. A. Karplus, M. H. Stipanuk, *J. Biol. Chem.* **2006**, *281*, 18723–18733, doi:10.1074/jbc.M601555200.
[39] H. Brkić, D. Buongiorno, M. Ramek, G. Straganz, S. Tomić, *J. Biol. Inorg. Chem.* **2012**, *17*, 801–815, doi:10.1007/s00775-012-0898-8.
[40] J. Chen, W. Li, M. Wang, G. Zhu, D. Liu, F. Sun, N. Hao, X. Li, Z. Rao, X. C. Zhang, *Protein Sci.* **2008**, *17*, 1362–1373, doi:10.1110/ps.035881.108.
[41] R. H. Holm, E. I. Solomon, *Chem. Rev.* **2004**, *104*, 347–348, doi:10.1021/cr0206364.
[42] L. Vicens, G. Olivo, M. Costas, *ACS Catal.* **2020**, *10*, 8611–8631, doi:10.1021/acscatal.0c02073.
[43] A. S. Borovik, *Acc. Chem. Res.* **2005**, *38*, 54–61, doi:10.1021/ar030160q.
[44] K. Cheaib, M. Q. E. Mubarak, K. Sénéchal-David, C. Herrero, R. Guillot, M. Clémancey, J.-M. Latour, S. P. de Visser, J.-P. Mahy, F. Banse, F. Avenier, *Angew. Chem. Int. Ed.* **2019**, *58*, 854–858, doi:10.1002/anie.201812724, *Angew. Chem.* **2019**, *131*, 864–868, doi:10.1002/ange.201812724.
[45] Z. Gordon, M. J. Drummond, E. M. Matson, J. A. Bogart, E. J. Schelter, R. L. Lord, A. R. Fout, *Inorg. Chem.* **2017**, *56*, 4852–4863, doi:10.1021/acs.inorgchem.6b03071.
[46] P. C. A. Bruijnincx, G. van Koten, R. J. M. Klein Gebbink, *Chem. Soc. Rev.* **2008**, *37*, 2716–2744, doi:10.1039/b707179p.
[47] A. R. McDonald, L. Que, *Coord. Chem. Rev.* **2013**, *257*, 414–428, doi:10.1016/j.ccr.2012.08.002.
[48] W. Nam, *Acc. Chem. Res.* **2015**, *48*, 2415–2423, doi:10.1021/acs.accounts.5b00218.
[49] D. A. Proshlyakov, T. F. Henshaw, G. R. Monterosso, M. J. Ryle, R. P. Hausinger, *J. Am. Chem. Soc.* **2004**, *126*, 1022–1023, doi:10.1021/ja039113j.
[50] J.-U. Rohde, J.-H. In, M. H. Lim, W. W. Brennessel, M. R. Bukowski, A. Stubna, E. Münck, W. Nam, L. Que, *Science* **2003**, *299*, 1037–1039, doi:10.1126/science.299.5609.1037.
[51] M. Puri, L. Que, *Acc. Chem. Res.* **2015**, *48*, 2443–2452, doi:10.1021/acs.accounts.5b00244.
[52] A. R. McDonald, Y. Guo, V. van Vu, E. L. Bominaar, E. Münck, L. Que, *Chem. Sci.* **2012**, *3*, 1680, doi:10.1039/c2sc01044e.
[53] A. Beck, A. Barth, E. Hübner, N. Burzlaff, *Inorg. Chem.* **2003**, *42*, 7182–7188, doi:10.1021/ic034097c.
[54] P. C. A. Bruijnincx, M. Lutz, A. L. Spek, E. E. van Faassen, B. M. Weckhuysen, G. van Koten, R. J. M. Klein Gebbink, *Eur. J. Inorg. Chem.* **2005**, *2005*, 779–787, doi:10.1002/ejic.200400830.
[55] P. D. Oldenburg, C.-Y. Ke, A. A. Tipton, A. A. Shteinman, L. Que, *Angew. Chem. Int.*

Ed. **2006**, *45*, 7975–7978, doi:10.1002/anie.200603486, *Angew. Chem.* **2006**, *118*, 8143–8146, doi:10.1002/ange.20060348.

[56] P. C. A. Bruijnincx, M. Lutz, A. L. Spek, W. R. Hagen, B. M. Weckhuysen, G. van Koten, R. J. M. K. Gebbink, *J. Am. Chem. Soc.* **2007**, *129*, 2275–2286, doi:10.1021/ja064816x.

[57] E. Folkertsma, E. F. de Waard, G. Korpershoek, A. J. van Schaik, N. Solozabal Mirón, M. Borrmann, S. Nijsse, M. A. H. Moelands, M. Lutz, M. Otte, M.-E. Moret, R. J. M. Klein Gebbink, *Eur. J. Inorg. Chem.* **2016**, *2016*, 1319–1332, doi:10.1002/ejic.201501406.

[58] C. R. Groom, I. J. Bruno, M. P. Lightfoot, S. C. Ward, *Acta Crystallogr. B* **2016**, *72*, 171–179, doi:10.1107/S2052520616003954.

[59] C. A. Grapperhaus, B. Mienert, E. Bill, T. Weyhermüller, K. Wieghardt, *Inorg. Chem.* **2000**, *39*, 5306–5317, doi:10.1021/ic0005238.

[60] J. T. Groves, R. C. Haushalter, M. Nakamura, T. E. Nemo, B. J. Evans, *J. Am. Chem. Soc.* **1981**, *103*, 2884–2886, doi:10.1021/ja00400a075.

[61] M. H. Lim, J.-U. Rohde, A. Stubna, M. R. Bukowski, M. Costas, R. Y. N. Ho, E. Munck, W. Nam, L. Que, *Proc. Natl. Acad. Sci. USA* **2003**, *100*, 3665–3670, doi:10.1073/pnas.0636830100.

[62] J. C. Price, E. W. Barr, B. Tirupati, J. M. Bollinger, C. Krebs, *Biochemistry* **2003**, *42*, 7497–7508, doi:10.1021/bi030011f.

[63] P. J. Riggs-Gelasco, J. C. Price, R. B. Guyer, J. H. Brehm, E. W. Barr, J. M. Bollinger, C. Krebs, *J. Am. Chem. Soc.* **2004**, *126*, 8108–8109, doi:10.1021/ja048255q.

[64] E. J. Klinker, J. Kaizer, W. W. Brennessel, N. L. Woodrum, C. J. Cramer, L. Que, *Angew. Chem. Int. Ed.* **2005**, *44*, 3690–3694, doi:10.1002/anie.200500485, *Angew. Chem.* **2005**, *117*, 3756–3760, doi:10.1002/ange.200500485.

[65] A. Thibon, J. England, M. Martinho, V. G. Young, J. R. Frisch, R. Guillot, J.-J. Girerd, E. Münck, L. Que, F. Banse, *Angew. Chem. Int. Ed.* **2008**, *47*, 7064–7067, doi:10.1002/anie.200801832, *Angew. Chem.* **2008**, *120*, 7172–7175, doi:10.1002/ange.200801832.

[66] J. England, Y. Guo, E. R. Farquhar, V. G. Young, E. Münck, L. Que, *J. Am. Chem. Soc.* **2010**, *132*, 8635–8644, doi:10.1021/ja100366c.

[67] D. C. Lacy, R. Gupta, K. L. Stone, J. Greaves, J. W. Ziller, M. P. Hendrich, A. S. Borovik, *J. Am. Chem. Soc.* **2010**, *132*, 12188–12190, doi:10.1021/ja1047818.

[68] S. Meyer, I. Klawitter, S. Demeshko, E. Bill, F. Meyer, *Angew. Chem. Int. Ed.* **2013**, *52*, 901–905, doi:10.1002/anie.201208044, *Angew. Chem.* **2013**, *125*, 935–939, doi:10.1002/ange.201208044.

[69] J. England, J. O. Bigelow, K. M. van Heuvelen, E. R. Farquhar, M. Martinho, K. K. Meier, J. R. Frisch, E. Münck, L. Que, *Chem. Sci.* **2014**, *5*, 1204–1215, doi:10.1039/C3SC52755G.

[70] J. Prakash, G. T. Rohde, K. K. Meier, E. Münck, L. Que, *Inorg. Chem.* **2015**, *54*, 11055–11057, doi:10.1021/acs.inorgchem.5b02011.

[71] S. Sahu, B. Zhang, C. J. Pollock, M. Dürr, C. G. Davies, A. M. Confer, I. Ivanović-Burmazović, M. A. Siegler, G. N. L. Jameson, C. Krebs, D. P. Goldberg, *J. Am. Chem. Soc.* **2016**, *138*, 12791–12802, doi:10.1021/jacs.6b03346.

[72] W. Rasheed, A. Draksharapu, S. Banerjee, V. G. Young, R. Fan, Y. Guo, M. Ozerov, J. Nehrkorn, J. Krzystek, J. Telser, L. Que, *Angew. Chem. Int. Ed.* **2018**, *57*, 9387–9391, doi:10.1002/anie.201804836, *Angew. Chem.* **2018**, *130*, 9531–9535, doi:10.1002/ange.201804836.

[73] S. Schaub, A. Miska, J. Becker, S. Zahn, D. Mollenhauer, S. Sakshath, V. Schünemann, S. Schindler, *Angew. Chem. Int. Ed.* **2018**, *57*, 5355–5358, doi:10.1002/anie.201800475, *Angew. Chem.* **2018**, *130*, 5453–5456, doi:10.1002/ange.201800475.

[74] W. Rasheed, R. Fan, C. S. Abelson, P. O. Peterson, W.-M. Ching, Y. Guo, L. Que, *J. Biol. Inorg. Chem.* **2019**, *24*, 533–545, doi:10.1007/s00775-019-01672-3.

[75] C. Cordes (née Kupper), M. Morganti, I. Klawitter, C. Schremmer, S. Dechert, F. Meyer, *Angew. Chem. Int. Ed.* **2019**, *58*, 10855–10858, doi:10.1002/anie.201900683, *Angew. Chem.* **2019**, *131*, 10971–10974, doi:10.1002/ange.201900683.

[76] D. Kass, T. Corona, K. Warm, B. Braun-Cula, U. Kuhlmann, E. Bill, S. Mebs, M. Swart, H. Dau, M. Haumann, P. Hildebrandt, K. Ray, *J. Am. Chem. Soc.* **2020**, *142*, 5924–5928,

doi:10.1021/jacs.9b13756.
[77] M. A. Dedushko, M. B. Greiner, A. N. Downing, M. Coggins, J. A. Kovacs, *J. Am. Chem. Soc.* **2022**, *144*, 8515–8528, doi:10.1021/jacs.1c07656.
[78] S. Munshi, A. Sinha, S. Yiga, S. Banerjee, R. Singh, M. K. Hossain, M. Haukka, A. F. Valiati, R. D. Huelsmann, E. Martendal, R. Peralta, F. Xavier, O. F. Wendt, T. K. Paine, E. Nordlander, *Dalton Trans.* **2022**, *51*, 870–884, doi:10.1039/d1dt03381f.
[79] S. Kal, S. Xu, L. Que, *Angew. Chem. Int. Ed.* **2020**, *59*, 7332–7349, doi:10.1002/anie.201906551, *Angew. Chem.* **2020**, *132*, 7400–7419, doi:10.1002/ange.201906551.
[80] P. Comba, M. Maurer, P. Vadivelu, *Inorg. Chem.* **2009**, *48*, 10389–10396, doi:10.1021/ic901702s.
[81] A. C. Lindhorst, S. Haslinger, F. E. Kühn, *Chem. Commun.* **2015**, *51*, 17193–17212, doi:10.1039/c5cc07146a.
[82] P. C. A. Bruijnincx, I. L. C. Buurmans, S. Gosiewska, M. A. H. Moelands, M. Lutz, A. L. Spek, G. van Koten, R. J. M. Klein Gebbink, *Chem. Eur. J.* **2008**, *14*, 1228–1237, doi:10.1002/chem.200700573.
[83] A. Mukherjee, M. Martinho, E. L. Bominaar, E. Münck, L. Que, *Angew. Chem. Int. Ed.* **2009**, *48*, 1780–1783, doi:10.1002/anie.200805342, *Angew. Chem.* **2009**, *121*, 1812–1815, doi:10.1002/ange.200805342.
[84] L. Chen, X.-J. Su, J. W. Jurss, *Organometallics* **2018**, *37*, 4535–4539, doi:10.1021/acs.organomet.8b00611.
[85] J. Bautz, P. Comba, C. Lopez de Laorden, M. Menzel, G. Rajaraman, *Angew. Chem. Int. Ed.* **2007**, *46*, 8067–8070, doi:10.1002/anie.200701681, *Angew. Chem.* **2007**, *119*, 8213–8216, doi:10.1002/ange.200701681.
[86] K. Chen, L. Que, *J. Am. Chem. Soc.* **2001**, *123*, 6327–6337, doi:10.1021/ja010310x.
[87] K. Chen, M. Costas, J. Kim, A. K. Tipton, L. Que, *J. Am. Chem. Soc.* **2002**, *124*, 3026–3035, doi:10.1021/ja0120025.
[88] W. N. Oloo, L. Que, *Acc. Chem. Res.* **2015**, *48*, 2612–2621, doi:10.1021/acs.accounts.5b00053.
[89] P. Comba, S. Fukuzumi, C. Koke, B. Martin, A.-M. Löhr, J. Straub, *Angew. Chem. Int. Ed.* **2016**, *55*, 11129–11133, doi:10.1002/anie.201605099, *Angew. Chem.* **2016**, *128*, 11295–11299, doi:10.1002/ange.201605099.
[90] I. Prat, A. Company, T. Corona, T. Parella, X. Ribas, M. Costas, *Inorg. Chem.* **2013**, *52*, 9229–9244, doi:10.1021/ic4004033.
[91] P. Comba, *Oxidation Catalysis with High-Valent Nonheme Iron Complexes*, chapter 6, 123–146, Wiley-VCH, Weinheim **2014**, doi:10.1002/9783527673278.ch6.
[92] W. Nam, *Acc. Chem. Res.* **2007**, *40*, 522–531, doi:10.1021/ar700027f.
[93] D. Macikenas, E. Skrzypczak-Jankun, J. D. Protasiewicz, *J. Am. Chem. Soc.* **1999**, *121*, 7164–7165, doi:10.1021/ja991094j.
[94] W. Nam, Y.-M. Lee, S. Fukuzumi, *Acc. Chem. Res.* **2014**, *47*, 1146–1154, doi:10.1021/ar400258p.
[95] M. S. Seo, N. H. Kim, K.-B. Cho, J. E. So, S. K. Park, M. Clémancey, R. Garcia-Serres, J.-M. Latour, S. Shaik, W. Nam, *Chem. Sci.* **2011**, *2*, 1039, doi:10.1039/c1sc00062d.
[96] J.-U. Rohde, A. Stubna, E. L. Bominaar, E. Münck, W. Nam, L. Que, *Inorg. Chem.* **2006**, *45*, 6435–6445, doi:10.1021/ic060740u.
[97] A. N. Biswas, M. Puri, K. K. Meier, W. N. Oloo, G. T. Rohde, E. L. Bominaar, E. Münck, L. Que, *J. Am. Chem. Soc.* **2015**, *137*, 2428–2431, doi:10.1021/ja511757j.
[98] J. P. Bigi, W. H. Harman, B. Lassalle-Kaiser, D. M. Robles, T. A. Stich, J. Yano, R. D. Britt, C. J. Chang, *J. Am. Chem. Soc.* **2012**, *134*, 1536–1542, doi:10.1021/ja207048h.
[99] F. Tiago de Oliveira, A. Chanda, D. Banerjee, X. Shan, S. Mondal, L. Que, E. L. Bominaar, E. Münck, T. J. Collins, *Science* **2007**, *315*, 835–838, doi:10.1126/science.1133417.
[100] A. M. Zima, O. Y. Lyakin, K. P. Bryliakov, E. P. Talsi, *Chem. Eur. J.* **2021**, *27*, 7781–7788, doi:10.1002/chem.202004395.
[101] A. M. Zima, O. Y. Lyakin, K. P. Bryliakov, E. P. Talsi, *ChemCatChem* **2019**, *11*, 5345–5352, doi:10.1002/cctc.201900842.

[102] A. M. Zima, D. E. Babushkin, O. Y. Lyakin, K. P. Bryliakov, E. P. Talsi, *ChemCatChem* **2022**, *14*, e20210143, doi:10.1002/cctc.202101430.
[103] W. N. Oloo, R. Banerjee, J. D. Lipscomb, L. Que, *J. Am. Chem. Soc.* **2017**, *139*, 17313–17326, doi:10.1021/jacs.7b06246.
[104] J. Serrano-Plana, W. N. Oloo, L. Acosta-Rueda, K. K. Meier, B. Verdejo, E. García-España, M. G. Basallote, E. Münck, L. Que, A. Company, M. Costas, *J. Am. Chem. Soc.* **2015**, *137*, 15833–15842, doi:10.1021/jacs.5b09904.
[105] R. Ezhov, A. K. Ravari, Y. Pushkar, *Angew. Chem. Int. Ed.* **2020**, *59*, 13502–13505, doi:10.1002/anie.202003278, *Angew. Chem.* **2020**, *132*, 13604–13607, doi:10.1002/ange.202003278.
[106] O. Y. Lyakin, A. M. Zima, D. G. Samsonenko, K. P. Bryliakov, E. P. Talsi, *ACS Catal.* **2015**, *5*, 2702–2707, doi:10.1021/acscatal.5b00169.
[107] S. Sahu, M. G. Quesne, C. G. Davies, M. Dürr, I. Ivanović-Burmazović, M. A. Siegler, G. N. L. Jameson, S. P. de Visser, D. P. Goldberg, *J. Am. Chem. Soc.* **2014**, *136*, 13542–13545, doi:10.1021/ja507346t.
[108] I. Prat, J. S. Mathieson, M. Güell, X. Ribas, J. M. Luis, L. Cronin, M. Costas, *Nat. Chem.* **2011**, *3*, 788–793, doi:10.1038/nchem.1132.
[109] J. Kaizer, E. J. Klinker, N. Y. Oh, J.-U. Rohde, W. J. Song, A. Stubna, J. Kim, E. Münck, W. Nam, L. Que, *J. Am. Chem. Soc.* **2004**, *126*, 472–473, doi:10.1021/ja037288n.
[110] R. Singh, G. Ganguly, S. O. Malinkin, S. Demeshko, F. Meyer, E. Nordlander, T. K. Paine, *Inorg. Chem.* **2019**, *58*, 1862–1876, doi:10.1021/acs.inorgchem.8b02577.
[111] O. Cussó, J. Serrano-Plana, M. Costas, *ACS Catal.* **2017**, *7*, 5046–5053, doi:10.1021/acscatal.7b01184.
[112] M. Costas, K. Chen, L. Que, *Coord. Chem. Rev.* **2000**, *200-202*, 517–544, doi:10.1016/S0010-8545(00)00320-9.
[113] I. Prat, A. Company, V. Postils, X. Ribas, L. Que, J. M. Luis, M. Costas, *Chem. Eur. J.* **2013**, *19*, 6724–6738, doi:10.1002/chem.201300110.
[114] S. T. Kleespies, W. N. Oloo, A. Mukherjee, L. Que, *Inorg. Chem.* **2015**, *54*, 5053–5064, doi:10.1021/ic502786y.
[115] M. A. Halcrow, *Dalton Trans.* **2020**, *49*, 15560–15567, doi:10.1039/d0dt01919d.
[116] M. M. Khusniyarov, *Chem. Eur. J.* **2016**, *22*, 15178–15191, doi:10.1002/chem.201601140.
[117] P. Gütlich, Y. Garcia, H. A. Goodwin, *Chem. Soc. Rev.* **2000**, *29*, 419–427, doi:10.1039/b003504l.
[118] P. Guionneau, *Dalton Trans.* **2014**, *43*, 382–393, doi:10.1039/c3dt52520a.
[119] S. Brooker, *Chem. Soc. Rev.* **2015**, *44*, 2880–2892, doi:10.1039/c4cs00376d.
[120] S. Rodríguez-Jiménez, A. S. Barltrop, N. G. White, H. L. C. Feltham, S. Brooker, *Inorg. Chem.* **2018**, *57*, 6266–6282, doi:10.1021/acs.inorgchem.8b00128.
[121] B. N. Livesay, M. P. Shores, *Inorg. Chem.* **2021**, *60*, 15445–15455, doi:10.1021/acs.inorgchem.1c02112.
[122] H. Toftlund, *Coord. Chem. Rev.* **1989**, *94*, 67–108, doi:10.1016/0010-8545(89)80045-1.
[123] M.-L. Boillot, B. Weber, *C. R. Chimie* **2018**, *21*, 1196–1208, doi:10.1016/j.crci.2018.01.006.
[124] H. Toftlund, *Monatsh. Chem.* **2001**, *132*, 1269–1277, doi:10.1007/s007060170017.
[125] S. Thies, C. Bornholdt, F. Köhler, F. D. Sönnichsen, C. Näther, F. Tuczek, R. Herges, *Chem. Eur. J.* **2010**, *16*, 10074–10083, doi:10.1002/chem.201000603.
[126] K. Keisers, H. M. Hüppe, L. Iffland-Mühlhaus, A. Hoffmann, C. Göbel, U.-P. Apfel, B. Weber, S. Herres-Pawlis, *Inorg. Chem.* **2020**, *59*, 15343–15354, doi:10.1021/acs.inorgchem.0c02306.
[127] M. A. Halcrow, *Chem. Soc. Rev.* **2011**, *40*, 4119–4142, doi:10.1039/c1cs15046d.
[128] J.-F. Létard, P. Guionneau, L. Goux-Capes, in *Spin Crossover in Transition Metal Compounds III*, 221–249, Springer, Berlin, Heidelberg **2004**, doi:10.1007/b95429.
[129] L. Yang, D. R. Powell, R. P. Houser, *Dalton Trans.* **2007**, 955–964, doi:10.1039/b617136b.
[130] A. W. Addison, T. N. Rao, J. Reedijk, J. van Rijn, G. C. Verschoor, *J. Chem. Soc., Dalton Trans.* **1984**, 1349–1356, doi:10.1039/DT9840001349.

[131] M. Llunell, D. Casanova, J. Ciera, P. Alemany, S. Alvarez, *SHAPE: Continous Shape Measures calculation* **2013**.
[132] S. Alvarez, D. Avnir, M. Llunell, M. Pinsky, *New J. Chem.* **2002**, *26*, 996–1009, doi:10.1039/b200641n.
[133] S. Alvarez, M. Llunell, *J. Chem. Soc., Dalton Trans.* **2000**, 3288–3303, doi:10.1039/b004878j.
[134] J. Cirera, P. Alemany, S. Alvarez, *Chem. Eur. J.* **2004**, *10*, 190–207, doi:10.1002/chem.200305074.
[135] U. Herber, J. Moegling, R. Siris, A. Hoffmann, P. Mayer, C. Göbel, C. Lochenie, B. Weber, S. Herres-Pawlis, *Z. Anorg. Allg. Chem.* **2018**, *644*, 1576–1592, doi:10.1002/zaac.201800095.
[136] K. Keisers, *Tetradentate C-scorpionates for iron(IV)oxo model systems and spin switch applications*, Ph.D. thesis, RWTH Aachen University **2021**, doi:10.18154/RWTH-2021-11383.
[137] S. Herres-Pawlis, R. D. Rittinghaus, P. M. Schäfer, P. Albrecht, C. Conrads, A. Hoffmann, A. Ksiazkiewicz, O. Bienemann, A. Pich, *ChemSusChem* **2019**, *12*, 2161–2165, doi:10.1002/cssc.201900481.
[138] A. Diebold, K. S. Hagen, *Inorg. Chem.* **1998**, *37*, 215–223, doi:10.1021/ic971105e.
[139] I. Sommer, *Bioinorganic studies of iron and copper complexes with bis(pyrazolyl)methane ligands*, Master's thesis, RWTH Aachen University **2017**.
[140] H. M. Hüppe, *Maleimid functionalized bis(pyrazolyl)methane ligands for the biomimetic iron coordination*, Master's thesis, RWTH Aachen University **2018**.
[141] A. Hoffmann, U. Flörke, M. Schürmann, S. Herres-Pawlis, *Eur. J. Org. Chem.* **2010**, *2010*, 4136–4144, doi:10.1002/ejoc.201000198.
[142] A. Hoffmann, S. Herres-Pawlis, *Z. Anorg. Allg. Chem.* **2013**, *639*, 1426–1432, doi:10.1002/zaac.201300103.
[143] A. Hoffmann, C. Citek, S. Binder, A. Goos, M. Rübhausen, O. Troeppner, I. Ivanović-Burmazović, E. C. Wasinger, T. D. P. Stack, S. Herres-Pawlis, *Angew. Chem. Int. Ed.* **2013**, *52*, 5398–5401, doi:10.1002/anie.201301249, *Angew. Chem.* **2013**, *125*, 5508–5512, 10.1002/ange.201301249.
[144] A. Hoffmann, U. Flörke, S. Herres-Pawlis, *Eur. J. Inorg. Chem.* **2014**, *2014*, 2296–2306, doi:10.1002/ejic.201400056.
[145] C. Wilfer, P. Liebhäuser, H. Erdmann, A. Hoffmann, S. Herres-Pawlis, *Eur. J. Inorg. Chem.* **2015**, *2015*, 494–502, doi:10.1002/ejic.201402957.
[146] C. Wilfer, P. Liebhäuser, A. Hoffmann, H. Erdmann, O. Grossmann, L. Runtsch, E. Paffenholz, R. Schepper, R. Dick, M. Bauer, M. Dürr, I. Ivanović-Burmazović, S. Herres-Pawlis, *Chem. Eur. J.* **2015**, *21*, 17639–17649, doi:10.1002/chem.201501685.
[147] U. Herber, A. Hoffmann, C. Lochenie, B. Weber, S. Herres-Pawlis, *Z. Naturforsch. B* **2014**, *69*, 1206–1214, doi:10.5560/znb.2014-4176.
[148] U. Herber, K. Hegner, D. Wolters, R. Siris, K. Wrobel, A. Hoffmann, C. Lochenie, B. Weber, D. Kuckling, S. Herres-Pawlis, *Eur. J. Inorg. Chem.* **2017**, *2017*, 1341–1354, doi:10.1002/ejic.201601345.
[149] J. Moegling, A. D. Benischke, J. M. Hammann, N. A. Vepřek, F. Zoller, B. Rendenbach, A. Hoffmann, H. Sievers, M. Schuster, P. Knochel, S. Herres-Pawlis, *Eur. J. Org. Chem.* **2015**, *2015*, 7475–7483, doi:10.1002/ejoc.201501117.
[150] J. Moegling, A. Hoffmann, F. Thomas, N. Orth, P. Liebhäuser, U. Herber, R. Rampmaier, J. Stanek, G. Fink, I. Ivanović-Burmazović, S. Herres-Pawlis, *Angew. Chem. Int. Ed.* **2018**, *57*, 9154–9159, doi:10.1002/anie.201713171, *Angew. Chem.* **2018**, *130*, 9294–9299, doi:10.1002/ange.201713171.
[151] P. Liebhäuser, K. Keisers, A. Hoffmann, T. Schnappinger, I. Sommer, A. Thoma, C. Wilfer, R. Schoch, K. Stührenberg, M. Bauer, M. Dürr, I. Ivanović-Burmazović, S. Herres-Pawlis, *Chem. Eur. J.* **2017**, *23*, 12171–12183, doi:10.1002/chem.201700887.
[152] F. Thomas, M. Oster, F. Schön, K. C. Göbgen, B. Amarouch, D. Steden, A. Hoffmann, S. Herres-Pawlis, *Dalton Trans.* **2021**, *50*, 6444–6462, doi:10.1039/D1DT00832C.
[153] F. Thomas, D. Steden, A. Eith, A. Hoffmann, S. Herres-Pawlis, *Z. Naturforsch. B* **2021**, *76*, 835–847, doi:10.1515/znb-2021-0140.

[154] J.-E. Park, S. K. Kang, J. O. Woo, K.-s. Son, *Dalton Trans.* **2015**, *44*, 9964–9969, doi:10.1039/c5dt00855g.
[155] D. L. Reger, T. Grattan, K. J. Brown, C. A. Little, J. J. Lamba, A. L. Rheingold, R. D. Sommer, *J. Organomet. Chem.* **2000**, *607*, 120–128, doi:10.1016/S0022-328X(00)00290-4.
[156] P. van der Sluis, A. L. Spek, *Acta Crystallogr. A* **1990**, *46*, 194–201, doi:10.1107/S0108767389011189.
[157] A. L. Spek, *Platon: A multipurpose crystallographic tool* **2008**.
[158] A. L. Spek, *Acta Crystallogr. D* **2009**, *65*, 148–155, doi:10.1107/S090744490804362X.
[159] W. S. Sheldrick, O. Stelzer, *Chem. Ber.* **1977**, *110*, 3421–3429, doi:10.1002/cber.19771101022.
[160] T. Astley, A. J. Canty, M. A. Hitchman, G. L. Rowbottom, B. W. Skelton, A. H. White, *J. Chem. Soc., Dalton Trans.* **1991**, 1981, doi:10.1039/DT9910001981.
[161] U. Herber, *From Ligand Design to Lactide Polymerisation Catalysis -A study on novel polydentate bis(pyrazolyl)methanes and their Fe(II), Cu(II) and Zn(II) complexes*, Ph.D. thesis, RWTH Aachen University **2017**, doi:10.18154/RWTH-2017-07524.
[162] P. J. Arnold, S. C. Davies, J. R. Dilworth, M. C. Durrant, D. V. Griffiths, D. L. Hughes, R. L. Richards, P. C. Sharpe, *J. Chem. Soc., Dalton Trans.* **2001**, 736–746, doi:10.1039/b008476j.
[163] L. Walz, H. Paulus, W. Haase, *J. Chem. Soc., Dalton Trans.* **1985**, 913, doi:10.1039/dt9850000913.
[164] W.-B. Shi, A.-L. Cui, H.-Z. Kou, *CrystEngComm* **2014**, *16*, 8027, doi:10.1039/C4CE01082E.
[165] X.-X. Shi, Q.-J. Chen, X.-L. Chen, Y. Zhang, M. Kurmoo, M.-H. Zeng, *Dalton Trans.* **2019**, *48*, 13094–13100, doi:10.1039/c9dt02890k.
[166] N. Lah, I. Leban, R. Clérac, *Eur. J. Inorg. Chem.* **2006**, *2006*, 4888–4894, doi:10.1002/ejic.200600596.
[167] B. Chiari, O. Piovesana, T. Tarantelli, P. F. Zanazzi, *Inorg. Chem.* **1987**, *26*, 952–955, doi:10.1021/ic00253a036.
[168] R. Paschke, S. Liebsch, C. Tschierske, M. A. Oakley, E. Sinn, *Inorg. Chem.* **2003**, *42*, 8230–8240, doi:10.1021/ic0301021.
[169] S. Tanase, E. Bouwman, W. L. Driessen, J. Reedijk, R. de Gelder, *Inorg. Chim. Acta* **2003**, *355*, 458–461, doi:10.1016/S0020-1693(03)00376-1.
[170] V. K. Muppidi, S. Pal, *Eur. J. Inorg. Chem.* **2006**, *2006*, 2871–2877, doi:10.1002/ejic.200600248.
[171] R. Mergehenn, W. Haase, R. Allmann, *Acta Crystallogr. B* **1975**, *31*, 1847–1853, doi:10.1107/S0567740875006358.
[172] W. Haase, *Chem. Ber.* **1973**, *106*, 3132–3148, doi:10.1002/cber.19731061006.
[173] M. Hamid, A. A. Tahir, M. Mazhar, M. Zeller, K. C. Molloy, A. D. Hunter, *Inorg. Chem.* **2006**, *45*, 10457–10466, doi:10.1021/ic060119u.
[174] S. Löw, J. Becker, C. Würtele, A. Miska, C. Kleeberg, U. Behrens, O. Walter, S. Schindler, *Chem. Eur. J.* **2013**, *19*, 5342–5351, doi:10.1002/chem.201203848.
[175] N. Matsumoto, I. Ueda, Y. Nishida, S. Kida, *Bull. Chem. Soc. Jpn.* **1976**, *49*, 1308–1312, doi:10.1246/bcsj.49.1308.
[176] L. Álvarez-Miguel, H. Barbero, A. Sacristán-Martín, J. M. Martín Álvarez, A. Pérez-Encabo, C. M. Álvarez, R. García-Rodríguez, D. Miguel, *Inorg. Chem.* **2018**, *57*, 264–276, doi:10.1021/acs.inorgchem.7b02448.
[177] M. Luo, Y.-H. Huang, J.-C. Zhang, *Acta Crystallogr. E* **2014**, *70*, m194, doi:10.1107/S1600536814009052.
[178] S. Putzien, S. Wirth, J. Nicolas Roedel, I.-P. Lorenz, *Polyhedron* **2011**, *30*, 1747–1751, doi:10.1016/j.poly.2011.02.004.
[179] D. Masi, C. Mealli, M. Sabat, A. Sabatini, A. Vacca, F. Zanobini, *Helv. Chim. Acta* **1984**, *67*, 1818–1826, doi:10.1002/hlca.19840670719.
[180] M. K. Chun, A. R. Jeong, K. S. Min, J. H. Jeong, *Inorg. Chem. Commun.* **2017**, *78*, 82–84, doi:10.1016/j.inoche.2017.03.011.
[181] O. Sall, F. B. Tamboura, A. Sy, A. H. Barry, E. I. Thiam, M. Gaye, J. Ellena, *Acta Crystallogr. E* **2019**, *75*, 1069–1075, doi:10.1107/S2056989019008922.

[182] A. Beheshti, E. S. Mousavi Fard, M. Kubicki, P. Mayer, C. T. Abrahams, S. E. Razatofighi, *CrystEngComm* **2019**, *21*, 251–262, doi:10.1039/C8CE01348A.
[183] R. D. Shannon, *Acta Crystallogr. A* **1976**, *32*, 751–767, doi:10.1107/S0567739476001551.
[184] A. Abedi, N. Safari, V. Amani, H. R. Khavasi, *Dalton Trans.* **2011**, *40*, 6877–6885, doi:10.1039/c0dt01508c.
[185] K. B. Yoon, J. K. Kochi, *Inorg. Chem.* **1990**, *29*, 869–874, doi:10.1021/ic00329a058.
[186] Y. Gao, J. Guery, C. Jacoboni, *Acta Crystallogr. C* **1993**, *49*, 147–151, doi:10.1107/S0108270192009892.
[187] M.-N. Collomb, A. Deronzier, K. Gorgy, J.-C. Leprêtre, J. Pécaut, *New J. Chem.* **1999**, *23*, 785–790, doi:10.1039/A901893J.
[188] H. Schroeder, J. Buback, S. Demeshko, K. Matyjaszewski, F. Meyer, M. Buback, *Macromolecules* **2015**, *48*, 1981–1990, doi:10.1021/acs.macromol.5b00023.
[189] H. M. Hüppe, K. Keisers, F. Fink, S. D. Mürtz, A. Hoffmann, L. Iffland, U.-P. Apfel, S. Herres-Pawlis, *Isr. J. Chem.* **2020**, *60*, 987–998, doi:10.1002/ijch.202000009.
[190] S.-M. Kuang, Z.-Z. Zhang, F. Xue, T. C. W. Mak, *Polyhedron* **1999**, *18*, 3465–3468, doi:10.1016/S0277-5387(99)00256-9.
[191] L. Wang, X. Wang, H. Hou, G. Zhu, Z. Han, W. Yang, X. Chen, Q. Wang, *Chem. Commun.* **2020**, *56*, 8846–8849, doi:10.1039/d0cc04122j.
[192] E. K. Byrne, D. S. Richeson, K. H. Theopold, *J. Chem. Soc., Chem. Commun.* **1986**, 1491, doi:10.1039/c39860001491.
[193] N. K. Thallaj, O. Rotthaus, L. Benhamou, N. Humbert, M. Elhabiri, M. Lachkar, R. Welter, A.-M. Albrecht-Gary, D. Mandon, *Chem. Eur. J.* **2008**, *14*, 6742–6753, doi:10.1002/chem.200701967.
[194] A. Machkour, D. Mandon, M. Lachkar, R. Welter, *Inorg. Chem.* **2004**, *43*, 1545–1550, doi:10.1021/ic034485e.
[195] A. Kejriwal, A. N. Biswas, A. Choudhury, P. Bandyopadhyay, *Transit. Met. Chem.* **2014**, *39*, 909–915, doi:10.1007/s11243-014-9875-0.
[196] J. Wang, M. S. Mashuta, Z. Sun, J. F. Richardson, D. N. Hendrickson, R. M. Buchanan, *Inorg. Chem.* **1996**, *35*, 6642–6643, doi:10.1021/ic9607494.
[197] L. Benhamou, H. Jaafar, A. Thibon, M. Lachkar, D. Mandon, *Inorg. Chim. Acta* **2011**, *373*, 195–200, doi:10.1016/j.ica.2011.04.015.
[198] M. C. Esmelindro, E. G. Oestreicher, H. Márquez-Alvarez, C. Dariva, S. M. S. Egues, C. Fernandes, A. J. Bortoluzzi, V. Drago, O. A. C. Antunes, *J. Inorg. Biochem.* **2005**, *99*, 2054–2061, doi:10.1016/j.jinorgbio.2005.07.007.
[199] N. Raffard-Pons Y Moll, F. Banse, K. Miki, M. Nierlich, J.-J. Girerd, *Eur. J. Inorg. Chem.* **2002**, *2002*, 1941–1944, doi:10.1002/1099-0682(200208)2002:8<1941::AID-EJIC1941>3.0.CO;2-B.
[200] N. Raffarda, V. Ballanda, J. Simaana, S. Létarda, M. Nierlichc, K. Mikib, F. Bansea, E. Anxolabéhère-Mallarta, J.-J. Girerda, *C. R. Chimie* **2002**, *5*, 99–109, doi:10.1016/S1631-0748(02)01359-0.
[201] W. Lin, L. Zhang, H. Suo, A. Vignesh, N. Yousuf, X. Hao, W.-H. Sun, *New J. Chem.* **2020**, *44*, 8076–8084, doi:10.1039/D0NJ00942C.
[202] Y. Yang, C. Lu, H. Wang, X. Liu, *Dalton Trans.* **2016**, *45*, 10289–10296, doi:10.1039/C6DT01411A.
[203] Y.-L. Feng, *Z. Kristallogr. N. Cryst.* **2005**, *220*, 211–212, doi:10.1524/ncrs.2005.220.14.211.
[204] B. J. Coe, S. J. Glenwright, *Coord. Chem. Rev.* **2000**, *203*, 5–80, doi:10.1016/S0010-8545(99)00184-8.
[205] M. Mitra, H. Nimir, S. Demeshko, S. S. Bhat, S. O. Malinkin, M. Haukka, J. Lloret-Fillol, G. C. Lisensky, F. Meyer, A. A. Shteinman, W. R. Browne, D. A. Hrovat, M. G. Richmond, M. Costas, E. Nordlander, *Inorg. Chem.* **2015**, *54*, 7152–7164, doi:10.1021/ic5029564.
[206] U. Bergmann, P. Glatzel, *Photosynth. Res.* **2009**, *102*, 255–266, doi:10.1007/s11120-009-9483-6.
[207] J. K. Kowalska, F. A. Lima, C. J. Pollock, J. A. Rees, S. DeBeer, *Isr. J. Chem.* **2016**, *56*, 803–815, doi:10.1002/ijch.201600037.
[208] W. Zhang, R. Alonso-Mori, U. Bergmann, C. Bressler, M. Chollet, A. Galler, W. Gawelda,

R. G. Hadt, R. W. Hartsock, T. Kroll, K. S. Kjær, K. Kubiček, H. T. Lemke, H. W. Liang, D. A. Meyer, M. M. Nielsen, C. Purser, J. S. Robinson, E. I. Solomon, Z. Sun, D. Sokaras, T. B. van Driel, G. Vankó, T.-C. Weng, D. Zhu, K. J. Gaffney, *Nature* **2014**, *509*, 345–348, doi:10.1038/nature13252.

[209] D. Khakhulin, F. Otte, M. Biednov, C. Bömer, T.-K. Choi, M. Diez, A. Galler, Y. Jiang, K. Kubicek, F. A. Lima, A. Rodriguez-Fernandez, P. Zalden, W. Gawelda, C. Bressler, *Appl. Sci.* **2020**, *10*, 995, doi:10.3390/app10030995.

[210] G. Vankó, P. Glatzel, V.-T. Pham, R. Abela, D. Grolimund, C. N. Borca, S. L. Johnson, C. J. Milne, C. Bressler, *Angew. Chem. Int. Ed.* **2010**, *49*, 5910–5912, doi:10.1002/anie.201000844, *Angew. Chem.* **2010**, *122*, 6046–6048, doi:10.1002/ange.201000844.

[211] K. S. Kjær, T. B. van Driel, T. C. B. Harlang, K. Kunnus, E. Biasin, K. Ledbetter, R. W. Hartsock, M. E. Reinhard, S. Koroidov, L. Li, M. G. Laursen, F. B. Hansen, P. Vester, M. Christensen, K. Haldrup, M. M. Nielsen, A. O. Dohn, M. I. Pápai, K. B. Møller, P. Chabera, Y. Liu, H. Tatsuno, C. Timm, M. Jarenmark, J. Uhlig, V. Sundstöm, K. Wärnmark, P. Persson, Z. Németh, D. S. Szemes, É. Bajnóczi, G. Vankó, R. Alonso-Mori, J. M. Glownia, S. Nelson, M. Sikorski, D. Sokaras, S. E. Canton, H. T. Lemke, K. J. Gaffney, *Chem. Sci.* **2019**, *10*, 5749–5760, doi:10.1039/c8sc04023k.

[212] G. Vankó, A. Bordage, M. Pápai, K. Haldrup, P. Glatzel, A. M. March, G. Doumy, A. Britz, A. Galler, T. Assefa, D. Cabaret, A. Juhin, T. B. van Driel, K. S. Kjær, A. Dohn, K. B. Møller, H. T. Lemke, E. Gallo, M. Rovezzi, Z. Németh, E. Rozsályi, T. Rozgonyi, J. Uhlig, V. Sundström, M. M. Nielsen, L. Young, S. H. Southworth, C. Bressler, W. Gawelda, *J. Phys. Chem. C* **2015**, *119*, 5888–5902, doi:10.1021/acs.jpcc.5b00557.

[213] A. M. March, T. A. Assefa, C. Boemer, C. Bressler, A. Britz, M. Diez, G. Doumy, A. Galler, M. Harder, D. Khakhulin, Z. Németh, M. Pápai, S. Schulz, S. H. Southworth, H. Yavaş, L. Young, W. Gawelda, G. Vankó, *J. Phys. Chem. C* **2017**, *121*, 2620–2626, doi:10.1021/acs.jpcc.6b12940.

[214] R. S. Khnayzer, V. S. Thoi, M. Nippe, A. E. King, J. W. Jurss, K. A. El Roz, J. R. Long, C. J. Chang, F. N. Castellano, *Energy Environ. Sci.* **2014**, *7*, 1477–1488, doi:10.1039/C3EE43982H.

[215] J. Chen, W. R. Browne, *Coord. Chem. Rev.* **2018**, *374*, 15–35, doi:10.1016/j.ccr.2018.06.008.

[216] D. Z. Zee, M. Nippe, A. E. King, C. J. Chang, J. R. Long, *Inorg. Chem.* **2020**, *59*, 5206–5217, doi:10.1021/acs.inorgchem.0c00455.

[217] Y. Qiu, J. F. Hartwig, *J. Am. Chem. Soc.* **2020**, *142*, 19239–19248, doi:10.1021/jacs.0c09157.

[218] S. Ménage, J.-B. Galey, J. Dumats, G. Hussler, M. Seité, I. G. Luneau, G. Chottard, M. Fontecave, *J. Am. Chem. Soc.* **1998**, *120*, 13370–13382, doi:10.1021/ja981123a.

[219] M. N. Mortensen, B. Jensen, A. Hazell, A. D. Bond, C. J. McKenzie, *Dalton Trans.* **2004**, 3396–3402, doi:10.1039/B409559F.

[220] P. J. Cappillino, J. R. Miecznikowski, L. A. Tyler, P. C. Tarves, J. S. McNally, W. Lo, B. S. T. Kasibhatla, M. D. Krzyaniak, J. McCracken, F. Wang, W. H. Armstrong, J. P. Caradonna, *Dalton Trans.* **2012**, *41*, 5662–5677, doi:10.1039/c2dt11096b.

[221] V. B. Romakh, B. Therrien, G. Süss-Fink, G. B. Shul'pin, *Inorg. Chem.* **2007**, *46*, 3166–3175, doi:10.1021/ic062207k.

[222] S. Nishino, Y. Takahashi, Y. Nishida, *Inorg. Chem. Commun.* **2002**, *5*, 609–611, doi:10.1016/S1387-7003(02)00509-9.

[223] C.-H. Ke, C.-H. Chen, M.-L. Tsai, H.-C. Wang, F.-T. Tsai, Y.-W. Chiang, W.-C. Shih, D. S. Bohle, W.-F. Liaw, *J. Am. Chem. Soc.* **2017**, *139*, 67–70, doi:10.1021/jacs.6b11454.

[224] M. Quesada, V. A. de la Peña-O'Shea, G. Aromí, S. Geremia, C. Massera, O. Roubeau, P. Gamez, J. Reedijk, *Adv. Mater.* **2007**, *19*, 1397–1402, doi:10.1002/adma.200602284.

[225] Q. Zhang, L. Xiang, L. Deng, *Organometallics* **2012**, *31*, 4537–4543, doi:10.1021/om300319n.

[226] S. E. Landau, R. H. Morris, A. J. Lough, *Inorg. Chem.* **1999**, *38*, 6060–6068, doi:10.1021/ic990876a.

[227] E. B. Hemming, B. Chan, P. Turner, L. Corcilius, J. R. Price, M. G. Gardiner, A. F. Masters, T. Maschmeyer, *Appl. Catal. B* **2018**, *223*, 234–241, doi:10.1016/j.apcatb.2017.04.053.

[228] J. A. Halfen, H. L. Moore, D. C. Fox, *Inorg. Chem.* **2002**, *41*, 3935–3943, doi:10.1021/ic025517l.

[229] J. Vela, J. M. Smith, Y. Yu, N. A. Ketterer, C. J. Flaschenriem, R. J. Lachicotte, P. L. Holland, *J. Am. Chem. Soc.* **2005**, *127*, 7857–7870, doi:10.1021/ja042672l.
[230] M. Narwane, Y.-L. Chang, W.-M. Ching, M.-L. Tsai, S. C. Hsu, *Inorg. Chim. Acta* **2019**, *495*, 118966, doi:10.1016/j.ica.2019.118966.
[231] Y. S. Spiridonova, Y. A. Nikolaeva, A. S. Balueva, E. I. Musina, I. A. Litvinov, I. D. Strelnik, V. V. Khrizanforova, Y. G. Budnikova, A. A. Karasik, *CCDC 2000582: Experimental Crystal Structure Determination* **2020**, doi:10.5517/CCDC.CSD.CC254RX0.
[232] W. R. Marks, E. W. Reinheimer, T. Seda, L. N. Zakharov, J. D. Gilbertson, *Inorg. Chem.* **2021**, *60*, 15901–15909, doi:10.1021/acs.inorgchem.1c02285.
[233] S. Alvarez, *Chem. Eur. J.* **2020**, *26*, 4350–4377, doi:10.1002/chem.201905453.
[234] D. W. Blakesley, S. C. Payne, K. S. Hagen, *Inorg. Chem.* **2000**, *39*, 1979–1989, doi:10.1021/ic990584.
[235] L. Benhamou, A. Thibon, L. Brelot, M. Lachkar, D. Mandon, *Dalton Trans.* **2012**, *41*, 14369–14380, doi:10.1039/C2DT31558K.
[236] G. J. P. Britovsek, J. England, A. J. P. White, *Inorg. Chem.* **2005**, *44*, 8125–8134, doi:10.1021/ic0509229.
[237] J. England, G. J. P. Britovsek, N. Rabadia, A. J. P. White, *Inorg. Chem.* **2007**, *46*, 3752–3767, doi:10.1021/ic070062r.
[238] A. Schober, S. Demeshko, F. Meyer, *Z. Anorg. Allg. Chem.* **2018**, *644*, 719–728, doi:10.1002/zaac.201800148.
[239] K. Bryliakov, E. Duban, E. Talsi, *Eur. J. Inorg. Chem.* **2005**, *2005*, 72–76, doi:10.1002/ejic.200400429.
[240] P. Comba, S. Wunderlich, *Chem. Eur. J.* **2010**, *16*, 7293–7299, doi:10.1002/chem.201000092.
[241] J. Heck, *Studies on Novel Copper Guanidine Quinoline Complexes: Examination of the Substituent Influence on the Properties and Ability as Entatic State Models for the Electron Transfer*, Ph.D. thesis, RWTH Aachen University **2023**, doi:10.18154/RWTH-2023-09447.
[242] H. M. Hüppe, L. Iffland-Mühlhaus, J. Heck, M. Eilers, H. Gildenast, S. Schönfeld, A. Dürrmann, A. Hoffmann, B. Weber, U.-P. Apfel, S. Herres-Pawlis, *Inorg. Chem.* **2023**, *62*, 4435–4455, doi:10.1021/acs.inorgchem.2c03890.
[243] P. Chaibuth, N. Chuaytanee, J. Hojitsiriyanont, K. Chainok, S. Wacharasindhu, O. Reiser, M. Sukwattanasinitt, *New J. Chem.* **2022**, *46*, 12158–12168, doi:10.1039/D2NJ01218A.
[244] S. McArthur, M. C. Baird, *Eur. Polym. J.* **2014**, *55*, 170–178, doi:10.1016/j.eurpolymj.2014.03.028.
[245] Y. Zang, J. Kim, Y. Dong, E. C. Wilkinson, E. H. Appelman, L. Que, *J. Am. Chem. Soc.* **1997**, *119*, 4197–4205, doi:10.1021/ja9638521.
[246] A. Thibon, L. Karmazin-Brelot, D. Mandon, *Dalton Trans.* **2013**, *42*, 6705–6707, doi:10.1039/c3dt50484k.
[247] A. Company, L. Gómez, X. Fontrodona, X. Ribas, M. Costas, *Chem. Eur. J.* **2008**, *14*, 5727–5731, doi:10.1002/chem.200800724.
[248] A. Company, L. Gómez, M. Güell, X. Ribas, J. M. Luis, L. Que, M. Costas, *J. Am. Chem. Soc.* **2007**, *129*, 15766–15767, doi:10.1021/ja077761n.
[249] M. Mitra, J. Lloret-Fillol, M. Haukka, M. Costas, E. Nordlander, *Chem. Commun.* **2014**, *50*, 1408–1410, doi:10.1039/C3CC47830K.
[250] D. M. Ekanayake, A. A. Fischer, M. E. Elwood, A. M. Guzek, S. V. Lindeman, C. V. Popescu, A. T. Fiedler, *Dalton Trans.* **2020**, *49*, 17745–17757, doi:10.1039/D0DT03403G.
[251] P. Spannring, I. Prat, M. Costas, M. Lutz, P. C. A. Bruijnincx, B. M. Weckhuysen, R. J. M. Klein Gebbink, *Catal. Sci. Technol.* **2014**, *4*, 708–716, doi:10.1039/c3cy00851g.
[252] S. Hayami, K. Hiki, T. Kawahara, Y. Maeda, D. Urakami, K. Inoue, M. Ohama, S. Kawata, O. Sato, *Chem. Eur. J.* **2009**, *15*, 3497–3508, doi:10.1002/chem.200802395.
[253] K. H. Sugiyarto, D. Onggo, H. Akutsu, V. R. Reddy, H. Sutrisno, Y. Nakazawa, A. Bhattacharjee, *CrystEngComm* **2021**, *23*, 2854–2861, doi:10.1039/D0CE01687J.
[254] A. Bhattacharjee, V. Ksenofontov, K. H. Sugiyarto, H. A. Goodwin, P. Gütlich, *Adv. Funct.*

Mater. **2003**, *13*, 877–882, doi:10.1002/adfm.200304356.
[255] A. L. Ward, L. Elbaz, J. B. Kerr, J. Arnold, *Inorg. Chem.* **2012**, *51*, 4694–4706, doi:10.1021/ic2026957.
[256] M. Kim, Y.-U. Kim, J. Han, *Polyhedron* **2007**, *26*, 4003–4008, doi:10.1016/j.poly.2007.04.041.
[257] L. Chu, K. I. Hardcastle, C. E. MacBeth, *Inorg. Chem.* **2010**, *49*, 7521–7529, doi:10.1021/ic1008347.
[258] N. S. Sickerman, Y. J. Park, G. K.-Y. Ng, J. E. Bates, M. Hilkert, J. W. Ziller, F. Furche, A. S. Borovik, *Dalton Trans.* **2012**, *41*, 4358–4364, doi:10.1039/c2dt12244h.
[259] S. Kisslinger, H. Kelm, S. Zheng, A. Beitat, C. Würtele, R. Wortmann, S. Bonnet, S. Herres-Pawlis, H.-J. Krüger, S. Schindler, *Z. Anorg. Allg. Chem.* **2012**, *638*, 2069–2077, doi:10.1002/zaac.201200237.
[260] A. L. Rheingold, *CCDC 1499258: Experimental Crystal Structure Determination* **2016**, doi:10.5517/ccdc.csd.cc1mb357.
[261] S. J. Lange, H. Miyake, L. Que, *J. Am. Chem. Soc. Society* **1999**, *121*, 6330–6331, doi:10.1021/ja990233u.
[262] M. Borrell, M. Costas, *J. Am. Chem. Soc.* **2017**, *139*, 12821–12829, doi:10.1021/jacs.7b07909.
[263] W. A. Hoffert, M. T. Mock, A. M. Appel, J. Y. Yang, *Eur. J. Inorg. Chem.* **2013**, *2013*, 3846–3857, doi:10.1002/ejic.201201499.
[264] M. P. Jensen, S. J. Lange, M. P. Mehn, E. L. Que, L. Que, *J. Am. Chem. Soc.* **2003**, *125*, 2113–2128, doi:10.1021/ja028478l.
[265] I. Šalitroš, N. T. Madhu, R. Boča, J. Pavlik, M. Ruben, *Monatsh. Chem.* **2009**, *140*, 695–733, doi:10.1007/s00706-009-0128-4.
[266] D. Y. Aleshin, I. Nikovskiy, V. V. Novikov, A. V. Polezhaev, E. K. Melnikova, Y. V. Nelyubina, *ACS omega* **2021**, *6*, 33111–33121, doi:10.1021/acsomega.1c05463.
[267] B. Weber, *Coord. Chem. Rev.* **2009**, *253*, 2432–2449, doi:10.1016/j.ccr.2008.10.002.
[268] E. C. Wilkinson, Y. Dong, L. Que, *J. Am. Chem. Soc.* **1994**, *116*, 8394–8395, doi:10.1021/ja00097a068.
[269] R. E. Norman, R. C. Holz, S. Menage, L. Que, J. H. Zhang, C. J. O'Connor, *Inorg. Chem.* **1990**, *29*, 4629–4637, doi:10.1021/ic00348a010.
[270] A. Mairata i Payeras, R. Y. N. Ho, M. Fujita, L. Que, *Chem. Eur. J.* **2004**, *10*, 4944–4953, doi:10.1002/chem.200400480.
[271] L. Gómez, I. Garcia-Bosch, A. Company, J. Benet-Buchholz, A. Polo, X. Sala, X. Ribas, M. Costas, *Angew. Chem. Int. Ed.* **2009**, *48*, 5720–5723, doi:10.1002/anie.200901865, *Angew. Chem.* **2009**, *121*, 5830–5833, doi:10.1002/ange.200901865.
[272] A. Hazell, J. McGinley, H. Toftlund, *J. Chem. Soc., Dalton Trans.* **1999**, 1271–1276, doi:10.1039/a900359b.
[273] A. Hazell, *Acta Crystallogr. E* **2006**, *62*, o5941–o5943, doi:10.1107/S160053680605080X.
[274] H. Sugimoto, H. Miyake, H. Tsukube, *J. Chem. Soc., Dalton Trans.* **2002**, 4535, doi:10.1039/b209331f.
[275] D. J. Harding, P. Harding, H. Adams, T. Tuntulani, *Inorg. Chim. Acta* **2007**, *360*, 3335–3340, doi:10.1016/j.ica.2007.03.046.
[276] D. J. Harding, P. Harding, H. Adams, *Acta Crystallogr. E* **2009**, *65*, m773, doi:10.1107/S1600536809021606.
[277] A. L. Rheingold, L. M. Liable-Sands, S. Trofimenko, *Inorg. Chem.* **2001**, *40*, 6509–6513, doi:10.1021/ic010751h.
[278] G. R. Fulmer, A. J. M. Miller, N. H. Sherden, H. E. Gottlieb, A. Nudelman, B. M. Stoltz, J. E. Bercaw, K. I. Goldberg, *Organometallics* **2010**, *29*, 2176–2179, doi:10.1021/om100106e.
[279] INEOS, *Acetonitrile: Safe storage and handling guide*, **2007**, https://www.ineos.com/globalassets/ineos-group/businesses/ineos-nitriles/she/2007_acetonitrile_brochure.pdf, checked on: 05.04.2023.
[280] C. F. Spencer, S. B. Adler, *J. Chem. Eng. Data* **1978**, *23*, 82–89, doi:10.1021/je60076a008.

[281] G. A. Bain, J. F. Berry, *J. Chem. Edu.* **2008**, *85*, 532, doi:10.1021/ed085p532.
[282] STOE, *X-Area Pilatus3_SV 1.31.131.0* **2017**.
[283] STOE, *X-Area Pilatus3_SV 1.31.170.0* **2020**.
[284] STOE, *X-Area Integrate 1.71.0.0* **2016**.
[285] STOE, *X-Area Integrate 1.78.3.0* **2020**.
[286] STOE, *X-Area Recipe 1.33.0.0* **2015**.
[287] STOE, *X-Area Recipe 1.36.0.0* **2020**.
[288] STOE, *X-Area LANA 1.71.4.0* **2017**.
[289] STOE, *X-Area LANA 1.83.8.0* **2020**.
[290] Bruker AXS Inc., *Smart* **2008**.
[291] Bruker AXS Inc., *Saint+* **2009**.
[292] Bruker AXS Inc., *Sadabs* **2008**.
[293] G. M. Sheldrick, *Acta Crystallogr. A* **2015**, *71*, 3–8, doi:10.1107/S2053273314026370.
[294] G. M. Sheldrick, *Acta Crystallogr. C* **2015**, *71*, 3–8, doi:10.1107/S2053229614024218.
[295] C. B. Hübschle, G. M. Sheldrick, B. Dittrich, *J. Appl. Crystallogr.* **2011**, *44*, 1281–1284, doi:10.1107/S0021889811043202.
[296] I. Prisecaru, *WMOSS4 Mössbauer Spectral Analysis Software* **2009–2016**.
[297] C. F. Macrae, I. J. Bruno, J. A. Chisholm, P. R. Edgington, P. McCabe, E. Pidcock, L. Rodriguez-Monge, R. Taylor, J. van de Streek, P. A. Wood, *J. Appl. Crystallogr.* **2008**, *41*, 466–470, doi:10.1107/S0021889807067908.
[298] J. Leonard, B. Lygo, G. Procter, *Praxis der organischen Chemie: Ein Handbuch*, VCH, Weinheim **1996**.
[299] K. S. Hagen, *Inorg. Chem.* **2000**, *39*, 5867–5869, doi:10.1021/ic000444w.
[300] B. J. Hathaway, D. G. Holah, A. E. Underhill, *J. Chem. Soc.* **1962**, *0*, 2444–2448, doi:10.1039/JR9620002444.
[301] N. E. Erickson, N. Sutin, *Inorg. Chem.* **1966**, *5*, 1834–1835, doi:10.1021/ic50044a050.
[302] N. S. Sommerfeld, J. Gülzow, A. Roller, K. Cseh, M. A. Jakupec, A. Grohmann, M. Galanski, B. K. Keppler, *Eur. J. Inorg. Chem.* **2017**, *2017*, 3115–3124, doi:10.1002/ejic.201700416.

Appendix

A.1 Additional Data for Chapter 3

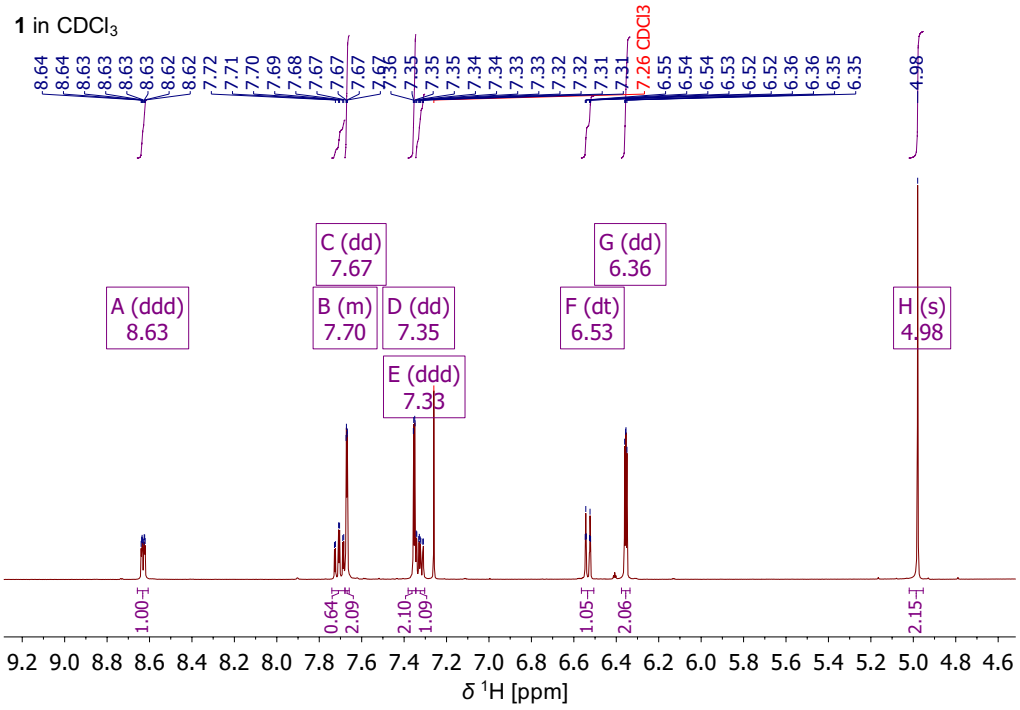

Figure A.1: ^{1}H-NMR spectrum of **1** in $CDCl_3$.

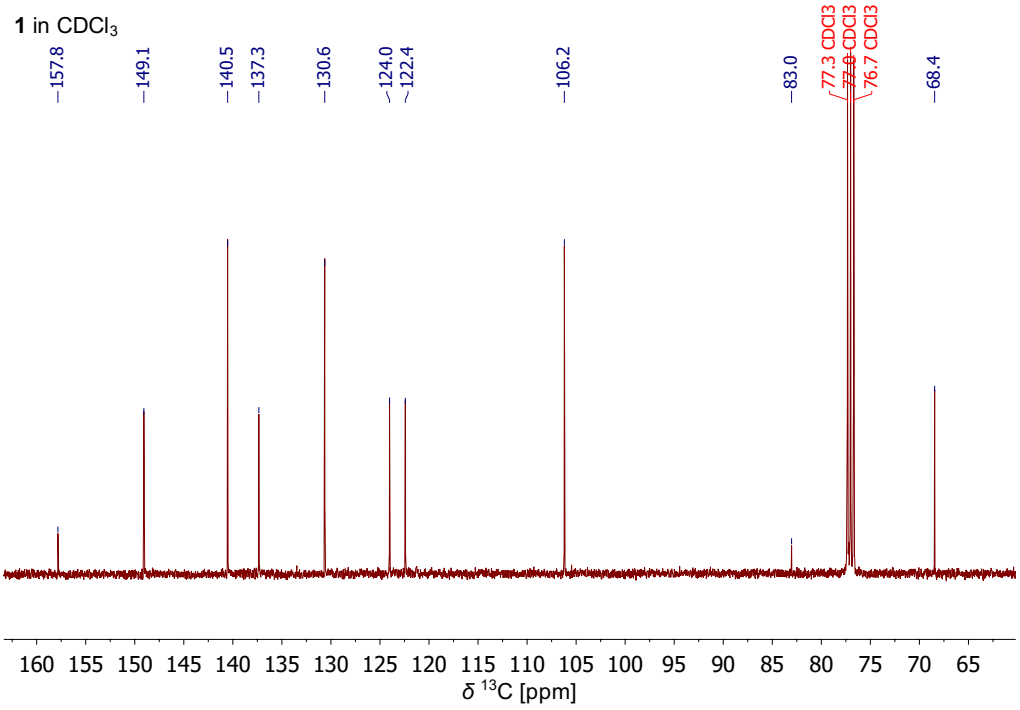

Figure A.2: ^{13}C-NMR spectrum of **1** in $CDCl_3$.

A.2 Additional Data for Chapter 4

Table A.1: Blank reactions for catalytic oxidation of cyclohexane with **2a**.

#		*A*/*K*	Efficiency [%]	TON	
	2a : mCPBA : cyclohexane				
1	0 : 10 : 1000	–	–	–	no *A* & *K* obtained
2	0 : 20 : 1000	–	–	–	no *A* & *K* obtained
	$Fe(OTf)_2 \cdot 2\,MeCN$: mCPBA : cyclohexane				
3	1 : 10 : 1000	1.6	26	3	

Table A.2: Blank reactions for catalytic oxidation of adamantane with **2a**.

#	**2a** : mCPBA : adamantane	3°/2°	Efficiency [%]	TON
	2a : mCPBA : adamantane			
1	0 : 10 : 1000	10	36	4
	$Fe(OTf)_2 \cdot 2\,MeCN$: mCPBA : adamantane			
2	1 : 20 : 100	19	29	3

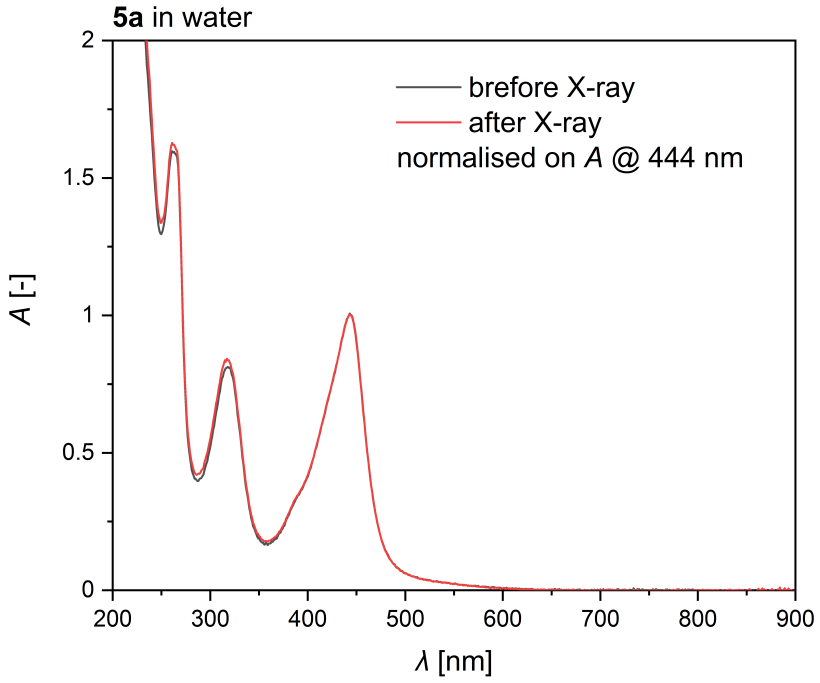

Figure A.3: UV/Vis spectra of **5a** before and after X-ray radiation of pump-probe XES measurements at European XFEL. To compensate for concentration differences, the values were normalised to the absorption at 444 nm.

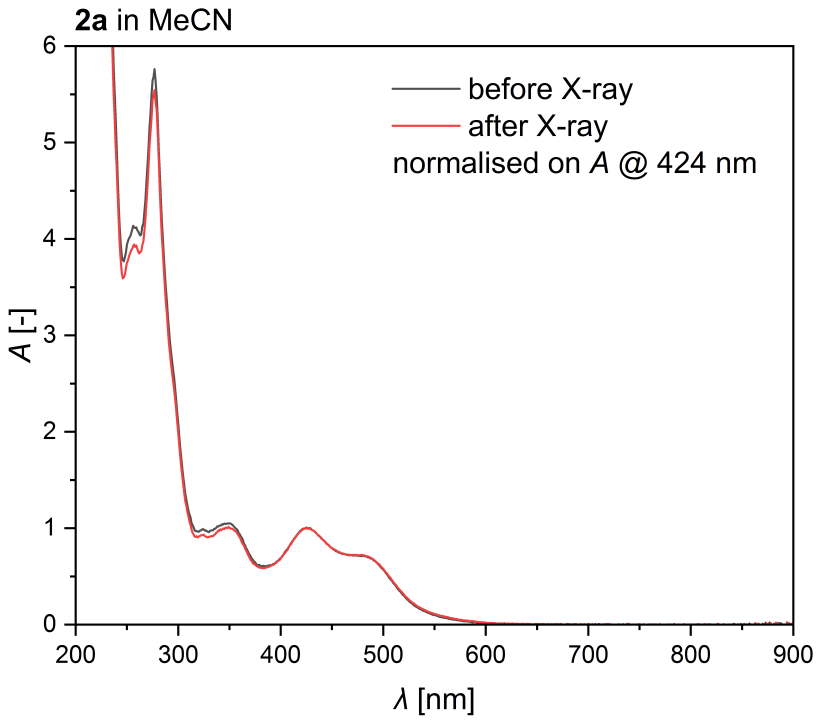

Figure A.4: UV/Vis spectra of **2a** before and after X-ray radiation of pump-probe XES measurements at European XFEL. To compensate for concentration differences, the values were normalised to the absorption at 424 nm.

A.3 Additional Data for Chapter 5

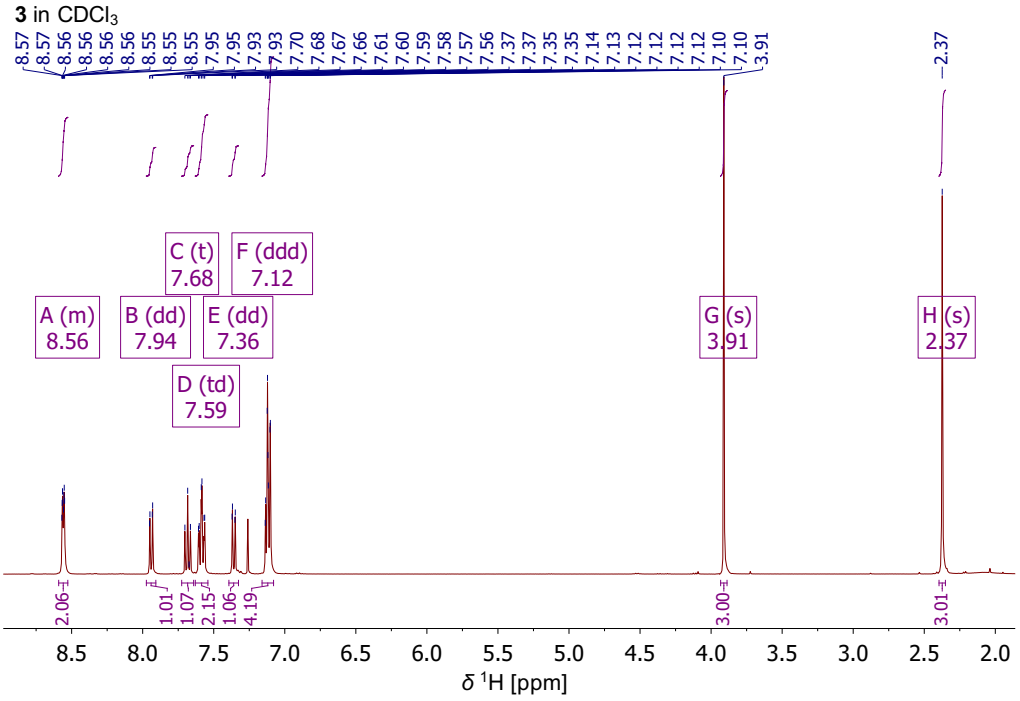

Figure A.5: ^{1}H-NMR spectrum of **3** in $CDCl_3$.

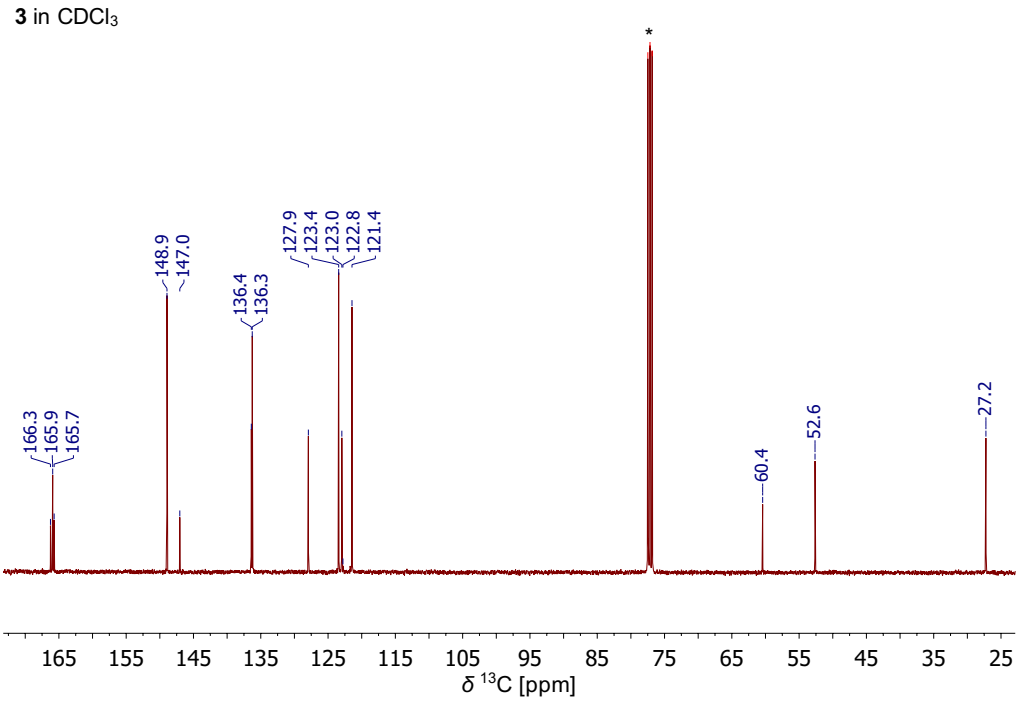

Figure A.6: ^{13}C-NMR spectrum of **3** in $CDCl_3$.

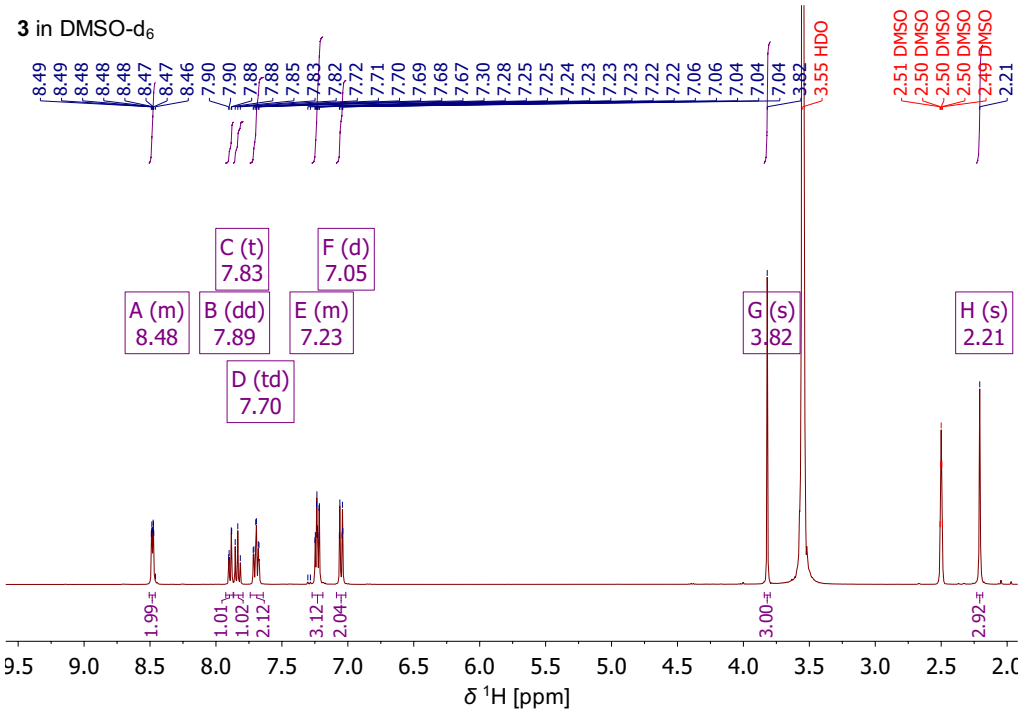

Figure A.7: ^{1}H-NMR spectrum of **3** in DMSO-d$_6$.

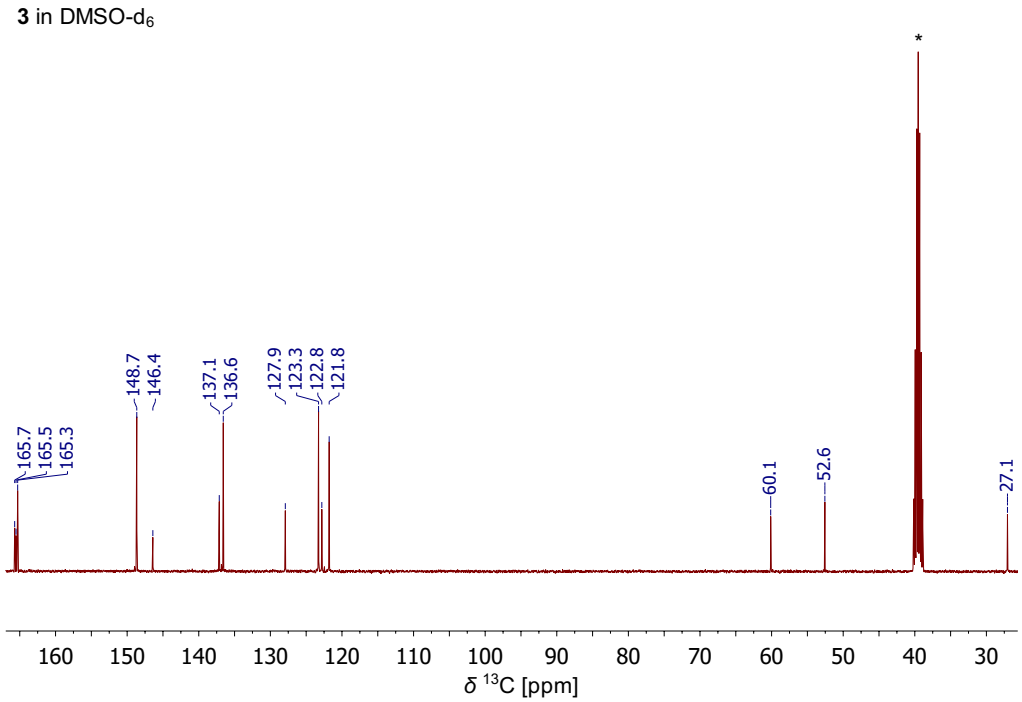

Figure A.8: ^{13}C-NMR spectrum of **3** in DMSO-d$_6$.

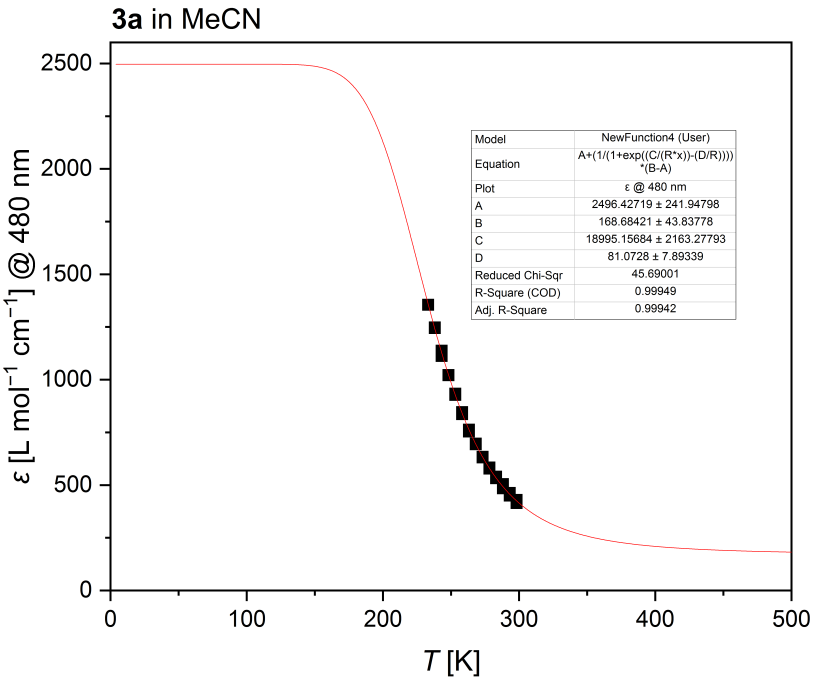

Figure A.9: Fit of extinction coefficients at 480 nm in UV/Vis spectra of **3a** in MeCN at different temperatures.

A.4 Additional Data for Chapter 6

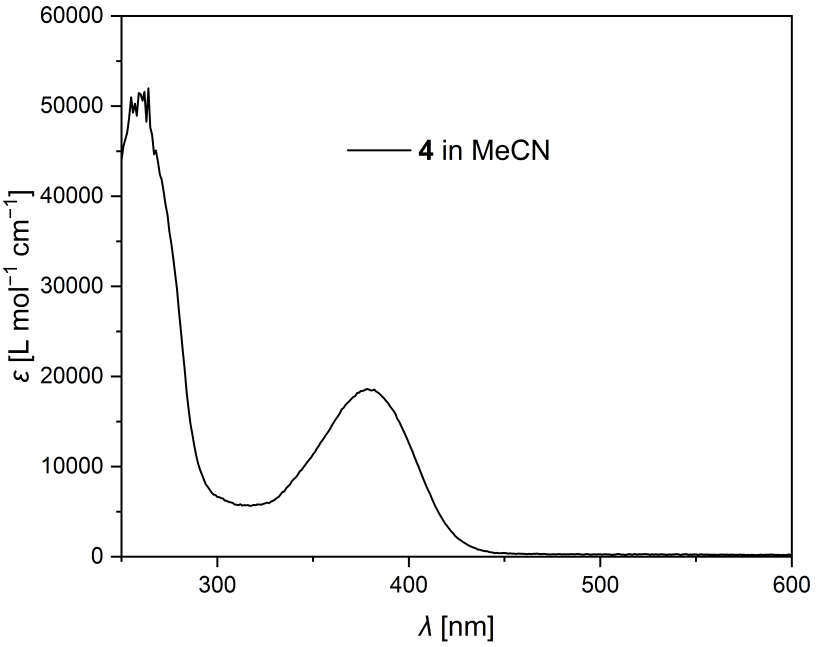

Figure A.10: UV/Vis spectra of **4** in MeCN at rt.

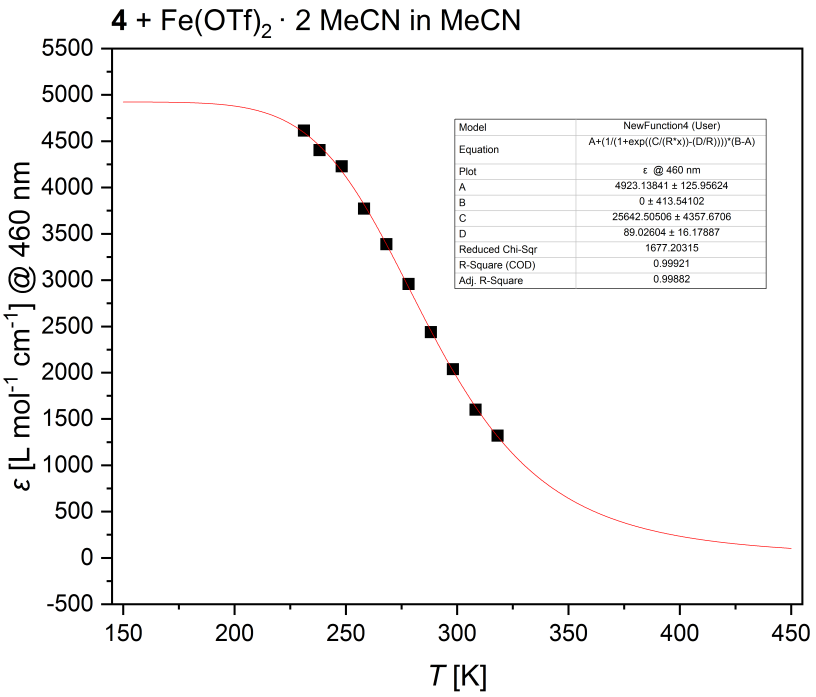

Figure A.11: Fit of extinction coefficients at 460 nm in UV/Vis spectra of $[Fe(OTf)_2] \cdot 2$ MeCN and **4** in MeCN at different temperatures.

Table A.3: C – H oxidation of cyclohexane in DCM with *in situ* complex formation of **4** and $Fe(OTf)_2 \cdot 2\,MeCN$ (iron complex : H_2O_2 : cyclohexane, 1 : 10 : 1000).

Oxidant	T [°C]	***A*/*K***	Efficiency [%]	TON	Workup
H_2O_2	0	7.5 / –	0 / –	0.0 / –	A1 / A2
H_2O_2	rt	13.1 / –	1 / –	0.1 / –	A1 / A2
H_2O_2	rt	7.5 / –	0 / –	0.0 / –	A3 / A4
H_2O_2	50	12.8 / –	1 / –	0.1 / –	A1 / A2
mCPBA	0	3.7	2	0.2	A2
mCPBA	rt	3.6	4	0.4	A2
mCPBA	rt	6.6 / 5.8	2 / 2	0.2 / 0.2	A3 / A4
mCPBA	50	6.7	2	0.2	A2
sPhIO	0	–	–	–	A2
sPhIO	0	– / 1.5	– / 1	– / 0.1	A3 / A4
sPhIO	rt	1.2	0	0.0	A2
sPhIO	rt	21.7 / 8.0	1 / 0	0.1 / 0.0	A3 / A4
sPhIO	50	–	–	–	A2
sPhIO	50	18.0 / 9.9	1 / 1	0.1 / 0.1	A3 / A4

– no products detected in GC analysis.

Table A.4: C – H oxidation of cyclohexane in MeCN with *in situ* complex formation of **4** and $Fe(OTf)_2 \cdot 2\,MeCN$ (iron complex : H_2O_2 : cyclohexane, 1 : 10 : 1000).

Oxidant	T [°C]	***A*/*K***	Efficiency [%]	TON	Workup
H_2O_2	0	2.4	1	0.1	A1
H_2O_2	rt	4.9	10	1.0	A1
H_2O_2	rt	5.3 */ 4.2 *	10 */ 9 *	1.0 */ 0.9 *	A3 / A4
H_2O_2	50	2.5	4	0.4	A1
H_2O_2 (10 steps)	rt	6.5	11	1.1	A3
H_2O_2 (without **4**)	rt	4.9	14	1.4	A3
mCPBA	0	2.6	3	0.3	A1
mCPBA	rt	3.5	4	0.4	A1
mCPBA	rt	4.6 / 4.5	6 / 6	0.6 / 0.6	A3 / A4
mCPBA	50	9.6	5	0.5	A1
sPhIO	0	2.4 / 1.9	1 / 1	0.1 / 0.1	A3 / A4
sPhIO	rt	2.1	2	0.2	A1
sPhIO	rt	17.1 / 8.9	1 / 1	0.1 / 0.1	A3 / A4
sPhIO	50	2.4 / 1.4	1 / 1	0.1 / 0.1	A3 / A4

*Average value of threefold determination.

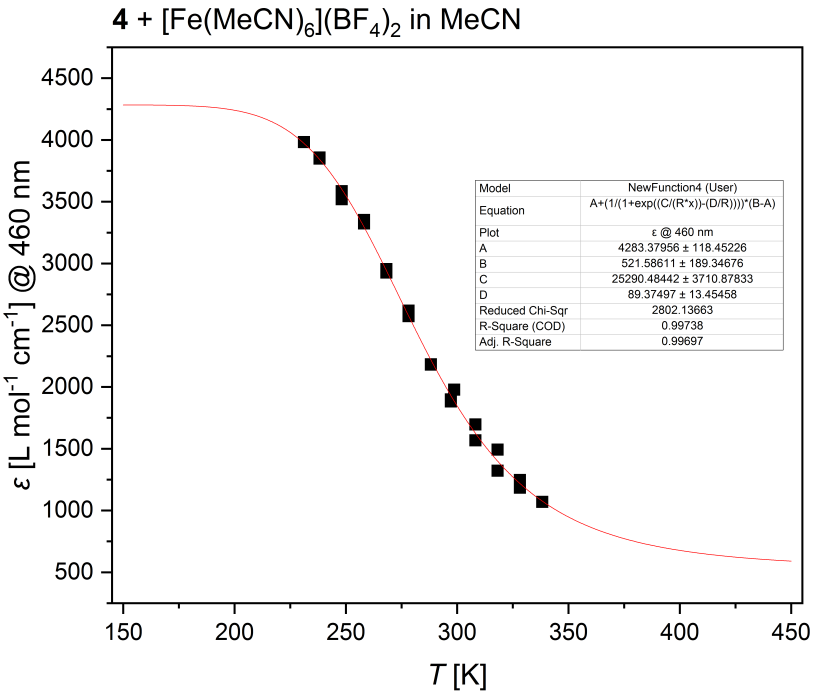

Figure A.12: Fit of extinction coefficients at 460 nm in UV/Vis spectra of $[Fe(MeCN)_6](BF_4)_2$ and **4** in MeCN at different temperatures; "OTf-free"-conditions.

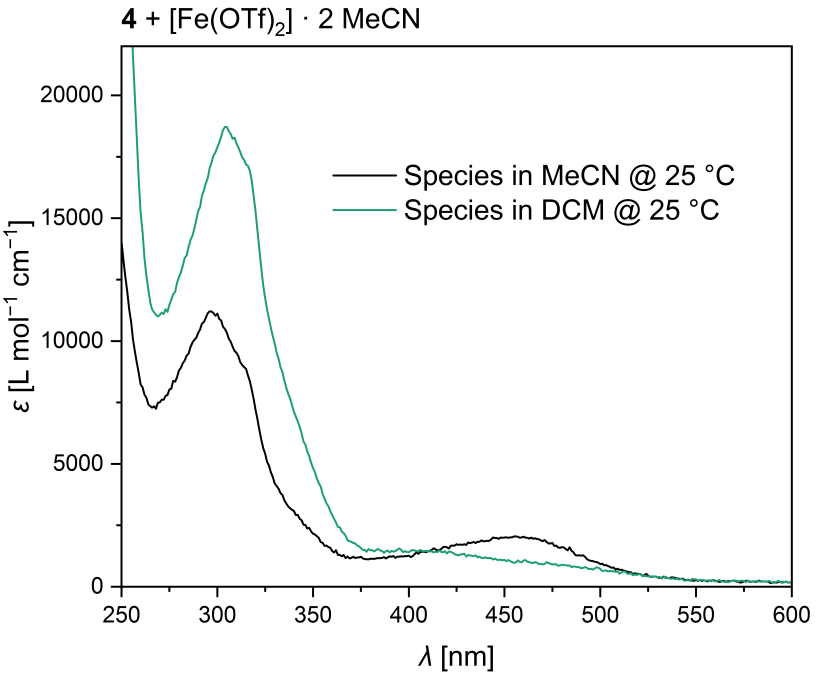

Figure A.13: Overlay of UV/Vis spectra of species formed by **4** (1 eq.) and $[Fe(OTf)_2] \cdot 2\,MeCN$ (1 eq.) in MeCN (black) and DCM (green) at 25 °C.

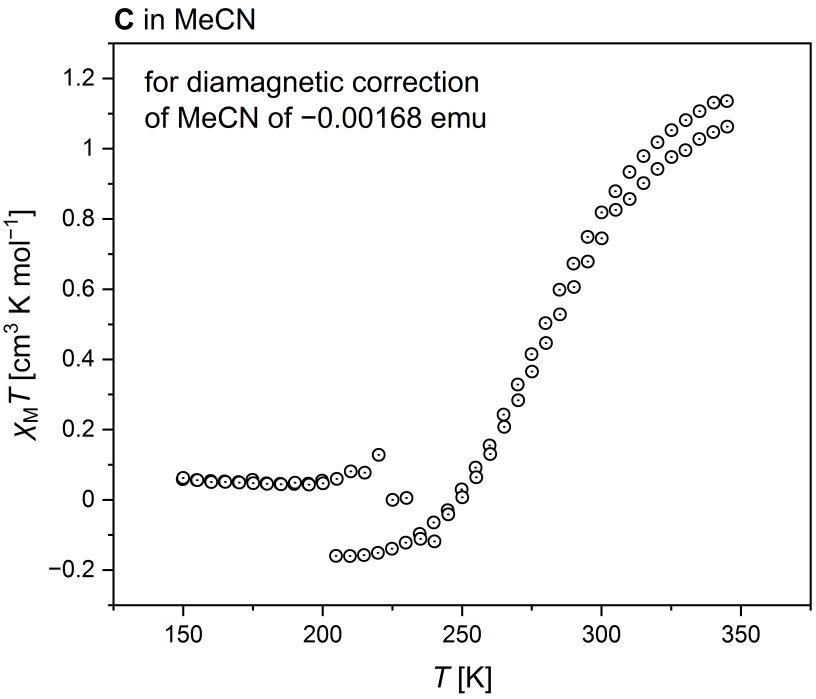

Figure A.14: Molar susceptibility vs. temperature data obtained by magnetic susceptibility measurement of **C** in MeCN under inert conditions if diamagnetic correction of solvent is considered to be −0.00168 emu.

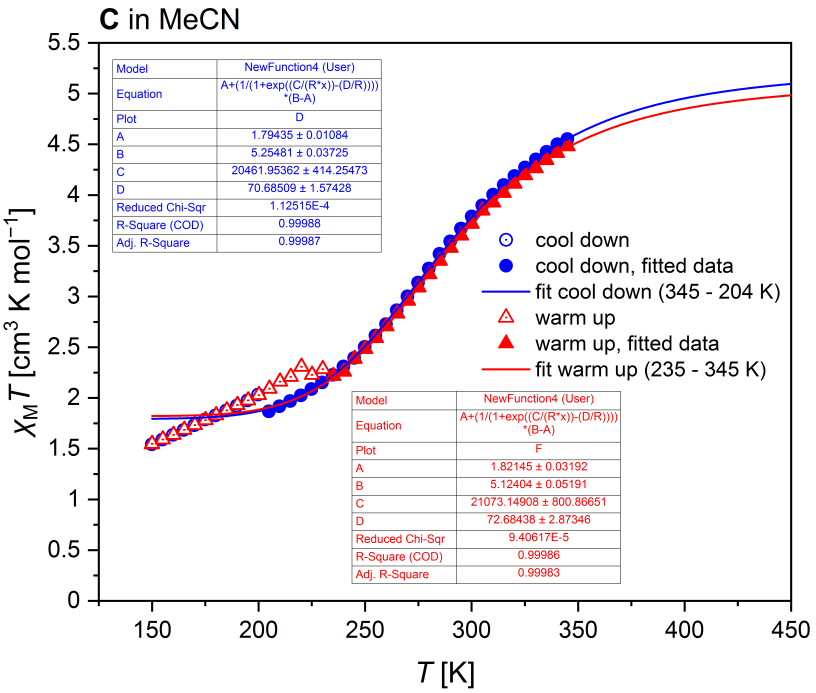

Figure A.15: Fit of magnetic measurement data ($\chi_M T$ at different temperatures) of **C** in MeCN. Data obtained when cooling the sample down was fitted in a range of 345–204 K and for warming the sample up between 235–345 K.

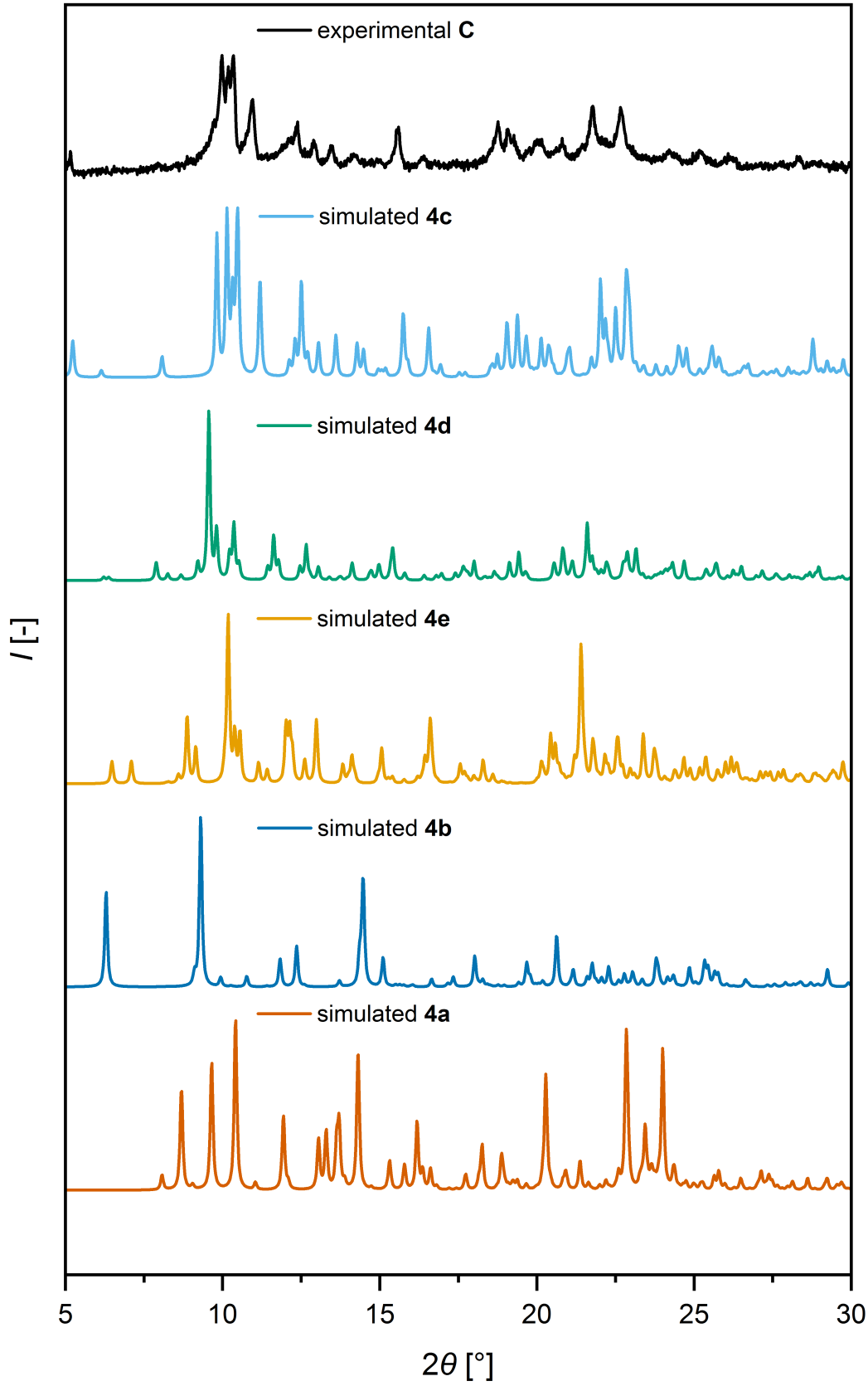

Figure A.16: Experimental PXRD of compound **C** (black, top) in comparison with the simulated patterns of **4c**, **4d**, **4e**, **4b** and **4a**.

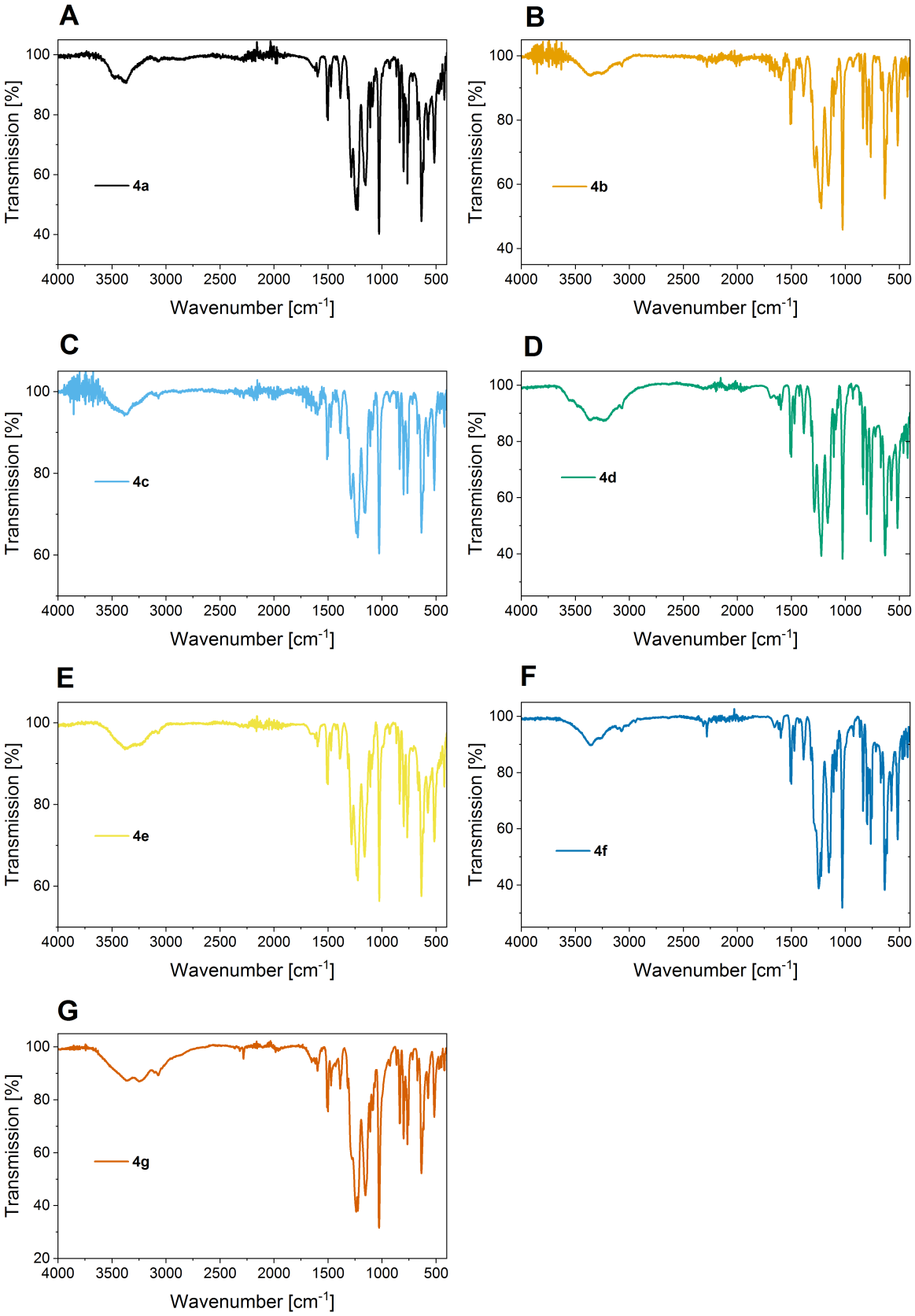

Figure A.17: IR spectra of solid compounds made from **4** and [Fe(OTf$_2$) · 2 MeCN] in MeCN in the range of 4000–400 cm^{-1}. Compounds: **4a**, **4b**, **4c**, **4d**, **4e**, **4f** and **4g**.

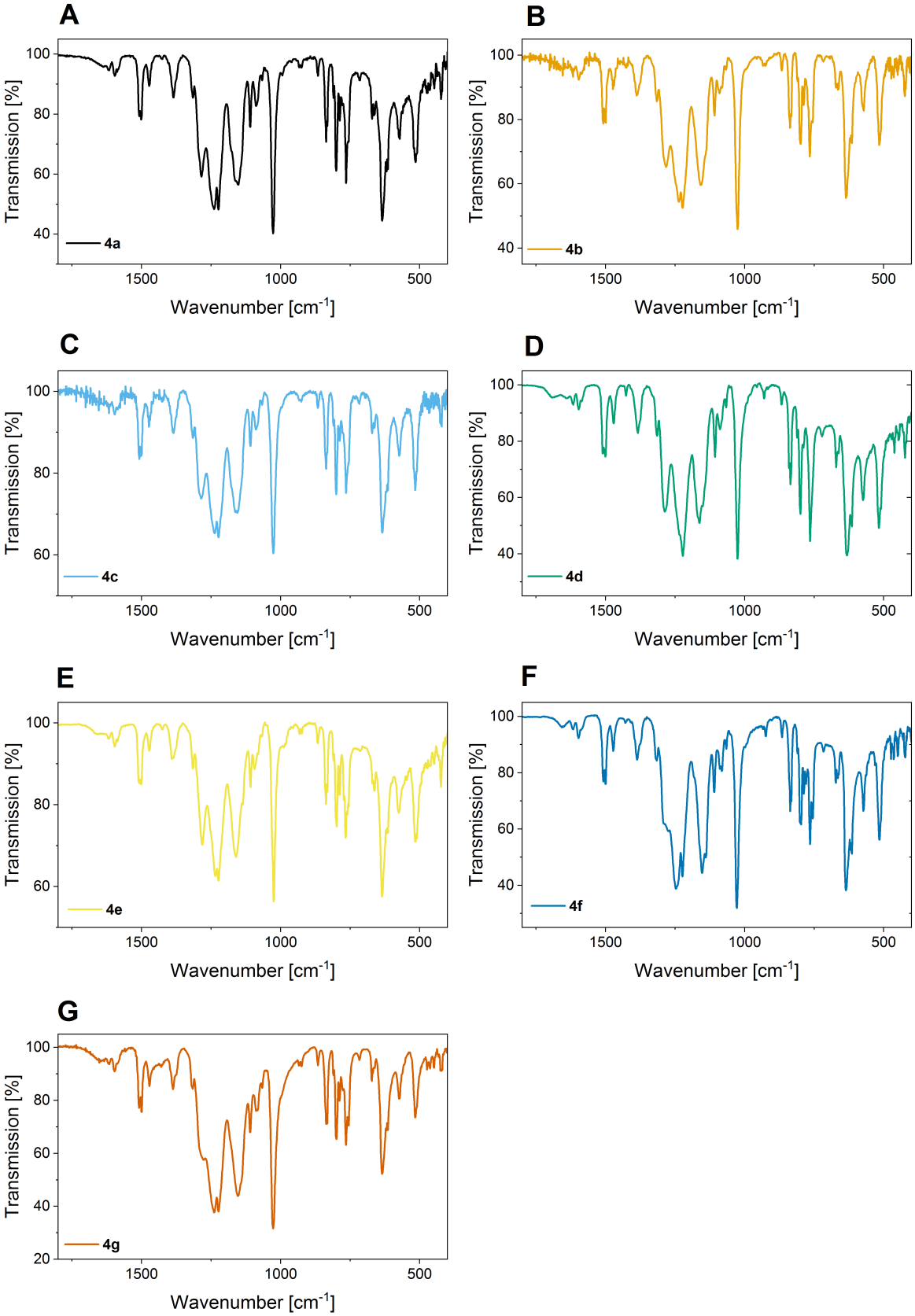

Figure A.18: IR spectra of solid complexes made from **4** and $[Fe(OTf_2) \cdot 2\,MeCN]$ in MeCN in the range of 1800–400 cm^{-1} (fingerprint area). Compounds: **4a**, **4b**, **4c**, **4d**, **4e**, **4f** and **4g**.

A.5 Crystallographic Data & Refinement Results

Table A.5: Crystallographic data and parameters of **1a**, **1b** and **1c**.

Compound	**1a** $[Fe(HOCH_2C(Pz)_2Py)_2]Br_2 \cdot MeCN$	**1b** $[Fe(HOCH_2C(Pz)_2Py)_2][FeBr_4]Br \cdot C_7H_8$	**1c** $[Fe(HOCH_2C(Pz)_2Py)_2][FeCl_4]Cl \cdot 2\,MeCN$
Measurement	SH_00815	SH_00802	SH_00803
Diffractometer	STOE	STOE	STOE
Empirical formula	$C_{28}H_{29}Br_2FeN_{11}O_2$	$C_{33}H_{34}Br_5Fe_2N_{10}O_2$	$C_{30}H_{32}Cl_5Fe_2N_{12}O_2$
Moiety formula	$C_{26}H_{26}FeN_{10}O_2$, 2 Br, C_2H_3N	$C_{26}H_{26}FeN_{10}O_2$, $FeBr_4$, Br, C_7H_8	$C_{26}H_{26}FeN_{10}O_2$, $FeCl_4$, Cl, $2\,C_2H_3N$
Formula weight [g mol^{-1}]	767.29	1113.19	881.61
Crystal size [mm]	$0.13 \times 0.10 \times 0.05$	$0.18 \times 0.16 \times 0.13$	$0.13 \times 0.12 \times 0.10$
T [K]	100(2)	100(2)	100(2)
Crystal system	triclinic	monoclinic	triclinic
Space group (№)	$P\bar{1}$ (2)	$P2_1/n$ (14)	$P\bar{1}$ (2)
a [Å]	11.196(2)	16.133(3)	9.7360(19)
b [Å]	12.407(3)	10.753(2)	13.861(3)
c [Å]	12.589(3)	20.722(4)	14.258(3)
α [°]	79.46(3)	90	96.05(3)
β [°]	66.51(3)	91.44(3)	94.95(3)
γ [°]	79.53(3)	90	105.13(3)
V [Å^3]	1565.3(7)	3593.6(12)	1834.1(7)
Z	2	4	2
ρ_{calc} [g cm^{-3}]	1.628	1.889	1.596
μ [mm^{-1}]	7.238	6.407	1.203
λ [Å]	1.54186	0.71073	0.71073
$F(000)$	772	1980	898
hkl range	$-13/12; -14/10; -12/14$	$-23/20; -15/15; -30/30$	$-14/14; -21/21; -21/21$
Refl. collected	9539	39803	45231
Independent refl.	5175	11901	13388
R_{int}	0.0289	0.0678	0.0459
№ of parameters	433	473	451
R_1 $[I > 2\sigma(I)]$	0.0607	0.0521	0.0443
wR_2 (all data)	0.1791	0.1055	0.1004
GoF	1.091	0.958	0.908
$\Delta\rho_{max}/\Delta\rho_{min}$ [e Å^{-3}]	$1.558/-1.056$	$0.778/-0.636$	$1.676/-1.666$
CCDC №	n.d.	n.d.	n.d.

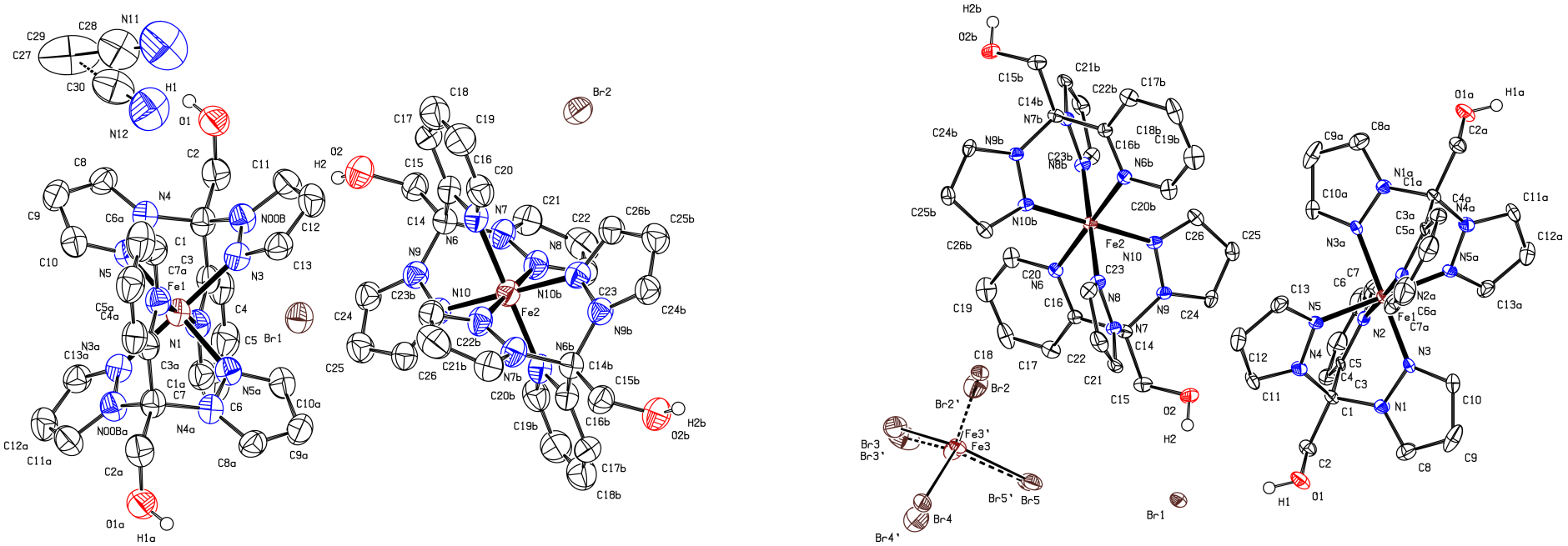

Figure A.19: Molecular structure of **1a** (left) and **1b** (right) in the solid state (displacement ellipsoid plot, 50 % probability, C bonded hydrogens omitted).

Note: In **1b** it was not possible to model the disordered toluene solvent molecules in an adequate manner, and the data set was treated with the BYPASS algorithm as implemented in PLATON/SQUEEZE.[156–158] The algorithm found a total volume of 400 Å^3 with 117 electrons in each unit cell. This approx. corresponds to one C_7H_8 molecule per complex molecule.

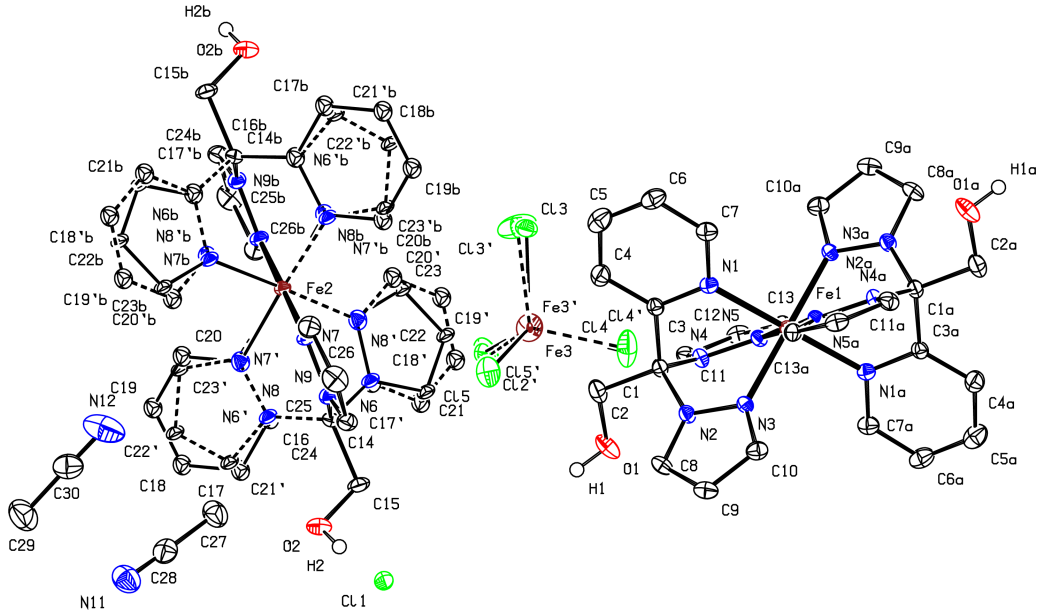

Figure A.20: Molecular structure of **1c** in the solid state (displacement ellipsoid plot, 50 % probability, C bonded hydrogens omitted).

Table A.6: Crystallographic data and parameters of **1d**, **1e** and **1f**.

Compound	**1d** $[Fe(HOCH_2C(Pz)_2Py)_2](OTf)_2 \cdot 2\,MeCN$	**1e** $[Zn(HOCH_2C(Pz)_2Py)_2][FeCl_4]$	**1f** $[Cu_2(\mu\text{-}Br)Br_2(HOCH_2C(Pz)_2Py)_2]Br \cdot C_7H_8$
Measurement	SH_01018	SH_00816	SH_00783
Diffractometer	STOE	STOE	STOE
Empirical formula	$C_{32}H_{32}F_6FeN_{12}O_8S_2$	$C_{26}H_{26}Cl_4N_{10}O_2Zn_2$	$C_{33}H_{34}Br_4Cu_2N_{10}O_2$
Moiety formula	$C_{26}H_{26}FeN_{10}O_2$, 2 CF_3O_3S, 2 C_2H_3N	$C_{26}H_{26}N_{10}O_2Zn$, $ZnCl_4$	$C_{26}H_{26}Br_3Cu_2N_{10}O_2$, Br, C_7H_8
Formula weight [g mol^{-1}]	946.66	783.11	1049.41
Crystal size [mm]	$0.36 \times 0.33 \times 0.30$	$0.09 \times 0.07 \times 0.05$	$0.22 \times 0.16 \times 0.09$
T [K]	100(2)	100(2)	100(2)
Crystal system	triclinic	monoclinic	monoclinic
Space group (№)	$P\bar{1}$ (2)	$P2_1/c$ (14)	$P2_1/n$ (14)
a [Å]	11.166(2)	12.094(2)	11.749(2)
b [Å]	12.396(3)	15.323(3)	16.248(3)
c [Å]	14.547(3)	16.814(3)	19.705(4)
α [°]	73.21(3)	90	90
β [°]	89.54(3)	92.94(3)	90.23(3)
γ [°]	89.80(3)	90	90
V [Å^3]	1927.7(7)	3112.0(11)	3761.5(13)
Z	2	4	4
ρ_{calc} [g cm^{-3}]	1.631	1.671	1.690
μ [mm^{-1}]	0.596	5.428	5.417
λ [Å]	0.71073	1.54186	0.71073
$F(000)$	968	1584	1864
hkl range	$-16/16; -18/18; -21/21$	$-14/11; -18/13; -20/16$	$-18/17; -16/24; -29/30$
Refl. collected	93678	19578	54440
Independent refl.	13857	5431	14298
R_{int}	0.0897	0.0169	0.0772
№ of parameters	810	399	402
R_1 [$I > 2\sigma(I)$]	0.0432	0.0517	0.0522
wR_2 (all data)	0.0998	0.1352	0.1185
GoF	0.833	1.097	0.950
$\Delta\rho_{max}/\Delta\rho_{min}$ [e Å^{-3}]	$0.722/-0.344$	$1.223/-0.602$	$1.413/-0.822$
CCDC №	n.d.	n.d.	n.d.

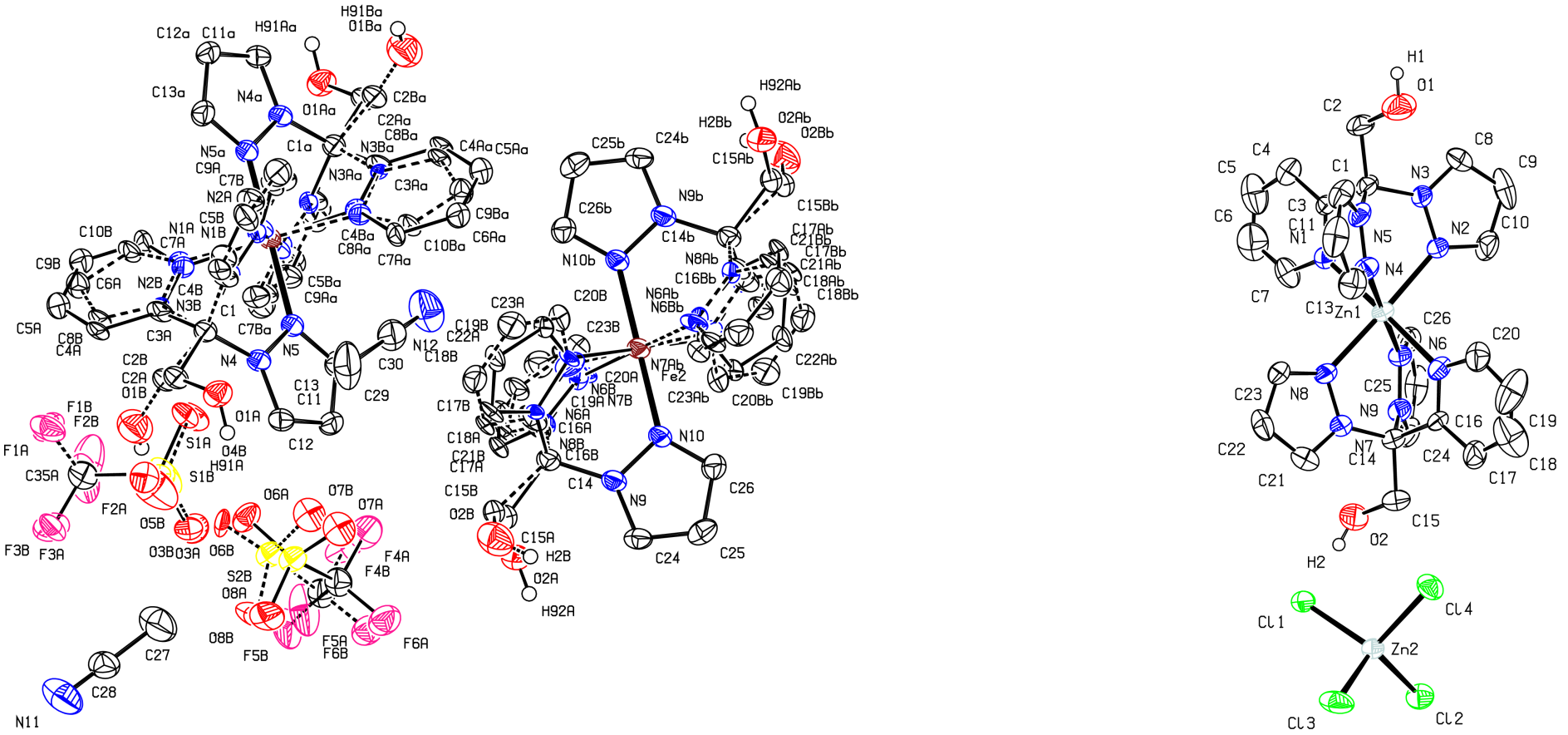

Figure A.21: Molecular structure of **1d** (left) and **1e** (right) in the solid state (displacement ellipsoid plot, 50 % probability, C bonded hydrogens omitted).

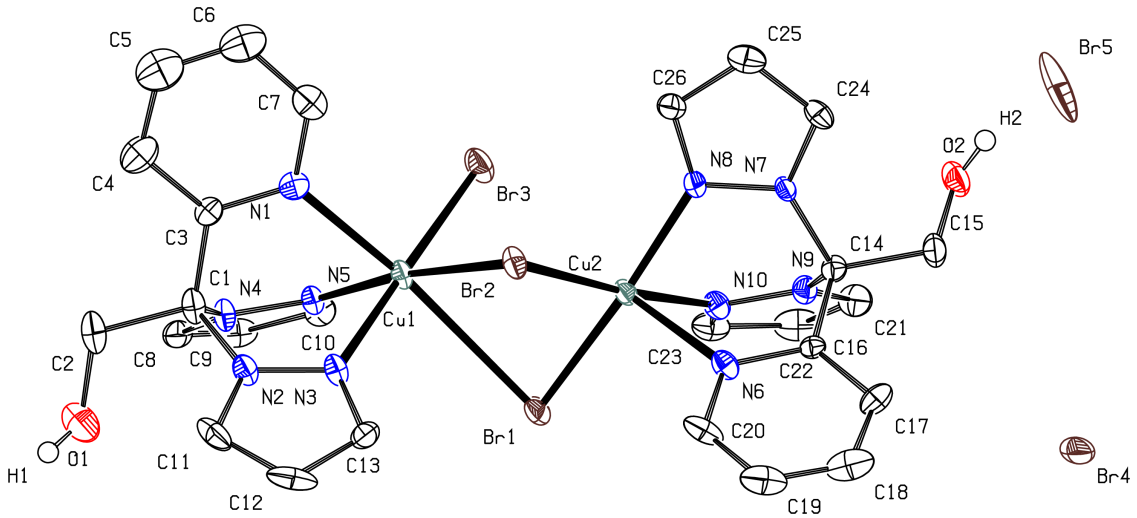

Figure A.22: Molecular structure of **1f** in the solid state (displacement ellipsoid plot, 50 % probability, asymmetric unit, C bonded hydrogens omitted).

Note: In **1f** it was not possible to model the disordered toluene solvent molecules in an adequate manner, and the data set was treated with the BYPASS algorithm as implemented in PLATON/SQUEEZE.[156–158] The algorithm found a total volume of 964 $Å^3$ with 275 electrons in each unit cell. This approx. corresponds to one C_7H_8 molecule per complex molecule.

Table A.7: Crystallographic data and parameters of **1g**, **1h**, **2b** and **2c**.

Compound	**1g** $[Cu_2(OCH_2C(Pz)_2Py)_2Cl_2]$	**1h** $[Cu_2(OCH_2C(Pz)_2Py)_2Br_2]$	**2b** $[Fe(MeC(Py)_2Phen)(MeCN)_2](BF_4)_2 \cdot MeCN$	**2c** $[Fe(MeC(Py)_2Phen)(\mu\text{-}Cl)_2FeCl_2]$
Measurement	SH_00744	SH_00731	SH_01007	SH_01321
Diffractometer	STOE	STOE	STOE	STOE
Empirical formula	$C_{52}H_{48}Cl_4Cu_4N_{20}O_4$	$C_{52}H_{48}Br_4Cu_4N_{20}O_4$	$C_{30}H_{27}B_2F_8FeN_7$	$C_{24}H_{18}Cl_4Fe_2N_4$
Moiety formula	$C_{52}H_{48}Cl_4Cu_4N_{20}O_4$	$C_{52}H_{48}Br_4Cu_4N_{20}O_4$	$C_{28}H_{24}FeN_6$, $2\,BF_4$, C_2H_3N	$C_{24}H_{18}Cl_4Fe_2N_4$
Formula weight [g mol^{-1}]	1413.06	1590.90	715.05	615.92
Crystal size [mm]	$0.11 \times 0.09 \times 0.07$	$0.19 \times 0.16 \times 0.11$	$0.31 \times 0.24 \times 0.20$	$0.21 \times 0.17 \times 0.12$
T [K]	100(2)	100(2)	100(2)	100(2)
Crystal system	triclinic	triclinic	triclinic	monoclinic
Space group (№)	$P\bar{1}$ (2)	$P\bar{1}$ (2)	$P\bar{1}$ (2)	$I2/a$ (15)
a [Å]	10.960(2)	11.101(2)	12.318(3)	14.476(3)
b [Å]	11.686(2)	11.921(2)	12.610(3)	10.619(2)
c [Å]	12.020(2)	12.107(2)	12.814(3)	31.318(10)
α [°]	89.36(3)	89.66(3)	62.55(3)	90
β [°]	74.04(3)	73.34(3)	63.00(3)	99.22(3)
γ [°]	70.62(3)	71.39(3)	87.61(3)	90
V [Å^3]	1390.9(6)	1448.3(6)	1538.0(7)	4752(2)
Z	1	1	2	8
ρ_{calc} [g cm^{-3}]	1.687	1.824	1.455	1.722
μ [mm^{-1}]	4.042	4.272	0.568	1.693
λ [Å]	1.54186	0.71073	0.71073	0.71073
$F(000)$	716	788	684	2480
hkl range	$-12/12; -10/13; -14/12$	$-14/13; -15/15; -15/14$	$-18/18; -18/18; -18/18$	$-22/21; -16/16; -32/47$
Refl. collected	12671	13121	27556	22903
Independent refl.	4610	6792	10240	8718
R_{int}	0.0238	0.0507	0.0204	0.0310
№ of parameters	255	255	495	308
R_1 $[I > 2\sigma(I)]$	0.0573	0.0620	0.0571	0.0596
wR_2 (all data)	0.1529	0.1727	0.1457	0.1349
GoF	1.069	1.000	1.090	1.164
$\Delta\rho_{max}/\Delta\rho_{min}$ [e Å^{-3}]	1.213/−1.147	1.461/−1.285	0.665/−0.679	0.849/−0.647
CCDC №	n.d.	n.d.	1980476	n.d.

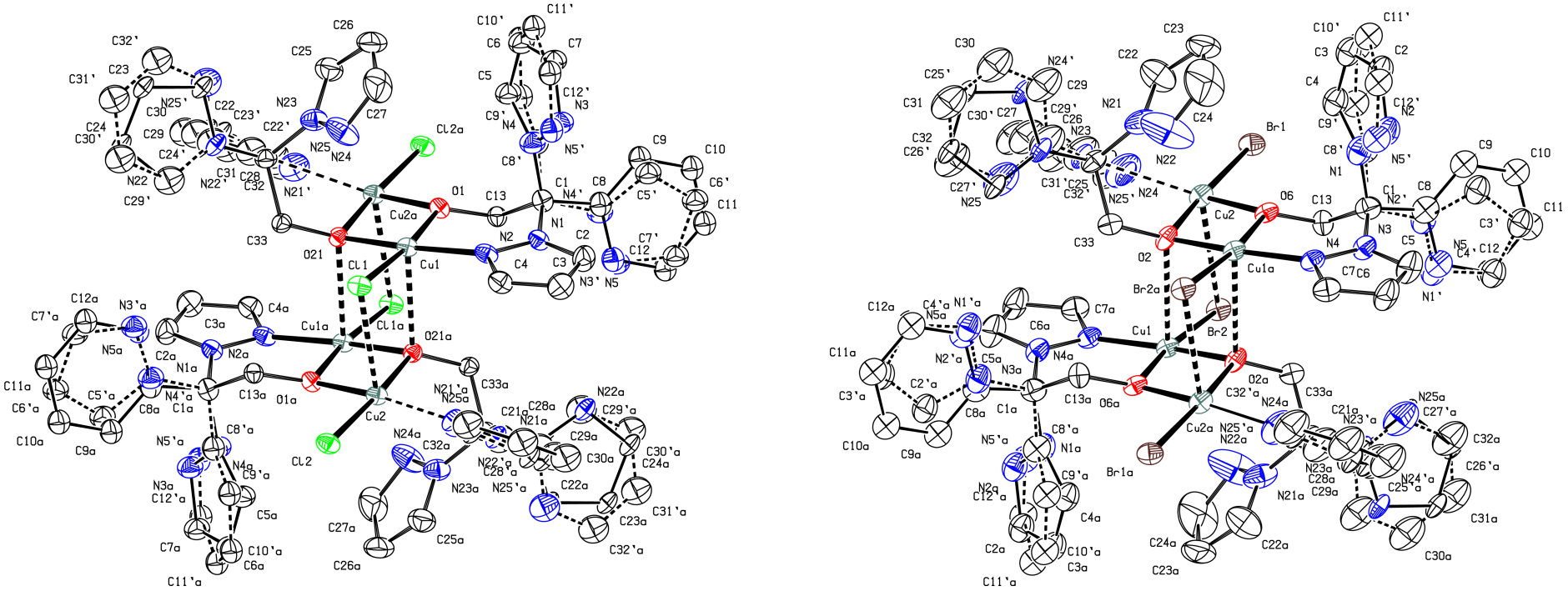

Figure A.23: Molecular structure of **1g** (left) and **1h** (right) in the solid state (displacement ellipsoid plot, 50 % probability, C bonded hydrogens omitted).

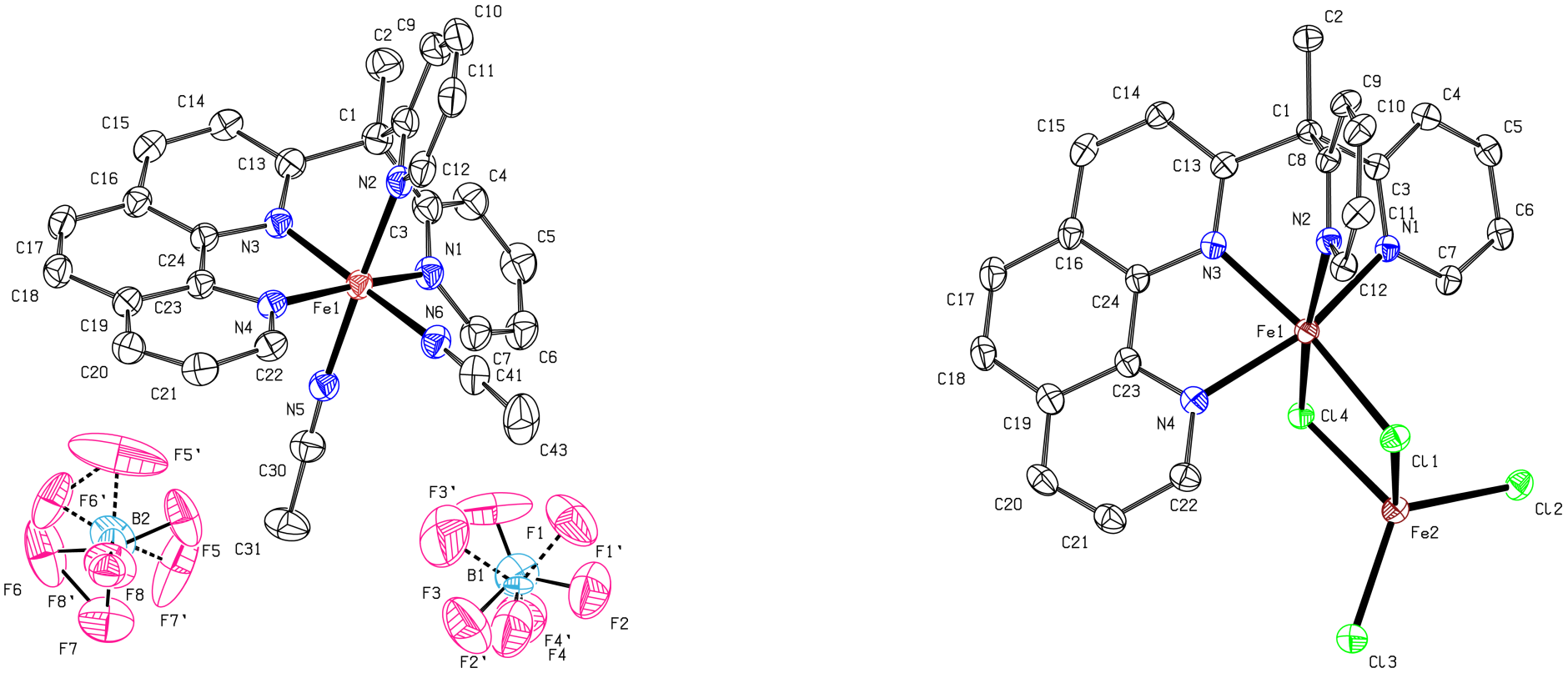

Figure A.24: Molecular structure of of **2b** (left) and **2c** (right) in the solid state (displacement ellipsoid plot, 50 % probability, asymmetric unit, C bonded hydrogens omitted).

Note: In **2b** it was not possible to model the disordered acetonitrile solvent molecules in an adequate manner, and the data set was treated with the BYPASS algorithm as implemented in PLATON/SQUEEZE.[156–158] The algorithm found a total volume of 178 Å^3 with 45 electrons in each unit cell. This approx. corresponds to one C_2H_3N molecule per unit complex molecule.

Table A.8: Crystallographic data and parameters of **2d**, **3a** and **3b**.

Compound	**2d** $[Fe(MeC(Py)_2Phen)Cl(\mu\text{-}O)FeCl_3] \cdot MeCN$	**3a** $[Fe(MeC(Py)_2PicMe)(OTf)_2]$	**3b** $[Fe_4(\mu\text{-}O)_2(MeC(Py)_2Pic)_4](OTf)_4 \cdot 4\,DCM \cdot THF$
Measurement	SH_02478	SH_00996	SH_00985
Diffractometer	STOE	STOE	STOE
Empirical formula	$C_{26}H_{21}Cl_4Fe_2N_5O$	$C_{21}H_{17}F_6FeN_3O_8S_2$	$C_{84}H_{72}Cl_8F_{12}Fe_4N_{12}O_{23}S_4$
Moiety formula	$C_{24}H_{18}Cl_4Fe_2N_4O$, C_2H_3N	$C_{21}H_{17}F_6FeN_3O_8S_2$	$C_{72}H_{64}Fe_4N_{12}O_{10}$, $4\,CF_3O_3S$, $4\,CH_2Cl_2$, C_4H_8O
Formula weight [g mol^{-1}]	672.98	673.34	2480.77
Crystal size [mm]	$0.16 \times 0.08 \times 0.03$	$0.19 \times 0.14 \times 0.10$	$0.13 \times 0.11 \times 0.08$
T [K]	100(2)	100(2)	100(2)
Crystal system	triclinic	triclinic	triclinic
Space group (№)	$P\bar{1}$ (2)	$P\bar{1}$ (2)	$P\bar{1}$ (2)
a [Å]	9.2624(19)	9.0519(18)	13.340(3)
b [Å]	11.910(2)	11.034(2)	13.879(3)
c [Å]	12.544(3)	14.108(3)	26.595(5)
α [°]	83.87(3)	109.36(3)	85.04(3)
β [°]	83.30(3)	91.37(3)	85.70(3)
γ [°]	81.25(3)	110.46(3)	87.51(3)
V [Å^3]	1352.7(5)	1229.8(5)	4888.1(17)
Z	2	2	2
ρ_{calc} [g cm^{-3}]	1.652	1.818	1.685
μ [mm^{-1}]	1.498	0.884	8.365
λ [Å]	0.71073	0.71073	1.54186
$F(000)$	680	680	2512
hkl range	$-11/11; -12/14; -15/15$	$-13/13; -16/16; -21/21$	$-4/15; -16/16; -31/31$
Refl. collected	24751	23653	28483
Independent refl.	5018	8994	15879
R_{int}	0.0472	0.0209	0.0402
№ of parameters	345	372	1363
R_1 $[I > 2\sigma(I)]$	0.0334	0.0374	0.0816
wR_2 (all data)	0.0903	0.0935	0.2323
GoF	0.973	1.086	1.050
$\Delta\rho_{max}/\Delta\rho_{min}$ [e Å^{-3}]	$0.619/-0.482$	$0.602/-0.542$	$1.450/-0.627$
CCDC №	n.d.	n.d.	n.d.

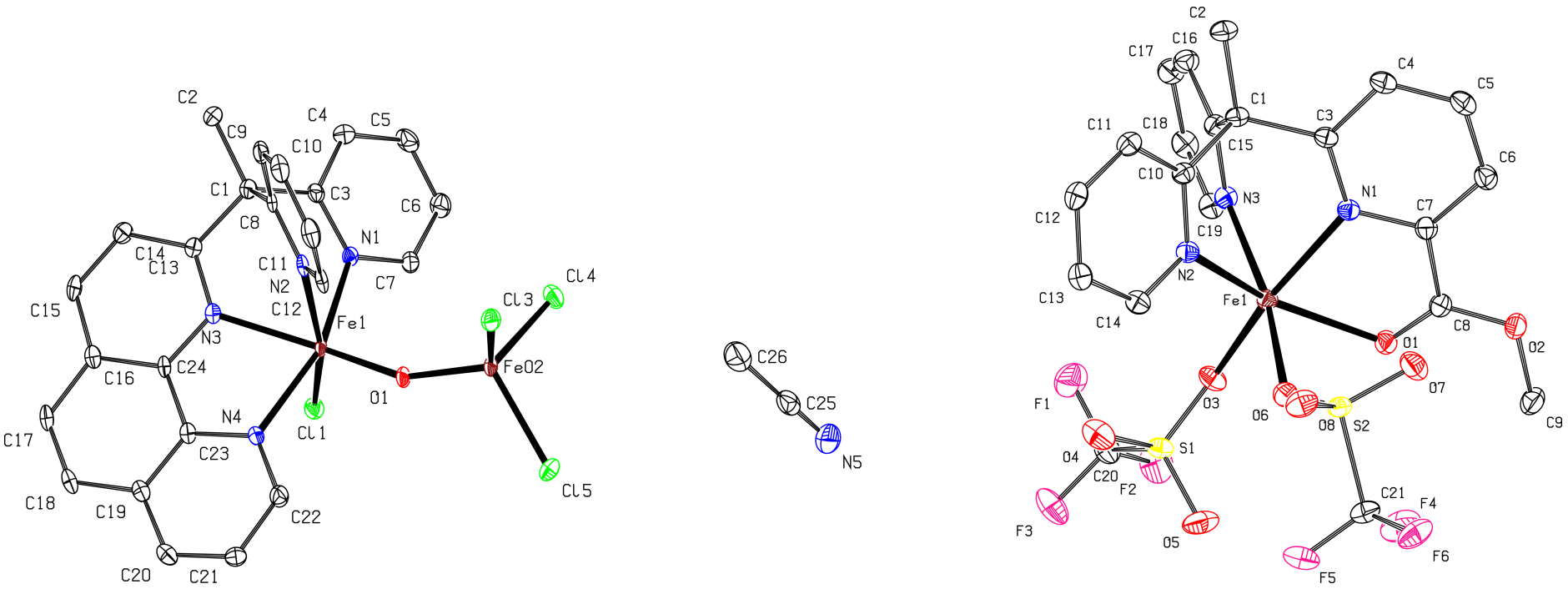

Figure A.25: Molecular structure of **2d** (left) and **3a** (right) in the solid state (displacement ellipsoid plot 50 % probability, asymmetric unit, C bonded hydrogens omitted).

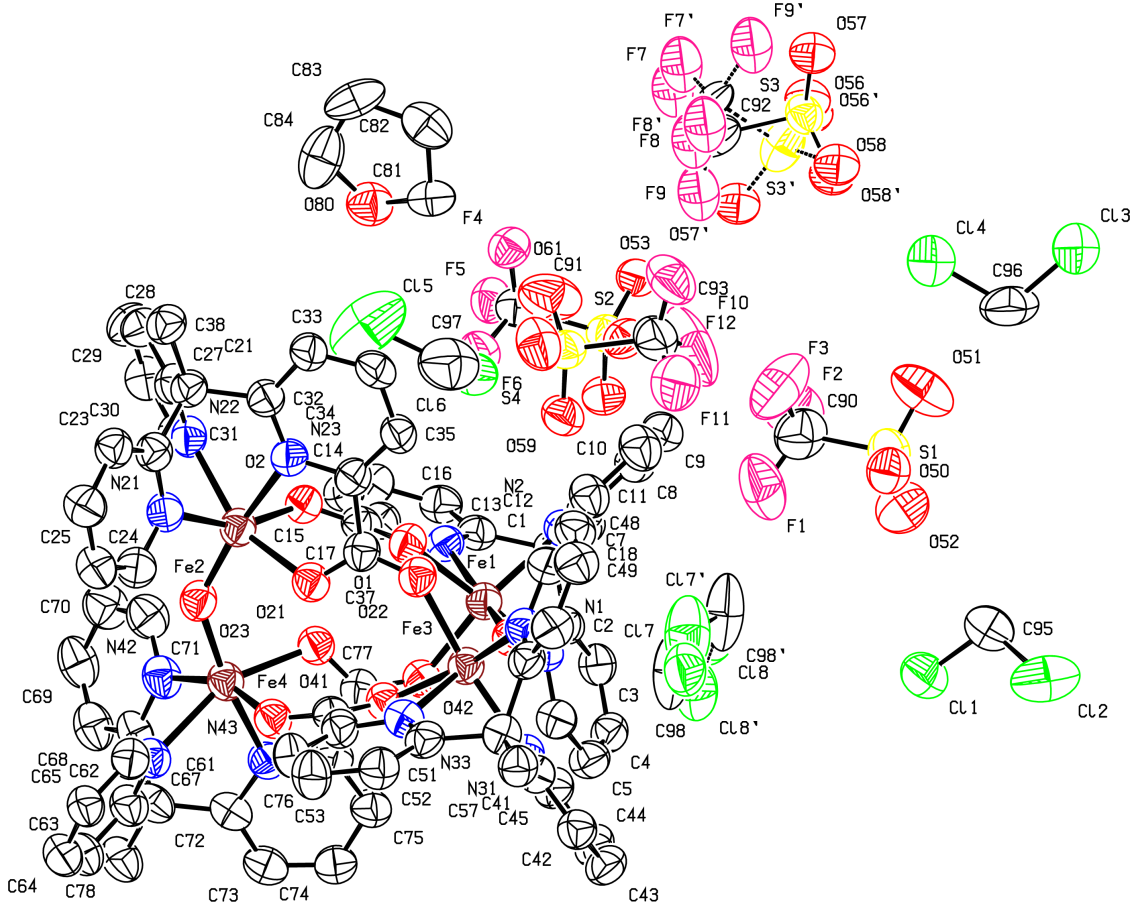

Figure A.26: Molecular structure of **3b** in the solid state (displacement ellipsoid plot, 50 % probability, asymmetric unit, C bonded hydrogens omitted).

Table A.9: Crystallographic data and parameters of **3c**, **3d** and **3e**.

Compound	**3c** $[Fe(MeC(Py)_2PicMe)Cl_2] \cdot 0.5\,MeCN$	**3d** $[Fe(MeC(Py)_2PicMe)(H_2O)(MeCN)](BF_4)_2 \cdot MeCN$	**3e** $[Fe(MeC(Py)_2PicMe)(BF_4)Cl] \cdot 3.5\,Et_2O$
Measurement	SH_01563	SH_01301	SH_01574
Diffractometer	STOE	STOE	STOE
Empirical formula	$C_{20}H_{18.5}Cl_2FeN_{3.5}O_2$	$C_{23}H_{25}B_2F_8FeN_5O_3$	$C_{33}H_{52}BClF_4FeN_3O_{5.5}$
Moiety formula	$C_{19}H_{17}Cl_2FeN_3O_2\ 0.5\,C_2H_3N$	$C_{21}H_{22}FeN_4O_3$, $2\,BF_4$, C_2H_3N	$C_{19}H_{17}BClF_4FeN_3O_2$, $3.5\,C_4H_{10}O$
Formula weight [g mol^{-1}]	466.64	648.95	756.89
Crystal size [mm]	$0.21 \times 0.16 \times 0.13$	$0.29 \times 0.25 \times 0.20$	$0.20 \times 0.18 \times 0.14$
T [K]	100(2)	100(2)	100(2)
Crystal system	monoclinic	monoclinic	monoclinic
Space group (№)	$C2/c$ (15)	$P2_1/c$ (14)	$P2_1/c$ (14)
a [Å]	16.350(3)	18.144(4)	12.372(3)
b [Å]	8.3363(17)	10.913(2)	11.946(2)
c [Å]	29.247(6)	13.929(3)	16.475(3)
α [°]	90	90	90
β [°]	94.01(3)	97.18(3)	95.16(3)
γ [°]	90	90	90
V [Å^3]	3976.5(14)	2736.5(10)	2425.1(9)
Z	8	4	4
ρ_{calc} [g cm^{-3}]	1.490	1.575	1.362
μ [mm^{-1}]	1.046	0.642	0.781
λ [Å]	0.71073	0.71073	0.71073
$F(000)$	1824	1320	1008
hkl range	$-24/11; -12/12; -44/44$	$-27/28; -16/16; -21/20$	$-16/16; -16/16; -22/22$
Refl. collected	35490	48219	33363
Independent refl.	7218	10304	6447
R_{int}	0.0745	0.0206	0.0263
№ of parameters	275	391	283
R_1 $[I > 2\sigma(I)]$	0.0877	0.0426	0.0395
wR_2 (all data)	0.2341	0.0948	0.0932
GoF	1.099	1.215	1.095
$\Delta\rho_{max}/\Delta\rho_{min}$ [e Å^{-3}]	$1.044/-0.657$	$0.738/-465$	$0.417/-0.413$
CCDC №	n.d.	n.d.	n.d.

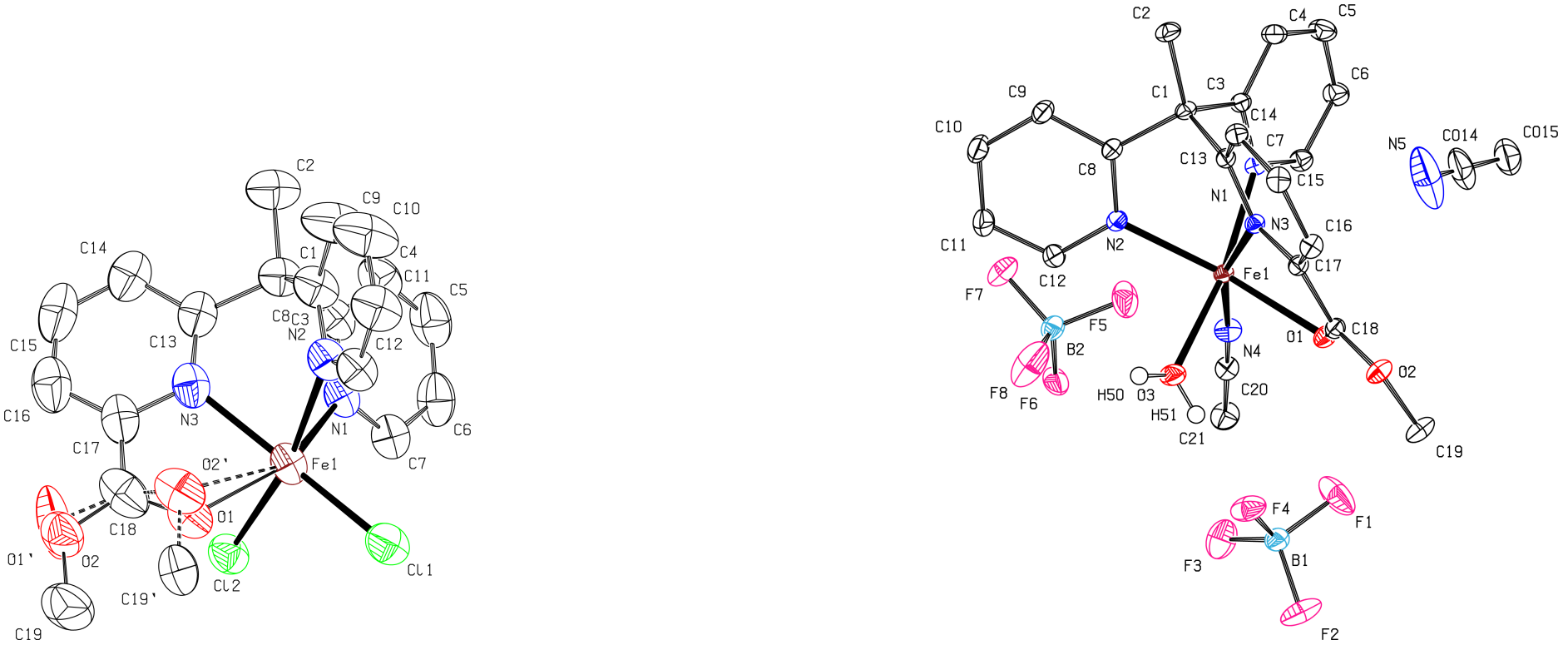

Figure A.27: Molecular structure of **3c** (left) and **3d** (right) in the solid state (displacement ellipsoid plot, 50 % probability, asymmetric unit, C bonded hydrogens omitted).

Note: In **3c** it was not possible to model the disordered acetonitrile solvent molecules in an adequate manner, and the data set was treated with the BYPASS algorithm as implemented in PLATON/SQUEEZE.[156–158] The algorithm found a total volume of 231 Å^3 with 60 electrons in each unit cell. This approx. corresponds to 0.5 C_2H_3N molecules per complex molecule.

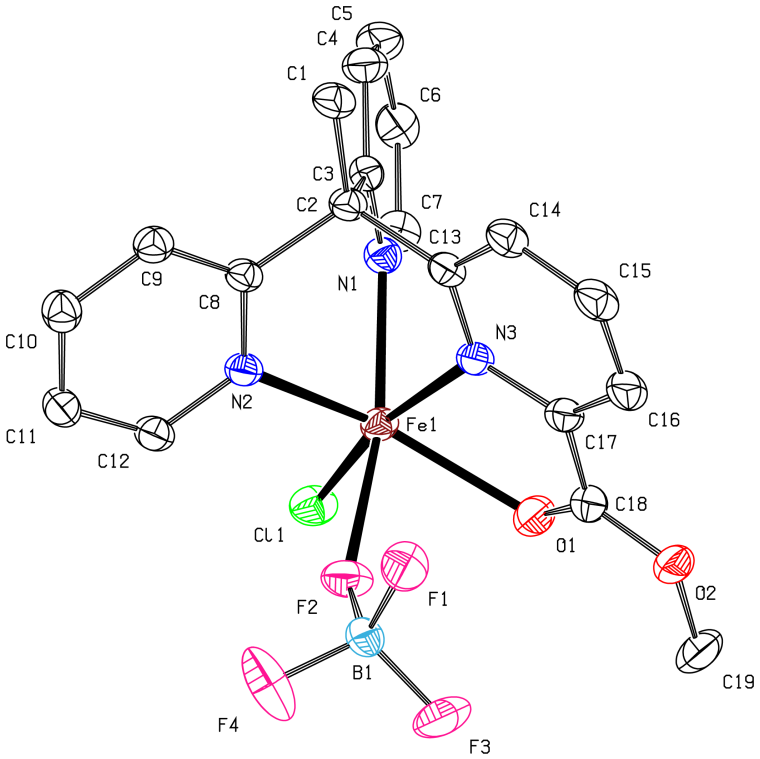

Figure A.28: Molecular structure of **3e** in the solid state (displacement ellipsoid plot, 50 % probability, asymmetric unit, C bonded hydrogens omitted).

Note: In **3e** it was not possible to model the disordered diethyl ether solvent molecules in an adequate manner, and the data set was treated with the BYPASS algorithm as implemented in PLATON/SQUEEZE.[156–158] The algorithm found a total volume of 575 Å^3 with 148 electrons in each unit cell. This approx. corresponds to 3.5 $C_4H_{10}O$ molecules per complex molecule.

Table A.10: Crystallographic data and parameters of **4a** and **4b**.

Compound	**4a** $[Fe(NQu_3)(MeCN)_2](OTf)_2 \cdot MeCN \cdot 0.5\,Et_2O$	**4b** $[Fe(NQu_3)(OTf)(MeCN)](OTf) \cdot 0.5\,Et_2O$
Measurement	h20_a03	SH_01705
Diffractometer	Bruker	STOE
Empirical formula	$C_{74}H_{64}F_{12}Fe_2N_{14}O_{13}S_4$	$C_{66}H_{52}F_{12}Fe_2N_{10}O_{13}S_4$
Moiety formula	$2\,C_{31}H_{24}FeN_6$, $4\,CF_3O_3S$, $C_4H_{10}O$, $2\,C_2H_3N$	$2\,C_{30}H_{21}F_3FeN_5O_3S$, $2\,CF_3O_3S$, $C_4H_{10}O$
Formula weight [g mol^{-1}]	1825.33	1661.11
Crystal size [mm]	$0.20 \times 0.17 \times 0.13$	$0.30 \times 0.25 \times 0.22$
T [K]	100(2)	100(2)
Crystal system	monoclinic	monoclinic
Space group (№)	$P2_1/c$ (14)	$P2_1/c$ (14)
a [Å]	20.555(3)	14.191(3)
b [Å]	12.9833(17)	12.900(3)
c [Å]	14.980(2)	19.623(4)
α [°]	90	90
β [°]	98.432(2)	98.60(3)
γ [°]	90	90
V [Å^3]	3954.4(9)	3551.9(13)
Z	2	2
ρ_{calc} [g cm^{-3}]	1.533	1.553
μ [mm^{-1}]	0.572	0.627
λ [Å]	0.71073	0.71073
$F(000)$	1868	1692
hkl range	$-27/27; -17/17; -19/20$	$-16/22; -19/19; -30/29$
Refl. collected	54195	85385
Independent refl.	9892	13495
R_{int}	0.0756	0.0779
№ of parameters	573	534
R_1 [$I > 2\sigma(I)$]	0.0495	0.0438
wR_2 (all data)	0.1358	0.1054
GoF	1.033	0.868
$\Delta\rho_{max}/\Delta\rho_{min}$ [e Å^{-3}]	$0.761/-0.544$	$0.469/-0.404$
CCDC №	2216548	2216549

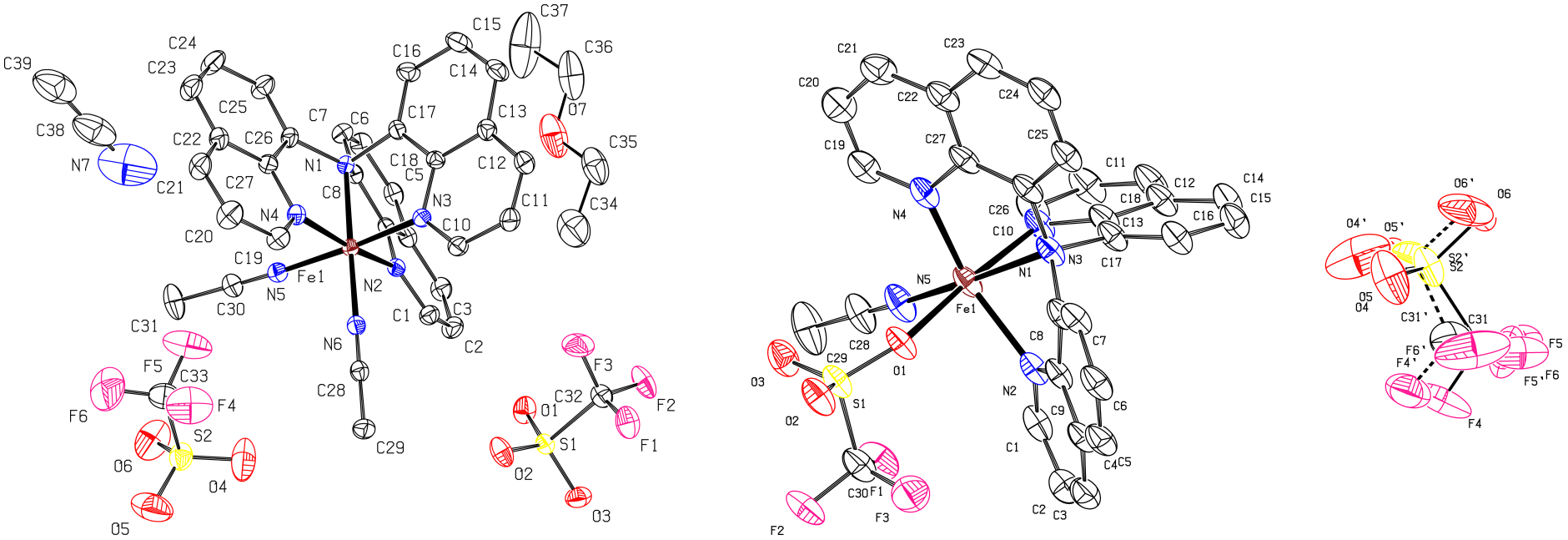

Figure A.29: Molecular structure of **4a** (left) and **4b** (right) in the solid state (displacement ellipsoid plot, 50 % probability, asymmetric unit, C bonded hydrogens omitted).

Note: In **4b** it was not possible to model the disordered solvent molecules in an adequate manner, and the data set was treated with the BYPASS algorithm as implemented in PLATON/SQUEEZE.[156–158] The algorithm found two voids of 240 $Å^3$ with 59 electrons, respectively, in each unit cell. Considered the solvent used, this approx. corresponds to two molecules of $C_4H_{10}O$.

Table A.11: Crystallographic data and parameters of **4c** and **4d**.

Compound	**4c** $[Fe(NQu_3)(OTf)_2]$	**4d** $[Fe(NQu_3)(OTf)_2] \cdot 0.45\,Et_2O$
Measurement	SH_01704	SH_01779
Diffractometer	STOE	STOE
Empirical formula	$C_{58}H_{36.36}F_{12}Fe_2N_8O_{12.18}S_4$	$C_{61.60}H_{45}F_{12}Fe_2N_8O_{12.90}S_4$
Moiety formula	$C_{29}H_{18}F_6FeN_4O_6S_2$, $C_{28.82}H_{18.36}F_{5.46}FeN_4O_{5.64}S_{1.82}$, $0.18\,CF_3O_3S$	$2\,C_{29}H_{18}F_6FeN_4O_6S_2$, $0.9\,C_4H_{10}O$
Formula weight [g mol^{-1}]	1508.13	1571.59
Crystal size [mm]	$0.15 \times 0.15 \times 0.13$	$0.18 \times 0.17 \times 0.16$
T [K]	100(2)	100(2)
Crystal system	triclinic	triclinic
Space group (№)	$P\bar{1}$ (2)	$P\bar{1}$ (2)
a [Å]	9.4553(5)	11.756(3)
b [Å]	17.6288(8)	15.539(4)
c [Å]	18.9131(10)	20.003(4)
α [°]	73.804(4)	112.08(3)
β [°]	81.445(4)	97.88(3)
γ [°]	83.556(4)	101.58(3)
V [Å^3]	2985.4(3)	3225.0(15)
Z	2	2
ρ_{calc} [g cm^{-3}]	1.678	1.618
μ [mm^{-1}]	0.735	0.685
λ [Å]	0.71073	0.71073
$F(000)$	1524	1596
hkl range	$-13/13; -25/14; -27/26$	$-18/17; -17/25; -32/30$
Refl. collected	38282	109250
Independent refl.	18023	27190
R_{int}	0.0658	0.0484
№ of parameters	975	913
R_1 $[I > 2\sigma(I)]$	0.0617	0.0539
wR_2 (all data)	0.1475	0.1465
GoF	0.885	1.032
$\Delta\rho_{max}/\Delta\rho_{min}$ [e Å^{-3}]	0.635/−0.493	1.070/−0.897
CCDC №	2216550	2216551

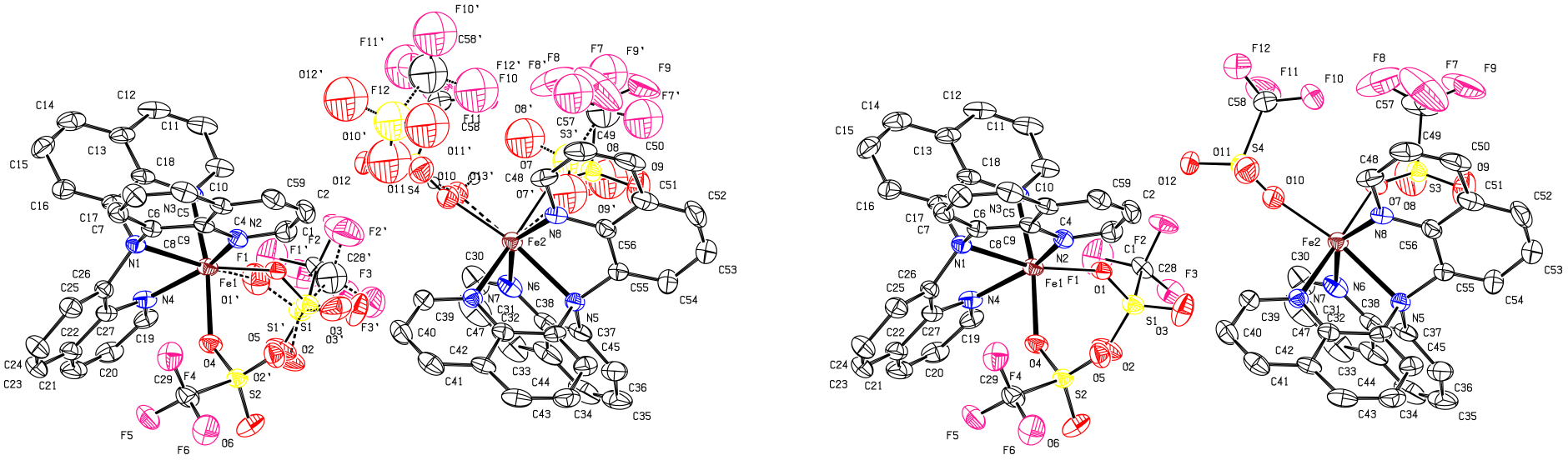

Figure A.30: Molecular structure of **4c** (left) and main residues of (Fe(1) 62.9 %, Fe(2) 82.2 %) of **4c** (right) in the solid state (displacement ellipsoid plot, 50 % probability, asymmetric unit, C bonded hydrogens omitted).

Note: In crystals of **4c** a minority species for the complex with Fe(2) was found to be present where the triflate anion in A position is replaced by a water co-ligand and the triflate anion that used to be at the A position is non-coordinating (17.8 %). In the structure model the Fe(2) – O_{H2O} distance was restrained to 2.01(1) Å and is thus not used for the discussion of bond lengths or angles.

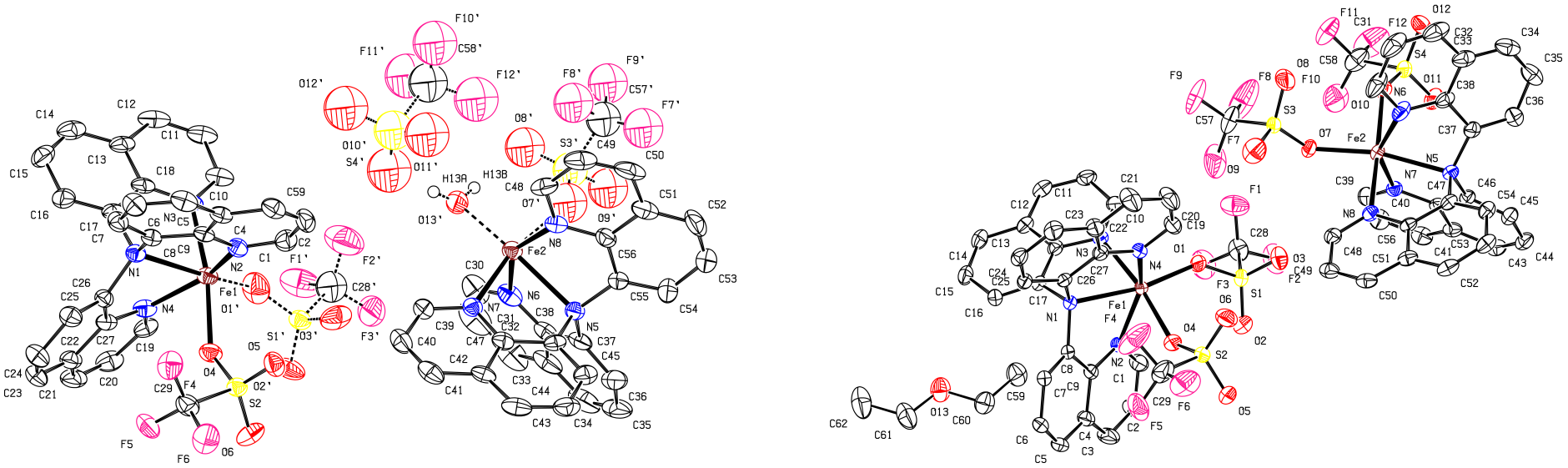

Figure A.31: Molecular structure of minority residues (Fe(1) 37.1 %, Fe(2) 17.8 %) of **4c** (left) and **4d** (right) in the solid state (displacement ellipsoid plot, 50 % probability, asymmetric unit, C bonded hydrogens omitted).

Note: In **4d** it was not possible to model the disordered solvent molecules in an adequate manner, and the data set was treated with the BYPASS algorithm as implemented in PLATON/SQUEEZE.[156–158] The algorithm found a void of 175 Å^3 with 36 electrons in each unit cell. This approx. corresponds to 0.45 $C_4H_{10}O$ molecules per complex molecule.

Table A.12: Crystallographic data and parameters of **4e** and **4f**.

Compound	**4e** $[Fe(NQu_3)(OTf)_2][Fe(NQu_3)(OTf)_2]_{0.5}\{[Fe(NQu_3)(OTf)(H_2O)](OTf)\}_{0.5}$	**4f** $[Fe(NQu_3)(H_2O)(MeCN)](OTf)_2$
Measurement	SH_01782	SH_01759
Diffractometer	STOE	STOE
Empirical formula	$C_{116}H_{74}F_{24}Fe_4N_{16}O_{25}S_8$	$C_{31}H_{23}F_6FeN_5O_7S_2$
Moiety formula	$C_{57}H_{38}F_9Fe_2N_8O_{10}S_3$, 2 $C_{29}H_{18}F_6FeN_4O_6S_2$, CF_3O_3S	$C_{29}H_{23}FeN_5O$, 2 CF_3O_3S
Formula weight [g mol^{-1}]	3027.79	811.51
Crystal size [mm]	$0.13 \times 0.13 \times 0.05$	$0.19 \times 0.11 \times 0.10$
T [K]	100(2)	100(2)
Crystal system	triclinic	triclinic
Space group (№)	$P\bar{1}$ (2)	$P\bar{1}$ (2)
a [Å]	12.5070(5)	9.8842(3)
b [Å]	13.6895(5)	17.5816(5)
c [Å]	17.3794(6)	19.9270(6)
α [°]	90.416(3)	84.653(3)
β [°]	91.880(3)	77.570(3)
γ [°]	95.491(3)	77.570(3)
V [Å^3]	2960.20(19)	3240.44(18)
Z	1	4
ρ_{calc} [g cm^{-3}]	1.698	1.663
μ [mm^{-1}]	0.742	0.686
λ [Å]	0.71073	0.71073
$F(000)$	1530	1648
hkl range	$-17/17; -18/17; -19/23$	$-14/15; -18/27; -31/31$
Refl. collected	60327	84282
Independent refl.	15884	24921
R_{int}	0.0909	0.0519
№ of parameters	940	1057
R_1 [$I > 2\sigma(I)$]	0.0509	0.0488
wR_2 (all data)	0.1033	0.1245
GoF	0.865	0.848
$\Delta\rho_{max}/\Delta\rho_{min}$ [e Å^{-3}]	$0.582/-0.575$	$0.815/-0.637$
CCDC №	2216552	2216553

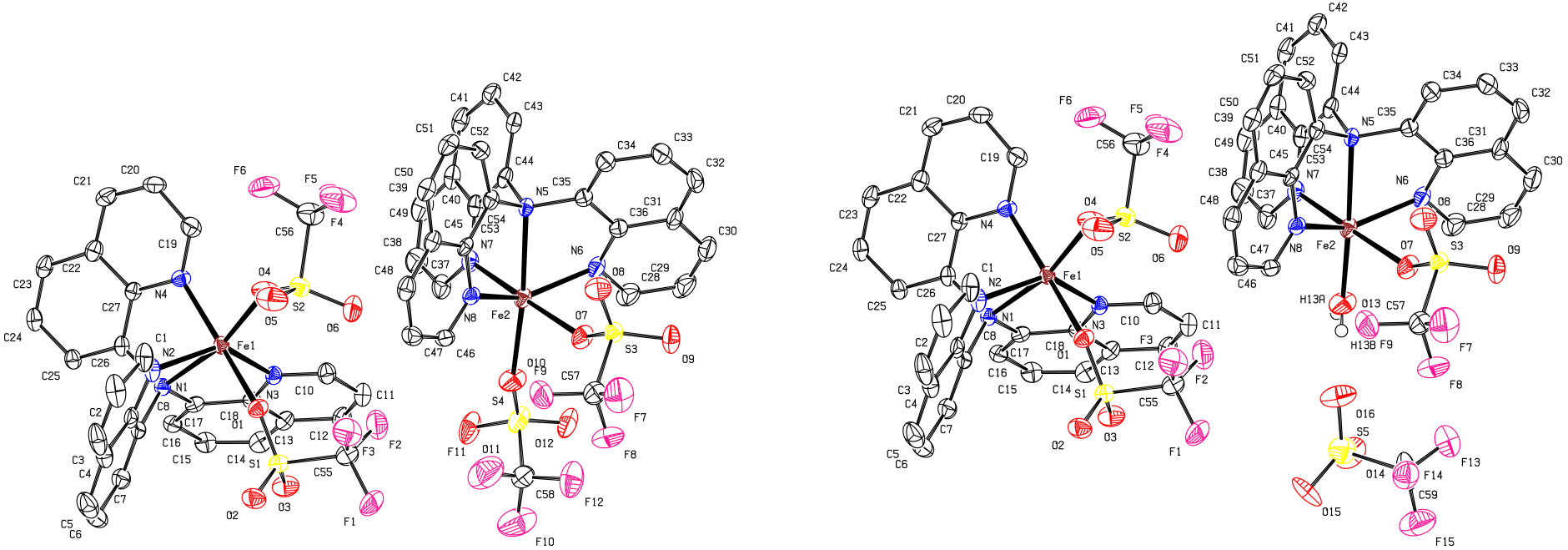

Figure A.32: Molecular structure of **4e** in [LFe(**4**)$(OTf)_2$]- (left) and [LFe(**4**)(OTf)(H_2O)]OTf-coordination (right) mode in the solid state (displacement ellipsoid plot, 50 % probability, asymmetric unit, C bonded hydrogens omitted).

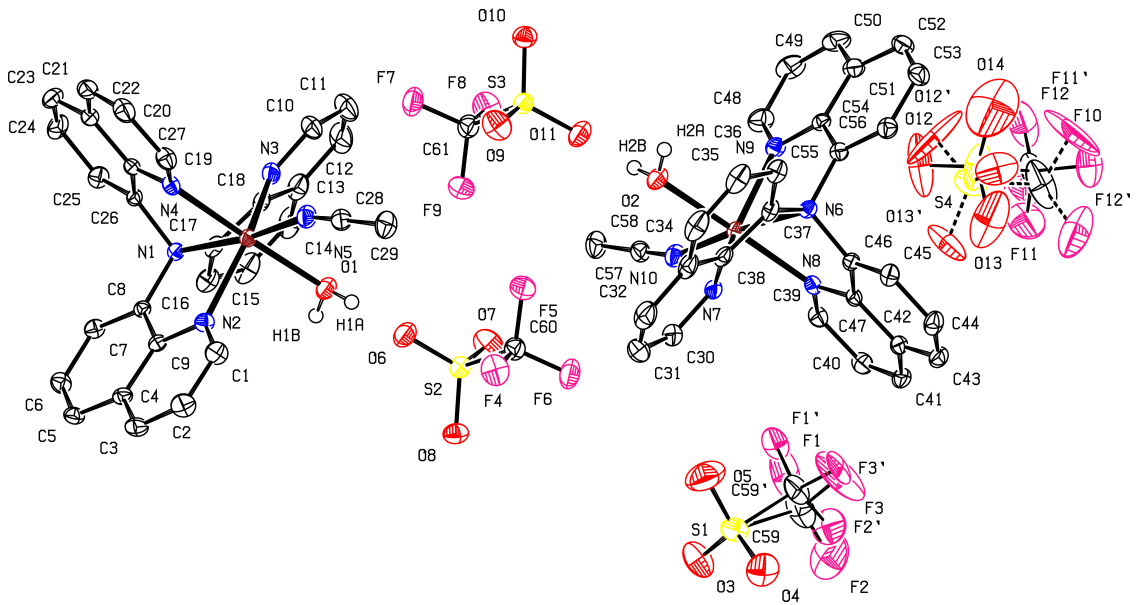

Figure A.33: Molecular structure of **4f** in the solid state (displacement ellipsoid plot, 50 % probability, asymmetric unit, C bonded hydrogens omitted).

Table A.13: Crystallographic data and parameters of **4g**, **4i** and **4j**.

Compound	**4g** $[Fe_2(\mu\text{-}O)(NQu_3)_2(OTf)_2](OTf)_2 \cdot 0.85\,MeCN$	**4i** $[Fe(NQu_3)(OTf)(H_2O)](OTf) \cdot DCM$	**4j** $[Fe(NQu_3)(EtCN)_2](OTf)_2$
Measurement	SH_02342	SH_01723	SH_02323
Diffractometer	STOE	STOE	STOE
Empirical formula	$C_{59.69}H_{38.53}F_{12}Fe_2N_{8.85}O_{13}S_4$	$C_{30}H_{22}Cl_2F_6FeN_4O_7S_2$	$C_{35}H_{28}F_6FeN_6O_6S_2$
Moiety formula	$C_{56}H_{36}F_6Fe_2N_8O_7S_2$, $2\,CF_3O_3S$, $0.85\,C_2H_3N$	$C_{28}H_{20}F_3FeN_4O_4S$,CF_3O_3S, CH_2Cl_2	$C_{33}H_{28}FeN_6$, $2\,CF_3O_3S$
Formula weight [g mol^{-1}]	1555.58	855.38	862.60
Crystal size [mm]	$0.20 \times 0.18 \times 0.15$	$0.18 \times 0.13 \times 0.07$	$0.19 \times 0.12 \times 0.06$
T [K]	100(2)	100(2)	100(2)
Crystal system	monoclinic	monoclinic	monoclinic
Space group (№)	$P2_1/c$ (14)	$C2/c$ (15)	$P2_1/c$ (14)
a [Å]	18.916(4)	31.868(6)	20.978(4)
b [Å]	22.816(5)	12.039(2)	8.7080(17)
c [Å]	14.585(3)	17.671(4)	20.667(4)
α [°]	90	90	90
β [°]	96.10(3)	93.36(3)	112.02(3)
γ [°]	90	90	90
V [Å^3]	6259(2)	6768(2)	3499.9(14)
Z	4	8	4
ρ_{calc} [g cm^{-3}]	1.651	1.679	1.637
μ [mm^{-1}]	0.705	0.814	0.640
λ [Å]	0.71073	0.71073	0.71073
$F(000)$	3146	3456	1760
hkl range	−21/22; −27/27; −17/17	−47/48; −18/18; −27/15	−32/32; −13/13, −25/32
Refl. collected	90103	77117	85664
Independent refl.	11468	12623	13420
R_{int}	0.1272	0.1239	0.1531
№ of parameters	964	486	507
R_1 [$I > 2\sigma(I)$]	0.0804	0.0603	0.0616
wR_2 (all data)	0.2524	0.1528	0.1627
GoF	0.970	0.861	0.916
$\Delta\rho_{max}/\Delta\rho_{min}$ [e Å^{-3}]	1.602/−1.152	0.906/−0.680	0.928/−0.760
CCDC №	2216554	2216555	2216556

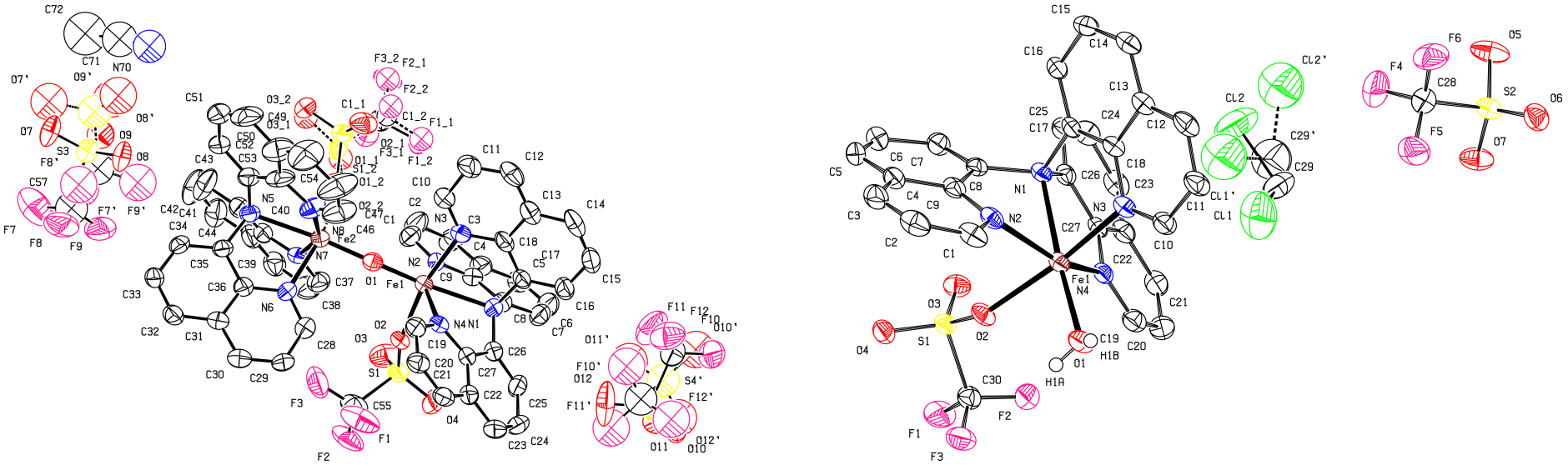

Figure A.34: Molecular structure of **4g** (left) and **4i** (right) in the solid state (displacement ellipsoid plot, 50 % probability, asymmetric unit, C bonded hydrogens omitted).

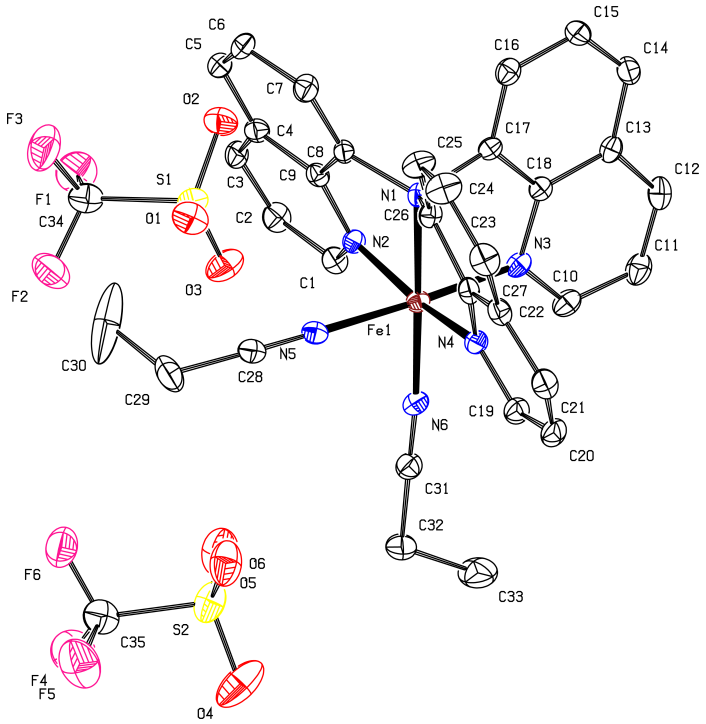

Figure A.35: Molecular structure of **4j** in the solid state (displacement ellipsoid plot, 50 % probability, asymmetric unit, C bonded hydrogens omitted).

Table A.14: Crystallographic data and parameters of **4k**, **4l**, **4m** and **4n**.

Compound	**4k** $[Fe(NQu_3)(OTf)(EtCN)](OTf) \cdot 0.5\,Et_2O$	**4l** $[Fe(NQu_3)(OTf)(MeOH)](OTf)$	**4m** $[Fe(NQu_3)(OTf)(MeOH)](OTf) \cdot MeOH$	**4n** $[Fe(NQu_3)Cl_2] \cdot 0.5\,DCM$
Measurement	SH_02357	SH_01755	SH_02491	SH_02107
Diffractometer	STOE	STOE	STOE	STOE
Empirical formula	$C_{68}H_{56}F_{12}Fe_2N_{10}O_{13}S_4$	$C_{30}H_{22}F_6FeN_4O_7S_2$	$C_{31}H_{26}F_6FeN_4O_8S_2$	$C_{27.5}H_{19}Cl_3FeN_4$
Moiety formula	$2\,C_{31}H_{23}F_3FeN_5O_3S$, $2\,CF_3O_3S$, $C_4H_{10}O$	$C_{29}H_{22}F_3FeN_4O_4S$, CF_3O_3S	$C_{29}H_{22}F_3FeN_4O_4S$, CH_4O, CF_3O_3S	$C_{27}H_{18}Cl_2FeN_4$, $0.5\,CH_2Cl_2$
Formula weight [$g\,mol^{-1}$]	1689.16	784.48	816.53	567.67
Crystal size [mm]	$0.24 \times 0.23 \times 0.22$	$0.29 \times 0.27 \times 0.25$	$0.14 \times 0.11 \times 0.04$	$0.190 \times 0.120 \times 0.040$
T [K]	100(2)	100(2)	100(2)	100(2)
Crystal system	triclinic	monoclinic	triclinic	triclinic
Space group (№)	$P\bar{1}$ (2)	$P2_1/c$ (14)	$P\bar{1}$ (2)	$P\bar{1}$ (2)
a [Å]	10.172(2)	10.1167(3)	10.101(2)	9.4894(3)
b [Å]	12.884(3)	17.5096(3)	11.003(2)	10.7865(3)
c [Å]	14.258(3)	18.0286(4)	15.459(3)	12.8614(3)
α [°]	90.95(3)	90	91.74(3)	83.090(2)
β [°]	103.12(3)	101.0271(18)	95.16(3)	82.821(3)
γ [°]	107.55(3)	90	104.58(3)	76.474(2)
V [$Å^3$]	1727.9(7)	3134.61(13)	1653.4(6)	1264.24(6)
Z	1	4	2	2
ρ_{calc} [$g\,cm^{-3}$]	1.623	1.662	1.640	1.491
μ [mm^{-1}]	0.646	0.705	0.674	0.938
λ [Å]	0.71073	0.71073	0.71073	0.71073
$F(000)$	862	1592	832	578
hkl range	$-16/13; -11/20; -22/22$	$-6/15; -25/26; -27/27$	$-9/15; -16/16; -24/23$	$-15/14; -10/17; -20/20$
Refl. collected	41040	71310	39755	50196
Independent refl.	13233	11409	12308	10500
R_{int}	0.0496	0.0245	0.0855	0.0483
№ of parameters	517	492	477	307
R_1 [$I > 2\sigma(I)$]	0.0524	0.0303	0.0539	0.0393
wR_2 (all data)	0.1326	0.0843	0.1146	0.0955
GoF	0.914	1.031	0.884	0.967
$\Delta\rho_{max}/\Delta\rho_{min}$ [$e\,Å^{-3}$]	0.634/−0.615	0.512/−0.446	0.890/−0.531	0.686/−0.539
CCDC №	2216557	2216558	2216559	2216560

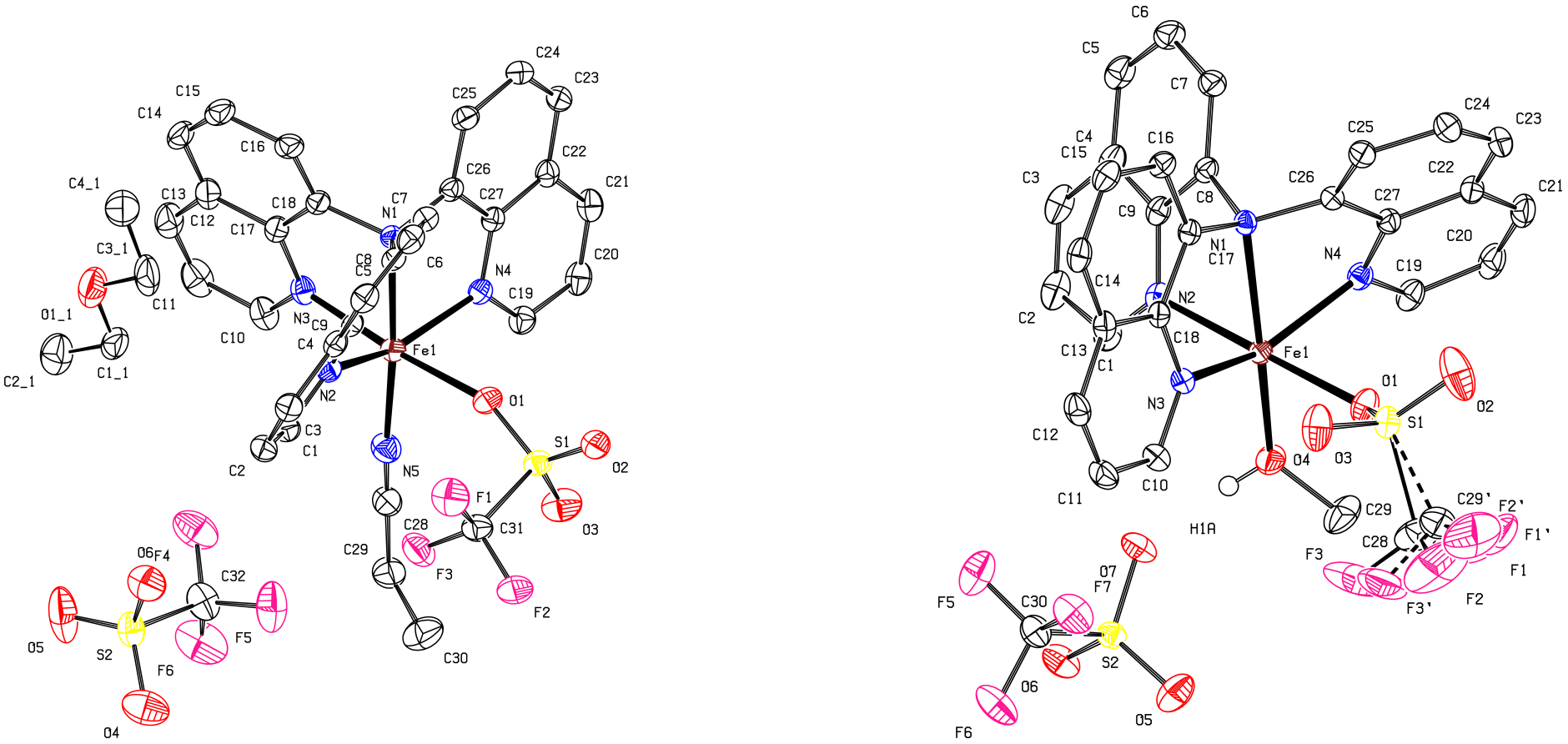

Figure A.36: Molecular structure of **4k** (left) and **4l** (right) in the solid state (displacement ellipsoid plot, 50 % probability, asymmetric unit, C bonded hydrogens omitted).

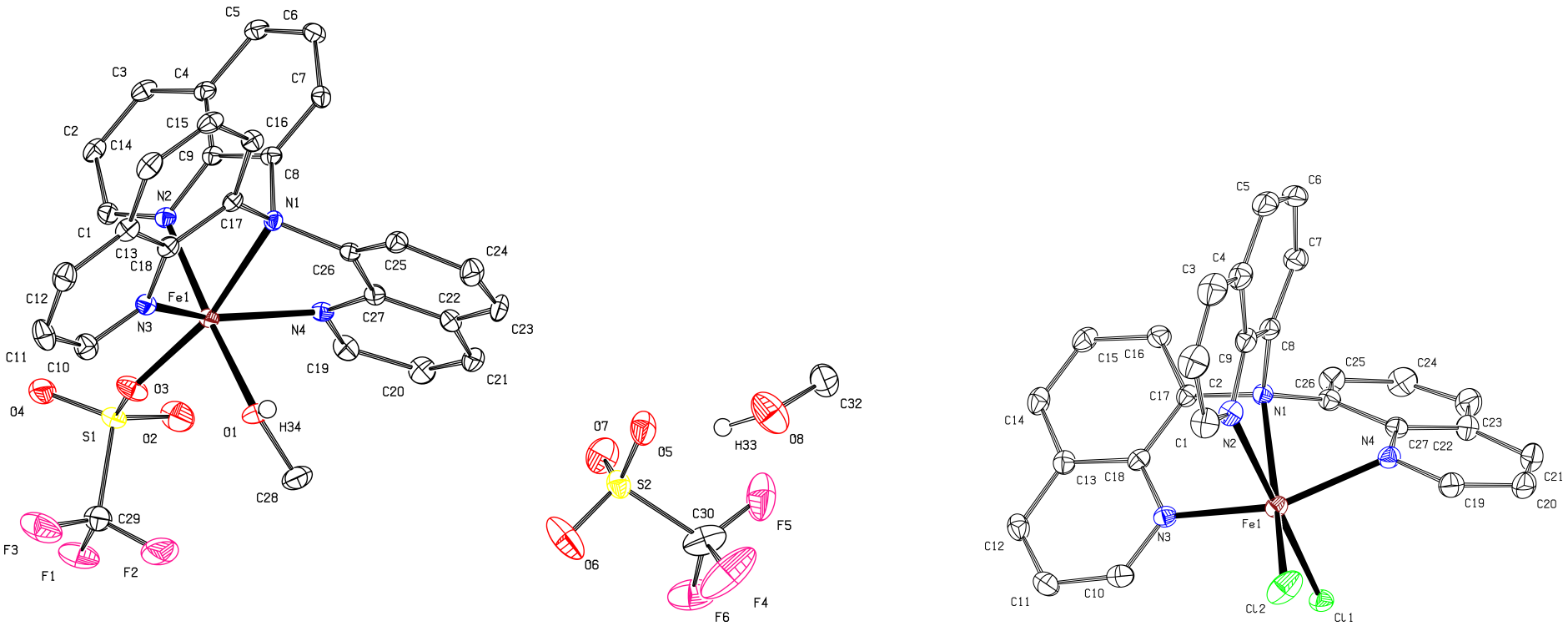

Figure A.37: Molecular structure of **4m** (left) and **4n** (right) in the solid state (displacement ellipsoid plot, 50 % probability, asymmetric unit, C bonded hydrogens omitted).

Note: In **4n** it was not possible to model the disordered solvent molecules in an adequate manner, and the data set was treated with the BYPASS algorithm as implemented in PLATON/SQUEEZE.[156–158] The algorithm found a void of 211 Å^3 with 55 electrons in each unit cell. Considered the solvent used, this approx. corresponds to one molecules of CH_2Cl_2 per unit cell.

Table A.15: Crystallographic data and parameters of **4o**, **4p** and **4q**.

Compound	**4o** $[Fe(NQu_3)Br_2] \cdot 0.5\,DCM$	**4p** $[Fe(NQu_3)Cl](PF_6) \cdot 1.5\,DCM$	**4q** $[Fe(NQu_3)(MeCN)_2](BF_4)_2 \cdot 0.5\,MeCN$
Measurement	SH_02113	SH_02041	SH_01694
Diffractometer	STOE	STOE	STOE
Empirical formula	$C_{27.5}H_{19}Br_2ClFeN_4$	$C_{28.50}H_{21}Cl_4F_6FeN_4P$	$C_{32}H_{25.5}B_2F_8FeN_{6.5}$
Moiety formula	$C_{27}H_{18}Br_2FeN_4$,0.5 CH_2Cl_2	$C_{27}H_{18}ClFeN_4P$, F_6P, 1.5 CH_2Cl_2	$C_{31}H_{24}FeN_6$, 2 BF_4, 0.5 C_2H_3N
Formula weight [g mol^{-1}]	656.59	762.11	730.56
Crystal size [mm]	$0.08 \times 0.05 \times 0.02$	$0.15 \times 0.11 \times 0.09$	$0.17 \times 0.13 \times 0.09$
T [K]	100(2)	100(2)	100(2)
Crystal system	triclinic	orthorhombic	triclinic
Space group (№)	$P\bar{1}$ (2)	*Pbcn* (60)	$P\bar{1}$ (2)
a [Å]	9.6295(19)	16.169(3)	11.4013(6)
b [Å]	10.997(2)	15.022(3)	12.3974(7)
c [Å]	12.947(3)	25.360(5)	12.6712(6)
α [°]	82.39(3)	90	71.334(4)
β [°]	82.80(3)	90	76.707(4)
γ [°]	76.18(3)	90	66.210(4)
V [Å^3]	1313.4(5)	6160(2)	1542.11(15)
Z	2	8	2
ρ_{calc} [g cm^{-3}]	1.660	1.644	1.573
μ [mm^{-1}]	3.742	8.195	0.574
λ [Å]	0.71073	1.54178	0.71073
$F(000)$	650	3064	742
hkl range	−12/12; −9/14; −17/17	−19/9; −15/18; −30/29	−17/17; −18/18; −11/19
Refl. collected	30209	73361	19252
Independent refl.	6491	5610	10844
R_{int}	0.1401	0.1872	0.0273
№ of parameters	302	436	474
R_1 $[I > 2\sigma(I)]$	0.0747	0.0599	0.0476
wR_2 (all data)	0.2127	0.1704	0.1266
GoF	0.987	0.930	1.002
$\Delta\rho_{max}/\Delta\rho_{min}$ [e Å^{-3}]	0.924/−1.978	0.554/−0.449	1.086/−0.913
CCDC №	2216561	2216562	2216563

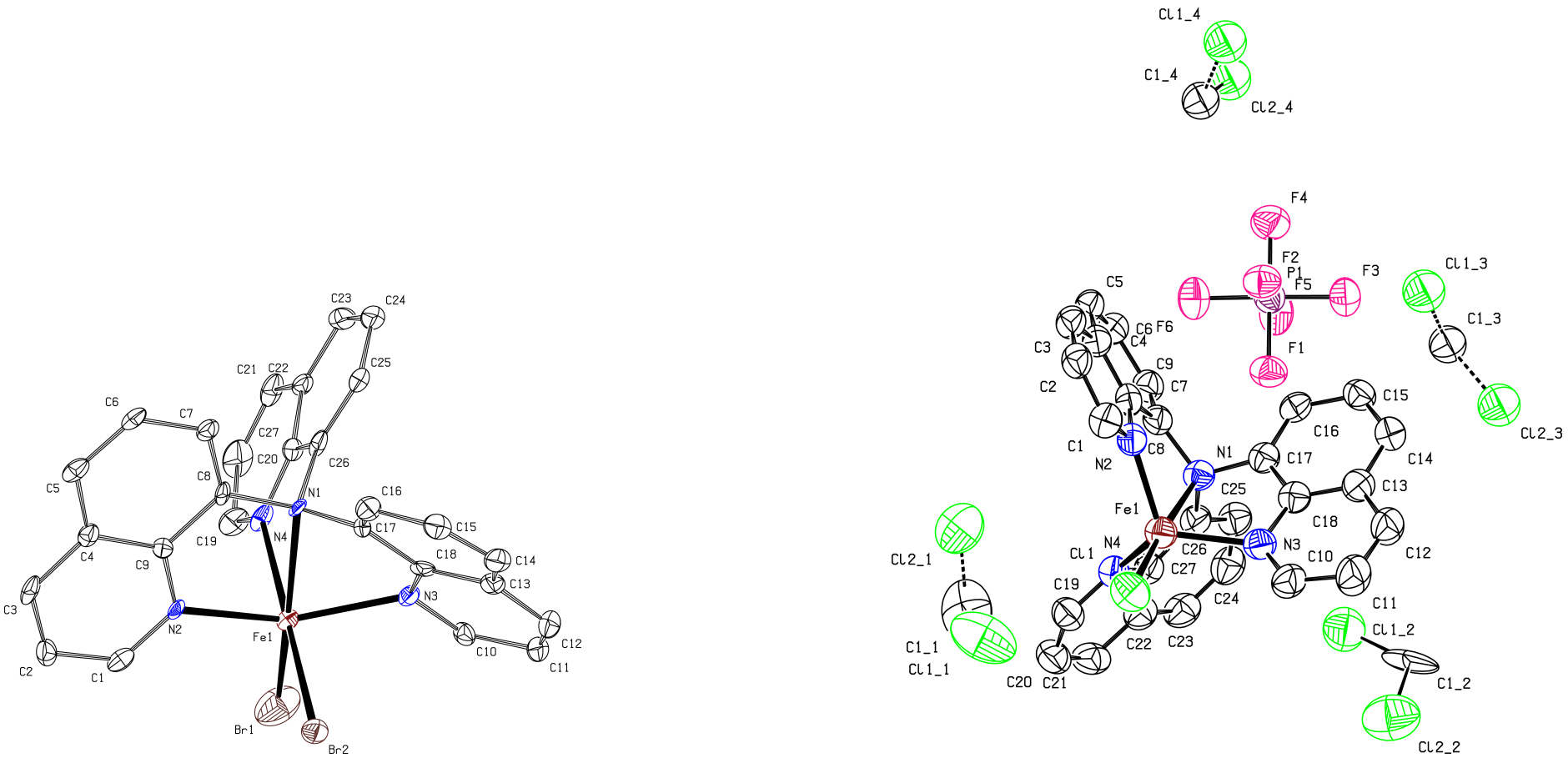

Figure A.38: Molecular structure of **4o** (left) and **4p** (right) in the solid state (displacement ellipsoid plot, 50 % probability, asymmetric unit, C bonded hydrogens omitted).

Note: In **4o** it was not possible to model the disordered solvent molecules in an adequate manner, and the data set was treated with the BYPASS algorithm as implemented in PLATON/SQUEEZE.[156–158] The algorithm found a void of 229 Å^3 with 42 electrons in each unit cell. Considered the solvent used, this approx. corresponds to one molecules of CH_2Cl_2 per unit cell.

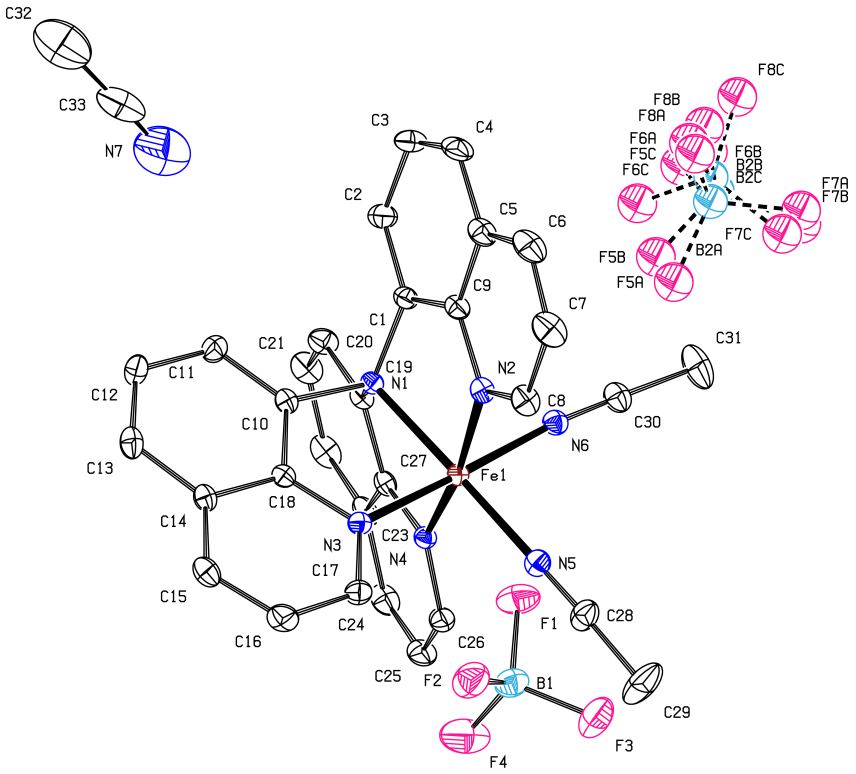

Figure A.39: Molecular structure of **4q** in the solid state (STOE (100 K), displacement ellipsoid plot, 50 % probability, asymmetric unit, C bonded hydrogens omitted).

Table A.16: Crystallographic data and parameters of **4q**.

Compound	**4q** $[Fe(NQu_3)(MeCN)_2](BF_4)_2 \cdot 0.5\,MeCN$	**4q** $[Fe(NQu_3)(MeCN)_2](BF_4)_2 \cdot 0.5\,MeCN$	**4q** $[Fe(NQu_3)(MeCN)_2](BF_4)_2 \cdot 0.5\,MeCN$
Measurement	h21_a01	h21_a02	h21_a03
Diffractometer	Bruker	Bruker	Bruker
Empirical formula	$C_{32}H_{25.5}B_2F_8FeN_{6.5}$	$C_{32}H_{25.5}B_2F_8FeN_{6.5}$	$C_{32}H_{25.5}B_2F_8FeN_{6.5}$
Moiety formula	$C_{31}H_{24}FeN_6$, 2 BF_4, 0.5 C_2H_3N	$C_{31}H_{24}FeN_6$, 2 BF_4, 0.5 C_2H_3N	$C_{31}H_{24}FeN_6$, 2 BF_4, 0.5 C_2H_3N
Formula weight [g mol^{-1}]	730.56	730.56	730.56
Crystal size [mm]	$0.53 \times 0.10 \times 0.14$	$0.53 \times 0.10 \times 0.14$	$0.53 \times 0.10 \times 0.14$
T [K]	100(2)	250(2)	273(2)
Crystal system	triclinic	triclinic	triclinic
Space group (№)	$P\bar{1}$ (2)	$P\bar{1}$ (2)	$P\bar{1}$ (2)
a [Å]	11.401(6)	11.481(2)	11.493(3)
b [Å]	12.413(7)	12.542(3)	12.556(3)
c [Å]	12.686(7)	12.793(3)	12.815(3)
α [°]	71.279(9)	71.333(3)	71.329(5)
β [°]	76.718(11)	76.987(3)	77.046(5)
γ [°]	66.252(9)	66.439(3)	66.440(5)
V [Å^3]	1545.9(14)	1589.7(5)	1596.0(6)
Z	2	2	2
ρ_{calc} [g cm^{-3}]	1.569	1.526	1.520
μ [mm^{-1}]	0.573	0.557	0.555
λ [Å]	0.71073	0.71073	0.71073
$F(000)$	742	742	742
hkl range	−13/13; −15/15; −15/15	−15/15; −16/16; −17/17	−15/15; −16/16; −17/16
Refl. collected	17975	21884	22140
Independent refl.	5934	7968	7928
R_{int}	0.1343	0.0961	0.1666
№ of parameters	457	457	457
R_1 [$I > 2\sigma(I)$]	0.0703	0.0789	0.0813
wR_2 (all data)	0.1775	0.2280	0.2245
GoF	0.985	1.062	0.982
$\Delta\rho_{max}/\Delta\rho_{min}$ [e Å^{-3}]	0.589/−0.739	0.855/−0.450	0.631/−0.471
CCDC №	2216564	2216565	2216566

Table A.17: Crystallographic data and parameters of **4r** and H_3(**4**)$(OTf)_3 \cdot DCM$.

Compound	**4r** $[Fe(NQu_3)(NCS)_2] \cdot 0.5\,Et_2O$	H_3(**4**)$(OTf)_3 \cdot DCM$ $H_3(NQu_3)(OTf)_3 \cdot DCM$
Measurement	h20_27	SH_02231
Diffractometer	Bruker	STOE
Empirical formula	$C_{31}H_{23}FeN_6S_2O_{0.5}$	$C_{31}H_{23}Cl_2F_9N_4O_9S_3$
Moiety formula	$C_{29}H_{18}FeN_6S_2$, $0.5\,C_4H_{10}O$	$C_{27}H_{21}N_4$, $3\,CF_3O_3S$, CH_2Cl_2
Formula weight [g mol^{-1}]	607.53	933.61
Crystal size [mm]	$0.44 \times 0.12 \times 0.04$	$0.10 \times 0.07 \times 0.03$
T [K]	200(2)	100(2)
Crystal system	monoclinic	triclinic
Space group (№)	$C2/c$ (15)	$P\bar{1}$ (2)
a [Å]	9.9526(11)	8.9112(18)
b [Å]	22.431(3)	12.741(3)
c [Å]	25.713(3)	16.966(3)
α [°]	90	86.34(3)
β [°]	95.578(2)	76.01(3)
γ [°]	90	77.97(3)
V [Å^3]	5713.2(12)	1827.9(7)
Z	8	2
ρ_{calc} [g cm^{-3}]	1.326	1.696
μ [mm^{-1}]	0.702	0.455
λ [Å]	0.71073	0.71073
$F(000)$	2336	944
hkl range	$-12/12; -28/28; -32/32$	$-11/11; -11/16; -22/21$
Refl. collected	34165	38946
Independent refl.	5889	8364
R_{int}	0.0825	0.1103
№ of parameters	343	532
R_1 $[I > 2\sigma(I)]$	0.0561	0.0549
wR_2 (all data)	0.1301	0.1095
GoF	1.042	0.879
$\Delta\rho_{max}/\Delta\rho_{min}$ [e Å^{-3}]	0.398/−0.342	0.629/−0.502
CCDC №	n.d.	2216547

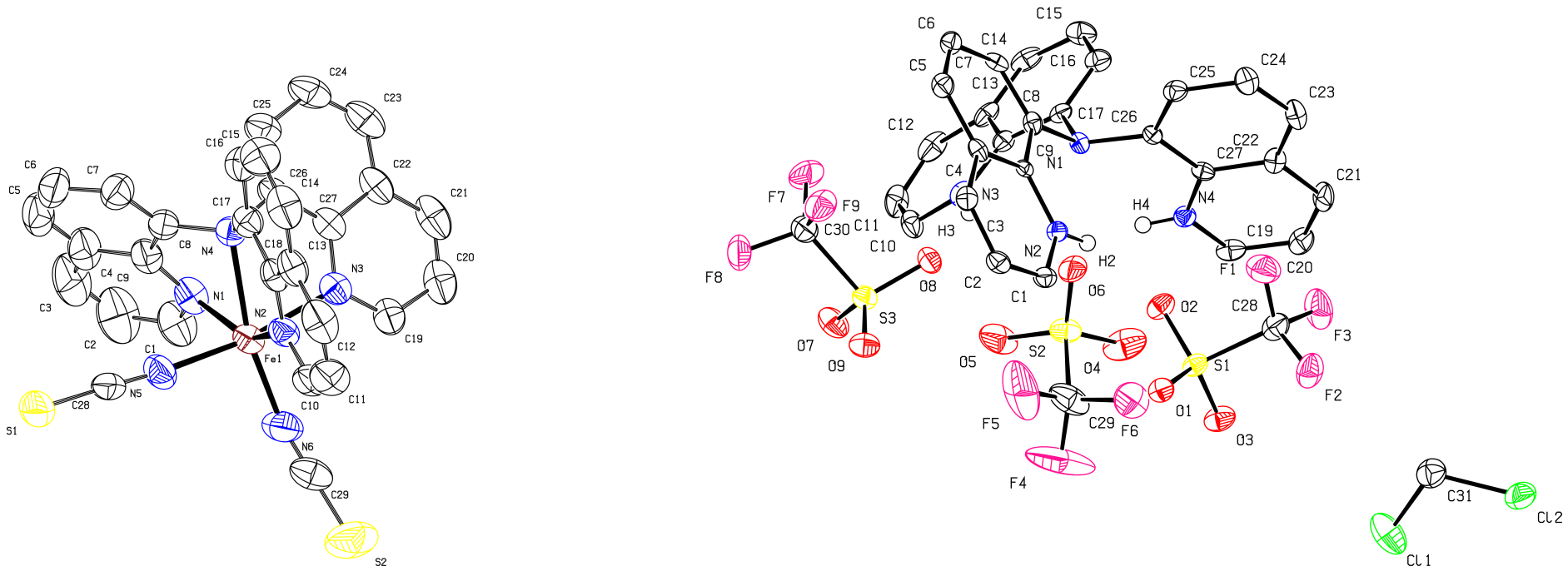

Figure A.40: Molecular structure of **4r** (left) and H_3(**4**)$(OTf)_3 \cdot$ DCM (right) in the solid state (displacement ellipsoid plot, 50 % probability, asymmetric unit, C bonded hydrogens omitted).

Note: In **4r** it was not possible to model the disordered diethyl ether solvent molecules in an adequate manner, and the data set was treated with the BYPASS algorithm as implemented in PLATON/SQUEEZE.[156–158] The algorithm found a total volume of 815 Å^3 with 174 electrons in each unit cell. This approx. corresponds to 0.5 $C_4H_{10}O$ molecules per complex molecule.

A.6 *x,y,z* Data for CSM Analysis

Table A.18: *x,y,z* Data for CSM Analysis.

Complex	Atom	*x*	*y*	*z*	Complex	Atom	*x*	*y*	*z*
1a	Fe1	8.106656	0.707259	5.729422	**1b**	Fe1	−0.259824	5.376550	10.357492
	N	7.235652	0.826895	7.456132		N	−1.392059	5.392787	8.779383
	N	6.311286	0.530032	4.936928		N	1.124192	6.249734	9.277744
	N	7.911958	2.630828	5.560794		N	0.456374	3.669119	9.688066
	N	8.977660	0.587624	4.002712		N	0.872410	5.360313	11.935600
	N	9.902025	0.884487	6.521916		N	−1.643840	4.503366	11.437239
	N	8.301353	−1.216309	5.898050		N	−0.976023	7.083981	11.026917
	Fe2	6.725051	6.100144	0.000000		Fe2	7.806576	5.376550	10.357492
	N	5.924972	4.535738	0.826744		N	7.015256	6.384890	8.908789
	N	6.648605	6.946193	1.783409		N	6.973457	6.509120	11.754510
	N	4.917132	6.770551	−0.295008		N	8.597895	4.368210	11.806194
	N	7.525131	7.664550	−0.826744		N	9.341002	6.575101	10.430678
	N	6.801497	5.254095	−1.783409		N	6.272150	4.177999	10.284306
	N	8.532970	5.429737	0.295008		N	8.639694	4.243980	8.960473
1c	Fe1	7.927278	6.690422	0.000000	**1d**	Fe1	5.683992	14.496059	6.963669
	N	6.543232	7.337213	1.205723		N	5.717327	13.463145	8.607666
	N	9.140719	6.605859	1.518551		N	7.480270	13.841303	6.581823
	N	7.366255	4.854172	0.492415		N	5.001423	12.884833	6.109881
	N	9.311323	6.043630	−1.205723		N	5.650657	15.528973	5.319672
	N	6.713836	6.774984	−1.518551		N	3.887714	15.150814	7.345515
	N	8.488300	8.526671	−0.492415		N	6.366561	16.107285	7.817457
	Fe2	0.635663	12.435748	7.039322		Fe1’	5.683992	14.496059	6.963669
	N	2.158252	11.405014	7.674241		N	5.717327	13.463145	8.607666
	N	−0.472571	10.871645	7.305451		N	4.919493	12.941462	5.987014
	N	1.036976	11.734551	5.248462		N	7.439401	13.718117	6.579038
	N	−0.886925	13.466482	6.404404		N	5.650657	15.528973	5.319672
	N	1.743898	13.999852	6.773194		N	6.448491	16.050656	7.940324
	N	0.234351	13.136945	8.830182		N	3.928583	15.274000	7.348300
	Fe2’	0.635663	12.435748	7.039322		Fe2	0.115778	4.200667	13.927338
	N	2.158252	11.405014	7.674241		N	−0.640379	5.768664	14.882169
	N	−0.382584	10.802382	7.355810		N	1.879961	4.967299	14.310187
	N	1.031727	11.825542	5.228823		N	0.074021	3.160933	15.568369
	N	−0.886925	13.466482	6.404404		N	0.871935	2.632670	12.972508
	N	1.653911	14.069115	6.722834		N	−1.648405	3.434035	13.544490
	N	0.239600	13.045955	8.849822		N	0.157535	5.240401	12.286308
1f	Cu	3.081423	9.731951	7.597181		Fe2’	0.115778	4.200667	13.927338
	N	2.193205	11.003162	8.884366		N	−0.640379	5.768664	14.882169
	N	2.254363	10.876850	6.187590		N	1.879961	4.967299	14.310187
	N	4.705083	11.290248	7.596708		N	0.074021	3.160933	15.568369
	Br	3.829511	8.308902	9.455820		N	0.871935	2.632670	12.972508
	Br	4.022891	8.210472	5.950602		N	−1.648405	3.434035	13.544490
	Br	0.753520	7.827571	7.855942		N	0.157535	5.240401	12.286308
	Cu	2.674018	6.463812	8.280616	**1e**	Zn	2.704356	11.207162	8.566740
	N	2.077262	5.305378	10.114803		N	1.200519	12.544731	7.805662
	N	4.328490	5.343041	8.381800		N	3.264781	12.880199	9.723880
	N	1.878492	4.929724	7.251897		N	4.170766	9.830259	9.379453
	Br	0.753520	7.827571	7.855942		N	3.945031	12.110811	7.095668
	Br	3.829511	8.308902	9.455820		N	2.156791	9.515660	7.435157
	Br	4.022891	8.210472	5.950602		N	1.403127	10.360806	10.011666
1g, 4-fold	Cu1	10.393410	8.969035	5.854042	**1h**, 4-fold	Cu1	8.051957	7.240155	−0.111531
	Cl	8.629439	9.569950	4.592289		N	9.132138	7.964140	−1.619704
	N	9.293184	8.196530	7.327945		O	6.672651	6.546540	1.105475

Continuation of Table A.18

Complex	Atom	x	y	z	Complex	Atom	x	y	z
	O	12.016804	8.415305	6.718515		O	6.407189	7.775119	−0.968021
	O	11.795668	9.697062	4.654774		Br	9.937155	6.651617	1.232999
	Cu2_Pz	13.429774	9.037374	5.571383		Cu2_Pz	5.015622	7.189523	0.227300
	N	14.511533	9.356798	4.015471		N	3.979981	6.797422	1.799189
	O	12.016804	8.415305	6.718515		O	6.672651	6.546540	1.105475
	O	11.795668	9.697062	4.654774		O	6.407189	7.775119	−0.968021
	Cl	15.146428	8.193538	6.752175		Br	3.162102	8.104323	−0.975873
	Cu2_Py	13.429774	9.037374	5.571383		Cu2_Py	5.015622	7.189523	0.227300
	N	14.514931	9.325222	3.892192		N	3.935270	6.830806	1.876299
	O	11.795668	9.697062	4.654774		O	6.672651	6.546540	1.105475
	O	12.016804	8.415305	6.718515		O	6.407189	7.775119	−0.968021
	Cl	15.146428	8.193538	6.752175		Br	3.162102	8.104323	−0.975873
1g, 5-fold	Cu1	10.393410	8.969035	5.854042	**1h**, 5-fold	Cu1	8.051957	7.240155	−0.111531
	N	9.293184	8.196530	7.327945		N	9.132138	7.964140	−1.619704
	O	12.016804	8.415305	6.718515		O	6.672651	6.546540	1.105475
	O	11.795668	9.697062	4.654774		O	6.407189	7.775119	−0.968021
	O	10.226240	11.330436	6.856943		O	8.232539	4.751627	−1.105475
	Cl	8.629439	9.569950	4.592289		Br	9.937155	6.651617	1.232999
	Cu2_Pz	13.429774	9.037374	5.571383		Cu2_Pz	5.015622	7.189523	0.227300
	N	14.511533	9.356798	4.015471		N	3.979981	6.797422	1.799189
	O	12.016804	8.415305	6.718515		O	6.672651	6.546540	1.105475
	O	11.795668	9.697062	4.654774		O	6.407189	7.775119	−0.968021
	Cl	13.392469	11.457548	6.919429		Br	4.968035	4.646550	−1.232999
	Cl	15.146428	8.193538	6.752175		Br	3.162102	8.104323	−0.975873
	Cu2_Py	13.429774	9.037374	5.571383		Cu_Py	5.015622	7.189523	0.227300
	N	14.514931	9.325222	3.892192		N	3.935270	6.830806	1.876299
	O	11.795668	9.697062	4.654774		O	6.672651	6.546540	1.105475
	O	12.016804	8.415305	6.718515		O	6.407189	7.775119	−0.968021
	Cl	13.392469	11.457548	6.919429		Br	4.968035	4.646550	−1.232999
	Cl	15.146428	8.193538	6.752175		Br	3.162102	8.104323	−0.975873
2b	Fe	6.484811	12.880233	5.723467	**2c**	Fe1	2.373491	7.130531	11.644052
	N	7.154297	14.436613	4.724295		N	2.681200	6.638670	9.549608
	N	4.986753	14.019794	6.252645		N	0.307788	7.094649	10.980681
	N	7.267858	13.504176	7.348460		N	1.922327	5.076126	11.890308
	N	6.169872	11.230800	6.849597		N	2.558946	6.827019	13.801126
	N	8.066007	11.894633	5.125345		Cl	2.693550	9.510493	11.768849
	N	5.504245	12.134359	4.219506		Cl	4.995552	6.978425	11.850182
2d	Fe1	8.561394	9.353749	3.427186		Fe2	5.113476	9.337435	11.811911
	N	8.054072	7.300596	3.659891		Cl	2.693550	9.510493	11.768849
	N	6.453613	9.574291	4.026344		Cl	5.846925	9.948835	9.751349
	N	7.428251	9.285880	1.601955		Cl	5.938829	10.339954	13.632771
	N	8.960687	11.262990	2.444601		Cl	4.995552	6.978425	11.850182
	Cl	10.455136	8.608840	2.234215	**3a**	Fe	2.094414	3.295367	9.527286
	O	9.183667	9.837725	5.051634		N	0.974449	4.579766	8.146946
	Fe2	9.341866	9.728957	6.812981		N	2.983539	5.192701	9.925647
	Cl	7.597867	10.674392	7.858743		N	0.559552	3.887350	10.883325
	Cl	9.503469	7.604375	7.443046		O	1.594587	1.610089	8.449157
	Cl	11.153763	10.787639	7.589300		O	4.220886	3.074816	8.941868
	O	9.183667	9.837725	5.051634		O	2.803561	2.052292	11.149854
3b	Fe1	10.174446	3.576322	5.363559	**3c**	Fe	2.621910	4.915774	3.254931
	N	10.646203	4.744231	3.598848		N	3.950777	6.617188	3.774955
	N	8.752909	5.194349	5.526618		N	4.388214	4.519650	2.113850
	N	8.498158	2.852164	4.253013		N	3.660045	4.049291	4.926598
	O	9.341588	2.109823	6.541126		Cl	1.686278	2.738199	2.623574
	O	11.340309	2.293475	4.243843		Cl	0.728549	5.884161	4.158700
	O	11.420469	4.067442	6.582511		O1	2.075945	5.327046	1.046582

Continuation of Table A.18

Complex	Atom	*x*	*y*	*z*	Complex	Atom	*x*	*y*	*z*
	Fe2	9.332509	−1.236084	7.717979		Fe	2.621910	4.915774	3.254931
	N	9.573491	−2.665302	9.330440		N	3.950777	6.617188	3.774955
	N	7.368620	−2.141546	7.709020		N	4.388214	4.519650	2.113850
	N	8.553916	−0.168515	9.453831		N	3.660045	4.049291	4.926598
	O	8.390879	0.079347	6.413268		Cl	1.686278	2.738199	2.623574
	O	10.736055	0.170611	8.209455		Cl	0.728549	5.884161	4.158700
	O	10.397351	−2.069705	6.524740		O2	2.512882	5.536429	0.915439
	Fe3	12.459982	3.177170	7.783784	**3d**	Fe	4.292903	5.413783	6.312139
	N	12.399571	4.339364	9.612899		N	4.239867	7.524950	5.946959
	N	14.308614	4.307429	7.613774		N	3.039505	5.340893	4.603026
	N	13.927021	1.919363	8.797525		N	2.583364	5.840438	7.451501
	O	12.701996	1.539496	6.583542		N	6.294529	5.159121	5.718384
	O	10.965746	2.278373	8.889599		O	4.860742	5.016931	8.428181
	O	11.420469	4.067442	6.582511		O	4.209329	3.272331	6.354662
	Fe4	11.666019	−1.586854	5.327644	**3e**	Fe	1.822413	3.259541	9.603967
	N	12.704483	−0.828381	3.575169		N	0.510757	3.977036	8.060703
	N	13.226560	−3.098535	5.292654		N	2.865250	5.077116	9.154523
	N	10.921770	−2.841203	3.731832		N	2.849135	2.501896	7.887200
	O	10.397351	−2.069705	6.524740		O	1.963738	1.083105	9.913020
	O	10.812484	0.227024	4.900863		Cl	0.550469	3.603637	11.473481
	O	12.992959	−0.676703	6.624558		F	3.756086	2.955035	10.854095
4a	Fe	4.863188	5.711185	3.413862	**4b**	Fe	3.184246	3.344841	10.887056
	N	4.138791	7.558695	3.002127		N	3.381432	1.170030	11.599705
	N	2.992850	5.245682	3.679624		N	1.990380	2.170683	9.553531
	N	4.723066	5.390095	1.495796		N	1.750843	3.236739	12.484841
	N	6.608955	6.564123	3.266867		N	4.848594	3.447138	12.181776
	N	4.986915	6.146009	5.320371		N	2.805843	5.350404	10.425862
	N	5.555267	3.951675	3.768933		O	4.651742	3.240093	9.196140
4c	Fe1	11.047836	3.212394	4.579637	**4d**	Fe1	−1.029077	−1.094594	14.648677
	N	11.047836	1.052638	5.305119		N	−2.703417	−2.638054	14.859880
	N	13.068188	3.273434	5.158761		N	−0.051387	−2.931676	15.172539
	N	10.340197	3.269295	6.600712		N	−1.839605	−0.680136	16.613656
	N	9.335105	2.079433	3.942836		N	−2.637845	−0.114810	13.713763
	O	11.614554	2.840412	2.517647		O	0.298602	0.423149	14.814107
	O	10.887090	5.238103	4.360100		O	−0.416313	−1.777799	12.650540
	Fe1'	11.047836	3.212394	4.579637		Fe2	1.452872	6.314750	12.455376
	N	11.411659	1.052638	5.305119		N	2.903403	7.138147	10.890818
	N	13.068188	3.273434	5.158761		N	0.355258	7.829174	11.298627
	N	10.340197	3.269295	6.600712		N	3.329236	5.618272	13.166473
	N	9.335105	2.079433	3.942836		N	1.380879	4.815533	10.912983
	O	11.614554	2.840412	2.517647		O	0.228726	5.197127	13.668531
	O	10.159888	4.971701	4.214103		O	1.361135	7.849856	13.930912
	Fe2	5.149375	10.488832	4.448239	**4f**	Fe1	5.417178	4.441717	−1.119651
	N	6.004114	11.741060	2.685454		N	4.412591	3.902464	0.885102
	N	3.416917	11.057478	3.370381		N	7.075080	4.140865	0.167257
	N	5.608110	8.982617	3.008812		N	3.331695	4.939003	−1.321333
	N	7.209321	10.915675	4.944631		N	5.105980	2.340128	−1.318221
	O	4.310346	9.124365	5.793039		N	6.249446	4.704861	−3.030663
	O	4.637669	11.967502	5.910919		O	5.681249	6.559720	−0.968536
4e	Fe1	0.689860	4.166450	5.622376		Fe2	11.769032	12.751330	10.792957
	N	−0.432188	2.176471	5.108077		N	12.607515	13.262290	8.715077
	N	0.700493	2.999605	7.407398		N	13.856155	12.180848	10.826019
	N	1.031085	3.949652	3.575602		N	12.159174	14.851152	10.949712
	N	−1.370421	4.699025	5.787557		N	10.007913	13.065112	9.647439
	O	2.878519	3.754266	5.841748		N	11.024634	12.468544	12.735864
	O	1.161968	6.100751	6.053130		O	11.459307	10.634692	10.622588
	Fe2	5.427493	9.707702	2.901681	**4g**	Fe1	13.950159	9.559220	9.121006

Continuation of Table A.18

Complex	Atom	x	y	z	Complex	Atom	x	y	z
	N	4.517413	11.669374	3.725324		N	15.882304	9.751558	9.908053
	N	5.541586	11.117263	1.283750		N	13.339162	8.373472	10.747743
	N	3.326828	9.359786	2.721737		N	14.845904	7.453987	8.720304
	N	5.611602	9.437063	4.975551		N	14.713550	9.735587	7.197551
	O	7.612448	10.087349	2.914013		O	12.153042	8.940678	8.247526
	O10	6.045618	7.785755	2.136399		O	13.396075	11.202656	9.542592
	Fe2	5.427493	9.707702	2.901681		Fe2	12.843118	12.903132	9.493428
	N	4.517413	11.669374	3.725324		N	11.956905	15.044870	9.468629
	N	5.541586	11.117263	1.283750		N	10.935197	12.567053	10.285115
	N	3.326828	9.359786	2.721737		N	11.979059	13.069005	7.615220
	N	5.611602	9.437063	4.975551		N	13.386725	13.707853	11.329290
	O	7.612448	10.087349	2.914013		O	14.547460	13.739795	8.610086
	O13	6.038476	7.990156	2.136399		O	13.396075	11.202656	9.542592
4i	Fe	11.880391	7.750588	6.014218		Fe2'	12.843118	12.903132	9.493428
	N	10.006379	8.848906	5.257259		N	11.956905	15.044870	9.468629
	N	10.568165	7.955251	7.722359		N	10.935197	12.567053	10.285115
	N	12.453281	9.788068	6.260128		N	11.979059	13.069005	7.615220
	N	12.136945	7.668121	3.924157		N	13.386725	13.707853	11.329290
	O	13.642729	6.866925	6.659512		O	14.549888	13.484256	8.817471
	O	11.170377	5.696855	6.095541		O	13.396075	11.202656	9.542592
4j	Fe	11.076021	4.949801	9.830308	**4k**	Fe	2.526339	2.503811	2.366989
	N	12.894773	4.615240	10.653587		N	3.386289	3.947872	3.659720
	N	10.702530	3.126172	10.429614		N	0.748970	2.266206	3.574958
	N	11.853421	4.306977	8.176276		N	1.590428	2.045652	0.545633
	N	11.766822	6.737380	9.484863		N	3.401185	0.677334	2.871139
	N	10.351744	5.535676	11.543350		N	1.372063	4.438115	1.939305
	N	9.327939	5.273565	9.083857		O	4.312629	3.031026	1.058079
4l	Fe	2.012379	11.256221	5.187505	**4m**	Fe	0.214293	6.092523	12.763325
	N	0.786574	12.566815	3.784587		N	0.808891	7.334433	14.421155
	N	1.682649	13.038874	6.361440		N	−1.582634	7.137538	12.317506
	N	3.518773	12.157265	4.055155		N	2.255501	5.670973	12.091830
	N	0.016102	10.484398	5.285362		N	0.994651	7.995059	11.731947
	O	2.358742	9.460087	3.902263		O	−0.652807	4.692174	13.970725
	O	2.929711	10.183583	6.695889		O	−0.328680	4.952663	11.039083
4n	Fe	2.739685	2.536167	9.217707	**4o**	Fe	2.788525	2.769673	9.248726
	N	4.749578	3.832377	9.157746		N	4.791818	4.039430	9.189464
	N	2.211463	4.551505	8.372793		N	3.696311	2.220694	7.401382
	N	3.629195	2.048694	7.348759		N	3.232304	3.428938	11.258531
	N	3.183838	3.210851	11.232747		N	2.303508	4.767215	8.396322
	Cl	3.592774	0.378666	10.080787		Br	0.448012	2.123683	9.179502
	Cl	0.502485	1.932623	9.165750		Br	3.639300	0.455209	10.185170
4q	Fe	7.443523	9.187143	2.747946	**4r**	Fe	4.341713	7.465620	15.915885
	N	6.397112	7.483115	3.039111		N	3.983882	9.208127	17.209139
	N	8.164552	8.809165	4.522241		N	3.951180	6.477333	14.075466
	N	8.773876	8.054743	1.904259		N	2.624218	6.417262	16.780306
	N	6.417749	9.327749	1.102779		N	2.481931	8.595178	15.088188
	N	8.465922	10.784243	2.453085		N	5.748782	8.682165	14.951428
	N	6.081522	10.283321	3.625019		N	5.682931	6.216191	16.796608
4p	Fe	7.189384	5.048444	2.298123					
	N	5.715742	4.514111	4.034776					
	N	6.894462	6.851534	3.292996					
	N	5.476440	4.368398	1.300968					
	N	8.234872	3.666870	3.501455					
	Cl	8.542083	5.473867	0.516583					